APRIL 2020

AJNR

VOLUME 41 • PP 551–736

AJNR

AMERICAN JOURNAL OF NEURORADIOLOGY

APRIL 2020
VOLUME 41
NUMBER 4
WWW.AJNR.ORG

THE JOURNAL OF DIAGNOSTIC AND INTERVENTIONAL NEURORADIOLOGY

MR thermometry in cerebrovascular disease
Hippocampal sclerosis detection with NeuroQuant
CTA diagnostic errors in evaluation of LVO
Enhancement of vestibular perilymph in Menière disease

Official Journal ASNR • ASFNR • ASHNR • ASPNR • ASSR

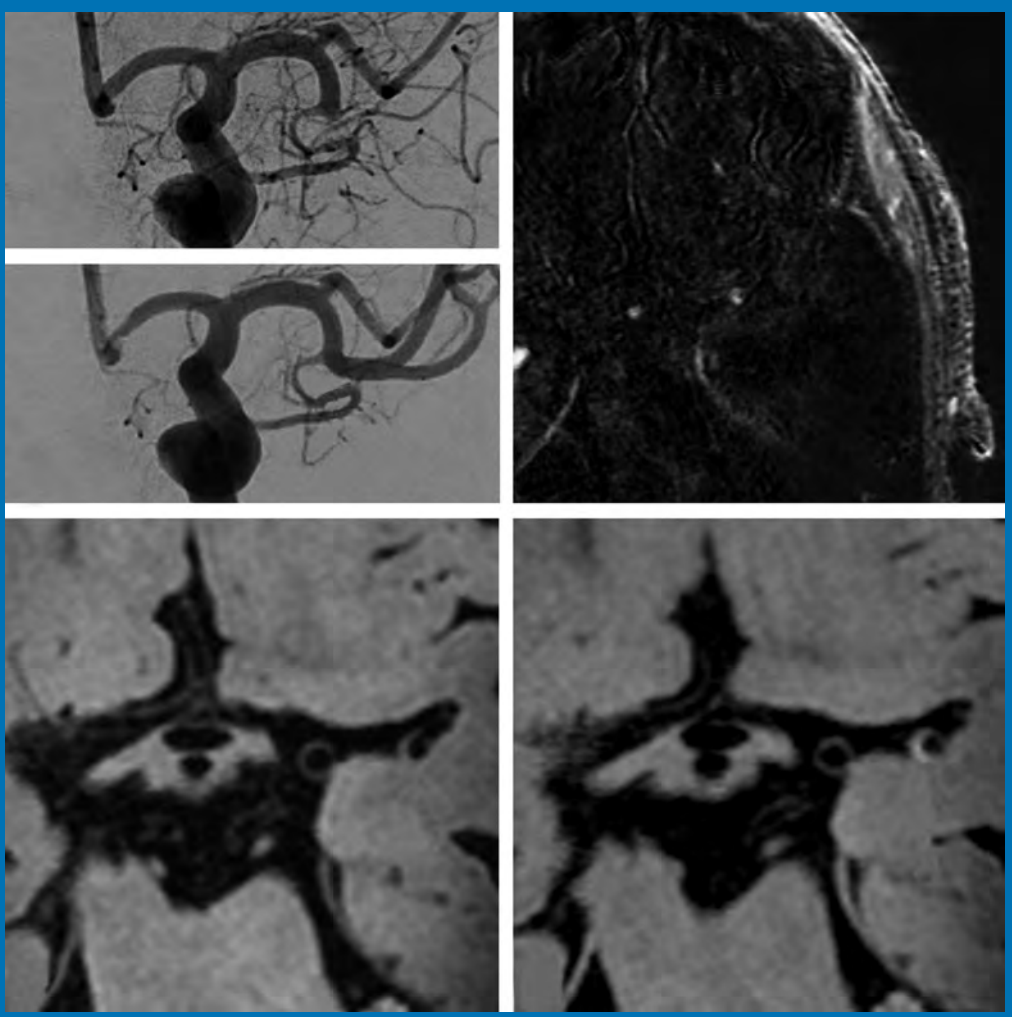

MicroVention®
TERUMO

FLOW DIVERSION.

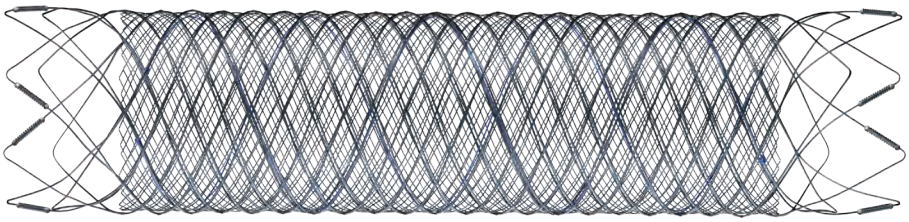

SIMPLIFIED.

FRED™
Flow **R**e-direction
Endoluminal **D**evice

The Flow Re-Direction Endoluminal Device (FRED) System is indicated for use in the internal carotid artery from the petrous segment to the terminus for the endovascular treatment of adult patients (22 years of age or older) with wide-necked (neck width ≥ 4 mm or dome-to-neck ratio < 2) saccular or fusiform intracranial aneurysms arising from a parent vessel with a diameter ≥ 2.0 mm and ≤ 5.0 mm.

Use of the FRED System is contraindicated under these circumstances: Patients in whom anticoagulant, anti-platelet therapy, or thrombolytic drugs are contraindicated. Patients with known hypersensitivity to metal such as nickel-titanium and metal jewelry. Patients with anatomy that does not permit passage or deployment of the FRED System. Patients with an active bacterial infection. Patients with a pre-existing stent in place at the target aneurysm. Patients in whom the parent vessel size does not fall within the indicated range. Patients who have not received dual anti-platelet agents prior to the procedure. For complete indications, contraindications, potential complications, warnings, precautions, and instructions, see instructions for use (IFU provided in the device).

HEADWAY Microcatheter Indications for Use: The HEADWAY Microcatheter is intended for general intravascular use, including the peripheral, coronary and neurovasculature for the infusion of diagnostic agents, such as contrast media, and therapeutic agents, such as occlusion coils.

SOFIA EX Catheter Indications for Use: The SOFIA EX Catheter is indicated for general intravascular use, including the neuro and peripheral vasculature. The SOFIA EX Catheter can be used to facilitate introduction of diagnostic agents or therapeutic devices. The SOFIA EX Catheter is not intended for use in coronary arteries.

SOFIA Catheter Indications for Use: The SOFIA Catheter is indicated for general intravascular use, including the neuro and peripheral vasculature. The SOFIA Catheter can be used to facilitate introduction of diagnostic or therapeutic devices. The SOFIA Catheter is not intended for use in coronary arteries.

RX Only: Federal (United States) law restricts this device to sale by or on the order of a physician.

Simplicity Begins

WITH ACCESS

Access Solutions

- **Easily accesses** tortuous anatomy and distal target lesions[4,5,6]
- **Precise and reliable** FRED Device delivery[1,2,3]
- **Minimized kick-back** and loss of access[7]

MicroVention® TERUMO

References:
1. TR11-211 2. TR13-171 3. TR15-055 4. TR13-192 5. TR15-072 6. TR19-145

MicroVention™, FRED™, Headway and SOFIA™ are registered trademarks of MicroVention, Inc. in the United States and other jurisdictions. © 2020 MicroVention, Inc. 03/2020

MicroVention Worldwide Innovation Center
35 Enterprise
Aliso Viejo, CA 92656 USA
PH 714.247.8000

MicroVention UK Limited PH 44 (0) 191 258 6777
MicroVention Europe S.A.R.L. PH +33 (1) 39 21 77 46
MicroVention Deutschland GmbH PH +49 211 210 798-0
Web **microvention.com**

stryker

The shape of **something better**

Being better means always being ahead

At Stryker, we invest heavily to create better technology that elevates outcomes. The result? We continue to make history, make a difference and make healthcare better, unlike any other company in the VCF space.

strykerIVS.com/VCF

Bone cement: Complications with the use of bone cement are rare. Serious adverse events, some with fatal outcome, associated with the use of bone cements for vertebroplasty, kyphoplasty and sacroplasty include myocardial infarction, cardiac arrest, cerebrovascular accident, pulmonary embolism, and cardiac embolism. Although it is rare, some adverse events have been known to occur up to one year post-operatively. Additional risks exist with the use of bone cement. Please see the IFU for a complete list of potential risks.

Stryker or its affiliated entities own, use, or have applied for the following trademarks or service marks: AVAflex, iVAS, SpineJack and Stryker. All other trademarks are trademarks of their respective owners or holders.

The absence of a product, feature, or service name, or logo from this list does not constitute a waiver of Stryker's trademark or other intellectual property rights concerning that name or logo.

D0000018655 | Copyright © 2020 Stryker

AJNR

AMERICAN JOURNAL OF NEURORADIOLOGY

APRIL 2020
VOLUME 41
NUMBER 4
WWW.AJNR.ORG

Publication Preview at www.ajnr.org features articles released in advance of print. Visit www.ajnrblog.org to comment on AJNR content and chat with colleagues and AJNR's News Digest at http://ajnrdigest.org to read the stories behind the latest research in neuroimaging.

AJNR (Am J Neuroradiol ISSN 0195–6108) is a journal published monthly, owned and published by the American Society of Neuroradiology (ASNR), 800 Enterprise Drive, Suite 205, Oak Brook, IL 60523. Annual dues for the ASNR include approximately 21% for a journal subscription. The journal is printed by Cadmus Journal Services, 5457 Twin Knolls Road, Suite 200, Columbia, MD 21045; Periodicals postage paid at Oak Brook, IL and additional mailing offices. Printed in the U.S.A. POSTMASTER: Please send address changes to American Journal of Neuroradiology, P.O. Box 3000, Denville, NJ 07834, U.S.A. Subscription rates: nonmember $410 ($480 foreign) print and online, $320 online only; institutions $470 ($540 foreign) print and basic online, $935 ($1000 foreign) print and extended online, $380 online only (basic), $825 online only (extended); single copies are $35 each ($40 foreign). Indexed by PubMed/MEDLINE, BIOSIS Previews, Current Contents (Clinical Medicine and Life Sciences), EMBASE, Google Scholar, HighWire Press, Q-Sensei, RefSeek, Science Citation Index, SCI Expanded, Meta/CZI, ReadCube, and Semantic Scholar. Copyright © American Society of Neuroradiology.

ONLINE FEATURES

LETTERS

BOOK REVIEWS *R.M. Quencer, Section Editor*

Please visit www.ajnrblog.org to read and comment on Book Reviews.

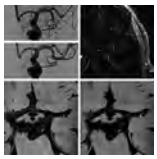

Occlusion of the left M1-M2 segment successfully treated using a thrombosuction device: Digital subtraction angiography directly before and after the thrombectomy procedure (including subtraction image from coregistered pre- and postcontrast vessel wall images) shows a hyperintense configuration at the thrombectomy site (top images). The bottom images show transverse pre- (left) and postcontrast (right) MPIR-TSE vessel wall images at 7T obtained 22 days after thrombectomy procedure. The eccentric vessel wall enhancement present after contrast administration is at the same location as the thrombectomy site.

Indicates Editor's Choices selection

Indicates Fellows' Journal Club selection

Indicates open access to non-subscribers at www.ajnr.org

Indicates article with supplemental on-line table

Indicates article with supplemental on-line photo

Indicates article with supplemental on-line video

Evidence-Based Medicine Level 1

Evidence-Based Medicine Level 2

AJNR

AMERICAN JOURNAL OF NEURORADIOLOGY

Publication Preview at www.ajnr.org features articles released in advance of print. Visit www.ajnrblog.org to comment on AJNR content and chat with colleagues and AJNR's News Digest at http://ajnrdigest.org to read the stories behind the latest research in neuroimaging.

APRIL 2020 • VOLUME 41 • NUMBER 4 • WWW.AJNR.ORG

EDITOR-IN-CHIEF

Jeffrey S. Ross, MD
Professor of Radiology, Department of Radiology, Mayo Clinic College of Medicine, Phoenix, AZ

SENIOR EDITORS

Harry J. Cloft, MD, PhD
Professor of Radiology and Neurosurgery, Department of Radiology, Mayo Clinic College of Medicine, Rochester, MN

Christopher G. Filippi, MD
Professor and Vice Chair of Biomedical and Translational Science, Donald and Barbara Zucker School of Medicine at Hofstra/Northwell, Lenox Hill Hospital and Greenwich Village Healthplex, New York, NY

Thierry A.G.M. Huisman, MD
Radiologist-in-Chief, Texas Children's Hospital, Houston, TX

Yvonne W. Lui, MD
Associate Professor of Radiology, Chief of Neuroradiology, New York University School of Medicine, New York, NY

C.D. Phillips, MD, FACR
Professor of Radiology, Weill Cornell Medical College, Director of Head and Neck Imaging, New York-Presbyterian Hospital, New York, NY

Lubdha M. Shah, MD, MS
Professor of Radiology and Director of Spine Imaging, University of Utah Department of Radiology and Imaging Sciences, Salt Lake City, UT

Charles M. Strother, MD
Professor of Radiology, Emeritus, University of Wisconsin, Madison, WI

STATISTICAL SENIOR EDITOR

Bryan A. Comstock, MS
Senior Biostatistician, Department of Biostatistics, University of Washington, Seattle, WA

ARTIFICIAL INTELLIGENCE DEPUTY EDITOR

Peter D. Chang, MD
Assistant Professor-in-Residence, Departments of Radiological Sciences, Computer Sciences, and Pathology, Director, Center for Artificial Intelligence in Diagnostic Medicine (CAIDM), University of California, Irvine, Irvine, CA

EDITORIAL BOARD

Ashley H. Aiken, *Atlanta, GA*
Lea M. Alhilali, *Phoenix, AZ*
Kubilay Aydin, *Istanbul, Turkey*
John D. Barr, *Dallas, TX*
Ari Blitz, *Baltimore, MD*
Barton F. Branstetter IV, *Pittsburgh, PA*
Jonathan L. Brisman, *Lake Success, NY*
Keith Cauley, *Danville, PA*
James Y. Chen, *San Diego, CA*
Asim F. Choudhri, *Memphis, TN*
Daniel Chow, *Irvine, CA*
J. Matthew Debnam, *Houston, TX*
Seena Dehkharghani, *New York, NY*
Yonghong Ding, *Rochester, MN*
Clifford J. Eskey, *Hanover, NH*
Saeed Fakhran, *Phoenix, AZ*
Massimo Filippi, *Milan, Italy*
Nils D. Forkert, Calgary, *Alberta, Canada*
Wende N. Gibbs, *Phoenix, AZ*
Christine M. Glastonbury, *San Francisco, CA*
John L. Go, *Los Angeles, CA*
Philipp Gölitz, *Erlangen, Germany*
Allison Grayev, *Madison, WI*
Brent Griffith, *Detroit, MI*
Ajay Gupta, *New York, NY*
Rakesh Kumar Gupta, *Haryana, India*
Lotfi Hacein-Bey, *Sacramento, CA*
Christopher P. Hess, *San Francisco, CA*
Andrei Holodny, *New York, NY*
Benjamin Huang, *Chapel Hill, NC*
Mahesh V. Jayaraman, *Providence, RI*
Valerie Jewells, *Chapel Hill, NC*
Christof Karmonik, *Houston, TX*
Timothy J. Kaufmann, *Rochester, MN*
Hillary R. Kelly, *Boston, MA*
Toshibumi Kinoshita, *Akita, Japan*
Kennith F. Layton, *Dallas, TX*
Alexander Lerner, *Los Angeles, CA*
Michael Lev, *Boston, MA*
Karl-Olof Lovblad, *Geneva, Switzerland*
Franklin A. Marden, *Chicago, IL*
Joseph C. McGowan, *Merion Station, PA*
Stephan Meckel, *Freiburg, Germany*
Christopher J. Moran, *St. Louis, MO*
Takahisa Mori, *Kamakura City, Japan*
Suresh Mukherji, *Ann Arbor, MI*
Alexander J. Nemeth, *Chicago, IL*
Renato Hoffmann Nunes, *Sao Paulo, Brazil*
Sasan Partovi, *Cleveland, OH*
Laurent Pierot, *Reims, France*
Jay J. Pillai, *Baltimore, MD*
Whitney B. Pope, *Los Angeles, CA*
Joana Ramalho, *Lisbon, Portugal*
Otto Rapalino, *Boston, MA*
Álex Rovira-Cañellas, *Barcelona, Spain*
Paul M. Ruggieri, *Cleveland, OH*
Amit M. Saindane, *Atlanta, GA*
Maksim Shapiro, *New York, NY*
Timothy Shepherd, *New York, NY*
Mark S. Shiroishi, *Los Angeles, CA*
Bruno P. Soares, *Baltimore, MD*
Maria Vittoria Spampinato, *Charleston, SC*
Khin Khin Tha, *Sapporo, Hokkaido, Japan*
Krishnamoorthy Thamburaj, *Hershey, PA*
Cheng Hong Toh, *Taipei, Taiwan*
Aquilla S. Turk, *Greenville, SC*
Anja G. van der Kolk, *Utrecht, the Netherlands*
Willem Jan van Rooij, *Tilburg, Netherlands*
Arastoo Vossough, *Philadelphia, PA*
Elysa Widjaja, *Toronto, Ontario, Canada*
Max Wintermark, *Stanford, CA*
Ronald L. Wolf, *Philadelphia, PA*
Kei Yamada, *Kyoto, Japan*
Carlos Zamora, *Chapel Hill, NC*
Vahe M. Zohrabian, *New Haven, CT*

EDITORIAL FELLOW

Hediyeh Baradaran, *Salt Lake City, UT*

SPECIAL CONSULTANTS TO THE EDITOR

AJNR Blog Editor
Neil Lall, *Denver, CO*
Case of the Month Editor
Nicholas Stence, *Aurora, CO*
Case of the Week Editors
Juan Pablo Cruz, *Santiago, Chile*
Sapna Rawal, *Toronto, Ontario, Canada*
Classic Case Editor
Sandy Cheng-Yu Chen, *Taipei, Taiwan*
Health Care and Socioeconomics Editor
Pina C. Sanelli, *New York, NY*
Physics Editor
Greg Zaharchuk, *Stanford, CA*
Podcast Editor
Wende N. Gibbs, *Phoenix, AZ*
Twitter Editor
Roger Jordan, *Houston, TX*

Official Journal:

American Society of Neuroradiology
American Society of Functional Neuroradiology
American Society of Head and Neck Radiology
American Society of Pediatric Neuroradiology
American Society of Spine Radiology

Founding Editor
Juan M. Taveras
Editors Emeriti
Mauricio Castillo, Robert I. Grossman, Michael S. Huckman, Robert M. Quencer

Managing Editor
Karen Halm
Assistant Managing Editor
Laura Wilhelm
Editorial Assistant
Margaret B. Sabato
Executive Director, ASNR
Mary Beth Hepp

AJNR go green

AJNR urges American Society of Neuroradiology members to reduce their environmental footprint by voluntarily suspending their print subscription.

The savings in paper, printing, transportation, and postage directly fund new electronic enhancements and expanded content.

The digital edition of *AJNR* presents the print version in its entirety, along with extra features including:

- **Publication Preview**
- **Case Collection**
- **Podcasts**
- **The *AJNR* News Digest**
- **The *AJNR* Blog**

It also reaches subscribers much faster than print. An electronic table of contents will be sent directly to your mailbox to notify you as soon as it publishes.

Readers can search, reference, and bookmark current and archived content 24 hours a day on www.ajnr.org.

ASNR members who wish to opt out of print can do so by using the AJNR Go Green link on the *AJNR* Website (http://www.ajnr.org/content/subscriber-help-and-services). Just type your name in the email form to stop print and spare our ecosystem.

AJNR
AMERICAN JOURNAL OF NEURORADIOLOGY

LUCIEN LEVY BEST RESEARCH ARTICLE

AWARD WINNER AND NOMINEES NAMED

This award is named for the late *AJNR* Senior Editor who championed its establishment and recognizes the best original research paper accepted in 2019. The winning paper was published electronically on March 12, 2020. It was selected by a vote of the *Journal's* Editor-in-Chief and Senior Editors.


ORIGINAL RESEARCH
ADULT BRAIN

Performance of Standardized Relative CBV for Quantifying Regional Histologic Tumor Burden in Recurrent High-Grade Glioma: Comparison against Normalized Relative CBV Using Image-Localized Stereotactic Biopsies

The Editors of *AJNR* are pleased to announce the annual Lucien Levy Best Research Article Award has been presented to

"Performance of Standardized Relative CBV for Quantifying Regional Histologic Tumor Burden in Recurrent High-Grade Glioma: Comparison against Normalized Relative CBV Using Image-Localized Stereotactic Biopsies"

by J.M. Hoxworth, J.M. Eschbacher, A.C. Gonzales, K.W. Singleton, G.D. Leon, K.A. Smith, A. Stokes, Y. Zhou, G.L. Mazza, A.B. Porter, M.M. Mrugala, R.S. Zimmerman, B.R. Bendok, D.P. Patra, C. Krishna, J.L. Boxerman, L.C. Baxter, K.R. Swanson, C.C. Quarles, K.M. Schmainda, and L.S. Hu

Other nominated papers were:

"A Method to Estimate Brain Volume from Head CT Images and Application to Detect Brain Atrophy in Alzheimer Disease" *by V. Adduru, S.A. Baum, C. Zhang, M. Helguera, R. Zand, M. Lichtenstein, C.J. Griessenauer, and A.M. Michael*

"Early Detection of Cancer: Evaluation of MRI Grading Systems in Patients with Suspected Nasopharyngeal Carcinoma" *by A.D. King, J.K.S. Woo, Q.-Y. Ai, F.K.F. Mo, T.Y. So, W.K.J. Lam, I.O.L. Tse, A.C. Vlantis, K.W.N. Yip, E.P. Hui, B.B.Y. Ma, R.W.K. Chiu, A.T.C. Chan, Y.M.D. Lo, and K.C.A. Cha*

"Defining Ischemic Core in Acute Ischemic Stroke Using CT Perfusion: A Multiparametric Bayesian-Based Model" *by K. Nael, E. Tadayon, D. Wheelwright, A. Metry, J.T. Fifi, S. Tuhrim, R.A. De Leacy, A.H. Doshi, H.L. Chang, and J. Mocco*

"Functional Connectivity Associated with Health-Related Quality of Life in Children with Focal Epilepsy" *by H. Nawani, M.L. Smith, A.L. Wheeler, and E. Widjaja*

"Thrombectomy with Conscious Sedation Compared with General Anesthesia: A DEFUSE 3 Analysis" *by C.J. Powers, D. Dornbos III, M. Mlynash, D. Gulati, M. Torbey, S.M. Nimjee, M.G. Lansberg, G.W. Albers, and M.P. Marks*

"Large Neck and Strong Ostium Inflow as the Potential Causes for Delayed Occlusion of Unruptured Sidewall Intracranial Aneurysms Treated by Flow Diverter" *by T. Su, P. Reymond, O. Brina, P. Bouillot, P. Machi, B.M.A. Delattre, L. Jin, K.O. Lövblad, and M.I. Vargas*

"Ensemble of Convolutional Neural Networks Improves Automated Segmentation of Acute Ischemic Lesions Using Multiparametric Diffusion-Weighted MRI" *by S. Winzeck, S.J.T. Mocking, R. Bezerra, M.J.R.J. Bouts, E.C. McIntosh, I. Diwan, P. Garg, A. Chutinet, W.T. Kimberly, W.A. Copen, P.W. Schaefer, H. Ay, A.B. Singhal, K. Kamnitsas, B. Glocker, A.G. Sorensen, and O. Wu*

Title: Morning Frost. This photograph was taken near the Spencer Butte in Eugene, Oregon.

Yulia Bronstein, MD, vRad (Virtual Radiologic) teleradiology service, Eugene, Oregon

Novel Coronavirus: What Neuroradiologists as Citizens of the World Need to Know

A. Mahajan and J.A. Hirsch

In December 2019, a novel β-coronavirus, initially called severe acute respiratory syndrome–coronavirus 2 (SARS-CoV-2) was introduced into the human population.[1] It is spreading rapidly. The World Health Organization has labeled the disease Coronavirus disease 2019 (COVID-19). This constitutes the seventh member of the Coronaviridae family known to infect humans, which includes the SARS and the Middle East Respiratory Syndrome (MERS) viruses. Considering the close identity of the virus with one found in bats, the disease is considered to be a zoonosis, ie, a disease that can be transmitted from animals to humans. The disease was declared a pandemic on March 11, 2020.

In this era of 24/7 news coverage available across much of the globe, people are watching the epidemic unfold in nearly real-time. This situation creates a unique dynamic in that for the first time ever, the global community is learning about this disease as it develops. Unfortunately, there is much misinformation that contributes to an overall climate of fear. The disease in question may not, for example, be as deadly as recent pandemics, eg, the Ebola virus. Simultaneously, we see an interplay between those who tend to play down the seriousness of the disease while there are those who are preparing for the worst with hoarding.

Neuroradiologists, as medical providers, are expected to provide guidance to the general public. Having the best available information will help us take better care of our families, friends, patients, and ourselves. In that context, it becomes imperative for neuroradiologists to learn as much as possible about this virus to educate the public about this entity.

The COVID-19 virus is an enveloped RNA virus with a single-strand, linear, positive-sense RNA, which means that the virus can use its RNA as the template from which to create proteins needed for propagation and spread. The genome length is 29,903 bases.[2] The virus was initially labeled as severe acute respiratory syndrome coronavirus 2 (SARS-CoV-2) due to its phylogenetic similarity to SARS-CoV (80% identical); however, it was more similar to the bat coronaviruses (96% identical).[3]

The name "coronavirus" refers to the crownlike appearance of these viruses seen on electron microscopy. The virus is around 70–220 nm in size. It is similar to the SARS-CoV regarding the mode of entry and the human receptor used for entry. The infectiousness of the virus is unclear but appears to be more infectious than SARS and MERS viruses, though less fatal.[4]

The virus gains entry into the cell after binding of the spike protein (S) on its surface with the angiotensin-converting enzyme 2 (ACE-2) on the surface of the host cell.[5] The S-protein interaction with ACE-2 appears to be essential for entry of the virus into the cell and is a candidate for vaccine development. The SARS-CoV spike (S) protein is composed of 2 subunits: The S1 subunit contains a receptor-binding domain that binds to the host cell receptor and the S2 subunit mediates fusion between the viral and host cell membranes.[6] None of the commercially available ACE inhibitors are effective against the ACE-2 enzyme. The neutralizing antibodies to the SARS-CoV bind to the ACE-2 receptor binding domain (RBD) of the SARS S-protein, highlighting the importance of this protein for virus entry. Although there is only 76.5% identity of amino acid sequences between COVID-19 and SARS-CoV, suggesting a difference in the RBD of SARS-CoV and COVID-19 viruses, they have almost identical 3D structures in the RBD with a strong binding to human ACE-2.[7] Active vaccine development against the S-protein is in progress currently.

The ACE-2 enzyme is involved with the degradation of angiotensin-II in the renin angiotensin system. Whether the interaction of the virus with angiotensin-II is important in the pathogenesis of COVID-19 is unknown. Most interesting, the ACE-2 expression is seen predominantly in the respiratory and intestinal tracts, which are the 2 sites of involvement of the coronavirus. In the respiratory epithelium, the ACE-2 was expressed in human airway epithelia as well as the lung parenchyma. ACE-2 may have a protective effect on the lung parenchyma, with alterations in the renin angiotensin system as the putative mechanism of lung injury.

The transmission of the coronavirus occurs via droplets and fomites during close unprotected contact. Fomites are objects or materials that are likely to carry infection, such as clothes, utensils, and furniture. Fecal shedding has been demonstrated, but fecal-oral transmission is not considered a driver of the epidemic. Aerosolization of fomites may contribute to airborne transmission, though currently this mode is not considered too important in the community. Transmission has been documented in the preclinical stage as well, even before the onset of symptoms.[8] Asymptomatic carriers as well as a prolonged incubation period up to 19 days has also been described, though reinfection may be another possibility in this case.[9]

The incubation is reported to be 2–7 days.[10] After virus isolation in various cell lines in vitro, cytopathic effects were observed 96 hours after inoculation. Whole genome sequencing of 104 strains of the virus from different locations around the globe reveals a 99.9% homology.

The severity of clinical symptoms may vary from

- Mild to moderate in 80%; most recover
- Severe in 13.8% (dyspnea, respiratory rate $>$ 30/min, O_2 saturation $\leq$ 93%, partial pressure of oxygen/fraction of inspired oxygen ratio $<$ 300, lung infiltrates $>$50% of the lung within 24–48 hours)
- Critical in 6.1% (respiratory failure, septic shock, and/or multiorgan dysfunction/failure).

http://dx.doi.org/10.3174/ajnr.A6526

Fever was the most common symptom seen in 89% of 1099 hospitalized patients in China,[10] though seen at initial presentation in only 44%. Sore throat was seen in only 14%; nasal congestion, in 5%; but cough, in 68%. Dyspnea may be a more serious presentation with severe acute respiratory distress syndrome seen in 17%–29%.[11] The time from onset to the development of severe disease, including hypoxia, is 1 week. There was no sex predilection. Among patients who have died, the time from symptom onset to death ranged from 2–8 weeks. Individuals at highest risk of severe disease and death include those older than 60 years of age and those with underlying conditions such as hypertension, diabetes, cardiovascular disease, chronic respiratory disease, and cancer.

The disease in children appears to be relatively rare and mild, with approximately 2.4% of the total reported cases among individuals younger than 19 years of age. A very small proportion of those younger than 19 years of age have developed severe (2.5%) or critical disease (0.2%).

The diagnosis is based on reverse transcription polymerase chain reaction (RT-PCR) of throat (oropharyngeal) and nasopharyngeal swabs, though sputum and bronchoalveolar lavage fluid had the best sensitivity. However, reports from China indicate that the RT-PCR sensitivity may have been as low as 60%–70%.[12]

Temporal changes seen on chest CT findings have been described by a panel of experts:[13] These included lack of abnormality in the first 2 days of illness in 50%. In early disease, peripheral, focal, or multifocal ground-glass opacities, affecting both lungs, may be seen in approximately 50%–75% of patients. With the progression of disease, crazy paving (ground-glass opacities with interlobular septal thickening) and consolidation became prominent, with a peak around 9–13 days, followed by slow clearing during a month or longer.

Chest CT was reported as better than RT-PCR in a recent article in *Radiology*.[12] Closer analysis of the data reveals that most patients with chest CT scans demonstrating lung pathology but PCR negative for COVID-19 were diagnosed on clinical grounds alone. However, only 15 cases had a positive PCR result on repeat testing. The PCR-negative patients with a positive CT result may reflect viral pneumonia related to other respiratory viruses, common during this time of the year. Chinese authorities had initially broadened the official definition of infection in Hubei province to include patients with typical findings of viral pneumonia on CT, with negative RT-PCR results. This inclusion caused a spike of 13,332 cases on February 12. This broader definition resulted in a higher number of presumptive cases of COVID-19 in China with a recommendation for a role for chest CT in the initial diagnosis of COVID-19 infection versus RT-PCR. However, chest CT was removed as a diagnostic criterion in the sixth version of the diagnostic criteria published on February 16, 2020.[14] RT-PCR remains the reference standard to make a definitive diagnosis of COVID-19 infection.[15]

Chest x-ray and chest CT may be used as adjuncts in case an initial RT-PCR has negative findings. The American College of Radiology[16] warns against using CT as a first-line tool in the diagnosis of coronavirus and it should be used sparingly and reserved for symptomatic hospitalized patients with specific clinical indications. Using portable radiography may be helpful, considering the ease of cleaning. CT scanners may need to be closed for an extended period—up to 1 hour after scanning a suspected patient—for cleaning and decontamination, affecting overall patient care.[17]

Remdesivir and chloroquine have shown efficacy in vitro.[18] Remdesivir inhibits the RNA-dependent RNA polymerase, essential for replication of the virus.[19] Chloroquine has shown apparent efficacy in the treatment of COVID-19–associated pneumonia in studies from China.[20] It supposedly exerts its antiviral activity, in part, by interfering with cell fusion by increasing endosomal pH, interfering with virus/cell fusion, and interfering with the glycosylation of cellular receptors of SARS-CoV. Clinical trials are underway, the results of which may be available in April. Recombinant ACE-2 trials are also underway (ClinicalTrials.gov NCT04287686).[5] A host of drugs being tested include interferon β; an HIV drug, lopinavir-ritonavir (Kaletra); and neuraminidase inhibitors like oseltamivir, among others.[21]

Vaccine development is also underway. Most promising is the vaccine targeting the spike protein (S). The molecule has been isolated, and the structure, elucidated.[22] First clinical trials of a mRNA based vaccine started on March 16, 2020 in Seattle though results may be months away.

The mortality rate was estimated at 3%–4%, though more recent estimates suggest 0.3%–1%; however, the risk to the immunosuppressed and the elderly is of great concern in the United States, especially with a large population of immunosuppressed patients and those on various immunosuppressive medications for a host of conditions. In a study of 1044 hospitalized patients in China, a mortality rate of 1.4% was identified,[10] which may have been lower if patients with fewer symptoms from the community had been included.

Infection control measures for health care professionals when coming in contact with infected individuals especially those performing lumbar punctures, myelograms and spine procedures in the neuroradiology community, should include contact and airborne precautions, which include hand hygiene, gloves, gowns, N95 masks, and eye protection. During the SARS epidemic, the hospital personnel who became infected had omitted at least one of these precautions.[23] There was no difference between using a surgical mask and a N95 mask in this case-control study from Hong Kong. Footwear protection should also be considered. More detailed instructions for use in the radiology department have recently been published.[24] An analysis of 22 studies[25] revealed that human coronaviruses such as SARS, MERS, or endemic human coronaviruses can persist on inanimate surfaces like metal, glass, or plastic for up to 9 days but can be efficiently inactivated by surface disinfection procedures with 62%–71% ethanol, 0.5% hydrogen peroxide, or 0.1% sodium hypochlorite within 1 minute of application, whereas 0.05%–0.2% benzalkonium chloride or 0.02% chlorhexidine digluconate are less effective.

Infection control measures like voluntary and mandated quarantine at an individual, community, national, and international level may ultimately be the only plausible way of controlling the spread of the disease.[26] These measures do work, as evidenced by the marked decrease in the incidence of cases from China.[27] On

an individual level, social distancing, self-isolation at the first appearance of symptoms, contact tracing, and informing the contacts may be the best measures to effectively control the spread of the disease. Availability of suitable testing methods may also go a long way to ensure peace of mind to the public at large.

In conclusion, in the midst of an ongoing epidemic, it is best to obtain as much information as we can about this virus so that we can take effective care of the community around us.

Disclosures: Joshua A. Hirsch—*UNRELATED*: *Consultancy*: Medtronic, Relievant Medsystems; *Grants/Grants Pending*: Neiman Health Policy, *Comments*: health policy and economics.

REFERENCES

1. Huang C, Wang Y, Li X, et al. **Clinical features of patients infected with 2019 novel coronavirus in Wuhan, China.** *Lancet* 2020;395:497–506 CrossRef Medline
2. **Report of the WHO-China Joint Mission on Coronavirus Disease 2019 (COVID-19).** February 16-24, 2020. https://www.who.int/docs/default-source/coronaviruse/who-china-joint-mission-on-covid-19-final-report.pdf. Accessed March 12, 2020
3. Zhou P, Yang XL, Wang XG, et al. **A pneumonia outbreak associated with a new coronavirus of probable bat origin.** *Nature* 2020;579:270–73 CrossRef Medline
4. Chen J. **Pathogenicity and transmissibility of 2019-nCoV:a quick overview and comparison with other emerging viruses.** *Microbes Infect* 2020 Feb 4. [Epub ahead of print] CrossRef
5. Zhang H, Penninger JM, Li Y, et al. **Angiotensin-converting enzyme 2 (ACE2) as a SARS-CoV-2 receptor: molecular mechanisms and potential therapeutic target.** *Intensive Care Med* 2020 Mar 3. [Epub ahead of print] CrossRef Medline
6. Du L, He Y, Zhou Y, et al. **The spike protein of SARS-CoV: a target for vaccine and therapeutic development.** *Nat Rev Microbiol* 2009;7:226–36 CrossRef Medline
7. Tian X, Li C, Huang A, et al. **Potent binding of 2019 novel coronavirus spike protein by a SARS coronavirus-specific human monoclonal antibody.** *Emerg Microbes Infect* 2020;9:382–85 CrossRef Medline
8. Rothe C, Schunk M, Sothmann P, et al. **Transmission of 2019-nCoV infection from an asymptomatic contact in Germany.** *N Engl J Med* 2020;382:970–71 CrossRef Medline
9. Bai Y, Yao L, Wei T, et al. **Presumed asymptomatic carrier transmission of COVID-19.** *JAMA* 2020 Feb 21. [Epub ahead of print] CrossRef Medline
10. Guan WJ, Ni ZY, Hu Y, et al. **Clinical characteristics of coronavirus disease 2019 in China.** *N Engl J Med* 2020 Feb 28. [Epub ahead of print] CrossRef Medline
11. Chen N, Zhou M, Dong X, et al. **Epidemiological and clinical characteristics of 99 cases of 2019 novel coronavirus pneumonia in Wuhan, China: a descriptive study.** *Lancet* 2020;395:507–13 CrossRef Medline
12. Ai T, Yang Z, Hou H, et al. **Correlation of chest CT and RT-PCR testing in coronavirus disease 2019 (COVID-19) in China: a report of 1014 cases.** *Radiology* 2020 Feb 26. [Epub ahead of print] CrossRef [Medline
13. Kanne JP, Little BP, Chung JH, et al. **Essentials for radiologists on COVID-19: An Update—Radiology Scientific Expert Panel.** *Radiology* 2020 Feb 27. [Epub ahead of print] CrossRef Medline
14. Jin YH, Cai L, Cheng ZS, et al; Zhongnan Hospital of Wuhan University Novel Coronavirus Management and Research Team, Evidence-Based Medicine Chapter of China International Exchange and Promotive Association for Medical and Health Care (CPAM), **A rapid advice guideline for the diagnosis and treatment of 2019 novel coronavirus (2019-nCoV) infected pneumonia (standard version).** *Mil Med Res* 2020;7:4 CrossRef Medline
15. Yang W, Yan F. **Patients with RT-PCR confirmed COVID-19 and normal chest CT.** *Radiology* 2020 Mar 6. [Epub ahead of print] CrossRef Medline
16. **ACR recommendations for the use of chest radiography and computed tomography (CT) for suspected COVID-19 infection.** March 11, 2020. https://www.acr.org/Advocacy-and-Economics/ACR-Position-Statements/Recommendations-for-Chest-Radiography-and-CT-for-Suspected-COVID19-Infection. Accessed March 12, 2020
17. Stempniak M. **CT should not be used as first-line tool against coronavirus, ACR warns following pandemic declaration.** *Radiology Business*. March 11, 2020. https://www.radiologybusiness.com/topics/care-delivery/ct-scan-coronavirus-chest-x-ray-radiology-covid-19. Accessed March 12, 2020
18. Wang M, Cao R, Zhang L, et al. **Remdesivir and chloroquine effectively inhibit the recently emerged novel coronavirus (2019-nCoV) in vitro.** *Cell Res* 2020;30:269–71 CrossRef Medline
19. Gordon CJ, Tchesnokov EP, Feng JY, et al. **The antiviral compound remdesivir potently inhibits RNA-dependent RNA polymerase from Middle East respiratory syndrome coronavirus.** *J Biol Chem* 2020 Feb 24. [Epub ahead of print] CrossRef Medline
20. Gao J, Tian Z, Yang X. **Breakthrough: Chloroquine phosphate has shown apparent efficacy in treatment of COVID-19 associated pneumonia in clinical studies.** *Biosci Trends* 2020 Feb 19. [Epub ahead of print] CrossRef Medline
21. Lu H. **Drug treatment options for the 2019-new coronavirus (2019-nCoV).** *Biosci Trends* 2020 Jan 28. [Epub ahead of print] CrossRef Medline
22. Wrapp D, Wang N, Corbett KS, et al. **Cryo-EM structure of the 2019-nCoV spike in the prefusion conformation.** *Science* 2020;367:1260–63 CrossRef Medline
23. Seto WH, Tsang D, Yung RW, et al; Advisors of Expert SARS group of Hospital Authority. **Effectiveness of precautions against droplets and contact in prevention of nosocomial transmission of severe acute respiratory syndrome (SARS).** *Lancet* 2003;361:1519–20 CrossRef Medline
24. Kooraki S, Hosseiny M, Myers L, et al. **Coronavirus (COVID-19) outbreak: what the department of radiology should know.** *J Am Coll Radiol* 2020 Feb 19. [Epub ahead of print] CrossRef Medline
25. Kampf G, Todt D, Pfaender S, et al. **Persistence of coronaviruses on inanimate surfaces and their inactivation with biocidal agents.** *J Hosp Infect* 2020;104:246–51 CrossRef Medline
26. Anderson RM, Heesterbeek H, Klinkenberg D, et al. **How will country-based mitigation measures influence the course of the COVID-19 epidemic?** *Lancet* 2020 March 6. [Epub ahead of print] CrossRef Medline
27. World Health Organization. **Coronavirus Disease 2019 (COVID-19) Situation Report—44.** March 4, 2020. https://www.who.int/docs/default-source/coronaviruse/situation-reports/20200304-sitrep-44-covid-19.pdf?sfvrsn=93937f92_6. Accessed March12, 2020

MR Thermometry in Cerebrovascular Disease: Physiologic Basis, Hemodynamic Dependence, and a New Frontier in Stroke Imaging

S. Dehkharghani and D. Qiu

ABSTRACT

SUMMARY: The remarkable temperature sensitivity of the brain is widely recognized and has been studied for its role in the potentiation of ischemic and other neurologic injuries. Pyrexia frequently complicates large-vessel acute ischemic stroke and develops commonly in critically ill neurologic patients; the profound sensitivity of the brain even to minor intraischemic temperature changes, together with the discovery of brain-to-systemic as well as intracerebral temperature gradients, has thus compelled the exploration of cerebral thermoregulation and uncovered its immutable dependence on cerebral blood flow. A lack of pragmatic and noninvasive tools for spatially and temporally resolved brain thermometry has historically restricted empiric study of cerebral temperature homeostasis; however, MR thermometry (MRT) leveraging temperature-sensitive nuclear magnetic resonance phenomena is well-suited to bridging this long-standing gap. This review aims to introduce the reader to the following: 1) fundamental aspects of cerebral thermoregulation, 2) the physical basis of noninvasive MRT, and 3) the physiologic interdependence of cerebral temperature, perfusion, metabolism, and viability.

ABBREVIATIONS: BOLD = blood oxygen level–dependent; BTR = brain thermal response; NMR = nuclear magnetic resonance; OEF = oxygen extraction fraction; PRESS = point-resolved spectroscopy; PRF = proton resonance frequency

Cerebral thermoregulation is a critical, but enigmatic aspect of brain physiology at the intersection of cerebral perfusion and metabolism. The brain exhibits exquisite sensitivity to disruptions in temperature homeostasis, with even small elevations rapidly potentiating ischemic or other neurologic injuries.[1-5] Nevertheless, formalized and experimentally tested theories of cerebral temperature control are lacking, due to the absence of pragmatic tools to measure spatiotemporally-resolved thermal gradients under physiologic and pathologic conditions. This review aims to introduce the reader to fundamental principles of cerebral temperature (dys)regulation and homeothermy, with an emphasis on temperature as a potential biomarker of cerebrovascular disease and the use of noninvasive approaches to measuring brain temperatures using MR thermometry.

Received November 13, 2019; accepted after revision January 2, 2020.

From the Department of Radiology (S.D.), New York University Langone Health, New York, New York; and Department of Radiology (D.Q.), Emory University Hospital, Atlanta, Georgia.

Portions of this work were supported by the American Society of Neuroradiology Scholar Award in Neuroradiology Research (2012–2013, 2013–2014), and an Emory University Research Committee (2013–2014) grant awarded to the lead author. This work was supported, in part, by National Center for Research Resources and the Office of Research Infrastructure Programs of the National Institutes of Health (P51RR000165, OD P51OD011132).

Please address correspondence to Seena Dehkharghani, MD, Center for Biomedical Imaging, Department of Radiology, New York University Langone Medical Center, 660 First Ave, 2nd Floor, Attention Hillary Gumiel, New York, NY 10016; e-mail: Seena.Dehkharghani@NYUMC.Org

Indicates open access to non-subscribers at www.ajnr.org

http://dx.doi.org/10.3174/ajnr.A6455

THERMOREGULATION AND TEMPERATURE HOMEOSTASIS

Body temperature is tightly controlled in humans at approximately 37°C and regulated through the balance of heat-conserving and heat-dissipating mechanisms mediated by the hypothalamus.[6] Most heat production arises from so-called obligatory thermogenesis—that is, the thermal energy of metabolically active organs, including the brain, with the remainder arising from voluntary and involuntary muscle activity or acquired passively from ambient sources.[6] While the body efficiently dissipates heat primarily through radiative as well as conductive, convective, and evaporative mechanisms, cerebral thermoregulation proves more complex. Throughout much of the highly metabolic brain (consuming 20% of the oxygen and 25% of the glucose at only 2%–3% of the total body weight),[7] the temperature exceeds that of the arterial inflow. While superficial cortical brain regions may dissipate heat to a greater extent through convention/conduction and radiation, cerebral temperature homeostasis largely depends on steady CBF to sustain countercurrent heat exchange mechanisms that prevent cerebral hyperthermia and prove critical to normal brain physiology.[6,8-10] The specific influence of systemic temperatures on cerebral thermoregulation, however, remains

poorly understood. Existing studies have produced discrepant and sometimes contradictory conclusions regarding: 1) the direction and magnitude of the brain-to-systemic temperature offset in certain brain regions, 2) the spatial distribution and magnitude of intracerebral temperature gradients, and 3) the specific mechanisms by which potentially mild pyrexia potentiates myriad forms of neurologic injury, including ischemia.

The implications of cerebral thermosensitivity, in fact, reach beyond a manifest susceptibility to injury and may even have steered the course of human evolution. Specifically, the development of efficient mechanisms of heat dissipation are proposed to have released human ancestors from fundamental thermal constraints to brain development and growth. Simply, the energetic cost and therefore the metabolic output of the large human brain poses considerable demands on such mechanisms of temperature control, the development of which facilitated the remarkable encephalization of early humans.[11-13] Thus, by comparison with other key constraints of human evolution, brain temperature was emphasized by Baker (1979)[13] to be the "single most important factor limiting the survival of man and other animals." Neuroprotective adaptations such as selective brain cooling—the maintenance of brain temperatures selectively despite rising peripheral temperatures by rerouting cooler, valveless facial/ocular and emissary venous supply—were therefore critical for thriving humans under thermal stress, exercise, and so forth.[8,13-15] Such adaptations are traceable to recognized changes in the human calvarial fossil record, developing in tandem with epochs of immense advancement, and may have compensated for the loss in humans of the rete caroticum (ie, the rete mirabilis) first proposed by Herophilus ~2000 years ago and documented later by Galen in other mammals including dogs, cats, and sheep.[14,16-20] From these insights, a coherent picture of the evolving human brain emerged, linking intelligence, the growing brain, bipedalism, and efficient cerebral heat exchange in a seminal paradigm known as the radiator hypothesis, which aptly underscores the importance of steady blood flow at the nexus of temperature homeostasis.[11-13,15,16] This point is easily contextualized when considering the thermogenicity of the metabolically active brain: Approximately 0.66 J/min/g are produced by the brain, primarily by the consumption of oxygen through chemical reaction with glucose which, absent heat dissipation, would produce a rise of 0.16°C/min.[18,21,22]

The study of cerebral thermoregulation, nevertheless, remains difficult. Past investigations have consisted mostly of surrogate measures of brain temperature (eg, tympanic, sublingual, and etc.) and sporadic human and animal studies using directly implanted temperature probes. Surrogate measures, however, are limited by the presence of temporally varying offsets relative to actual brain temperatures.[23-26] Implantable probes are similarly suboptimal for large-scale experimentation due to their requisite invasiveness and cost,[27-30] which limit their widespread placement throughout the brain and in turn, their suitability for interrogation of spatially distributed temperature gradients.[27,29,31,32] Notwithstanding their limitations, a small number of animal and human studies have confirmed the presence of measurable spatial temperature gradients that can be altered during brain injury.[2,9,21,29,33-41] A theoretic framework for understanding temperature homeostasis has also been established through numeric simulations often based in the seminal bioheat equations proposed by Pennes (1948),[42] and the reader is referred to excellent resources on the topic.[8-10,43-47]

CENTRAL FEVER AND CEREBRAL TEMPERATURE DYSREGULATION DURING HYPOPERFUSION

Systemic and cerebral temperature dysregulation during and following neurovascular ischemia is well-described, yet the mechanisms underpinning this relationship remain unclear.

The sensitivity of neuronal substrate to hyperthermia has been the focus of multiple human and animal stroke studies, and identification of this potentially modifiable biomarker has naturally promoted investigation into therapeutic cooling protocols following different forms of neurologic injury.[1,2,4-6,48] Indeed, therapeutic cooling remains among the most potent neuroprotectants following ischemia and cardiac arrest, dating to landmark studies of the mid-20th century.[49,50] Early canine studies by Hosler (1953)[49] found that at a body temperature of 20°C, no neurologic injury was observed following resuscitation from 11–13 minutes of cardiac fibrillation. Similarly, Donnelly (1956)[51] reported that brain anoxia can be tolerated for only 3 minutes at physiologic temperatures, but remarkably with full resistance for 9 minutes when cooling to 26.5°C. In part through depression of metabolic demand—a 2.2-fold reduction in oxygen consumption for each 10°C decrease in temperature—as well as protection against immediate and programmed cytotoxicity and vascular permeability, brisk hypothermia (~ 20°–32°C) permits prolonged circulatory arrest potentially with little neurologic injury.[7] Decades of subsequent investigation have highlighted the protective attributes of corporeal and brain cooling following brain injury, yet a number of large-scale prospective trials have failed to capture a population-level benefit from cooling, owing perhaps to systemic adverse effects or, we posit, the use of non-neurologic temperature benchmarks. This latter point, we believe, holds tremendous potential promise for noninvasive brain thermometry, with which the known variability between systemic surrogates and brain temperatures can be disentangled toward more guided therapeutic hypothermia protocols.

In contradistinction, hyperthermia proves a strong potentiator of neurologic injury.[1,2,5,52] Fever, an adaptation intended to raise host defenses, has been shown to influence clinical outcomes negatively following stroke, potentially even when mild.[1,2,4-6,53-59] Fever following neurologic injury is unfortunately common, even without direct hypothalamic injury.[60] While the mechanisms of central fever following ischemic stroke are incompletely understood, the aforementioned impairment in radiative heat exchange may act in concert with cytokine-mediated influences involving the hypothalamus, as well as more regional and zonal inflammatory trafficking as described by the inflammatory penumbra paradigm.[6,7,41,53,61,62] These inflammatory cascades may be moderated through hypothermia which, together with reduced expression of pro-apoptotic genes, may provide a powerful potential target for intervention.[63-66]

Radiologic progression of ischemia due to hyperthermia remains comparatively less explored. We previously reported on the tendency for greater consumption of penumbral (ie, at risk)

tissues in fully reperfused patients with acute ischemic stroke when fevers exceeded 37.5°C in the early stroke aftermath. While infarction expansion following reperfusion comprises an array of reported causes, identification of a potentially modifiable and readily attainable biomarker may significantly influence imaging and clinical outcomes.[53,67]

Larger studies, including a series of 4295 patients, have firmly established the detrimental effects of fever as producing longer intensive care unit and hospital stays, higher mortality, and overall worse outcomes, even when controlling for disease severity, complications, and age.[68] We propose that the frequency with which pyrexia occurs in neurologically injured patients—up to 47% of neurologic patients in intensive care units (increasing to 93% after 2 weeks[69])—itself motivates investigation into the use of noninvasive, direct brain thermography in diagnosis, prognostication, and perhaps treatment selection or response to therapy.

MR THERMOMETRY

Principles and Techniques

2D MRI thermometry dates to initial experimentation by Parker et al,[70] who studied the temperature sensitivity of proton longitudinal relaxation (T1) times in human blood specimens, decades after the far earlier discovery of temperature-sensitive nuclear magnetic resonance (NMR) phenomena in the mid-20th century. While a strong linear relationship and sensitivity of ~2°C was reported from a 5-minute scan, the speed and accuracy of T1 thermometry have limited its application in neuroscience. Subsequently, other temperature-sensitive MRI contrast mechanisms were explored, including transverse relaxation time (T2), equilibrium magnetization/susceptibility, spin density, microscopic diffusion, and the proton resonance frequency (PRF), the latter now most commonly used, particularly for thermal ablative procedures (eg, laser interstitial thermal therapy, high-intensity focused ultrasound, and radiofrequency ablation).[71] While each approach may offer relative, application-specific advantages, PRF thermometry, which exploits either of 2 attributes of the proton resonance frequency, is the most accurate, versatile, and widely used technique and will be the subject of the remainder of this review.[72] Specifically, this review will emphasize clinically pragmatic approaches allowing the sufficient spatial, temporal, and temperature resolution to probe dynamic thermal gradients in the healthy brain and during cerebrovascular impairment. Emerging strategies, including potentially promising and accurate temperature-sensitive contrast agents, remain unfit for translational human or clinical imaging and are beyond the intended scope of this review; however, the interested reader is referred to thorough topical reviews on the subject.[73-75]

PRF Thermometry

PRF thermometry stems from the temperature dependence of the water proton chemical shift. Due to the shielding effects of their surrounding electron currents, the magnetic field experienced by hydrogen protons varies slightly relative to that of the externally applied field (B_0). The effect manifests in a temperature-dependent chemical shift (s) as follows:

$$1) \qquad \omega(T) = \gamma \cdot [1 - s(T)] \times B_{local,}$$

where $\omega(T)$ represents the angular frequency of proton precession; γ, the gyromagnetic ratio (~42 MHz/T for the hydrogen nucleus); and $s(T)$, the temperature-dependent chemical shift modulated by the electron-shielding effect on the local magnetic field (B_{local}), itself a function of both the externally applied (B_0) field and spatially varying magnetic susceptibility. The shielding effect of the water proton is influenced heavily by the strength of hydrogen bonds, which is a function of temperature. Hydrogen bonds are formed between the hydrogen of 1 water molecule and the electronegative oxygen atom of another water molecule (Fig 1*A*). Hydrogen bonds among water molecules, therefore, reduce the opposing electron currents about the bound hydrogen proton, exposing the proton to less attenuated B_{local} fields, thereby inducing higher precessional frequencies. (Fig 1*B*). At higher temperatures, however, the hydrogen bonds between water molecules become less stable and/or disrupted, resulting in greater electronic shielding and therefore reduced magnetic flux density and a lower frequency of precession of the hydrogen proton. It has been shown in multiple studies, including our own, that the water proton chemical shift $s(T)$ is largely a linear function of temperature T, (Fig 1*C*):

$$2) \qquad s(T) \approx s_0 + \beta \times (T - 37),$$

where S_0 denotes the chemical shift at 37°C and β denotes change in chemical shift per unit increase in temperature. β has been measured to be between −0.009 and −0.011 ppm per degree Celsius,[29,72,76,77] dating to its initial description in NMR by Hindman (1966).[77]

While most MR thermometry applications have sought to measure relative temperature changes (eg, during and following thermal ablation), they are poorly suited for the study of baseline temperatures and pathophysiologic temperature gradients between brain regions, comparisons between subjects, or longitudinal study, together motivating the development of quantitative techniques approximating absolute temperatures. As apparent from Equation 1, an accurate measure of the chemical shift difference would require precise measurement of B_{local} down to 0.01 ppm. To resolve this issue, a stable (ie, non-temperature-dependent) reference frequency is necessary to normalize the water frequency, thereby allowing nearly absolute thermometry based on the temperature-dependent chemical shift difference between the 2 (or sometimes more) metabolites. Such self-referenced thermometry has been the subject of considerable study using the chemical shift difference between the temperature-sensitive water resonance and a non-temperature-sensitive reference metabolite, such as the methyl resonance of neuronal NAA at ~1.98 ppm.

By comparison, when the primary interest is simply the collection of relative changes in temperature across time, for example during ablative procedures, explicit measurement of either water or reference metabolite frequency is unnecessary, and a baseline water resonance phase can instead be measured before treatment begins. Thereafter, a relative temperature

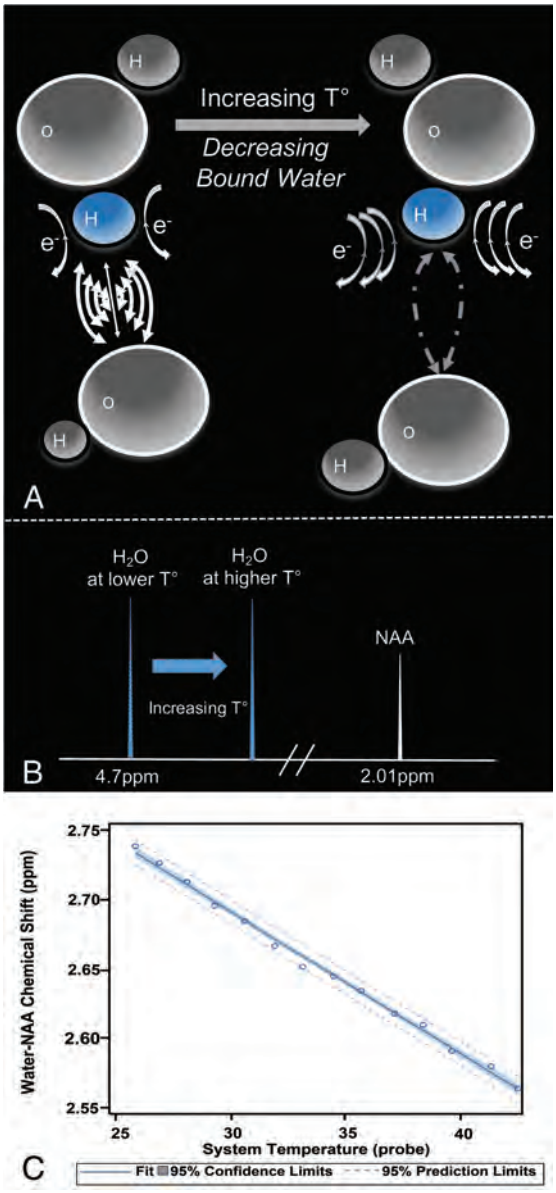

FIG 1. *A*, Schematic representation of the temperature-dependency of the water proton resonance frequency chemical shift. A water hydrogen bonding scenario for water molecules in two milieu of differing temperatures is depicted. Increasing temperatures drive the water hydrogen bonding equilibrium towards greater free water proportions through disruption of hydrogen bonds. Electronic currents ("e-") about the hydrogen proton shield it from the main magnetic flux, but will vary in strength between strongly (left) and weakly (right) bound water pools. The greater shielding of free water hydrogens (right) yields lower precessional frequencies, governed by the gyromagnetic ratio of hydrogen, ~42MHz/T. *B*, Within the hydrogen PRF spectrum, higher temperatures translate the water resonance upfield (i.e. towards lower chemical shifts), reducing the chemical shift difference between water and a non-temperature dependent reference such as the methyl resonance of NAA, producing a linear correlation coefficient (*C*) of ~−0.01 ppm/C. As shown, the relationship between hydrogen bonding equilibrium, PRF, and temperature remains linear across even supraphysiologic temperature ranges as demonstrated in an aqueous cytosolic phantom during real time fiberoptic temperature monitoring. *Adapted from* Dehkharghani et al.[76]

change can be estimated following ablation using an additional phase estimation, and the phase shift can be used to estimate a relative temperature change on the basis of the aforementioned temperature-dependent frequency changes. In this case, the phase evolution arising from the PRF change relates to the relative temperature change as follows:

$$3)\qquad \Delta\varphi_t = -2\pi\cdot\Delta\omega_t \times TE$$
$$= -2\pi \times \big(\omega(T_1) - \omega(T_0)\big) \times TE$$
$$= 2\pi \times \gamma \times \beta_w \times B_{local} \times TE \times \Delta T,$$

where β_w reflects the thermal chemical shift coefficient of water. Importantly, however, non-temperature-dependent changes in phase, including, for instance, those due to magnetic field drifts across time resulting from gradient heating or subject motion can engender errors in the imputed temperature change. In either case, phase imaging can be used only to estimate relative temperature changes across time, though with comparatively higher spatial and temporal resolution than most quantitative thermometry techniques.[71] In principle, any sequence that is sensitive to PRF can be used to measure the phase change across time, and the most common approach is through phase imaging from a gradient-echo sequence, according to the equation $\Delta\varphi_t = -2\pi \times \Delta\omega_t \times TE$, where $\Delta\varphi_t$ represents the phase change across time, and *TE*, the echo time. More recently, "reference-less" phase thermometry methods have been proposed, which assume temperature changes occurring only in a local region and essentially using the phase from the neighboring regions as an in-line reference, though their robustness and accuracy as alternatives to truly self-referenced techniques have not been conclusively demonstrated.[78]

As introduced above, using the chemical shift difference as measured from proton spectroscopy, absolute thermometry can be approached through the additional, simultaneous measurement of the PRF of another proton chemical group lacking in temperature-dependent hydrogen bonds. Provided that intravoxel susceptibility effects are small as shown by De Poorter,[85] the use of a reference frequency devoid of temperature-dependent chemical shifts is thus performed as follows:

$$4)\ \Delta\omega = \Delta\omega_w - \Delta\omega_r$$
$$= -\gamma \times \big(s_{0,w} - s_{0,r} + (\beta_w - \beta_r) \times (T - 37)\big),$$

where, in contrast to Equation 3, $\Delta\omega$ denotes the difference in angular frequency between the water proton and the reference compound, such as NAA, choline, or other candidate hydrogen metabolites; $s_{0,w}$ and $s_{0,r}$ denote chemical shifts of water and the reference compound, respectively, at 37°C; and $\beta_w$and β_r represent thermal chemical shift coefficients for water and the reference compound, respectively.[79] NAA, the dominant nonwater metabolite in the conventional brain PRF spectrum, has proved generally well-suited due to its uniformly high concentration and extremely small temperature dependency (<0.0007 ppm/°C) related to the absence of hydrogen bonds. Accordingly, MR spectroscopy can be used to measure the PRF difference between water and reference compounds simultaneously, facilitating

quantitative temperatures at single time points or longitudinally, either between or among individual subjects and across experimental conditions.[29,41,59,76,80]

MR Thermometry in Stroke and Cerebrovascular Disease

Acute Ischemic Stroke. Noninvasive cerebral MRT has been explored in small-but-growing numbers of human and animal studies, aiming to capture empirically the link between brain temperature and hemodynamic compromise. While such mechanistic insights are valuable motivations for noninvasive MRT, the development of biomarkers of tissue viability and outcome arguably remain the most compelling long-term objective of thermometry in this setting.

Corbett et al[29] first described the use of single-voxel proton MR spectroscopy for in vivo brain thermometry in a piglet model of ischemic stroke using a 4.7T NMR spectroscopy system. Using water-NAA chemical shift thermometry, their in vivo experiments recapitulated the linearly changing water-NAA chemical shift difference coefficient of approximately 0.01 ppm/°C across both physiologic and ischemic conditions (slope, 1.00 ± 0.03, $r^2 = 0.96$), importantly, with little impact by either pH or protein concentration in physiologically relevant ranges. The authors furthermore reported that even with falling NAA concentrations in ischemic and infarcted tissues, sufficient concentrations remained to allow peak assignment of the NAA resonance. The potential for alternative candidate reference frequencies such as choline or trimethylamines was, nevertheless, tested and confirmed by the authors in subsequent studies, further supporting the feasibility of in vivo brain thermometry in scenarios of falling or undetectable NAA.[31,32] Of particular interest, the authors reproduced centripetal temperature gradients as measured from directly implanted thermocouples at varying depths, on order of 1°C temperature drop from a 1-cm depth to the brain surface.

Later work by Corbett et al[31] in healthy human adults again used individual, single-voxel point-resolved spectroscopy spectra (PRESS). By interrogating temperatures in both superficial and deep brain loci, the authors demonstrated, for the first time, that centripetal temperature gradients within the brain itself are amenable to noninvasive detection under clinically practicable conditions. The preceding, however, left the need for noninvasive, real-time detection of fully spatially-resolved temperature gradients unmet, motivating the expansion of existing single-voxel spectroscopy techniques to multivoxel thermographs in 2D or 3D. Such multivoxel MR spectroscopic imaging or chemical shift imaging is not, however, without inherent challenges.[72,81,82] While Ishihara et al[83] had reported on the preliminary development of relative cerebral thermal maps using phase-contrast thermography, the dependence of phase-based PRF thermometry on baseline phase mapping (see above) and its potential vulnerability to poorly compensated effects, such as from susceptibility changes, limited its applicability for the reasons detailed above.[72,81,84,85] Successful extension of single-voxel spectroscopy to MR spectroscopic imaging–based thermometry was, thereafter, reported by Kuroda et al[81,84] in in vitro and in vivo animal studies, though long acquisition times and analytic errors related to chemical shift misregistration and data corruption by lipid contamination are well-recognized challenges to experimentation and clinical use. Acceleration, such as with echo-planar spectroscopic imaging, and more robust signal localization, such as with adiabatic imaging techniques, have been reported with success by multiple investigators, including in our group, with the common goal of robust in vivo thermography (Fig 2).[41,59,84,86]

In vivo multivoxel thermography in human subjects was reported initially by Karaszewski et al[39] among a cohort of adult patients with ischemic stroke. The authors attempted to operationalize thermography profiles relative to infarcted and at-risk tissues as defined by diffusion-weighted imaging, reporting generally greater temperatures in possibly abnormal tissues (ie, regions along the immediate periphery of the pathologic DWI lesion). Notwithstanding significant study limitations, including the heterogeneous duration from stroke onset, the absence of perfusion-to-diffusion penumbral estimation, and variable treatment effects, the authors observed that the greatest heating may occur in viably hypoperfused, metabolically active tissues. In contradistinction, somewhat lower temperatures were observed within the more definitively devitalized tissues in the infarction core, in line with past experiments documenting the potential for temperature reduction within the infarcted core of rat brains early after stroke induction using direct thermometry.[3]

Subsequent work by the authors reproduced the findings that the greatest brain temperatures are found in the infarction margins and, importantly, identified unanticipated nonuniformities in temperatures elsewhere throughout the brain; specifically, temperatures in the brain hemisphere contralateral to the stroke were also found to be significantly higher in subjects who were imaged at later times. While such studies are small, observational, and far from conclusive, it can be posited that the convolved effects of perfusion (reduced, absent, or restored following ischemia), metabolic heat production (aerobic and anaerobic), systemic temperatures (physiologic or pyrexic), and variable inflammatory mechanisms (the inflammatory penumbra; mitochondrial uncoupling protein-2) in aggregate determine the temperature profile of infarcted, viably ischemic, and normal/compensated oligemic tissues. These studies confirm the presence of measurable temperature perturbations in ischemic tissues and motivate the further development of operational paradigms of temperature disturbance in stroke.

The preceding human studies of thermometry were inherently limited by the inability to control for the timing of thermometry relative to stroke onset or to track changes longitudinally with sufficient temporal resolution to formalize temperature changes following stroke. Furthermore, the opportunity for local calibration of chemical shift thermometry under clinical scanning conditions has generally been lacking. While several small animal stroke-induction studies attempted to address the former, the generalization of rodent and lower mammal studies to human physiology poses widely cited challenges and may impede translatability in mechanistic and pharmacologic studies.[87] This issue has motivated further study across stroke neuroscience in gyrencephalic nonhuman primates to facilitate translation.

Our group has undertaken serial studies of noninvasive thermometry in the phylogenetically similar rhesus macaque,

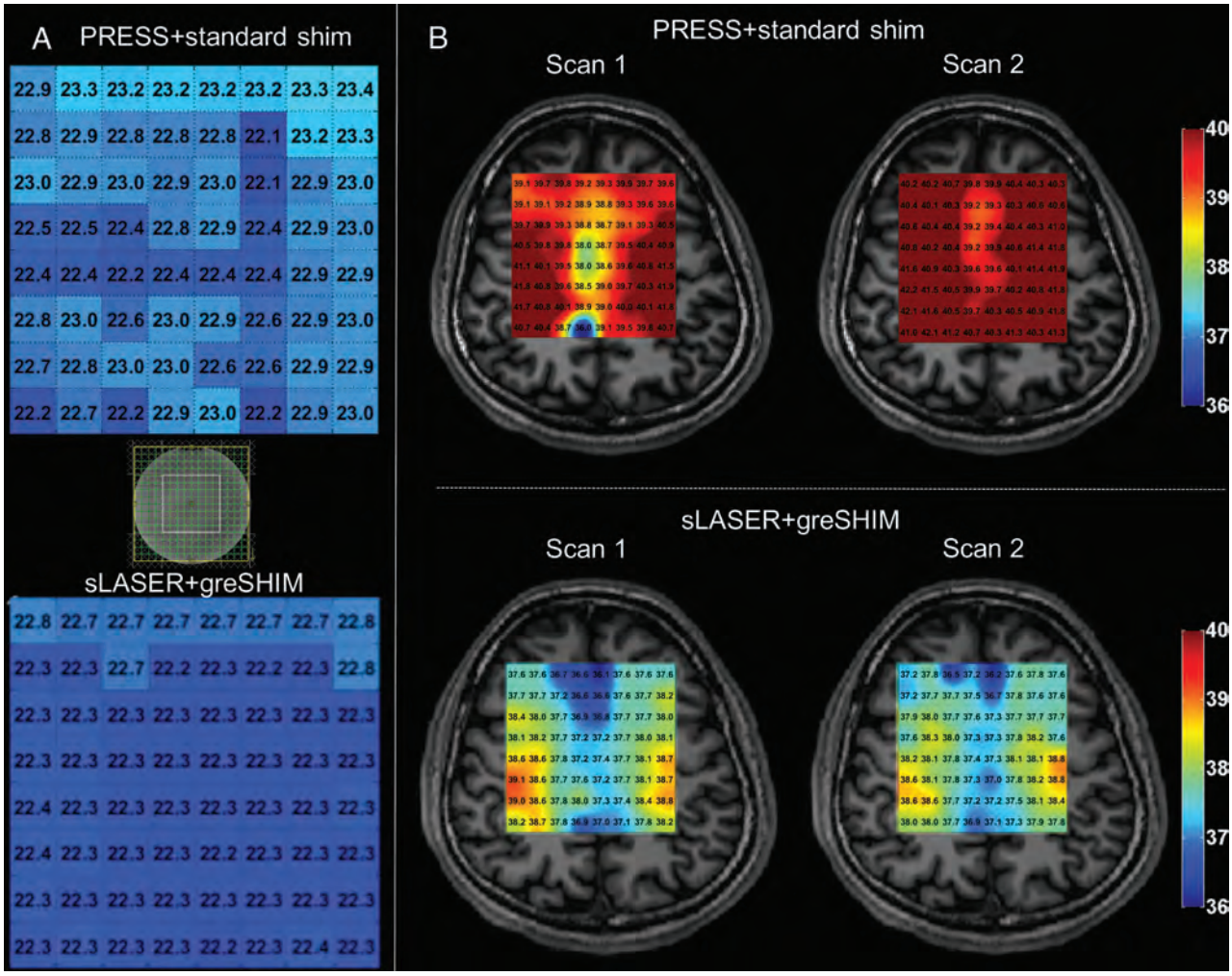

FIG 2. Phantom (*A*) and human in vivo PRF thermometry in a healthy volunteer (*B*) using the water-NAA chemical shift, demonstrating the impact of adiabatic (semiLASER) versus conventional volume localization (PRESS) and improvements in the shimming conditions using 3D gradient-echo (greSHIM). Spatially uniform phantom temperatures are noted in *A* with improvements in SNR, fitted line widths, and test-retest repeatability (not shown) by comparison with conventional point-resolved spectroscopy using sLASER at 3T. Greater test-retest stability obtained 30 minutes apart and the presence of physiologically meaningful temperature gradients are demonstrated to greater advantage in the *lower row* of *B* when using sLASER for spatial localization together with greSHIM. Adapted from Dehkharghani et al.,[86,88] with permission from the International Society of Magnetic Resonance in Medicine.

specifically in efforts to bridge this gap.[41,76] Using robust adiabatic multivoxel chemical shift imaging strategies (sLASER, Siemens Healthineers, Erlangen, Germany) with greater performance against chemical shift misregistration, together with higher order magnetic field shimming, we recently reported on dynamic brain temperature changes following highly-controlled endovascular stroke induction in NHP.[41] This experimental design permits repeated production of thermographs under physiologic and postischemic conditions without the confounding effects of surgery and ambient heat loss, the constraints of focally implanted temperature probes, or the limitations of unknown disease onset. The preoperative calibration of water-NAA chemical shift thermometry under essentially identical imaging conditions using clinical 3T scanning conditions also facilitates future translation. While the potentially nontrivial effect of anesthesia induction on cerebral blood flow, metabolism, and temperature regulation cannot be overlooked in such models, dynamic imaging immediately following anesthesia induction in control and ischemic experimental sessions fortuitously produces an additional form of physiologic contrast during which temperatures can be measured and compared between conditions.

Across all subjects in our protocol, we observed gradually increasing brain and systemic temperatures, importantly, with steady divergence in brain-to-systemic temperature gradients occurring as the cerebral hyperthermia steadily outpaced even the worsening systemic pyrexia (Fig 3). This dynamic and unpredictable offset stresses the importance of direct brain thermometry in the monitoring of brain injury, owing to the inaccuracies of systemic temperature surrogates in this setting. Furthermore, significant differences in the temperature evolution across time were observed among tissues, independent of worsening systemic hyperthermia, further suggesting the potential for mixed mechanisms of temperature change throughout the brain.

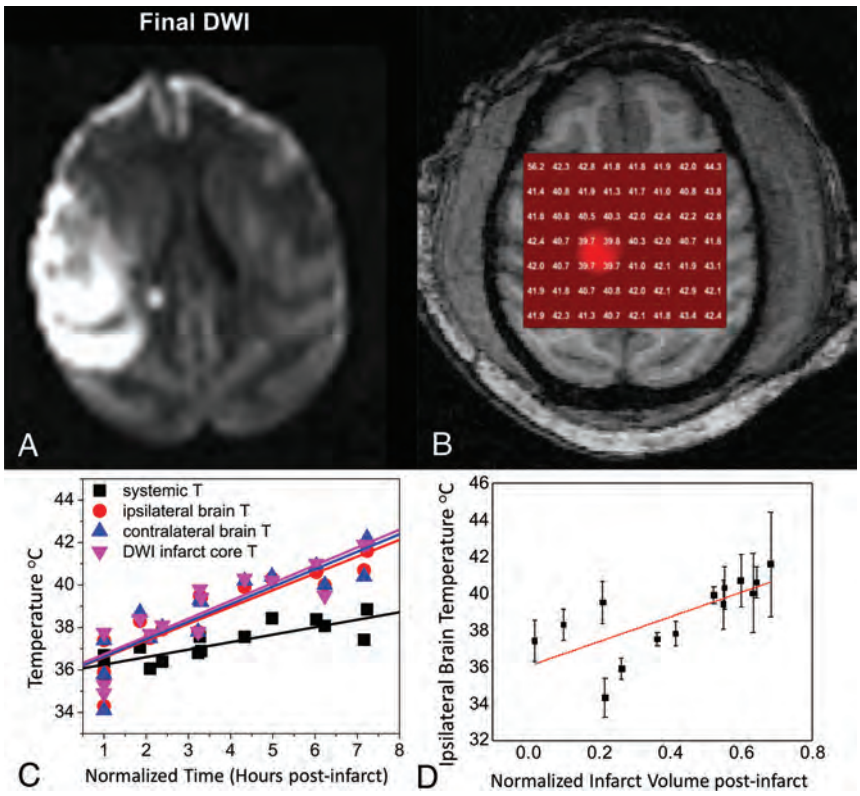

FIG 3. Dynamic MR thermometry following superselective right MCA endovascular stroke induction in an adult rhesus macaque using a low-profile suture embolus. DWI (*A*) obtained at approximately 7 hours following complete occlusion and contemporaneous 2D axial sLASER chemical shift thermography (see MR Thermometry in Stroke and Cerebrovascular Disease: Acute Ischemic Stroke) following automated and manual shimming (*B*) demonstrate extensive right-hemispheric ischemic injury and generalized cerebral hyperthermia, respectively. Through the course of the experiment, temperatures in both hemispheres were noted to rise, importantly with a differing temporal course and, in both cases, outpacing the influences of the steadily increasing systemic pyrexia (*C*), measured continuously from an indwelling rectal probe and aggregated over all subjects. The correlation between both normalized infarction size (*C*) and time from infarction relative to cerebral temperatures was similarly observed across all experimental NHP strokes, and aggregated results are depicted. Adapted from Dehkharghani et al.[41]

Chronic Cerebrovascular Ischemia. Hemodynamic and thermoregulatory theory predict a strong dependency of brain temperature on blood flow, which has largely been confirmed during experimentation in low-flow states such as ischemic stroke as described above. The theoretic, converse cooling effects of hemodynamic augmentation are, however, more difficult to test experimentally. A brief review of the dynamic autoregulatory process underlying hemodynamic failure is worthwhile at this stage. The response of the cerebrovascular system to falling perfusion pressures was expounded in initial work by Powers and further by Derdeyn et al.[89,90] using ^{15}O-PET.[89-93] A sequential, quasi-stepwise response to incremental hemodynamic failure is commonly encountered, culminating in the up-regulation of the oxygen extraction fraction (OEF) from the heme moiety of hemoglobin to sustain the cerebral metabolic rate of oxygen when falling perfusion pressures outstrip the cerebrovascular reserve. This tenuous state of so-called misery perfusion would, on the basis of cerebral thermoregulatory theory, seem conducive to heating. Specifically, one would anticipate that viable (ie, with continued but potentially reduced metabolic activity) tissue beds downstream from chronic steno-occlusive lesions could exhibit a particular propensity for heating through the combination of increased thermogenic oxygen cleavage and reduced perfusion.

Cerebral oximetry and the identification of misery perfusion by MR imaging remain elusive aims and areas of active study by many groups including our own.[94-98] The unambiguous demonstration of misery perfusion proves challenging without direct MR oximetry, which remains difficult under clinically pragmatic conditions.[99,100] The characterization of cerebral temperatures could, however, reflect a measurable epiphenomenon of the hemodynamic and metabolic derangements inherent to misery perfusion. In a study of contemporaneous ^{15}O-PET and single-voxel point-resolved spectroscopy by Ishigaki et al,[101] local temperatures and the OEF were estimated in the deep white matter of healthy subjects and patients with unilateral, anterior circulation steno-occlusive disease. As expected, uniformly normal distributions of OEF were measured in healthy subjects, while elevations of OEF in the diseased territories of patients with steno-occlusive disease were observed as compensations for reduced blood flow. The authors also confirmed the hypothesized interactions between interhemispheric temperature offset and OEF. While the findings are compelling as potential evidence for brain temperatures as an imaging biomarker in chronic ischemia, the comprehensive characterization of tissue thermal signatures in hemodynamic failure would require acquisition of thermographs to assess the spatiotemporal relationship between perfusion and temperature.

To this end, we recently reported on cerebral multivoxel thermography in patients with chronic, unilateral anterior circulation steno-occlusive disease, leveraging the hemodynamic contrast of acetazolamide augmentation.[80] We hypothesized the presence of a detectable modulation of cerebral temperatures by cerebrovascular augmentation, which we have coined the "brain thermal response" (BTR, Fig 4), which we compared with both CBF (using multidelay arterial spin-labeling) and blood oxygen level–dependent (BOLD) augmentation. In accordance with aforementioned observations by Ishigaki et al,[101] while highly significant interactions were observed between augmentation and temperature, the relationship appears to be unsurprisingly

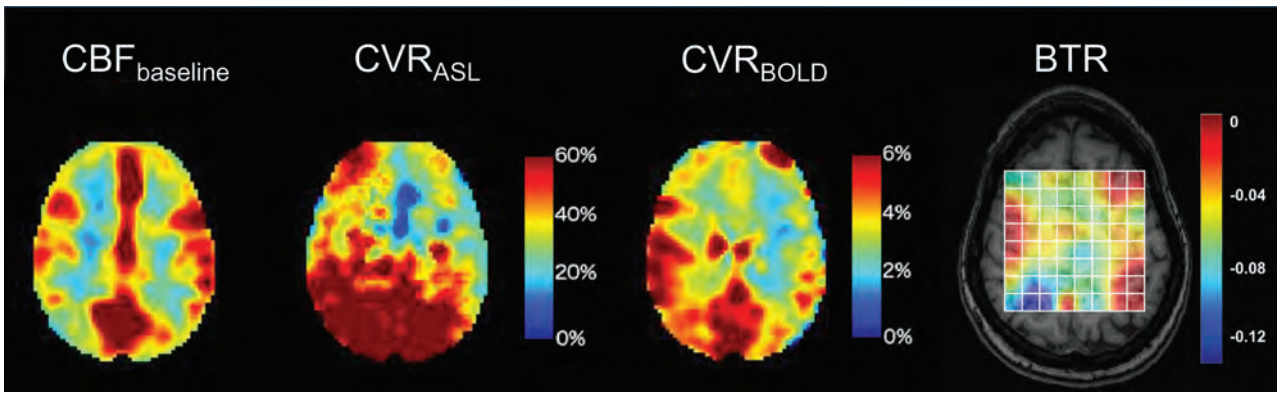

FIG 4. Cerebrovascular reserve (CVR) percentage augmentation maps calculated with BOLD and arterial spin-labeling (ASL), as well as a BTR map overlaid on a T1-weighted anatomic image. Images are all from the same subject (a 32-year-old woman with unilateral left MCA stenosis and multiple TIAs). The *white grid* overlay represents the MR thermometry VOI derived from multivoxel spectroscopy analysis using the water-NAA chemical shift difference. Images are displayed in the radiologic convention. Impaired cerebrovascular reserve in the left hemisphere is present in both BOLD and ASL, with a greater severity of impairment in arterial spin-labeling, likely related to tag decay and residual delay sensitivity despite the use of 10 separate, in-line postlabel delays of varying duration. The BTR map demonstrates an asymmetric thermal response, with less brain cooling following vasodilatory stimulus in the diseased left hemisphere, indicated by reduced (ie, less negative) BTR values and corresponding primarily to the areas of greatest impairment in the anterior and posterior MCA borderzone territories. Maximal (most negative) BTRs are noted in the regions spatially concordant with the greatest hemodynamic augmentation (blue regions) in the right parietal lobe. Adapted from Fleischer et al.[80]

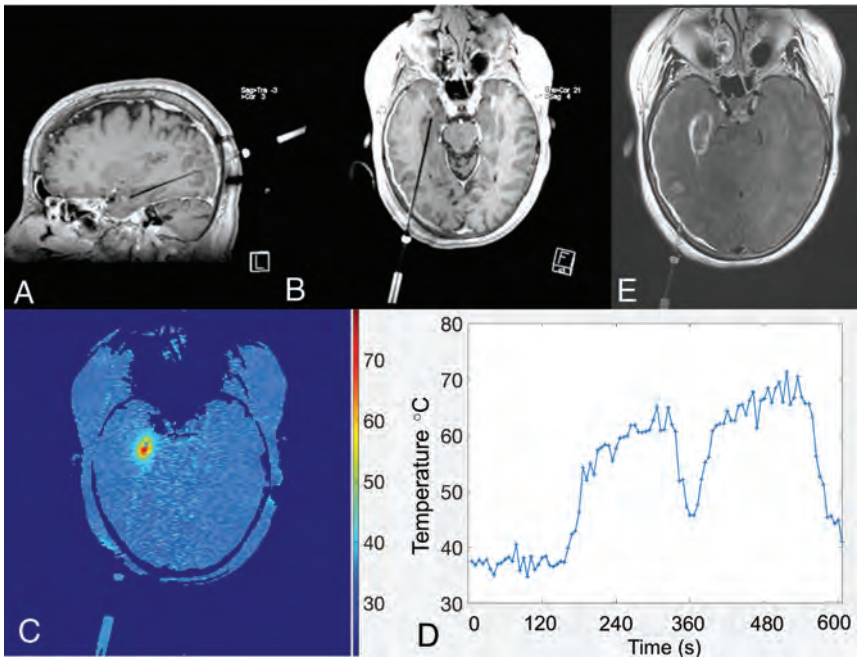

FIG 5. Real-time temperature mapping using phase-based PRF thermometry during stereotactic laser amygdalohippocampectomy for mesial temporal lobe epilepsy. Multiplanar spoiled gradient T1-weighted images obtained with intravenous gadolinium (*A* and *B*) demonstrate a stereotactically introduced, right-posterior-approach ablative probe, terminating within the right hippocampal formation. A parametric thermal map with inset scale and a temperature-time course graph (*C* and *D*, respectively) demonstrate that the estimated, relative temperature change from baseline following ablation exceeded 30°C. Contrast-enhanced T2-FLAIR axial image (*E*) through the treatment bed confirms the final zone of ablative injury.

complex and nonlinear. In particular, BOLD augmentation reflects a convolved effect of flow and volume and also, critically, of blood oxygenation/oxygen extraction. This latter effect, which may be variably up-regulated at baseline, depending on the metabolic need and also on vasoreactivity and disease chronicity, is difficult to measure directly. However, in concert, these variables likely determine the direction of the baseline arterial blood-to-brain temperature offset and, therefore, the magnitude and direction of the BTR. While further investigation into the diagnostic and prognostic merits of BTR are underway, we anticipate that the overarching mechanisms are governed by already well-recognized principles of cerebral hemodynamic control and thermoregulation and reflect a tendency for tissue heating arising from impaired perfusion and up-regulated OEF.[80,101]

An interesting potential implication of such thermal disturbance in cerebrovascular disease was described recently by Murakami et al,[103] who explored the potential for preoperative hyperthermia as a predictor of post-carotid endarterectomy hyperperfusion syndrome. A strong and highly significant correlation was observed between baseline temperature elevation and potentially dangerous post-carotid endarterectomy blood flow augmentation ($r = 0.763$, $P < .001$). Similarly, our experience with the BTR demonstrated a significant negative relationship between baseline temperatures and cerebrovascular reserve capacity, in line with past reports of impaired cerebrovascular reserve capacity as a strong predictor of hyperperfusion syndrome.[104]

MR Thermometry in Thermal Therapy. MR thermometry has found broad applications in the real-time monitoring of thermal therapies, and despite obvious differences from the preceding sections, for completeness, we introduce the reader to this emergent application of cerebral thermometry.

The coagulative response of thermally injured tissue is a function of both maximal temperature and the duration over which it is sustained beyond the ablative threshold. In such applications, MRT can be used to ensure that temperatures in target regions are sustained at prespecified levels to achieve coagulation and fatal thermal dose. In combination with sophisticated dose and thermal models, the use of real-time monitoring affords greater safety in such procedures by ensuring that ablative doses not exceed cavitation thresholds and by confirming that temperatures in vulnerable and eloquent nearby regions remain below injurious ranges (Fig 5). The scale of temperature change in these applications is on the order of tens of degrees Celsius and, hence, much larger than that described either in basal cerebral temperature gradients or occurring in the pathophysiologic states discussed elsewhere in this review. During thermal therapy, the baseline cerebral temperature gradient can therefore be neglected and the temperatures assumed to be spatially homogeneous and equal to the systemic temperature. By freeing the methodology from the demands for absolute, baseline temperature estimation, many alternative approaches to thermometry can be used in such applications beyond those discussed for the study of cerebral thermoregulation described herein.[71]

CONCLUSIONS

This review introduces the reader to fundamental aspects of cerebral and systemic thermoregulation, emphasizing the importance of tight cerebral thermoregulation in homeotherms and specifically the vulnerability of the ischemic neurovascular unit to the effects of hyperthermia. Temperature represents a powerful biomarker of brain function and a potentially valuable target for interrogation through noninvasive means as permitted by emerging cerebral MR thermometry techniques. We believe that cerebral temperatures are, therefore, well-suited for diagnostic and prognostic purposes and mechanistic study and hope to see them find their way deeper into the scientific agenda of the neuroimaging community.

Disclosures: Seena Dehkharghani—*RELATED: Grant*: Foundation of the ASNR, Emory University Research Council, *Comments*: Scholar Award in Neuroradiology Research in the name of the lead author in successive years, Emory University Research Council Grant to the lead author*; *Support for Travel to Meetings for the Study or Other Purposes:* Foundation of the ASNR*; *UNRELATED: Travel/Accommodations/Meeting Expenses Unrelated to Activities Listed:* ISchemaView, *Comments*: travel costs. Deqiang Qiu—*UNRELATED: Grants/Grants Pending*: Siemens.* *Money paid to the institution.

REFERENCES

1. Busto R, Dietrich WD, Globus MY, et al. **The importance of brain temperature in cerebral ischemic injury.** *Stroke* 1989;20:1113–14 CrossRef Medline
2. Busto R, Dietrich WD, Globus MY, et al. **Small differences in intraischemic brain temperature critically determine the extent of ischemic neuronal injury.** *J Blood Flow Metab* 1987;7:729–38 CrossRef Medline
3. Minamisawa H, Mellergard P, Smith ML, et al. **Preservation of brain temperature during ischemia in rats.** *Stroke* 1990;21:758–64 CrossRef CrossRef Medline
4. Minamisawa H, Nordstrom CH, Smith ML, et al. **The influence of mild body and brain hypothermia on ischemic brain damage.** *J Cereb Blood Flow Metab* 1990;10:365–74 CrossRef Medline
5. Wass CT, Lanier WL, Hofer RE, et al. **Temperature changes of > or = 1 degree C alter functional neurologic outcome and histopathology in a canine model of complete cerebral ischemia**. *Anesthesiology* 1995;83:325–35 CrossRef Medline
6. Axelrod YK, Diringer MN. **Temperature management in acute neurologic disorders.** *Neurol Clin* 2008;26:585–603, xi CrossRef Medline
7. Saad H, Aladawy M. **Temperature management in cardiac surgery.** *Glob Cardiol Sci Pract* 2013;2013:44–62 CrossRef Medline
8. Baker MA. **Brain cooling in endotherms in heat and exercise.** *Annu Rev Physiol* 1982;44:85–96 CrossRef Medline
9. Zhu M, Ackerman JJ, Sukstanskii AL, et al. **How the body controls brain temperature: the temperature shielding effect of cerebral blood flow.** *J Appl Physiol* 2006;101:1481–88 CrossRef Medline
10. Zhu M, Ackerman JJ, Yablonskiy DA. **Body and brain temperature coupling: the critical role of cerebral blood flow.** *J Comp Physiol B* 2009;179:701–10 CrossRef Medline
11. Falk D. **Brain evolution in homo: the "radiator" theory.** *Behav Brain Sci* 1990;13:333–44 CrossRef
12. Baker MA, Hayward JN. **Intracranial heat exchange and regulation of brain temperature in sheep.** *Life SCI* 1968;7:349–57 CrossRef Medline
13. Baker MA. **A brain-cooling system in mammals.** *Sci Am* 1979; 240:130–39 CrossRef Medline
14. Cabanac M, Caputa M. **Natural selective cooling of the human brain: evidence of its occurrence and magnitude.** *J Physiol* 1979; 286:255–64 CrossRef Medline
15. Hayward JN, Baker MA. **Role of cerebral arterial blood in the regulation of brain temperature in the monkey.** *Am J Physiol* 1968; 215:389–403 CrossRef Medline
16. Cabanac M. **Selective brain cooling in humans: "fancy" or fact?** *FASEB J* 1993;7:1143–46; discussion 1146–47 Medline
17. Caputa M. **Selective brain cooling: a multiple regulatory mechanism.** *J Therm Biol* 2004;29:691–702 CrossRef
18. Falk D. **Brain evolution in homo: the radiator theory.** *Behavioral and Brain Sciences* 1990;13:333–34 CrossRef
19. Falk D. Evolution of the primate brain. In: *Handbook of Paleoanthropology*. Berlin: Springer-Verlag; 2007:1133–62
20. Kuhnen G, Jessen C. **Thermal signals in control of selective brain cooling.** *Am J Physiol* 1994;267:R355–59 CrossRef Medline
21. Yablonskiy DA, Ackerman JJ, Raichle ME. **Coupling between changes in human brain temperature and oxidative metabolism during prolonged visual stimulation.** *Proc Natl Acad Sci U S A* 2000;97:7603–08 CrossRef Medline
22. Zhu L, Diao C. **Theoretical simulation of temperature distribution in the brain during mild hypothermia treatment for brain injury.** *Med Biol Eng Comput* 2001;39:681–87 CrossRef Medline
23. Stone JG, Young WL, Smith CR, et al. **Do standard monitoring sites reflect true brain temperature when profound hypothermia is rapidly induced and reversed?** *Anesthesiology* 1995;82:344–51 CrossRef Medline
24. Simon E. **Tympanic temperature is not suited to indicate selective brain cooling in humans: a re-evaluation of the thermophysiological basics.** *Eur J Appl Physiol* 2007;101:19–30 CrossRef Medline
25. Baker MA, Stocking RA, Meehan JP. **Thermal relationship between tympanic membrane and hypothalamus in conscious cat and monkey.** *J Appl Physiol* 1972;32:739–42 CrossRef Medline
26. McCaffrey TV, McCook RD, Wurster RD. **Effect of head skin temperature on tympanic and oral temperature in man.** *J Appl Physiol* 1975;39:114–18 CrossRef Medline

27. Cady EB, D'Souza PC, Penrice J, et al. **The estimation of local brain temperature by in vivo 1H magnetic resonance spectroscopy.** *Magn Reson Med* 1995;33:862–67 CrossRef Medline
28. Childs C, Hiltunen Y, Vidyasagar R, et al. **Determination of regional brain temperature using proton magnetic resonance spectroscopy to assess brain-body temperature differences in healthy human subjects.** *Magn Reson Med* 2007;57:59–66 CrossRef Medline
29. Corbett RJ, Laptook AR, Tollefsbol G, et al. **Validation of a noninvasive method to measure brain temperature in vivo using 1H NMR spectroscopy.** *J Neurochem* 1995;64:1224–30 CrossRef Medline
30. Schwab S, Spranger M, Aschoff A, et al. **Brain temperature monitoring and modulation in patients with severe MCA infarction.** *Neurology* 1997;48:762–67 CrossRef Medline
31. Corbett R, Laptook A, Weatherall P. **Noninvasive measurements of human brain temperature using volume-localized proton magnetic resonance spectroscopy.** *J Cereb Blood Flow Metab* 1997;17: 363–69 CrossRef Medline
32. Corbett RJ, Purdy PD, Laptook AR, et al. **Noninvasive measurement of brain temperature after stroke.** *AJNR Am J Neuroradiol* 1999;20:1851–57 Medline
33. Verlooy J, Heytens L, Veeckmans G, et al. **Intracerebral temperature monitoring in severely head injured patients.** *Acta Neurochir (Wien)* 1995;134:76–78 CrossRef Medline
34. Sun Z, Zhang J, Chen Y, et al. **Differential temporal evolution patterns in brain temperature in different ischemic tissues in a monkey model of middle cerebral artery occlusion.** *J Biomed Biotechnol* 2012;2012:980961 CrossRef Medline
35. Sukstanskii AL, Yablonskiy DA. **Theoretical limits on brain cooling by external head cooling devices.** *Eur J Appl Physiol* 2007;101: 41–49 CrossRef Medline
36. Soukup J, Rieger A, Holz C, et al. **Temperature gradient between brain tissue and arterial blood mirrors the flow-metabolism relationship in uninjured brain: an experimental study.** *Acta Anaesthesiol Scand* 2007;51:872–79 CrossRef Medline
37. Otawara Y, Ogasawara K, Kubo Y, et al. **Brain and systemic temperature in patients with severe subarachnoid hemorrhage.** *Surg Neurol* 2003;60:159–64; discussion 164 CrossRef Medline
38. Mellergard P. **Changes in human intracerebral temperature in response to different methods of brain cooling.** *Neurosurgery* 1992;31:671–77; discussion 677 Medline
39. Karaszewski B, Wardlaw JM, Marshall I, et al. **Measurement of brain temperature with magnetic resonance spectroscopy in acute ischemic stroke.** *Ann Neurol* 2006;60:438–46 CrossRef Medline
40. Kalmbach AS, Waters J. **Brain surface temperature under a craniotomy.** *J Neurophysiol* 2012;108:3138–46 CrossRef Medline
41. Dehkharghani S, Fleischer CC, Qiu D, et al. **Cerebral temperature dysregulation: MR thermographic monitoring in a nonhuman primate study of acute ischemic stroke.** *AJNR Am J Neuroradiol* 2017;38:712–20 CrossRef Medline
42. Pennes HH. **Analysis of tissue and arterial blood temperatures in the resting human forearm.** *J Appl Physiol* 1948;1:93–22 CrossRef Medline
43. Nelson DA, Nunneley SA. **Brain temperature and limits on transcranial cooling in humans: quantitative modeling results.** *Eur J Appl Physiol Occup Physiol* 1998;78:353–59 CrossRef Medline
44. Sukstanskii AL, Yablonskiy DA. **An analytical model of temperature regulation in human head.** *J Therm Biol* 2004;29:583–87 CrossRef
45. Sukstanskii AL, Yablonskiy DA. **Theoretical model of temperature regulation in the brain during changes in functional activity.** *Proc Natl Acad Sci USA* 2006;103:12144–49 CrossRef Medline
46. Wissler EH. **Pennes' 1948 paper revisited.** *J Appl Physiol* 1998;85: 35–41 CrossRef Medline
47. Collins CM, Smith MB, Turner R. **Model of local temperature changes in brain upon functional activation.** *J Appl Physiol* 2004; 97:2051–55 CrossRef Medline
48. Minamisawa H, Smith ML, Siesjo BK. **The effect of mild hyperthermia and hypothermia on brain damage following 5, 10, and 15 minutes of forebrain ischemia.** *Ann Neurol* 1990;28:26–33 CrossRef Medline
49. Hosler RM. **The emergency treatment of cardiac arrest.** *J Int Coll Surg* 1953;19:336–40 Medline
50. Wolfe KB. **Effect of hypothermia on cerebral damage resulting from cardiac arrest.** *Am J Cardiol* 1960;6:809–12 CrossRef Medline
51. Donnelly CJ, Frobese AS, Stone HH. **The effect of lowered body temperature on the cerebral hemodynamics and metabolism of man.** *Surg Gynecol Obstet* 1956;103:313–7 Medline
52. Ginsberg MD, Sternau LL, Globus MY, et al. **Therapeutic modulation of brain temperature: relevance to ischemic brain injury.** *Cerebrovasc Brain Metab Rev* 1992;4:189–25 Medline
53. Dehkharghani S, Bowen M, Haussen DC, et al. **Body temperature modulates infarction growth following endovascular reperfusion.** *AJNR Am J Neuroradiol* 2017;38:46–51 CrossRef Medline
54. Dietrich WD, Busto R, Halley M, et al. **The importance of brain temperature in alterations of the blood-brain barrier following cerebral ischemia.** *J Neuropathol Exp Neurol* 1990;49:486–97 CrossRef Medline
55. Dietrich WD, Busto R, Valdes I, et al. **Effects of normothermic versus mild hyperthermic forebrain ischemia in rats.** *Stroke* 1990;21: 1318–25 CrossRef Medline
56. Ginsberg MD, Busto R. **Combating hyperthermia in acute stroke: a significant clinical concern.** *Stroke* 1998;29:529–34 CrossRef Medline
57. Karaszewski B, Thomas RG, Dennis MS, et al. **Temporal profile of body temperature in acute ischemic stroke: relation to stroke severity and outcome.** *BMC Neurol* 2012;12:123 CrossRef Medline
58. Karaszewski B, Wardlaw JM, Marshall I, et al. **Early brain temperature elevation and anaerobic metabolism in human acute ischaemic stroke.** *Brain* 2009;132:955–64 CrossRef Medline
59. Maudsley AA, Goryawala MZ, Sheriff S. **Effects of tissue susceptibility on brain temperature mapping.** *Neuroimage* 2017;146:1093–1101 CrossRef Medline
60. Wrotek SE, Kozak WE, Hess DC, et al. **Treatment of fever after stroke: conflicting evidence.** *Pharmacotherapy* 2011;31:1085–91 CrossRef Medline
61. Gauberti M, De Lizarrondo SM, Vivien D. **The "inflammatory penumbra" in ischemic stroke: from clinical data to experimental evidence.** *Eur Stroke J* 2016;1:20–27 CrossRef Medline
62. Gauberti M, Montagne A, Marcos-Contreras OA, et al. **Ultra-sensitive molecular MRI of vascular cell adhesion molecule-1 reveals a dynamic inflammatory penumbra after strokes.** *Stroke* 2013;44: 1988–96 CrossRef Medline
63. Han HS, Karabiyikoglu M, Kelly S, et al. **Mild hypothermia inhibits nuclear factor-kappa B translocation in experimental stroke.** *J Cereb Blood Flow Metab* 2003;23:589–98 CrossRef Medline
64. Inamasu J, Suga S, Sato S, et al. **Postischemic hypothermia attenuates apoptotic cell death in transient focal ischemia in rats.** *Acta Neurochir Suppl* 2000;76:525–27 CrossRef Medline
65. Ohmura A, Nakajima W, Ishida A, et al. **Prolonged hypothermia protects neonatal rat brain against hypoxic-ischemia by reducing both apoptosis and necrosis.** *Brain Dev* 2005;27:517–26 CrossRef Medline
66. Wang GJ, Deng HY, Maier CM, et al. **Mild hypothermia reduces ICAM-1 expression, neutrophil infiltration and microglia/monocyte accumulation following experimental stroke.** *Neuroscience* 2002;114:1081–90 CrossRef Medline
67. Haussen DC, Nogueira RG, Elhammady MS, et al. **Infarct growth despite full reperfusion in endovascular therapy for acute ischemic stroke.** *J Neurointerv Surg* 2016;8:117–21 CrossRef Medline
68. Diringer MN, Reaven NL, Funk SE, et al. **Elevated body temperature independently contributes to increased length of stay in neurologic intensive care unit patients.** *Crit Care Med* 2004; 32:1489–95 CrossRef Medline
69. Kilpatrick MM, Lowry DW, Firlik AD, et al. **Hyperthermia in the neurosurgical intensive care unit.** *Neurosurgery* 2000;47:850–55; discussion 855–56 CrossRef Medline

70. Parker DL, Smith V, Sheldon P, et al. **Temperature distribution measurements in two-dimensional NMR imaging.** *Med Phys* 1983; 10:321–25 CrossRef Medline
71. Rieke V, Butts Pauly K. **MR thermometry.** *J Magn Reson Imaging* 2008;27:376–90 CrossRef Medline
72. Kuroda K. **Non-invasive MR thermography using the water proton chemical shift.** *Int J Hyperthermia* 2005;21:547–60 CrossRef Medline
73. Coman D, Trubel HK, Rycyna RE, et al. **Brain temperature and pH measured by (1)H chemical shift imaging of a thulium agent.** *NMR Biomed* 2009;22:229–39 CrossRef Medline
74. Hekmatyar SK, Kerkhoff RM, Pakin SK, et al. **Noninvasive thermometry using hyperfine-shifted MR signals from paramagnetic lanthanide complexes.** *Int J Hyperthermia* 2005;21:561–74 CrossRef Medline
75. Lindner LH, Reinl HM, Schlemmer M, et al. **Paramagnetic thermosensitive liposomes for MR-thermometry.** *Int J Hyperthermia* 2005;21:575–88 CrossRef Medline
76. Dehkharghani S, Mao H, Howell L, et al. **Proton resonance frequency chemical shift thermometry: experimental design and validation toward high-resolution noninvasive temperature monitoring and in vivo experience in a nonhuman primate model of acute ischemic stroke.** *AJNR Am J Neuroradiol* 2015;36:1128–35 CrossRef Medline
77. Hindman J. **Proton resonance shift of water in the gas and liquid states.** *The Journal of Chemical Physics* 1966;44:4582–92 CrossRef
78. Zou C, Tie C, Pan M, et al. **Referenceless MR thermometry-a comparison of five methods.** *Phys Med Biol* 2017;62:1–16 CrossRef Medline
79. Cady EB, Penrice J, Robertson NJ. **Improved reproducibility of MRS regional brain thermometry by "amplitude-weighted combination."** *NMR Biomed* 2011;24:865–72 CrossRef Medline
80. Fleischer CC, Wu J, Qiu D, et al. **The brain thermal response as a potential neuroimaging biomarker of cerebrovascular impairment.** *AJNR Am J Neuroradiol* 2017;38:2044–51 CrossRef Medline
81. Kuroda K, Suzuki Y, Ishihara Y, et al. **Temperature mapping using water proton chemical shift obtained with 3D-MRSI: feasibility in vivo.** *Magn Reson Med* 1996;35:20–29 CrossRef Medline
82. Kuroda K, Oshio K, Chung AH, et al. **Temperature mapping using the water proton chemical shift: a chemical shift selective phase mapping method.** *Magn Reson Med* 1997;38:845–51 CrossRef Medline
83. Ishihara Y, Calderon A, Watanabe H, et al. **A precise and fast temperature mapping using water proton chemical shift.** *Magn Reson Med* 1995;34:814–23 CrossRef Medline
84. Kuroda K, Mulkern RV, Oshio K, et al. **Temperature mapping using the water proton chemical shift: self-referenced method with echo-planar spectroscopic imaging.** *Magn Reson Med* 2000; 43:220–25 CrossRef Medline
85. De Poorter J. **Noninvasive MRI thermometry with the proton resonance frequency method: study of susceptibility effects.** *Magn Reson Med* 1995;34:359–67 CrossRef Medline
86. Dehkharghani S, Wei L, Mao H, et al. **Multivoxel proton spectroscopy for non-invasive MR thermometry: phantom comparison of PRESS and semiLASER-localized chemical shift imaging for temperature monitoring.** In: *Proceedings of the Joint Meeting of the International Society of Magnetic Resonance in Medicine and the European Society of Magnetic Resonance in Medicine and Biology*, Milan, Italy. May 10–16, 2014; 2828
87. Cook DJ, Tymianski M. **Nonhuman primate models of stroke for translational neuroprotection research.** *Neurotherapeutics* 2012;9: 371–79 CrossRef Medline
88. Dehkharghan S, Fleischer CC, Qiu D, et al. *Non-Invasive Brain MR Thermometry in a Nonhuman Primate Model of Acute Ischemic Stroke*, ISMRM Annual Meeting 2017; Honolulu, HI
89. Derdeyn CP, Videen TO, Fritsch SM, et al. **Compensatory mechanisms for chronic cerebral hypoperfusion in patients with carotid occlusion.** *Stroke* 1999;30:1019–24 CrossRef Medline
90. Derdeyn CP, Videen TO, Yundt KD, et al. **Variability of cerebral blood volume and oxygen extraction: stages of cerebral haemodynamic impairment revisited.** *Brain* 2002;125:595–607 CrossRef Medline
91. Powers WJ. **Cerebral hemodynamics in ischemic cerebrovascular disease.** *Ann Neurol* 1991;29:231–40 CrossRef Medline
92. Powers WJ. **Stroke: misery perfusion in cerebrovascular disease—is it important?** *Nat Rev Neurol* 2012;8:479–80 CrossRef Medline
93. Powers WJ, Press GA, Grubb RL Jr, et al. **The effect of hemodynamically significant carotid artery disease on the hemodynamic status of the cerebral circulation.** *Ann Intern Med* 1987;106:27–34 CrossRef Medline
94. Yablonskiy DA, Sukstanskii AL, He X. **Blood oxygenation level-dependent (BOLD)-based techniques for the quantification of brain hemodynamic and metabolic properties: theoretical models and experimental approaches.** *NMR Biomed* 2013;26:963–86 CrossRef Medline
95. Wu J, Dehkharghani S, Nahab F, et al. **Acetazolamide-augmented dynamic BOLD (aczBOLD) imaging for assessing cerebrovascular reactivity in chronic steno-occlusive disease of the anterior circulation: an initial experience.** *Neuroimage Clin* 2017;13:116–22 CrossRef Medline
96. Wu J, Dehkharghani S, Nahab F, et al. **The effects of acetazolamide on the evaluation of cerebral hemodynamics and functional connectivity using blood oxygen level-dependent MR imaging in patients with chronic steno-occlusive disease of the anterior circulation.** *AJNR Am J Neuroradiol* 2017;38:139–45 CrossRef Medline
97. Leatherday C, Dehkharghani S, Nahab F, et al. **Cerebral MR oximetry during acetazolamide augmentation: beyond cerebrovascular reactivity in hemodynamic failure.** *J Magn Reson Imaging* 2019; 50:175–82 CrossRef Medline
98. Christen T, Bolar DS, Zaharchuk G. **Imaging brain oxygenation with MRI using blood oxygenation approaches: methods, validation, and clinical applications.** *AJNR Am J Neuroradiol* 2013;34: 1113–23 CrossRef Medline
99. Atkinson IC, Thulborn KR. **Feasibility of mapping the tissue mass corrected bioscale of cerebral metabolic rate of oxygen consumption using 17-oxygen and 23-sodium MR imaging in a human brain at 9.4 T.** *Neuroimage* 2010;51:723–33 CrossRef Medline
100. Lakshmanan K, Dehkharghani S, Madelin G, et al. **A dual-tuned (17) O/(1) H head array for direct brain oximetry at 3 Tesla.** *Magn Reson Med* 2020;83:1512–18 CrossRef Medline
101. Ishigaki D, Ogasawara K, Yoshioka Y, et al. **Brain temperature measured using proton MR spectroscopy detects cerebral hemodynamic impairment in patients with unilateral chronic major cerebral artery steno-occlusive disease: comparison with positron emission tomography.** *Stroke* 2009;40:3012–16 CrossRef Medline
102. Nanba T, Nishimoto H, Yoshioka Y, et al. **Apparent brain temperature imaging with multi-voxel proton magnetic resonance spectroscopy compared with cerebral blood flow and metabolism imaging on positron emission tomography in patients with unilateral chronic major cerebral artery steno-occlusive disease.** *Neuroradiology* 2017;59:923–35 CrossRef Medline
103. Murakami T, Ogasawara K, Yoshioka Y, et al. **Brain temperature measured by using proton MR spectroscopy predicts cerebral hyperperfusion after carotid endarterectomy.** *Radiology* 2010;256: 924–31 CrossRef Medline
104. Buczek J, Karliński M, Kobayashi A, et al. **Hyperperfusion syndrome after carotid endarterectomy and carotid stenting.** *Cerebrovasc Dis* 2013;35:531–37 CrossRef Medline

The Lateral Ventricles: A Detailed Review of Anatomy, Development, and Anatomic Variations

C.L. Scelsi, T.A. Rahim, J.A. Morris, G.J. Kramer, B.C. Gilbert, and S.E. Forseen

ABSTRACT

SUMMARY: The cerebral ventricles have been studied since the fourth century BC and were originally thought to harbor the soul and higher executive functions. During the infancy of neuroradiology, alterations to the ventricular shape and position on pneumoencephalography and ventriculography were signs of mass effect or volume loss. However, in the current era of high-resolution cross-sectional imaging, variation in ventricular anatomy is more easily detectable and its clinical significance is still being investigated. Interpreting radiologists must be aware of anatomic variations of the ventricular system to prevent mistaking normal variants for pathology. We will review of the anatomy and development of the lateral ventricles and discuss several ventricular variations.

The cerebral ventricles were the center of attention among philosophers, priests, anatomists, and physicians as far back as Aristotle in the fourth century BC.[1] They were originally thought to harbor the soul and "vital" spirits responsible for higher functions. After the influence of Christianity and the Renaissance, the ventricles were conceptualized as 3 cavities where common sense, creative imagination, and memory were individually allocated. It was not until the 16th century that anatomists Andreas Vesalius and Constanzo Varolio identified ventricles as being filled with CSF.[2]

Before the era of cross-sectional imaging, when ventriculography and pneumoencephalography were the only modalities available, variations in ventricular morphology were used as signs of parenchymal volume loss or mass effect.[3,4] Currently, asymmetries and anatomic variations are frequently identified and accepted as normal variations. Although they are not frequently a diagnostic dilemma, imaging interpreters must be aware of these anatomic variants to prevent mistaking them for pathology. In this review, we discuss normal anatomy, ventricular development, and anatomic variations of the lateral ventricles along with a deep look into the investigation of these entities. Pathologic states (ie, hydrocephalus, degenerative disease, traumatic encephalopathy, and so forth) can affect ventricular size and morphology but have been studied extensively and will be left out of this review.

ANATOMY

Lateral Ventricles

The lateral ventricles are paired C-shaped structures comprising a body and atrium along with 3 projections into the frontal, temporal, and occipital lobes, termed "horns." The lateral ventricles communicate with the third ventricle through the interventricular foramina of Monro.[5] Each lateral ventricle has an estimated capacity of 7–10 mL.[6]

The frontal horn (Fig 1) extends anteriorly from the foramina of Monro and communicates with the body of the lateral ventricles posteriorly. The anterior wall and roof are formed by the genu of the corpus callosum, and the floor is formed by the rostrum. The head of the caudate nucleus forms the lateral wall. The columns of the fornix form the inferior portion of the medial wall.[6-8]

The body of the lateral ventricle communicates with the atrium posteriorly from the foramina of Monro to the corpus callosum and psalterium of the fornix, also called the hippocampal commissure. The roof is formed by the body of the corpus callosum, and the floor is formed by the thalamus. The septum pellucidum and body of the fornix form the superior and inferomedial walls, respectively. The lateral wall is formed by the caudate nucleus and thalamus. In the groove between the caudate nucleus and thalamus along the lateral wall sits the stria terminalis, a main outlet pathway of the amygdala and the location of the thalamostriate vein.[9]

The atrium (Fig 2) is a triangular cavity that communicates with the body, temporal horn, and occipital horn. The body and

Received November 12, 2019; accepted after revision January 6, 2020.

From the Departments of Radiology (C.L.S., T.A.R., J.A.M., G.J.K.) and Neuroradiology (B.C.G., S.E.F.), Medical College of Georgia, Augusta, Georgia.

Please address correspondence to Chris L. Scelsi, DO, 1120 15th St, Augusta, GA, 30912; e-mail: cscelsi@augusta.edu

Indicates open access to non-subscribers at www.ajnr.org

http://dx.doi.org/10.3174/ajnr.A6456

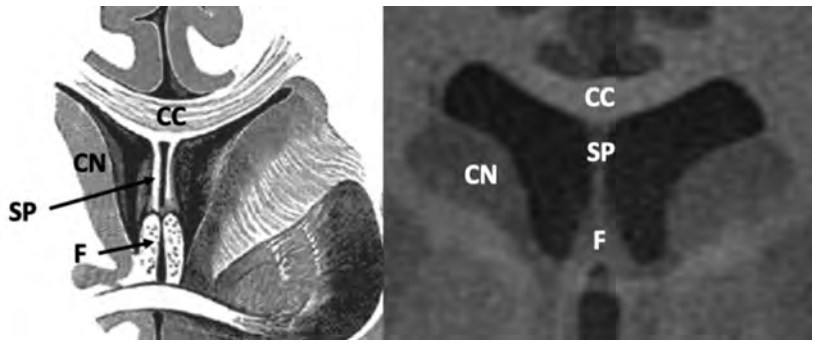

FIG 1. Anatomy of the frontal horns of the lateral ventricles. Coronal T1-weighted MR image from a healthy 22-year-old man. CN indicates caudate nucleus; CC, body of the corpus callosum; F, columns of the fornices; SP, septum pellucidum. Illustration adapted with permission from Gray.[64]

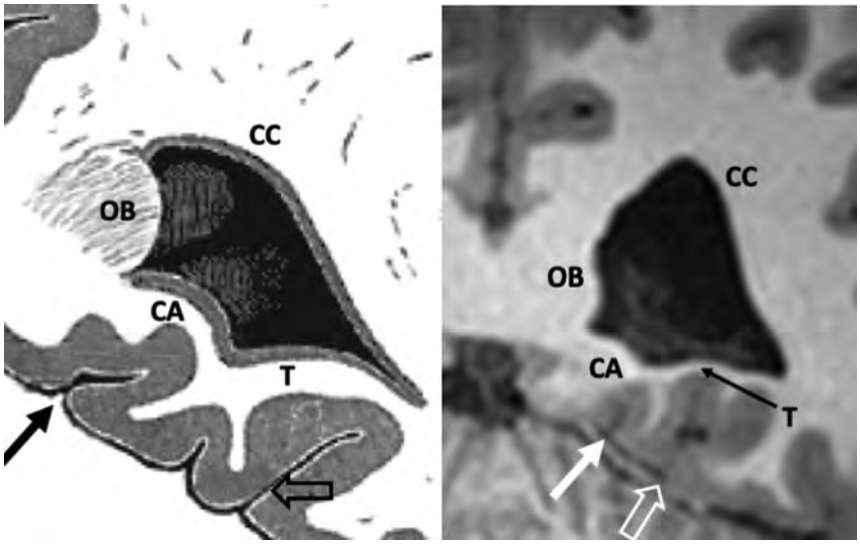

FIG 2. Anatomy of the atrium of the left lateral ventricle. Coronal T1-weighted MR image from a healthy 21-year-old woman. OB indicates occipital bulb containing fibers of forceps major; CA, calcar avis; T, collateral trigone; CC, tapetum of the corpus callosum; *solid arrow*, calcarine sulcus; *open arrow*, collateral sulcus. Illustration adapted with permission from Gray.[65]

splenium of the corpus callosum form the roof. The tapetum, which is a sheetlike bundle of decussating fibers in the splenium of the corpus callosum, arches over the atrium and forms the roof. The tapetum continues laterally and comprises the lateral wall and the caudate nucleus. The floor is created by the collateral trigone, a continuation of the collateral eminence formed by the collateral sulcus. The contour of the medial wall is formed by the calcar avis and bulb of the corpus callosum, which is a bulging created by the forceps major.[5,9] The calcar avis was previously known as the hippocampus minor and represents an indentation formed by the calcarine fissure.[10] When prominent, the calcar avis can mimic hemorrhage on cranial sonography.[11]

The temporal horn is the longest and largest horn, extending anteriorly from the atrium below the thalamus and terminating at the amygdala. The collateral eminence and hippocampus form the floor, which is separated from the hippocampus by a thin layer of white matter called the alveus.[11,12] The roof is created by the thalamus, tail of the caudate nucleus, and tapetum. The striothalamic sulcus separates the caudate tail and thalamus. The tapetum also runs inferiorly to comprise the lateral wall and separates the lateral wall from the optic radiations. The choroidal fissure runs along the medial wall.[12]

The occipital horn curves posteriorly and medially from the atrium and varies in size. The tapetum forms the roof and lateral wall and separates it from the optic radiations.[7,9,11] The collateral trigone forms the floor. Similar to the atrium, the bulb of the corpus callosum and calcar avis form the medial wall.[9]

Choroid Plexus and Choroidal Fissure

The choroid plexus is present within the lateral, third, and fourth ventricles and is the primary source of CSF, producing approximately 500 mL per day.[13,14] Within the lateral ventricles, the choroid plexus runs along a cleft between the fornix and thalamus called the choroidal fissure. The choroidal fissure forms a C-shape extending from the foramina of Monro to its inferior terminal point, which is termed the "inferior choroidal point."[9,15] Within the atria, there is a prominent triangular tuft called the glomus.[15] The tela choroidea is an invagination of the pia mater and ependyma, which gives rise to the choroid plexus within the choroidal fissure and along the roof of the third ventricle.[9,16]

The choroidal fissure is an important neurosurgical structure because it opens up access to the basal cisterns and to structures that would be otherwise inaccessible through an extracerebral route.[9] Recently, excess CSF has been shown to pass through the inferior choroidal point in patients with idiopathic normal pressure hydrocephalus. Its anatomic relationship may explain disproportionate enlargement of the basal cisterns and Sylvian fissures in patients with idiopathic normal pressure hydrocephalus.[17]

DEVELOPMENT

After closure of the neural tube during the fourth week of gestation, the lateral ventricles begin forming from the 2 outpouchings of the telencephalon, a derivative of the prosencephalon.[18,19] The lateral walls of the telencephalon evaginate, and there is rapid growth of the medial basal portion of the cerebral hemispheres called the corpus striatum, which ultimately gives rise to the basal ganglia. This rapid growth shapes the floor and narrows the foramina of Monro (Fig 3).[18,20-22]

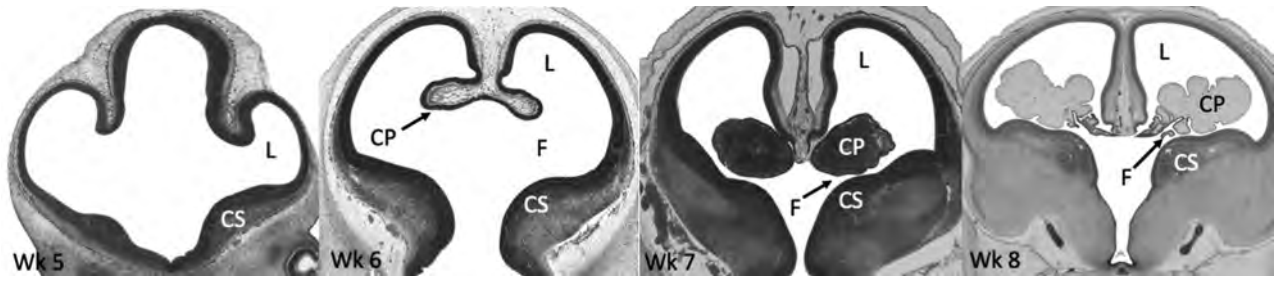

FIG 3. Histologic sections of the telencephalon in the developing embryo from weeks 5 to 8. The lateral ventricles (L) arise as outpouchings from the telencephalon. Rapid growth of the corpus striatum (CS) shapes the floor of the lateral ventricles and narrows the foramina of Monro (F). The primitive choroid plexus (CP) comprises a large portion of the ventricular cavity by the eighth week. Also note that the lateral ventricles occupy a large majority of the cerebral hemisphere at 8 weeks. Images courtesy of Dr John Cork, PhD, Department of Cell Biology and Anatomy at Louisiana State University Health Sciences Center and the Virtual Human Embryo Project. Images used were the following: Carnegie Stage 17, section 410; Carnegie stage 18, section 302; Carnegie stage 20, section 131; Carnegie stage 23, section 50. https://www.ehd.org/virtual-human-embryo.

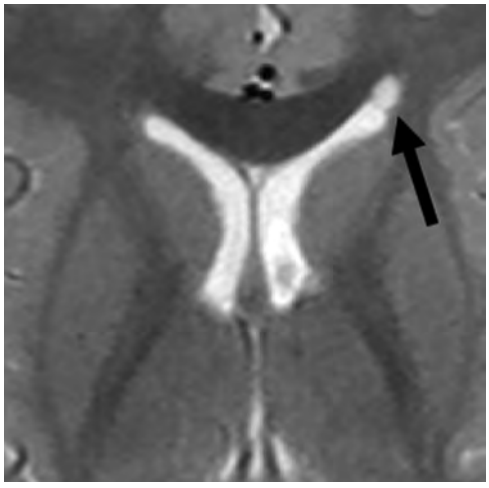

FIG 4. Coarctation of the frontal horn. Axial T2-weighted MR image from a 3-year-old boy showing coarctation of the left frontal horn with connatal cyst formation (*black arrow*).

During the sixth week, the foramina of Monro begins to narrow (Fig 3), and the choroidal fissure forms.[20,21] By the eighth week, further growth of the corpus striatum forms the C-shaped appearance of the lateral ventricles. The frontal and temporal horns are now well-defined, and the choroid plexus nearly fills the entirety of the lateral ventricles (Fig 3).[21]

At the end of the first trimester, the lateral ventricles continue to expand rapidly, occupying a large majority of the cerebral hemispheres, outpacing parenchymal growth.[23] Transient occlusion of the central canal of the spinal cord may facilitate this rapid increase in ventricle size.[24] Parenchymal growth hastens during the second trimester, and by 21 weeks, the frontal, temporal, and occipital horns are well-defined. By 31 weeks, the lateral ventricles resemble the adultlike appearance.[25,26]

ANATOMIC VARIANTS

Coarctation

Coarctation (Fig 4) refers to the apposition or fusion of 2 ventricular walls, resulting in partial or complete obliteration of the lumen.[27] When focal, coarctation can isolate a portion of the ventricle, creating multiple small rosettes or an ependymal-lined cyst, commonly referred to as a connatal cyst (Fig 4).[28,29] The incidence of unilateral or bilateral frontal horn coarctation has been reported to be between 0.38% and 6.0%, with a majority of studies reporting incidences below 1%.[30-32] Coarctation of the occipital horns is much more common, with a reported incidence of 21.3%.[33]

Coarctation is thought to occur at sites where opposing walls are in close proximity as is in the case with the ventricular horns, but it also has been described as occurring in the body.[28,31,33] The exact mechanism of ventricular coarctation is currently unknown. Bates and Netsky[28] described intermingling of subependymal glial cells at sites where the ventricular wall lacks ependyma. Davidoff[27] reported similar findings in cases of congenital aqueductal stenosis.[34] No histologic evidence of inflammation or gliosis has been associated with coarctation, suggesting that it is developmental in nature.[27,28]

Ventricular coarctation is accepted as benign and is associated with normal neurodevelopmental outcomes when occurring in isolation.[29,35] When identified in neonates, coarctation often resolves spontaneously by 2 months of age.[36] However, it can commonly be mistaken for similar-appearing subependymal cysts or periventricular leukomalacia, which can be associated with less favorable outcomes.[36-38] Identifying the location of the cyst with respect to the superolateral angles of the lateral ventricles, which are formed by the most superior and lateral margins, is a key distinguishing feature. Connatal cysts (Fig 5*A*) occur anterior to the foramina of Monro and at the level of the angles. Periventricular leukomalacia (Fig 5*B*) should be considered when cyst formation is located above the angles, and subependymal cysts (Fig 5*C*) should be considered when it is located below the angles and at the caudothalamic groove.[11,39,40]

Asymmetric Size and Morphology

Size asymmetry between the lateral ventricles (Fig 6) occurs in 5%–12% of healthy individuals.[41] In healthy patients, some studies have found that either the right or left lateral ventricle

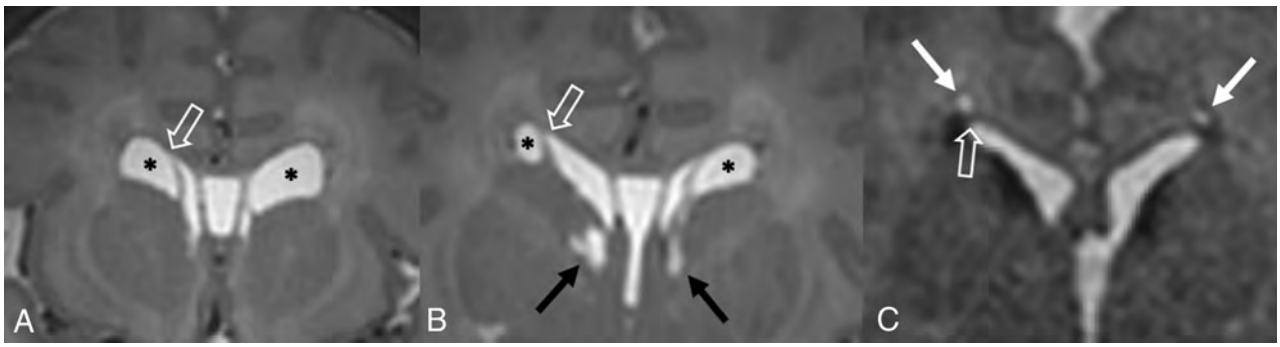

FIG 5. Periventricular cysts. *A*, Coronal T2-weighted MR image from a 1-week-old girl with a history of germinal matrix hemorrhage demonstrating coarctation of the bilateral frontal horns with connatal cyst formation (*asterisks*). Note that these cysts are at the level of the superolateral angles of the lateral ventricle (*open arrow*). *B*, Coronal T2-weighted MR image from the same patient demonstrating subependymal cysts (*black arrows*) located near the caudothalamic groove below the level of the superolateral angles (*open arrow*). Additional connatal cysts are present (*asterisks*). *C*, Coronal T2-weighted MR image from a 1-month-old boy with a history of germinal matrix hemorrhage and peripartum hypoxia demonstrating small bilateral periventricular cysts (*white arrows*) located above the level of the superolateral angles (*open arrow*). This appearance is consistent with cystic periventricular leukomalacia.

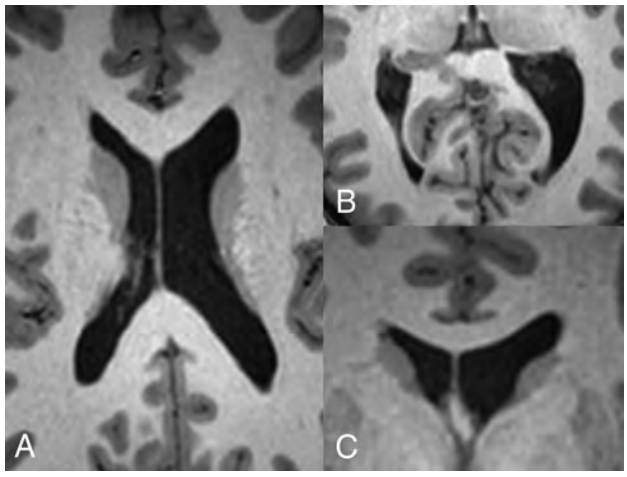

FIG 6. Variations in lateral ventricular size and shape in a healthy 16-year-old girl. Axial T1-weighted MR images through the bodies of the lateral ventricles (*A*) and occipital horns (*B*) demonstrate a larger left lateral ventricle. Note the differences in morphology of the occipital horns. *C*, Coronal T1-weighted MR image through the frontal horns demonstrates relative enlargement of the left lateral ventricle.

was consistently larger than the other,[26,42-47] while other studies have reported no significant difference in size between the two.[48,49] The association between lateral ventricle asymmetry, handedness, and sex is also controversial, with multiple studies showing a significant difference in lateral ventricle size in right- versus left-handed individuals and males versus females.[45,49,50] Other studies have shown no significant difference in these populations.[41,43,47,48]

The shape of the lateral ventricles has also been investigated extensively, with multiple studies classifying various lateral ventricular morphologies and rotational differences.[42,51-53] The occipital horn of the lateral ventricle seems to be the most inconsistent portion, which can range from being completely absent to being present in variable lengths (Fig 6*B*).[33,48,54] The temporal horn, especially the anterior tip, is also variable in shape but to a lesser extent compared with the occipital horn.[55]

The clinical significance of varying lateral ventricular asymmetries is currently controversial. On the basis of the association of ventricular morphologic abnormalities due to underlying white matter damage, it has been suggested that mild ventricular asymmetries may be a sign of subtle white matter or deep gray matter abnormalities that may not be seen on imaging. Paquette et al[51] proposed that differences in the left lateral ventricle in preterm neonates may be related to subcortical white matter alterations, suggesting subcortical vulnerability to preterm birth.[42] Sadan et al[56] studied fetuses with normal-sized-but-asymmetric ventricles (defined as width of < 10 mm and a difference in width of > 2 mm) and demonstrated increased behavioral abnormalities in these children.

To our knowledge, no definitive large-scale investigation of variations in lateral ventricle morphology and long-term neurologic outcome has been performed. Therefore, it is generally accepted that small volumetric or morphologic differences between normal-sized lateral ventricles are likely of no clinical significance and have no effect on long-term neurodevelopmental outcome.[3,41,44,48,52,57-59] However, interpreting radiologists should evaluate adjacent parenchymal disease, an intraventricular lesion, or obstruction at the foramina of Monro before dismissing ventricular asymmetry as a anormal variant (Fig 7).[60]

Cavum Septi Pellucidi, Cavum Vergae, and Cavum Veli Interpositi

The septum pellucidum forms the medial walls of the lateral ventricles and consists of 2 thin laminae, which normally fuse shortly after birth. If the laminae fail to fuse, the potential space can expand with CSF, termed "cavum septi pellucidi." If there is an extension posterior to a vertical plane created by the columns of the fornix, the term cavum vergae (Fig 8) is used.[6,39] The clinical significance of cavum septi pellucidi and cavum vergae is unknown, and they are considered a normal variant.[39] However, studies have suggested that their presence

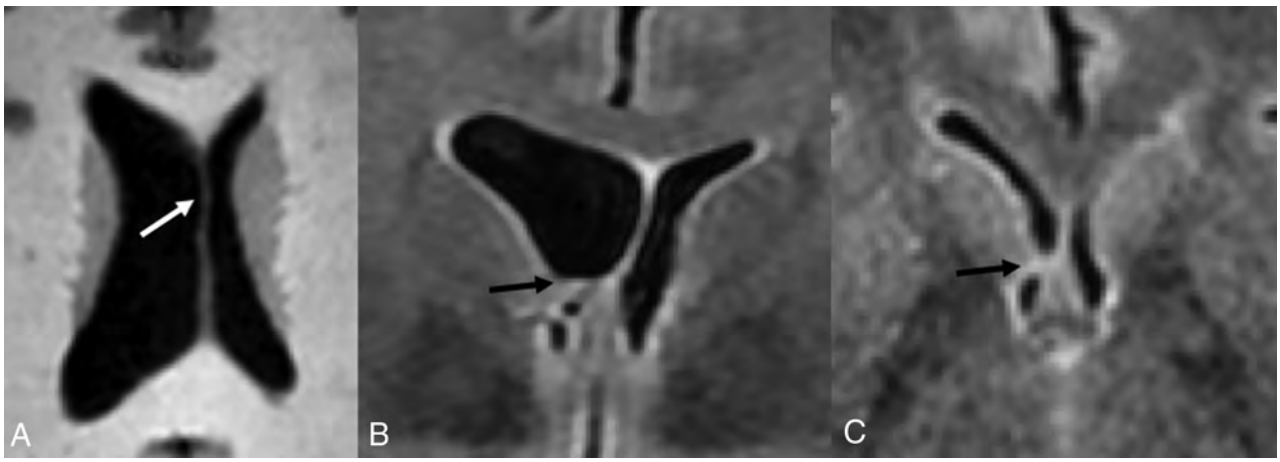

FIG 7. Lateral ventricular asymmetry in a 56-year-old woman referred from a separate institution for the management of a suspected intraventricular mass. *A*, Axial T1-weighted MR images demonstrate asymmetric enlargement of the right lateral ventricle. There is mild bulging of the septum pellucidum (*white arrow*), which prompted careful evaluation of the lateral ventricular outflow. Coronal (*B*) and Axial (*C*) T2-weighted FLAIR images show no intraventricular mass but rather coaptation of the ependyma covering the caudate nucleus and fornix (*black arrow*). These imaging findings causes partial outflow obstruction and unilateral hydrocephalus. This remained stable on multiple subsequent follow-up MRIs and was favored to represent coarctation versus scar.

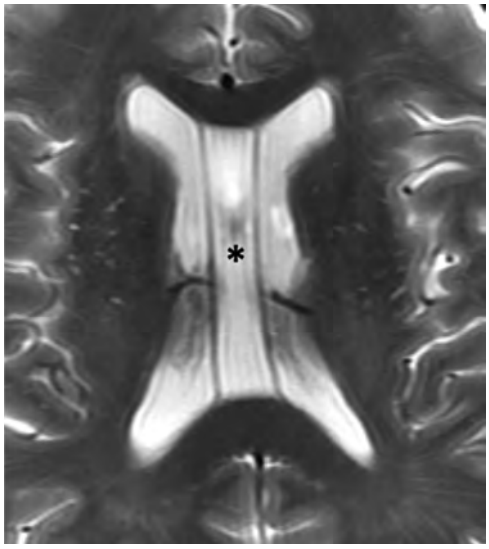

FIG 8. Cavum septi pellucidi and vergae. Axial T2-weighted MR image of a 67-year-old man demonstrating expansion of the cavum septi, consistent with cavum septi pellucidi (*asterisk*). There is extension posterior to the vertical plane of the columns of the fornix (not shown here) consistent with coexisting cavum vergae.

is associated with cognitive dysfunction in patients with prior head trauma.[61] Also, the size and frequency of cavum septi pellucidi and cavum vergae were greater in patients with schizophrenia, alcoholism, and prior head trauma.[62] The cavum septi pellucidi is a normal finding in fetuses between 18 and 37 weeks of gestation, and its absence is associated with multiple significant CNS abnormalities.[63]

The cavum veli interpositi results from expansion of the cistern of the velum interpositum, which is located above the third ventricle and below the columns of the fornices. When large, it may mimic a cyst. The cavum veli interpositi is accepted as a normal variant, and no association with cognitive dysfunction or neuropsychiatric disorders has been reported.[39]

Choroid Plexus Cysts

Choroid plexus cysts may be acquired or congenital. The acquired cysts are common in adults and are formed by accumulation of xanthogranulomatous debris; hence, these are more frequently referred to as xanthogranulomas. Xanthogranulomas are usually bilateral and demonstrate T1 and T2 signal characteristics similar to those of CSF but may not be completely suppressed on FLAIR. They are also typically hyperintense on DWI, with isointense signal on ADC (Fig 9*A*).[5,6]

Choroid plexus cysts are typically found incidentally, mainly in the glomera, and they are usually asymptomatic. In the antenatal period, choroid plexus cysts may be associated with chromosomal abnormalities when large or when present with other CNS abnormalities.[39]

An important differential consideration is a choroidal metastasis, which may mimic xanthogranulomas, especially when cystic. However, the typical bilateral occurrence of xanthogranulomas and lack of internal enhancement can help differentiate the two (Fig 9*B*). An ependymal cyst is also a differential consideration, but these typically more closely follow CSF signal. They also arise outside the choroid plexus and displace the glomera, unlike xanthogranulomas.[5]

CONCLUSIONS

Isolated anatomic variations of the lateral ventricles are very common in healthy individuals. In this article, we describe several anatomic variants of the lateral ventricles and review multiple studies of these entities. We also review the anatomy and embryology of the lateral ventricles. These variations are often mentally noted while interpreting studies, and because they are generally accepted as normal and of no clinical significance to the patient, they are infrequently mentioned in radiology reports. Although

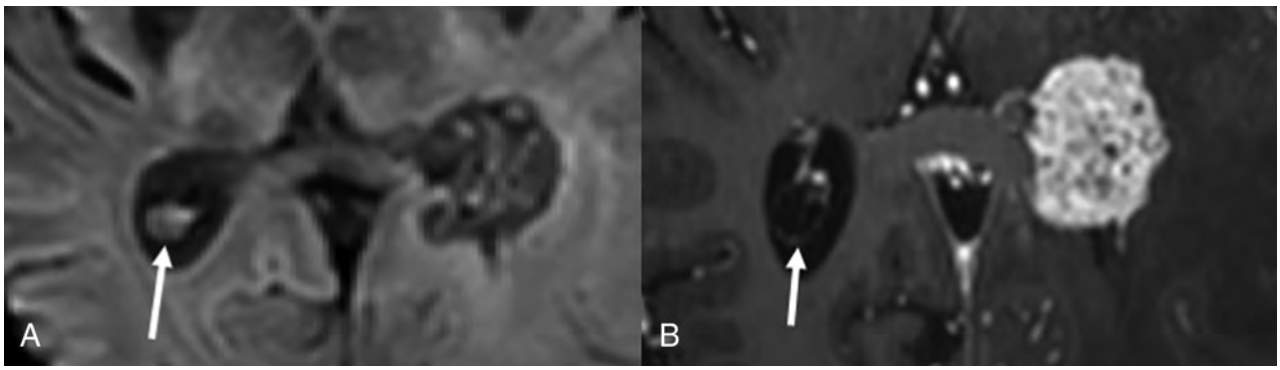

FIG 9. Xanthrogranuloma and choroid plexus metastasis. Axial DWI (*A*) and postgadolinium T1-weighted (*B*) MR images of a 56-year-old woman with metastatic renal cell carcinoma. Images demonstrate a cystic lesion centered within the right choroid plexus glomus, which demonstrates increased DWI signal but no central enhancement (*arrow*), consistent with a xanthogranuloma. This finding is in contrast to the solidly-enhancing lesion centered within the left glomus, consistent with a hypervascular metastasis.

identification of these is rarely a diagnostic dilemma, interpreting radiologists should be aware of these entities because some cases may mimic pathology.

REFERENCES

1. Engelhardt E. **Cerebral localization of the mind and higher functions: the beginnings.** *Dement Neuropsychol* 2018;12:321–25 CrossRef Medline
2. Schiller F. **The cerebral ventricles: from soul to sink.** *Arch Neurol* 1997;54:1158–62 CrossRef Medline
3. Shapiro R, Galloway SJ, Shapiro MD. **Minimal asymmetry of the brain: a normal variant.** *AJR Am J Roentgenol* 1986;147:753–56 CrossRef Medline
4. Hoeffner EG, Mukherji SK, Srinivasan A, et al. **Neuroradiology back to the future: brain imaging.** *AJNR Am J Neuroradiol* 2012;33:5–11 CrossRef Medline
5. Osborn AG, Hedlund GL, Salzman KL. *Osborn's Brain*. Philadelphia: Elsevier; 2018:1119–25
6. Stratchko L, Filatova I, Agarwal A, et al. **The ventricular system of the brain: anatomy and normal variations.** *Semin Ultrasound CT MR* 2016;37:72–83 CrossRef Medline
7. Snell RS. *Clinical Neuroanatomy*. Baltimore: Lippincott Williams & Wilkins; 2001:444–56
8. Mortazavi MM, Adeeb N, Griessenauer CJ, et al. **The ventricular system of the brain: a comprehensive review of its history, anatomy, histology, embryology and surgical considerations.** *Childs Nerv Syst* 2014;30:19–35 CrossRef Medline
9. Rhoton AL. **The lateral and third ventricles.** *Neurosurgery* 2002;51: S207–71 Medline
10. Owen CM, Howard A, Binder DK. **Hippocampus minor, calcar avis and the Huxley-Owen debate.** *Neurosurgery* 2009;65:1098–1105 CrossRef Medline
11. Enríquez G, Correa F, Lucaya J, et al. **Potential pitfalls in cranial sonography.** *Pediatr Radiol* 2003;33:110–17 CrossRef Medline
12. Singh I. *Textbook of Human Neuroanatomy*. New Delhi: Jaypee Brothers Medical Publishers; 2018:228–38
13. Mortazavi MM, Griessenauer CJ, Adeeb N, et al. **The choroid plexus: a comprehensive review of its history, anatomy, function, histology, embryology and surgical considerations.** *Childs Nerv Syst* 2014; 30:205–14 CrossRef Medline
14. Brinker T, Stopa E, Morrison J, et al. **A new look at cerebrospinal fluid circulation.** *Fluids Barriers CNS* 2014;11:10 CrossRef Medline
15. Holodny AI, George AE, Golomb J, et al. **The perihippocampal fissures: normal anatomy and disease states.** *Radiographics* 1998;18: 653–65 CrossRef Medline
16. Zagorska-Swiezy K, Litwin JA, Gorczyca J, et al. **Arterial supply and venous drainage of the choroid plexus of the human lateral ventricle in the prenatal period as revealed by vascular corrosion casts and SEM.** *Folia Morphol (Warsz)* 2008;67:209–13 Medline
17. Yamada S, Ishikawa M, Iwamuro Y, et al. **Choroidal fissure acts as an overflow device in cerebrospinal fluid drainage: morphological comparison between idiopathic and secondary normal-pressure hydrocephalus.** *Sci Rep* 2016;6:39070 CrossRef Medline
18. Sadler TW. *Langman's Medical Embryology*. Baltimore: Lippincott Williams & Wilkins; 2012:287–308
19. O'Rahilly R, Müller F. *Human Embryology &Teratology*. New York: Wiley-Liss; 2001: 405–29
20. Moore KL, Persaud T. *The Developing Human: Clinically Oriented Embryology*. Philadelphia: W.B. Saunders; 1998:451–77
21. O'Rahilly R, Müller F. **Ventricular system and choroid plexuses of the human brain during the embryonic period proper.** *Am J Anat* 1990;189:285–302 CrossRef Medline
22. Yamada S, Samtani RR, Lee ES, et al. **Developmental atlas of the early first trimester human embryo.** *Dev Dyn* 2010;239:1585–95 CrossRef Medline
23. Lowery LA, Sive H. **Totally tubular: the mystery behind function and origin of the brain ventricular system.** *Bioessays* 2009;31:446–58 CrossRef Medline
24. Desmond ME. **Description of the occlusion of the spinal cord lumen in early human embryos.** *Anat Rec* 1982;204:89–93 CrossRef Medline
25. Kinoshita Y, Okudera T, Tsuru E, et al. **Volumetric analysis of the germinal matrix and lateral ventricles performed using MR images of postmortem fetuses.** *AJNR Am J Neuroradiol* 2001;22:382–88 Medline
26. Li Z, Xu F, Zhang Z, et al. **Morphologic evolution and coordinated development of the fetal lateral ventricles in the second and third trimesters.** *AJNR Am J Neuroradiol* 2019;40:718–25 CrossRef Medline
27. Davidoff LM. **Coarctation of the walls of the lateral angles of the lateral cerebral ventricles.** *J Neurosurg* 1946;3:250–56 CrossRef Medline
28. Bates JI, Netsky MG. **Developmental anomalies of the horns of the lateral ventricles.** *J Neuropathol Exp Neurol* 1955;14:316–25 CrossRef Medline
29. Cooper S, Bar-Yosef O, Berkenstadt M, et al. **Prenatal evaluation, imaging features, and neurodevelopmental outcome of prenatally diagnosed periventricular pseudocysts.** *AJNR Am J Neuroradiol* 2016;37:2382–88 CrossRef Medline
30. Chang CL, Chiu NC, Ho CS, et al. **Frontal horn cysts in normal neonates.** *Brain Dev* 2006;28:426–30 CrossRef Medline
31. Sener RN. **MRI and asymptomatic coarctation of the frontal lateral ventricle horn.** *J Neuroradiol* 1997;24:163–67 Medline

32. Pal BR, Preston PR, Morgan MEI, et al. **Frontal horn thin walled cysts in preterm neonates are benign.** *Arch Dis Child Fetal Neonatal Ed* 2001;85:F187–93 CrossRef Medline
33. Hori A, Bardosi A, Tsuboi K, et al. **Accessory cerebral ventricle of the occipital lobe: morphogenesis and clinical and pathological appearance.** *J Neurosurg* 1984;61:767–71 CrossRef Medline
34. Beckett RS, Netsky MG, Zimmerman HM. **Developmental stenosis of the aqueduct of Sylvius.** *Am J Pathol* 1950;26:755–87 Medline
35. Unger S, Salem S, Wylie L, et al. **Newborn frontal horn cysts: cause for concern?** *J Perinatol* 2011;31:98–103 CrossRef Medline
36. Sun RL, Tekes A, Golden WC, et al. **Connatal cyst in a preterm twin infant with maternal comorbidities.** *Pediatr Neurol* 2014;51:444–47 CrossRef Medline
37. Rosenfeld DL, Schonfeld SM, Underberg-Davis S. **Coarctation of the lateral ventricles: an alternative explanation for subependymal pseudocysts.** *Pediatr Radiol* 1997;27:895–97 CrossRef Medline
38. Lu JH, Emons D, Kowalewski S. **Connatal periventricular pseudocysts in the neonate.** *Pediatr Radiol* 1992;22:55–58 CrossRef Medline
39. Epelman M, Daneman A, Blaser S, et al. **Differential diagnosis of intracranial cystic lesions at head US: correlation with CT and MR imaging.** *Radiographics* 2006;26:173–96 CrossRef Medline
40. Fickenscher K, Bailey Z, Saettele M, et al. **Pediatric cranial ultrasound: techniques, variants and pitfalls.** In: Bright P, ed. *Neuroimaging: Methods*. London: IntechOpen; 2012:217–32
41. Kiroğlu Y, Karabulut N, Oncel C, et al. **Cerebral lateral ventricular asymmetry on CT: how much asymmetry is representing pathology?** *Surg Radiol Anat* 2008;30:249–55 CrossRef Medline
42. Trimarchi F, Bramanti P, Marino S, et al. **MRI 3D lateral cerebral ventricles in living humans: morphological and morphometrical age-, gender-related preliminary study.** *Anat Sci Int* 2013;88:61–69 CrossRef Medline
43. Zipursky RB, Lim KO, Pfefferbaum A. **Volumetric assessment of cerebral asymmetry from CT scans.** *Psychiatry Res* 1990;35:71–89 CrossRef Medline
44. Ichihashi K, Iino M, Eguchi Y, et al. **Difference between left and right lateral ventricular sizes in neonates.** *Early Hum Dev* 2002; 68:55–64 CrossRef Medline
45. Lu Z, He J, Yu Y, et al. **Measurement of lateral ventricle volume of normal infant based on magnetic resonance imaging.** *Chinese Neurosurg Journal* 2019;5 CrossRef
46. Brouwer MJ, de Vries LS, Groenendaal F, et al. **New reference values for the neonatal cerebral ventricles.** *Radiology* 2012;262:224–33 CrossRef Medline
47. Allen JS, Damasio H, Grabowski TJ. **Normal neuroanatomical variation in the human brain: an MRI-volumetric study.** *Am J Phys Anthropol* 2002;118:341–58 CrossRef Medline
48. Tubbs RS, Shoja M, Loukas M. *Bergman's Comprehensive Encyclopedia of Human Anatomic Variation*. Hoboken: Wiley Blackwell; 2016: 943–53
49. Erdogan AR, Dane S, Aydin MD, et al. **Sex and handedness differences in size of cerebral ventricles of normal subjects.** *Int J Neurosci* 2004;114:67–73 CrossRef Medline
50. McRae DL, Branch CL, Milner B. **The occipital horns and cerebral dominance.** *Neurology* 1968;18(1 Pt 1):95–98 Medline
51. Paquette N, Shi J, Wang Y, et al. **Ventricular shape and relative position abnormalities in preterm neonates.** *Neuroimage Clin* 2017;15: 483–43 CrossRef Medline
52. Torkildsen A. **The gross anatomy of the lateral ventricles.** *J Anat* 1934;68:480–91 Medline
53. Shen EY, Huang FY. **Sonographic findings of ventricular asymmetry in neonatal brain.** *Arch Dis Child* 1989;64:730–44 CrossRef Medline
54. Vandewalle G, Beuls E, Vanormelingen L, et al. **Accessory intraventricular prominence of the occipital horn of the lateral ventricle.** *J Neurosurg* 2003;99:151–55 Medline
55. Bronen RA, Cheung G. **MRI of the temporal lobe: normal variations, with special reference toward epilepsy.** *Magn Reson Imaging* 1991;9:501–07 CrossRef Medline
56. Sadan S, Malinger G, Schweiger A, et al. **Neuropsychological outcome of children with asymmetric ventricles or unilateral mild ventriculomegaly identified in utero.** *BJOG* 2007;114:596–602 CrossRef Medline
57. Cha S, George AE. **How much asymmetry should be considered normal variation or within normal range in asymmetrical frontal horns of the lateral ventricles noted during CT brains scans without evidence of midline shift or any other significant lesion?** *AJR Am J Roentgenol* 2002;178:240 CrossRef Medline
58. Achiron R, Yagel S, Rotstein Z, et al. **Cerebral lateral ventricular asymmetry: is this a normal ultrasonographic finding in the fetal brain?** *Obstet Gynecol* 1997;89:233–37 CrossRef Medline
59. Meyer R, Bar-Yosef O, Barzilay E, et al. **Neurodevelopmental outcome of fetal isolated ventricular asymmetry without dilation: a cohort study.** *Ultrasound Obstet Gynecol* 2018;52:467–72 CrossRef Medline
60. Pfeiffer G, Friede RL. **Unilateral hydrocephalus from early developmental occlusion of one foramen of Monro.** *Acta Neuropathol* 1984; 64:75–77 CrossRef Medline
61. Lee JK, Wu J, Bullen J, et al. **Association of cavum septum pellucidum and cavum vergae with cognition, mood, and brain volumes in professional fighters.** *JAMA Neurol* 2019 Sep 9. [Epub ahead of print] CrossRef Medline
62. Filipovic B, Prostran M, Ilankovic N, et al. **Predictive potential of cavum septi pellucidi (CSP) in schizophrenics, alcoholics and persons with past head trauma.** *Eur Arch Psychiatry Clin Neurosci* 2004;254:228–30 CrossRef Medline
63. Hosseinzadeh K, Luo J, Borhani A, et al. **Non-visualisation of cavum septi pellucidi: implication in prenatal diagnosis?** *Insights Imaging* 2013;4:357–67 CrossRef Medline
64. Gray H. *Anatomy of the Human Body*. New York: Lea and Fibiger; 1918: plate 744
65. Gray H. *Anatomy of the Human Body*. New York: Lea and Fibiger; 1918: plate 738

Polymorphous Low-Grade Neuroepithelial Tumor of the Young as a Partially Calcified Intra-Axial Mass in an Adult

J.C. Benson, D. Summerfield, C. Carr, P. Cogswell, S. Messina, J.V. Gompel, and K. Welker

ABSTRACT

SUMMARY: Polymorphous low-grade neuroepithelial tumors of the young (PLNTYs) are recently described CNS tumors. Classically, PLNTYs are epileptogenic and are a subtype of a heterogeneous group of low-grade neuroepithelial tumors that cause refractory epilepsy, such as angiocentric gliomas, oligodendrogliomas, gangliogliomas, and pleomorphic xanthoastrocytomas. Although they are a relatively new entity, a number of imaging and histologic characteristics of PLNTYs are already known. We present the imaging and pathologic findings of such a tumor as well as the surgical approach and clinical management.

ABBREVIATIONS: LGNT = low-grade neuroepithelial tumor; PLNTY = polymorphous low-grade neuroepithelial tumor of the young

A 44-year-old left-handed woman with a history of depression and bipolar 1 disorder presented to our institution for suicidal ideation. She reported that her depressive symptoms had substantially worsened during the past year, and she had recently developed intermittent episodes of emotional lability, with sudden feelings of irritability and rage. In addition, she reported approximately 5 recent episodes of extreme fatigue in which she would fall asleep and be unarousable for hours, as well as shorter-duration spells characterized by facial and body paresthesias. The patient was admitted for psychiatric care and underwent neuroimaging to rule out a structural cause for her symptoms.

Imaging

An initial noncontrast head CT showed a partially calcified intra-axial mass in the left temporal lobe (Fig 1). MR imaging confirmed the presence of the lesion, which demonstrated heterogeneous signal, intralesional calcifications, and cystic components. Faint T1 hyperintensity was seen within the tumor, while other areas demonstrated minimal enhancement. Punctate areas of minimal intralesional restricted diffusion were present. Focal areas of elevated relative CBV were noted within the tumor on DSC perfusion imaging. A mild associated mass effect was seen, with effacement of the adjacent left lateral ventricle and expansion of an overlying left temporal lobe gyrus. However, there was no midline shift or herniation.

Preoperative imaging was completed on a 7T MR imaging scanner to optimize fMRI and DTI. On this examination, signal in the cystic areas was hypointense to CSF on T2-weighted images (Fig 2), which was thought to represent proteinaceous fluid within this region, particularly given its signal heterogeneity.

Initial imaging raised concern for an oligodendroglioma, though the distinct tumor borders and dense central calcifications were thought to be atypical. A ganglioglioma and dysembryoplastic neuroepithelial tumor were also considered, though these are usually cortically based and have fainter internal calcifications.

Preoperative language fMRI was predominantly used to establish the patient's hemispheric language dominance; because of the tumor location, left-hemispheric language dominance would have necessitated an awake resection with electrocortical stimulation mapping to prevent a postoperative language deficit. The patient performed 5 different fMRI language tasks in the scanner (Fig 3). The derived statistical maps demonstrated strong right-hemispheric language dominance for 3 expressive language–related activation sites (Broca area, dorsolateral prefrontal cortex, presupplementary motor area). Similarly, there was strong right-hemispheric language dominance for 3 receptive language sites (Wernicke area, Geschwind area, and visual word form area). The patient was consequently determined to be globally right-hemispheric-dominant for language, and intraoperative language mapping was unnecessary. Additionally, the patient's right-hemispheric dominance

Received December 5, 2019; accepted after revision February 13, 2020.

From the Departments of Radiology (J.C.B., C.C., P.C., S.M., K.W.), Pathology (D.S.), and Neurosurgery (J.V.G.), Mayo Clinic, Rochester, Minnesota.

Please address correspondence to John C. Benson, MD, Department of Radiology, Mayo Clinic, 200 1st St SW, Rochester MN 55905; e-mail: benson.john3@mayo.edu

http://dx.doi.org/10.3174/ajnr.A6500

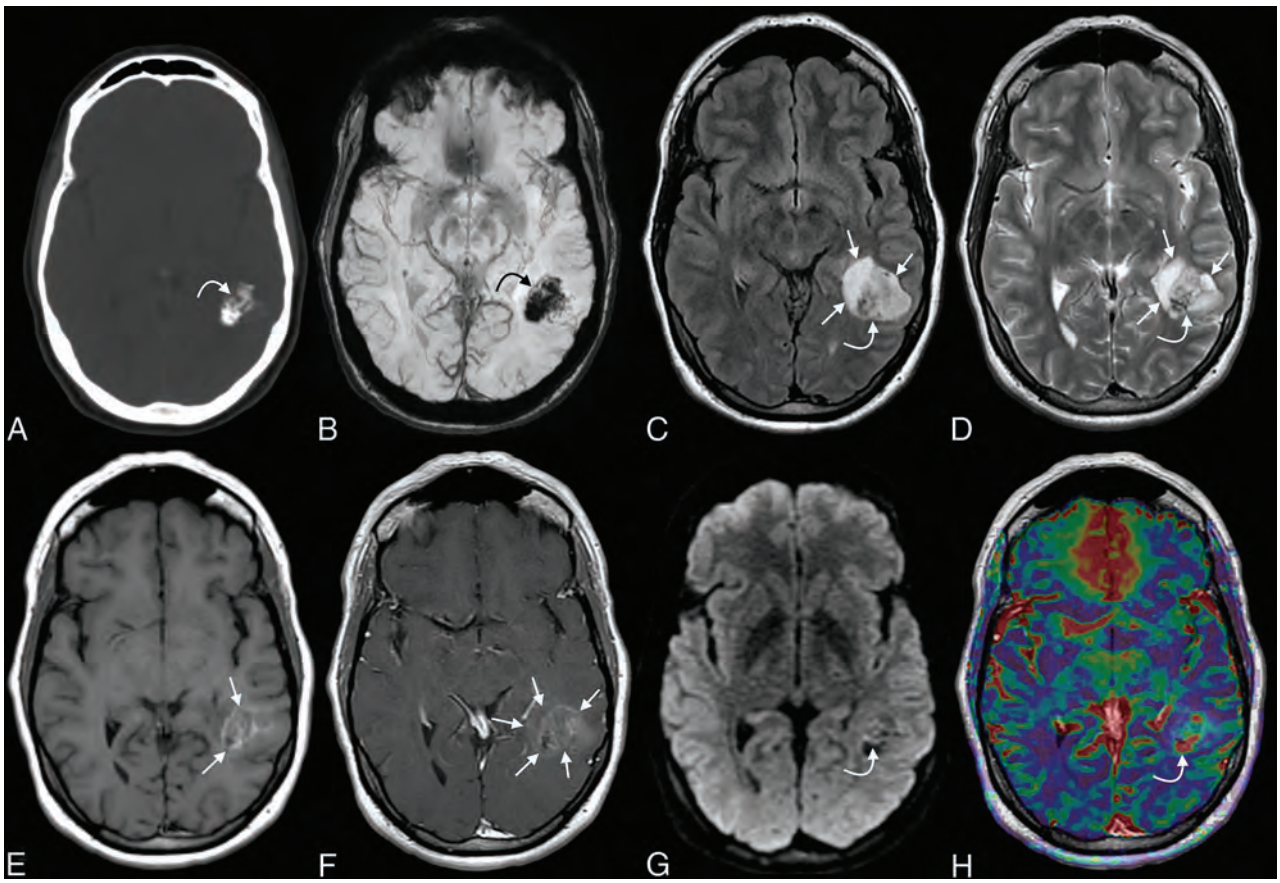

FIG 1. Initial CT and 1.5T MR imaging. Axial CT (*A*) image shows a sharply delineated mass within the left temporal lobe with dense intralesional calcifications, with blooming signal on the corresponding SWI (*B*) (*curved arrows* in *A* and *B*). Heterogeneous signal was noted within the mass on both FLAIR (*C*) and T2WI (*D*) (*curved arrows* on *C* and *D*). Some peripheral areas appeared cystic (*straight arrows, C* and *D*). No substantial surrounding vasogenic edema was observed. A mild associated mass effect was observed, including partial effacement of the left lateral ventricle. Faint T1-hyperintense signal was noted in the central components of the tumor (*straight arrows*, *E*), while a greater extent of the mass demonstrated mild enhancement (*straight arrows*, *F*). A few tiny foci of mildly restricted diffusion were observed centrally (*curved arrow*, *G*), which corresponded with low-intensity signal on ADC images (not shown), though these may have been artifactual because no high-grade features were seen on pathology. Some of the solid-appearing components demonstrated elevated relative CBV (*curved arrow*, *H*).

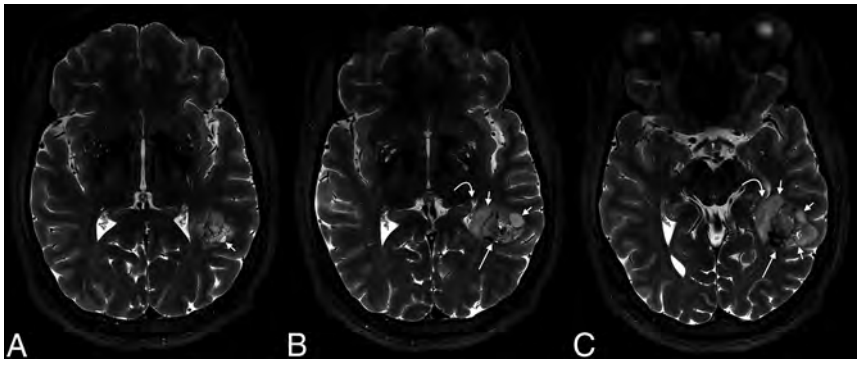

FIG 2. 7T MR imaging demonstrates internal characteristics of the mass on T2WI. From left to right (*A–C*), heterogeneous solid material is seen centrally (*long straight arrows*), while cystic components are located peripherally (*short straight arrows*). Fluid within the cysts is heterogeneous, but typically hypointense to CSF. A mild associated mass effect is seen, including partial effacement of the left lateral ventricle (*curved arrows*).

suggested that the tumor may have been long-standing because its left-sided location may have prevented it from being symptomatic.

Although marked intratumoral perfusion may result in arteriovenous shunting and hence confound fMRI blood oxygen level–dependent images, the intralesional relative CBV within this tumor was considered too minor to have such an effect. Thus, the determination of global right-hemisphere dominance was based solely on the fMRI findings.

The patient underwent gross total resection of the tumor approximately 3 months after presentation.

Operative Report

The patient underwent resection of the mass via a left temporal craniotomy. The surgeons elected to approach the tumor through a corticectomy of the left middle temporal gyrus, which was the shortest route to the tumor given the reassuring fMRI data. Intraoperative evaluation of the tumor demonstrated a hemorrhagic lesion. The tumor was

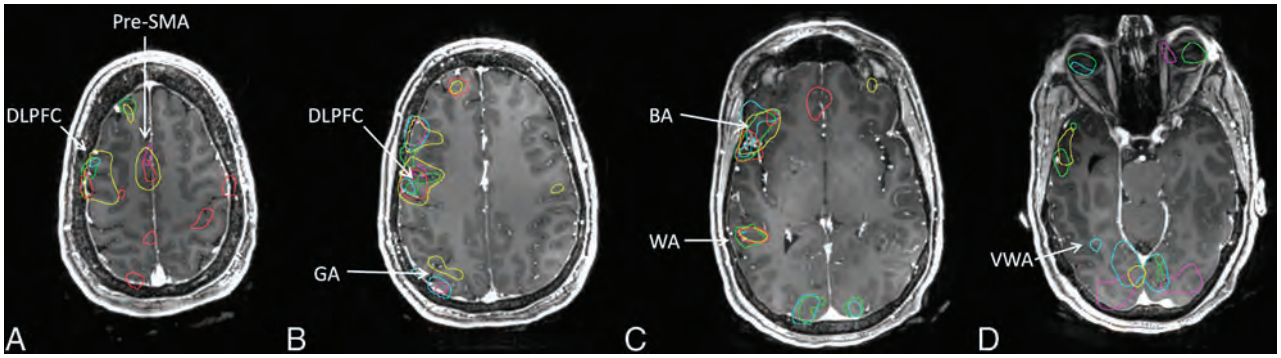

FIG 3. Presurgical mapping with fMRI and DTI performed on a 7T MR imaging scanner. Language fMRI (*A–D*) was accomplished using 5 different tasks: silent word generation (red), sentence completion (yellow), rhyming (cyan), reading comprehension (green), and semantic decision (magenta). In this left-handed patient, these tasks collectively demonstrated strong right-hemispheric lateralization of all 6 commonly identified language-activation sites, including the presupplementary motor area (Pre-SMA), language-related dorsolateral prefrontal cortex (DLPFC), Geschwind area (GA), Broca area (BA), Wernicke area (WA), and visual word form area (VWA).

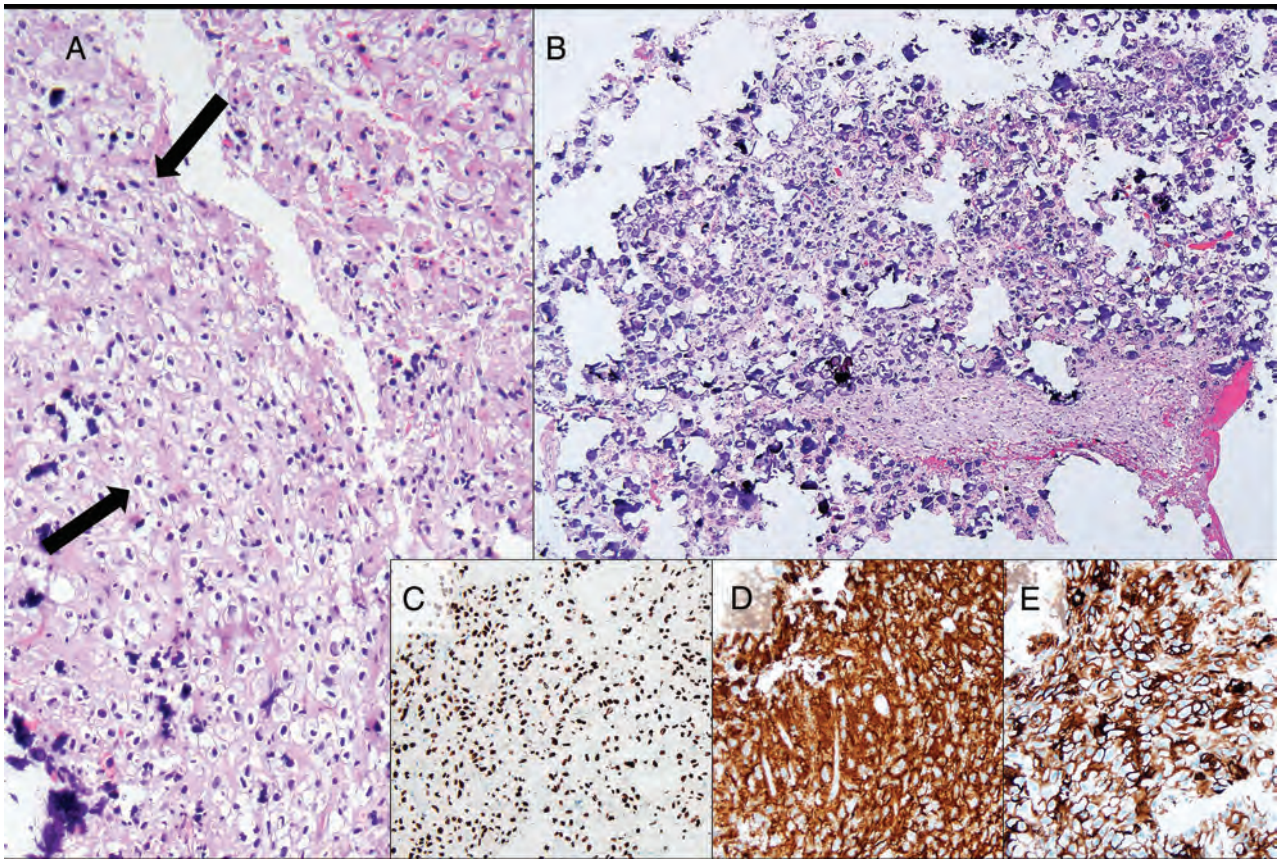

FIG 4. Hematoxylin-eosin-stained photomicrographs show a prominent population of oligodendroglial cells with round-to-ovoid nuclei (*arrow, A*, scaled from 100×) as well as abundant calcifications, which appear as purple spherules of amorphous material (*B*, scaled from 100×). Immunohistochemical staining demonstrates uniformly positive nuclear *OLIG2* expression (*C*, scaled from 100×), strong cytoplasmic expression of *BRAF V600E* (*D*, scaled from 200×), and widespread membranous expression of CD34 (*E*, scaled from 200×).

ultimately removed in a piecemeal fashion. No obvious residual tumor was identified at the conclusion of the procedure. The patient did well postoperatively without immediate complication.

Pathology

Histologic analysis of the tumor demonstrated cells of variable size, with round-to-ovoid nuclei, as well as abundant coarse calcifications. Although the cells were similar to an oligodendroglioma, several distinguishing features were present (Fig 4). The nuclei of oligodendroglioma cells are typically more monotonous and rounder, and the focal microcalcifications seen are finer and much less extensive than those seen in the present case. More important, the tumor lacked *isocitrate dehydrogenase 1/2* (*IDH1*/*IDH2*) mutations and codeletion of chromosomes 1p

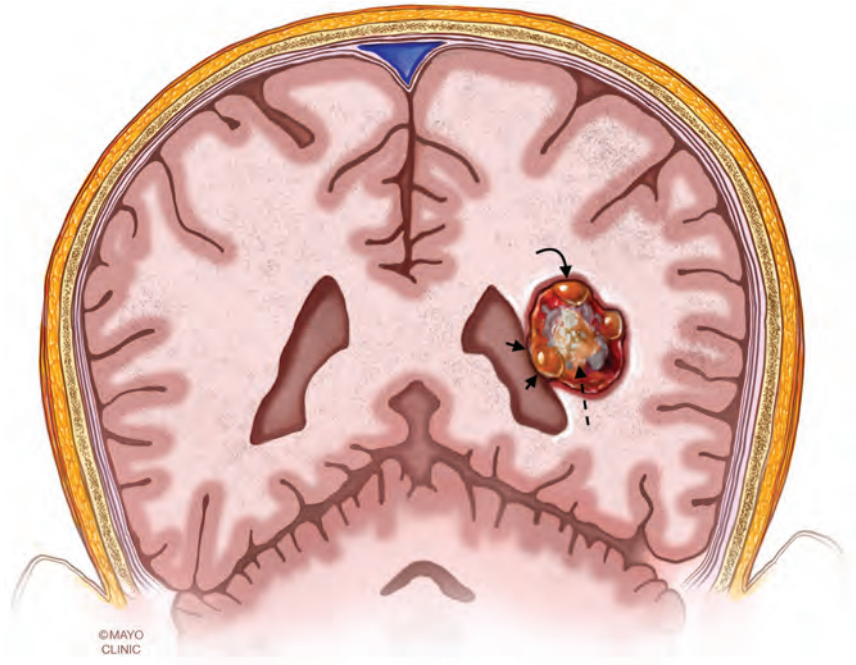

FIG 5. An artist's illustration of a prototypical PLNTY. The tumors are typically located in the temporal lobe, well-circumscribed, and made up of mixed solid tissue, central calcifications (*dashed arrow*), and peripherally located cysts (*curved arrow*). Mass effect, if present, is usually minimal (*short straight arrows*). Reprinted with permission of the Mayo Foundation for Medical Education and Research. All rights reserved.

and 19q (see below), thereby precluding the diagnosis of an oligodendroglioma. High-grade features (microvascular proliferation, necrosis, and mitotic activity) were also absent.

The next step in the histologic classification of this tumor was to differentiate it from other subtypes of low-grade neuroepithelial tumors (LGNTs), which can manifest a wide degree of histopathologic features. The abundant calcifications visualized are often seen in polymorphous low-grade neuroepithelial tumors of the young (PLNTYs). In addition, the tumor demonstrated strong CD34 expression and the diffuse positivity of *oligodendrocyte transcription factor 2* (*OLIG2*) and *B-Raf proto-oncogene, serine/threonine kinase* (*BRAF* V600E), which are additional features of PLNTYs. Furthermore, characteristic histologic features of other LGNTs (eg, eosinophilic granular bodies, Rosenthal fibers, gemistocytes, specific glioneruonal element, ganglion cells) were absent.

Additional immunohistochemical studies showed no overexpression of *p53* as well as retained *ATRX chromatin remodeler* (*ATRX*) expression. The Ki67 labeling index, a marker of proliferative activity, was minimal (<1%), supporting the diagnosis of a low-grade tumor.

A neuro-oncology-targeted next-generation sequencing panel examined 150 genes and confirmed the *BRAF* V600E mutation. No other sequence alterations of known pathologic significance were found; notably, there were no *fibroblast growth factor receptor 2* or *3* (*FGFR2* or *FGFR3*) fusions or *IDH1* or *IDH2* mutations. Chromosomal microarray showed no alterations of chromosomes 1p or 19q. Along with the lack of *IDH1* or *IDH2* mutation, the lack of 1p19q codeletion guides the differential diagnosis away from oligodendroglioma. *BRAF* V600E mutations are a recurrent genomic alteration described in PLNTYs (30% of tumors in the index series) and are mutually exclusive with *FGFR* fusions (identified in 40% of cases).[1] Both *BRAF* and *FGFR* fusions cause downstream activation of the mitogen-activated protein (MAP) kinase pathway, and at present, the histology and subsequent behavior are similar in the presence of either alteration. Of note, *BRAF* alterations can be seen in other LGNTs, including gangliogliomas and pilocytic astrocytomas.

The diagnosis was PLNTY.

DISCUSSION

PLNTYs represent a nonependymal and non-neuronal subtype of LGNTs. The tumor has been recently recognized; it was first described by Huse et al,[1] in 2017. The ages of affected patients within the original cohort were 4–32 years of age, with a median age of 17.5 years.[1] Multiple subsequent case reports have described this tumor in patients in or near this age range.[2-4] The sex of individuals in the index study was nearly evenly split (6 females, 4 males). As yet, PLNTY tumors remain unclassified by the World Health Organization. However, they are thought to be benign and appear to progress in a fashion similar to grade I tumors.[5]

Symptomatically, LGNTs often cause epilepsy that is early-onset and resistant to antiepileptogenic agents.[3] These lesions have also been designated as long-term epilepsy–associated tumors.[6-8] Gangliogliomas, dysembryoplastic neuroepithelial tumors, pleomorphic xanthoastrocytomas, and angiocentric gliomas are all subtypes of this growing list of such tumors. Nevertheless, like oligodendrogliomas, PLNTYs may also present with headaches or be found incidentally.[5]

Because it is a new and rare diagnostic entity, the imaging characteristics of PLNTY remain somewhat unknown. Johnson et al,[4] in the largest imaging review conducted on such tumors, found them to be well-circumscribed, with heterogeneous intralesional signal. Most tumors have macroscopic calcification visible on CT. These calcifications are located centrally within the lesions, a distinct feature that may help radiologists distinguish them from other processes. The location of tumors, too, may be characteristic: PLNTYs are usually located in the temporal lobe, though lesions in the parietal, frontal, and occipital lobes have also been reported. Finally, cystic components were noted in 89% of cases, which were typically located peripherally (Fig 4).[4]

The index case fits these imaging characteristics neatly: A well-circumscribed temporal lobe mass with central

Comparison of clinical, imaging, and histopathologic characteristics of PLNTYs and oligodendrogliomas

	PLNTY	Oligodendroglioma
Age at diagnosis (yr)	16–18	40–60
Most common location	Temporal lobe	Frontal lobe
Tumoral border	Well-circumscribed	Poorly defined
Calcification	Heavily calcified, central location of calcifications	Less prominent; calcifications are classically gyriform
Intralesional signal	Heterogeneous	Heterogeneous
Enhancement	Minority of tumors, typically mild	Minority of tumors, typically mild (described as dotlike)
Intratumoral cysts	~90%	~50%

calcifications, peripheral cysts, and heterogeneous internal signal should have raised suspicion of a PLNTY (Fig 5). An oligodendroglioma, too, may have demonstrated many of these imaging features, though the imaging findings overall favored a PLNTY (Table). Most notably, oligodendrogliomas have indistinct margins; sharp tumor borders are rarely seen in 1p19q-codeleted tumors.[9] Oligodendrogliomas tend to have calcifications that are more typically gyriform/cortically-based.[10] Extremely dense calcifications can also be seen in low-grade astrocytomas, albeit rarely.[11] Intralesional signal in oligodendrogliomas is nearly always equal on FLAIR and T2 images, as opposed to astrocytomas, though this has not yet been studied in PLNTYs.[12] The patient's age was somewhat atypical for a PLNTY tumor: Forty-four years of age is outside the range of the largest prior case reviews, though PLNTY tumors have been found in patients as old as 57 years.[13] Oligodendrogliomas, in comparison, are more likely to be diagnosed in adults, with a peak between 40 and 60 years of age.[14] Finally, it is not entirely clear whether the patient's spells represented true seizures; her symptoms were nonfocal, and findings of electroencephalography were normal. It is possible that the patient had seizures that propagated along cortical/subcortical pathways that were occult on electroencephalographic monitoring. However, 2 of the 10 patients first diagnosed with a PLNTY by Huse et al[1] had clinical presentations other than seizures: one with headaches and the other with visual disturbances. As with most CNS tumors, clinically, presentations are variable and do not always predict pathology.

A discrepancy was noted between the imaging features and pathology: Intratumoral perfusion was elevated, though the tumor lacked hypervascularity on histologic analysis. The findings on perfusion imaging were not thought to be artifactual because inherent susceptibility tends to cause absence or substantial reduction in relative CBV.

The patient in the index case had an excellent postoperative course following her surgical resection. She had complete resolution of her paroxysmal neuropsychiatric symptoms and subjective improvement of her cognitive status. Her language function was completely preserved postoperatively. Seven of 8 patients in the cohort originally described by Huse et al[1] were disease-free following gross total resection (mean follow-up, 50.6 months). Only 1 patient had breakthrough seizures and follow-up imaging findings that were considered possibly concerning for tumor recurrence at 36 months after her operation.[1]

Case Summary

- Although scantly described, PLNTY tumors have multiple characteristic imaging features: well-circumscribed masses, typically in the temporal lobe, with admixed heterogeneous solid and densely calcific material centrally and cysts peripherally.
- Differential considerations include the following: oligodendroglioma, calcified low-grade astrocytoma, dysembryoplastic neuroepithelial tumor, pleomorphic xanthoastrocytoma, and ganglioglioma.
- PLNTYs remain unclassified by the World Health Organization but appear to progress in a manner similar to grade I tumors.
- Histologically, PLNTYs typically show calcifications and oligodendroglioma-like elements, though additional histologic elements can be present in variable amounts. Mutually exclusive *BRAF* mutations or *FGFR2/3* fusions are common, and both activate the MAP kinase pathway.
- Here, fMRI allowed a safe approach to the patient's tumor without intraoperative language mapping.

REFERENCES

1. Huse JT, Snuderl M, Jones DT, et al. **Polymorphous low-grade neuroepithelial tumor of the young (PLNTY): an epileptogenic neoplasm with oligodendroglioma-like components, aberrant CD34 expression, and genetic alterations involving the MAP kinase pathway.** *Acta Neuropathol* 2017;133:417–29 CrossRef Medline
2. Zhang K, Sassoon A. **Polymorphous low-grade neuroepithelial tumor of the young (PLNTY): two cases of the recently described epileptogenic neoplasm with oligodendroglioma-like components and heavy calcification.** *Am J Clin Pathol* 2018;150(Suppl 1):S16–17 CrossRef
3. Bitar M, Danish SF, Rosenblum MK. **A newly diagnosed case of polymorphous low-grade neuroepithelial tumor of the young.** *Clin Neuropathol* 2018;37:178–81 CrossRef Medline
4. Johnson DR, Giannini C, Jenkins RB, et al. **Plenty of calcification: imaging characterization of polymorphous low-grade neuroepithelial tumor of the young.** *Neuroradiology* 2019;61:1327–32 CrossRef Medline
5. Sumdani H, Shahbuddin Z, Harper G, et al. **Case report of rarely described polymorphous low-grade neuroepithelial tumor of the young and comparison with oligodendroglioma.** *World Neurosurg* 2019;127:47–51 CrossRef Medline
6. Kasper BS, Kasper EM. **New classification of epilepsy-related neoplasms: the clinical perspective.** *Epilepsy Behav* 2017;67:91–97 CrossRef Medline
7. Blümcke I, Aronica E, Becker A, et al. **Low-grade epilepsy-associated neuroepithelial tumours: the 2016 WHO classification.** *Nat Rev Neurol* 2016;12:732–40 CrossRef Medline
8. Thom M, Blümcke I, Aronica E. **Long-term epilepsy-associated tumors.** *Brain Pathol* 2012;22:350–79 CrossRef Medline
9. Johnson DR, Diehn FE, Giannini C, et al. **Genetically defined oligodendroglioma is characterized by indistinct tumor borders at MRI.** *AJNR Am J Neuroradiol* 2017;38:678–84 CrossRef Medline

10. Smits M. **Imaging of oligodendroglioma.** *Br J Radiol* 2016;89:20150857 CrossRef Medline
11. Berhouma M, Jemel H, Kchir N. **Calcified pilocytic astrocytoma of the medulla mimicking a brainstem "stone."** *Pathologica* 2008;100:408–10 Medline
12. Lasocki A, Gaillard F, Gorelik A, et al. **MRI 1p/19q status in intracranial gliomas.** *AJNR Am J Neuroradiol* 2018;39:687–92 CrossRef Medline
13. Riva G, Cima L, Villanova M, et al. **Low-grade neuroepithelial tumor: unusual presentation in an adult without history of seizures.** *Neuropathology* 2018;38:557–60 CrossRef Medline
14. Nielsen MS, Christensen HC, Kosteljanetz M, et al. **Incidence of and survival from oligodendroglioma in Denmark, 1943-2002.** *Neuro Oncol* 2009;11:311–17 CrossRef Medline

Brain Metastases: Insights from Statistical Modeling of Size Distribution

M. Buller, K.M. Chapple, and C.R. Bird

ABSTRACT

BACKGROUND AND PURPOSE: Brain metastases are a common finding on brain MRI. However, the factors that dictate their size and distribution are incompletely understood. Our aim was to discover a statistical model that can account for the size distribution of parenchymal metastases in the brain as measured on contrast-enhanced MR imaging.

MATERIALS AND METHODS: Tumor volumes were calculated on the basis of measured tumor diameters from contrast-enhanced T1-weighted spoiled gradient-echo images in 68 patients with untreated parenchymal metastatic disease. Tumor volumes were then placed in rank-order distributions and compared with 11 different statistical curve types. The resultant R^2 values to assess goodness of fit were calculated. The top 2 distributions were then compared using the likelihood ratio test, with resultant R values demonstrating the relative likelihood of these distributions accounting for the observed data.

RESULTS: Thirty-nine of 68 cases best fit a power distribution (mean $R^2 = 0.938 \pm 0.050$), 20 cases best fit an exponential distribution (mean $R^2 = 0.957 \pm 0.050$), and the remaining cases were scattered among the remaining distributions. Likelihood ratio analysis revealed that 66 of 68 cases had a positive mean R value (1.596 ± 1.316), skewing toward a power law distribution.

CONCLUSIONS: The size distributions of untreated brain metastases favor a power law distribution. This finding suggests that metastases do not exist in isolation, but rather as part of a complex system. Furthermore, these results suggest that there may be a relatively small number of underlying variables that substantially influence the behavior of these systems. The identification of these variables could have a profound effect on our understanding of these lesions and our ability to treat them.

In patients with cancer, brain metastases are a common finding on MR imaging, and their presence has important implications for staging and treatment. Metastases to the brain are a well-established but incompletely understood process. Although the hematogeneous spread of tumors to the brain is widely accepted, the mechanisms responsible for malignant cell clusters establishing themselves and becoming detectable masses remain unclear. A multitude of factors may potentially play a role, including factors specific to the metastatic tumor cluster cells, those specific to the local tissues at the deposition site, and systemic factors affecting the entire patient. An increased understanding of which variables dictate the behavior of this complex system would be invaluable in advancing our knowledge of brain metastases, as well as in advancing our ability to detect, make prognoses for, and treat metastatic lesions.

We have anecdotally noted that intracranial metastases seem to present with a limited array of size distributions across all patients, regardless of age or primary tumor type. In patients with multiple intracranial metastases, there is often 1 relatively large metastasis and a number of smaller metastases. This pattern seems to be independent of the number of metastatic lesions within the brain. These findings appear to be inconsistent with a typical Gaussian distribution of lesion sizes, in which tumor sizes are evenly distributed about a mean. In this study, we attempted to elucidate the specific distribution that would best explain this observation.

MATERIALS AND METHODS

We searched all patient records between February 1, 2016, and July 1, 2017, for MR imaging reports of intracranial metastases. We then excluded patients who had previously treated metastases or metastases based in the dura. This search revealed 105 patients with untreated, parenchymal metastases. Subsequently, patients with fewer than 3 metastases were omitted because these metastases could

Received July 22, 2019; accepted after revision February 12, 2020.

From the Department of Neuroradiology, Barrow Neurological Institute, St. Joseph's Hospital and Medical Center, Phoenix, Arizona.

Please address correspondence to C. Roger Bird, MD, c/o Neuroscience Publications, Barrow Neurological Institute, St. Joseph's Hospital and Medical Center, 350 W Thomas Rd, Phoenix, AZ 85013; e-mail: Neuropub@barrowneuro.org

Indicates article with supplemental on-line table.

http://dx.doi.org/10.3174/ajnr.A6496

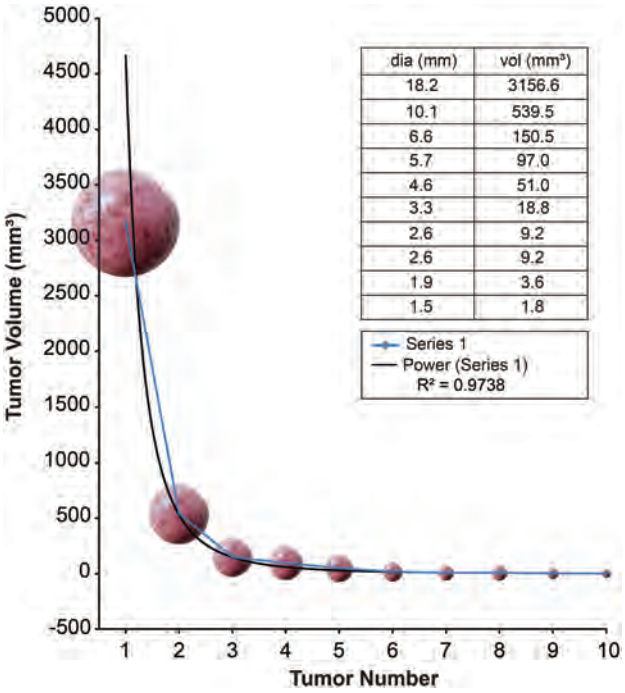

FIG 1. Example of a rank-order distribution of the volumes of intracranial metastases in 1 patient (patient 37). Used with permission from Barrow Neurologic Institute, Phoenix, Arizona.

not be accurately plotted for nonlinear distributions. This criterion reduced our study population to a total of 68 eligible patients.

For each patient, axial T1-weighted, contrast-enhanced spoiled gradient-echo sequences were examined, and a diameter was recorded for each metastatic lesion. Each lesion was measured manually by an experienced subspecialty board-certified neuroradiologist. Diameter measurements were acquired at the midpoint of each lesion in the craniocaudal plane, and the long and short axis measurements were averaged in cases of nonspherical lesions to obtain a diameter. These measurements were then used to calculate a volume for each tumor by the equation $V = \frac{4}{3}\pi r^3$; for these purposes, a spherical shape was assumed.

The Shapiro-Wilk test for normality was performed for each patient. The null hypothesis tested that the data were normally distributed, and significant P values reflected non-normality. Each volume measurement was then placed in a rank-order distribution and plotted for each individual patient (Fig 1). The resulting curves were then compared with 11 possible distributions using regression curve-fit analysis. The possible distributions included linear, logarithmic, inverse, quadratic, cubic, compound, power, "S," growth, exponential, and logistic plots. Coefficient of determination values, designated by R^2, were generated for each patient and curve type using SPSS software (IBM, Armonk, New York). The R^2 value is a measure of the goodness-of-fit of data to a particular model and ranges from 0 to 1. This value indicates what portion of the variability seen within a given dataset can be explained using the chosen model. The curves with the highest R^2 value for each patient were then collected and grouped on the basis of curve type, with power law and exponential curve types being the most common.

A logistic regression was used to determine whether the number of lesions was independent of the distribution "power" versus others. We also ran this model with power and exponential dichotomized against all other distributions.

Given that power law and exponential curve types best accounted for the tumor distribution in most patients, we then sought to determine whether the power law distribution or the exponential distribution was a better fit for our observed data. We calculated likelihood ratios for each patient's lesions comparing the power law and exponential curves. The likelihood ratio test is used to compare 2 statistical models on the basis of the ratio of the probabilities of each model accounting for the observed data. The probability that a given model accounts for the observed data is called the "likelihood" for that model. Initially, the goodness-of-fit of observed data is compared with 2 models, in this case power and exponential distributions. The logarithm of the ratio of the 2 likelihoods—the R value—is then calculated. In our study, positive R values are consistent with the power distribution providing a better fit than the exponential distribution, with more extreme values suggesting a stronger likelihood than values close to zero. Conversely, negative values confer similar implications in favor of the exponential distribution over the power distribution.

Finally, each distribution was treated as a power law type $[Y(x) = Cx^{\alpha}]$, and α values were calculated for each curve. The α value represents the slope of the linear distribution obtained by plotting a power distribution logarithmically.

RESULTS

The total number of metastases per patient ($n = 68$) ranged from 3 to 84, with a mean of approximately 11 metastases per patient.

The tumor distribution in 39 patients best fit a power distribution, with a mean R^2 value of 0.938 ± 0.050. The next most prevalent curve type was exponential, accounting for 20 patients (mean R^2 = 0.957 ± 0.050). The remaining 9 cases were composed of 5 cubic distributions (mean R^2 = 0.985 ± 0.006), 1 logarithmic distribution ($R^2 = 0.972$), 2 S distributions ($R^2 = 0.972, 0.998$), and 1 inverse distribution ($R^2 = 0.962$).

Results from the Shapiro-Wilk test suggest that tumor distributions were normal for 17 patients. Nine of these cases also fit power ($n = 2$), exponential ($n = 4$), cubic ($n = 1$), log ($n = 1$), and S ($n = 1$) distributions as demonstrated by P values $< .05$. The remaining 8 cases had R^2 values for non-normal distributions that ranged from 0.762 to 0.993; however, associated P values exceeded .05.

The tumor distributions in 66 of 68 patients had likelihood ratios skewed toward a power law distribution, with R values ranging from 0.020 to 6.049 (Fig 2). The mean R value was 1.596 ± 1.316.

Results from the logistic regression analysis regarding tumor number and distribution suggested that the number of lesions did not predict a power distribution ($P = .246$) or combined power and exponential distributions ($P = .198$).

Calculated α values ranged from 0.494 to 9.29. Data are summarized in the On-line Table.

DISCUSSION

Our results indicate that metastases within the brain largely follow a non-normal distribution, particularly in cases with >7 metastases.

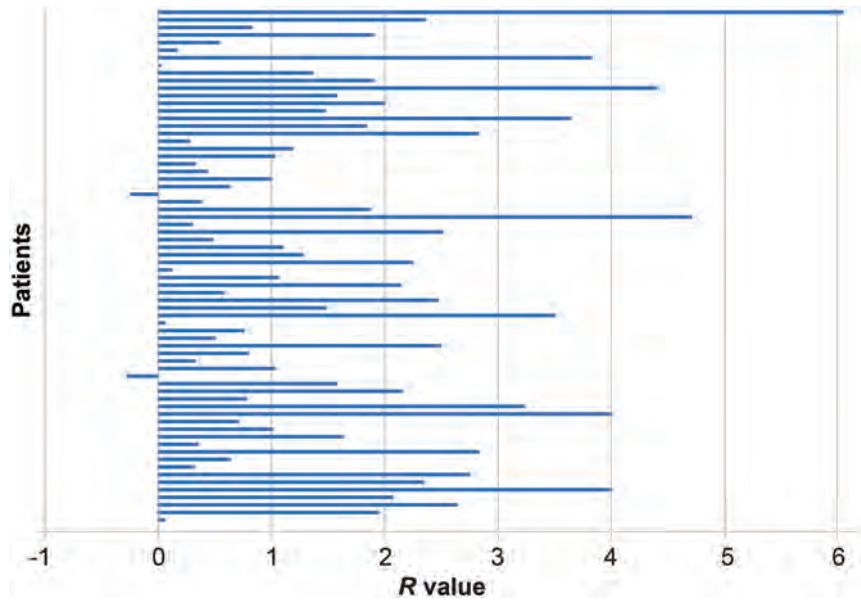

FIG 2. Likelihood ratio analysis with *R* value distributions for all 68 patients. Values to the right of zero indicate that the distribution is more likely to fit a power law, with higher numbers indicating a stronger fit. Values to the left of zero indicate that the distribution is more likely to fit an exponential distribution. Used with permission from Barrow Neurologic Institute, Phoenix, Arizona.

These results also suggest that it is statistically reasonable to posit that brain metastases likely follow a size distribution best described by a power law. On the basis of our data, this relationship is independent of the number of metastases present.

Power law relationships exist within multiple areas of scientific inquiry, including biology, ecology, and economics. Some of the earliest work with such distributions in biology was performed by Rubner,[1] in 1883, in which he found a relationship between the size and basal metabolic rate of various organisms. Nearly 50 years later, Swiss biologist Kleiber[2] used a power law to relate oxygen consumption and body mass across multiple species of mammals (later dubbed the Kleiber law). Since that time, there have been many other applications of power laws. Some of the more well-known applications include the Pareto principle (regarding the distribution of wealth in a population), the Zipf law (describing the frequency of words in written language), and the Richter scale (measuring the strength of earthquakes). More recently, power laws have been used to elicit differences between "traditional" wars and modern insurgency conflicts and to assess the stability of such conflicts.[3]

Power law relationships can be expressed as follows:

1) $$Y(x) = Cx^{\alpha}.$$

When these equations are plotted on a log-log curve, they yield a linear relationship:

2) $$log\ [Y(x)] = logC + \alpha log\ x.$$

In Equation 2, the term α dictates the slope of the linear relationship.

Power law relationships fall broadly into 3 categories.[4] The first category involves relationships that demonstrate self-symmetry. In these relationships, the α value is constrained to multiples of a single value. Examples of this type of power law relationship include Euclidian geometry (multiples of 1/3) and biologic allometries related to mass (multiples of 1/4). The second type of power law relationship is one in which the α values occur over a small range of values. Population densities of certain species of insects and birds are examples of this type of power law relationship.[4] These 2 types of power laws are united in that they evidence self-similarity, which implies the presence of a small set of underlying variables accounting for the behavior of the system. The third type of power law involves those cases in which other distributions fit the data just as well as the power distribution, and although these relationships demonstrate apparent self-similarity across multiple values, this effect does not hold across multiple orders of magnitude.[4]

Our data suggest that the size distribution of intracranial metastases follows a power law distribution of the second type. To our knowledge, this has not yet been explained in the literature. Several previous works that have modeled tumor growth have suggested that tumor growth is more appropriately modeled using power laws, as opposed to the more commonly accepted Gompertz model.[5-7] Additional work with cellular automata also supports a power law model for tumor growth in 1, 2, and 3 dimensions.[8] This work was later supported with both in vivo and in vitro results, suggesting that tumor growth as a power law distribution should not be excluded.[9] In addition to evidence of power law tumor growth, there is also evidence that the metastatic cell clusters released from primary tumors can also be modeled with a decaying power law.[10]

Our data suggest that intracranial metastases are not simply individual tumors growing in isolation but instead form part of a complex system in which these tumors are interdependent. Additionally, we suggest the possibility that a small number of variables may substantially influence the behavior of metastatic lesions within the brain. Although our study did not attempt to elucidate these factors, other work in this area has suggested multiple possibilities, including competition for local resources, host immune response, anti-angiogenic factors, or anti-cell cycle factors.[11-17] Recent work using mathematical modeling within this area supports a systemic effect over local factors and suggests that while the model best supports anti-cell cycle factors, a combination of anti-cell, anti-angiogenesis, and immune factors would also be a reasonable conclusion.[18]

This research, in combination with mathematic modeling based on these findings, could expand our understanding of the

factors that influence the growth of metastases in the brain. Although work is already ongoing to identify factors that regulate metastatic growth within the brain, the addition of the insights detailed in this article may allow more focused mathematic modeling and an increased understanding of these processes. These, in turn, could have ramifications on new treatment for brain metastases or increasingly sensitive tests for the early detection of systemic metastatic disease. Furthermore, the nature of power laws may allow us to determine the stability of the system at a given point in time, thus allowing clinicians to be more selective with regard to the prognosis and efficacy of treatment.

Our methods were based on the work of Clauset et al,[19] which describes a well-established and state-of-the-art method for elucidating power law relationships. However, there are limitations to the statistical methods for determining power law relationships that are particularly problematic in small datasets, which Clauset defines as $n < 100$. Clauset et al noted in their article: "In practice, we can rarely, if ever, be certain that an observed quantity is drawn from a power law distribution. The most we can say is that x is drawn from a distribution in the form of Eq. 1 [sic]."[19]

In our study, both the number of patients and the maximum number of tumors per patient are below this dataset threshold. However, single patients presenting with >100 metastases are rare, and we deemed it statistically incorrect to lump all tumors from multiple patients into a single dataset. In addition, given the limitations in orders of magnitude imposed by the fixed volume of the intracranial compartment and the minimum spatial resolution of current MR imaging technology, there is debate within the scientific community as to whether one can distinguish between the type 2 and 3 power law distributions described above.[4] Within the bounds of these fundamental limitations, we believe that our findings represent a best possible scenario using current imaging techniques.

We are currently working to expand our dataset. We plan to assess whether primary tumor type has any effect on the power law relationship to determine whether size distribution could be useful in typing intracranial metastases. Data on patient outcomes could also help determine whether the magnitude of the α value could indicate the stability of the system and may help to predict the rapidity of disease progression in a manner similar to the conclusions of Bohorquez et al[3] regarding the stability of insurgency conflicts. Furthermore, mathematic modeling using cellular automata is currently underway to preliminarily identify some of the potentially limited variables for targeted study based on our hypothesis.

CONCLUSIONS

We found that intracranial metastases follow a size distribution consistent with a power law distribution. This distribution pattern implies that these tumors are not growing in isolation but are rather interconnected parts of a complex system. Given the small range of α values, it is possible that a small number of variables may markedly influence the variance within this system and that identification of these variables could be valuable for making prognoses and treating patients with metastatic cancer. Further work, both theoretic and experimental, will be required to identify these factors. To this end, we intend to pursue mathematic modeling using cellular automata to preliminarily identify possible variables for more targeted investigation.

ACKNOWLEDGMENTS

The authors thank the staff of Neuroscience Publications at Barrow Neurologic Institute for assistance with manuscript preparation. We also thank Rebecca Freed and Morgan Snopko of the School of Mathematical and Statistical Sciences at Arizona State University for assistance with likelihood ratios.

REFERENCES

1. Rubner M. **Uber den Einfluss der Körpergröβe auf Stoff-und Kraftwechsel.** *Zeitschrift für Biologie* 1883;19:535–62
2. Kleiber M. **Body size and metabolism.** *Hilgardia* 1932;6:315–53 CrossRef
3. Bohorquez JC, Gourley S, Dixon AR, et al. **Common ecology quantifies human insurgency.** *Nature* 2009;462:911–14 CrossRef Medline
4. Brown JH, Gupta VK, Li BL, et al. **The fractal nature of nature: power laws, ecological complexity and biodiversity.** *Philos Trans R Soc Lond B Biol Sci* 2002;357:619–26 CrossRef Medline
5. Bru A, Albertos S, Luis Subiza J, et al. **The universal dynamics of tumor growth.** *Biophys J* 2003;85:2948–61 CrossRef Medline
6. Gatenby RA, Frieden BR. **Information dynamics in carcinogenesis and tumor growth.** *Mutat Res* 2004;568:259–73 CrossRef Medline
7. Hart D, Shochat E, Agur Z. **The growth law of primary breast cancer as inferred from mammography screening trials data.** *Br J Cancer* 1998;78:382–87 CrossRef Medline
8. Vainstein V, Kirnasovsky OU, Kogan Y, et al. **Strategies for cancer stem cell elimination: insights from mathematical modeling.** *J Theor Biol* 2012;298:32–41 CrossRef Medline
9. Hochman G, Kogan Y, Vainstein V. **Evidence for power law tumor growth and implications for cancer radiotherapy.** http://www.imbm.org/PDF/HKVetal.pdf. Accessed October 30, 2017
10. Scott JG, Gerlee P, Basanta D. **Mathematical modeling of the metastatic process.** In: Malek A, ed. *Experimental Metastasis: Modeling and Analysis* Heidelberg: Springer Netherlands; 2013:189–208
11. Ruggiero RA, Bruzzo J, Chiarella P, et al. **Tyrosine isomers mediate the classical phenomenon of concomitant tumor resistance.** *Cancer Res* 2011;71:7113–24 CrossRef Medline
12. Ruggiero RA, Bruzzo J, Chiarella P, et al. **Concomitant tumor resistance: the role of tyrosine isomers in the mechanisms of metastases control.** *Cancer Res* 2012;72:1043–50 CrossRef Medline
13. Gershon RK, Carter RL. **Factors controlling concomitant immunity in tumor-bearing hamsters: effects of prior splenectomy and tumor removal.** *J Natl Cancer Inst* 1969;43:533–43 Medline
14. Gorelik E, Segal S, Feldman M. **On the mechanism of tumor "concomitant immunity.** *Int J Cancer* 1981;27:847–56 CrossRef Medline
15. O'Reilly MS, Holmgren L, Shing Y, et al. **Angiostatin: a novel angiogenesis inhibitor that mediates the suppression of metastases by a Lewis lung carcinoma.** *Cell* 1994;79:315–28 CrossRef Medline
16. Erlich P. **Experimentelle Karzinomstudien an Maüsen.** *Arb Aus Dem K Inst Für Exp Ther Zu Frankf Am Main* 1906;75–102
17. O'Reilly MS, Boehm T, Shing Y, et al. **Endostatin: an endogenous inhibitor of angiogenesis and tumor growth.** *Cell* 1997;88:277–85 CrossRef Medline
18. Benzekry S, Lamont C, Barbolosi D, et al. **Mathematical modeling of tumor-tumor distant interactions supports a systemic control of tumor growth.** *Cancer Res* 2017;77:5183–93 CrossRef Medline
19. Clauset A, Shalizi CR, Newman ME. **Power-law distributions in empirical data.** *SIAM Review* 2009;51:661–703 CrossRef

Discrimination between Glioblastoma and Solitary Brain Metastasis: Comparison of Inflow-Based Vascular-Space-Occupancy and Dynamic Susceptibility Contrast MR Imaging

X. Li, D. Wang, S. Liao, L. Guo, X. Xiao, X. Liu, Y. Xu, J. Hua, J.J. Pillai, and Y. Wu

ABSTRACT

BACKGROUND AND PURPOSE: Accurate differentiation between glioblastoma and solitary brain metastasis is of vital importance clinically. This study aimed to investigate the potential value of the inflow-based vascular-space-occupancy MR imaging technique, which has no need for an exogenous contrast agent, in differentiating glioblastoma and solitary brain metastasis and to compare it with DSC MR imaging.

MATERIALS AND METHODS: Twenty patients with glioblastoma and 22 patients with solitary brain metastasis underwent inflow-based vascular-space-occupancy and DSC MR imaging with a 3T clinical scanner. Two neuroradiologists independently measured the maximum inflow-based vascular-space-occupancy–derived arteriolar CBV and DSC-derived CBV values in intratumoral regions and peritumoral T2-hyperintense regions, which were normalized to the contralateral white matter (relative arteriolar CBV and relative CBV, inflow-based vascular-space-occupancy relative arteriolar CBV, and DSC-relative CBV). The intraclass correlation coefficient, Student *t* test, or Mann-Whitney *U* test and receiver operating characteristic analysis were performed.

RESULTS: All parameters of both regions had good or excellent interobserver reliability (0.74∼0.89). In peritumoral T2-hyperintese regions, DSC-relative CBV ($P < .001$), inflow-based vascular-space-occupancy arteriolar CBV ($P = .001$), and relative arteriolar CBV ($P = .005$) were significantly higher in glioblastoma than in solitary brain metastasis, with areas under the curve of 0.94, 0.83, and 0.72 for discrimination, respectively. In the intratumoral region, both inflow-based vascular-space-occupancy arteriolar CBV and relative arteriolar CBV were significantly higher in glioblastoma than in solitary brain metastasis (both $P < .001$), with areas under the curve of 0.91 and 0.90, respectively. Intratumoral DSC-relative CBV showed no significant difference ($P = .616$) between the 2 groups.

CONCLUSIONS: Inflow-based vascular-space-occupancy has the potential to discriminate glioblastoma from solitary brain metastasis, especially in the intratumoral region.

ABBREVIATIONS: AUC = area under the curve; CBVa = arteriolar CBV; GBM = glioblastoma; iVASO = inflow-based vascular-space-occupancy; rCBV = relative CBV; rCBVa = relative arteriolar CBV; PTH = peritumoral T2-hyperintesity region; SBM = solitary brain metastasis

Glioblastoma (GBM) accounts for 40%∼50% of all primary malignant brain tumors in adults. Brain metastases are the most common complication of systemic cancer, and half of them are solitary at diagnosis.[1] It is clinically important to distinguish GBM from solitary brain metastasis (SBM) because of the vast differences in these 2 entities with regard to tumor staging, treatment approach, and clinical outcomes.[2-4] Structural gadolinium-enhanced MR imaging is the preferred imaging examination for brain tumors, but with a limited capacity to differentiate GBM and SBM. They share similar imaging features, such as extensive

Received July 23, 2019; accepted after revision February 03, 2020.

From the Department of Medical Imaging (X. Li, S.L., L.G., X.X., X. Liu, Y.X., Y.W.), Nanfang Hospital, Southern Medical University, Guangzhou, P.R. China; School of Biomedical Engineering (D.W.), Shanghai Jiao Tong University, Shanghai, P.R. China; Division of CT and MR, Radiology Department (S.L.), First Affiliated Hospital of Gannan Medical University, Ganzhou, P.R. China; Neurosection, Division of MR Research (J.H.); Division of Neuroradiology (J.P.); Russell H. Morgan Department of Radiology and Radiological Science and Department of Neurosurgery (J.P.), Johns Hopkins University School of Medicine, Baltimore, Maryland; and F.M. Kirby Research Center for Functional Brain Imaging (J.H.), Kennedy Krieger Institute, Baltimore, Maryland.

Xiaodan Li and Danni Wang contributed equally to this study.

This study has received funding from the Natural Science Foundation of Guangdong Province, China (grant No. S201301005689), the Science and Technology Program of Guangzhou, China (grant No. 201707010003), and the Special Foundation of President of Nanfang Hospital, Southern Medical University (grant No. 2016B026).

Abstract previously presented orally at: Annual Meeting and Exhibition of the International Society for Magnetic Resonance in Medicine, May 11–16, 2019; Montreal, Quebec, Canada.

Please address correspondence to Yuankui Wu, MD, Department of Medical Imaging, Nanfang Hospital, Southern Medical University, No. 1838 Guangzhou Avenue North, Guangzhou, P.R. China; e-mail: ripleyor@126.com

Indicates open access to non-subscribers at www.ajnr.org
Indicates article with supplemental on-line tables.

http://dx.doi.org/10.3174/ajnr.A6466

edema and ring-enhancement, which is a great challenge in clinical practice.[5-7]

Many studies have demonstrated that PWI is a promising technique to discriminate GBM from SBM, due to its capability to disclose the differences between them in angiogenesis and vascularity.[8,9] In particular, DSC MR imaging is the most robust perfusion technique to perform such a task.[10,11] However, most studies found that DSC-derived relative CBV (rCBV) in intratumoral regions does not permit reliable differentiation between high-grade gliomas and metastases,[1,6,12-15] which was thought to be related to contrast leakage from tumor vessels and, consequently, unreliable estimation of CBV.[10,16,17] rCBV measured in peritumoral regions may be effective in this regard, but this method inherently has some major disadvantages due to indefinite tumoral boundary and various definitions of the peritumoral area.[15,18] Besides, the administration of exogenous contrast agents required for DSC raises concerns about the adverse effects of gadolinium, especially the deposits in brain, even using macrocyclic gadolinium-based contrast agents.[19-22]

Inflow-based vascular-space-occupancy (iVASO) is a completely noninvasive perfusion method that does not involve administration of an exogenous contrast agent.[23] Instead, proton spins in the water molecules in blood are exploited as an endogenous contrast agent by applying spatially selective radiofrequency inversion pulses.[24] iVASO emphasizes the perfusion blood volume in arteries and arterioles. The absolute CBV of pial arteries and precapillary arterioles (arteriolar CBV [CBVa]) can be calculated from the different signals between a scan with arterial blood signal selectively zeroed out (nulled) and a control scan without blood nulling.[24,25] Notably, previous studies have demonstrated that pial arteries and arterioles are the most sensitive vessels to respond via adaptive hemodynamic adjustment to changes in cerebral metabolism status in the human body.[26-28] According to recent studies, CBVa measured with iVASO MR imaging (iVASO-CBVa) has proved sensitive in disclosing microvascular abnormalities in the early stage of some mental and cognitive disorders, such as Huntington disease, Alzheimer disease, and schizophrenia.[29-31] Furthermore, a previous study has demonstrated that iVASO-CBVa is strongly correlated with glioma grades and might be superior to DSC-derived rCBV.[32] Therefore, we hypothesized that iVASO can distinguish GBM from SBM. To validate this hypothesis, we performed iVASO MR imaging on patients with GBM or SBM on a clinical 3T MR imaging scanner.

MATERIALS AND METHODS

Study Participants

This retrospectively reviewed study was prospectively controlled and conducted between December 2015 and March 2017. All examinations were performed in accordance with institutional (Nanfang Hospital Southern Medical University) review board guidelines with an approved study protocol. Inclusion criteria were as follows: 1) patients with a single, solitary enhancing brain mass with a clinical question of SBM versus GBM; 2) pretreatment acquisition of a 3T MR imaging brain tumor protocol, including structural MR imaging, iVASO, and DSC; and 3) the mass pathologically confirmed by stereotactic biopsy or surgical sample within 2 weeks after MR imaging. Ten patients were excluded (4 for obvious movement artifacts, 4 for susceptibility artifacts hampering ROI placement, 2 for small lesions greatly influenced by partial volume averaging effect). The remaining 20 patients with GBM and 22 with SBM were eventually included in the study.

MR Imaging Acquisition

MR imaging examinations were implemented with a clinical 3T imaging unit (Achieva 3T; Philips Healthcare, Best, the Netherlands) equipped with an 8-channel head coil. DSC, iVASO, and structural MR imaging were performed for each subject in the same scan session.

The structural MR imaging protocol included an axial FLAIR scan (TR/TI/TE = 11,000/2200/125 ms, voxel = $0.7 \times 0.7 \times 6$ mm^3, 20 slices), T2WI (TR/TE = 3000/80 ms, voxel = $0.5 \times 0.7 \times 6$ mm^3, 20 slices), and T1WI (TR/TE = 2000/20 ms, voxel = $0.5 \times 0.9 \times 6$ mm^3, 20 slices) (detailed in On-line Table 1). Contrast-enhanced fat-suppressed T1WI (TR/TE = 297/4.6 ms, voxel = $0.5 \times 0.7 \times 6$ mm^3, 20 slices) was obtained after DSC.

3D iVASO was performed before contrast agent administration. Parameters for the iVASO pulse sequence were the following: TR/TI = 5000/1040, 3100/862, 2500/756, 2000/641, 1700/558, 1300/430 ms; 3D gradient spin-echo readout (TE = 10 ms; voxel = $2.5 \times 2.5 \times 6$ mm^3, 14 slices); parallel imaging acceleration (sensitivity encoding) = 2×2; crusher gradients of $b = 0.3$ s/mm^2 and Venc = 10 cm/s along the z-direction. A reference scan (TR = 20 seconds, other parameters identical) was obtained to determine the scaling factor M0 in iVASO images so that absolute CBVa values could be calculated. The total duration of all iVASO-related scans combined was 7 minutes for each patient.

DSC perfusion images were acquired immediately after contrast agent injection with fast-field echo, echo-planar imaging, TR/TE = 1700/40 ms, FOV = 210 × 210 mm, pixel = 2.3 × 2.3 mm, matrix = 90 × 90, thickness/gap = 6/0 mm, 20 slices, 60 dynamics, flip angle = 75°. Contrast agent (gadodiamide, Omniscan; GE Healthcare, Piscataway, New Jersey) was administered at a dose of 0.2 mmol/kg and a rate of 4.5 mL/s, using a power injector (Spectris Solaris EP; MedRad, Indianola, Pennsylvania) through the antecubital vein, followed by a 20- mL sterile saline flush at the same rate. The total acquisition time of DSC was 1 minute 42 seconds.

MR Imaging Analysis

All iVASO data were preprocessed using the Statistical Parametric Mapping software package (Version 8; http://www.fil.ion.ucl.ac.uk/spm/software/spm12). The iVASO images were analyzed with in-house routines programmed in Matlab (MathWorks, Natick, Massachusetts), which were used for a previously published report.[32] DSC images were processed on an Advantage Workstation using FuncTool (Version 4.6; GE Healthcare) to obtain CBV maps.

Color-coded iVASO-CBVa and DSC-CBV maps were generated, respectively. The region of maximal abnormality of each parameter within the lesion volume (hotspot) was determined via visual inspection. This methodology was demonstrated to provide the most optimal interobserver and intraobserver reproducibility.[33] Four ROIs of about 20 pixels were carefully placed on the hotspots,

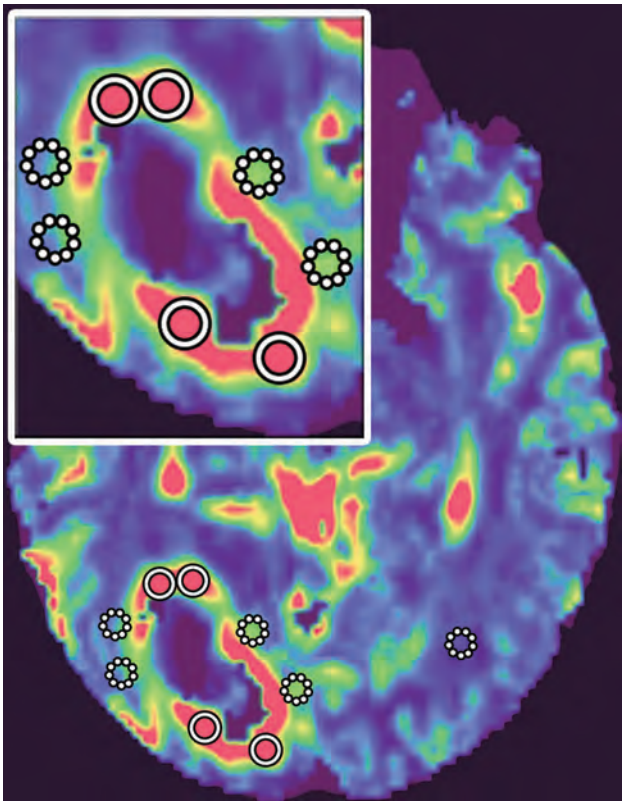

FIG 1. ROI placements. Four to six ROIs were drawn in both intratumoral (*circle with solid line*) and peritumoral (*circle with dotted line*) regions, and the maximum value was recorded. Also, an ROI in the contralateral white matter (*circle with dotted line*) was chosen as a reference. The insert is the magnification of lesion area.

respectively, in the intratumoral region and the peritumoral T2-hyperintense region (PTH), to obtain the maximum iVASO-CBVa and CBV of each region. The PTH was defined as the T2-hyperintense region within 1 cm around the enhancing tumor.[13] ROIs were drawn in the contralateral white matter as references for normalization (iVASO-rCBVa and DSC-rCBV) (Fig 1). All ROIs were placed independently by 2 blinded experienced neuroradiologists (X. Li and Y. Wu, with 5 and 12 years of experience, respectively). The measurement results of the 2 radiologists were used to assess the interobserver reliability. The average of the 2 measurement results was used for further statistical analysis.

Statistical Analysis

Statistical analysis was performed using SPSS Statistics 22.0 (IBM, Armonk, New York). Interobserver reliability of the parameters between the 2 neuroradiologists was assessed by the intraclass correlation coefficient with 95% confidence intervals. Intraclass correlation coefficient values of $\leq$0.40, between 0.41 and 0.60, between 0.61 and 0.80, and $\geq$0.81 were interpreted as poor, moderate, good, and excellent reliability, respectively. iVASO-CBVa, rCBVa, and DSC-rCBV in intratumoral and peritumoral regions were correlated with each other by calculating Pearson correlation coefficients. The Shapiro-Wilk test was used to assess the normality of data distribution. Comparisons between the GBM and SBM groups were performed using the Student *t* test or Mann-Whitney *U* test accordingly. Receiver operating characteristic and area under the curve (AUC) were used to assess the diagnostic value of parameters for discrimination. An area under the receiver operating characteristic curve greater than 0.90 was considered excellent; 0.80–0.90 was considered good; 0.70–0.80 was considered fair; 0.60–0.70 was considered poor; and $<$0.50 was considered a failure. The cutoff value was established by maximizing the Youden index (Youden index = sensitivity + specificity −1). A statistical significance of a P value $<$ .05 was used.

RESULTS

Twenty GBMs (16 men and 4 women, with a mean age of 46.1 years; range, 18–62 years), which included 19 patients without the *isocitrate dehydrogenase 1* (*IDH1*) mutation and 1 with the *IDH1* mutation, and 22 SBMs (13 men and 9 women, with a mean age of 56.6 years; range, 44–65 years), which included 18 patients with primary non-small cell lung adenocarcinoma, 2 with breast adenocarcinoma, 1 with prostate cancer, and 1 with hepatocellular carcinoma, finally met all of our inclusion and exclusion criteria. Among them, 2 patients with GBMs and 17 with SBMs were diagnosed on the basis of stereotactic biopsy samples, and the conditions of the others were confirmed by gross total resection.

The interobserver reliability was excellent for iVASO-CBVa in PTH (intraclass correlation coefficient = 0.82) and was good for DSC-rCBV (intraclass correlation coefficient = 0.80) and iVASO-rCBVa (intraclass correlation coefficient = 0.74). In the intratumoral region, all the parameters demonstrated excellent reliability (intraclass correlation coefficient = 0.86∼0.89).

The results of correlation analysis are given in On-line Table 2. In the intratumoral region, no substantial correlation was observed between iVASO-CBVa or rCBVa and DSC-rCBV (P = .23 and .18), while in the peritumoral region, a mild correlation was observed between iVASO-CBVa or rCBVa and DSC-rCBV (P < .001).

Perfusion values are plotted in Fig 2. In intratumoral regions, both iVASO-CBVa and rCBVa were significantly higher in patients with GBM than in those with SBM (P = .001 and .005, respectively), while DSC-rCBV showed no significant difference between them (P = .616). In PTH, DSC-rCBV, iVASO-CBVa, and rCBVa revealed higher values in GBM than in SBM (P < .001). Representative cases including iVASO and DSC perfusion MR images are shown in Fig 3.

The results of receiver operating characteristic analysis of each parameter for differentiating GBM and SBM are listed in the Table and plotted in Fig 4. In intratumoral regions, both iVASO-CBVa and rCBVa showed excellent performance, with AUCs of 0.91 and 0.90, a sensitivity of 80% and 70%, and a specificity of 100% and 100%, respectively, which was comparable with that of DSC-rCBV in PTH (AUC, 0.94; sensitivity, 80%; specificity, 100%). In PTH, the AUCs of iVASO-CBVa and rCBVa were 0.83 and 0.72, respectively.

DISCUSSION

Reliable differentiation between GBM and SBM is of vital clinical importance. Our preliminary study investigated the capacity of

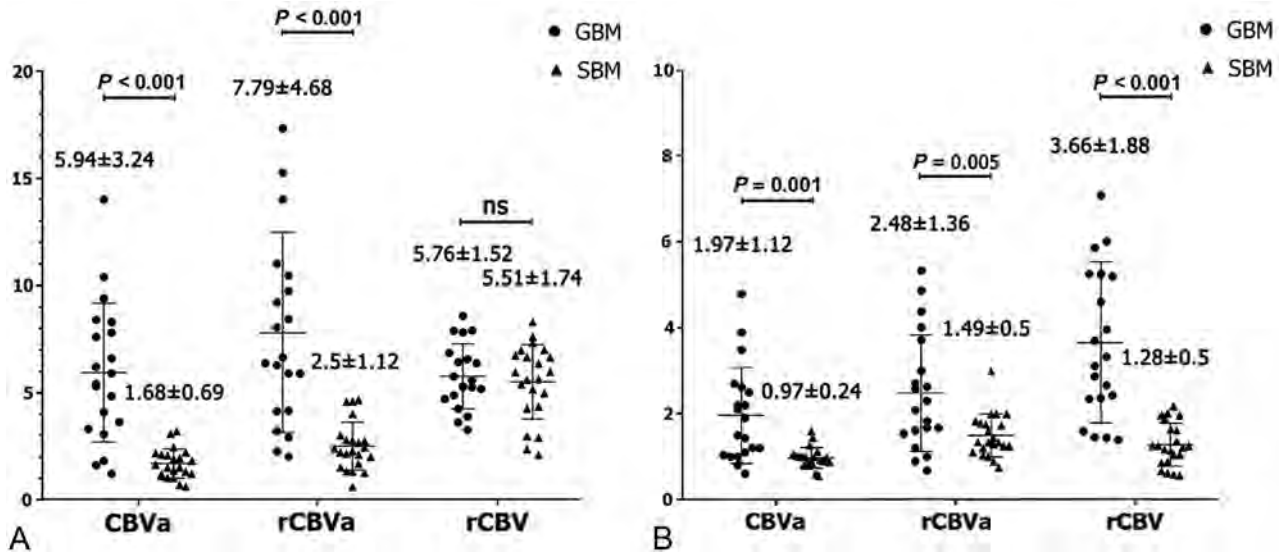

FIG 2. iVASO-CBVa, rCBVa, and DSC-rCBV in the intratumoral region (*A*) and in peritumoral T2-hyperintense region (*B*) of glioblastoma and single brain metastasis. Data are presented as mean value ± SD. Ns indicates not significant.

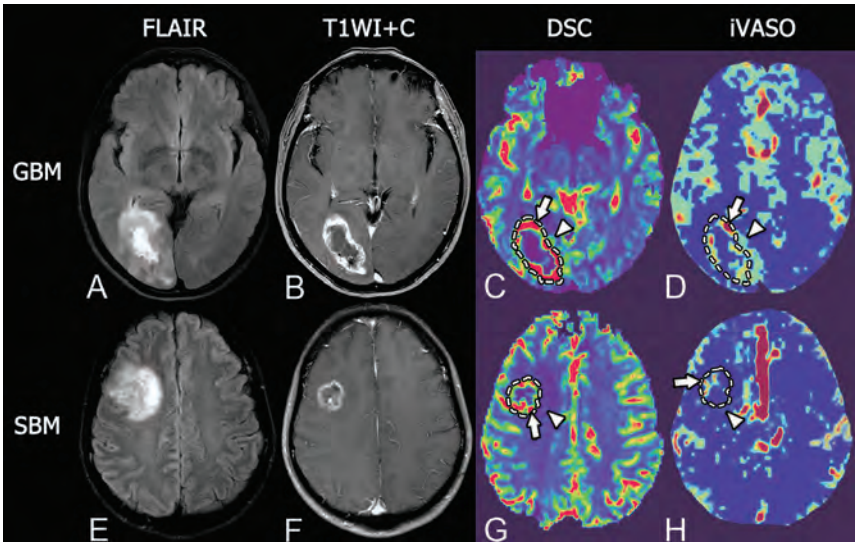

FIG 3. Representative MR images of glioblastoma and single brain metastasis. *Upper row*, A GBM in a 51-year-old woman. *Lower row*, SBM in a 46-year-old man. Both GBM and SBM present as hyperintense masses on T2 FLAIR with extensive peritumoral edema (*A* and *E*) and show a ring-enhancement pattern on fat-suppressed postcontrast T1WI with prominent necrosis in the tumor center (*B* and *F*). In intratumoral regions, GBM shows maximum DSC-rCBV similar to that of SBM (5.29 versus 4.98, *arrows* in *C* and *G*), but higher maximum iVASO-CBVa than SBM (5.90/100 mL versus 1.30/100 mL, *arrows* in *D* and *H*). In the peritumoral region, GBM shows prominently higher DSC-rCBV and iVASO-CBVa than SBM (DSC-rCBV, 3.11 versus 1.25, *arrowheads* in *C* and *G*; iVASO-CBVa, 1.20/100 mL versus 0.55/100 mL, *arrowheads* in *D* and *H*).

iVASO MR imaging to differentiate these 2 types of tumors. The results showed that iVASO-derived CBVa and rCBVa in both intratumoral and peritumoral PTH can accurately discriminate GBM and SBM and that DSC-rCBV was powerful for the discrimination between them only in PTH.

Within PTH, DSC-rCBV can accurately discriminate GBM from SBM according to our study, which was concordant with previous reports.[5,14,15] This finding may be explained by the obviously different perfusion values in the PTH between these entities. Histopathologically, GBM tends to grow in an invasive manner and extends to the PTH beyond the contrast-enhancing margins.[34-39] On the contrary, SBM tends to grow in an expansile way, leading to no prominent infiltration of tumor cells in the PTH beyond the area of contrast enhancement.[15,35,40] However the definition of the tumor boundary is a common issue of controversy within this field. Researchers have defined the tumoral and peritumoral areas in various ways.[1,13,15,41] For gliomas, the so-called peritumoral regions pathologically consist of benign changes, such as vasogenic edema and inflammatory reaction, as well as infiltration by tumor cells. Besides, the peritumoral edema areas of GBM and metastasis are usually extensive and may include different lobes and even extend to the whole cerebral hemisphere and the contralateral hemisphere. This feature will make drawing the ROI relatively difficult and thus affect the interobserver reliability,[42] as shown in our present study in which the interobserver reliability of the peritumoral region (0.74∼0.82) was lower than that of the intratumoral region (0.86∼0.89).

According to most previous studies, the intratumoral region is the mainstream region for measurement.[43,44] The intratumoral perfusion is closely related to tumor biologic characteristics, gene mutation status, therapeutic response, and prognosis.[45-48] Unfortunately, most of these studies have demonstrated that

intratumoral DSC-rCBV was not powerful for differentiating GBM from SBM,[1,6,12-15] as shown in our study. Of note, this finding does not mean that these 2 types of tumors share the same characteristics of microvasculature. Weber et al[13] observed significantly larger microvessel density in GBM than in brain adenocarcinoma metastases. According to the study of Jinnouchi et al,[49] the capillaries of brain metastasis resemble those from the site of the original systemic cancer and thus have no similarity to the normal brain capillaries and completely lack BBB components. On the other hand, GBM is primary brain tumor and has a blood-brain barrier, albeit a heterogeneous, disrupted one.[8,50] Lai et al[51] and Fu et al[52] reported that the degree of intralesional susceptibility signal was significantly higher in GBM than in SBM. Intralesional susceptibility signal reflects the conglomerates of tumor microvascularity, and the degree of intralesional susceptibility signal showed a significant correlation with the value of maximum DSC-rCBV in the same tumor segments.[44,53,54] Furthermore, a few investigators reported significant perfusion differences between GBM and SBM, using parameters of peak height or percentage signal recovery[35,55,56] or histogram analysis of rCBV.[57]

Results of receiver operating characteristic analysis of each parameter

Technique/Parameter	AUC	*P* Value	Cutoff	Se (%)	Sp (%)
Intratumoral region					
iVASO					
CBVa	0.91	<.001	3.25	80.0	100.0
rCBVa	0.90	<.001	5.28	70.0	100.0
DSC					
rCBV	0.51	.920	3.11	100.0	18.2
Peritumoral region					
iVASO					
CBVa	0.83	<.001	1.03	80.0	77.3
rCBVa	0.72	.014	2.04	55.0	95.5
DSC					
rCBV	0.94	<.001	2.26	80.0	100.0

Note: Se indicates sensitivity; Sp, specificity.

In the present study, both iVASO-CBVa and rCBVa accurately differentiated GBM from SBM and outperformed DSC-rCBV without leakage correlation via assessment of the intratumoral regions. Interobserver reliability analysis demonstrated poor reliability between iVASO-derived parameters and DSC-rCBV in intratumoral regions. This may be mainly due to the different compartments assessed by iVASO and DSC. iVASO is designed to quantify the blood volume of the arterioles, while DSC quantifies the perfusion of the whole microvasculature.[23,24] Physiologically, arterioles and pial arteries are the most actively regulated blood vessels in the microvasculature.[27,58,59] They control the cerebral perfusion of the whole microvasculature unit through the contraction and relaxation of smooth-muscle and elastic lamina.[60,61] Also, there is evidence that generation of arterioles occurs before capillary growth in angiogenesis.[62] The predominant arterial origin of the iVASO signal was validated in a previous study by measuring the transverse relaxation times (T2*/T2) of iVASO difference signals, which are highly oxygenation-level dependent.[63] Besides, the iVASO signal changes during functional stimulation, such as somatosensory stimulus and forepaw stimulation, preceded the changes in total CBV,[24] which corresponded to animal studies showing earlier changes in arterioles upon neuronal activation.[64,65] Therefore, the ability to measure arteriolar CBV separately from the rest of the microvasculature (capillaries and venous vessels) may furnish information that is not obtainable from total CBV measures (ie, DSC-CBV) and may make the measurement more sensitive in reflecting hemodynamics changes.[31] Notably, the wall of the arterioles is not permeable to magnetically labeled spin protons. Hence, the CBVa value would not be affected by the disrupted blood-brain barrier. In contrast, the measurement of DSC-rCBV is

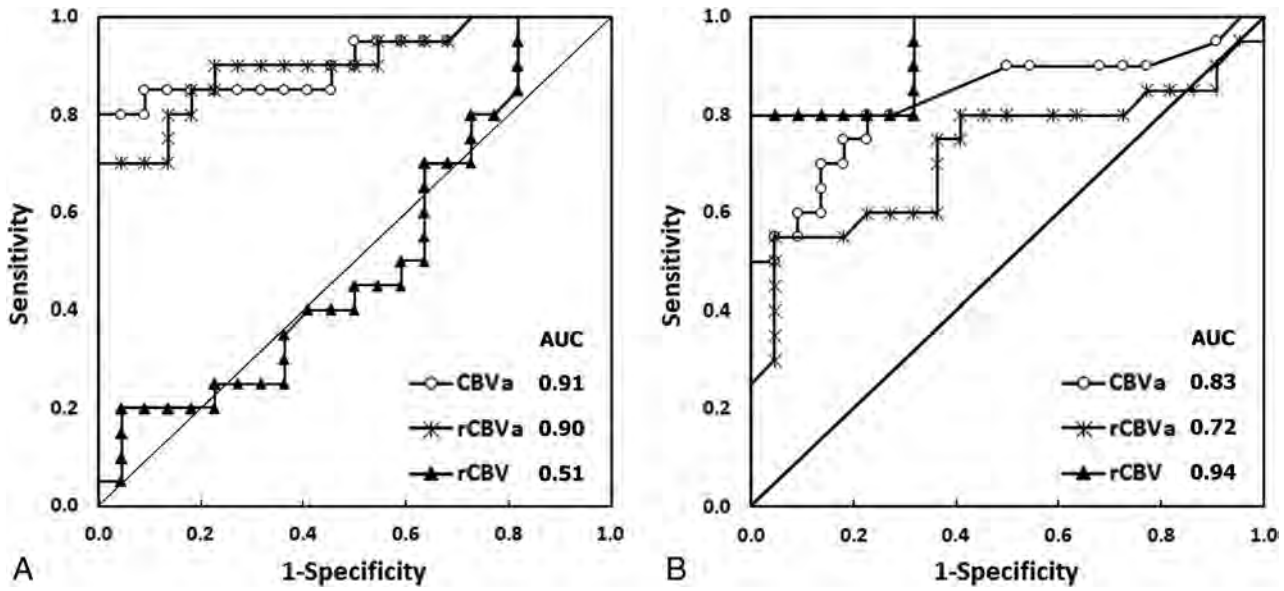

FIG 4. Receiver operating characteristic curves of parameters of iVASO and DSC MR imaging in differentiating glioblastoma and solitary brain metastasis. In the intratumoral region (*A*), both iVASO-CBVa (AUC = 0.91) and rCBVa (AUC = 0.90) show higher AUCs than DSC-rCBV (AUC = 0.51). In the PTH (*B*), the AUC of DSC-rCBV (0.94) is higher than that of iVASO-CBVa (0.83) or rCBVa (0.72).

remarkably confounded by the disrupted blood-brain barrier. Our results demonstrated significant differences in iVASO-CBVa between GBM and SBM. This finding indicates the difference in the arteriolar compartment between them, which is in line with the results revealed by previous studies.[8,13,49-52]

Most interesting, intratumoral iVASO-CBVa had a diagnostic value approximate to that of iVASO-rCBVa. This finding may suggest that the discrimination between GBM and SBM can be achieved by measuring the perfusion value within the intratumoral region alone, which will enhance the clinical applicability of iVASO, whereas iVASO-CBVa and rCBVa in the PTH showed lower capability than their intratumoral counterparts in distinguishing these 2 groups of tumors. This might be related to the heterogeneity and complexity of the microenvironment in the PTH. Also, according to the theory of iVASO, the measurement of iVASO-CBVa is based on the arterial transit time of gray matter, so it is sensitive to blood flow with a relatively high speed.[23] However, the arterial transit time in white matter is relatively long, which will reduce the sensitivity of iVASO in quantifying perfusion.[24,66,67] In contrast, DSC is designed to mainly quantify the capillary bed, so it will not be affected by the relatively slow blood flow in the white matter regions.[32]

DSC MR imaging, the most widely used perfusion MR imaging technique, was recommended as a routine protocol by the 2018 European Guidelines in brain tumor MR scanning.[11] However, the deposit of exogenous contrast agent of gadolinium is a major issue of public concern.[19-22] Also, logistically, the inconvenience of the bolus injection of contrast agent in children and elderly patients has limited the application of DSC scanning.[32,67] Besides, according to most studies,[1,12] DSC failed to discriminate GBM from SBM via analysis of the intratumoral region, just as shown in our present study. iVASO is a totally noninvasive perfusion technique without the need for exogenous contrast agents. Of note, the actual scan time of iVASO MR imaging is usually several minutes longer than DSC MR imaging. However, one important practical advantage of iVASO is that the perfusion data can be obtained in a flexible manner and can be integrated into a conventional MR imaging examination at any time as long as no contrast agent has been administered.[32,67]

Our study has several limitations. First, the sample size is relatively small. Therefore, a larger cohort study is needed to validate these results in the future. Also, metastases of other different cancer subtypes were not included in our study. Second, we did not use histogram analysis to study the tumor perfusion. Generally, histogram analysis reveals more objective results. However, the additional time-consuming postprocessing involved may lower its clinical practicability. Considering that the hotspot method showed good reliability, we believed that this would not essentially affect our main results. Moreover, we did not apply the leakage-correction analysis method or preload gadolinium-based contrast agent in our DSC protocol to reduce the variance of gadolinium rCBV estimates.[68] However, a recent DSC study applying preload of contrast agent failed to discriminate these 2 groups of tumors in the intratumoral region.[12] Moreover, the complexity of the operation and the consumption of more time, which greatly hinder patient compliance and cause motion artifacts, limit the use of leakage-correction and preload strategy in clinical practice.[69] In addition, it would be better to perform imaging-pathology correlation analysis. However, because the section thickness (6 mm) of the current iVASO technique is inferior to the requirement for stereotactic biopsy, one-to-one correspondence between the biopsied regions and imaged regions is not possible.

CONCLUSIONS

This preliminary study demonstrated that iVASO might be useful for discriminating GBM from SBM based on the analysis of either PTH or intratumoral region. Due to its completely noninvasive nature, iVASO might greatly benefit patients with brain tumor in daily clinical practice, especially for elderly populations and those with compromised renal function.

Disclosures: Jay Pillai—*UNRELATED*: *Royalties*: Springer Science & Business Media, Elsevier, *Comments*: royalties for books published.

REFERENCES

1. Bauer AH, Erly W, Moser FG, et al. **Differentiation of solitary brain metastasis from glioblastoma multiforme: a predictive multiparametric approach using combined MR diffusion and perfusion.** *Neuroradiology* 2015;57:697–703 CrossRef Medline
2. Soffietti R, Abacioglu U, Baumert B, et al. **Diagnosis and treatment of brain metastases from solid tumors: guidelines from the European Association of Neuro-Oncology (EANO).** *Neuro Oncol* 2017;19:162–74 CrossRef Medline
3. Ahmed R, Oborski MJ, Hwang M, et al. **Malignant gliomas: current perspectives in diagnosis, treatment, and early response assessment using advanced quantitative imaging methods.** *Cancer Manag Res* 2014;6:149–70 CrossRef Medline
4. Giese A, Westphal M. **Treatment of malignant glioma: a problem beyond the margins of resection.** *J Cancer Res Clin Oncol* 2001; 127:217–25 CrossRef Medline
5. Lee EJ, Ahn KJ, Lee EK, et al. **Potential role of advanced MRI techniques for the peritumoural region in differentiating glioblastoma multiforme and solitary metastatic lesions.** *Clin Radiol* 2013;68: e689–97 CrossRef Medline
6. Server A, Orheim TE, Graff BA, et al. **Diagnostic examination performance by using microvascular leakage, cerebral blood volume, and blood flow derived from 3-T dynamic susceptibility-weighted contrast-enhanced perfusion MR imaging in the differentiation of glioblastoma multiforme and brain metastasis.** *Neuroradiology* 2011;53:319–30 CrossRef Medline
7. Maluf FC, DeAngelis LM, Raizer JJ, et al. **High-grade gliomas in patients with prior systemic malignancies.** *Cancer* 2002;94:3219–24 CrossRef Medline
8. Wesseling P, Ruiter DJ, Burger PC. **Angiogenesis in brain tumors; pathobiological and clinical aspects.** *J Neurooncol* 1997;32:253–65 CrossRef Medline
9. Long DM. **Capillary ultrastructure in human metastatic brain tumors.** *J Neurosurg* 1979;51:53–58 CrossRef Medline
10. Cha S, Knopp EA, Johnson G, et al. **Intracranial mass lesions: dynamic contrast-enhanced susceptibility-weighted echo-planar perfusion MR imaging.** *Radiology* 2002;223:11–29 CrossRef Medline
11. Thust SC, Heiland S, Falini A, et al. **Glioma imaging in Europe: a survey of 220 centres and recommendations for best clinical practice.** *Eur Radiol* 2018;28:3306–17 CrossRef Medline
12. Suh CH, Kim HS, Jung SC, et al. **Perfusion MRI as a diagnostic biomarker for differentiating glioma from brain metastasis: a systematic review and meta-analysis.** *Eur Radiol* 2018;28:3819–31 CrossRef Medline
13. Weber MA, Zoubaa S, Schlieter M, et al. **Diagnostic performance of spectroscopic and perfusion MRI for distinction of brain tumors.** *Neurology* 2006;66:1899–906 CrossRef Medline

14. Chiang IC, Kuo YT, Lu CY, et al. **Distinction between high-grade gliomas and solitary metastases using peritumoral 3-T magnetic resonance spectroscopy, diffusion, and perfusion imagings.** *Neuroradiology* 2004;46:619–27 CrossRef Medline
15. Law M, Cha S, Knopp EA, et al. **High-grade gliomas and solitary metastases: differentiation by using perfusion and proton spectroscopic MR imaging.** *Radiology* 2002;222:715–21 CrossRef Medline
16. Boxerman JL, Schmainda KM, Weisskoff RM. **Relative cerebral blood volume maps corrected for contrast agent extravasation significantly correlate with glioma tumor grade, whereas uncorrected maps do not.** *AJNR Am J Neuroradiol* 2006;27:859–67 Medline
17. Sunwoo L, Yun TJ, You SH, et al. **Differentiation of glioblastoma from brain metastasis: qualitative and quantitative analysis using arterial spin labeling MR imaging.** *PLoS One* 2016;11:e0166662 CrossRef Medline
18. Lemee JM, Clavreul A, Menei P. **Intratumoral heterogeneity in glioblastoma: don't forget the peritumoral brain zone.** *Neuro Oncol* 2015;17:1322–32 CrossRef Medline
19. Gulani V, Calamante F, Shellock FG, et al; International Society for Magnetic Resonance in Medicine. **Gadolinium deposition in the brain: summary of evidence and recommendations.** *Lancet Neurol* 2017;16:564–70 CrossRef Medline
20. Kuo PH, Kanal E, Abu-Alfa AK, et al. **Gadolinium-based MR contrast agents and nephrogenic systemic fibrosis.** *Radiology* 2007;242:647–49 CrossRef Medline
21. Schieda N, Blaichman JI, Costa AF, et al. **Gadolinium-based contrast agents in kidney disease: a comprehensive review and clinical practice guideline issued by the Canadian Association of Radiologists.** *Can J Kidney Health Dis* 2018;5:2054358118778573 CrossRef Medline
22. Bjornerud A, Vatnehol SAS, Larsson C, et al. **Signal enhancement of the dentate nucleus at unenhanced MR imaging after very high cumulative doses of the macrocyclic gadolinium-based contrast agent gadobutrol: an observational study.** *Radiology* 2017;285:434–44 CrossRef Medline
23. Hua J, Liu P, Kim T, et al. **MRI techniques to measure arterial and venous cerebral blood volume.** *Neuroimage* 2019;187:17–31 CrossRef Medline
24. Hua J, Qin Q, Donahue MJ, et al. **Inflow-based vascular-space-occupancy (iVASO) MRI.** *Magn Reson Med* 2011;66:40–56 CrossRef Medline
25. Hua J, Qin Q, Pekar JJ, et al. **Measurement of absolute arterial cerebral blood volume in human brain without using a contrast agent.** *NMR Biomed* 2011;24:1313–25 CrossRef Medline
26. Huber L, Goense J, Kennerley AJ, et al. **Investigation of the neurovascular coupling in positive and negative BOLD responses in human brain at 7 T.** *Neuroimage* 2014;97:349–62 CrossRef Medline
27. Ito H, Ibaraki M, Kanno I, et al. **Changes in the arterial fraction of human cerebral blood volume during hypercapnia and hypocapnia measured by positron emission tomography.** *J Cereb Blood Flow Metab* 2005;25:852–57 CrossRef Medline
28. van Zijl PC, Eleff SM, Ulatowski JA, et al. **Quantitative assessment of blood flow, blood volume and blood oxygenation effects in functional magnetic resonance imaging.** *Nat Med* 1998;4:159–67 CrossRef Medline
29. Hua J, Unschuld PG, Margolis RL, et al. **Elevated arteriolar cerebral blood volume in prodromal Huntington's disease.** *Mov Disord* 2014;29:396–401 CrossRef Medline
30. Hua JL, Blair NIS. **Abnormal grey matter arteriolar cerebral blood volume and its association with the presence of E4 allele of the apolipoprotein E (APOE) gene in elderly subjects at risk for Alzheimer's disease.** In: *Proceedings of the Scientific Meeting and Exhibition of the International Society for Magnetic Resonance in Medicine*, May 7–13, 2016. Singapore; 4030
31. Hua J, Brandt AS, Lee S, et al. **Abnormal grey matter arteriolar cerebral blood volume in schizophrenia measured with 3D inflow-based vascular-space-occupancy MRI at 7T.** *Schizophr Bull* 2017;43:620–32 CrossRef Medline
32. Wu Y, Agarwal S, Jones CK, et al. **Measurement of arteriolar blood volume in brain tumors using MRI without exogenous contrast agent administration at 7T.** *J Magn Reson Imaging* 2016;44:1244–55 CrossRef Medline
33. Wetzel SG, Cha S, Johnson G, et al. **Relative cerebral blood volume measurements in intracranial mass lesions: interobserver and intraobserver reproducibility study.** *Radiology* 2002;224:797–803 CrossRef Medline
34. Ricci R, Bacci A, Tugnoli V, et al. **Metabolic findings on 3T 1H-MR spectroscopy in peritumoral brain edema.** *AJNR Am J Neuroradiol* 2007;28:1287–91 CrossRef Medline
35. Cha S, Lupo JM, Chen MH, et al. **Differentiation of glioblastoma multiforme and single brain metastasis by peak height and percentage of signal intensity recovery derived from dynamic susceptibility-weighted contrast-enhanced perfusion MR imaging.** *AJNR Am J Neuroradiol* 2007;28:1078–84 CrossRef Medline
36. Cha S. **Perfusion MR imaging of brain tumors.** *Top Magn Reson Imaging* 2004;15:279–89 CrossRef Medline
37. Bertossi M, Virgintino D, Maiorano E, et al. **Ultrastructural and morphometric investigation of human brain capillaries in normal and peritumoral tissues.** *Ultrastruct Pathol* 1997;21:41–49 CrossRef Medline
38. Kelly PJ, Daumas-Duport C, Scheithauer BW, et al. **Stereotactic histologic correlations of computed tomography- and magnetic resonance imaging-defined abnormalities in patients with glial neoplasms.** *Mayo Clin Proc* 1987;62:450–59 CrossRef Medline
39. Daumas-Duport C, Monsaigneon V, Blond S, et al. **Serial stereotactic biopsies and CT scan in gliomas: correlative study in 100 astrocytomas, oligo-astrocytomas and oligodendrocytomas.** *J Neurooncol* 1987;4:317–28 CrossRef Medline
40. Server A, Josefsen R, Kulle B, et al. **Proton magnetic resonance spectroscopy in the distinction of high-grade cerebral gliomas from single metastatic brain tumors.** *Acta Radiol* 2010;51:316–25 CrossRef Medline
41. Halshtok NO, Sadetzki S, Chetrit A, et al. **Perfusion-weighted imaging of peritumoral edema can aid in the differential diagnosis of glioblastoma mulltiforme versus brain metastasis.** *Isr Med Assoc J* 2013;15:103–05 Medline
42. Oei MTH, Meijer FJA, Mordang JJ, et al. **Observer variability of reference tissue selection for relative cerebral blood volume measurements in glioma patients.** *Eur Radiol* 2018;28:3902–11 CrossRef Medline
43. Usinskiene J, Ulyte A, Bjornerud A, et al. **Optimal differentiation of high- and low-grade glioma and metastasis: a meta-analysis of perfusion, diffusion, and spectroscopy metrics.** *Neuroradiology* 2016;58:339–50 CrossRef Medline
44. Park MJ, Kim HS, Jahng GH, et al. **Semiquantitative assessment of intratumoral susceptibility signals using non-contrast-enhanced high-field high-resolution susceptibility-weighted imaging in patients with gliomas: comparison with MR perfusion imaging.** *AJNR Am J Neuroradiol* 2009;30:1402–08 CrossRef Medline
45. Hu LS, Ning S, Eschbacher JM, et al. **Radiogenomics to characterize regional genetic heterogeneity in glioblastoma.** *Neuro Oncol* 2017;19:128–37 CrossRef Medline
46. Nguyen TB, Cron GO, Bezzina K, et al. **Correlation of tumor immunohistochemistry with dynamic contrast-enhanced and DSC-MRI parameters in patients with gliomas.** *AJNR Am J Neuroradiol* 2016;37:2217–23 CrossRef Medline
47. Meyer M, Reimand J, Lan X, et al. **Single cell-derived clonal analysis of human glioblastoma links functional and genomic heterogeneity.** *Proc Natl Acad Sci USA* 2015;112:851–56 CrossRef Medline
48. Stieber D, Golebiewska A, Evers L, et al. **Glioblastomas are composed of genetically divergent clones with distinct tumourigenic potential and variable stem cell-associated phenotypes.** *Acta Neuropathol* 2014;127:203–19 CrossRef Medline
49. Jinnouchi T, Shibata S, Fukushima M, et al. **Ultrastructure of capillary permeability in human brain tumor, Part 6: metastatic brain**

tumor with brain edema [in Japanese]. *No Shinkei Geka* 1988;16(5 Suppl):563–68 Medline
50. Sarkaria JN, Hu LS, Parney IF, et al. **Is the blood-brain barrier really disrupted in all glioblastomas? A critical assessment of existing clinical data.** *Neuro Oncol* 2018;20:184–91 CrossRef Medline
51. Lai PH, Chung HW, Chang HC, et al. **Susceptibility-weighted imaging provides complementary value to diffusion-weighted imaging in the differentiation between pyogenic brain abscesses, necrotic glioblastomas, and necrotic metastatic brain tumors.** *Eur J Radiol* 2019;117:56–61 CrossRef Medline
52. Fu JH, Chuang TC, Chung HW, et al. **Discriminating pyogenic brain abscesses, necrotic glioblastomas, and necrotic metastatic brain tumors by means of susceptibility-weighted imaging.** *Eur Radiol* 2015;25:1413–20 CrossRef Medline
53. Pinker K, Noebauer-Huhmann IM, Stavrou I, et al. **High-resolution contrast-enhanced, susceptibility-weighted MR imaging at 3T in patients with brain tumors: correlation with positron-emission tomography and histopathologic findings.** *AJNR Am J Neuroradiol* 2007;28:1280–86 CrossRef Medline
54. Park SM, Kim HS, Jahng GH, et al. **Combination of high-resolution susceptibility-weighted imaging and the apparent diffusion coefficient: added value to brain tumour imaging and clinical feasibility of non-contrast MRI at 3 T.** *Br J Radiol* 2010;83:466–75 CrossRef Medline
55. Mouthuy N, Cosnard G, Abarca-Quinones J, et al. **Multiparametric magnetic resonance imaging to differentiate high-grade gliomas and brain metastases.** *J Neuroradiol* 2012;39:301–07 CrossRef Medline
56. Vallée A, Guillevin C, Wager M, et al. **Added value of spectroscopy to perfusion MRI in the differential diagnostic performance of common malignant brain tumors.** *AJNR Am J Neuroradiol* 2018;39:1423–31 CrossRef Medline
57. Ma JH, Kim HS, Rim NJ, et al. **Differentiation among glioblastoma multiforme, solitary metastatic tumor, and lymphoma using whole-tumor histogram analysis of the normalized cerebral blood volume in enhancing and perienhancing lesions.** *AJNR Am J Neuroradiol* 2010;31:1699–706 CrossRef Medline
58. Iadecola C, Nedergaard M. **Glial regulation of the cerebral microvasculature.** *Nat Neurosci* 2007;10:1369–76 CrossRef Medline
59. Kim T, Hendrich KS, Masamoto K, et al. **Arterial versus total blood volume changes during neural activity-induced cerebral blood flow change: implication for BOLD fMRI.** *J Cereb Blood Flow Metab* 2007;27:1235–47 CrossRef Medline
60. Gitiaux C, Kostallari E, Lafuste P, et al. **Whole microvascular unit deletions in dermatomyositis.** *Ann Rheum Dis* 2013;72:445–52 CrossRef Medline
61. Shen Z, Lu Z, Chhatbar PY, et al. **An artery-specific fluorescent dye for studying neurovascular coupling.** *Nat Methods* 2012;9:273–76 CrossRef Medline
62. Hansen-Smith F, Egginton S, Zhou AL, et al. **Growth of arterioles precedes that of capillaries in stretch-induced angiogenesis in skeletal muscle.** *Microvasc Res* 2001;62:1–14 CrossRef Medline
63. Zhao JM, Clingman CS, Narvainen MJ, et al. **Oxygenation and hematocrit dependence of transverse relaxation rates of blood at 3T.** *Magn Reson Med* 2007;58:592–97 CrossRef Medline
64. Vanzetta I, Hildesheim R, Grinvald A. **Compartment-resolved imaging of activity-dependent dynamics of cortical blood volume and oximetry.** *J Neurosci* 2005;25:2233–44 CrossRef
65. Hillman EM, Devor A, Bouchard MB, et al. **Depth-resolved optical imaging and microscopy of vascular compartment dynamics during somatosensory stimulation.** *Neuroimage* 2007;35:89–104 CrossRef Medline
66. Gunther M, Bock M, Schad LR. **Arterial spin-labeling in combination with a look-locker sampling strategy: inflow turbo-sampling EPI-FAIR (ITS-FAIR).** *Magn Reson Med* 2001;46:974–84 CrossRef Medline
67. Warmuth C, Gunther M, Zimmer C. **Quantification of blood flow in brain tumors: comparison of arterial spin labeling and dynamic susceptibility-weighted contrast-enhanced MR imaging.** *Radiology* 2003;228:523–32 CrossRef Medline
68. Boxerman JL, Prah DE, Paulson ES, et al. **The role of preload and leakage correction in gadolinium-based cerebral blood volume estimation determined by comparison with MION as a criterion standard.** *AJNR Am J Neuroradiol* 2012;33:1081–87 CrossRef Medline
69. Welker K, Boxerman J, Kalnin A, et al; American Society of Functional Neuroradiology MR Perfusion Standards and Practice Subcommittee of the ASFNR Clinical Practice Committee. **ASFNR recommendations for clinical performance of MR dynamic susceptibility contrast perfusion imaging of the brain.** *AJNR Am J Neuroradiol* 2015;36:E41–51 CrossRef Medline

Hippocampal Sclerosis Detection with NeuroQuant Compared with Neuroradiologists

S. Louis, M. Morita-Sherman, S. Jones, D. Vegh, W. Bingaman, I. Blumcke, N. Obuchowski, F. Cendes, and L. Jehi

ABSTRACT

BACKGROUND AND PURPOSE: NeuroQuant is an FDA-approved software that performs automated MR imaging quantitative volumetric analysis. This study aimed to compare the accuracy of NeuroQuant analysis with visual MR imaging analysis by neuroradiologists with expertise in epilepsy in identifying hippocampal sclerosis.

MATERIALS AND METHODS: We reviewed 144 adult patients who underwent presurgical evaluation for temporal lobe epilepsy. The reference standard for hippocampal sclerosis was defined by having hippocampal sclerosis on pathology ($n = 61$) or not having hippocampal sclerosis on pathology ($n = 83$). Sensitivities, specificities, positive predictive values, and negative predictive values were compared between NeuroQuant analysis and visual MR imaging analysis by using a McNemar paired test of proportions and the Bayes theorem.

RESULTS: NeuroQuant analysis had a similar specificity to neuroradiologist visual MR imaging analysis (90.4% versus 91.6%; $P = .99$) but a lower sensitivity (69.0% versus 93.0%, $P < .001$). The positive predictive value of NeuroQuant analysis was comparable with visual MR imaging analysis (84.0% versus 89.1%), whereas the negative predictive value was not comparable (79.8% versus 95.0%).

CONCLUSIONS: Visual MR imaging analysis by a neuroradiologist with expertise in epilepsy had a higher sensitivity than did NeuroQuant analysis, likely due to the inability of NeuroQuant to evaluate changes in hippocampal T2 signal or architecture. Given that there was no significant difference in specificity between NeuroQuant analysis and visual MR imaging analysis, NeuroQuant can be a valuable tool when the results are positive, particularly in centers that lack neuroradiologists with expertise in epilepsy, to help identify and refer candidates for temporal lobe epilepsy resection. In contrast, a negative test could justify a case referral for further evaluation to ensure that false-negatives are detected.

ABBREVIATIONS: HS = hippocampal sclerosis; PPV = positive predictive value; NPV = negative predictive value

Hippocampal sclerosis (HS) is one of the most common neuropathologic substrates of temporal lobe epilepsy, which often requires surgical resection in patients who are drug resistant. The current clinical standard of practice for the evaluation of drug-resistant seizures requires a neuroradiologist's assessment of the patient's brain MR imaging. The ability to detect lesions (HS or other lesions) is known to correlate with marked improvement in surgical outcomes and may motivate the treating neurologist to initiate a surgical evaluation. Literature that compares the ability of general radiologists with that of neuroradiologists with expertise in epilepsy in identifying HS is limited but suggests a superiority that favors trained specialists.

A study from 2002 by Von Oertzen et al[1] claimed that "non-expert" neuroradiologists who evaluated standard MRIs in patients with temporal and extra-temporal epilepsies had a sensitivity of 39% in detecting epileptogenic abnormalities compared with 50% by neuroradiologists who had expertise in epilepsy reading standard MRIs and 91% when reading epilepsy-dedicated MRIs. These figures include different types of lesions; however, the exact figures for HS sensitivity and specificity are not clear in that study.[1] Nevertheless, such performance discrepancies contribute to a health care delivery gap that needs to be bridged to allow centers without dedicated expertise to detect epileptogenic lesions, including HS, and to better identify patients in need of

Received November 7, 2019; accepted after revision January 17, 2020.

From the Epilepsy Center (S.L., M.M.-S., S.J., D.V., W.B., L.J.), and Quantitative Health Sciences (N.O.), Cleveland Clinic, Cleveland, Ohio; Institute of Neuropathology (I.B.), University Hospitals Erlangen, Erlangen, Germany; and Department of Neurology (F.C.), University of Campinas–UNICAMP, Campinas, São Paulo, Brazil.

This research was supported by National Institute of Neurological Disorders and Stroke of the National Institutes of Health under award number 1R01NS097719-01A1.

Please address correspondence to Lara Jehi, MD, Department of Neurology, Cleveland Clinic, 9500 Euclid Ave. Cleveland, OH 44195; e-mail: Jehil@ccf.org; @LaraJehiMD

Indicates open access to non-subscribers at www.ajnr.org

http://dx.doi.org/10.3174/ajnr.A6454

surgical evaluation. This gap is particularly relevant, given abundant literature that demonstrates the underutilization of epilepsy surgery, partly attributed to the reluctance to refer patients who are "nonlesional" for a surgical evaluation for fear of a lower odds of postoperative seizure freedom.[2-4]

NeuroQuant is the first FDA-approved automated software (CorTechs Labs, San Diego, California) that provides absolute volumes of brain structures as well as the relative volume between left- and right-sided structures (eg, left hippocampus relative to the right hippocampus) and compares the structural volumes to a normative control (with results reported as percentiles compared with the normative cohort). It was previously used to assess hippocampal volume changes in patients with Alzheimer disease,[5] traumatic brain injury,[6] and multiple sclerosis,[7,8] but studies in epilepsy have been limited by heterogeneous patient cohorts,[9,10] and small sample sizes.[11] Furthermore, none of these studies were based on a histopathologic confirmation of HS as a reference standard. These limitations complicate the clinical applicability and generalizability of NeuroQuant analysis for epilepsy. The purpose of this study was to compare the clinical accuracy, sensitivity, and specificity of a neuroradiologist with expertise in epilepsy with that of volumetric analysis with NeuroQuant.

METHODS

Study Design and Patient Selection

We selected adult patients from our tertiary-care center who underwent a comprehensive presurgical evaluation for temporal lobe epilepsy resections from 2010 to 2017. The presurgical evaluation consisted of clinical history, video electroencephalography, PET, and MR imaging, in addition to SPECT, magnetoencephalography, and invasive electroencephalography when indicated. Patients were included if they had a 3T preoperative MR imaging and a postoperative hippocampal pathology report. We excluded patients with hippocampal tumors on pathology ($n = 8$) to avoid the volumetric software counting tumor as hippocampal volume or patients with a history of epilepsy surgery ($n = 22$). We included a total of 144 patients in the analysis, 61 with HS confirmed by histopathology and 83 patients with histopathology negative results for HS. This study was approved by the Cleveland Clinic Institutional Review Board.

Definition of HS

Postoperative histologic analysis was reviewed by an epilepsy-trained neuropathologist (I.B.). Each patient in this study was classified as HS+ (histopathology diagnostic of HS) as defined by using the most recent International League Against Epilepsy classification system of clinical-neuropathologic subtypes of mesial temporal sclerosis,[12,13] or as HS– (the hippocampus is normal on histopathology or shows nonspecific findings). This histologic classification was the reference standard that we used to assess the accuracy of expert visual MR imaging analysis relative to NeuroQuant analysis in identifying HS.

MR Imaging Visual Analysis

All MRIs in this study were acquired on a 3T scanner and were reviewed before surgery by a neuroradiologist with expertise in epilepsy in the setting of an interdisciplinary epilepsy patient management conference in which patients are assessed for potential surgical interventions. The interdisciplinary team consists of neuroradiologists with epilepsy expertise, epileptologists, epilepsy-trained neurosurgeons, and neuropsychologists. There are 4 main neuroradiologists at our institution who provide the preoperative MR imaging assessments for the patient management conferences, with an average of 20 years of experience (minimum of 3 years) with epilepsy imaging and research. Only 1 neuroradiologist at a time attends the meeting to provide an official reading of the MR imaging.

After the case is presented, the MR imaging is reviewed and the neuroradiologist confirms the final impression. The standard MR imaging protocol for this study consisted of a 3T sagittal T1-weighted sequence, axial FLAIR and DWI sequences, volumetric coronal T1-weighted MPRAGE, thin-section coronal FLAIR, and T2-weighted sequences. In addition, the team had access to past MR imaging studies, the patient's semiology, and other studies (eg, PET, SPECT, electroencephalography) to aid in the holistic determination of the patient's HS status. The inclusion of other studies beyond MR imaging also helped to lower the risk of favoring a solely imaging-based diagnosis because patients could be referred for surgery even in the absence of MR imaging findings.

Criteria for MR Imaging Signs of HS

Each patient was classified as having MR imaging signs of HS (visual MR imaging HS+) or not (visual MR imaging HS–) by using features such as an increased T2/FLAIR signal, loss of hippocampal architecture, and loss of hippocampal volume. Ancillary signs included volume loss of the temporal pole and a corresponding subcortical white matter signal abnormality. There were a total of 80 visual MR imaging HS– and 64 visual MR imaging HS+ included in this study. Any MR imaging studies that showed questionable signs of HS were classified as visual MR imaging HS–.

Quantitative Hippocampal Volumetric Analysis by Using NeuroQuant Software

T1 MRIs were de-identified before uploading to the NeuroQuant servers. The NeuroQuant software segments T1 volumetric images, quantifies various volumes of the brain, and compares them against a normative data base adjusted for age (3 to 100 years), sex, and cranial volume.[14] NeuroQuant is easy to use and is compatible with 1.5T and 3T noncontrast MR imaging, which creates volumetric reports in roughly 5–10 minutes (Figs 1 and 2).

After uploading de-identified 3D volumetric T1 images, we used the NeuroQuant hippocampal asymmetry report to classify all hippocampal volumes less than the 5th percentile (compared with the normative control group) as hippocampal atrophy (NeuroQuant HA+ group). To further ensure that we selected an adequate cutoff point, we also analyzed cutoff values of 7, 6, 4, 3, and 2, and found that the 5th percentile cutoff mark recommended by NeuroQuant analysis was the most sensitive and specific for hippocampal atrophy (Table 1). We further classified the hippocampal volumes based on the side of surgery as right or left, and used the surgical side to compare with pathology and visual analysis results.

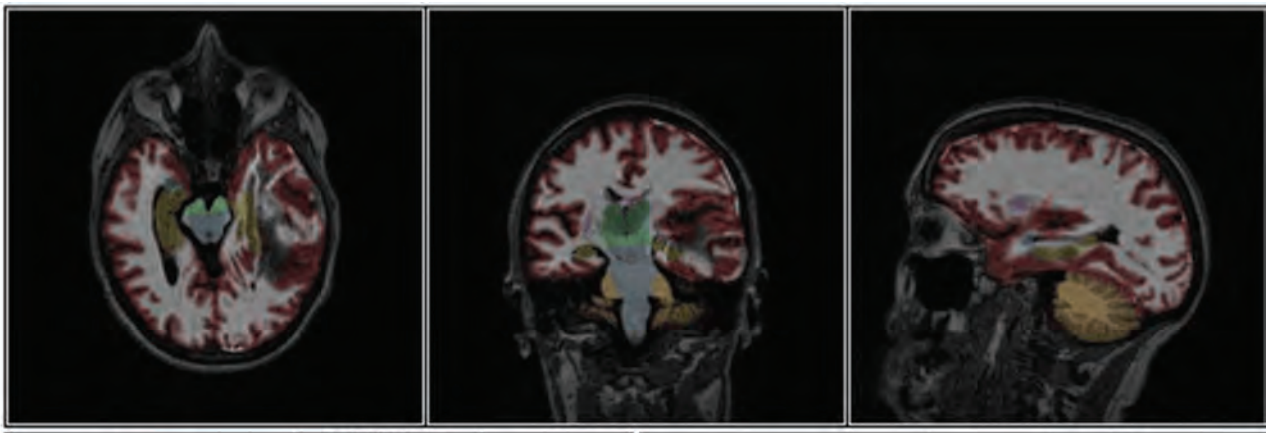

Structure	Total Volume (cm^3)	Percentile
Intracranial Volume	1579	78
Whole Brain	1286	99
Forebrain Parenchyma	1144	99

Total Volumes	Percentiles		
	Left	Right	Total
Cerebral White Matter	98	99	99
Cortical Gray Matter	99	19	96
Ventricles	6	20	11
Cerebral WM Hypointensities*	99	1	99
Subcortical Structures			
Cerebellar White Matter	10	11	10
Cerebellar Gray Matter	16	18	17
Brainstem	-	-	67
Thalamus	53	87	75
Ventral Diencephalon	72	80	77
Basal Ganglia			
Putamen	3	15	7
Caudate	1	17	1
Nucleus Accumbens	96	96	97
Pallidum	1	25	6
Cingulate	85	69	79
Anterior Cingulate	90	92	93
Posterior Cingulate	84	61	75
Isthmus Cingulate	40	8	21

Cortical Brain Regions	Percentiles		
	Left	Right	Total
Frontal Lobes	99	19	89
Superior Frontal	99	31	82
Middle Frontal	76	54	68
Inferior Frontal	99	9	88
Lateral Orbitofrontal	53	14	31
Medial Orbitofrontal	24	40	33
Paracentral	95	80	92
Primary Motor	99	14	99
Parietal Lobes	99	19	93
Primary Sensory	99	46	98
Medial Parietal	99	45	91
Superior Parietal	63	9	29
Inferior Parietal	89	42	71
Supramarginal	99	22	99
Occipital Lobes	40	10	22
Medial Occipital	27	3	10
Lateral Occipital	52	33	42
Temporal Lobes	99	53	99
Transverse Temporal + Superior Temporal	99	43	99
Posterior Superior Temporal Sulcus	99	4	99
Middle Temporal	87	85	89
Inferior Temporal	98	6	66
Fusiform	99	59	98
Parahippocampal	99	28	80
Entorhinal Cortex	78	80	83
Temporal Pole	95	63	88
Amygdala	30	96	75
Hippocampus	99	67	98

FIG 1. NeuroQuant triage brain atrophy report provides volumetric percentiles of left and right regions of the brain.

Statistical Analysis

We used the first 30 cases to determine the a priori discordance rate (how many times the results from MR imaging and NeuroQuant analysis differed), and, by using an alpha of 0.05 to achieve a power of 0.80, we determined that we needed at least 60 study subjects with HS and 60 without HS. Our final study had 61 patients with HS and 83 patients without HS. A McNemar paired test of proportions was then used for sensitivity and specificity testing between NeuroQuant analysis and MR imaging (Table 2). Because the positive predictive value (PPV) and negative predictive value (NPV) in this study are specific to the Cleveland Clinic's epilepsy population and the prevalence of HS in that population, we wanted to evaluate how the PPV and NPV would change with changes in HS prevalence so that our results could be applied in settings with a varying prevalence of HS. We used the Bayes theorem (Equations 1 and 2) to calculate PPV and NPV based on the prevalence, sensitivity, and specificity found in this study (Figs 1 and 2).

1) $$PPV = sensitivity \times prevalence / sensitivity \times prevalence + (1 - specificity) \times (1 - prevalence)$$

2) $$NPV = specificity \times (1 - prevalence) / (1 - sensitivity) \times prevalence + specificity = (1 - prevalence)$$

RESULTS

Cohort Characteristics

To examine potential confounding variables, we analyzed sex, mean age at surgery, hippocampal volume, and side of surgery in

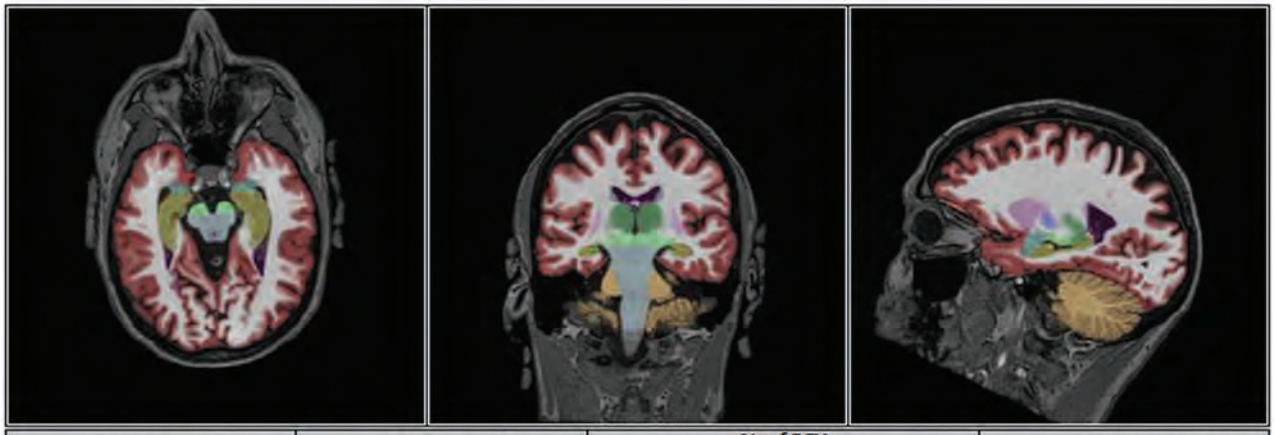

Hippocampus	Volume (cm³)	% of ICV (5%-95% Normative Percentile)	Normative Percentile
Left	3.99	0.28 (0.23 - 0.30)	78
Right	3.54	0.25 (0.24 - 0.31)	16
Left-Right Asymmetry Index*: 11.8			99

AGE-MATCHED REFERENCE CHARTS

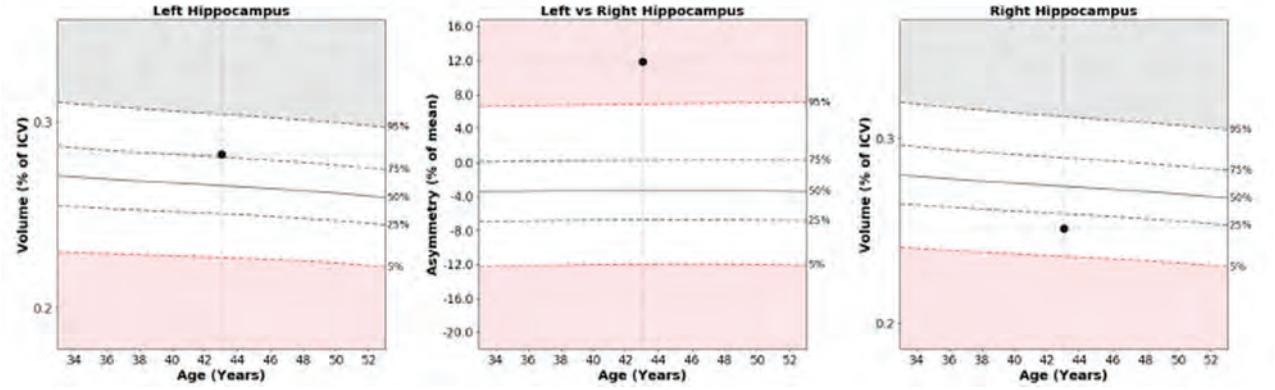

FIG 2. NeuroQuant hippocampal atrophy report provides volumetric percentiles of the left and right regions of the hippocampus as well as the normative percentile of the hippocampus compared with the normative control group of patients.

Table 1: Sensitivities, specificities, PPVs, and NPVs, with varying cutoff points of NeuroQuant analysis

NeuroQuant Cutoff Point	Sensitivity, %	Specificity, %	PPV, %	NPV, %
<7%	44.3	68.7	50.9	62.6
<6%	42.6	68.7	50.0	62.0
<5%	68.8	90.4	84.0	79.8
<4%	39.3	71.1	50.0	61.5
<3%	37.7	74.7	52.3	62.0
<2%	31.1	78.3	51.4	60.7

Table 2: Results for NeuroQuant analysis vs visual MR imaging analysis in identifying HS by using histopathology as the reference standard for HS

	Sensitivity and Specificity Analysis			
	Pathology Positive HS+ (n = 61)		Pathology Negative HS– (n = 83)	
NeuroQuant Analysis	Visual MR Imaging HS+	Visual MR Imaging HS–	Visual MR Imaging HS+	Visual MR Imaging HS–
HS+[a]	41	1	4	4
HS–[b]	16	3	3	72

[a] Defined as a NeuroQuant value of <5%.
[b] Defined as a NeuroQuant value of >5%.

the pathology HS+ and pathology HS– groups. There were no differences between these 2 groups, except for age at surgery with the pathology HS– group having a lower mean age (35.36 years) compared with the pathology HS+ group (40.4 years; $P = .047$), with otherwise comparable cohorts (Table 3).

NeuroQuant Analysis versus MR Imaging Visual Analysis Comparison

Next, we compared the sensitivity and specificity of NeuroQuant analysis with MR imaging visual analysis. By using a cutoff value of 5% for volume, NeuroQuant analysis correctly identified 42 of 61 positive cases of pathology HS+, whereas expert visual MR imaging analysis detected 57 of 61 cases of pathology HS+ (Table 2). NeuroQuant analysis correctly identified 75 of 83 cases of pathology HS–, whereas expert visual MR imaging analysis correctly identified 76 of 83 cases of pathology HS– (Table 2). The sensitivity of the NeuroQuant analysis in detecting HS was 68.8% compared with 93.4% for visual MR imaging analysis

Table 3: Sample Demographics

	Pathology HS+	Pathology HS–	*P*
Female, *n*/total *n* (%)	27/61 (44.3)	57.8/83 (57.8)	.13
Age at surgery, mean ± SD, y	40.40 ± 14.3	35.36 ± 15.6	.05
MR imaging positive for HS, *n*/total *n* (%)	57/61 (93.4)	7/83 (8.4)	<.0001
Ipsilateral hippocampus volume, mean ± SD (cm^3)	9.98 ± 22.1	56.04 ± 32.3	<.0001
Contralateral hippocampus volume, mean ± SD (cm^3)	52.79 ± 32.9	58.51 ± 30.0	.29
Surgery side - left, *n*/total *n* (%)	33/61 (54.1)	43/83 (51.8)	.87

Note:—SD indicates standard deviation.

Table 4: Sensitivity and specificity values for NeuroQuant analysis and visual MR imaging analysis

	NeuroQuant Analysis	Visual MR Imaging Analysis	*P*
Sensitivity, %	68.8	93.4	.0007
Specificity, %	90.4	91.6	.99

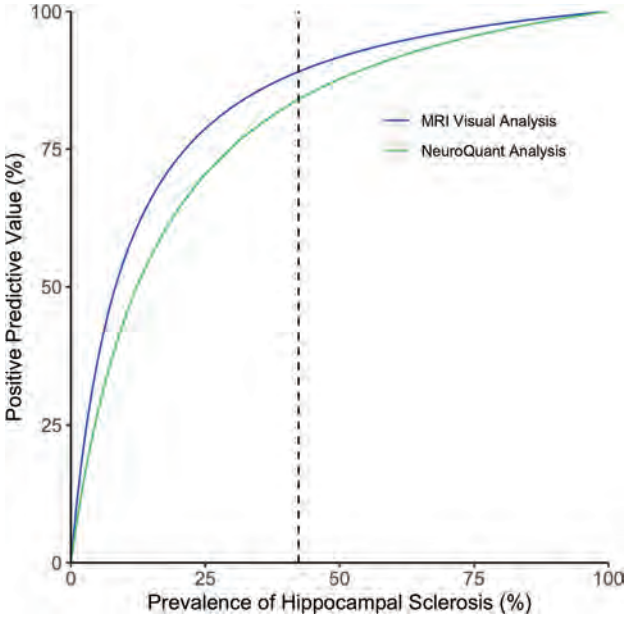

FIG 3. PPV of visual MR imaging analysis and NeuroQuant analysis results as the prevalence of HS increases. In our study, HS had a prevalence of 42.4% (*black dotted line*), NeuroQuant analysis had a PPV of 84%, and MR imaging had a PPV of 89.1%. With a decreased prevalence of HS, both MR imaging and NeuroQuant (NQ) have a decreased PPV, whereas an increased prevalence of HS results in a higher PPV for both analytic methods.

($P = .0007$) (Table 4). The specificity of the NeuroQuant analysis was 90.4% compared with 91.6% for visual MR imaging analysis ($P = 1$) (Table 4).

By using different cutoff values of 7%, 6%, 4%, 3%, and 2%, we found that the NeuroQuant analysis had the highest sensitivity and specificity at the cutoff value of 5, which we selected for this study (Table 1). When using a cutoff of 7 or 6 (including some values that NeuroQuant analysis deems normal) for HS, we found that the sensitivity was higher than when using a narrower cutoff window of 4, 3, or 2 (Table 1). PPV, however, was low, at 50–52%, for all cutoff values, except for the cutoff value of 5, at which the PPV was 84.0% (Table 1). The NPV was roughly 60–62% at cutoff values of 7, 6, 4, 3, and 2, and was 79.8% at a cutoff value of 5.

The PPV and NPV of the NeuroQuant analysis in this study were 84.0% and 79.8%, respectively, whereas the PPV and NPV of the visual MR imaging analysis were 89.1% and 95.0%, respectively (Figs 3 and 4). How the PPV changes for both MR imaging and NeuroQuant analysis as the prevalence of HS changes with an increase in PPV that occurs at a higher disease prevalence of HS is shown in Fig 3. How NPV changes for MR imaging and NeuroQuant analysis, with an increase in NPV as the prevalence of HS decreases is show in Fig 4. For both NPV and PPV, the MR imaging visual analysis had higher predictive probabilities than did NeuroQuant analysis overall.[9]

DISCUSSION

Typically, HS is identified by MR imaging visual analysis based on 3 features: increased T2 signal, structural changes or loss of structure of the hippocampus, and decreased volume of the hippocampus itself.[13] In this study, we sought to determine how the automated quantitative volumetric results reported by the NeuroQuant analysis compared with visual MR imaging analysis in detecting HS and found that NeuroQuant had a lower sensitivity compared with visual MR imaging analysis. Because NeuroQuant only evaluates volume changes in the hippocampus, in contrast to a neuroradiologist's evaluation of T2 signal and structural changes, it makes sense that, overall, neuroradiologists had a higher sensitivity than did NeuroQuant analysis.

Furthermore, neuroradiologists had access to clinical information (eg, semiology and past MR images) to which NeuroQuant did not have access. As a result, there was some bias toward a neuroradiologist being able to identify a lesion on MR imaging and having a higher sensitivity compared with the volumetric software of NeuroQuant, which does not use clinical information. Clinically, due to the lower sensitivity of NeuroQuant analysis, if a NeuroQuant test came back negative, then follow-up work with a neuroradiologist's assessment is recommended to truly rule out HS.

We acknowledge the possible selection bias due to the retrospective nature of this study and because all the patients in this study were surgical candidates. Another possible limitation was that current MR imaging sequence protocols, including other contrasts such as double inversion recovery, may improve on the sensitivity and specificity of visual analyses for the detection of HS compared with the protocol used in this study. However, even if contemporary protocols could improve the sensitivity and specificity for visual analysis in the detection of HS (which were already high, at 93.4% and 91.6% in this study), it would not change the performance of NeuroQuant because high-resolution T1-weighted volumetric sequences as used in this study are still the reference standard for volumetric measurements.

Another potential limitation was that we excluded secondary causes of mesial temporal sclerosis, for example, temporal lobe

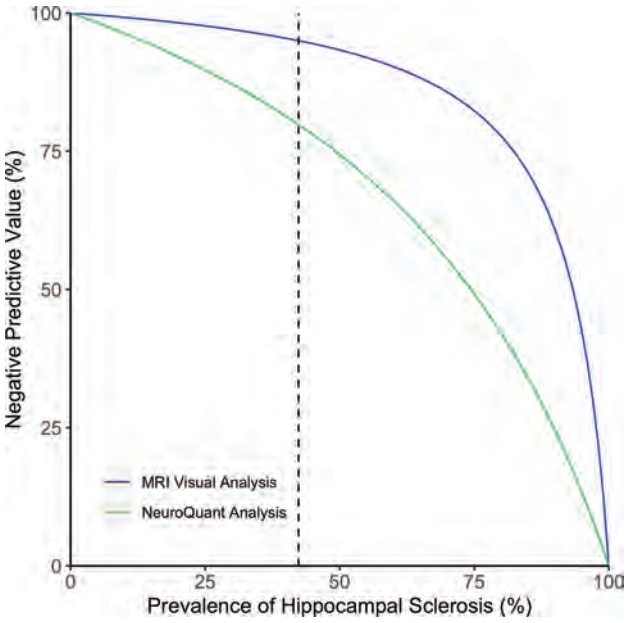

FIG 4. NPV of visual MR imaging analysis and NeuroQuant analysis results as the prevalence of HS increases. In our study, HS had a prevalence of 42.4% (*black dotted line*). In areas with a lower prevalence of HS than our institution, the NPV increases for both MR imaging and NeuroQuant.

tumors, that encroached on the hippocampal area; therefore, the generalizability of dual pathology needs to be further evaluated because the results of this study could not be applied to patients with hippocampal tumors. Similarly, patients with a previous stroke, trauma, or surgery would likely not benefit from a NeuroQuant analysis due to morphologic variation that NeuroQuant is likely not equipped to account for at this time.

Furthermore, it is not possible to make direct comparisons with our study and that of Von Oertzen et al.[1] This is because Von Oertzen et al[1] primarily analyzed the results of standard MRIs reported by "nonexpert" radiologists, standard MRIs evaluated by epilepsy "expert" radiologists, and then epilepsy-specific MR imaging protocols read by "expert" radiologists in 123 patients with temporal and extratemporal lobe epilepsies with varying types of underlying lesions. In addition, because Von Oertzen et al[1] evaluated 1.5T MRIs acquired between 1996 and 1999, the resolution in our study was superior because MRIs were acquired in a 3T scanner between 2010 and 2017.

The specificity between NeuroQuant analysis and visual MR imaging analysis was not statistically different ($P = 1$). Given the high specificity of both NeuroQuant analysis and visual MR imaging analysis by a neuroradiologist, along with NeuroQuant's PPV of 84% (compared with the visual MR imaging analysis PPV of 89.1%), if a NeuroQuant test came back positive, then the treating neurologist could be confident that HS is very likely the potential epileptic substrate and may consider referral for an epilepsy surgery evaluation if clinically indicated: the PPV and specificity of the NeuroQuant report is comparable with that of a neuroradiologist's assessment.

This would especially be of use in centers with limited resources and that do not have neuroradiologists with expertise in epilepsy. These centers could use NeuroQuant to help decide when a further work-up and referral to a center with a trained radiologist is essential (negative NeuroQuant assessment for HS) versus when a patient can be referred for surgery (positive result on NeuroQuant analysis for probable HS). Even in tertiary centers where specialized neuroradiology resources are available, NeuroQuant could help streamline workflows and optimize resource utilization, even if it may not be able to capture all true cases of HS due to its low sensitivity.

Other studies looked into quantifying structural changes of the hippocampus and changes in the T2 signal as a means of capturing HS on MR imaging. However, these tools are not FDA-approved; NeuroQuant is.[15,16] It is hoped that, in the future, these tools will be more readily available to better supplement the detection capability of NeuroQuant.

Given that many complex epilepsy cases with refractory epilepsy are often referred to the Cleveland Clinic, we may have an overinflated population of medically refractory HS (a prevalence of 42.4% in this study). We are aware that the PPV and NPV for visual MR imaging analysis and NeuroQuant analysis in this study are specific to the Cleveland Clinic's population of patients with temporal lobe epilepsy (particularly those with medically intractable epilepsy) and that the predictive power of NeuroQuant may change with a varying prevalence of HS. To account for ranges in HS prevalence based on different institutions across the United States and their prevalence of pharmacoresistant temporal lobe epilepsies, we plotted how the PPV and NPV would change with a lower and higher prevalence of HS in Figs 3 and 4, respectively.

The PPV of MR imaging and NeuroQuant analysis decreased with a lower prevalence of HS; however, overall, the PPV of MR imaging and NeuroQuant analysis were similar, with the largest difference in PPV being 10.9% at a prevalence of 11% for HS. This suggests that, even if the prevalence of HS at other institutions is slightly under our prevalence of 42.4%, the PPVs of MR imaging and NeuroQuant analysis are comparable enough that a positive result on NeuroQuant analysis could potentially hold the same value as a positive MR imaging radiologist assessment in referring a patient for surgery without needing to refer the patient to other centers. However, at any prevalence of HS, MR imaging had an overall higher NPV, which suggests a negative test on NeuroQuant should always be followed up with a neuroradiologist's assessment to ensure that any true HS cases are not missed (Fig 3).

Because NeuroQuant works by uploading a patient's T1 MR imaging volumetric sequence, it is a quick and easy test to run because most of these patients will already have MR imaging as part of their presurgical evaluation. As a result, a positive NeuroQuant result could be a very useful tool in helping neurologists better define and recommend patients with temporal lobe epilepsy for surgical resection.

CONCLUSIONS

Overall, MR imaging analysis by a neuroradiologist with expertise in epilepsy has both a higher sensitivity and specificity than NeuroQuant analysis, which makes it an overall better assessment tool for HS. However, there is a potential clinical role for

NeuroQuant in lower resource centers that do not have access to epilepsy-trained radiologists to use NeuroQuant to assess drops in hippocampal volume status to consider referring patients with positive NeuroQuant test results for surgery, while pursuing follow-up and trained neuroradiologist consults for patients with negative NeuroQuant test results.

Disclosures: Marcia Morita-Sherman—*RELATED: Grant:* National Institutes of Health (NIH), *Comments*: NIH grant 1R01NS097719-01A1*; *UNRELATED: Employment:* Cleveland Clinic, *Comments*: Cleveland Clinic pays me as a research fellow; *Grants/Grants Pending:* NIH, *Comments*: NIH grant 1R01NS097719-01A1*. Stephen Jones—*RELATED: Grant:* NIH*; *Support for Travel to Meetings for the Study or Other Purposes:* NIH, *Comments*: Travel is part of the NIH grant*; *UNRELATED: Consultancy:* Monteris International; *Expert testimony:* Law firm in South Carolina*; *Grants/Grants Pending:* NIH, Biogen, St Jude, DoD; *Payment for Lectures including Service on Speakers Bureaus**: St Jude Hospital; *Royalties:* Book; *Payment for Development of Educational Presentations:* Cleveland Clinic Educational Material; *Travel/Accommodations/Meeting Expenses Unrelated to Activities Listed:* Siemens Ultra High Field meeting, *Comments*: Covered travel expenses.* Deborah Vegh—*RELATED: Grant:* Cleveland Clinic, *Comments*: NIH funded grant activity where I serve as research coordinator and am salaried via the grant*; *Support for Travel to Meetings for the Study or Other Purposes:* Cleveland Clinic.* Nancy Obuchowski—*UNRELATED: Consultancy:* IBM, Siemens, QIBA, *Comments*: Dr Obuchowski provides statistical consulting through a contract with her institution.* Fernando Cendes—*RELATED: Grant:* São Paulo Research Foundation (FAPESP), Grant 2013/07559-3*; *UNRELATED: Consultancy:* UCB Pharma; *Employment:* Universidade Estadual de Campinas-UNICAMP, Brazil; *Grants/Grants Pending:* CNPq-Conselho Nacional de Desenvolvimento Científico e Tecnológico, Brazil; *Payment for Lectures, Including Service on Speakers Bureaus:* UCB Pharma. Lara Jehi—*RELATED: Grant:* NINDS*; *UNRELATED: Grants/Grants Pending:* Eisai Inc.* *Money paid to institution.

REFERENCES

1. Von Oertzen J, Urbach H, Jungbluth S, et al. **Standard magnetic onance imaging is inadequate for patients with refractory focal epilepsy.** *J Neurol Neurosurg Psychiatry* 2002;73:643–47 CrossRef Medline
2. Jehi L, Mathern GW. **Who's responsible to refer for epilepsy surgery? We all are!** *Neurology* 2015;84:112–13 CrossRef Medline
3. Erba G, Moja L, Beghi E, et al. **Barriers toward epilepsy surgery. A survey among practicing neurologists.** *Epilepsia* 2012;53:35–43 CrossRef Medline
4. Hakimi AS, Spanaki MV, Schuh LA, et al. **A survey of neurologists' views on epilepsy surgery and medically refractory epilepsy.** *Epilepsy Behav* 2008;13:96–101 CrossRef Medline
5. Borba EM, Duarte JA, Bristot G, et al. **Brain-derived neurotrophic factor serum levels and hippocampal volume in mild cognitive impairment and dementia due to Alzheimer disease.** *Dement Geriatr Cogn Dis Extra* 2016;6:559–67 CrossRef Medline
6. Ross DE, Ochs AL, Seabaugh JM, et al. **Man versus machine: comparison of radiologists' interpretations and NeuroQuant volumetric analyses of brain MRIs in patients with traumatic brain injury.** *J Neuropsychiatry Clin Neurosci* 2013;25:32–39 CrossRef Medline
7. Wang C, Beadnall HN, Hatton SN, et al. **Automated brain volumetrics in multiple sclerosis: a step closer to clinical application.** *J Neurol Neurosurg Psychiatry* 2016;87:754–57 CrossRef Medline
8. Pareto D, Sastre-Garriga J, Alberich M, et al. **Brain regional volume estimations with NeuroQuant and FIRST: a study in patients with a clinically isolated syndrome.** *Neuroradiology* 2019;61:667–74 CrossRef Medline
9. Azab M, Carone M, Ying SH, et al. **Mesial temporal sclerosis: accuracy of NeuroQuant versus neuroradiologist.** *AJNR Am J Neuroradiol* 2015;36:1400–06 CrossRef Medline
10. Brinkmann BH, Guragain H, Kenney-Jung D, et al. **Segmentation errors and intertest reliability in automated and manually traced hippocampal volumes.** *Ann Clin Transl Neurol* 2019;6:1807–14 CrossRef Medline
11. Farid N, Girard HM, Kemmotsu N, et al. **Temporal lobe epilepsy: quantitative MR volumetry in detection of hippocampal atrophy.** *Radiology* 2012;264:542–50 CrossRef Medline
12. Blümcke I, Coras R, Miyata H, et al. **Defining clinico-neuropathological subtypes of mesial temporal lobe epilepsy with hippocampal sclerosis.** *Brain Pathol* 2012;22:402–11 CrossRef Medline
13. Blümcke I, Thom M, Aronica E, et al. **International consensus classification of hippocampal sclerosis in temporal lobe epilepsy: a task force report from the ILAE Commission on Diagnostic Methods.** *Epilepsia* 2013;54:1315–29 CrossRef Medline
14. Luo W, Airriess C, Albright J. **The NeuroQuant normative database: Comparing individual brain structures.** *CorTechs Labs, Inc*; 2015. http://www.cortechslabs.com/whitepapers. Accessed January 16, 2017
15. Rodionov R, Bartlett PA, He C, et al. **T2 mapping outperforms normalised FLAIR in identifying hippocampal sclerosis.** *NeuroImage Clin* 2015;7:788–91 CrossRef Medline
16. Ver Hoef LW, Paige AL, Riley KO, et al. **Evaluating hippocampal internal architecture on MRI: inter-rater reliability of a proposed scoring system.** *Epilepsy Res* 2013;106:146–54 CrossRef Medline

Anoxic Brain Injury Detection with the Normalized Diffusion to ASL Perfusion Ratio: Implications for Blood-Brain Barrier Injury and Permeability

N. Li, M.A. Wingfield, J.P. Nickerson, D.R. Pettersson, and J.M. Pollock

ABSTRACT

BACKGROUND AND PURPOSE: Anoxic brain injury is a result of prolonged hypoxia. We sought to describe the nonquantitative arterial spin-labeling perfusion imaging patterns of anoxic brain injury, characterize the relationship of arterial spin-labeling and DWI, and evaluate the normalized diffusion-to-perfusion ratio to differentiate patients with anoxic brain injury from healthy controls.

MATERIALS AND METHODS: We identified all patients diagnosed with anoxic brain injuries from 2002 to 2019. Twelve ROIs were drawn on arterial spin-labeling with coordinate-matched ROIs identified on DWI. Linear regression analysis was performed to examine the relationship between arterial spin-labeling perfusion and diffusion signal. Normalized diffusion-to-perfusion maps were generated using a custom-built algorithm.

RESULTS: Thirty-five patients with anoxic brain injuries and 34 healthy controls were identified. Linear regression analysis demonstrated a significant positive correlation between arterial spin-labeling and DWI signal. By means of a combinatory cutoff of slope of >0 and R^2 of > 0.78, linear regression using arterial spin-labeling and DWI showed a sensitivity of 0.86 (95% CI, 0.71–0.94) and specificity of 0.82 (95% CI, 0.66–0.92) for anoxic brain injuries. A normalized diffusion-to-perfusion color map demonstrated heterogeneous ratios throughout the brain in healthy controls and homogeneous ratios in patients with anoxic brain injuries.

CONCLUSIONS: In anoxic brain injuries, a homogeneously positive correlation between qualitative perfusion and DWI signal was identified so that areas of increased diffusion signal showed increased ASL signal. By exploiting this relationship, the normalized diffusion-to-perfusion ratio color map may be a valuable imaging biomarker for diagnosing anoxic brain injury and potentially assessing BBB integrity.

ABBREVIATIONS: ASL = arterial spin-labeling; NDP = normalized diffusion-to-perfusion; BBB = blood brain barrier; CBF = cerebral blood flow

Anoxic or hypoxic brain injury has several classic, well-described imaging findings, including symmetric diffusion restriction in the basal ganglia and cortex.[1,2] In the neonatal population, the classic diffusion findings may not be as readily apparent due to the high water content and immature morphology of the brain.[3] Arterial spin-labeling (ASL) perfusion is a unique, noninvasive measurement of cerebral blood flow (CBF). ASL perfusion relies on the magnetic tagging of arterial blood water, which is then used as a tracer for brain perfusion.[4-7] ASL is uniquely positioned to be incorporated into pediatric and neonatal stroke protocols because it is a noncontrast and repeatable perfusion measurement.[8] The ASL tracer has been assumed to be freely diffusible across the blood-brain barrier.[5,9-11] However, animal models have shown BBB disruption, due to mannitol or stroke, increased the ASL perfusion signal relative to the dynamic susceptibility contrast perfusion; this finding suggests that the measured ASL perfusion is dependent on BBB integrity, and the ASL signal increases when there is BBB disruption.[9] This BBB dependency has not been shown in humans to date.

The ASL sequence has been used to measure perfusion in a variety of pathologies, including anoxic brain injury[8,12-18] and ischemic strokes.[19,20] Quantitative forms of ASL have demonstrated a global increase in CBF[12] as well as relative hyperperfusion in regions with demonstrated injury on conventional MR imaging[14,15,21] in patients with anoxic brain injury. This hyperperfusion has been theorized to represent flow restoration exceeding the metabolic demands of the injured brain regions with subsequent neurovascular uncoupling, loss of autoregulation, and further brain damage with potential future poor neurologic outcomes.[13,22-25] In addition to the quantitative form of ASL, qualitative forms of ASL

Received August 26, 2019; accepted after revision January 28, 2020.

From the Department of Radiology (N.L., M.A.W., J.P.N., D.R.P., and J.M.P.), Oregon Health & Science University, Portland, Oregon

Please address correspondence to Jeffrey M. Pollock, MD, Department of Radiology, Oregon Health & Science University, 3181 SW Sam Jackson Park Rd, CR 135, Portland, OR, 97239; e-mail: pollockj@ohsu.edu

http://dx.doi.org/10.3174/ajnr.A6461

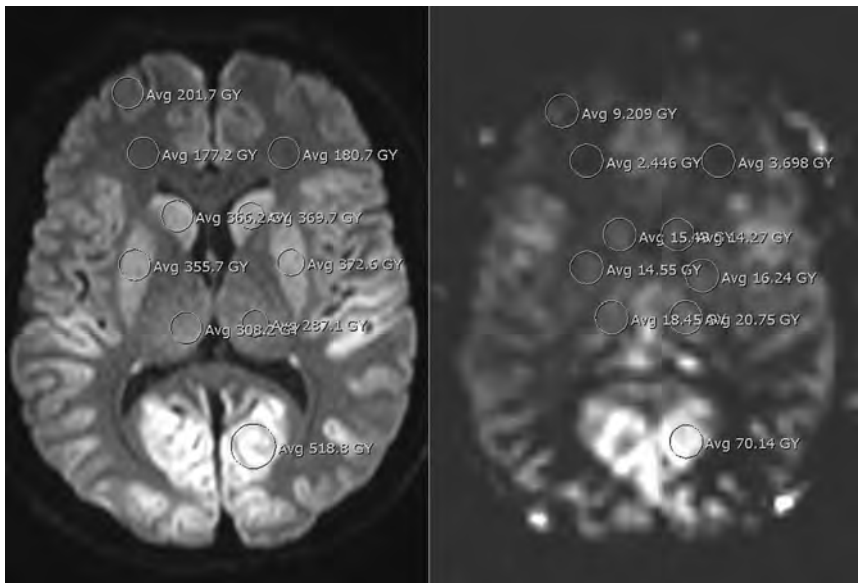

FIG 1. Sample image showing 10 of the 12 ROI measurements on DWI (*left*) and ASL (*right*) at the level of the basal ganglia in a patient who had anoxic brain injury.

perfusion are available, which display relative differences in CBF. Qualitative ASL has some advantages over quantitative ASL. The qualitative version of ASL is available in clinical practice from all major vendors, whereas quantitative techniques are not as readily available, require more complex processing, and may only be available with research licenses at academic centers. Qualitative ASL is much simpler, only requiring subtraction between the control and label pairs, whereas quantification requires the assumption or measurement of multiple variables, including the T1 of tissue, T1 of blood, tagging efficiency, M0 blood and the M0 white matter correction factors, and it depends on accurate segmentation of a high resolution T1.[16,26] Each of these variables not only complicates quantification but is also a potential source of error in quantification. The imaging pattern of anoxic brain injury has not been described with nonquantitative forms of ASL perfusion nor has there been an effort to quantify the relationship between quantitative or nonquantitative ASL perfusion and DWI. In this study, we sought to describe the nonquantitative ASL perfusion imaging patterns of anoxic brain injury, characterize the relationship of ASL and DWI, and evaluate a new metric: the normalized diffusion-to-perfusion (NDP) ratio to differentiate patients with anoxic brain injury from healthy controls.

MATERIALS AND METHODS

With institutional review board approval, we retrospectively identified and reviewed medical records of all patients imaged at our institution between 2002 and 2019 whose brain MR imaging report contained the words "anoxic" or "hypoxic" using an institutional radiology search engine. Patients with anoxia were included if their MR imaging study contained diagnostic ASL perfusion and DWI sequences. Patients were excluded if there were severe motion artifacts or the ASL or DWI sequence was otherwise nondiagnostic. Age-matched controls imaged with ASL and DWI without a history of anoxic or hypoxic injury were also collected and analyzed. Similar to the anoxic group, control patients were excluded if the ASL or DWI sequence was nondiagnostic. In addition, patients with prior operations, intracranial hemorrhage, and ischemic injuries of any age were excluded. Patient age, cause of anoxic injury, and time from anoxic injury to imaging were recorded. Our institutional review board approved this retrospective study.

ASL CBF maps were generated using the single-phase pulsed ASL clinical sequence on 3T and 1.5T Ingenia systems (Philips Healthcare, Best, the Netherlands). Imaging parameters were as follows: 30 dynamics with tag and control pairs; TE, 25 ms; label delay, 1200–900 ms; flip angle, 70°; TR, 4000 ms; FOV, 24 × 24 cm; acquisition matrix, 68 × 66 (12 sections, 6-mm thickness, 0.6-mm section gap). A subtraction of the control and labeled pairs was performed to generate a qualitative gray-scale CBF map. No vascular suppression gradients were used because they are not part of the standard Philips ASL sequence.

DWI parameters were as follows: TR, 5355 ms; TE, 81 ms; matrix, 116 × 116; FOV, 23 × 23 cm (3-mm thickness, 0.3-mm section gap). B_0 and $b = 1000$ images were used to calculate the ADC images using the in-line vendor software during image acquisition.

Ten ROIs were manually drawn on the ASL sequence in the caudate, putamen, thalamus, frontal cerebral cortex, and cerebral white matter bilaterally (Fig 1). An additional ROI was placed in the brain stem and cerebellum and served to normalize the perfusion values; in patients in whom the brain stem and/or the cerebellum showed restricted diffusion, another area free of involvement was selected for normalization for either white matter, gray matter, or both. Corresponding ROIs were placed on the DWI and ADC images. The signal intensity of each ROI was recorded in gray.

Statistical Analysis

ASL perfusion and DWI measurements for each ROI were normalized using the ROI signal intensity in the cerebellum or the brain stem for gray matter and white matter, respectively. A linear best fit was performed between the normalized DWI and the normalized ASL values, and the slope was recorded, allowing identification and removal of up to 4 outliers. A triple-variable receiver operating characteristic analysis involving the number of outliers, best-fitted line slopes, and their respective R^2 values was performed to determine the optimal cutoff. A similar analysis was performed using the quantitative and normalized ADC measurements.

The relationship between the estimated time interval from the inciting event to imaging and the linear regression slopes as well

Table 1: Patient characteristics of the anoxic injury group and the healthy control group

Variable	Anoxic (n = 35)	Healthy (n = 34)	P Value
Age (mean) (yr)	21.1 ± 4.4	24.1 ± 2.3	.05
Sex (Female)	16 (45.7%)	15 (44.1%)	.87
Survived	13 (37.1%)		
Interval to imaging (day)	3.8 ± 0.5		
Received CPR	15 (42.9%)		
CPR time (mean) (min)	22.7 ± 4.3		
Witnessed seizure	8 (22.9%)		
Neonatal hypoxic-ischemic encephalopathy	10 (28.6%)		
Mechanical (asphyxiation, hanging, drowning, and so forth)	8 (22.9%)		

Note:—CPR indicates cardiopulmonary resuscitation.

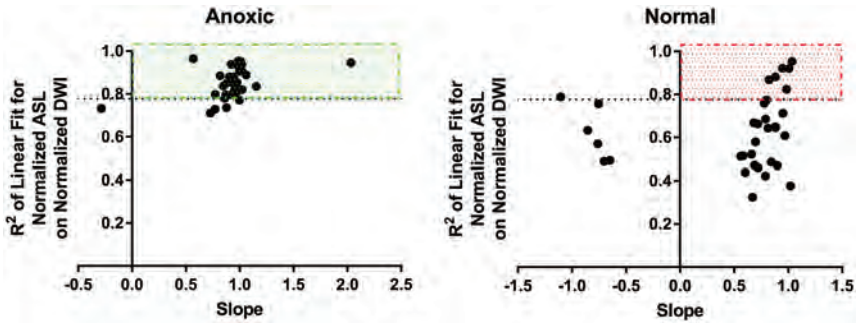

FIG 2. Twelve-point ROI linear regression analysis using DWI and ASL sequences. *A*, R^2-versus-slope scatterplot for patients with anoxic brain injuries identified 30 of 35 cases positive for anoxic brain injury using a receiver operating characteristic analysis–determined cutoff of positive slopes and R^2 higher than 0.78. *B*, R^2-versus-slope scatterplot for healthy controls excludes 28 of 34 cases negative for anoxic brain injury using the same slope and R^2 cutoffs.

as R^2 values were examined to determine the dependence on the timing of imaging. Calculations were also performed to determine the dependence on the number of ROI measurements. Two random raw (non-normalized) DWI and ASL ROIs were selected for each patient, and the slope was calculated using the 2 points alone. All possible combinations of 2 ROI selections were segregated into 3 different groups: both ROIs within basal ganglia and thalamus, either ROI within basal ganglia and thalamus, or no ROI within basal ganglia and thalamus.

Data were presented as mean ± standard error of the mean and frequency (percentage) for numeric and categoric variables, respectively. Analysis was completed using the Fisher exact test and the Mann-Whitney nonparametric t test. A 2-tailed P value $< .05$ was considered significant. Šidák multiple comparison correction was used.

Normalized Diffusion-to-Perfusion Ratio Color Map Generation

DICOM files of the ASL and DWI sequences were coregistered using Advanced Normalization Tools (ANTs, Version 2.3.2; ANTsPy, Version 0.1.6; http://stnava.github.io/ANTs/).[27-29] To decrease the impact of punctate heterogeneous noisy signals, we applied an anisotropic diffusion-smoothing function to both sequences (Insight Toolkit, Version5.0.1; Anisotropic Diffusion Library, Version 1.0.2; https://itk.org/).[30-32] The NDP color map was then generated using the ratio of the z score–normalized DWI and ASL sequences. A value of "not a number" was assigned and subsequently rendered black on the final color map if the ASL value was zero.

RESULTS

Forty-five patients with anoxic injuries were initially identified using our institutional radiology search engine from 2002 to 2019 with 2-reader confirmation. Nine patients were excluded due to nondiagnostic imaging sequences; 1 patient was excluded due to remote injury (imaging was obtained 253 days after initial inciting event). The remaining 35 patients with anoxic injuries had imaging ranging from 0 to 14 days after the reported inciting event with a mean of 3.8 ± 0.5 days. Thirty-four age-matched patients with an MR imaging with normal findings performed between September 2010 and May 2019 were selected. Of these 34 patients in the control group, 30 (88.2%) had studies performed to rule out stroke, given concerning mental status changes, headache, vertigo, facial or extremity weakness or paresthesia, and vision changes. Three (8.8%) had studies ordered for follow-up of surgery, seizure, and prior remote punctate stroke. The remaining patient (3.0%) had an MR imaging performed to rule out asphyxiation from nonaccidental trauma, which was subsequently cleared. Four of the 34 (11.8%) patients in the control group had additional brain imaging in our system and continued to be negative for significant radiographic findings. Patient characteristics of the anoxic group and the healthy group are shown in Table 1.

Triple-variable receiver operating characteristic analysis involving the allowable number of outliers, best linear-fitted line slopes, and their respective R^2 values was performed using the normalized DWI and ASL measurements. Identification of up to 3 outliers (25%) yielded the best diagnostic performance. Under this constraint, the best-fitted lines of anoxic injuries demonstrated significantly higher slopes of 0.93 ± 0.05 compared with those of healthy controls at 0.53 ± 0.11, $P < .001$. The best-fitted lines of anoxic injuries also had significantly higher R^2 values of 0.85 ± 0.01, compared with 0.63 ± 0.03 in healthy controls, with $P < .001$. Scatterplots of the best-fitted lines of R^2 and their corresponding slopes were generated (Fig 2). By means of a combinatory cutoff of slopes higher than 0 and R^2 values higher than 0.78 as determined per the receiver operating characteristic analysis, the following diagnostic characteristics for anoxic injuries were obtained using normalized DWI and ASL: sensitivity of 0.86 (95% CI, 0.71–0.94), specificity of 0.82 (95% CI, 0.66–0.92), positive predictive value of 0.83 (95% CI, 0.68–0.92), and negative predictive value of 0.85 (95% CI, 0.69–0.94). The contingency table is shown in Table 2, with the Fisher exact test, $P < .001$.

A similar analysis was performed on the raw quantitative ADC measurements with the following diagnostic characteristics for anoxic injuries: sensitivity of 0.57 (95% CI, 0.41–0.72), specificity of 0.71 (95% CI, 0.54–0.83), positive predictive value of 0.67 (95% CI, 0.49–0.81), and negative predictive value of 0.62 (95% CI, 0.46–0.75) with the Fisher exact test, $P = .03$.

To determine the effects of time, we examined the relationship between the time interval from the inciting event to imaging and the linear regression slopes and R^2 (Fig 3). Both failed to demonstrate significantly nonzero slopes ($y = 0.01055 \times x + 0.8847$ with $P = .58$ and $y = 0.003945 \times x + 0.8327$ with $P = .38$, for linear regression slopes and R^2, respectively).

Permutations of all possible "12 select 2" ($C_2^{12} = 66$) ROI raw (non-normalized) DWI and ASL signal densities were examined to determine the dependence on ROI selection. Using a cutoff of positive-versus-negative slopes for anoxic and healthy diagnostic predictions, we calculated specificity and sensitivity. Data were segregated into 3 groups: both ROIs within the basal ganglia and thalamus, either ROI within the basal ganglia and thalamus, or no ROI within the basal ganglia and thalamus. A combination of the caudate and contralateral putamen was able to achieve a sensitivity of 0.71 and specificity of 0.76. Another combination, the putamen and contralateral cortex, showed a sensitivity of 0.89 and specificity of 0.74. The overall diagnostic performance of this "2-location ROI" method was inferior to that of the "12-location ROI linear regression" method ($P < .001$ for both sensitivity and specificity).

The NDP ratio color map was generated using the coregistered, smoothed, and z score–normalized DWI ($b = 1000$) and ASL sequences (Fig 4). The NDP ratio color map of anoxic injuries demonstrated homogeneous color distribution throughout the brain (Fig 4*A*, *-B*). The NDP ratio color map of healthy controls demonstrated heterogeneous color distribution bilaterally (Fig 4*E*, *-F*). If one highlighted the differences between the anoxic and nonanoxic patterns, the NDP ratio color map of predominately unilateral anoxic injury secondary to strangulation demonstrated homogeneous signals in the primarily affected right hemisphere and heterogeneous signals in the preserved left hemisphere (Fig 4*I*, *-J*).

DISCUSSION

Anoxic brain injury is a medical condition with devastating outcomes.[12,33,34] Discriminating anoxic from nonanoxic injuries, especially in the neonatal period, is important for medical management,[35] potential therapeutic hypothermia protocol adjustment,[22] and prognostic estimation.[13,34,35] Classic findings of diffusion restriction as well as quantitative hyperperfusion, especially in the regions of higher metabolic demand such as the basal ganglia and cortex, have been described previously in the literature.[1-3,12-14,22] However, there remains a gap in the literature regarding the anoxic brain injury patterns on nonquantitative ASL sequences. In this article, we characterized the qualitative ASL perfusion findings in anoxic injury. We identified the relationship between ASL perfusion and diffusion restriction, which demonstrated a homogeneously positive correlation in patients with anoxic brain injuries so that areas of restricted diffusion showed increased ASL perfusion signal (Fig 5*D*–*F*).

Review of the 35 patients with anoxic brain injuries demonstrated classic diffusion restriction findings (hyperintense on DWI and hypointense on ADC). Ischemic changes including energy metabolism variations and cytotoxic edema reflected by diffusion-weighted imaging were prominent in the metabolically active tissue in the brain,[36] most commonly in the basal ganglia (especially the

Table 2: Contingency table of normalized DWI and normalized ASL linear regression for the diagnosis of anoxic injury using a combinatory cutoff of slope of >0 and R^2 of >0.78[a]

Case Count, Total (%), Column (%), Row (%)	Anoxic	Healthy	Total
Positive slope and $R^2 > 0.78$	30	6	36
	43.48%	8.70%	52.17%
	85.71%	17.65%	
	83.33%	16.67%	
Negative slope or $R^2 \leq 0.78$	5	28	33
	7.25%	40.58%	47.83%
	14.29%	82.35%	
	15.15%	84.85%	
Total	35	34	69
	50.72%	49.28%	100%

[a] Fisher exact test $P < .001$.

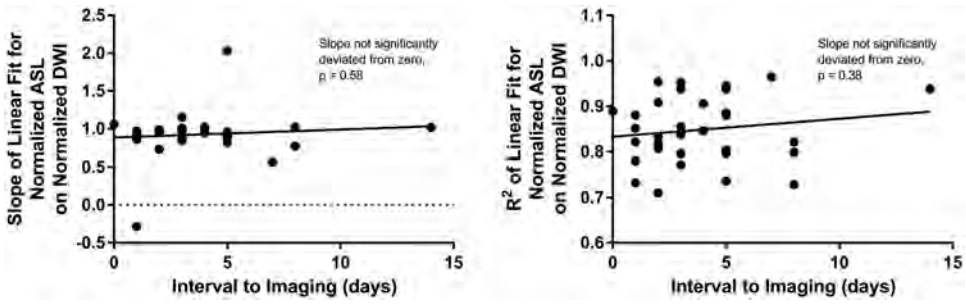

FIG 3. Linear regression analysis demonstrates no significant linear dependence between slopes and interval to imaging (*left*) or between R^2 and interval to imaging (*right*), using DWI and the ASL sequences. Nonetheless, both exhibited positive trends. Linear fit equations: $y = 0.01055 \times x + 0.8847$, $P = .58$ (*left*); $y = 0.003945 \times x + 0.8327$, $P = .38$ (*right*).

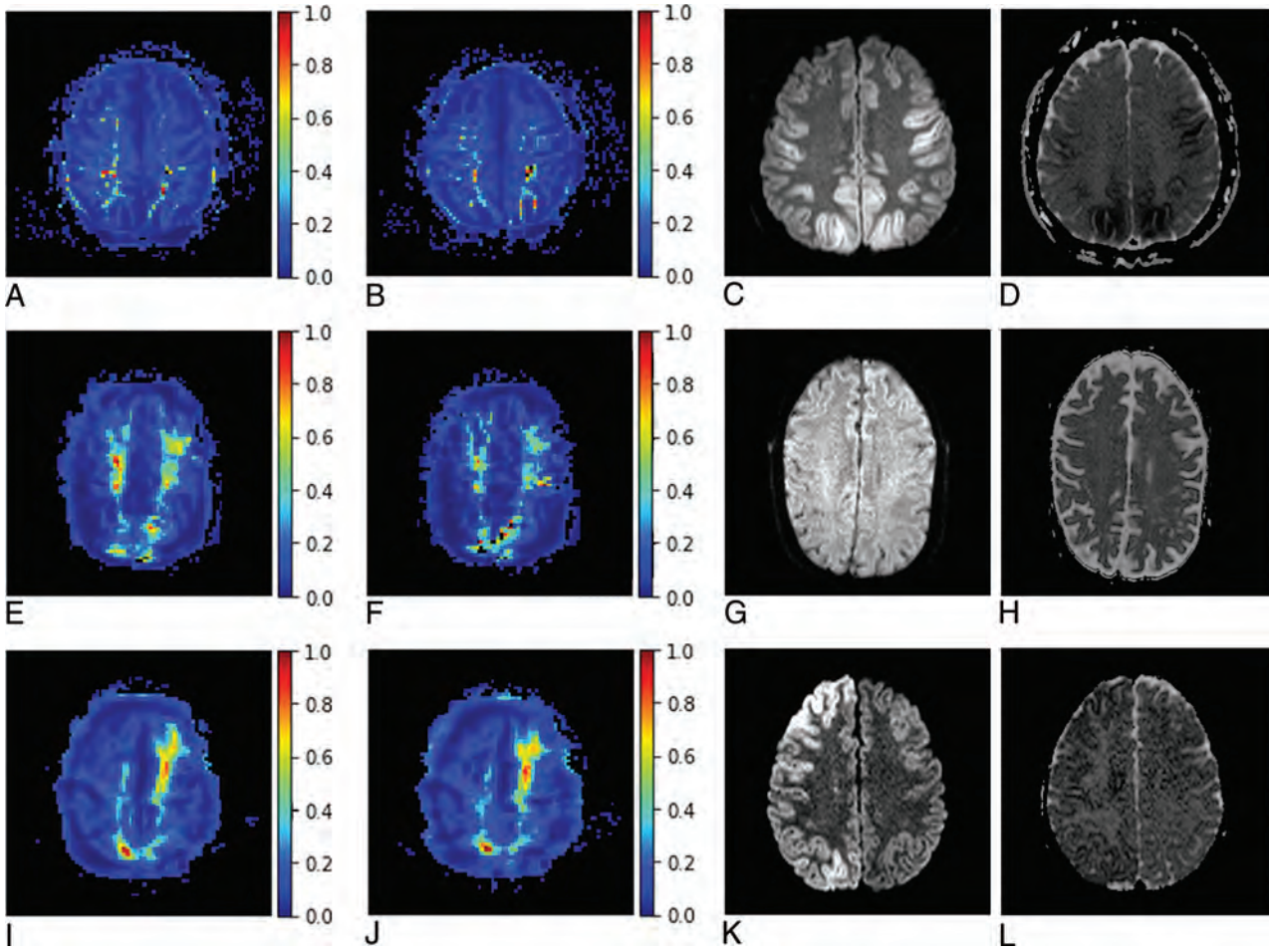

FIG 4. Representative slices of voxelwise normalized NDP color map generation and corresponding DWI and ADC images. Anoxic brain injury (*A* and *B*) demonstrates homogeneous NDP ratios throughout the brain. *B* = 1000 DWI (*C*) and ADC (*D*) images show symmetric diffusion restriction in the frontal and parietal gray matter. *E* and *F*, A healthy control demonstrates heterogeneous NDP ratios throughout the brain. The heterogeneity is most pronounced in the white matter. *B* = 1000 DWI (*G*) and ADC map (*H*) show no diffusion restriction. Unilateral anoxic brain injury with NDP (*I* and *J*) showing 1 predominately homogeneous (anoxic) right hemisphere and 1 heterogeneous (nonaffected) left hemisphere. *J*, The asymmetry is most pronounced at the vertex. *B* = 1000 DWI (*K*) and ADC map (*L*) demonstrate unilateral cortical diffusion restriction in the right anoxic hemisphere, corresponding to the more homogeneous NDP ratios.

posterior putamina), ventrolateral thalami, and cortex.[1-3,37-39] In addition to a pattern of global hyperperfusion seen with prior quantitative ASL studies (Fig 5*A*–*C*), review of the qualitative ASL perfusion images also demonstrated regional signal increases that correlated with the areas of increased DWI signal (Fig 5*D*–*F*).[12,13] We suspect that the regional ASL perfusion differences are detectable with quantitative techniques, but on typical color maps that might not be adequately scaled, global hyperperfusion may render these relative differences less apparent because the entire brain is at the high end of the color spectrum.

ROI analyses demonstrated a uniform homogeneously positive relationship between the ASL perfusion signal and the DWI signal in the selected regions among patients with anoxic brain injuries (Fig 2). This relationship held true not only in the more commonly described basal ganglia region but also in the cortical gray matter and white matter regions.[15,21] Analysis of the ADC signal revealed a similar relationship, consistent with prior literature demonstrating significant correlations between decreased ADC and elevated ASL cerebral blood perfusion signals;[25] however, the diagnostic performance of the ADC and normalized ADC was inferior, likely due to higher susceptibility to volume-averaging artifacts from the surrounding CSF or intrinsic properties yet to be delineated causing higher ASL cerebral blood perfusion elevation than the corresponding ADC abnormality.[25]

This homogeneously positive relationship between ASL and DWI may be related to changes in global BBB permeability. Tanaka et al[9] previously showed that the ASL perfusion sequence tends to overestimate CBF in ischemic stroke in an animal model. Unilateral injection of mannitol in healthy animals, which increased the permeability of the BBB, also increased the ASL signal. Assuming that the magnetically tagged water molecules are freely diffusible across the BBB,[5,10,11] they postulated that ischemic stroke injuries, with subsequent disruption of the BBB, allowed increased extravasation of water molecules, implying that ASL perfusion signal is dependent on BBB integrity.

On the basis of the results of the animal studies and our current observations, we hypothesize that in an anoxic injury, there

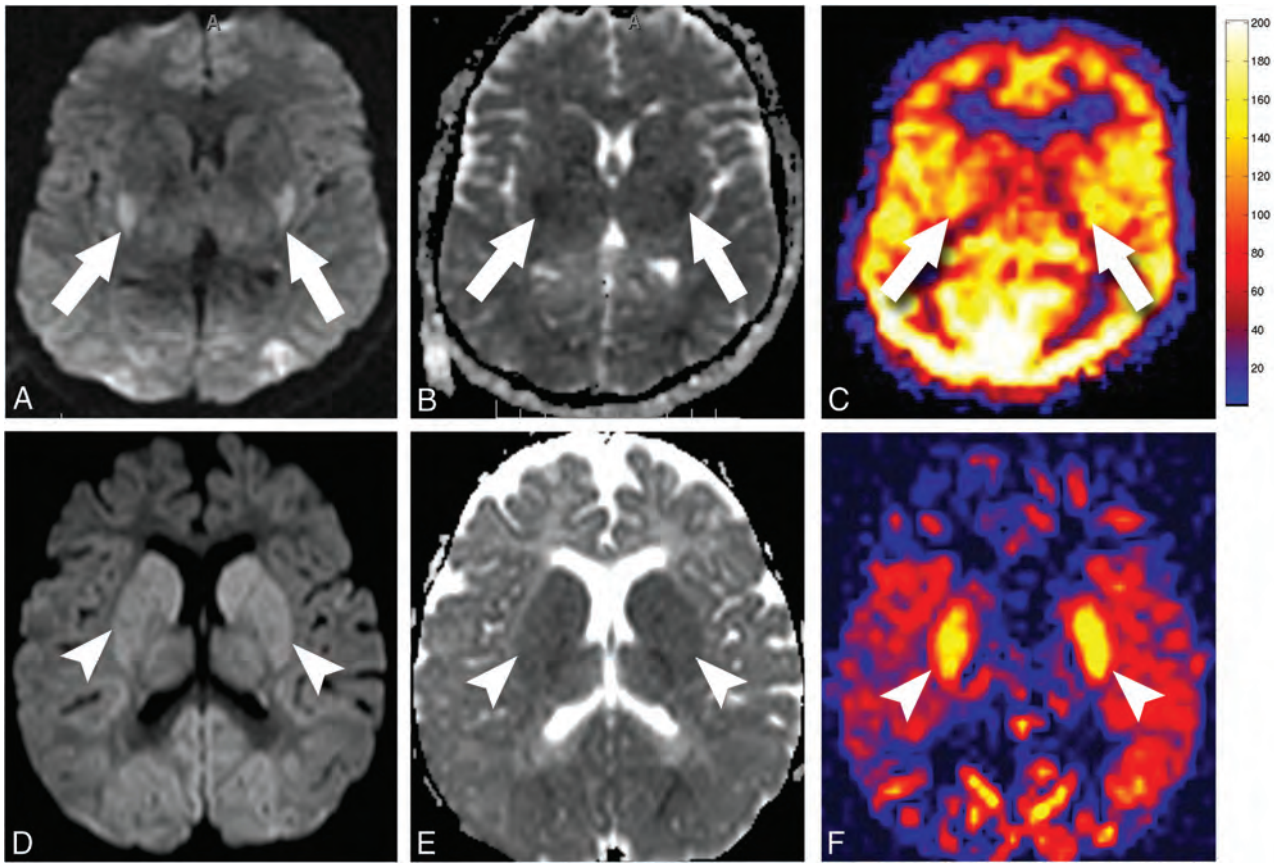

FIG 5. Quantitative-versus-nonquantitative ASL perfusion in anoxic brain injury. *A–C*, Quantitative perfusion imaging in a 31-year-old patient who had an anoxic brain injury after cardiac arrest. *B* = 1000 DWI (*A*) and ADC map (*B*) show diffusion restriction in the posterior putamen (*arrows*) and occipital cortex. *C*, Quantitative pulsed ASL image shows global hyperperfusion. Subtle increased cerebral blood flow is seen in the posterior putamen and occipital lobes, corresponding to the areas of diffusion restriction (*arrows*). *D–F*, Nonquantitative perfusion imaging in a 22-month-old child who had an anoxic injury after cardiac arrest. *B* = 1000 DWI (*D*) and ADC map (*E*) show diffusion restriction in the basal ganglia (*arrowheads*) and occipital cortex. *F*, Nonquantitative colorized pulsed ASL image demonstrates marked increases in the ASL signal in the putamen (*arrowheads*) and occipital cortex, corresponding to the areas of diffusion restriction.

is both a global and regional disruption of the BBB, especially in the regions of higher metabolic demands, leading to regional increases in ASL signal that correlate with the areas of greatest diffusion restriction (Fig 5*D–F*). Nondependence of the positive relationship between ASL and DWI signal on the time interval from injury to imaging (Fig 3) suggests that the BBB injury is present and enduring up to 14 days (range, 0–14 days after the reported inciting event). This BBB disruption is normally seen on gadolinium contrast-enhanced MR imaging 2–3 days after ischemic injury and may persist for months;[40] however, it is conceivable that the BBB injury occurs earlier than 2–3 days, and it is only after 2–3 days that the BBB disruption is large enough for the gadolinium particles to cross the BBB.

Gadoterate meglumine, a commonly used chelated gadolinium contrast medium, is 2 nm,[41] compared with 0.275 nm for a water molecule. ASL uses the protons within the blood water,[4,5,42,43] making the ASL sequence much more sensitive to early changes in the BBB pore size. Although there is not a significantly nonzero slope, positive trends of both the linear regression slope and R^2 over interval to imaging were observed (Fig 3). These may suggest that the repair of the BBB is gradual and lags behind the pseudonormalization of the diffusion signals, a phenomenon in which diffusion-weighted imaging improves and appears to have normal findings by the end of the first week.[3] Gradually decreasing metabolic demands due to delayed cell death during the energy failure component of the reperfusion phase[21,44,45] with persistent BBB disruption could theoretically have contributed to a similar relationship. Further research with animal models and survival studies is needed to delineate the underlying physiologic response and to evaluate the effects of BBB disruption in humans and the recovery of BBB integrity.

The animal studies showing an increase in ASL signal with BBB disruption alone highlight 1 potential limitation of quantitative ASL techniques. Quantitative ASL equations are based on the assumption that the ASL tag is a freely diffusible tracer and is able to freely cross the BBB. If the animal studies and our hypothesis are true, then nonquantitative methods may be advantageous when studying entities such as anoxic brain injury. Prior quantitative studies looking at anoxic brain injury showed marked global hyperperfusion with mean gray matter perfusion values reaching up to 204 mL/100 g of tissue/min (Fig 5*A–C*).[12] These exceptionally high perfusion values are 3–4 times normal and would mean between 45% and 60% of cardiac output would be directed to the brain.[46] On the basis of these

superphysiologic values, we believe that the cerebral perfusion has increased to a degree; however, changes in BBB permeability have also influenced the quantitative ASL measurements. Future studies may evaluate quantitative and nonquantitative ASL perfusion in a human BBB disruption model to validate this hypothesis.

Another potential cause of the diffusion and perfusion ratio observations would be loss of autoregulation, leading to loss of global vasoreactivity after anoxic brain injury.[47,48] Loss of vasoreactivity has been suggested in neonates with hypoxic-ischemic encephalopathy.[49] Additionally, global hyperperfusion affecting the white matter could artificially increase the ratio in the white matter regions by increasing their perfusion values to a level similar to that of the gray matter. Future studies could investigate this possibility by applying gray-white matter segmentation and analyzing the mean diffusion-to-perfusion ratios in the gray matter and white matter, respectively.

Among healthy controls, significantly lower R^2 values and lower slopes of the linear regression models implied underlying heterogeneity of the relationship between the ASL perfusion and the DWI signal. Analyses of the ADC also demonstrated similar results. The lack of a homogeneous relationship is likely secondary to a much lower signal-to-noise ratio among the intracranial structures in healthy controls. Small variability in metabolic demand, regional perfusion, BBB permeability, and the inherent delay of the autoregulation feedback loop may also contribute to the demonstrated heterogeneities.[47,48]

Generation of the voxelwise NDP color map highlights 2 key concepts. First, in patients with anoxic brain injuries, for reasons that remain elusive, the ratio between ASL and DWI signal was homogeneous throughout the brain, including the white and gray matter (Fig 4*A*, -*B*). In patients with anoxia, this voxelwise global homogeneous relationship supersedes any larger manual or automated ROI methodology by showing that as long as enough ROIs are selected and the locations of the DWI and ASL are matched, the actual location of the ROI in a particular structure is not significant. Second, in healthy controls, the NDP color map (Fig 4*E*, -*F*) demonstrated global heterogeneity, evident by the large distribution of DWI/ASL ratios through the brain structures. Thus, in the healthy population, ROI placement and, most important, the number of ROIs become significant due to the global heterogeneity. This is most pronounced in the white matter regions where perfusion values are very low. The NDP color map of the predominately unilateral case, which was an unfortunate patient with nonaccidental trauma with anoxic brain injury secondary to unilateral carotid occlusion from strangulation, demonstrated more uniform color distribution in the affected right hemisphere and heterogeneous color distribution in the nonaffected left hemisphere (Fig 4*I–J*). With future automatic implementation, we believe the NDP color map can be an additional imaging biomarker for anoxic brain injuries, especially in the neonatal population. The NDP ratio map avoids the dependence, complexity, and inherit limitations of manual or automated ROI selection and ratio calculations.

In an attempt to simplify the NDP ratio generation for a neuroradiologist in a general clinical practice who might not have a pipeline to generate these NDP maps or have time to select 10 ROIs, we examined the diagnostic performance of choosing 2 random ROIs. The positivity of the slope of the line between the 2 points on a graph of ASL-versus-DWI signal was determined. Positive slopes would be consistent with anoxic injuries. Negative slopes would be consistent with healthy patients. The diagnostic performance of this method was inferior to that of the 12-point ROI linear regression method. This was expected because the inherent heterogeneity of the NDP ratios in the healthy population could not be accurately captured by a random 2-point selection (Fig 4*E*, -*F*). If the NDP ratio color map cannot be obtained while one is trying to confirm the diagnosis of anoxic brain injury, alternatively, 2 different basal ganglia or thalamus structures from the opposite hemisphere can be selected for slope determination with reasonable sensitivity (0.78) and specificity (0.71).

This study has several limitations, in addition to the inherent limitations of being a retrospective study. First, despite recent progress in the understanding of BBB permeability and ASL perfusion, our knowledge of their characteristics, especially in the context of anoxic brain injuries, remains limited. The exact underlying physiologic property that the NDP ratio is reflecting remains uncertain. Further research is needed for better characterization of the physical and molecular properties of the BBB during anoxic brain injury, timing, and its subsequent repair and also to evaluate the NDP ratio in models of BBB disruption. Second, we performed a strict comparison between patients with a confirmed diagnosis of anoxic brain injury and control subjects with normal imaging examination findings. This improves our statistical power and highlights our findings. Further studies will aim to examine the NDP ratios in other isolated and mixed etiologies, including tumor, stroke, and metabolic diseases. Third, we used the in-line vendor software for automatic ADC map generation. Prior comparative studies have demonstrated significant variations in the generation of ADC maps across different postprocessing software.[50] Future studies could be repeated with an open-source postprocessing software, such as Horos (https://sourceforge.net/projects/horos/). Moreover, manually placed ROI regions could have signal interference from surrounding structures, volume averaging, or incompletely matched locations. An automated atlas-based process for brain parcellation, region selection, and location-matching across series could be more accurate if performed with a high-resolution T1 series.

Last, the ASL perfusion sequence remains suboptimal in the neonatal population due to the small head size and requires optimization to ensure good-quality imaging. Our postlabel delay times at 1200 ms differ from the International Society for Magnetic Resonance in Medicine Perfusion Study Group ASL parameter recommendations, but most of our cases were scanned before the release of these recommendations. It is possible that the shorter postlabel delay has influenced the findings and observations with the NDP map. These findings can be further validated and confirmed at longer postlabel delay times in future studies.[51]

CONCLUSIONS

In patients with anoxic brain injury, there is a global homogeneously positive relationship between qualitative ASL perfusion and diffusion-weighted signal so that areas of restricted diffusion show significantly increased ASL perfusion signal. This relationship

suggests that ASL perfusion signal may be dependent on BBB integrity, consistent with prior animal models. A new metric, the NDP ratio color map, may be a valuable imaging biomarker to differentiate patients with anoxic brain injury from healthy controls and to potentially assess BBB integrity. Further studies are necessary to better understand the underlying physiology reflected in the NDP ratio map observations in anoxic brain injury.

Disclosures: Ningcheng Li—*UNRELATED: Patents (Planned, Pending or Issued)*: A Patent application has been filed for this work. We have not received any payments. Jeffrey M. Pollock—*UNRELATED: Patents (Planned, Pending or Issued)*: A Patent application has been filed for this work. We have not received any payments.

REFERENCES

1. Chao CP, Zaleski CG, Patton AC. **Neonatal hypoxic-ischemic encephalopathy: multimodality imaging findings.** *Radiographics* 2006;26 (Suppl 1):S159–72 CrossRef Medline
2. Heinz ER, Provenzale JM. **Imaging findings in neonatal hypoxia: a practical review.** *AJR Am J Roentgenol* 2009;192:41–47 CrossRef Medline
3. Huang BY, Castillo M. **Hypoxic-ischemic brain injury: imaging findings from birth to adulthood.** *Radiographics* 2008;28:417–39 CrossRef Medline
4. Petersen ET, Zimine I, Ho YC, et al. **Non-invasive measurement of perfusion: a critical review of arterial spin labelling techniques.** *Br J Radiol* 2006;79:688–701 CrossRef Medline
5. Detre JA, Leigh JS, Williams DS, et al. **Perfusion imaging.** *Magn Reson Med* 1992;23:37–45 CrossRef Medline
6. Detre JA, Williams DS, Koretsky AP. **Nuclear magnetic resonance determination of flow, lactate, and phosphate metabolites during amphetamine stimulation of the rat brain.** *NMR Biomed* 1990;3:272–78 CrossRef Medline
7. Wong EC, Buxton RB, Frank LR. **Quantitative perfusion imaging using arterial spin labeling.** *Neuroimaging Clin N Am* 1999;9:333–42 Medline
8. McGehee BE, Pollock JM, Maldjian JA. **Brain perfusion imaging: how does it work and what should I use?** *J Magn Reson Imaging* 2012;36:1257–72 CrossRef Medline
9. Tanaka Y, Nagaoka T, Nair G, et al. **Arterial spin labeling and dynamic susceptibility contrast CBF MRI in postischemic hyperperfusion, hypercapnia, and after mannitol injection.** *J Cereb Blood Flow Metab* 2011;31:1403–11 CrossRef Medline
10. Kim SG. **Quantification of relative cerebral blood flow change by flow-sensitive alternating inversion recovery (FAIR) technique: application to functional mapping.** *Magn Reson Med* 1995;34:293–301 CrossRef Medline
11. Kwong KK, Belliveau JW, Chesler DA, et al. **Dynamic magnetic resonance imaging of human brain activity during primary sensory stimulation.** *Proc Natl Acad Sci USA* 1992;89:5675–79 CrossRef Medline
12. Pollock JM, Whitlow CT, Deibler AR, et al. **Anoxic injury-associated cerebral hyperperfusion identified with arterial spin-labeled MR imaging.** *AJNR Am J Neuroradiol* 2008;29:1302–07 CrossRef Medline
13. De Vis JB, Hendrikse J, Petersen ET, et al. **Arterial spin-labelling perfusion MRI and outcome in neonates with hypoxic-ischemic encephalopathy.** *Eur Radiol* 2015;25:113–21 CrossRef Medline
14. Massaro AN, Bouyssi-Kobar M, Chang T, et al. **Brain perfusion in encephalopathic newborns after therapeutic hypothermia.** *AJNR Am J Neuroradiol* 2013;34:1649–55 CrossRef Medline
15. Wintermark P, Hansen A, Gregas MC, et al. **Brain perfusion in asphyxiated newborns treated with therapeutic hypothermia.** *AJNR Am J Neuroradiol* 2011;32:2023–29 CrossRef Medline
16. Deibler AR, Pollock JM, Kraft RA, et al. **Arterial spin-labeling in routine clinical practice, Part 1: technique and artifacts.** *AJNR Am J Neuroradiol* 2008;29:1228–34 CrossRef Medline
17. Deibler AR, Pollock JM, Kraft RA, et al. **Arterial spin-labeling in routine clinical practice: Part 2, hypoperfusion patterns.** *AJNR Am J Neuroradiol* 2008;29:1235–41 CrossRef Medline
18. Deibler AR, Pollock JM, Kraft RA, et al. **Arterial spin-labeling in routine clinical practice, Part 3: hyperperfusion patterns.** *AJNR Am J Neuroradiol* 2008;29:1428–35 CrossRef Medline
19. De Vis JB, Petersen ET, Kersbergen KJ, et al. **Evaluation of perinatal arterial ischemic stroke using noninvasive arterial spin-labeling perfusion MRI.** *Pediatr Res* 2013;74:307–13 CrossRef Medline
20. Wintermark P, Warfield SK. **New insights in perinatal arterial ischemic stroke by assessing brain perfusion.** *Transl Stroke Res* 2012;3:255–62 CrossRef Medline
21. Proisy M, Corouge I, Leghouy A, et al. **Changes in brain perfusion in successive arterial spin labeling MRI scans in neonates with hypoxic-ischemic encephalopathy.** *Neuroimage Clin* 2019;24:101939 CrossRef Medline
22. Wintermark P. **Injury and repair in perinatal brain injury: insights from non-invasive MR perfusion imaging.** *Semin Perinatol* 2015;39:124–29 CrossRef Medline
23. Wang J, Licht DJ. **Pediatric perfusion MR imaging using arterial spin labeling.** *Neuroimaging Clin N Am* 2006;16:149–67 CrossRef Medline
24. Huisman T, Sorensen AG. **Perfusion-weighted magnetic resonance imaging of the brain: techniques and application in children.** *Eur Radiol* 2004;14:59–72 CrossRef Medline
25. Pienaar R, Paldino MJ, Madan N, et al. **A quantitative method for correlating observations of decreased apparent diffusion coefficient with elevated cerebral blood perfusion in newborns presenting cerebral ischemic insults.** *Neuroimage* 2012;63:1510–08 CrossRef Medline
26. Alsop DC, Detre JA. **Multisection cerebral blood flow MR imaging with continuous arterial spin labeling.** *Radiology* 1998;208:410–16 CrossRef Medline
27. Avants B, Tustison N, Song G. **Advanced Normalization Tools (ANTS).** *Insight J* 2009;1–35. www.picsl.upenn.edu/ANTS. Accessed January 20, 2020
28. Avants BB, Tustison NJ, Song G, et al. **A reproducible evaluation of ANTs similarity metric performance in brain image registration.** *Neuroimage* 2011;54:2033–44 CrossRef Medline
29. Avants BB, Tustison NJ, Stauffer M, et al. **The Insight ToolKit image registration framework.** *Front Neuroinform* 2014;8:44 CrossRef Medline
30. Mirebeau J-M, Fehrenbach J, Risser L, et al. **Anisotropic Diffusion in ITK.** *Insight J* 2014;Dec. http://hdl.handle.net/10380/3505.
31. Perona P, Malik J. **Scale-space and edge detection using anisotropic diffusion.** *IEEE Trans Pattern Anal Mach Intell* 1990;12:629–39
32. Yoo TS, Ackerman MJ, Lorensen WE, et al. Engineering and algorithm design for an image processing API: a technical report on ITK—The Insight Toolkit. In: J Westwood, ed. *Proceedings of Medicine Meets Virtual Reality*. Amsterdam: IOS Press; 2002:586–92
33. Dilenge ME, Majnemer A, Shevell MI. **Topical review: long-term developmental outcome of asphyxiated term neonates.** *J Child Neurol* 2001;16:781–92 CrossRef Medline
34. Martinez-Biarge M, Diez-Sebastian J, Kapellou O, et al. **Predicting motor outcome and death in term hypoxic-ischemic encephalopathy.** *Neurology* 2011;76:2055–61 CrossRef Medline
35. Volpe JJ. **Neonatal encephalopathy: an inadequate term for hypoxic-ischemic encephalopathy.** *Ann Neurol* 2012;72:156–66 CrossRef Medline
36. Le Bihan D, Johansen-Berg H. **Diffusion MRI at 25: exploring brain tissue structure and function.** *Neuroimage* 2012;61:324–41 CrossRef Medline
37. Forbes KP, Pipe JG, Bird R. **Neonatal hypoxic-ischemic encephalopathy: detection with diffusion-weighted MR imaging.** *AJNR Am J Neuroradiol* 2000;21:1490–96 Medline
38. Grant PE, Yu D. **Acute injury to the immature brain with hypoxia with or without hypoperfusion.** *Radiology Clin North Am* 2006;44:63–77 CrossRef Medline

39. Wijdicks EF, Campeau NG, Miller GM. **MR imaging in comatose survivors of cardiac resuscitation.** *AJNR Am J Neuroradiol* 2001;22:1561–65 Medline
40. Elster AD. **MR contrast enhancement in brainstem and deep cerebral infarction.** *AJNR Am J Neuroradiol* 1991;12:1127–32 Medline
41. Le Duc G, Remy C, Peoc'h M, et al. **Evaluation of blood-brain barrier rupture in a rat glioma model by using a contrast agent for magnetic resonance imaging.** In: *Biology and Physiology of the Blood-Brain Barrier: Transport, Cellular Interactions, and Brain Pathologies*. Paris: Plenum Press; 2013:369–72
42. Grade M, Hernandez Tamames JA, Pizzini FB, et al. **A neuroradiologist's guide to arterial spin labeling MRI in clinical practice.** *Neuroradiology* 2015;57:1181–202 CrossRef Medline
43. Alsaedi A, Thomas D, Bisdas S, et al. **Overview and critical appraisal of arterial spin labelling technique in brain perfusion imaging.** *Contrast Media Mol Imaging* 2018;2018:5360375 CrossRef Medline
44. Saliba E, Debillon T. **Neuroprotection par hypothermie contrôlée dans l'encéphalopathie hypoxique-ischémique du nouveau-né à terme: hypothermia for hypoxic-ischemic encephalopathy in fullterm newborns.** *Arch Pédiatrie* 2010;17(Suppl 3):S67–77 CrossRef
45. Greisen G. **Cerebral blood flow and oxygenation in infants after birth asphyxia: clinically useful information?.** *Early Hum Dev* 2014;90:703–05 CrossRef Medline
46. Walters FJ. **Neuropharmacology: intracranial pressure and cerebral blood flow.** *Update in Anaesthia* 1998:9:29–37
47. Sundgreen C, Larsen FS, Herzog TM, et al. **Autoregulation of cerebral blood flow in patients resuscitated from cardiac arrest.** *Stroke* 2001;32:128–32 CrossRef Medline
48. Paulson OB, Strandgaard S, Edvinsson L. **Cerebral autoregulation.** *Cerebrovasc Brain Metab Rev* 1990;2:161–92 Medline
49. Carrasco M, Perin J, Jennings JM, et al. **Cerebral autoregulation and conventional and diffusion tensor imaging magnetic resonance imaging in neonatal hypoxic-ischemic encephalopathy.** *Pediatr Neurol* 2018;82:36–43 CrossRef Medline
50. Ghosh A, Singh T, Singla V, et al. **Comparison of absolute apparent diffusion coefficient (ADC) values in ADC maps generated across different postprocessing software: reproducibility in endometrial carcinoma.** *AJR Am J Roentgenol* 2017;209:1312–20 CrossRef Medline
51. Alsop DC, Detre JA, Golay X, et al. **Recommended implementation of arterial spin-labeled perfusion MRI for clinical applications: a consensus of the ISMRM perfusion study group and the European consortium for ASL in dementia.** *Magn Reson Med* 2015;73:102–16 CrossRef Medline

CT Angiography in Evaluating Large-Vessel Occlusion in Acute Anterior Circulation Ischemic Stroke: Factors Associated with Diagnostic Error in Clinical Practice

B.A.C.M. Fasen, R.J.J. Heijboer, F.-J.H. Hulsmans, and R.M. Kwee

ABSTRACT

BACKGROUND AND PURPOSE: It is currently not completely clear how well radiologists perform in evaluating large-vessel occlusion on CTA in acute ischemic stroke. The purpose of this study was to investigate potential factors associated with diagnostic error.

MATERIALS AND METHODS: Five hundred twenty consecutive patients with a clinical diagnosis of acute ischemic stroke (49.4% men; mean age, 72 years) who underwent CTA to evaluate large-vessel occlusion of the proximal anterior circulation were included. CTA scans were retrospectively reviewed by a consensus panel of 2 neuroradiologists. Logistic regression analysis was performed to investigate the association between several variables and missed large-vessel occlusion at the initial CTA interpretation.

RESULTS: The prevalence of large-vessel occlusion was 16% (84/520 patients); 20% (17/84) of large-vessel occlusions were missed at the initial CTA evaluation. In multivariate analysis, non-neuroradiologists were more likely to miss large-vessel occlusion compared with neuroradiologists (OR = 5.62; 95% CI, 1.06–29.85; $P = .04$), and occlusions of the M2 segment were more likely to be missed compared with occlusions of the distal internal carotid artery and/or M1 segment (OR = 5.69; 95% CI, 1.44–22.57; $P = .01$). There were no calcified emboli in initially correctly identified large-vessel occlusions. However, calcified emboli were present in 4 of 17 (24%) initially missed or misinterpreted large-vessel occlusions.

CONCLUSIONS: Several factors may have an association with missing a large-vessel occlusion on CTA, including the CTA interpreter (non-neuroradiologists versus neuroradiologists), large-vessel occlusion location (M2 segment versus the distal internal carotid artery and/or M1 segment), and large-vessel occlusion caused by calcified emboli. Awareness of these factors may improve the accuracy in interpreting CTA and eventually improve stroke outcome.

ABBREVIATIONS: EVT = endovascular thrombectomy; LVO = large-vessel occlusion

Stroke is a leading cause of global mortality and disability.[1] Randomized controlled trials have recently shown that endovascular thrombectomy (EVT) significantly reduces disability in patients with acute ischemic stroke caused by large-vessel occlusion (LVO) of the proximal anterior circulation.[2-4] Therefore, EVT is currently considered the standard of care, and it is recommended that all potential EVT candidates (ie, patients with clinically suspected LVO [eg, Los Angeles Motor Scale score of ≥4] and presentation within 6 hours of symptom onset) are rapidly screened for LVO using CTA.[5] This paradigm shift has a great impact on the workflow of radiology departments in stroke centers worldwide because they are required to provide rapid and accurate CTA evaluation with 24/7 coverage. In our hospital, which is one of the largest general hospitals in the Netherlands and a primary stroke center (ie, capable of administering intravenous thrombolytics but not EVT), CTA was introduced as a standard of care after the results from the Multicenter Randomized Clinical Trial of Endovascular Treatment for Acute Ischemic Stroke in the Netherlands (MR CLEAN) were published in January 2015.[2]

However, it is currently not completely clear how well radiologists perform in interpreting CTA in clinical practice. Unfamiliarity in reading CTA particularly among non-neuroradiologists, the crucial need for rapid diagnosis often during on-call hours, and the relatively small caliber of the M2 and A2 segments may lead to diagnostic error. Knowledge of potential factors associated with diagnostic error may be helpful to optimize accurate interpretation of CTA. Therefore, the purpose of our study was to investigate potential factors associated with diagnostic error in evaluating LVO on CTA in acute ischemic stroke.

Received October 9, 2019; accepted after revision January 27, 2020.

From the Department of Radiology, Zuyderland Medical Center, Heerlen/Sittard/Geleen, the Netherlands.

Please address correspondence Robert M. Kwee, MD, PhD, Department of Radiology, Zuyderland Medical Center, Henri Dunantstraat 5, 6419 PC Heerlen, the Netherlands; e-mail: rmkwee@gmail.com

http://dx.doi.org/10.3174/ajnr.A6469

Table 1: Anatomic distribution of LVOs

Location of LVO	No. (%)	No. of Missed LVOs at Initial CTA Evaluation (%)
Distal intracranial carotid artery	1 (1.2%)	0 (0%)
Distal intracranial carotid artery and M1 segment	10 (11.9%)	0 (0%)
Distal intracranial carotid artery and M2 segment	1 (1.2%)	0 (0%)
M1 segment	31 (36.9%)	3 (17.6%)
M2 segment	40 (47.6%)	14 (82.4%)
A1 segment	1 (1.2%)	0 (0%)
A2 segment	0	0 (0%)

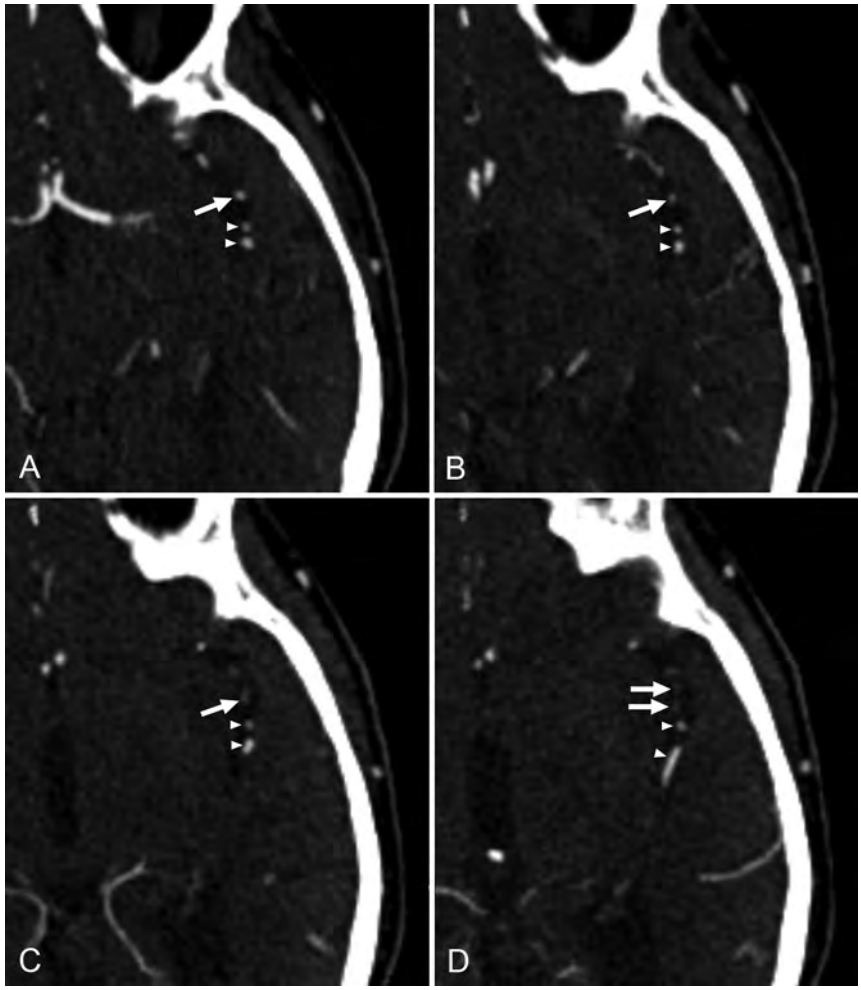

FIG 1. A 75-year-old male patient with acute ischemic stroke. At initial CTA evaluation, occlusion of 1 of the M2 segment branches of the left middle cerebral artery (*arrows* on all slices) was missed. Consecutive axial CTA slices in a caudocranial direction (*A–D*) show a contrast filling defect in a branch of the left M2 segment (*arrows* in *C* and *D*). Note that 2 adjacent branches of the left M2 segment show normal contrast filling on all slices (*arrowheads*).

MATERIALS AND METHODS

Patients

This retrospective study was approved by the institutional review board of our hospital (No. Z2019102), and patient consent was waived. Five hundred twenty consecutive patients with a clinical diagnosis of acute ischemic stroke (49% men; mean age, 72 years; range, 19–100 years) who underwent CTA to evaluate LVO of the proximal anterior circulation at Zuyderland Medical Center between January 2019 and August 2019 were included. Patients with suspected posterior circulation symptoms or occlusion were excluded from the study.

CTA Protocol

CT was performed using either 64-section CT scanners (Brilliance, 168 patients, Incisive, 43 patients, Philips Healthcare, Best, the Netherlands; or Somatom Definition AS, 302 patients, Siemens, Erlangen, Germany) or on a 64-section dual-source scanner (Somatom Definition Flash, 7 patients; Siemens). CTA was performed with 60 mL of iobitridol (Xenetix 300; Guerbet, Aulnay-sous-Bois, France) using a bolus-tracking technique (Philips scanners) or after a test bolus (Siemens scanners) at an injection speed of 5 mL/s. Scanning parameters were the following: collimation = 64 × 0.625 mm (Philips scanners) or 64 × 0.6 mm (Siemens scanners), 120 kV(peak) (Philips scanners) or 100 kVp (Siemens scanners), 250 mAs (Philips Brilliance) or 117 mAs (Philips Incisive) or 130 mAs (Siemens scanners), pitch = 0.391 (Philips Brilliance) or 0.60 (Philips Incisive) or 1.2 (Siemens scanners), and matrix size = 512 × 512. CTA images were reconstructed in the transverse plane with 0.67-mm section thickness and a 0.33-mm increment (Philips scanners) or with 1.0-mm section thickness and a 0.5-mm increment (Siemens scanners).

Initial CTA Interpretation

CTA scans were prospectively read and reported by either neuroradiologists (n = 4), non-neuroradiologists (n = 15), or senior radiology residents (n = 10) during office hours (8:00 AM to 5:00 PM on weekdays) and on-call hours (5:00 PM to 8:00 AM on weekdays, weekends, and official holidays). LVO was defined as the presence of a contrast filling defect in any of the following segments of the proximal anterior circulation: the distal intracranial carotid artery, M1 and M2 segments of the middle cerebral artery, and A1 and A2 segments of the anterior cerebral artery. Readers were able to interpret CTA in conjunction with noncontrast head CT, which was acquired just before

Table 2: Variables potentially associated with missing LVO at initial CTA evaluation; results of univariate logistic regression analysis[a]

Variables	Odds Ratio (95% CI)	*P* Value
Interpreter		
Non-neuroradiologists ($n = 33$) vs neuroradiologists ($n = 27$)	7.14 (1.43–35.57)	.02
Senior residents ($n = 24$) vs neuroradiologists ($n = 27$)	1.79 (0.27–11.71)	.55
Senior residents ($n = 24$) vs non-neuroradiologists ($n = 33$)	0.25 (0.06–1.02)	.05
Time of CTA interpretation, on-call hours ($n = 40$) vs office hours ($n = 44$)	1.89 (0.63–5.70)	.26
Reporting of lateralizing symptoms/signs or suspected location of stroke on the request form for CTA; yes ($n = 58$) vs no ($n = 26$)	0.91 (0.29–2.92)	.88
Location of LVO; M2 segment ($n = 40$) vs distal internal carotid artery and/or M1 segment ($n = 42$)	6.77 (1.79–25.57)	.005

[a] Nos. in parentheses in column 1 represent the number of CTA scans.

Table 3: Variables potentially associated with missing LVO at initial CTA evaluation; results of multivariate logistic regression analysis[a]

Variables	Odds Ratio (95% CI)	*P* Value
Interpreter		
Non-neuroradiologists ($n = 33$) vs neuroradiologists ($n = 27$)	5.62 (1.06–29.85)	.04
Senior residents ($n = 24$) vs neuroradiologists ($n = 27$)	1.63 (0.23–11.37)	.62
Senior residents ($n = 24$) vs non-neuroradiologists ($n = 33$)	0.29 (0.07–1.26)	.10
Location of LVO; M2 segment ($n = 40$) vs distal internal carotid artery and/or M1 segment ($n = 42$)	5.69 (1.44–22.57)	.01

[a] Nos. in parentheses in column 1 represent the number of CTA scans.

CTA. CT images were analyzed on a PACS workstation with MIP and MPR capabilities.

Reference Standard

CTA scans were retrospectively reviewed for the presence or absence of LVO by a consensus panel of 2 neuroradiologists (R.M.K. and F.-J.H.H.). In case of LVO, whether it was caused by a calcified embolus was also recorded. Calcified emboli are considerably more attenuated (mean, 162 HU; range, 79–435 HU) than intraluminal thrombi (typical range, 50–70 HU) and are round or ovoid (not tubular or linear-like vascular wall calcifications).[6] There were no disagreements between the 2 neuroradiologists.

Statistical Analysis

Statistical analyses were performed using MedCalc statistical software for Windows, Version 12.6.0 (MedCalc Software, Mariakerke, Belgium). Logistic regression analysis was performed to investigate the association among interpreters (neuroradiologists, non-neuroradiologists, or senior residents), time of CTA interpretation (on-call hours versus office hours), availability of specified clinical information (lateralizing symptoms/signs or suspected location of stroke reported on the request form for CTA), location of LVO (M2 segment versus distal internal carotid artery and/or M1 segment), and missed LVO at initial interpretation. Significant variables in univariate analysis (ie, predefined *P* value $< .10$) were considered for multivariate analysis.[7]

RESULTS

The prevalence of LVO was 16% (84/520 patients). The anatomic distribution of LVOs is shown in Table 1. Twenty percent of LVOs (17/84) were missed at initial CTA evaluation. In univariate analysis, non-neuroradiologists were more likely to miss LVOs compared with neuroradiologists, and occlusions of the M2 segment (Fig 1) were more likely to be missed compared with occlusions of the distal internal carotid artery and/or M1 segment (Table 2). The time of CTA interpretation and the availability of specified clinical information (lateralizing symptoms/signs or suspected location of stroke reported on the request form for CTA) were not significantly associated with missing LVO (Table 2). In multivariate analysis, the type of interpreter (non-neuroradiologists versus neuroradiologists, OR = 5.62; 95% CI, 1.06–29.85, $P = .04$) and the location of the LVO (M2 segment versus the distal internal carotid artery and/or M1 segment, OR = 5.69; 95% CI, 1.44–22.57, $P = .01$) remained significantly associated with missing the LVO at initial CTA evaluation (Table 3). In all correctly identified LVOs at initial CTA interpretation, there were no calcified emboli. However, calcified emboli were present in 4 of 17 (24%) initially missed or misinterpreted LVOs. In 3 patients, calcified emboli were missed (2 in the M1 segment, 1 in the M2 segment), whereas in 1 patient, a calcified embolus in the M2 segment was misinterpreted as clinically irrelevant calcification (Fig 2). In 16 patients with missed anterior circulation LVO, mRS scores after a median follow-up of 46.5 days (range, 6–163 days) were 1 ($n = 5$), 2 ($n = 7$), 3 ($n = 1$), 4 ($n = 1$), and 6 ($n = 2$). One patient with a missed anterior circulation LVO was lost to follow-up: This patient was transferred to a comprehensive stroke center because of complete hemiparesis with brain swelling requiring possible decompressive craniectomy.

DISCUSSION

In patients experiencing a typical large-vessel acute ischemic stroke, 1.9 million neurons are destroyed each minute that the stroke is untreated.[8] Rapid and accurate detection of LVO on CTA is of crucial importance so that EVT can be performed as soon as possible to reduce disability. The prevalence of LVO in our study was 16%, which is comparable with prevalence values reported in the literature.[9,10] Most striking, we found that as much as 20% of LVOs were missed or misinterpreted at initial CTA interpretation in clinical practice.

Errors and discrepancies are uncomfortably common, with an estimated day-to-day rate of 3%–5% of radiology studies

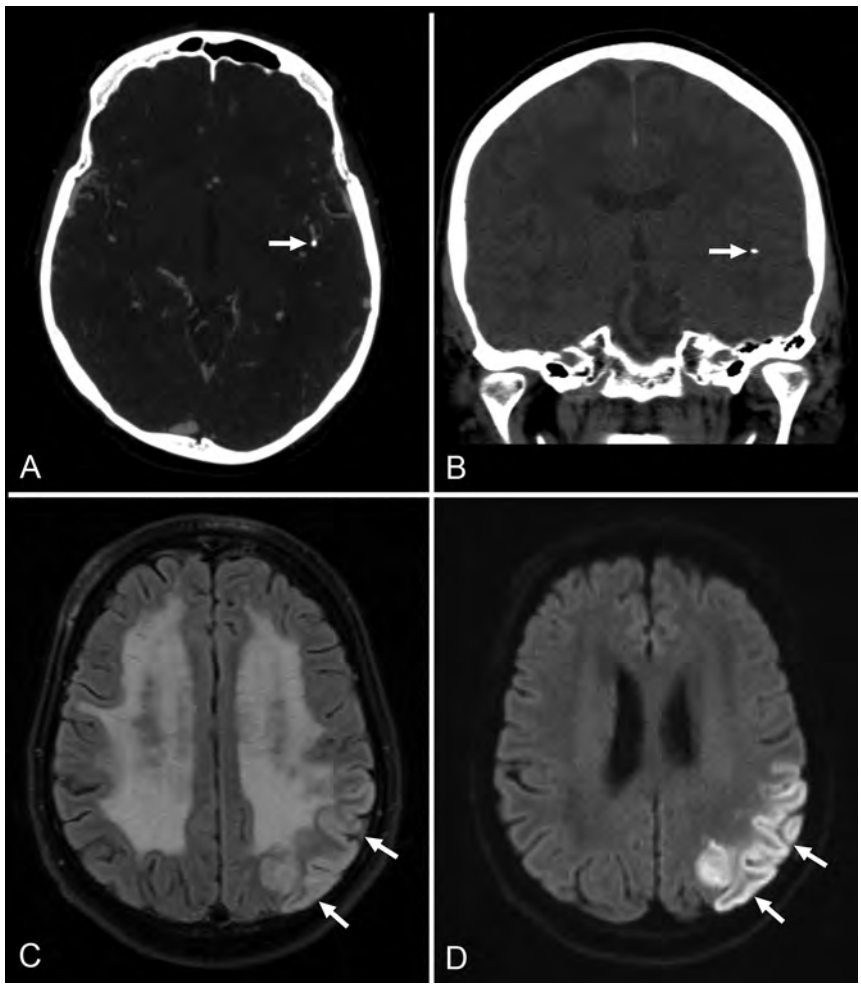

FIG 2. A 70-year-old male patient with acute ischemic stroke. At initial CTA evaluation, LVO due to a calcified embolus in the M2 segment of the left middle cerebral artery (*arrows* in CTA image, *A*; and in a noncontrast head CT image, *B*) was misinterpreted as clinically irrelevant calcification. Follow-up MR imaging (FLAIR image, *C*; and diffusion-weighted image, *D*) 1 day after CTA reveals infarction in the left middle cerebral artery territory (*arrows*).

reported, and even higher rates reported in many targeted studies.[11] CTA evaluation for intracranial LVO appears to be no exception, with a total error rate of 3.3% (17 of all 520 CTA scans analyzed in this study). Potential factors associated with diagnostic error need to be uncovered and highlighted to prevent repetition and improve patient care. We found that nonneuroradiologists were more likely to miss LVOs compared with neuroradiologists. A plausible explanation could be that neuroradiologists are more experienced in evaluating CTA of the intracranial vasculature. We also found that occlusions in the M2 segment of the middle cerebral artery were more likely to be missed compared with occlusions in the distal internal carotid artery and/or M1 segment. The relatively smaller caliber, tortuous course, and variable branching pattern of the M2 segment[12] may be potential causes of perception error. Radiologists should be aware of these causes and carefully scrutinize branches of the M2 segment. The use of MIP and/or MPR may be helpful.[13,14] In addition, the use of wavelet-based reconstruction (which improves image quality),[15] multiphase CTA,[16,17] CT perfusion maps,[17,18] angiographic volume perfusion CT reconstructions (4D CTA),[18] and/or automated software[19] may help to further improve the detection of LVO.

All 4 calcified emboli (2 in the M1 segment and 2 in the M2 segment) were either missed or misinterpreted at initial CTA evaluation in our study. The most probable reason for this diagnostic error is unfamiliarity with this entity. In a previous study, 27% of calcified emboli were misinterpreted and 9% were overlooked on noncontrast head CT.[6] Once thought to be rare,[20] calcified emboli are now considered more common than previously assumed.[6] The prevalence in a former study in patients with stroke with acute LVO was 1.3%,[21] whereas it was even higher in our study: 4.8% (4 of 84 patients with acute LVO). Removal of calcified emboli may be challenging, but successful recanalization can be achieved by mechanical thrombectomy.[21,22] We believe that it is critical to interpret CTA in conjunction with thin-section noncontrast CT because calcified emboli may be more conspicuous on nonenhanced CT images. Furthermore, hyperdense thrombus may also be identified more easily using thin-section noncontrast CT.[23] We speculated that LVOs may be more easily missed during on-call hours. However, our study findings do not support this hypothesis. Although the availability of specified clinical information (lateralizing symptoms/signs or suspected location of stroke reported on the request form for CTA) enables a more targeted search, we did not find evidence that its absence was associated with missing LVOs.

Our study has some potential limitations. First, we did not have confirmation of CTA findings with DSA. However, CTA using modern CT scanners provides equivalent information of the large intracranial arteries compared with DSA.[24] Second, CTA evaluation may be subject to some degree of interobserver variation. However, the purpose of our study was to evaluate potential factors associated with diagnostic error rather than investigating interobserver variability. Moreover, retrospective review of CTA scans in a calm research setting does not reflect CTA evaluation in a usually busy clinical setting needing rapid diagnosis. Third, because of the retrospective nature of our study and the complexity, we could not investigate other potential sources of diagnostic error, including reading speed, fatigue, workload, and frequency of interruptions and distractions during CTA evaluation. Fourth, because A1 and A2 segment occlusions

were scarce (only 1.2% of all LVOs) in our study, no conclusions can be drawn for these segments. However, A1 and A2 segment occlusions are overall less relevant from an incidence point of view (only 0.6% of all anterior circulation LVOs in the MR CLEAN trial).[2]

CONCLUSIONS

Twenty percent of LVOs were missed at initial CTA evaluation in clinical practice. Several factors may have an association with missing an LVO on CTA, including CTA interpreter (non-neuroradiologists versus neuroradiologists), LVO location (M2 segment versus distal internal carotid artery and/or M1 segment), and LVO caused by calcified emboli. Awareness of these factors may improve accuracy in interpreting CTA and eventually improve stroke outcome.

REFERENCES

1. GBD 2016 Neurology Collaborators. **Global, regional, and national burden of neurological disorders, 1990-2016: a systematic analysis for the Global Burden of Disease Study 2016.** *Lancet Neurol* 2019;18:459–80 CrossRef Medline
2. Berkhemer OA, Majoie CB, Dippel DW; MR CLEAN Investigators. **Endovascular therapy for ischemic stroke.** *N Engl J Med* 2015;372:2363 CrossRef Medline
3. van den Berg LA, Dijkgraaf MG, Berkhemer OA, et al; MR CLEAN Investigators. **Two-year outcome after endovascular treatment for acute ischemic stroke.** *N Engl J Med* 2017;376:1341–49 CrossRef Medline
4. Goyal M, Menon BK, van Zwam WH, et al; HERMES Collaborators, **Endovascular thrombectomy after large-vessel ischaemic stroke: a meta-analysis of individual patient data from five randomised trials.** *Lancet* 2016;387:1723–31 CrossRef Medline
5. Almekhlafi MA, Kunz WG, Menon BK, et al. **Imaging of patients with suspected large-vessel occlusion at primary stroke centers: available modalities and a suggested approach.** *AJNR Am J Neuroradiol* 2019;40:396–400 CrossRef Medline
6. Walker BS, Shah LM, Osborn AG. **Calcified cerebral emboli, a "do not miss" imaging diagnosis: 22 new cases and review of the literature.** *AJNR Am J Neuroradiol* 2014;35:1515–19 CrossRef Medline
7. Ranganathan P, Pramesh CS, Aggarwal R. **Common pitfalls in statistical analysis: logistic regression.** *Perspect Clin Res* 2017;8:148–51 CrossRef Medline
8. Saver JL. **Time is brain–quantified.** *Stroke* 2006;37:263–66 CrossRef Medline
9. Zubkov AY, Uschmann H, Rabinstein AA. **Rate of arterial occlusion in patients with acute ischemic stroke.** *Neurol Res* 2008;30:835–38 CrossRef Medline
10. Kummer BR, Gialdini G, Sevush JL, et al. **External validation of the Cincinnati prehospital stroke severity scale.** *J Stroke Cerebrovasc Dis* 2016;25:1270–74 CrossRef Medline
11. Brady AP. **Error and discrepancy in radiology: inevitable or avoidable?** *Insights Imaging* 2017;8:171–82 CrossRef Medline
12. Gibo H, Carver CC, Rhoton AL Jr, et al. **Microsurgical anatomy of the middle cerebral artery.** *J Neurosurg* 1981;54:151–69 CrossRef Medline
13. Saba L, Sanfilippo R, Montisci R, et al. **Assessment of intracranial arterial stenosis with multidetector row CT angiography: a postprocessing techniques comparison.** *AJNR Am J Neuroradiol* 2010;31:874–79 CrossRef Medline
14. Ota H, Takase K, Rikimaru H, et al. **Quantitative vascular measurements in arterial occlusive disease.** *Radiographics* 2005;25:1141–58 CrossRef Medline
15. Kunz WG, Sommer WH, Havla L, et al. **Detection of single-phase CTA occult vessel occlusions in acute ischemic stroke using CT perfusion-based wavelet-transformed angiography.** *Eur Radiol* 2017;27:2657–64 CrossRef Medline
16. Yu AY, Zerna C, Assis Z, et al. **Multiphase CT angiography increases detection of anterior circulation intracranial occlusion.** *Neurology* 2016;87:609–16 CrossRef Medline
17. Byrne D, Sugrue G, Stanley E, et al. **Improved detection of anterior circulation occlusions: the "delayed vessel sign" on multiphase CT angiography.** *AJNR Am J Neuroradiol* 2017;38:1911–16 CrossRef Medline
18. Becks MJ, Manniesing R, Vister J, et al. **Brain CT perfusion improves intracranial vessel occlusion detection on CT angiography.** *J Neuroradiol* 2019;46:124–29 CrossRef Medline
19. Amukotuwa SA, Straka M, Smith H, et al. **Automated detection of intracranial large vessel occlusions on computed tomography angiography.** *Stroke* 2019;50:2790–98 CrossRef Medline
20. Kavanagh EC, Fenton DM, Heran MK, et al. **Calcified cerebral emboli.** *AJNR Am J Neuroradiol* 2006;27:1996–99 Medline
21. Dobrocky T, Piechowiak E, Cianfoni A, et al. **Thrombectomy of calcified emboli in stroke: does histology of thrombi influence the effectiveness of thrombectomy?** *J Neurointerv Surg* 2018;10:345–50 CrossRef Medline
22. Kwak HS, Park JS. **Successful recanalization using the Embolus Retriever with Interlinked Cage for acute stroke due to calcified cerebral emboli.** *Interv Neuroradiol* 2018;24:674–77 CrossRef Medline
23. Mair G, Boyd EV, Chappell FM, et al; IST-3 Collaborative Group. **Sensitivity and specificity of the hyperdense artery sign for arterial obstruction in acute ischemic stroke.** *Stroke* 2015;46:102–07 CrossRef Medline
24. Klingebiel R, Kentenich M, Bauknecht HC, et al. **Comparative evaluation of 64-slice CT angiography and digital subtraction angiography in assessing the cervicocranial vasculature.** *Vasc Health Risk Manag* 2008;4:901–07 CrossRef Medline

Reliability of CT Angiography in Cerebral Vasospasm: A Systematic Review of the Literature and an Inter- and Intraobserver Study

L. Letourneau-Guillon, B. Farzin, T.E. Darsaut, M. Kotowski, F. Guilbert, M. Chagnon, A. Diouf, D. Roy, A. Weill, M. Lemus, C. Bard, M. Belair, D. Landry, L. Nico, A. Tellier, R. Jabre, C. Kauffmann, and J. Raymond

ABSTRACT

BACKGROUND AND PURPOSE: Computed tomography angiography offers a non-invasive alternative to DSA for the assessment of cerebral vasospasm following subarachnoid hemorrhage but there is limited evidence regarding its reliability. Our aim was to perform a systematic review (Part I) and to assess (Part II) the inter- and intraobserver reliability of CTA in the diagnosis of cerebral vasospasm.

MATERIALS AND METHODS: In Part I, articles reporting the reliability of CTA up to May 2018 were systematically searched and evaluated. In Part II, 11 raters independently graded 17 arterial segments in each of 50 patients with SAH for the presence of vasospasm using a 4-category scale. Raters were additionally asked to judge the presence of any moderate/severe vasospasm ($\geq$ 50% narrowing) and whether findings would justify augmentation of medical treatment or conventional angiography $\pm$ balloon angioplasty. Four raters took part in the intraobserver reliability study.

RESULTS: In Part I, the systematic review revealed few studies with heterogeneous vasospasm definitions. In Part II, we found interrater reliability to be moderate at best ($\kappa \leq 0.6$), even when results were stratified according to specialty and experience. Intrarater reliability was substantial ($\kappa > 0.6$) in 3/4 readers. In the per arterial segment analysis, substantial agreement was reached only for the middle cerebral arteries, and only when senior raters' judgments were dichotomized (presence or absence of $\geq$50% narrowing). Agreement on the medical or angiographic management of vasospasm based on CTA alone was less than substantial ($\kappa \leq 0.6$).

CONCLUSIONS: The diagnosis of vasospasm using CTA alone was not sufficiently repeatable among observers to support its general use to guide decisions in the clinical management of patients with SAH.

ABBREVIATION: EBM = Evidence-Based Medicine

Cerebral vasospasm is the main cause of delayed cerebral ischemia after rupture of an intracranial aneurysm.[1-3] To detect and manage vasospasm, CTA and DSA are commonly used, particularly in comatose or sedated patients, to guide the use of medical and/or endovascular interventions that aim to prevent poor outcomes.[3,4] The reliability of CTA in this context has not been rigorously evaluated.[5-8]

This article is divided in 2 parts. First, we systematically reviewed the literature on the CTA evaluation of vasospasm with emphasis on grading classifications and interobserver reliability. Second, we performed a local reliability study to assess whether clinicians agreed in making the diagnosis of moderate or severe vasospasm using CTA and in recommending further investigations or treatments based on CTA results in a series of 50 patients.

Received October 18, 2019; accepted after revision January 27, 2020.

From the Radiology Department (L.L.-G., B.F., M.K., F.G., A.D., D.R., A.W., M.L., C.B., M.B., D.L., L.N., A.T., J.R.), Centre Hospitalier de l'Universite de Montreal (CHUM), Centre de Recherche du CHUM (CRCHUM), Universite de Montreal, Montreal, Quebec, Canada; Neurosurgery Division, Surgery Department (R.J.), Centre Hospitalier de l'Universite de Montreal, Universite de Montreal, Montreal, Quebec, Canada; Department of Surgery (T.E.D.), Division of Neurosurgery, University of Alberta Hospital, Edmonton, Alberta, Canada; Statistical Consultation Services (M.C.), Department of Mathematics and Statistics, Universite de Montreal, Quebec, Canada; and Laboratoire Clinique du Traitement de l'Image (C.K.), Centre de Recherche du Centre Hospitalier de l'Universite de Montreal, Universite de Montreal, Montreal, Quebec, Canada.

Preliminary results previously presented at: Annual Meeting of the Eastern Neuroradiological Society, August 22–25, 2019; Brooklyn, New York.

Laurent Letourneau-Guillon received Can $1125.00 from the ninth competition of the Program de Support Professoral du département de radiologie, radio-oncologie et médecine nucléaire de l'Université de Montréal to cover statistical analysis fees (internal funding program).

Please address correspondence to Laurent Letourneau-Guillon, MD, Pavillon D, 1051, Rue Sanguinet, porte D03.5481, Montreal (Quebec) H2X 0C1 Canada; e-mail: laurent.letourneau-gillon.1@umontreal.ca

Indicates article with supplemental on-line appendix and tables.

Indicates article with supplemental on-line photos.

http://dx.doi.org/10.3174/ajnr.A6462

MATERIALS AND METHODS

Part I: Systematic Review

Classification systems used to quantify the degree of vasospasm with DSA and/or CTA and intra-/interobserver agreement studies on the diagnosis of vasospasm using CTA were systematically reviewed. A detailed protocol for the search strategy was prepared according to the Preferred Reported Items for Systematic Reviews and Meta-Analysis statement.[9] The EMBASE, CINAHL, Evidence-Based Medicine (EBM), Cochrane, and MEDLINE databases were searched with no starting date specification, capturing English and French publications up to May 3, 2018. The search strategy is available in On-line Tables 1–5. One author (B.F.) tested the search strategy for its ability to recover pertinent articles. The data were collected and reviewed in detail by 2 authors with 5 and 6 years of experience, respectively (B.F. and L.L.-G.). Discrepancies were resolved by consensus.

Part II: Reliability Study

The Guidelines for Reporting Reliability and Agreement Studies were followed.[10] The Centre de Recherche du Centre Hospitalier Universitaire de Montreal review board waived informed consent to access the patients' clinical and radiologic data. Written informed consent was obtained from all raters participating in the study.

Patients. We assembled a portfolio of 50 patients. The number of patients was predefined using the method of Donner and Rotondi[11] and the *kappaSize* package[12] in R, Version 3.4.4 (https://www.r-project.org/),[13] taking into account pragmatic factors such as the willingness of observers to complete segment-by-segment evaluations.

All consecutive patients presenting to our institution from January 2005 to May 2017 with nontraumatic nonperimesencephalic SAH[14] and who had undergone at least 2 CTAs (one on admission, the other follow-up CTA performed 2–21 days later to assess the presence of vasospasm) were retrospectively recovered from our radiology information system. The 2- to 21-day interval was chosen to cover the typical vasospasm window, assuming that the initial CTA could potentially be delayed by up to 24 hours since the onset of symptoms.[4,15,16] The admission CTA was used as a reference when evaluating vasospasm on follow-up CTA.[7,8] To minimize the issue of the κ paradox, CTAs were chosen in approximately equal proportions of vasospasm severity with reference to the official radiology report.[17-19] We did not exclude examinations degraded by coil or clip artifacts unless the study was rendered nondiagnostic (1 patient with 3 coiled aneurysms). All radiologic studies were de-identified and sent to the PACS for this study. The retrieved clinical information included demographic data (age, sex) and initial SAH-related patient characteristics (Hunt and Hess scale,[20] hydrocephalus, ventricular drainage, craniectomy, anatomic location of the culprit vascular lesion causing the SAH, type of treatment of the vascular lesion) as well as the reason for performing the follow-up CTA in search of vasospasm and the time delay between the initial and follow-up CTA. One author (L.L.-G.) retrospectively graded each admission noncontrast head CT for SAH using the modified Fisher scale.[21]

Readers. Eleven clinicians involved in the diagnosis and management of vasospasm, from different specialties (radiology, neurosurgery) and with different levels of experience in the management of vasospasm from our institution participated in the study. Readers were stratified by experience as junior (residents and fellows) or senior (attending physicians with $\geq$5 years of experience; range, 5–35 years).

Evaluations and Categories. For each case, readers were asked to grade the degree of vasospasm of 17 arterial segments on a 4-category scale (none, mild [<50%], moderate [50%–74%], and severe [$\geq$75% narrowing]) compared with the initial CTA.[8,22] Arterial segments were predefined as proximal (intracranial internal carotid arteries, A1, M1, and P1 segments, basilar and vertebral arteries) or distal (A2–3, M2–3, P2–3 segments), as previously reported.[7] For each patient, there were 3 additional questions (yes/no): 1) Is there moderate-severe vasospasm at any location? 2) Presuming the presence of a new neurologic deficit corresponding to the territory of the artery affected by vasospasm, would you recommend a change in medical management? 3) Would you recommend DSA with or without balloon angioplasty? The latter 2 clinical decisions were based on the readers' clinical experience.

All the aforementioned readings were performed using only the pair of de-identified admission and follow-up CTAs, with the reader blinded to the initial report, other clinical information, or follow-up imaging as well as other reader assessments. For the intrarater portion of the study, all cases were read a second time by 4 raters. The second set of readings was permutated and performed at least 4 weeks following the initial readings to minimize recall bias.

CTAs. All CTAs were performed on a 64-section Somatom Sensation scanner (Siemens, Erlangen, Germany), using 60-mL injections of iohexol (350 mg iodine per millimeter, Omnipaque; GE Healthcare, Piscataway, New Jersey), followed by a 30-mL saline bolus at 5 mL/s. Scanning parameters were 120-kV tube voltage, 250 mAs, pitch of 0.6, section thickness of 0.6 with 0.4-mm intervals from C2 to the vertex, matrix of 512 $\times$ 512, FOV of 30–32 cm. Minimal reformations were (section thickness/increments): 1/1-mm axial MPR images, 3/1-mm coronal and sagittal MIP images, as well as 30/3-mm axial MIP images.

Data Analyses. Intra- and interobserver reliability statistics were computed using STATA/IC, Version 14.2 (StataCorp, College Station, Texas) and R[13] using the *irr* package[23] under the supervision of a statistician (M.C.). Cohen and Fleiss κ reliability coefficients were calculated for intraobserver and multirater interobserver analyses, respectively, using 1000 bootstrap samples (bias-corrected) to obtain 95% confidence intervals. In the per-patient analysis, the 3 main questions generated dichotomous results (yes/no). In the per-segment analysis, the 4-point grading system for vasospasm (none, mild, moderate, severe) generated an ordinal scale (0–3). We did not add weightings to the κ calculation for the latter data. This scale was then dichotomized (none-mild versus moderate-severe, corresponding to <50 versus $\geq$50% arterial narrowing) for a secondary analysis. An exploratory analysis was also performed,

removing all arterial segments obscured by clip or coil artifacts. All κ coefficients were stratified according to experience (junior versus senior) and specialty among senior readers (diagnostic versus interventional neuroradiology). κ coefficients were interpreted using Landis and Koch guidelines,[24] predefining $\kappa > 0.6$ as "substantial agreement."

RESULTS

Part I: Systematic Review

A total of 5761 titles were reviewed, 2780 abstracts were examined, and 304 full-text articles were read in detail, leaving 14 articles for the systematic review (On-line Fig 1). In these studies, 8 different classification systems were used (with 3–5 categories) with various arbitrary cutoffs (On-line Table 6). All 14 were diagnostic accuracy studies, but 3 also assessed interobserver agreement on cerebral vasospasm using CTA. One of the interobserver variability studies had 3 raters, while the other 2 studies had 2. No study assessed intraobserver reliability. Results are summarized in On-line Table 7. The degree of blinding of the raters was not reliably reported. The paucity of data and the heterogeneity of methods and end points precluded the performance of a meta-analysis.

Part II: Reliability Study

Patients and their characteristics are summarized in Table 1 and On-line Fig 2, respectively. The CTAs were performed between March 27, 2008, and April 6, 2017. The mean time interval between the initial and follow-up CTA was 7.1 days (range, 2–15 days). Characteristics related to follow-up CTAs as well as subsequent vasospasm management are summarized in Table 2.

The 11 readers were 3 interventional neuroradiologists (>15 years of experience each in evaluating CTAs for vasospasm), 3 diagnostic neuroradiologists (15, 12, and 5 years of experience), 2 interventional neuroradiology fellows, 2 senior diagnostic radiology residents, and 1 senior neurosurgery resident.

The interobserver agreement for the detection of moderate-to-severe vasospasm (≥50% narrowing in any segment) was only fair (κ = 0.340; 95% CI, 0.232–0.462) for all raters (Fig 1, data in On-line Table 8). Agreement between senior raters improved to moderate (κ = 0.433; 95% CI, 0.266–0.582). Perfect agreement was found for few patients: Six of 50 (12%) patients were judged by all raters to have moderate-severe vasospasm, while 3/50 (6%) were judged by all raters not to have any vasospasm. These proportions improved slightly when only senior readers were considered, reaching 7/50 (14%) and 16/50 (32%), respectively. There were significant differences ($p < .001$) in the proportions of patients judged to have moderate-to-severe vasospasm between junior and senior raters, as well as between diagnostic and interventional neuroradiologists (On-line Table 9 and On-line Fig 3*A*).

Interobserver agreement regarding augmentation of medical treatment based on CTA alone was fair (κ = 0.245; 95% CI, 0.179–0.336) (Fig 1, data in On-line Table 8). Interobserver agreement on recommending DSA ± balloon angioplasty based on CTA alone was also fair (κ = 0.272; 95% CI, 0.159–0.415) (Fig 1, data in On-line Table 8). There were only 2/50 (4%) cases in which all raters agreed that DSA ± angioplasty should be performed (On-line Fig 3*C*).

Table 1: Baseline demographics, clinical, and radiologic characteristics of the patients[a]

Characteristics	
Age (median) (range, IQR) (yr)	60 (38–88, 56–69)
Female sex	27 (54)
Hunt and Hess scale	
1	5 (10)
2	12 (24)
3	8 (16)
4	17 (34)
5	8 (16)
Hydrocephalus	47 (94)
EVD placement	38 (76)
Craniectomy	4 (8)
Modified Fisher scale	
1	1 (2)
2	8 (16)
3	2 (4)
4	39 (78)
Treatment of culprit vascular lesion	
Endovascular	39 (78)
Surgical	9 (18)
None[b]	2 (4)
>1 Lesion treated[c]	3 (6)
Ruptured aneurysm/lesion location[d]	
Anterior communicating artery	19 (38)
Posterior communicating artery	8 (16)
Middle cerebral artery bifurcation	6 (12)
PICA	6 (12)
Carotid ophthalmic	3 (6)
Pericallosal	2 (4)
Basilar tip	1 (2)
Carotid terminus	1 (2)
Posterior cerebral artery (P1)	1 (2)
Vertebral artery dissection	1 (2)
None[b]	2 (4)

Note:—IQR indicates interquartile range; PICA, posterior inferior cerebellar artery; EVD, external ventricular drain.

[a] Data in parentheses are percentages except where indicated.

[b] No culprit lesion identified on repeat DSA examinations.

[c] Three aneurysms, 2 treated by endovascular coiling, and 1, by surgical clipping.

[d] In case of >1 treated aneurysm, this reflects the most likely source of hemorrhage.

Table 2: Vasospasm-related characteristics[a]

Characteristics	
Reason to perform follow-up CTA (vasospasm assessment)	
Altered level of consciousness	14 (28)
New neurologic deficit	12 (24)
Raised intracranial pressure	4 (8)
New ischemic lesion on CT	2 (4)
None other than rule out vasospasm	18 (36)
Vasospasm severity according to original CTA reports	
None	10 (20)
Mild	17 (34)
Moderate	18 (36)
Severe	5 (10)
Invasive vasospasm management performed following CTA	
DSA	4 (8)
Intra-arterial milrinone	1 (2)
Angioplasty	0 (0)

[a] Data in parentheses are percentages except where indicated.

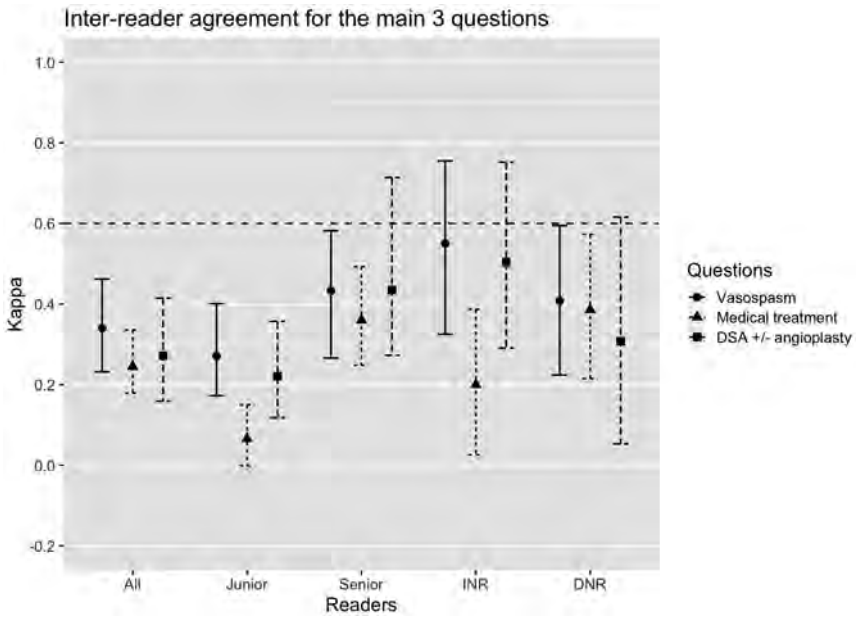

FIG 1. Interreader reliability coefficients (95% confidence intervals) including all subgroups (senior, junior, interventional, and diagnostic neuroradiologists) for the 3 main questions: detection of moderate-severe vasospasm in any arterial segment (≥ 50% narrowing), recommendations of medical treatment augmentation, and DSA ± angioplasty based on imaging findings. The horizontal *dashed line* indicates the threshold for substantial agreement ($\kappa > 0.6$). INR indicates interventional neuroradiology; DNR, diagnostic neuroradiology.

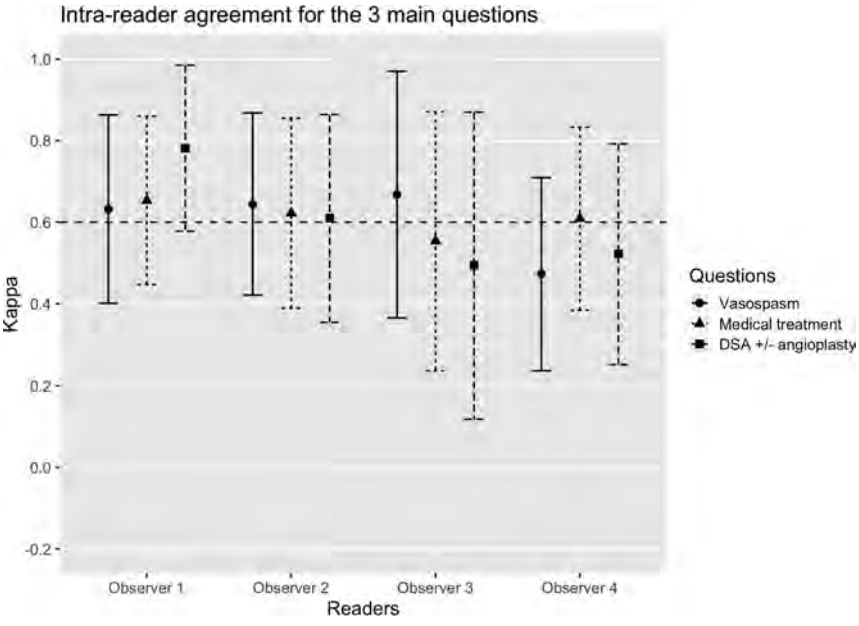

FIG 2. Intrareader reliability coefficients for the 3 main questions (95% confidence intervals) among 4 observers: detection of moderate-severe vasospasm in any arterial segment (≥ 50% narrowing), recommendations for medical treatment augmentation, and DSA ± angioplasty based on imaging findings. The *horizontal dashed line* indicates the threshold for substantial agreement ($\kappa > 0.6$).

The segment-by-segment analysis evaluating the presence of moderate-severe vasospasm did not reach substantial agreement for any arterial segment when considering all raters (On-line Fig 4, full data in On-line Tables 11 and 12). Judgments regarding proximal segments (M1, A1, vertebral and basilar arteries) were, in general, more repeatable than judgments regarding distal segments, with the exception of the internal carotid artery, for which agreement remained only slight. When only senior raters were considered, agreement for the presence of moderate-severe vasospasm (dichotomous scale) in the M1 segments improved to substantial (On-line Fig 4*D*). Examples of maximal agreement and maximal disagreement for the M1 segments are illustrated in On-line Fig 5.

An exploratory analysis was conducted to examine the role of metal artifacts from endovascular coils or surgical clips in affecting the repeatability of diagnoses. Thirty-six A1, 13 A2–A3, 11 ICA, and 7 M1 segments were excluded from this analysis, retaining only arterial segments that were not obscured by artifacts (On-line Fig 6, full data in On-line Table 13). κ coefficients remained below the 0.6 threshold, except for the left M1 segment, which reached the substantial agreement threshold among all observers.

Four observers completed the intraobserver study (3 interventional neuroradiologists and 1 radiology resident). Intraobserver reliability was "substantial" ($\kappa > 0.6$) in 3/4 readers (Fig 2, data in On-line Table 10) for the detection of moderate-to-severe vasospasm. For the management recommendations based on imaging findings, intraobserver reliability was substantial for 3 readers for medical management and for 2 readers for the decision to perform DSA.

DISCUSSION

The systematic review revealed a wide variation in grading systems of vasospasm. In addition, few studies evaluated the reliability of CTA for the diagnosis of vasospasm. Most reports were primarily diagnostic accuracy studies, dedicated to a comparison with DSA, while agreement studies were limited to 2–3 raters. The relatively good agreement between readers in these studies could not be confirmed in our center.

The main finding of our reliability study, which included a higher number of observers and wider range of experience compared with prior reports, is that the reliability of CTA alone in the diagnosis of moderate-to-severe cerebral vasospasm was not substantially repeatable between observers, even when verdicts were dichotomized and even when analyses were restricted to experienced raters.

This problem has previously been identified.[25] When a noninvasive imaging test is proposed to replace a more invasive one (here conventional angiography), the emphasis is usually placed on diagnostic accuracy, rather than on studying the repeatability of judgments made with the new imaging technique by multiple observers.[10,25] A major difficulty is the shift in the clinical spectrum of patients who are undergoing the test, which naturally occurs as the imaging test becomes widely accepted in routine clinical applications. Initially, for the diagnostic accuracy studies, the new test is likely to be compared with DSA for patients on the "severe" end of the spectrum (patients for whom DSA is judged to be indicated). Later on, at the time of clinical usage, the less invasive test is increasingly used in patients who have less severe disease, for whom DSA would not necessarily be performed. The consequence is that the relatively good interobserver agreement typically found between 2 or 3 expert raters in early diagnostic accuracy studies cannot be reproduced in real-world practice.

The poor repeatability of CTA judgments on vasospasm may not be surprising when one considers a number of unresolved problems. Despite the fact that CTA has been used for decades in the diagnosis of post-SAH cerebral vasospasm, there is no consensus on diagnostic criteria and our systematic review revealed a wide range of grading scales with various arbitrary cutoff values. Whether observers can reliably differentiate 25% or 30% luminal narrowing is questionable, given the small caliber of arteries and the limited spatial resolution of CTA. Even if precise and reliable measurements were possible, there is no agreement on which baseline reference value should be used. Some authors, similar to our study, use the baseline examination (when available) as a reference while others use the ipsilateral or contralateral "uninvolved" arteries. Various methods (eyeballing versus measuring with a caliper, for example) are commonly used. The rationale for various grading scales and the exact procedural methodology have not been clearly stated or validated.

In general, scales should be valid, reliable, and clinically relevant.[26] A scale that is too complex or that introduces too many categories is less repeatable, leaving too much room for variations in interpretation by different observers. There is also no standardized way to summarize the findings of each arterial segment in 1 global verdict that concerns the individual patient. We chose a grading system that had been used previously.[8,22] We also predefined a 50% diameter narrowing cutoff to explore whether better agreement could be achieved by simplifying responses through dichotomization and also because the 50% threshold has been suggested to correlate with decreased cerebral perfusion in the setting of cerebral vasospasm.[2,27-29] Further exploration of the diagnostic value of other threshold values may be warranted, given the low reliability found in the current study as well as possible lack of specificity of the 50% narrowing cutoff to predict ischemia.[15,28,30]

The primary end point of the study was the identification of moderate-to-severe vasospasm in any arterial segment for a given patient. If agreement between observers failed to reach the substantial ($\kappa > 0.6$) threshold, even for experienced raters, at least the intrarater agreement was better for most readers. There remains hope that better interobserver agreement could be attained, at least for major proximal arterial segments (excluding the carotid arteries), with more precise definitions and standardized procedures.

No matter how vasospasm is interpreted, the most important questions concern the clinical relevance of the CTA verdict. We were interested in exploring whether agreement existed, if not for the grade of vasospasm, at least for the clinical significance of the CTA findings in terms of whether medical treatment should be increased or whether DSA ± balloon angioplasty should be performed. We were careful not to provide clinical information that could bias the interpretation of the clinical history by different observers.[31] Despite this effort and contrary to a previous report,[7] interrater agreement remained below the substantial level.

A striking finding was the difference in the severity of vasospasm adjudicated by readers of different experiences and specialties. Diagnostic radiologists had a higher proportion of moderate-to-severe vasospasm diagnoses compared with interventional neuroradiologists. Junior readers had a higher proportion of positive answers to the 3 main questions, compared with more experienced readers. Interventional neuroradiologists, who are exposed to the most severe end of the disease spectrum because they may be required to treat these patients, may have a higher threshold for diagnosing severe vasospasm than other clinicians.

Segment-by-segment analyses were performed to explore potential ways to improve the reliability of CTA. This analysis also showed lower agreement than previously reported.[7] However, the relatively low reliability of the assessment of the carotid arteries and the relatively better agreement found in the evaluation of middle cerebral arteries have previously been noted.[6] These observations suggest that readers looking for vasospasm on CTA should perhaps focus on more reliable segments such as the M1 segments and basilar artery and not on less reliable segments such as carotid arteries or distal vessels.

The present study did not select the best cases or exclude patients with clip or coil artifacts, to reflect real-life clinical conditions. Including mainly patients without metal artifacts, as in a previous report,[6] would hardly have reflected normal clinical usage, for most patients at risk of vasospasm have already undergone endovascular or surgical treatment of the aneurysm at the time of the CTA assessment. Metal artifacts remain a limitation of CTA, a problem that could perhaps be mitigated by specific algorithms and/or dual-energy CT.[32] However, agreement improved only minimally when a second analysis excluding arterial segments obscured by beam-hardening artifacts was performed.

Several factors may explain the lower reliability we found compared with previous reports. Reliability is the complex product of interactions among the test, subjects, raters, and the

context of assessment.[33,34] κ coefficients based on a limited number of subjects and raters can result in overestimates.[35] Our study included a larger number of readers and index cases than in previous reports. The spectrum of patients included in our study also differed, as we discussed previously. Grading scales, exact methods of measurement, and statistical analyses also differed. One frequent source of artificial inflation of agreement is the lack of blinding of raters to other raters' observations, to the reference test, or to clinical information or clues.[31] In our study, observers independently analyzed anonymized images; they could not access the clinical or radiologic file of patients.

CTA is performed at our institution in patients with severe SAH grades in whom neurologic monitoring is difficult or impossible and/or when transcranial Doppler sonography findings are concerning for cerebral vasospasm. Angiography was performed in only 8% of studied patients; only 1 patient received intra-arterial milrinone. This is in contrast to almost 50% of patients undergoing angioplasty in the study by Shankar et al.[7] A retrospective review at our institution during the same period revealed that most patients with vasospasm treated with angioplasty had lateralizing neurologic symptoms despite maximal medical treatment. They were directly referred to the angiography suite without CTA. In such patients, the addition of CTA in the investigation of vasospasm may be superfluous. It seems that in our institution, CTA is most often used as a screening test for patients in intensive care, who are difficult to monitor clinically. Unfortunately, our study suggests that in this context, CTA interpretations are not repeatable enough to guide management decisions. If CTA is to be used as a screening test in patients with a low prior probability of symptomatic vasospasm, our study suggests that interpretations should be cautious, perhaps using a diagnostic threshold at a higher level than 50% narrowing, limited to more reliable proximal arterial segments.

Our study had several limitations. The portfolio of cases was artificially constructed, and raters were self-selected. A different set of cases and observers could have produced different results. Given our low prevalence of severe vasospasm in individual arterial segments, our κ coefficients could potentially be underestimated due to a skewed rating distribution in the per-segment analysis.[19] We did not try to differentiate focal-versus-diffuse vasospasm when a narrowing was present.[30] The experimental setup and the use of a portfolio differ from the case-by-case evaluation of real patients, and we can only surmise that responders took the time and care to respond as if they were evaluating real patients.

CONCLUSIONS

The systematic review found few reliability studies, limited to 2–3 readers. Our agreement study, which included a larger number of observers, revealed that the diagnosis of moderate-severe vasospasm was not sufficiently repeatable to support the use of CTA alone to guide decisions in the clinical management of patients with SAH. The repeatability of verdicts could potentially be improved by raising the diagnostic threshold above 50% narrowing for substantial vasospasm, by focusing on proximal arterial segments such as the M1 and basilar arteries, and by standardizing interpretation protocols.

ACKNOWLEDGMENT

We thank Guylaine Gevry for support during manuscript writing, editing, and submission as well as Daniela Ziegler, MSI (librarian) for support during the systematic review.

Disclosures: Laurent Letourneau-Guillon—*RELATED*: *Grant*: Laurent Letourneau-Guillon received Can $1125.00 from the ninth competition of the Program de Support Professoral du département de radiologie, radio-oncologie et médecine nucléaire de l'Université de Montréal to cover statistical analysis fees (internal funding program). The full amount was transferred to the statistician.* Miguel Chagnon—*RELATED*: *Consulting Fee or Honorarium*: University of Montreal.* Daniel Roy—*UNRELATED*: *Payment for Lectures Including Service on Speakers Bureaus*: Société des sciences vasculaires du Québec (Can $500); *Payment for Development of Educational Presentations*: Société des Radiologues du Québec (Can $5000); *Travel/Accommodations/Meeting Expenses Unrelated to Activities Listed*: ABC Win 2019, WFITN 2019, *Comments*: ABC Win, guest speaker (travel and accommodations), WFITN 2019, faculty (accommodations). *Money paid to institution.

REFERENCES

1. Macdonald RL. **Origins of the concept of vasospasm.** *Stroke* 2016;47:e11–15 CrossRef Medline
2. Budohoski KP, Guilfoyle M, Helmy A, et al. **The pathophysiology and treatment of delayed cerebral ischaemia following subarachnoid haemorrhage.** *J Neurol Neurosurg Psychiatry* 2014;85:1343–53 CrossRef Medline
3. Findlay JM, Nisar J, Darsaut T. **Cerebral vasospasm: a review.** *Can J Neurol Sci* 2016;43:15–32 CrossRef Medline
4. Francoeur CL, Mayer SA. **Management of delayed cerebral ischemia after subarachnoid hemorrhage.** *Crit Care* 2016;20:277 CrossRef Medline
5. Greenberg ED, Gold R, Reichman M, et al. **Diagnostic accuracy of CT angiography and CT perfusion for cerebral vasospasm: a meta-analysis.** *AJNR Am J Neuroradiol* 2010;31:1853–60 CrossRef Medline
6. Chaudhary SR, Ko N, Dillon WP, et al. **Prospective evaluation of multidetector-row CT angiography for the diagnosis of vasospasm following subarachnoid hemorrhage: a comparison with digital subtraction angiography.** *Cerebrovasc Dis* 2008;25:144–50 CrossRef Medline
7. Shankar JJ, Tan IY, Krings T, et al. **CT angiography for evaluation of cerebral vasospasm following acute subarachnoid haemorrhage.** *Neuroradiology* 2012;54:197–203 CrossRef Medline
8. Binaghi S, Colleoni ML, Maeder P, et al. **CT angiography and perfusion CT in cerebral vasospasm after subarachnoid hemorrhage.** *AJNR Am J Neuroradiol* 2007;28:750–58 Medline
9. Moher D, Liberati A, Tetzlaff J, et al; PRISMA Group. **Preferred reporting items for systematic reviews and meta-analyses: the PRISMA statement.** *J Clin Epidemiol* 2009;62:1006–12 CrossRef Medline
10. Kottner J, Audige L, Brorson S, et al. **Guidelines for Reporting Reliability and Agreement Studies (GRRAS) were proposed.** *J Clin Epidemiol* 2011;64:96–106 CrossRef Medline
11. Donner A, Rotondi MA. **Sample size requirements for interval estimation of the kappa statistic for interobserver agreement studies with a binary outcome and multiple raters.** *Int J Biostat* 2010;6: Article 31 CrossRef Medline
12. Rotondi M. **kappaSize: sample size estimation functions for studies of interobserver agreement. R package version 1.1 2013.** https://CRAN.R-project.org/package=kappaSize. Accessed January 10, 2018
13. R Core Team. **R: A language and environment for statistical computing. Version 3.4.4.** R Foundation for Statistical Computing 2018. https://www.R-project.org. Accessed April 2, 2018
14. Cruz JP, Sarma D, Noel de Tilly L. **Perimesencephalic subarachnoid hemorrhage: when to stop imaging?** *Emerg Radiol* 2011;18:197–202 CrossRef Medline

15. Budohoski KP, Czosnyka M, Kirkpatrick PJ, et al. **Clinical relevance of cerebral autoregulation following subarachnoid haemorrhage.** *Nat Rev Neurol* 2013;9:152–63 CrossRef Medline
16. Lazaridis C, Naval N. **Risk factors and medical management of vasospasm after subarachnoid hemorrhage.** *Neurosurg Clin N Am* 2010;21:353–64 CrossRef Medline
17. Feinstein AR, Cicchetti DV. **High agreement but low kappa, I: the problems of two paradoxes.** *J Clin Epidemiol* 1990;43:543–49 CrossRef Medline
18. Cicchetti DV, Feinstein AR. **High agreement but low kappa, II: resolving the paradoxes.** *J Clin Epidemiol* 1990;43:551–58 CrossRef Medline
19. Quarfoot D, Levine RA. **How robust are multirater interrater reliability indices to changes in frequency distribution?** *The American Statistician* 2016;70:373–84 CrossRef
20. Hunt WE, Hess RM. **Surgical risk as related to time of intervention in the repair of intracranial aneurysms.** *J Neurosurg* 1968;28:14–20 CrossRef Medline
21. Frontera JA, Claassen J, Schmidt JM, et al. **Prediction of symptomatic vasospasm after subarachnoid hemorrhage: the modified Fisher scale.** *Neurosurgery* 2006;59:21–27; discussion 21–27 CrossRef Medline
22. Takagi R, Hayashi H, Kobayashi H, et al. **Three-dimensional CT angiography of intracranial vasospasm following subarachnoid haemorrhage.** *Neuroradiology* 1998;40:631–35 CrossRef Medline
23. Gamer M, Lemon J, Fellows I, et al. **irr: Various coefficients of interrater reliability and agreement. R package version 0.84.** https://CRAN.R-project.org/package=irr. Accessed June 1, 2018
24. Landis JR, Koch GG. **The measurement of observer agreement for categorical data.** *Biometrics* 1977;33:159–74 Medline
25. Farzin B, Gentric JC, Pham M, et al. **Agreement studies in radiology research.** *Diagn Interv Imaging* 2017;98:227–33 CrossRef Medline
26. Cloft HJ, Kallmes DF. **Scaling back on scales with a scale of scales.** *AJNR Am J Neuroradiol* 2011;32:219–20 CrossRef Medline
27. Kelly PJ, Gorten RJ, Grossman RG, et al. **Cerebral perfusion, vascular spasm, and outcome in patients with ruptured intracranial aneurysms.** *J Neurosurg* 1977;47:44–49 CrossRef Medline
28. Ohkuma H, Manabe H, Tanaka M, et al. **Impact of cerebral microcirculatory changes on cerebral blood flow during cerebral vasospasm after aneurysmal subarachnoid hemorrhage.** *Stroke* 2000;31:1621–27 CrossRef Medline
29. Voldby B, Enevoldsen EM, Jensen FT. **Regional CBF, intraventricular pressure, and cerebral metabolism in patients with ruptured intracranial aneurysms.** *J Neurosurg* 1985;62:48–58 CrossRef Medline
30. Lodi CA, Ursino M. **Hemodynamic effect of cerebral vasospasm in humans: a modeling study.** *Ann Biomed Eng* 1999;27:257–73 CrossRef Medline
31. Lucas NP, Macaskill P, Irwig L, et al. **The development of a quality appraisal tool for studies of diagnostic reliability (QAREL).** *J Clin Epidemiol* 2010;63:854–61 CrossRef Medline
32. Winklhofer S, Hinzpeter R, Stocker D, et al. **Combining monoenergetic extrapolations from dual-energy CT with iterative reconstructions: reduction of coil and clip artifacts from intracranial aneurysm therapy.** *Neuroradiology* 2018;60:281–91 CrossRef Medline
33. Barth J, de Boer WE, Busse JW, et al. **Inter-rater agreement in evaluation of disability: systematic review of reproducibility studies.** *BMJ* 2017;356:14 CrossRef Medline
34. Spanjer J, Krol B, Brouwer S, et al. **Sources of variation in work disability assessment.** *Work* 2010;37:405–11 CrossRef Medline
35. Gwet KL. *Handbook of Inter-Rater Reliability: The Definitive Guide to Measuring the Extent of Agreement Among Raters.* Gaithersburg: Advanced Analytics; 2014
36. Schneck SA, Kricheff, II. **Intracranial Aneurysm Rupture, Vasospasm, and Infarction.** *Arch Neurol* 1964;11:668–80 CrossRef Medline
37. Kassell NF, Helm G, Simmons N, et al. **Treatment of cerebral vasospasm with intra-arterial papaverine.** *J Neurosurg* 1992;77:848–52 CrossRef Medline
38. Anderson GB, Ashforth R, Steinke DE, et al. **CT angiography for the detection of cerebral vasospasm in patients with acute subarachnoid hemorrhage.** *AJNR American journal of neuroradiology* 2000;21:1011–15 Medline
39. Otawara Y, Ogasawara K, Ogawa A, et al. **Evaluation of Vasospasm after Subarachnoid Hemorrhage by Use of Multislice Computed Tomographic Angiography.** *Neurosurgery* 2002;51:939–43 CrossRef Medline
40. Yoon DY, Choi CS, Kim KH, et al. **Multidetector-Row CT Angiography of Cerebral Vasospasm after Aneurysmal Subarachnoid Hemorrhage: Comparison of Volume-Rendered Images and Digital Subtraction Angiography.** *American Journal of Neuroradiology* 2006;27:370–77 Medline
41. Joo SP, Kim TS, Kim YS, et al. **Clinical utility of multislice computed tomographic angiography for detection of cerebral vasospasm in acute subarachnoid hemorrhage.** *Minim Invasive Neurosurg* 2006;49:286–90 CrossRef Medline
42. Aralasmak A, Akyuz M, Ozkaynak C, et al. **CT angiography and perfusion imaging in patients with subarachnoid hemorrhage: correlation of vasospasm to perfusion abnormality.** *Neuroradiology* 2009;51:85–93 CrossRef Medline
43. Zhang H, Zhang B, Li S, et al. **Whole brain CT perfusion combined with CT angiography in patients with subarachnoid hemorrhage and cerebral vasospasm.** *Clinical neurology and neurosurgery* 2013;115:2496–501 CrossRef Medline
44. Danura H, Schatlo B, Marbacher S, et al. **Acute angiographic vasospasm and the incidence of delayed cerebral vasospasm: preliminary results.** *Acta neurochirurgica Supplement* 2015;120:187–90 CrossRef Medline
45. Stecco A, Fabbiano F, Amatuzzo P, et al. **Computed tomography perfusion and computed tomography angiography in vasospasm after subarachnoid hemorrhage.** *Journal of neurosurgical sciences* 2018;62:397–405 CrossRef Medline

Suspected Metallic Embolization Distal to Coiled Intracranial Aneurysms Detectable by Susceptibility-Weighted MR Imaging

D.H. Yoo, Y.D. Cho, H.S. Lee, S.H. Kim, D. Jang, S.H. Lee, W.-S. Cho, H.-S. Kang, J.E. Kim, and M.H. Han

ABSTRACT

BACKGROUND AND PURPOSE: After endovascular coiling of intracranial aneurysms, round dark parenchymal lesions believed to be particulate metal are sometimes encountered in MR imaging studies of the brain. We used SWI to assess the frequency of such occurrences, in addition to exploring likely causes and clinical implications.

MATERIALS AND METHODS: We reviewed 700 MR imaging studies performed between September 2018 and March 2019 at our institution as follow-up monitoring of coiled intracranial aneurysms. Any sizeable (>5 mm) rounded dark-signal lesions encountered were presumed to be metallic. The magnitudes and locations of such lesions were recorded. In patients with these lesions, pertinent procedural documentation was screened for devices used, including coils, microcatheters, microguidewires, and stents. Medical records were also examined to determine whether any related symptoms ensued.

RESULTS: Twenty patients (2.8%) exhibited a total of 25 lesions on SWI. Diameters ranged from 5 to 11 mm (median, 8 mm). All except 2 lesions were located in brain regions downstream from aneurysms, but all lesions occupied vascular territories of vessels used to place guiding catheters. Other than the Synchro 14, which was routinely deployed, no device was regularly used in patients with SWI-detectable lesions; and none of the affected patients developed focal neurologic symptoms as a consequence.

CONCLUSIONS: Although the origins remain unclear, distal embolization of particulate metal distal to coiled cerebral aneurysms is occasionally observed on follow-up MR imaging studies. Such lesions, however, seem to have no apparent clinical impact.

ABBREVIATIONS: AcomA = anterior communicating artery; ICA = internal carotid artery; MCA = middle cerebral artery

Although endovascular coiling has become an established treatment option for intracranial aneurysms, the relatively high rates of recanalization in initially occluded aneurysms have necessitated periodic follow-up imaging.[1,2] DSA is still the criterion standard for evaluating saccular occlusions, despite the inherent thromboembolic risk, radiation exposure, and use of contrast. Multiple studies have also found MRA to be a reliable means of monitoring coiled aneurysms.[3] Furthermore, TOF-MRA has the added advantage of no contrast requirement, and axial source images of TOF-MRA may be especially useful in screening aneurysms for recurrence.[4] On inspecting TOF-MRA source images of coiled intracranial aneurysms, we sometimes encounter peculiar, rounded dark-signal lesions (other than the coiled masses themselves) within the brain parenchyma. These lesions are thought to be particulate metal, as previously determined in a series of patients using T1, T2, diffusion, and T2*-weighted imaging.[5]

The present study was conducted to evaluate the frequency with which distal embolization of metallic material occurs in conjunction with the coiling of intracranial aneurysms. We also explored potential causes and clinical implications of these lesions. Because the entire brain is not accessible by TOF-MRA, SWI was engaged as well. SWI additionally offers ready visibility of lesions owing to pronounced blooming artifacts, thus heightening the diagnostic sensitivity.

MATERIALS AND METHODS

This study was approved by our institutional review boards (Seoul National University Hospital). Given the retrospective nature of this study, written informed consent was waived. We

Received December 10, 2019; accepted after revision February 19, 2020.

From the Departments of Radiology (D.H.Y., Y.D.C., H.S.L., S.H.K., M.H.H.), and Neurosurgery (D.J., S.H.L., W.-S.C., H.-S.K., J.E.K.), Seoul National University Hospital, Seoul National University College of Medicine, Seoul, Korea; and Department of Neurosurgery and Radiology (M.H.H.), Veterans Health Service Medical Center, Seoul, Korea.

Please address correspondence to Young Dae Cho, MD, PhD, Department of Radiology, Seoul National University College of Medicine, 28 Yongon-Dong, Jongno-Gu, Seoul, 110-744, Korea: e-mail: aronnn@naver.com

Indicates article with supplemental on-line table.

http://dx.doi.org/10.3174/ajnr.A6506

retrieved and reviewed MR imaging studies performed at our institution (Seoul National University Hospital) between September 2018 and March 2019, each as follow-up in patients with coiled intracranial aneurysms. Our routine institutional follow-up protocol calls for monitoring by TOF-MRA at 6, 18, and 36 months after procedures, with additional interim or subsequent testing as clinically required. Within the study period, SWI was added for improved sensitivity and full coverage of the brain. Multislab TOF-MRA was performed using 3 axial slabs of 40–45 sections per slab at section thickness/overlap of 1.0 mm/50% or 0.5 mm/0%. Most TOF-MRA images addressed the base of the skull to the mid-Sylvian region, depending on the proximity or remoteness of coiled aneurysms. SWI was acquired at 2.0- to 2.5-mm thickness, extending from the base of the skull to the vertex.

The SWI studies of each patient were first reviewed to check for dark-signal lesions. We presumed that metallic fragments would be rounded and >5 mm in diameter. Lesions of irregular shapes or <4 mm across were excluded as potential microhemorrhages. If such lesions were detected by SWI, TOF-MRA source images were scrutinized to pinpoint their presence. If available, we also reviewed the following: 1) preprocedural MR imaging studies establishing the procedure-related nature of lesions, 2) other postprocedural MR imaging examinations reflecting temporal changes, and 3) pre- and postprocedural brain CT examinations.

Table 1: Characteristics of treated aneurysms in the study population

Characteristic	Aneurysm (*n* = 859)
Ruptured/unruptured	78 (9.1%)/781 (90.9%)
Size of aneurysm	
Mean (mm)	5.2 ± 3.1
Distribution (mm)	
–3	222 (25.8%)
4–6	475 (55.3%)
7–9	119 (13.9%)
10–	43 (5.0%)
Location of aneurysm	
Internal carotid artery	363 (42.2%)
Anterior cerebral artery[a]	193 (22.5%)
Middle cerebral artery	207 (24.1%)
Vertebrobasilar artery	96 (11.2%)

[a] Including an anterior communicating artery aneurysm.

Most endovascular procedures were conducted with the patient under general anesthesia. Antiplatelet premedication was routinely administered to patients with unruptured aneurysms. A bolus of heparin (3000 IU), administered on placement of the femoral arterial sheath, was thereafter sustained by hourly doses (1000 IU); activated clotting time was monitored each hour. Continuance of dual-antiplatelet therapy was advised for at least 3 months postoperatively, followed by single-agent maintenance for at least 1 year in patients with stents deployed. In the absence of stent placement, antiplatelet therapy was selectively dispensed in instances of prior antiplatelet medication use, coil protrusion, or procedural thromboembolism.

Patient demographics and characteristics of coiled aneurysms, such as size, location, and rupture status, were collected. In patients with dark-signal lesion on SWI, their locations and magnitudes were recorded, with particular attention paid to any restriction within the vascular territories of catheterized arteries. Procedural data were similarly reviewed to identify devices used, including coils, microcatheters, microguidewires, and stents. Finally, medical records were screened for any related patient symptoms.

RESULTS

MR imaging studies of 700 patients were subject to review. The study population included 189 men (27%) and 511 women (73%), with a mean age of 61.4 years (range, 18–86 years) at the time of MR imaging. In all except 12 patients, a 3T MR imaging unit was used. The interval between the most recent coiling session and current MR imaging ranged from 4 to 177 months (mean, 26.5 months), distributed as follows: ≤6 months, 227 (32.4%); 7–18 months, 218 (31.2%); 19–36 months, 133 (19.0%); and >36 months, 122 (17.4%). In this patient population, 859 aneurysms were treated overall, the characteristics of which are detailed in Table 1. Multiple aneurysms were found in 131 patients, and 77 patients were retreated due to recanalization. Twelve patients had additional aneurysms managed by surgical clipping.

A total of 25 dark-signal lesions suspicious for particulate metal were detected by SWI in 20 patients (2.8%) with 24 treated aneurysms (Figs 1 and 2). Specific features of their treated aneurysms and the dark-signal lesions observed are summarized in Table 2. Although 2 patients (patients 11 and 12) had undergone prior coiling of other aneurysms, no dark-signal lesions had previously resulted. In the 2 instances of retreatment due to recanalization of coiled aneurysms (patients 6 and 16), no dark-signal lesion was detected after initial treatment. The mean procedure-to-MR imaging interval was 16 months (range, 4–67 months).

The diameters of dark-signal lesions ranged from 5 to 11 mm (median, 8 mm). Among the 25 lesions identified on SWI, 14 (56%) were covered in the

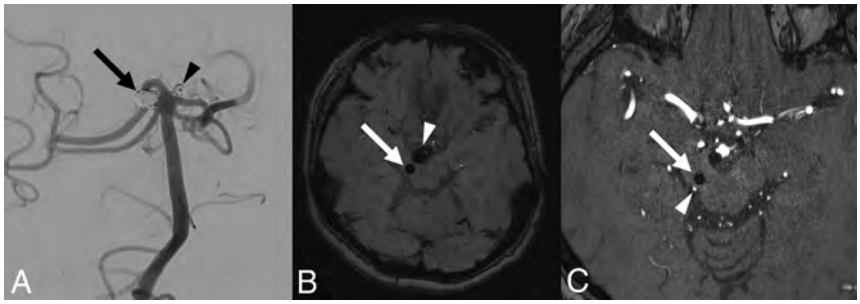

FIG 1. *A*, Coil embolization of 2 aneurysms involving the right superior cerebellar artery (*arrow*) and basilar tip (*arrowhead*). *B*, SWI 20 months later shows an 8-mm rounded, dark-signal lesion of the right midbrain (*arrow*) and another dark signal representing a coil mass (*arrowhead*). *C*, Source image from TOF-MRA depicts the same lesion, measured at 4 mm (*arrow*), with the right superior cerebellar artery (*arrowhead*) coursing posteriorly.

Table 2: Details of patients with dark-signal lesions

Case No.	Age (yr)/Sex	Aneurysm		Lesion			Anticoagulant or Antiplatelet Maintenance[b]
		Location	Size (mm)	Location	Size (mm)	TOF-MRA[a]	
1	44/F	Rt ICA	6	Rt parietal	11	No	Antiplatelet
2	57/M	AcomA	4	Lt temporal	10	Yes	None
3	72/M	Lt ICA	5	Lt temporal	10	Yes	Antiplatelet
		AcomA	5				
4	72/M	AcomA	5	Rt frontal	7	No	Antiplatelet
5	60/F	Rt SCA	5	Rt midbrain	8	Yes	None
		Lt PCA	3				
6	68/F	Lt ICA[c]	3	Lt parietal	11	No	Antiplatelet
7	49/M	Lt ICA	4	Lt temporal	9	Yes	Antiplatelet
8	63/F	Rt ICA	4	Rt temporal	9	Yes	None
9	52/F	Rt MCA	4	Rt temporal	10	Yes	Antiplatelet
		Rt ICA	4	Rt CC	10	Yes	
10	19/F	Lt ICA	15	Rt frontal	6	Yes	Antiplatelet
				Lt frontal	5	No	
				Lt frontal	5	No	
11	59/F	Rt ICA	3	Lt parietal	8	No	None
12	66/F	AcomA	3	Lt frontal	10	No	Antiplatelet
13	49/F	Rt ICA	7	Rt frontal	5	Yes	Antiplatelet
14	39/F	Lt ICA[c]	4	Lt BG	7	Yes	Antiplatelet
				Rt parietal	7	Yes	
				Rt parietal	7	No	
15	60/F	Rt MCA	11	Rt parietal	8	No	None
16	62/F	Rt SCA[c]	8	Rt occipital	10	Yes	Antiplatelet
17	63/F	Rt ICA	4	Rt frontal	6	Yes	Antiplatelet
		Lt ICA	3				
18	71/M	AcomA	6	Rt frontal	5	No	Antiplatelet
19	54/F	Lt ICA	4	Lt CC	5	Yes	None
20	58/F	Rt MCA	5	Rt frontal	7	No	None

Note:—Rt indicates right; Lt, left; PCA, posterior cerebral artery; CC, corpus callosum; SCA, superior cerebellar artery; BG, basal ganglia.
[a] Indicates whether the dark-signal lesion on SWI was covered in the source image of TOF-MRA.
[b] Indicates maintenance >1 month after coil embolization.
[c] Denotes ruptured aneurysm.

scan range of TOF-MRA source images (Fig 1). Preprocedural MR imaging studies were available in 11 of 20 patients with dark-signal lesions. No evidence of pre-existing dark-signal lesions was documented in all 11 patients. Postprocedural CT scans of the brain available in 3 patients (patients 9, 14, and 16) were devoid of lesions at corresponding dark-signal locations (not detected on CT). Six patients (patient 5, 8, 15, 17, 18, and 19) underwent earlier postprocedural MR imaging examinations during the follow-up (TOF-MRA in 5 patients, and T2*-weighted imaging in 1 patient) with a mean interval of 21 months (range, 6–49 months). In all 6 patients, there was no change in the lesions at all when compared with the same available sequence of MR images (SWI in case of T2*-weighted imaging).

Except for 2 instances (patients 2 and 15), all lesions occupied regions of the brain downstream from coiled aneurysms. However, all were within vascular territories of vessels used to place guiding catheters. In patient 2, the left ICA served for placement of the guiding catheter during the coiling of an anterior communicating artery (AcomA) aneurysm, leaving a dark-signal lesion in the left MCA territory. In patient 15, the dark-signal lesion appeared within the parasagittal right parietal lobe in the anterior cerebral artery territory after coiling of a right MCA aneurysm. The bilateral anterior cerebral artery territory was solely or predominantly supplied by the right or left ICA in 4 patients (patients 4, 10, 11, and 18), resulting in dark-signal lesions contralateral to coiled aneurysms. In patient 14, the left ICA alone provided bilateral hemispheric perfusion due to chronic right ICA occlusion. Dark-signal lesions appeared within the right MCA territory after coiling of a left-sided aneurysm.

No device common to patients with the dark-signal lesions was identified, except for the Synchro 14 (Stryker, Kalamazoo, Michigan), which was routinely deployed in our study population (withheld in 2 patients [0.3%] only). Devices used for each patient with dark-signal lesions are itemized in the On-line Table. None of the patients with dark-signal lesions developed focal neurologic symptoms attributable to corresponding lesions.

DISCUSSION

In cerebral angiographic procedures, whether diagnostic or therapeutic, there is a certain risk of cerebral embolism.[6] Ischemic lesions may be seen by diffusion-weighted imaging in about half of patients after endovascular coiling of intracranial aneurysms, though most are not neurologically evident.[7] The potential causes of these include air bubbles, thrombi, and disrupted atherosclerotic plaque. A variety of foreign materials have also been implicated. Since the advent of cerebral angiography, reports of embolic cotton or synthetic fibers have surfaced, their origins traced to surgical drapes or gauze.[8-10] More recently, the hydrophilic polymer coating of catheters and guidewires has become a documented source of downstream emboli following cerebral angiography or interventional procedures.[11-14]

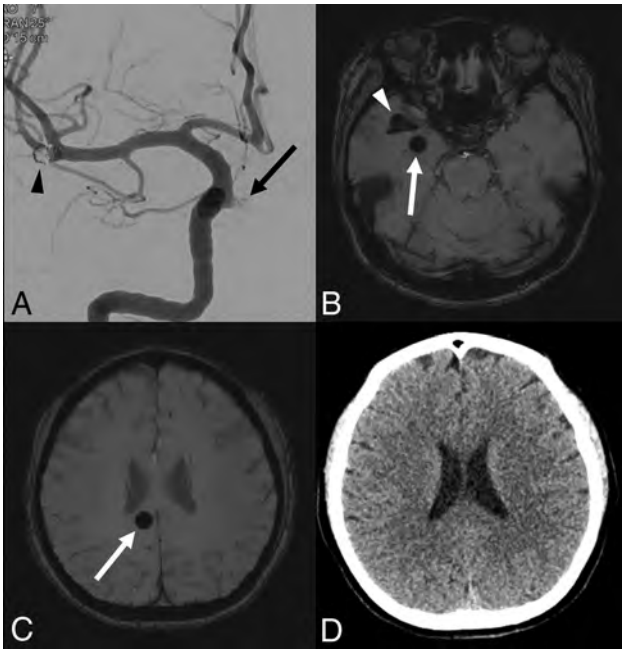

FIG 2. *A*, Coil embolization of 2 aneurysms arising from the right ICA (*arrow*) and MCA at the bifurcation (*arrowhead*). *B*, SWI 6 months later demonstrates a 10-mm rounded dark-signal lesion within right temporal lobe (*arrow*) and another dark signal representing a coil mass and stent (*arrowhead*). *C*, A second rounded dark-signal lesion (10 mm) is present within the right corpus callosum (*arrow*). *D*, The lesion of right corpus callosum is undetectable by postprocedural CT.

Devices intended for interventional procedures contain metallic substances by design to confer fluoroscopic visibility and enhance biostability/durability. Still, reports of suspected particulate metal emboli after endovascular treatment of intracranial aneurysms or cardiac catheterization have been surprisingly few.[5] In the present study, suspicious metallic emboli were identified by MR imaging in 2.8% of a sizeable patient population ($n = 700$) with coiled intracranial aneurysms. This figure is somewhat lower than that cited in a previous study, in which 5.5% of patients (6/110) displayed metallic embolic phenomena in postprocedural MR imaging studies under similar circumstances.[5]

Most dark-signal lesions encountered herein fell within vascular territories of vessels used to place guiding catheters. The exceptions in 2 instances suggest that such embolization is not always linked to coil deployment/detachment or positioning of stents during endovascular procedures. Instead, it may occur while navigating to or from aneurysms, gaining access or retrieving devices. The only device shared by patients with dark-signal lesions was the Synchro 14 microwire (Stryker). We have often found that microguidewire coatings may be peeled off as torque is applied, serving as a potential cause of dark-signal lesions (microfragments of the coating). However, the Synchro 14 was used in essentially all of our procedures, so it can hardly be considered the culprit device.

Coil detachment may be achieved in a variety of ways, including mechanical, electrolytic, electrothermal, and hydraulic methods. When the present study was conceived, we wondered whether some coil-detachment strategies might precipitate micrometallic fragmentation. However, our data have dispelled any relation between dark-signal lesions and a single detachment system, and no other devices (ie, guiding catheters, microcatheters, or stents) were consistently used in the presence of dark-signal lesions.

Previous reports on inadvertent distal embolization of foreign matter have confirmed subsequent neurologic symptoms due to hemorrhage or focal edema,[11,13,14] whereas we encountered no clinical manifestations owing to dark-signal lesions. In addition, FLAIR images available in 3 patients with dark-signal lesions revealed no abnormal signal around the lesion. It is feasible that, despite their various sizeable appearance on SWI, such minute fragments of metal, small enough to escape detection by CT, are too small to induce embolic infarction. In addition, these lesions were unchanged with time in 6 patients, underscoring the relative biostability of such emboli and the likely absence of foreign body reaction.

Our study has several acknowledged limitations. First, the dark-signal lesions present on SWI were never pathologically confirmed as metallic in nature because none of the patients had clinical conditions calling for biopsy. Furthermore, preprocedural MR imaging and immediate postprocedural MR imaging were not available in all patients, so we could not conclusively ascertain whether all dark-signal lesions were procedure-related. The possibility of pre-existing hemorrhage or calcification still remained. In addition, patients who underwent stent-assisted coiling routinely received antiplatelet medication for at least a year, which might increase incidence of microhemorrhage.[15] Another pitfall was the potential to underestimate the incidence of metallic emboli by excluding lesions of <4 mm or by failing to detect lesions near the base of the skull, the latter explained by susceptibility artifacts from bone and air. Finally, our study was retrospective by design, incorporating MR imaging protocols and follow-up intervals that were not consistent within the study population. A prospective investigation involving controlled perioperative MR imaging studies would perhaps yield more reliable results.

CONCLUSIONS

Although a causative device or mechanism has yet to be implicated, embolization of particulate metal distal to coiled cerebral aneurysms is not an infrequent finding in follow-up MR imaging studies. In this setting, however, the patients seem unaffected clinically.

Disclosures: Moon Hee Han—*UNRELATED*: *Consultancy*: MicroVention.* *Money paid to the institution.

REFERENCES

1. Molyneux A, Kerr R, Stratton I, et al. **International Subarachnoid Aneurysm Trial (ISAT) of neurosurgical clipping versus endovascular coiling in 2143 patients with ruptured intracranial aneurysms: a randomised trial.** *Lancet* 2002;360:1267–74 CrossRef CrossRef Medline
2. Lecler A, Raymond J, Rodriguez-Regent C, et al. **Intracranial aneurysms: recurrences more than 10 years after endovascular treatment-a prospective cohort study, systematic review, and meta-analysis.** *Radiology* 2015;277:173–80 CrossRef Medline
3. Ahmed SU, Mocco J, Zhang X, et al. **MRA versus DSA for the follow-up imaging of intracranial aneurysms treated using endovascular**

techniques: a meta-analysis. *J Neurointerv Surg* 2019;11:1009–14 CrossRef Medline

4. Cho YD, Kim KM, Lee WJ, et al. **Time-of-flight magnetic resonance angiography for follow-up of coil embolization with Enterprise stent for intracranial aneurysm: usefulness of source images.** *Korean J Radiol* 2014;15:161–68 CrossRef Medline
5. Yasuda R, Maeda M, Umino M, et al. **Suspected metallic embolism following endovascular treatment of intracranial aneurysms.** *AJNR Am J Neuroradiol* 2016;37:1696–99 CrossRef Medline
6. Bendszus M, Koltzenburg M, Burger R, et al. **Silent embolism in diagnostic cerebral angiography and neurointerventional procedures: a prospective study.** *Lancet* 1999;354:1594–97 CrossRef Medline
7. Bond KM, Brinjikji W, Murad MH, et al. **Diffusion-weighted imaging-detected ischemic lesions following endovascular treatment of cerebral aneurysms: a systematic review and meta-analysis.** *AJNR Am J Neuroradiol* 2017;38:304–09 CrossRef Medline
8. Silberman J, Cravioto H, Feigin I. **Foreign body emboli following carotid angiography.** *Arch Neurol* 1960;3:711–17 CrossRef
9. Chason JL, Landers JW, Swanson RE. **Cotton fiber embolism: a frequent complication of cerebral angiography.** *Neurology* 1963;13:558–60 CrossRef CrossRef Medline
10. Shannon P, Billbao JM, Marotta T, et al. **Inadvertent foreign body embolization in diagnostic and therapeutic cerebral angiography.** *AJNR Am J Neuroradiol* 2006;27:278–82 Medline
11. Shapiro M, Ollenschleger MD, Baccin C, et al. **Foreign body emboli following cerebrovascular interventions: clinical, radiographic, and histopathologic features.** *AJNR Am J Neuroradiol* 2015;36:2121–26 CrossRef Medline
12. Oh SW, Shin NY, Lee HJ, et al. **Delayed enhancing lesions after coil embolization of aneurysms: clinical experience and benchtop analyses.** *J Neurointerv Surg* 2017;9:1243–47 CrossRef Medline
13. Ansari SA, Anderson RR, Caron MJ, et al. **Hydrophilic polymer embolic complication during diagnostic cerebral angiography presenting with delayed intracranial hemorrhage: case report and literature review.** *J Neurointerv Surg* 2019;11:80–83 CrossRef Medline
14. Geisbush TR, Marks MP, Heit JJ. **Cerebral foreign body reaction due to hydrophilic polymer embolization following aneurysm treatment by Pipeline flow diversion device.** *Interv Neuroradiol* 2019;25:447–53 CrossRef Medline
15. Qiu J, Ye H, Wang J, et al. **Antiplatelet therapy, cerebral microbleeds, and intracerebral hemorrhage: a meta-analysis.** *Stroke* 2018;49:1751–54 CrossRef Medline

MRI Vessel Wall Imaging after Intra-Arterial Treatment for Acute Ischemic Stroke

A. Lindenholz, I.C. van der Schaaf, A.G. van der Kolk, H.B. van der Worp, A.A. Harteveld, L.J. Kappelle, and J. Hendrikse

ABSTRACT

BACKGROUND AND PURPOSE: Vessel wall imaging is increasingly performed in the diagnostic work-up of patients with ischemic stroke. The aim of this study was to compare vessel wall enhancement after intra-arterial thrombosuction with that in patients not treated with thrombosuction.

MATERIALS AND METHODS: From 2009 to 2017, forty-nine patients with an ischemic stroke underwent 7T MR imaging within 3 months after symptom onset as part of a prospective intracranial vessel wall imaging study. Fourteen of these patients underwent intra-arterial treatment using thrombosuction (intra-arterial treatment group). In the intra-arterial treatment group, vessel walls were evaluated for major vessel wall changes. All patients underwent pre- and postcontrast vessel wall imaging to assess enhancing foci of the vessel wall using coregistered subtraction images. A Wilcoxon signed rank test was performed to test for differences.

RESULTS: In the intra-arterial treatment group, 11 of 14 patients (79%) showed vessel wall enhancement compared with 17 of 35 patients without intra-arterial treatment (49%). In the intra-arterial treatment group, more enhancing foci were detected on the ipsilateral side ($n = 18.5$) compared with the contralateral side ($n = 3$, $P = .005$). Enhancement was more often concentric on the ipsilateral side ($n = 8$) compared with contralateral side ($n = 0$, $P = .01$). No differences were found in the group without intra-arterial treatment between the number and configuration of ipsilateral and contralateral enhancing foci.

CONCLUSIONS: Patients with intra-arterial treatment by means of thrombosuction showed more (concentric) enhancing foci of the vessel wall ipsilateral compared with contralateral to the treated artery than the patients without intra-arterial treatment, suggesting reactive changes of the vessel wall. This finding should be taken into account when assessing vessel wall MR images in patients with stroke.

ABBREVIATIONS: IAT = intra-arterial treatment; MPIR = magnetization prepared inversion recovery

Intra-arterial treatment (IAT) has proved beneficial in selected patients with an anterior circulation acute ischemic stroke.[1] With IAT, revascularization of the occluded artery by means of mechanical thrombectomy can be achieved in most patients, restoring blood flow to the brain tissue. Although the overall effects of IAT on clinical outcome are well-known,[1,2] not much is known about the effects of thrombectomy on the local intracranial vessel wall. Recently, there has been concern that IAT might damage the arterial vessel wall.[3-6]

Thrombectomy can be performed with different devices: Stent retrievers or thrombosuction devices have been used most often.[2] Damage to the intracranial vessel wall may be caused by repeated mechanical sheer stress of the stent retriever on the vessel wall[4] or the negative pressure (up to −50 cm Hg) when using a thrombosuction device.[5,7] This damage may consist of dissections, vessel wall edema, and rupture or damage to the endothelium, potentially leading to recurrent thrombosis and distal embolism.[3-6] Histopathologic preclinical studies have shown endothelial damage to the vessel wall after thrombectomy, more evident with stent-retriever devices than with thrombosuction devices.[3-5,8-10] In recent MR imaging studies and other imaging studies performed after IAT, damage to a major vessel wall such as dissection or stenosis was only rarely reported.[5,8-12] However, the arterial vessel wall more often showed contrast enhancement or wall thickening than arteries of patients who did not undergo

Received May 12, 2019; accepted after revision January 28, 2020.

From the Departments of Radiology (A.L., I.C.v.d.S., A.G.v.d.K., A.A.H., J.H.) and Neurology and Neurosurgery (H.B.v.d.W., L.J.K.), University Medical Center Utrecht, Utrecht, the Netherlands

The research of Jeroen Hendrikse was funded by the European Research Council under the European Union's Horizon 2020 Program (H2020)/European Research Council Grant agreement No. 637024 (HEARTOFSTROKE).

Please address correspondence to Arjen Lindenholz, MD, MSc, Department of Radiology, University Medical Center Utrecht, Postbox 85500, 3508 GA Utrecht, the Netherlands; e-mail: A.Lindenholz@umcutrecht.nl

Indicates open access to non-subscribers at www.ajnr.org
Indicates article with supplemental on-line table.
http://dx.doi.org/10.3174/ajnr.A6460

IAT.[11-13] In these series, patients were treated mostly with stent retrievers, and scanning was performed with 3T MR imaging scanners in the acute setting (first day to first week) after IAT. The longer-term effects after IAT performed by thrombosuction have not been reported yet.

Intracranial vessel wall imaging is expected to be increasingly performed in the diagnostic work-up and follow-up of patients with stroke. The aim of this study was to assess the frequency of longer-term vessel wall changes by assessing the presence and severity of intracranial vessel wall enhancement in patients with stroke after IAT with thrombosuction and compare them with patient with stroke without IAT. Potential differences may support the diagnostic interpretation of intracranial vessel wall changes after acute stroke treatment.

MATERIALS AND METHODS

Study Population

From December 2009 to November 2017, patients with an acute ischemic stroke in the anterior circulation who were treated at the neurology department of the University Medical Center Utrecht were screened for inclusion. Patients were retrieved from the ongoing Intracranial Vessel Wall Imaging study (NTR2119; www.trialregister.nl), a prospective vessel wall MR imaging study recruiting patients who presented with clinical symptoms of anterior circulation ischemia (TIA or stroke).[14] Main inclusion criteria for the current study were age older than 18 years and the possibility of undergoing a 7T MR imaging examination within 3 months after symptom onset. The patients without IAT were selected on the basis of an anterior circulation nonlacunar infarct. Patients with contraindications for MR imaging or for gadolinium-containing contrast agents were excluded, as well as patients with ischemic stroke caused by vasculitis, reversible cerebral vasoconstriction syndrome, small-vessel disease, or secondary to a recent surgical or interventional procedure. Additional exclusion criteria for the current study were primary treatment with a different strategy than a thrombosuction device for the IAT-group to improve study population homogeneity and previous IAT or TIA as final diagnosis for the non-IAT group. Findings of 23 patients without IAT have been published before.[15,16] These prior articles dealt with sequence development and vessel wall lesion prevalence, whereas in this study, we report longer-term intracranial vessel wall enhancement after IAT using thrombosuction compared with patients not treated with IAT. This study was approved by the institutional review board of our hospital, and all patients gave written informed consent. For all patients, baseline characteristics including age, sex, vascular risk factors, stroke severity expressed using the NIHSS, as well as stroke classification and time intervals between IAT and imaging were collected. For the IAT-group, time intervals between symptom onset and treatment, procedural time, number of passes needed for thrombus removal, and concomitant treatment with IV recombinant tissue-type plasminogen activator (alteplase) were additionally collected.

Treatment

Treatment was performed as part of standard clinical care. All patients who were eligible for intravenous thrombolysis received IV alteplase within the 4.5-hour time window from symptom onset. IAT was introduced in our center during the study period after the international IAT trial results, and the first patient treated with a thrombosuction device was included in 2014. The main criteria for IAT were derived from the Multicenter Randomized Clinical Trial of Endovascular Treatment for Acute Ischemic Stroke in The Netherlands (MR CLEAN) trial:[1] 1) a clinical diagnosis of acute ischemic stroke caused by an intracranial anterior circulation occlusion that was visible on CTA, MRA, or DSA; and 2) the ability to perform treatment within 6 hours from symptom onset. All patients in the IAT-group were treated under general anesthesia. A thrombosuction device (Penumbra System®, Alameda, California) was used in all patients included in this study. Procedural complications involving the vessel wall, including dissection or perforation, were noted.

Imaging

Imaging was performed on a 7T whole-body MR imaging system (Philips Healthcare, Best, the Netherlands) with either a 16- or a 32-channel receive coil and a volume transmit/receive coil for transmission (Quad TR; Nova Medical, Wilmington, Massachusetts). Vessel wall visualization at 7T MR imaging has been shown to be superior compared with 3T MR imaging because of a higher contrast-to-noise ratio and image quality.[17,18] The imaging protocol included a dedicated pre- and postcontrast 3D whole-brain T1-weighted magnetization-prepared inversion recovery TSE (MPIR-TSE) vessel wall sequence and a TOF-MRA.[16] For the postcontrast image acquisitions, a gadolinium-containing contrast agent (gadobutrol, Gadovist 1.0 mmol/mL; Bayer Schering Pharma, Berlin, Germany), dose-adjusted to patient weight, was administered intravenously. The TOF-MRA images were used for anatomic verification of the vessels seen on the MPIR-TSE images. The following scan parameters were used for the MPIR-TSE sequence: FOV = 220 × 180 × 13 mm^3, which was optimized to 250 × 250 × 190 mm^3 and satisfactorily tested for equality in vessel wall lesion detection during the study period;[16] acquired spatial resolution = 0.8 × 0.8 × 0.8 mm^3; reconstructed spatial resolution = 0.49 × 0.49 × 0.49 mm^3; TR = 3952 ms; TE = 37 ms; TI = 1375 ms; flip angle = 120°; readout bandwidth = 935 Hz; and an acquisition time of 10 min 40 sec. For the small-FOV sequence, the FOV was placed so that the distal intracranial carotid artery and middle cerebral artery were included in the FOV. Scan parameters for the TOF-MRA were as follows: FOV = 190 × 190 × 102 mm^3, acquired spatial resolution = 0.4 × 0.5 × 0.6 mm^3, reconstructed spatial resolution = 0.4 × 0.4 × 0.3 mm^3, TR = 21 ms, TE = 2.3 ms, flip angle = 30°, readout bandwidth = 557 Hz, and acquisition time = 9 min 18 sec.

Image Assessment

Image assessment was performed off-line on a PACS. All images were independently assessed by 2 readers with expertise in reading neurovascular vessel wall images (A.G.v.d.K., 9 years of experience and A.L., 4 years of experience). Readers were blinded to any patient characteristics. The arterial segments that were analyzed included the left and right intracranial ICAs (the clinoid, supraclinoid, and terminal segments) and the left and right MCAs (M1 and M2 segments). Recanalization after IAT was assessed with TICI grading on postprocedural DSA images.[19]

First, in the IAT-group postprocedural DSA, 7T MR vessel wall, and 7T MRA images were assessed for dissections and stenoses as major vessel wall changes. Intracranial stenoses were classified into <50% stenosis (minor), 50%–69% stenosis (moderate), 70%–99% stenosis (severe), and occlusion.[20] Second, all 7T MR vessel wall images were assessed for the presence and number of enhancing foci per arterial segment. The mean numbers of enhancing foci of both readers were used for the analyses. Assessment was blinded to IAT and non-IAT. In all patients (IAT-group and non-IAT group), the arteries in the hemisphere ipsilateral to the ischemic infarction were compared with those of the contralateral side. All enhancing foci were further classified as either concentric (circumference of the vessel wall >50% enhancing) or eccentric (<50% circumference enhancement) type enhancement. Intracranial atherosclerosis more often shows eccentric vessel wall enhancement, and an inflammatory state of the vessel wall shows most often concentric vessel wall enhancement.[21,22]

The method and cutoff point for the configuration of vessel wall lesion assessment by visual inspection has been described before as a clinically usable tool for vessel wall assessment.[21] In the assessment of contrast enhancement, a focus was considered enhancing when the signal intensity approximated the signal intensity of the (enhancing) pituitary stalk and was present in at least 2 slices. Next, pre- and postcontrast vessel wall images were compared side-by-side to confirm the enhancement. As a double confirmation of enhancement, subtraction images were calculated and used. Thus, pre- and postcontrast vessel wall images were coregistered for the whole 3D volume using the elastix toolbox in MeVisLab (Version 2.7; MeVis Medical Solutions, Bremen, Germany).[23] Subsequently, precontrast vessel wall images were subtracted from the coregistered postcontrast vessel wall images and were assessed for contrast enhancement. The registration parameters, ΔRotation (in degrees) and ΔTranslation (in millimeters), were used as a measure of motion between pre- and postcontrast vessel wall sequences. The ΔRotation and ΔTranslation parameters were calculated as $\sqrt{(\text{X-axis}^2 + \text{Y-axis}^2 + \text{Z-axis}^2)}$. When >1 enhancing focus was detected within 1 arterial segment, they were counted separately when they were separated from each other by a normal-appearing vessel wall segment. Also, enhancing foci at the location where the ICA crosses the dura mater from extracranial to intracranial, suspicious for vasa vasorum, were not considered vessel wall enhancement.

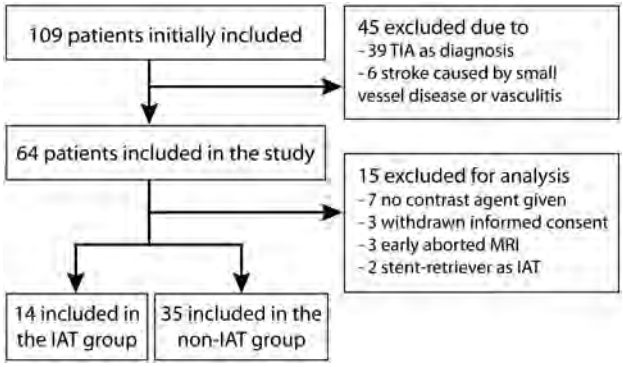

FIG 1. Flowchart of study inclusion.

Statistical Analysis

SPSS, Version 21.0 for Windows (IBM, Armonk, New York) was used for statistical analysis. Descriptive statistics were used for the frequency of intracranial dissection or stenosis. Counts are given in proportions (percentages), including their 95% confidence intervals. The intraclass correlation coefficient using a 2-way mixed, average measurement, consistency model, and the Dice similarity coefficient to correct for the location of the enhancement were calculated to evaluate the interrater agreement. A Wilcoxon signed rank test was used for comparison between the number of enhancing foci ipsilateral and contralateral to the ischemic site as seen on the vessel wall images. A Mann-Whitney *U* test was performed to compare the number of enhancing foci between the IAT-group and non-IAT group. A 2-sided *P* value < .05 was considered statistically significant.

Table 1: Baseline characteristics, specified by patients with stroke with and without IAT

	IAT Total (%)	Non-IAT Total (%)	*P* Value
Age (mean) (range) (yr)	65 (42–85)	60 (35–81)	.23[a]
Sex (male)	10 (71%)	18 (51%)	.34[b]
Hypertension	4 (29%)	18 (51%)	.21[b]
Hyperlipidemia	7 (50%)	18 (51%)	.99[b]
Diabetes mellitus	0 (0%)	4 (11%)	.31[b]
Current smoking	3 (21%)	12 (34%)	.46[c]
Former smoking	5 (36%)	7 (20%)	.46[c]
Atrial fibrillation	3 (21%)	4 (11%)	.39[b]
NIHSS score (mean) (range)	10.5 (3–20)	6.3 (0–21)	.02[a]
TOAST criteria[30]			.62[c]
Large-artery atherosclerosis	7 (50%)	21 (60%)	
Cardioembolism	4 (29%)	5 (14%)	
Small-vessel occlusion	0 (0%)	0 (0%)	
Other determined etiology	1 (7%)	5 (14%)	
Undetermined	2 (14%)	4 (12%)	
Time to 7T MR imaging (mean) (SD) (day)	55 (±22)	16 (±23)	<.001[a]
Time to 7T MR imaging (median) (range) (day)	58 (22–87)	6 (1–84)	

[a] Mann-Whitney *U* test.
[b] Fisher exact test.
[c] Pearson χ^2 test.

RESULTS

Patients and Treatment

Between December 2009 and October 2017, forty-nine patients were included in this study. A flowchart of the study inclusion is shown in Fig 1. Baseline characteristics for both patient groups can be found in the Table 1.

Fourteen patients underwent IAT using thrombosuction; 2 of them had an occlusion in the distal intracranial ICA, and 12 patients had occlusion in the MCA (Table 2). Twelve patients received intravenous alteplase before intra-arterial mechanical thrombectomy; the other 2 patients exceeded the 4.5-hour time window for alteplase treatment. In 2 patients, a stent retriever (Solitaire, Covidien, Irvine, California; or

Table 2: Location of occlusion and treatment details, including detected enhancing vessel wall foci, in the IAT-group[a]

Patient No.	Occlusion Site	NIHSS Score	NOP	Time Symptom Onset to IAT (Min)	Procedural Time (Min)	TICI Score	Alteplase	Time IAT to MRI (Day)	Ipsilateral Enhancing Foci	Contralateral Enhancing Foci
1	M1 right	10	1	190	35	TICI 3	Yes	33	–	–
2	M1–M2 right	11	1	208	34	TICI 3	Yes	67	–	M1-E
3	Distal carotid left	8	3	318	50	TICI 2b	No	84	M1-C	–
4	M2 left	5	5	170	83	TICI 2b	Yes	49	ICA-E, M2-E	ICA-E
5	M2 left	5	1	127	42	TICI 3	Yes	65	–	–
6	(Large) M3 right	3	1	135	60	TICI 0	Yes	67	ICA-C	–
7	Distal carotid left	12	2	201	60	TICI 2b	Yes	80	ICA-C	–
8	M2 left	4	3	275	70	TICI 2b	No	59	ICA-C, M1-E	ICA-E
9	M1–M2 left	15	1	150	35	TICI 3	Yes	22	M1-E	–
10	M1 left	14	1	150	39	TICI 3	Yes	24	M1-E	–
11	M1 right	12	1	145	29	TICI 3	Yes	25	ICA-E 2x, M1-E	–
12	M1–M2 right	20	1	76	40	TICI 3	Yes	51	–	–
13	M1 right	15	0	44	42	TICI 3	Yes	57	–	–
14	M1–M2 left	14	2	180	50	TICI 2b	Yes	87	M1-C, M2-C	–

Note:—C indicates concentric; E, eccentric; M, segment of the middle cerebral artery (M1 and M2); NOP, number of passes; –, no enhancing foci detected.

[a] Treatment details of the 14 patients including the number and location of the detected foci of contrast enhancement (by A.G.v.d.K.). In patient 3, the enhancing focus detected in the M1 segment was located distal to the occlusion but directly adjacent to the occlusion site and therefore identified as the same location as the thrombosuction site.

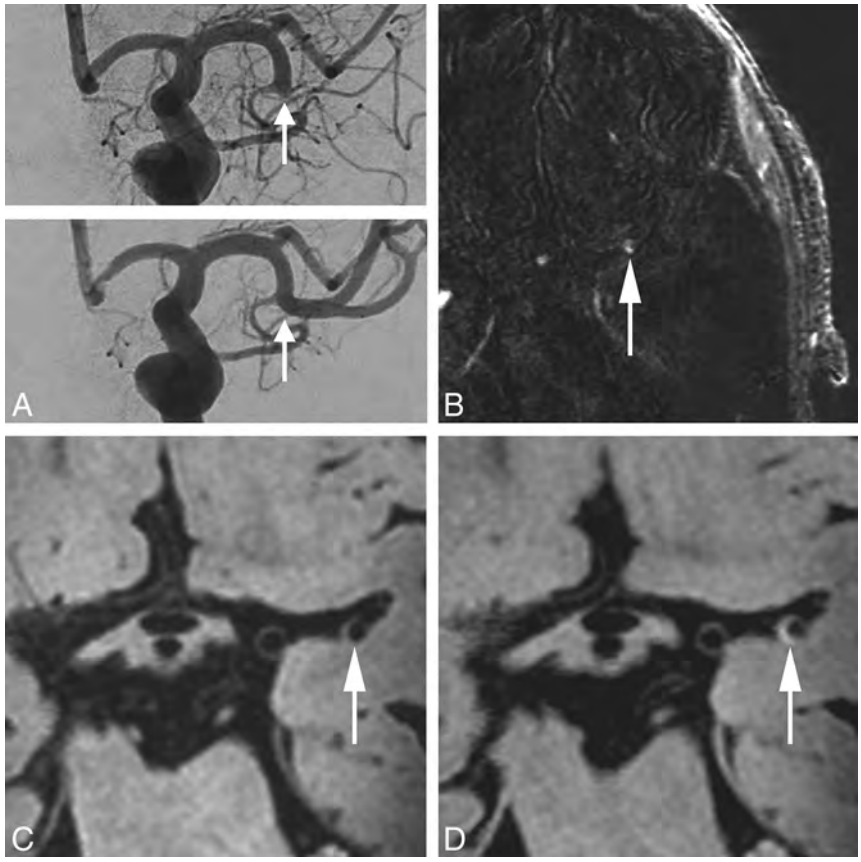

FIG 2. An 85-year-old man with an occlusion of the left M1–M2 segment (*arrow*), successfully treated with a thrombosuction device (patient 9 in Table 2). *A*, Digital subtraction angiography directly before and after the thrombectomy procedure. *B*, Subtraction image from coregistered pre- and postcontrast vessel wall images confirms a hyperintense configuration at the thrombectomy site. The transverse pre- (*C*) and postcontrast (*D*) MPIR-TSE vessel wall images at 7T (voxel size = 0.8 × 0.8 × 0.8 mm^3) were obtained 22 days after thrombectomy procedure. The eccentric vessel wall enhancement present after contrast administration is at the same location as the thrombectomy site (*arrow*, *D*).

Trevo, Stryker, Kalamazoo, Michigan) was used in addition to the thrombosuction device (patients 4 and 14, Table 2). IAT was technically successful in 13 of 14 patients. No procedure-related hemorrhagic complications occurred during the procedures in any of the patients. In 9 patients, 1 pass was sufficient; in the remaining 5 patients, more passes were needed (range, 2–5 passes) to remove the culprit thrombus.

In the non-IAT group, 5 of 35 patients had an ICA infarction (right-sided, $n = 3$) and 30 patients had an MCA infarction (right-sided, $n = 16$) (On-line Table). Twelve patients received intravenous alteplase as standard ischemic stroke treatment. In the remaining 23 patients, the 4.5-hour time window was exceeded or only minor symptoms were still present on admission.

Vessel Wall Assessment

Major Vessel Wall Changes in the IAT-Group. Besides a postprocedural moderate stenosis in the treated artery of 1 patient, no other major vessel wall changes were detected. This stenosis in the proximal left M2 segment was detected by MR vessel wall imaging and TOF-MRA (>6 weeks after IAT) at the same location as the removed thrombus and was not yet visible on the postprocedural angiogram obtained in the same session as the

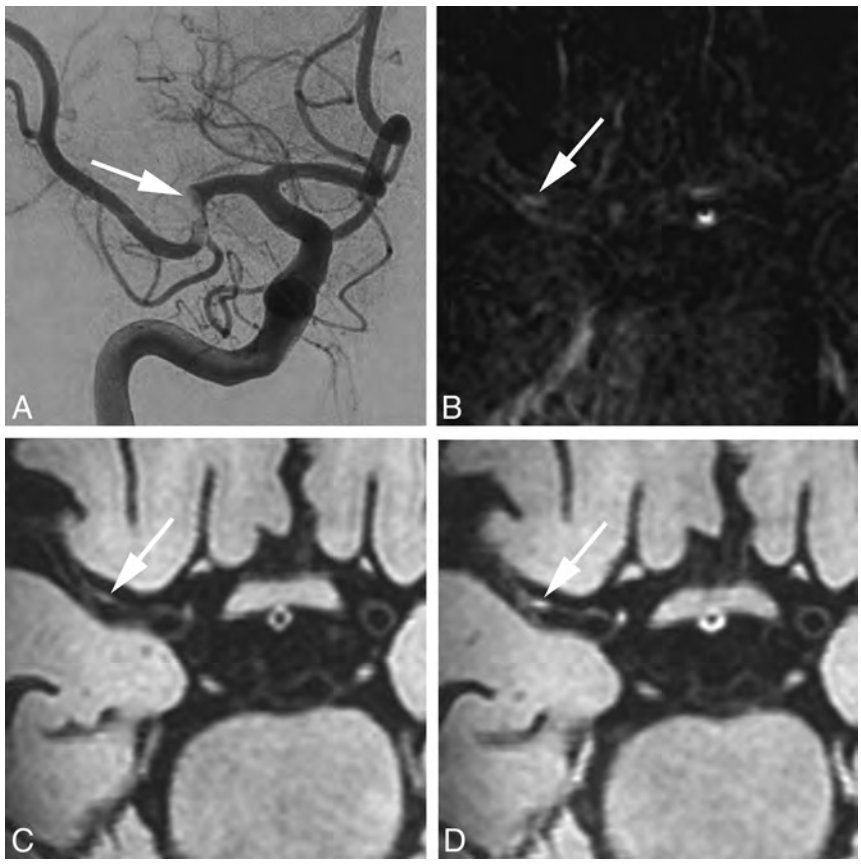

FIG 3. A 72-year-old woman with an occlusion of the right M1 segment, successfully treated with a thrombosuction device (patient 11 in Table 2). Digital subtraction angiography directly before the thrombectomy procedure shows an acute occlusion in the right middle cerebral artery (*A*, *arrow*). *B*, Subtraction image from coregistered pre- and postcontrast (*C* and *D*) vessel wall images confirms a hyperintense rim (*arrow*) at the vessel wall. Transverse pre- (*C*) and postcontrast (*D*) MPIR-TSE vessel wall images at 7T were obtained 25 days after the thrombectomy procedure. The area of eccentric vessel wall enhancement (*D*) is seen in the right M1 segment, at the same location as the thrombectomy site, confirmed on the subtraction image in *B* (*arrows*).

thrombectomy. It is not clear whether this was caused by an atherosclerotic plaque or restenosis or was treatment-induced. In patients with a middle cerebral artery occlusion, no T1-hyperintensity before contrast was found, nor did we find an MR imaging vessel wall indication suggesting an intramural hemorrhage.

Vessel Wall Enhancement. The interrater agreement for the number and location of the enhancing foci was an intraclass correlation coefficient of 0.91 (95% CI, 0.84–0.95) and a Dice similarity coefficient of 0.87. Examples of foci of vessel wall enhancement at the thrombectomy site are shown in Figs 2–4. An example of vessel wall enhancement of the non-IAT group is shown in Fig 5. In the IAT-group, 11 of 14 patients (79%) showed vessel wall enhancement compared with 17 of 35 patients (49%) in the non-IAT group. As an average of both readers, in total, 21.5 foci of vessel wall enhancement were detected in the 84 vessel segments (26%) of the patients with IAT compared with 30 foci of vessel wall enhancement in the 210 vessel segments (14%) in the patients without IAT (IAT-group versus non-IAT group, *P* value = .04). In the IAT-group, there were more foci of vessel wall enhancement ipsilateral ($n = 18.5$, 86%) to the treated artery compared with the contralateral side ($n = 3$, 14%) ($P = .005$). In the non-IAT group, there was no difference in the number of enhancing foci between the ipsilateral ($n = 18$; 60%) and the contralateral sides ($n = 12$, 40%) ($P = .47$). In the IAT-group, vessel wall enhancement was more often concentric on the ipsilateral side ($n = 8$) compared with contralateral side ($n = 0$) ($P = .01$). In the non-IAT group, there was no significant difference in concentric enhancement between the ipsilateral ($n = 7$) and the contralateral sides ($n = 5$) ($P = .14$). No differences were found between eccentric enhancing foci on the ipsilateral-versus-contralateral side and in the IAT-group versus non-IAT group. The locations of all enhancing foci are shown in Table 2 and the Online Table, and all statistical analyses are shown in Table 3. The degree of movement calculated over all patients was with a mean of 0.77° ± 0.51° for ΔRotation and 0.81 ± 0.59 mm for ΔTranslation.

DISCUSSION

In the current study, we show the patterns of vessel wall changes that can be anticipated in diagnostic vessel wall MR imaging studies in patients with stroke after IAT with a thrombosuction device compared with patients with stroke in whom no thrombectomy was performed. MR vessel wall imaging, in the subacute and chronic stages after IAT, showed more foci of vessel wall enhancement on the side treated with thrombectomy, while no difference between ipsi- and contralateral enhancement was found in the patients with stroke without IAT. Additionally, in the IAT-group, these enhancing foci were more often concentric in the vessels ipsilateral to the thrombectomy site compared with the contralateral side.

The higher number of ipsilateral foci of (concentric) contrast enhancement may be explained by several mechanisms: 1) the direct effect of the mechanical forces of the used thrombosuction device; 2) the indirect effect of the removed occluded thrombus by the release of (local) inflammatory molecules; and 3) pre-existent atherosclerotic plaques with possible active inflammation. First, the direct effects of the mechanical forces of the thrombectomy procedure may induce vessel wall changes that cause vessel wall enhancement. This potential explanation is supported by previous imaging that studied the effect of IAT using a stent retriever (and one also including patients treated with a thrombosuction device) on the vessel wall on 3T MR imaging.[10-13,24] The

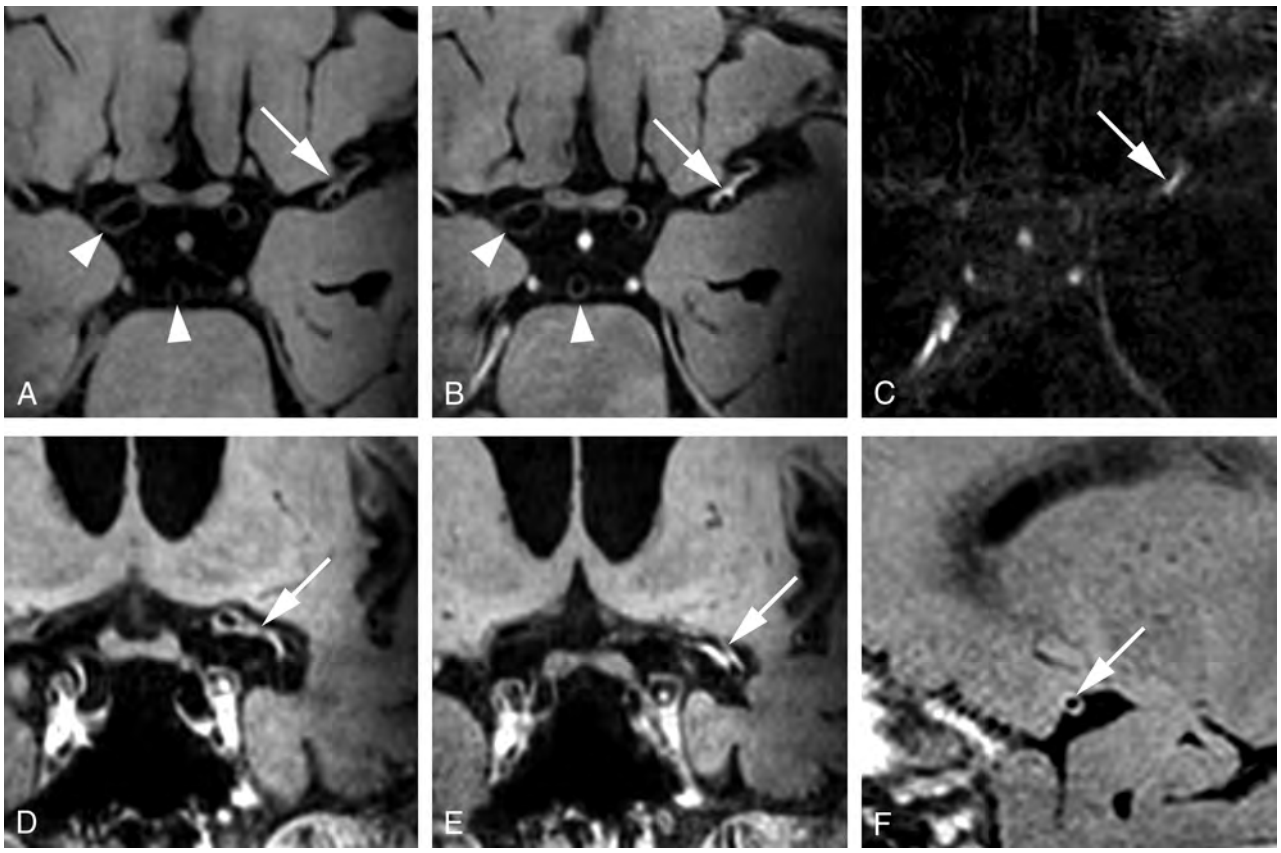

FIG 4. A 67-year-old man with an occlusion of the left M1–M2 segment, successfully treated with intra-arterial thrombectomy (patient 14 in Table 2). The patient was treated with both a stent-retriever device and a thrombosuction device. Axial pre- (*A*) and postcontrast (*B*) MPIR-TSE vessel wall images at 7T, 87 days after the thrombectomy procedure. Clear contrast enhancement is present (*white arrows*) at the same location where the thrombectomy was performed. The carotid and basilar arteries appear normal (*white arrowheads*, *A* and *B*). *C*, Subtraction image of the pre- and postcontrast vessel wall images confirms the enhancement at the same location. *D* and *E*, Coronal views of the postcontrast MPIR-TSE vessel wall images show enhancement over a long trajectory of the left M1 and M2 segments. *F*, Sagittal view of the postcontrast MPIR-TSE vessel wall image shows that the enhancement has a concentric configuration.

study that also included patients treated with a thrombosuction device showed that concentric vessel wall enhancement, which occurred in, respectively, 67% and 14% of the patients in the IAT-group ($n = 15$) versus the non-IAT group ($n = 14$), was associated with the number of attempts, type of device, and more frequent hemorrhagic transformation of the ischemic infarct (mean interval of treatment to MR imaging, 3.66 ± 1.52 days).[13]

In another series (IAT-group, $n = 6$, versus non-IAT group, $n = 10$), MR vessel wall imaging showed wall thickening in 83% versus 30% and contrast enhancement in 67% versus 20% of patients, respectively, (mean interval of treatment to MR imaging, 3.44 ± 2.58 days).[11] Also, in a recent study, more contrast-enhancing vessel wall areas were found in the post thrombectomy group ($n = 6$), scanned within 24 hours after treatment, compared with a control group ($n = 5$).[12] In addition, some follow-up studies (ranging from several days to 2 years) reported delayed arterial vessel wall abnormalities, postulating that these might be attributable to endothelial damage after IAT.[3,6,8,25,26] On the other hand, in a study with 23 patients with stroke who were scanned within 1 week after thrombectomy, major vessel wall damage such as disruption and stenosis was rare.[10]

We limited our study to patients treated with a thrombosuction device. In this study, 7T MR imaging was used, but previous 3T MR imaging and 7T MR imaging comparison studies showed that 3T MR vessel wall imaging can also detect most vessel wall lesions.[17,18] Furthermore, previous 3T MR imaging studies assessing vessel wall enhancement after treatment with stent-retriever devices have comparable findings.[10-13,24] Second, the observed vessel wall enhancement may be the result of the former occluding thrombus on the arterial vessel wall that caused reactive, inflammatory changes or a local "scarring" of the vessel wall. This possibility is supported by studies that have shown an increased level of inflammatory markers after an ischemic stroke.[27,28] A third, more hypothetic explanation for the higher number of ipsilateral foci of contrast enhancement is the presence of pre-existent intracranial atherosclerotic lesions, possibly with active inflammation, in the revascularized segment.[29] However, the absence of a significant difference in enhancement between the ipsi- and contralateral arteries in our non-IAT group suggests that not all of the observed enhancing foci can be explained by pre-existent atherosclerotic lesions. Furthermore, atherosclerotic lesions often have a more eccentric configuration, which is in contrast to the high number of concentric-type enhancing foci seen in our study and might indicate an inflammatory state of the whole vessel wall rather than an eccentric atherosclerotic plaque.[22]

It is unknown how long contrast enhancement of the arterial vessel wall persists after IAT in patients with stroke. In our study, we used a relatively long time interval between thrombectomy and MR imaging (up to 3 months) compared with that in previously published articles (range, 1–11 days).[10,11] Our results indicate that vessel wall enhancement also persists in the subacute-to-chronic phase.

This study has limitations. First, because local areas of ischemia appear as hypointense parenchymal lesions on the T1-weighted vessel wall sequences, we were unable to blind the observers to the side of thrombectomy in the IAT-group or the side of infarction in the non-IAT group (left or right). Second, IAT was introduced in our center as standard clinical care during the study inclusion period, after the successful international IAT trials. Therefore, the first 28 patients in the non-IAT group did not have IAT as a treatment option. Retrospectively, 10 of all 35 patients without IAT had a proximal occlusion (ICA, M1, or M2) similar to the patients with IAT. In the remaining 25 patients without IAT, no acute occlusion and a better overall NIHSS score was recorded in the final reports (On-line Table). This result may have led to a selection bias in the group without IAT, with the inclusion of lesser affected patients that may have biased the true results. Nevertheless, we believe that the comparison of the ipsilateral-to-contralateral side in the IAT-group is most relevant because in this comparison, all potential individual risk factors are the similar. Third, the number of patients with IAT enrolled in this study is relatively low. Including more patients would benefit the statistical power and enable the possibility of additional analyses. Fourth, for most patients without IAT, the time window between symptom onset and 7T MR imaging was shorter. Nevertheless, there were significantly more enhancing foci in the IAT-group, despite the longer time window. Finally, discrimination between eccentric or concentric enhancing foci can be challenging, and in clinical practice, certainly there is an overlap in the enhancement configuration and the causes of vessel wall enhancement. Histopathologic validation of the detected enhancement would have given insight into the true nature/composition of the enhancing vessel wall areas (due to the IAT procedure and thrombus-related or pre-existing atherosclerotic plaques); however, this necessitates ex vivo tissue, which was not available. Therefore, some of the

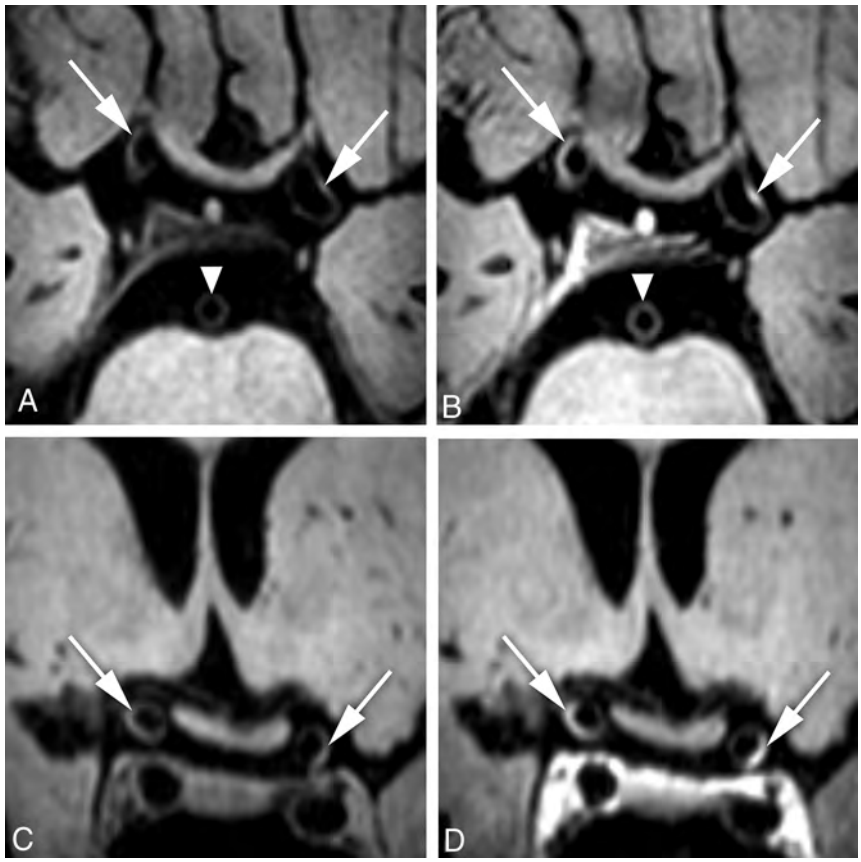

FIG 5. A 75-year-old woman with an anterior circulation ischemic infarction of the left MCA territory (non-IAT group, patient 30 in On-line Table). Transverse and coronal precontrast (*A* and *C*) and postcontrast (*B* and *D*) MPIR-TSE vessel wall images at 7T were obtained 10 days after symptom onset of the ischemic infarction. Note eccentric vessel wall enhancement of the supraclinoid portion of both intracranial carotid arteries (*B* and D, *arrows*). The basilar artery appears normal (*white arrowheads*, *A* and *B*).

Table 3: Comparison of enhancing foci between the IAT-group and the non-IAT group and between the ipsilateral and contralateral sides

	IAT-Group	Non-IAT Group	*P* Value
Total No. of enhancing foci	21.5	30	.04[a]
Total No. of ipsilateral enhancing foci	18.5	18.0	.003[a]
Total No. of contralateral enhancing foci	3.0	12.0	.74[a]
Total No. of concentric ipsilateral foci	9.0	8.5	.02[a]
Total No. of eccentric ipsilateral foci	9.5	9.5	.07[a]
Total No. of enhancing foci ipsilateral vs contralateral (proportion) *P* value	(18.5 vs 3.0) .005[b]	(18.0 vs 12.0) .47[b]	
Total No. of concentric enhancing foci ipsilateral vs. contralateral (proportion) *P* value	(9.0 vs 0.0) .011[b]	(8.5 vs 3.0) .14[b]	
Total No. of eccentric enhancing foci ipsilateral vs. contralateral (proportion) *P* value	(9.5 vs 3.0) 06[b]	(9.5 vs 9.0) .97[b]	

[a] Mann-Whitney *U* test.
[b] Wilcoxon signed rank test.

enhancing foci detected in our study participants might be explained by one of these other mechanisms of wall enhancement. Patients should ideally also have been scanned before the IAT procedure, but due to the limited timeframe in which IAT can be performed, this is difficult to accomplish in clinical practice.

CONCLUSIONS

IAT using thrombosuction did show more concentric enhancing foci of the vessel wall ipsilateral to the occlusion site compared with the patients without IAT, suggesting reactive changes of the vessel wall. In an era in which MR vessel wall imaging studies are expected to be increasingly performed in the diagnostic work-up and follow-up of patients with acute stroke, the patterns of vessel wall enhancement after thrombectomy need to be known to avoid misinterpretation of these enhancing patterns in the follow-up MR imaging examinations after acute stroke treatment.

Disclosures: Arjen Lindenholz—*RELATED*: *Grant*: European Research Council, *Comments*: The research of Dr Jeroen Hendrikse has received funding from the European Research Council under the European Union's Horizon 2020 Program (H2020)/European Research Council Grant agreement no 637024 (HEARTOFSTROKE).* H. Bart van der Worp—*UNRELATED*: *Consultancy*: Boehringer Ingelheim, Bayer AG, LivaNova, *Comments*: member of Advisory Board (Boehringer Ingelheim, Bayer AG), outcome adjudication (LivaNova)*; *Grants/Grants Pending*: European Union, Dutch Heart Foundation, *Comments*: grants for stroke research.* *Money paid to the institution.

REFERENCES

1. Berkhemer OA, Fransen PS, Beumer D, et al; MR CLEAN Investigators. **A randomized trial of intraarterial treatment for acute ischemic stroke.** *N Engl J Med* 2015;372:11–20 CrossRef Medline
2. Rodrigues FB, Neves JB, Caldeira D, et al. **Endovascular treatment versus medical care alone for ischaemic stroke: systematic review and meta-analysis.** *BMJ* 2016;353:i1754 CrossRef Medline
3. Gory B, Bresson D, Kessler I, et al. **Histopathologic evaluation of arterial wall response to 5 neurovascular mechanical thrombectomy devices in a swine model.** *AJNR Am J Neuroradiol* 2013;34:2192–98 CrossRef Medline
4. Teng D, Pannell JS, Rennert RC, et al. **Endothelial trauma from mechanical thrombectomy in acute stroke: in vitro live-cell platform with animal validation.** *Stroke* 2015;46:1099–1106 CrossRef Medline
5. Peschillo S, Diana F, Berge J, et al. **A comparison of acute vascular damage caused by ADAPT versus a stent retriever device after thrombectomy in acute ischemic stroke: a histological and ultrastructural study in an animal model.** *J Neurointerv Surg* 2017;9:743–49 CrossRef Medline
6. Kurre W, Perez MA, Horvath D, et al. **Does mechanical thrombectomy in acute embolic stroke have long-term side effects on intracranial vessels? An angiographic follow-up study.** *Cardiovasc Interv Radiol* 2013;36:629–36 CrossRef Medline
7. Penumbra Pivotal Stroke Trial Investigators. **The Penumbra pivotal stroke trial: safety and effectiveness of a new generation of mechanical devices for clot removal in intracranial large vessel occlusive disease.** *Stroke* 2009;40:2761–68 CrossRef Medline
8. Renu A, Laredo C, Lopez-Rueda A, et al. **Vessel wall enhancement and blood-cerebrospinal fluid barrier disruption after mechanical thrombectomy in acute ischemic stroke.** *Stroke* 2017;48:651–57 CrossRef Medline
9. Gascou G, Lobotesis K, Machi P, et al. **Stent retrievers in acute ischemic stroke: complications and failures during the perioperative period.** *AJNR Am J Neuroradiol* 2014;35:734–40 CrossRef Medline
10. Hsieh K, Verma RK, Schroth G, et al. **Multimodal 3 Tesla MRI confirms intact arterial wall in acute patients with stroke after stent-retriever thrombectomy.** *Stroke* 2014;45:3430–32 CrossRef Medline
11. Power S, Matouk C, Casaubon LK, et al. **Vessel wall magnetic resonance imaging in acute ischemic stroke: effects of embolism and mechanical thrombectomy on the arterial wall.** *Stroke* 2014;45:2330–34 CrossRef Medline
12. Abraham P, Scott Pannell J, Santiago-Dieppa DR, et al. **Vessel wall signal enhancement on 3-T MRI in acute patients with stroke after stent retriever thrombectomy.** *Neurosurg Focus* 2017;42:E20 CrossRef Medline
13. Seo WK, Oh K, Suh SI, et al. **Clinical significance of wall changes after recanalization therapy in acute stroke: high-resolution vessel wall imaging.** *Stroke* 2017;48:1077–80 CrossRef Medline
14. van der Kolk AG, Zwanenburg JJ, Brundel M, et al. **Intracranial vessel wall imaging at 7.0-T MRI.** *Stroke* 2011;42:2478–84 CrossRef Medline
15. van der Kolk AG, Zwanenburg JJ, Brundel M, et al. **Distribution and natural course of intracranial vessel wall lesions in patients with ischemic stroke or TIA at 7.0 Tesla MRI.** *Eur Radiol* 2015;25:1692–1700 CrossRef Medline
16. van der Kolk AG, Hendrikse J, Brundel M, et al. **Multi-sequence whole-brain intracranial vessel wall imaging at 7.0 Tesla.** *Eur Radiol* 2013;23:2996–3004 CrossRef Medline
17. Harteveld AA, van der Kolk AG, van der Worp HB, et al. **High-resolution intracranial vessel wall MRI in an elderly asymptomatic population: comparison of 3T and 7T.** *Eur Radiol* 2017;27:1585–95 CrossRef Medline
18. Zhu C, Haraldsson H, Tian B, et al. **High-resolution imaging of the intracranial vessel wall at 3 and 7 T using 3D fast spin echo MRI.** *MAGMA* 2016;29:559–70 CrossRef Medline
19. Fugate JE, Klunder AM, Kallmes DF. **What is meant by "TICI"?** *AJNR Am J Neuroradiol* 2013;34:1792–97 CrossRef Medline
20. Samuels OB, Joseph GJ, Lynn MJ, et al. **A standardized method for measuring intracranial arterial stenosis.** *AJNR Am J Neuroradiol* 2000;21:643–46 Medline
21. Lindenholz A, van der Kolk AG, Zwanenburg JJM, et al. **The use and pitfalls of intracranial vessel wall imaging: how we do it.** *Radiology* 2018;286:12–28 CrossRef Medline
22. Swartz RH, Bhuta SS, Farb RI, et al. **Intracranial arterial wall imaging using high-resolution 3-Tesla contrast-enhanced MRI.** *Neurology* 2009;72:627–34 CrossRef Medline
23. Klein S, Staring M, Murphy K, et al. **Elastix: a toolbox for intensity-based medical image registration.** *IEEE Trans Med Imaging* 2010;29:196–205 CrossRef Medline
24. Li Y, Turan TN, Chaudry I, et al. **High-resolution magnetic resonance imaging evidence for intracranial vessel wall inflammation following endovascular thrombectomy.** *J Stroke Cerebrovasc Dis* 2017;26:e96–98 CrossRef Medline
25. Akpinar S, Yilmaz G. **Early middle cerebral artery stenosis following stent-assisted thrombectomy.** *Interv Neuroradiol* 2015;21:337–40 CrossRef Medline
26. Eugene F, Gauvrit JY, Ferre JC, et al. **One-year MR angiographic and clinical follow-up after intracranial mechanical thrombectomy using a stent retriever device.** *AJNR Am J Neuroradiol* 2015;36:126–32 CrossRef Medline
27. Schuhmann MK, Gunreben I, Kleinschnitz C, et al. **Immunohistochemical analysis of cerebral thrombi retrieved by mechanical thrombectomy from patients with acute ischemic stroke.** *Int J Mol Sci* 2016;17:298 CrossRef Medline
28. Jin R, Liu L, Zhang S, et al. **Role of inflammation and its mediators in acute ischemic stroke.** *J Cardiovasc Transl Res* 2013;6:834–51 CrossRef Medline
29. Qiao Y, Zeiler SR, Mirbagheri S, et al. **Intracranial plaque enhancement in patients with cerebrovascular events on high-spatial-resolution MR images.** *Radiology* 2014;271:534–42 CrossRef Medline
30. Chung JW, Park SH, Kim N, et al. **Trial of ORG 10172 in Acute Stroke Treatment (TOAST) classification and vascular territory of ischemic stroke lesions diagnosed by diffusion-weighted imaging.** *J Am Heart Assoc* 2014;3 CrossRef Medline

Contrast-Induced Acute Kidney Injury in Radiologic Management of Acute Ischemic Stroke in the Emergency Setting

J.W. Myung, J.H. Kim, J. Cho, I. Park, H.Y. Kim, and J.H. Beom

ABSTRACT

BACKGROUND AND PURPOSE: The use of invasive cerebral angiography with CTA for active treatment of patients with suspected ischemic strokes has been increasing recently. This study aimed to identify the incidence of postcontrast acute kidney injury using baseline renal function when CTA and cerebral angiography were performed sequentially.

MATERIALS AND METHODS: This retrospective observational study evaluated adults (18 years of age or older) with ischemic stroke who underwent CTA and cerebral angiography sequentially between 2010 and 2018. The incidence of postcontrast acute kidney injury was determined using the baseline estimated glomerular filtration rate. The value of the baseline estimated glomerular filtration rate at which the occurrence of postcontrast acute kidney injury increased was also determined.

RESULTS: Postcontrast acute kidney injury occurred in 57/601 (9.5%) patients. Those with a baseline estimated glomerular filtration rate of <30 mL/min/1.73 m^2 showed a higher incidence of acute kidney injury. Age, chronic kidney disease, medication (nonsteroidal anti-inflammatory drugs, angiotensin-converting enzyme inhibitors, angiotensin II receptor blockers, β blockers, statins, and insulin) use following contrast media exposure, and serum albumin affected the incidence of postcontrast acute kidney injury. The incidence of postcontrast acute kidney injury increased when the baseline estimated glomerular filtration rate was <43 mL/min/1.73 m^2.

CONCLUSIONS: Patients with low baseline renal function had the highest incidence of postcontrast acute kidney injury after CTA and cerebral angiography, but no fatal adverse effects were documented. Thus, patients suspected of having a stroke should be actively managed with respect to neurovascular function.

ABBREVIATIONS: AKI = acute kidney injury; ED = emergency department; eGFR = estimated glomerular filtration rate; PC-AKI = postcontrast acute kidney injury

Acute ischemic stroke requires active management in the emergency setting to prevent long-term sequelae and curb mortality.[1,2] The recently published 2018 American Heart Association/American Stroke Association guidelines for early treatment of stroke recommend endovascular recanalization after 6 hours of symptom onset, shifting the focus to a more active and invasive approach.[3] The guidelines also recommend CTA to improve diagnosis, aid in the treatment of acute ischemic cerebral infarction, and assist patient selection in interventional radiology on the basis of the head and neck vascular status[4,5]—that is, once a CTA is performed, on the basis of the time of neurologic symptom onset and its severity, there is a high probability of active intervention with intra-arterial thrombolysis via cerebral angiography for early reperfusion.[6-8]

However, the incidence of postcontrast acute kidney injury (PC-AKI) is expected to increase in such conditions because of patient exposure to approximately 200 mL of contrast media in a short time.[9,10] PC-AKI can lead to irreversible kidney damage and an increased risk of morbidity and mortality, particularly because no established treatments are available. Therefore, there is a need for emergency department (ED) personnel to perform evidence-based risk/benefit assessment for performing CTA and cerebral angiography in patients with suspected ischemic strokes.[9-11]

Previous studies have drawn conflicting conclusions on the risk factors associated with PC-AKI.[12-14] Even though there are studies on PC-AKI after either CTA or cerebral angiography, studies that consider concomitant CTA and cerebral angiography performed within a short duration are lacking.[10,11] In addition,

Received December 8, 2019; accepted after revision February 5, 2020.

From the Department of Emergency Medicine (J.W.M., J.H.K., J.C., I.P., J.H.B.), and Biostatistics Collaboration Unit, Department of Biomedical Systems Informatics (H.Y.K.), Yonsei University College of Medicine, Seoul, Republic of Korea.

Please address correspondence to Jin Ho Beom, MD, Department of Emergency Medicine, Yonsei University College of Medicine, 50-1, Yonsei-ro, Seodaemun-gu, Seoul, 03722, Republic of Korea; e-mail: wangtiger@yuhs.ac

Indicates open access to non-subscribers at www.ajnr.org
Indicates article with supplemental on-line table.

http://dx.doi.org/10.3174/ajnr.A6472

there is scant literature on the occurrence of PC-AKI according to the baseline renal function. Furthermore, there are no clear guidelines on the use of contrast media in patients with renal disease.[1,15-17]

Therefore, this study aimed to identify the incidence of PC-AKI in terms of the baseline renal function in patients who underwent both CTA and cerebral angiography for suspected ischemic stroke in the ED. Furthermore, we aimed to present a reference value of the baseline of the estimated glomerular filtration rate (eGFR) that increases the likelihood of PC-AKI, to serve as a basis for decision-making in the ED.

MATERIALS AND METHODS

Ethics

The institutional review board of Yonsei University Health System Clinical Trial Center approved the study (approval number, 4–2019–0170) and waived the requirement for informed consent on the basis of the retrospective observational study design. The study was conducted according to the tenets of the Declaration of Helsinki as revised in 2013.

Study Design and Population

This retrospective study was conducted using data from patients enrolled in the Brain Salvage through Emergent Stroke Therapy critical pathway protocol implemented at our tertiary university hospital in Seoul, South Korea. The necessary data for the study were collected from the electronic medical records.

We evaluated data of adult patients (18 years of age or older) who visited the ED between October 2010 and September 2018 and underwent both CTA and cerebral angiography for differentiation and treatment of ischemic stroke, respectively. The exclusion criteria were the following: 1) CTA performed at another hospital or not performed, 2) death within 48 hours of CTA, 3) transfer or discharge within 48 hours of CTA, 4) CTA and cerebral angiography performed at an interval longer than 48 hours, 5) the presence of end-stage renal disease, and 6) no serum creatinine data within 72 hours of contrast media use.

Brain Salvage through Emergent Stroke Therapy Protocol

The Brain Salvage through Emergent Stroke Therapy critical pathway is a medical process protocol implemented by the ED to perform rapid thrombolytic therapy for patients with suspected acute ischemic stroke. This protocol identifies patients with symptoms indicative of stroke, such as single-sided weakness, speech disorder, gait disturbance, loss of consciousness, visual field symptoms, and sudden headache. Once the critical pathway is activated by an ED physician, a neurologist examines the patient and CTA is performed subsequently. Thrombolytic therapy through cerebral angiography is performed in the angiography suite as necessary.

CTA

All imaging was performed using a high-resolution CT scanner (Revolution EVO; GE Healthcare, Milwaukee, Wisconsin). For CTA, isotonic contrast material (iopamidol 755 mg/mL, Iopamiro 370; Bracco, Milan, Italy) was injected at a rate of 4 mL/s. The upper limit volume of the contrast material was 100 mL.

Cerebral Angiography

Cerebral angiography was performed on an angiography system (Allura Clarity FD 20/20; Philips Healthcare, Best, the Netherlands). For cerebral angiography, isotonic contrast material (iodixanol 652 mg/mL, Visipaque 320; GE Healthcare) was injected at a rate of 3–4 mL/s.

Definition of Exposure and Outcome

In this study, the eGFR was calculated using the Chronic Kidney Disease Epidemiology Collaboration equation (https://www.kidney.org/content/ckd-epi-creatinine-equation-2009), according to the current guidelines. The enrolled patients were then divided into 4 groups based on eGFR (milliliters/minute/1.73 m^2) values that increase the risk of PC-AKI as follows: eGFR <30, eGFR 30–59, eGFR 60–89, and eGFR ≥ 90.[18] Although there are diverse definitions of PC-AKI, we used the absolute increase in serum creatinine levels by ≥ 0.5 mg/dL or a relative increase in serum creatinine levels by $\geq 25\%$ from baseline observed within 72 hours after contrast media exposure as proposed by Barrett and Parfrey.[19]

Statistical Analysis

Post hoc analyses were performed to determine the PC-AKI incidence according to the baseline eGFR groups. In addition, univariate logistic analysis was performed to determine the impact of each variable on PC-AKI occurrence. Statistically significant variables in the univariate logistic analysis were subjected to multivariable logistic regression analysis through a stepwise variable selection to determine independent variables. Subsequently, the baseline eGFR cutoff value was determined using the maximum area under the curve. All statistical analyses were performed using SAS, Version 9.4 (SAS Institute, Cary, North Carolina), and P values $< .05$ were considered statistically significant.

RESULTS

Of the 726 patients identified, 125 patients were excluded. Thus, 601 patients were included in the analysis. PC-AKI occurred in 57 (9.5%) patients (Fig 1). In total, 15 (2.5%) patients had an eGFR of <30 mL/min/1.73 m^2; 97 (16.14%) patients, eGFR of 30–59 mL/min/1.73 m^2; 302 (50.25%) patients, eGFR of 60–89 mL/min/1.73 m^2; and 187 (31.11%) patients, eGFR of ≥ 90 mL/min/1.73 m^2. The incidences of PC-AKI significantly differed among the baseline eGFR groups ($P < .001$) (Table 1). Post hoc analysis showed that the group with an eGFR of <30 mL/min/1.73 m^2 had a higher PC-AKI incidence than the other groups, and the differences in incidences among the remaining groups were not significant (Table 2).

In the univariate analyses, the significant risk factors (all $P < .05$) for PC-AKI were age older than 75 years, diabetes mellitus, chronic kidney disease, atrial fibrillation, use of angiotensin-converting enzyme inhibitors and angiotensin II receptor blockers before CTA, medication (nonsteroidal anti-inflammatory drugs, angiotensin-converting enzyme inhibitors, angiotensin II receptor blockers, β blockers, statins, and insulin) use after

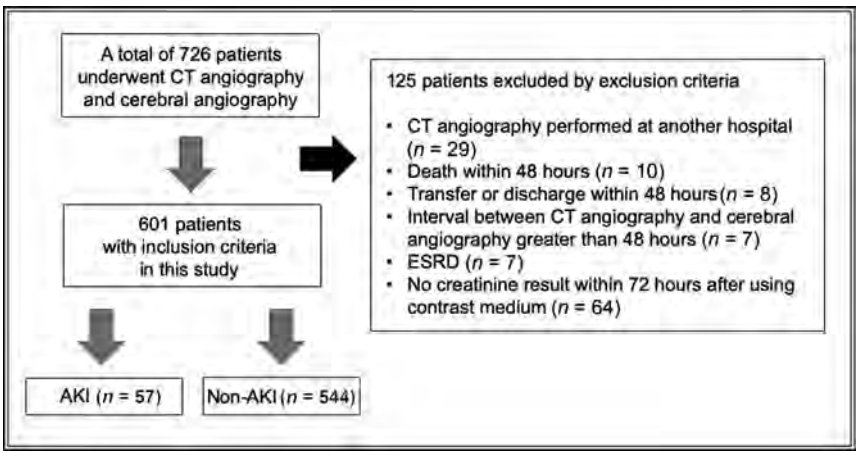

FIG 1. Patient inclusion flowchart. ESRD indicates end-stage renal disease.

Table 1: PC-AKI incidence based on baseline eGFR[a]

Group	eGFR (mL/min/1.73 m^2)	Non-AKI	PC-AKI	*P*
1	<30	8 (1.47)	7 (12.28)	<.001
2	30–59	91 (16.73)	6 (10.53)	
3	60–89	269 (49.45)	33 (57.89)	
4	≥90	176 (32.35)	11 (19.30)	

[a] Data are number of patients and percentage.

Table 2: Post hoc analysis for comparison of PC-AKI incidence between baseline eGFR groups

Adjusted *P*					
1 vs 2	1 vs 3	1 vs 4	2 vs 3	2 vs 4	3 vs 4
.001	.005	<.001	>.999	>.999	.349

contrast exposure, proteinuria, low hemoglobin and hematocrit levels, a high Δ neutrophil index, low platelet count, low serum albumin level, and low sodium concentration. In the multivariate model, age older than 75 years, chronic kidney disease, medication (nonsteroidal anti-inflammatory drugs, angiotensin-converting enzyme inhibitors, angiotensin II receptor blockers, β blockers, statins, insulin) use after contrast exposure, and serum albumin levels were found to significantly (all $P < .05$) influence the occurrence of PC-AKI (On-line Table).

The maximum area under the curve value in the receiver operating characteristic curve analysis was obtained for the variables, and the baseline eGFR value corresponding to the maximum area under the curve value was identified. The resulting cutoff value of baseline eGFR was found to be 43 mL/min/1.73 m^2 (Fig 2). This value retained significance in the univariate analysis.

DISCUSSION

Patients with acute ischemic stroke who visit the ED have high short-term mortality rates (16%–23%).[20,21] Even mild ischemic stroke is associated with poor prognosis during long-term follow-up.[22] Therefore, rapid and accurate diagnosis and treatment of ischemic stroke are essential in the ED for such patients. Noncontrast brain CT has been used as a standard test in the evaluation of patients with acute stroke because of the short amount of time required, its convenience, and wide availability at many hospitals.[23] The recently updated American Heart Association/American Stroke Association guidelines recommend endovascular recanalization therapy for patients with suspected stroke arriving at the ED after 6 hours of symptom onset. In line with aggressive treatment, CTA is a tool optimized for cerebral angiographic treatment with the advantage of rapidly detecting cerebrovascular large-vessel occlusion with high accuracy in the emergency department.[24] However, concomitant use of CTA and cerebral angiography exposes the patient to excessive contrast media in a short time. This can be burdensome to not only the patient but also the physicians. To date, studies on contrast media administration and acute kidney injury (AKI) incidence have reported diverse results according to the underlying diseases and general patient condition. Furthermore, studies that include cases with simultaneous contrast media use for diagnosis and treatment are lacking.

The task of accurately predicting contrast-induced kidney injury in patients with suspected stroke who require rapid management in the ED could likely delay the decision-making by neurologists and ED physicians.[12-14] Therefore, presenting grounds for treatment that can be the criteria for judgment by ED physicians can be very important. Recently, Jia et al[9] reported no significant difference in the incidence of PC-AKI between CTA only and with a combination of CTA and DSA. However, this study with a small sample size did not control for factors that affect AKI. In the present study, the PC-AKI incidence was compared among groups classified according to baseline eGFR without any adjustments. PC-AKI occurred in 7/15 (46.6%) patients in the group with an eGFR of <30 mL/min/1.73 m^2, and the incidence of PC-AKI was also significantly higher in this group compared with the other groups. This result was similar to the results of other previous studies.[25] However, this result was judged to be inaccurate because the patients' underlying medical conditions were not considered. Therefore, the risk factors of AKI other than the contrast medium were determined and adjusted for to determine the cutoff value of eGFR at which the risk of AKI occurrence increases. We found that when CTA and cerebral angiography were performed consecutively, the probability of PC-AKI occurrence increased when the baseline eGFR was <43 mL/min/1.73 m^2.

However, this result cannot be an absolute guideline to prevent examinations that are indispensable due to the risk of PC-AKI in patients with eGFR <43 mL/min/1.73 m^2. In fact, continuous renal replacement therapy was performed in only 5/57 patients (8.7%) with PC-AKI, corresponding to only 0.8% of the 601 patients evaluated. All 5 patients fully recovered within 4 days of continuous renal replacement therapy. In addition, the renal function of the remaining patients who developed PC-AKI but did not undergo hemodialysis or continuous renal replacement therapy also recovered within

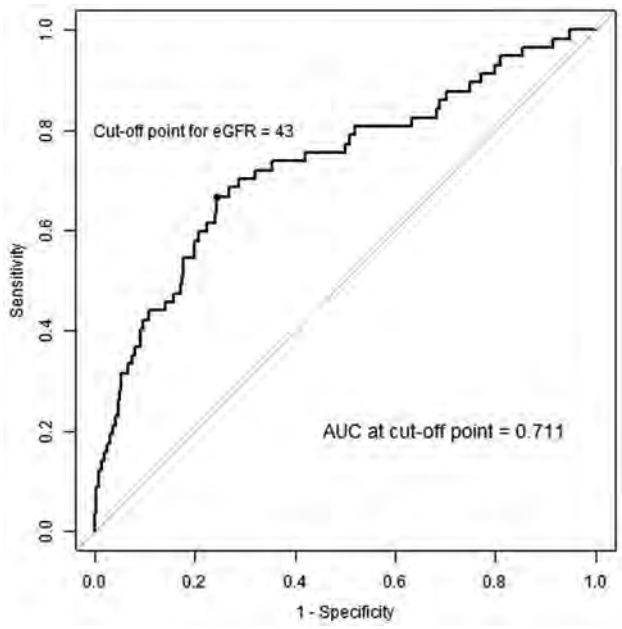

FIG 2. Receiver operating characteristic (ROC) curves showing the probability of PC-AKI. The ROC curve was drawn for PC-AKI prediction probabilities using significant variables from the multivariate analysis. Baseline eGFR: ROC curve drawn on the basis of the baseline eGFR variables. eGFR is in milliliter/minute/1.73 m^2. AUC indicates area under the curve.

several days. Therefore, in this study, even when PC-AKI occurred, its degree was not severe. Hence, the treatment decisions must be according to the neurologic symptoms and patient status. However, on the basis of the significant variables noted in the univariate analysis, physicians can predict patients at high risk of PC-AKI. Therefore, physicians will be able to perform sufficient IV hydration for these patients and plan an individual nephron-protective strategy for each patient.[26,27] This process will enable performance of relevant tests after sufficiently explaining the predictable results to patients and their caregivers and is expected to be helpful in clinical practice.

The strength of this study is that data on various factors known to be related to PC-AKI were collected from patients treated using the Brain Salvage through Emergent Stroke Therapy critical pathway protocol that has been implemented consistently for a long time at a single institution. Many studies on the relationship between contrast media and renal diseases exist. However, to the best of our knowledge, this is the first study to identify the relationship between contrast media and AKI based on the baseline eGFR in patients who undergo CTA and cerebral angiography sequentially within a short interval. Furthermore, the cutoff value of eGFR for predicting PC-AKI was calculated with adjustment for various factors associated with PC-AKI. These results can be helpful for accurate treatment planning. Moreover, our findings will be valuable in the prevention of AKI because the cutoff values of eGFR presented here can be used to identify patients at high risk for PC-AKI, which, in turn, will enable physicians to provide individualized treatment.

However, our study has several limitations. Because this study was conducted at a single center, the results may have limited generalizability. Due to the retrospective design of the study, selection biases may have occurred because in some cases, laboratory data for creatinine levels after CTA and cerebral angiography were missing. Furthermore, additional biases owing to seriously ill patients who died within 48 hours after the examinations and those who were discharged or transferred within 48 hours for other reasons not included in the study may also exist. In our study, the postcontrast exposure to medication can also be thought of as a confounder because the more severe the disease state of the patient is, such as in patients with PC-AKI, the more medication is prescribed after contrast exposure. In addition, for patients with an extremely low baseline eGFR, cerebral angiography was performed after noncontrast brain CT without performing CTA, and there is a possibility that this feature may have affected the results to some extent. Finally, the area under the curve after adjustment for risk factors in this study was 0.7310, indicating that PC-AKI is influenced by more risk factors. Therefore, our findings need to be validated in future studies. Last, because PC-AKI is affected by many variables, AKI should ideally be diagnosed on the basis of clinically important adverse effects instead of a simple creatinine level elevation.

CONCLUSIONS

Among patients with acute ischemic stroke who underwent CTA and cerebral angiography in the ED, those with a baseline eGFR of <30 mL/min/1.73 m^2 had a higher incidence of PC-AKI compared with those with other eGFR levels. After we adjusted for risk factors of PC-AKI, the risk of PC-AKI was high in the group with a baseline eGFR of <43 mL/min/1.73 m^2. Hence, physicians could consider noncontrast CT and MR imaging/MRA testing for the patients in this group. However, because PC-AKI was not associated with fatal adverse effects in this study, it is recommended that patients suspected of having a stroke be actively managed with respect to neurovascular function on the basis of risk/benefit analyses.

REFERENCES

1. Brinjikji W, Demchuk AM, Murad MH, et al. **Neurons over nephrons: systematic review and meta-analysis of contrast-induced nephropathy in patients with acute stroke.** *Stroke* 2017;48:1862–68 CrossRef Medline
2. Demel SL, Grossman AW, Khoury JC, et al. **Association between acute kidney disease and intravenous dye administration in patients with acute stroke: a population-based study.** *Stroke* 2017;48:835–39 CrossRef Medline
3. Powers WJ, Rabinstein AA, Ackerson T, et al; American Heart Association Stroke Council. **2018 guidelines for the early management of patients with acute ischemic stroke: a guideline for healthcare professionals from the American Heart Association/American Stroke Association.** *Stroke* 2018;49:e46–110 CrossRef Medline
4. Esteban JM, Cervera V. **Perfusion CT and angio CT in the assessment of acute stroke.** *Neuroradiology* 2004;46:705–15 CrossRef Medline
5. Wildermuth S, Knauth M, Brandt T, et al. **Role of CT angiography in patient selection for thrombolytic therapy in acute hemispheric stroke.** *Stroke* 1998;29:935–38 CrossRef Medline
6. van den Berg LA, Dijkgraaf MG, Berkhemer OA, et al; MR CLEAN Investigators. **Two-year outcome after endovascular treatment for**

acute ischemic stroke. *N Engl J Med* 2017;376:1341–49 CrossRef Medline

7. Jovin TG, Chamorro A, Cobo E, et al; REVASCAT Trial Investigators. **Thrombectomy within 8 hours after symptom onset in ischemic stroke.** *N Engl J Med* 2015;372:2296–2306 CrossRef Medline
8. Fransen PS, Berkhemer OA, Lingsma HF, et al; Multicenter Randomized Clinical Trial of Endovascular Treatment of Acute Ischemic Stroke in the Netherlands Investigators. **Time to reperfusion and treatment effect for acute ischemic stroke: a randomized clinical trial.** *JAMA Neurol* 2016;73:190–96 CrossRef Medline
9. Jia ZY, Wang SX, Zhao LB, et al. **Risk of acute kidney injury with consecutive, multidose use of iodinated contrast in patients with acute ischemic stroke.** *AJNR Am J Neuroradiol* 2019;40:652–54 CrossRef Medline
10. Hall SL, Munich SA, Cress MC, et al. **Risk of acute kidney injury associated with neuroimaging obtained during triage and treatment of patients with acute ischemic stroke symptoms.** *J Neurointerv Surg* 2016;8:1231–34 CrossRef Medline
11. Sharma J, Nanda A, Jung RS, et al. **Risk of contrast-induced nephropathy in patients undergoing endovascular treatment of acute ischemic stroke.** *J Neurointerv Surg* 2013;5:543–55 CrossRef Medline
12. Tao Y, Dong W, Li Z, et al. **Proteinuria as an independent risk factor for contrast-induced acute kidney injury and mortality in patients with stroke undergoing cerebral angiography.** *J Neurointerv Surg* 2017;9:445–48 CrossRef Medline
13. Ang TE, Bivard A, Levi C, et al. **Multi-modal CT in acute stroke: wait for a serum creatinine before giving intravenous contrast? No!** *Int J Stroke* 2015;10:1014–17 CrossRef Medline
14. Lima FO, Lev MH, Levy RA, et al. **Functional contrast-enhanced CT for evaluation of acute ischemic stroke does not increase the risk of contrast-induced nephropathy.** *AJNR Am J Neuroradiol* 2010;31:817–21 CrossRef Medline
15. Ehrlich ME, Turner HL, Currie LJ, et al. **Safety of computed tomographic angiography in the evaluation of patients with acute stroke: a single-center experience.** *Stroke* 2016;47:2045–50 CrossRef Medline
16. Wilhelm-Leen E, Montez-Rath ME, Chertow G. **Estimating the risk of radiocontrast-associated nephropathy.** *J Am Soc Nephrol* 2017;28:653–59 CrossRef Medline
17. McDonald RJ, McDonald JS, Newhouse JH, et al. **Controversies in contrast material-induced acute kidney injury: closing in on the truth?** *Radiology* 2015;277:627–32 CrossRef Medline
18. Molen A, Reimer P, Dekkers IA, et al. **Post-contrast acute kidney injury, Part 1: definition, clinical features, incidence, role of contrast medium and risk factors.** *Eur Radiol* 2018;28:2845–55 CrossRef Medline
19. Barrett BJ, Parfrey PS. **Prevention of nephrotoxicity induced by radiocontrast agents.** *N Engl J Med* 1994;331:1449–50 CrossRef Medline
20. Feigin VL, Lawes CM, Bennett DA, et al. **Stroke epidemiology: a review of population-based studies of incidence, prevalence, and case-fatality in the late 20th century.** *Lancet Neurol* 2003;2:43–53 CrossRef Medline
21. Grysiewicz RA, Thomas K, Pandey DK. **Epidemiology of ischemic and hemorrhagic stroke: incidence, prevalence, mortality, and risk factors.** *Neurol Clin* 2008;26:871–95, vii CrossRef Medline
22. Prencipe M, Culasso F, Rasura M, et al. **Long-term prognosis after a minor stroke: 10-year mortality and major stroke recurrence rates in a hospital-based cohort.** *Stroke* 1998;29:126–32 CrossRef Medline
23. Mair G, Wardlaw JM. **Imaging of acute stroke prior to treatment: current practice and evolving techniques.** *Br J Radiol* 2014;87:20140216 CrossRef Medline
24. Lev MH, Farkas J, Rodriguez VR, et al. **CT angiography in the rapid triage of patients with hyperacute stroke to intraarterial thrombolysis: accuracy in the detection of large vessel thrombus.** *J Comput Assist Tomogr* 2001;25:520–28 CrossRef Medline
25. Davenport MS, Khalatbari S, Cohan RH, et al. **Contrast material-induced nephrotoxicity and intravenous low-osmolality iodinated contrast material: risk stratification by using estimated glomerular filtration rate.** *Radiology* 2013;268:719–28 CrossRef Medline
26. Weisbord SD, Gallagher M, Jneid H, et al; PRESERVE Trial Group. **Outcomes after angiography with sodium bicarbonate and acetylcysteine.** *N Engl J Med* 2018;378:603–14 CrossRef Medline
27. Partovi S, Trischman T, Kang PS. **Lessons learned from the PRESERVE trial.** *Br J Radiol* 2018;91:20180092 CrossRef

Save the Brain First: CTA and Mechanical Thrombectomy in Patients at Risk for Contrast-Induced Nephropathy

Stroke is one of the most common diseases affecting 800,000 Americans each year. It ranks fourth among all-cause mortality in the United States.[1] When patients present with stroke-like symptoms, the current American Heart Association/American Stroke Association (AHA/ASA) guidelines recommend an immediate non-contrast CT of the head. If large-vessel occlusion is suspected, CTA or MRA should be performed to assess the vascular anatomy and plan for endovascular therapy. If the patient is a candidate for mechanical thrombectomy, cerebral angiography is performed.[2] Both CTA and mechanical thrombectomy will subject patients to intravenous contrast.

The concern for exposing patients to a large amount of intravenous contrast is the development of contrast-induced nephropathy (CIN). It is defined as an increase in the plasma creatinine level of 0.5 mg/dL or >25% increase from the baseline within 2–5 days of contrast exposure without any other attributable cause.[3] Multiple risk factors can predispose patients to CIN. Tsai et al[4] have shown that severe chronic kidney disease (CKD), defined as an estimated glomerular filtration rate (eGFR) of <30 mL/min/1.72m^2, was the most significant risk factor for the development of CIN. Most important, acute kidney injury (AKI) in patients with stroke has been associated with an increased risk of in-hospital mortality.[5] Therefore, CIN is a relevant clinical entity and needs to be managed appropriately.

When the initial head CT is negative for bleeding, the question arises as to when and whether the patient should undergo CTA and subsequent revascularization. The current AHA/ASA guidelines recommend proceeding with CTA in patients without a history of renal disease.[2] However, for patients with a history of CKD, there is no current consensus guideline. Therefore, we believe the article by Myung et al[6] has shed valuable light on the risk-stratification and clinical decision-making for this patient population.

The authors conducted a retrospective observational study examining the relationship between CIN and baseline renal function in a large cohort involving 601 patients undergoing CTA and cerebral angiography. The authors demonstrated that patients with severe CKD (eGFR of <30 mL/min/1.73 m^2) were at a higher risk of CIN ($P < .001$). The CIN incidence rate was 12.5% in all patients with CKD and 46.6% in patients with severe CKD. Furthermore, the cutoff eGFR value for an increased CIN risk was found to be 43 mL/min/1.73 m^2. Most important, there was no reported mortality in the patients with CIN. Only 5 patients underwent dialysis, and all patients fully recovered renal function within 4 days. Due to its retrospective observational nature, in this study, a causal relationship could not be established between intravenous contrast and CIN. Furthermore, the absolute CIN incidence rate in patients with CKD was low. Patients with severe CKD were at an increased risk of CIN. However, the clinical consequence is not necessarily significant because all patients recovered successfully after a short course of dialysis and no in-hospital mortality was reported. The authors concluded that neurological interventions should take precedence over concerns of renal injury. However, the understanding of CIN risk factors may help guide individualized renal protective therapy.

Similar to the authors' conclusion, it is absolutely reasonable to proceed with endovascular therapy regardless of the patient's baseline renal function. It is important to proceed with neurovascular interventions before the creatinine level is drawn to avoid a prolonged time to intervention.

First, there is a growing body of evidence showing that intravenous contrast may not cause CIN, particularly in patients with unremarkable baseline renal function. A 2013 systematic review and meta-analysis showed no difference in the rate of AKI between patients with and without contrast exposure.[7] In 2017, a systematic review of 14 studies revealed that CTA and CT perfusion scans were not significantly associated with an increased risk of developing AKI.[8] Furthermore, Lima et al[9] have shown that there was no difference in the AKI rate between patients undergoing CTA and thrombectomy and those without any contrast exposure. Other studies have found similar results.[10,11] Of course, the major critique is that high-risk patients might be scanned much less frequently than the generally healthy patient population owing to the concern for CIN. Therefore, the CIN incidence in the contrast-exposure group may have been erroneously low. On the other hand, stroke may disrupt neurohormonal pathways and may contribute to the development of AKI.[12]

Second, although CIN has been reported to range as high as 20%–30% in the high-risk renal population, the true incidence rate may be much lower. A 2013 study showed that 9%–11% of the at-

risk patients developed postcontrast AKI.[13] A 2017 meta-analysis showed that 2.3% of the patients with CKD undergoing CTA were affected by AKI.[7] Similarly, other studies have found that the absolute CIN rate was low in at-risk patients.[14] The often-quoted high CIN incidence rate was partially due to the use of older hyperosmolar contrast agents, which have been associated with an increased risk of CIN.[15] Furthermore, the incidence of CIN in patients undergoing neurovascular therapy is also low. In a study including 185 high-risk patients undergoing cerebral angiography and mechanical thrombectomy, only 1 patient developed CIN.[16] Similarly, Loh et al[17] found that 3 of 99 patients undergoing endovascular therapy had AKI. In a more recent study, 12 of 93 patients with CKD developed AKI after CTA and thrombectomy, though CKD was not an independent risk factor for AKI in this study.[18]

Last, although CIN has been associated with an increased in-hospital mortality, the true clinical significance of CIN may also be overestimated. It is plausible that CIN is a surrogate marker of rather than a causative factor for worse clinical outcome. For example, the degree of renal impairment is typically minor. McDonald et al[7] have shown that the rate of dialysis was 0.3% in patients developing CIN. Furthermore, effort to reduce renal impairment does not improve the overall mortality rate. Coca et al[19] have shown that reducing the AKI rate by >50% did not reduce the risk of long-term mortality.

Currently, there is no prospective, randomized controlled trial comparing the risk of AKI in patients with CKD with and without contrast exposure. Therefore, no true causal relationship can be established. However, based on existing literature, there is evidence indicating that intravascular contrast does not cause CIN. Furthermore, the absolute rate of CIN remains low, and the clinical significance is unclear. It is more likely that CIN is a surrogate marker reflecting critical illness and multimorbidity rather than a factor determining patient outcome. In that case, assessing a patient's renal function before CTA and mechanical thrombectomy may have no clinical benefit from a renal-protective perspective, even for patients with CKD. Furthermore, each minute wasted on obtaining laboratory data may cost patients 1.9 million neurons in the stroke population.[20] Therefore, it is prudent to proceed with CTA and mechanical thrombectomy on the basis of neurologic status regardless of the patient's renal function. In the future, prospective, randomized controlled trials for patients with severe CKD may be considered, but ethically, it will be difficult not to treat patients if they are otherwise candidates for mechanical thrombectomy. Time is indeed brain, and brain should be saved first.

REFERENCES

1. Koton S, Schneider AL, Rosamond WD, et al. **Stroke incidence and mortality trends in US communities, 1987 to 2011.** *JAMA* 2014;312:259–68 CrossRef Medline
2. Powers WJ, Rabinstein AA, Ackerson T, et al; American Heart Association Stroke Council. **2018 Guidelines for the Early Management of Patients with Acute Ischemic Stroke: A Guideline for Healthcare Professionals From the American Heart Association/American Stroke Association.** *Stroke* 2018;49:e46–110 CrossRef Medline
3. Nijssen EC, Rennenberg RJ, Nelemans PJ, et al. **Prophylactic hydration to protect renal function from intravascular iodinated contrast material in patients at high risk of contrast-induced nephropathy (AMACING): a prospective, randomised, phase 3, controlled, open-label, non-inferiority trial.** *Lancet* 2017;389:1312–22 CrossRef Medline
4. Tsai TT, Patel UD, Chang TI, et al. **Contemporary incidence, predictors, and outcomes of acute kidney injury in patients undergoing percutaneous coronary interventions: insights from the NCDR cath-PCI registry.** *JACC Cardiovasc Interv* 2014;7:1–9 CrossRef Medline
5. Gadalean F, Simu M, Parv F, et al. **The impact of acute kidney injury on in-hospital mortality in acute ischemic stroke patients undergoing intravenous thrombolysis.** *PLoS One* 2017;12:e0185589 CrossRef Medline
6. Myung JW, Kim JH, Cho JH, et al. **Contrast-induced acute kidney injury in radiologic management of acute ischemic stroke in the emergency setting.** *AJNR* 2020;41:632–36 CrossRef Medline
7. McDonald JS, McDonald RJ, Comin J, et al. **Frequency of acute kidney injury following intravenous contrast medium administration: a systematic review and meta-analysis.** *Radiology* 2013;267:119–28 CrossRef Medline
8. Brinjikji W, Demchuk AM, Murad MH, et al. **Neurons over nephrons; systematic review and meta-analysis of contrast-induced nephropathy in patients with acute stroke.** *Stroke* 2017;48:1862–68 CrossRef Medline
9. Lima FO, Lev MH, Levy RA, et al. **Functional contrast-enhanced CT for evaluation of acute ischemic stroke does not increase the risk of contrast-induced nephropathy.** *AJNR Am J Neuroradiol* 2010;31:817–21 CrossRef Medline
10. Jia ZY, Wang SX, Zhao LB, et al. **Risk of acute kidney injury with consecutive, multidose use of iodinated contrast in patients with acute ischemic stroke.** *AJNR Am J Neuroradiol* 2019;40:652–54 CrossRef Medline
11. Langner S, Stumpe S, Kirsch M, et al. **No increased risk for contrast-induced nephropathy after multiple CT perfusion studies of the brain with a nonionic, dimeric, iso-osmolal contrast medium.** *AJNR Am J Neuroradiol* 2008;29:1525–29 CrossRef Medline
12. Zhao Q, Yan T, Chopp M, et al. **Brain–kidney interaction: renal dysfunction following ischemic stroke.** *J Cereb Blood Flow Metab* 2020;40:246–62 CrossRef Medline
13. McDonald RJ, McDonald JS, Bida JP, et al. **Intravenous contrast material-induced nephropathy: causal or coincident phenomenon?** *Radiology* 2013;267:106–18 CrossRef Medline
14. Hopyan JJ, Gladstone DJ, Mallia G, et al. **Renal safety of CT angiography and perfusion imaging in the emergency evaluation of acute stroke.** *AJNR Am J Neuroradiol* 2008;29:1826–30 CrossRef Medline
15. Lautin EM, Freeman NJ, Schoenfeld AH, et al. **Radiocontrast-associated renal dysfunction: a comparison of lower-osmolality and conventional high-osmolality contrast media.** *Am J Roentgenol* 1991;157:59–65 Medline
16. Kim J, Male S, Jagadeesan BD, et al. **Safety of cerebral angiography and neuroendovascular therapy in patients with chronic kidney disease.** *Neuroradiology* 2018;60:529–33 CrossRef Medline
17. Loh Y, McArthur DL, Vespa P, et al. **The risk of acute radiocontrast-mediated kidney injury following endovascular therapy for acute ischemic stroke is low.** *AJNR Am J Neuroradiol* 2010;31:1584–87 CrossRef Medline
18. Weber R, van Hal R, Stracke P, et al. **Incidence of acute kidney injury after computed tomography angiography±computed tomography perfusion followed by thrombectomy in patients with stroke using a postprocedural hydration protocol.** *J Am Heart Assoc* 2020;9:e014418 CrossRef Medline
19. Coca SG, Zabetian A, Ferket BS, et al. **Evaluation of short-term changes in serum creatinine level as a meaningful end point in randomized clinical trials.** *J Am Soc Nephrol* 2016;27:2529–42 CrossRef Medline
20. Saver JL. **Time is brain: quantified.** *Stroke* 2006;37:263–66 CrossRef

X. Li
S. Partovi
Section of Interventional Radiology, Imaging Institute
Cleveland Clinic Foundation
Cleveland, Ohio

http://dx.doi.org/10.3174/ajnr.A6515

White Matter Disease and Outcomes of Mechanical Thrombectomy for Acute Ischemic Stroke

E.A. Mistry, A.M. Mistry, T. Mehta, N. Arora, A.K. Starosciak, F.D.L.R. La Rosa, J.E. Siegler, S.E. Kasner, R. Chitale, M. Fusco, M. Froehler, S. Yaghi, M. Schrag, and P. Khatri, on behalf of BEST Collaborators

ABSTRACT

BACKGROUND AND PURPOSE: The increased severity of white matter disease is associated with worse outcomes and an increased rate of intracerebral hemorrhage in patients with ischemic stroke undergoing thrombolytic treatment. However, whether white matter disease is associated with outcomes in patients undergoing endovascular treatment remains unclear.

MATERIALS AND METHODS: In this prespecified exploratory analysis of our prospective multi-institutional study that enrolled consecutive adult patients with anterior circulation ischemic stroke undergoing endovascular treatment from November 2017 to September 2018, we compared the following outcomes between patients with none-to-minimal (van Swieten score, 0–2) and moderate-to-severe (van Swieten score, 3–4) white matter disease using logistic regression: 90-day mRS 3–6, death, intracerebral hemorrhage, successful recanalization, and early neurologic recovery.

RESULTS: Of the 485 patients enrolled in the Blood Pressure after Endovascular Stroke Therapy (BEST) study, 389 had white matter disease graded (50% women; median age, 68 years; range, 58–79 years). A van Swieten score of 3–4 ($n = 74/389$, 19%) was associated with a higher rate of 90-day mRS of 3–6 (45% versus 18%; adjusted OR, 2.73; 95% CI, 1.34–5.93; $P = .008$). Although the death rate was higher in patients with van Swieten scores of 3–4 (26% versus 15%), the adjusted likelihood was not significantly different (adjusted OR, 1.14; 95% CI, 0.56–2.26; $P = .710$). Ordered regression revealed a shift toward worse mRS scores with increasing van Swieten scores (adjusted common OR, 3.04; 95% CI, 1.93–4.84; $P < .001$). No associations between white matter disease severity and intracerebral hemorrhage, successful recanalization, and early neurologic recovery were observed.

CONCLUSIONS: Moderate-to-severe white matter disease is associated with worse outcomes in patients undergoing endovascular treatment without a significant increase in hemorrhagic complications. Studies comparing patients with and without endovascular treatment are necessary to determine whether the benefit of endovascular treatment is attenuated with greater white matter disease.

ABBREVIATIONS: aOR = adjusted OR; EVT = endovascular treatment; ICH = intracerebral hemorrhage; VSS = van Swieten score; WMD = white matter disease

Endovascular treatment (EVT) drastically improves outcomes for select patients with an acute large-vessel occlusion and is the treatment technique with the highest level of evidence according to the most recent guidelines.[1,2] Thus, the use of EVT as the definitive treatment technique for large-vessel occlusion strokes is increasing.[3] Moreover, the indications for EVT are expanding to populations that were previously thought to not derive many benefits from EVT, such as those with delayed presentation.[4,5] Additional populations that may derive benefit are also under study, such as those with a large infarct core,[6,7] older age,[8] and low NIHSS scores.[9] White matter disease (WMD) is easily detectable on baseline routine imaging performed in all

Received December 10, 2019; accepted after revision January 31, 2020.

From the Departments of Neurology (E.A.M., M.S.) and Neurosurgery (A.M.M., R.C., M. Fusco), and Cerebrovascular Program (M. Froehler), Vanderbilt University Medical Center, Nashville, Tennessee; Department of Neurology and Neurosurgery (T.M.), University of Minnesota, Minneapolis, Minnesota; Department of Neurology (N.A.), University of Missouri, Columbia, Missouri; Baptist Health Neuroscience Center (A.K.S., F.D.L.R.L.R.), Miami, Florida; Department of Neurology (J.E.S., S.E.K.), University of Pennsylvania, Philadelphia, Pennsylvania; New York University Langone Health (S.Y.), Brooklyn, New York; and Department of Neurology and Rehabilitation Medicine (P.K.), University of Cincinnati, Cincinnati, Ohio.

This work was supported by the National Institutes of Health/National Institute of Neurological Disorders and Stroke (K23NS113858; Mistry), University of Cincinnati Gardner Neuroscience Institute pilot grant, and Society of Vascular and Interventional Neurology pilot grant.

Please address correspondence to Eva A. Mistry, MBBS, 2525 West End Ave, Suite 612, Nashville TN 37232; e-mail: eva.a.mistry@vumc.org

Indicates open access to non-subscribers at www.ajnr.org
Indicates article with supplemental on-line tables.
http://dx.doi.org/10.3174/ajnr.A6478

patients with stroke. Moderate-to-severe WMD is associated with poorer outcomes in patients with stroke from any etiology and increases the rate of hemorrhagic complications in those treated with intravenous thrombolysis.[10,11] However, outcomes of patients with moderate-to-severe WMD in the context of EVT remain less well-studied, and the rates of early neurologic recovery and hemorrhagic complications remain unknown. In this prespecified exploratory analysis of our prospective, multicenter, cohort study, Blood Pressure after Endovascular Stroke Therapy (BEST), we sought to determine whether patients with acute stroke with moderate-to-severe WMD undergoing EVT have worse functional outcomes and increased rates of hemorrhagic complications compared with those with no-to-minimal WMD.

MATERIALS AND METHODS

Study Design and Patient Selection

The BEST study prospectively enrolled consecutive adult patients undergoing EVT for an anterior cerebral circulation large-vessel occlusion (internal carotid artery or the M1 or M2 segments of the middle cerebral artery) at 12 comprehensive stroke centers across the United States from November 2017 to September 2018. We excluded from the study patients with the following conditions: 1) a known prestroke mRS score of less than 2; 2) terminal medical diagnoses such as a stage IV cancer; 3) a left ventricular assist device; or 4) a stroke in the perioperative or inpatient setting. Additional details on methods have been previously published.[12] The BEST study was approved by the institutional review boards of 11 sites and was deemed exempt by 1 site, and informed consent was waived. The results presented here are a prespecified secondary analysis of the BEST study. The data that support the findings of this study are available from the corresponding author on reasonable request.

Study Variables and Covariates

The primary study variable was the severity of WMD, graded prospectively. A single physician collected data on WMD on the first CT scan at presentation for each patient using the van Swieten score (VSS), after undergoing centralized training on the grading.[13] The VSS was graded on the contralateral hemisphere of the known large-vessel occlusion. This technique has been used by previous studies to avoid mislabeling the ipsilateral acute stroke-related hypodensities on the CT scan as WMD.[14] Furthermore, the van Swieten method of WMD grading has been deemed comparable with other CT- and MR imaging–based grading systems.[15]

We collected the following variables: the ASPECTS, available from the radiology report of the first noncontrast brain CT or calculated by trained local study personnel; core and penumbra volumes automatically calculated by the RApid processing of PerfusIon and Diffusion software (RAPID; iSchemaView, Stanford, California) from the initial pre-EVT CT perfusion scan; time from last known well to final recanalization assessed as a modified TICI score (or angiogram completion if the final modified TICI was 0); and the presence of any intraparenchymal hemorrhage (ICH; excluding subarachnoid hemorrhage) on either MR imaging or CT within the 72 hours post-EVT.

Outcomes

The primary study outcome was the dichotomized 90-day mRS 0–2 (functional independence) versus 3–6. Secondary outcomes included a 90-day mRS 0–3 (ambulatory independence) versus 4–6, any ICH, symptomatic ICH (associated with a ≥4-point increase in the NIHSS score from baseline to 24 hours), a change in the mRS distribution, successful recanalization (defined as modified TICI 2b–3), and early neurologic recovery (NIHSS 0–1 or ≥8-point decrease in the NIHSS score from baseline to 24 hours).

Statistical Analysis

The baseline characteristics between the group of patients with no-to-minimal (VSS 0–2) and moderate-to-severe (VSS 3–4) WMD were compared using a χ^2 test, *t* test, or Mann-Whitney *U* test, as appropriate. Associations between WMD with outcomes were determined using logistic regression. These models were subsequently adjusted for the following covariables selected a priori: age, hypertension, initial glucose level, NIHSS score on presentation, time to recanalization, intravenous thrombolysis, ASPECTS, systolic blood pressure on admission, and successful recanalization (except when used as the dependent variable). A subgroup analysis was then undertaken on only those patients with a successful recanalization. All analyses and plots were generated using R statistical and computing software, Version 3.6 (http://www.r-project.org/). Statistical significance α was set at $<.05$ for all statistical analyses. All *P* values are 2-sided.

RESULTS

Of the 485 patients included in BEST, 389 had WMD graded on the baseline CT scan, of whom 90-day follow-up was available for 365 (94%). A total of 74 (19%) had moderate-to-severe WMD (VSS 3–4). Table 1 outlines the baseline characteristics and outcomes according to moderate-to-severe and no-to-minimal WMD. Patients with VSS 3–4 were older and had a higher proportion with hypertension in addition to having a higher baseline blood glucose level and systolic blood pressure. The remaining baseline characteristics were not different between the 2 groups.

A total of 13 (18%) of the 70 patients with VSS 3–4 had a 90-day mRS 0–2 compared with 141 (45%) of the 295 with VSS 0–2 ($P < .001$, Table 1). Compared with patients with VSS 0–2, those with VSS 3–4 had higher odds of being functionally dependent or dead (OR, 4.01; 95% CI, 2.17–7.94; $P < .001$; adjusted OR [aOR], 2.73; 95% CI, 1.34–5.93; $P = .008$ for having a 90-day mRS 3–6). The complete results of the model are depicted in On-line Table 1. Patients with VSS 3–4 were less likely to have an mRS 0–3, denoting ambulatory independence, in unadjusted analysis (OR, 0.43; 95% CI, 0.25–0.73; $P = .002$) but not in the adjusted analysis (aOR, 0.75; 95% CI, 0.40–1.43; $P = .38$). Ordered logistic regression revealed an overall shift toward a worse outcome in patients with VSS 3–4 with unadjusted common OR of 2.86; 95% CI, 1.83–4.52; $P < .001$; and adjusted common OR of 3.04; 95% CI, 1.93–4.84; $P < .001$ (Fig 1). A shift toward worse outcomes with each incremental grade of VSS was also observed (Fig 1). Compared with VSS 0, patients with a baseline VSS 3 and 4 had higher odds of having a 90-day mRS 3–6 (OR, 3.58; 95% CI, 1.61–8.64; $P = .003$; and OR 7.25; 95% CI, 2.63–25.73; $P < .001$,

respectively). After adjustment for covariables, VSS 4 continued to have a higher odds of 90-day mRS 3–6 (On-line Table 2).

Patients with VSS 3–4 demonstrated a higher likelihood of death by 90 days on unadjusted (OR, 1.97; 95% CI, 1.06–3.57; $P = .029$) but not on adjusted analysis (aOR, 1.14; 95% CI, 0.56–2.26; $P = .71$). The rates and odds of early neurologic improvement and successful recanalization were not significantly different among the 2 groups (Table 2). Notably, the rate of any ICH was also not significantly different between the 2 groups (22%, $n = 66$, in patients with VSS 0–2 versus 20%, $n = 15$, in patients with VSS 3–4; $P = .86$).

A successful recanalization was achieved in 343 (88%) patients. Of these, 90-day outcome was available for 323 (94%) patients. Outcomes of this subgroup of patients are outlined in Table 3. Overall, futile recanalization was observed in 80% of the patients with VSS 3–4 compared with 48% in those with VSS 0–2 ($P < .001$) when futile recanalization was defined as 90-day mRS 3–6 in patients with successful recanalization (OR, 4.19; 95% CI, 2.24–8.37,

Table 1: Baseline characteristics of patients with no-to-minimal (van Sweeten score, 0–2) and moderate-to-severe (van Swieten score, 3–4) white matter disease

	van Swieten 0–2 ($n = 315$)	van Swieten 3–4 ($n = 74$)	*P* Value
Age (mean) (±SD) (yr)	66 (±15)	76 (±12)	<.001
Male (%)	164 (52)	32 (43)	.2
Hypertension (%)	224 (71)	68 (92)	<.001
Diabetes (%)	92 (29)	23 (31)	.78
Glucose (median) (IQR)	122 (102–146)	131 (115–162)	.009
NIHSS (median) (IQR)	15 (10–20)	17 (11–21)	.16
ASPECTS (median) (IQR)	8 (7–10)	8 (7–9)	.07
Core volume (mean) (±SD)	20 (±24)	19 (±26)	.85
Penumbra volume (mean) (±SD)	119 (±71)	124 (±71)	.69
Systolic BP on admission (mean) (± SD)	154 (±29)	168 (±29)	<.001
Time from last known well to reperfusion (median) (IQR)	274 (180–534)	286 (190–676)	.2
Intravenous thrombolysis (%)	160 (51)	29 (39)	.09
Prior stroke (%)	52 (16)	19 (26)	.09

Note:—BP indicates blood pressure; IQR, interquartile range.

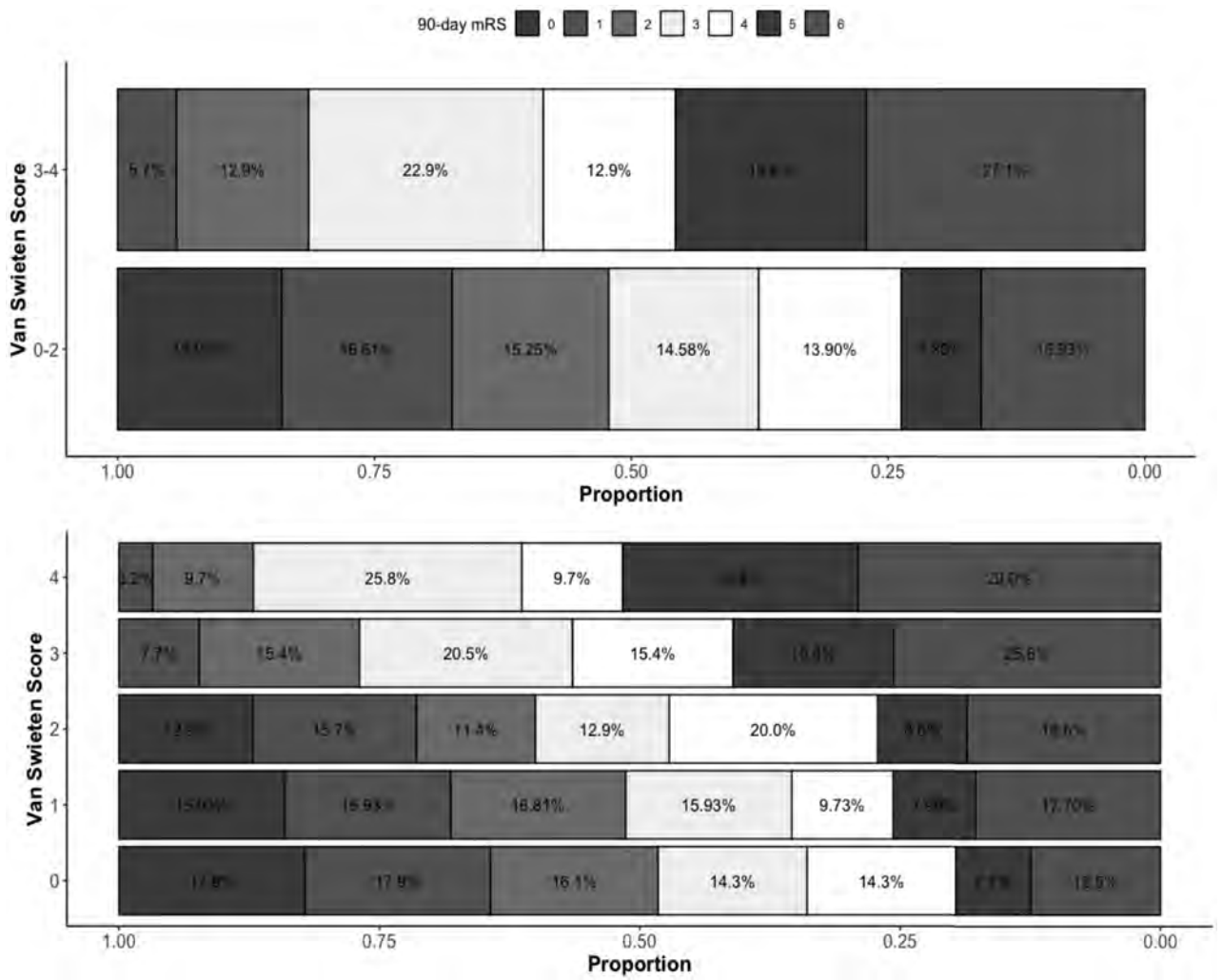

FIGURE. Distribution of the 90-day mRS score according to white matter disease severity graded with the van Swieten scale score.

Table 2: Outcomes of patients with no-to-minimal (van Swieten score, 0–2) and moderate-to-severe (van Swieten score, 3–4) white matter disease

Outcome	van Swieten 0–2 ($n = 315$)	van Swieten 3–4 ($n = 74$)	Unadjusted OR with 95% CI	*P* Value	Adjusted OR with 95% CI	*P* Value
90-Day mRS 0–2 (%)	141/295 (45)	13/70 (18)	0.25 (0.13–0.46)	<.001	0.37 (0.17–0.75)	.008
90-Day mRS 0–3 (%)	184/295 (58)	29/70 (39)	0.43 (0.25–0.73)	.002	0.75 (0.40–1.43)	.38
Shift in the 90-day mRS	NA	NA	2.86 (1.83–4.52)	<.001	3.05 (1.93–4.84)	<.001
Death (%)	47 (15)	19 (26)	1.97 (1.06–3.57)	.029	1.14 (0.56–2.26)	.71
Symptomatic ICH (%)	13 (4)	4 (5)	1.33 (0.37–3.88)	.629	NA	NA
mTICI ≥ 2b (%)	275 (87)	68 (92)	1.65 (0.72–4.47)	.27	NA	NA
ENI (%)	132 (42)	30 (40)	0.95 (0.56–1.58)	.83	NA	NA

Note:—mTICI indicates modified TICI; ENI, early neurologic improvement; NA, not applicable.

Table 3: Outcomes of patients with successful recanalization (mTICI ≥ 2b) according to the severity of baseline white matter disease

Outcome	van Swieten 0–2 ($n = 275$)	van Swieten 3–4 ($n = 68$)	*P* Value
90-Day mRS 0–2 (%)	132/258 (52)	13/65 (20)	<.001
90-Day mRS 0–3 (%)	169/258 (65.5)	28/65 (43)	.002
Death (%)	34 (12.4)	17 (25.0)	.013
Symptomatic ICH (%)	10 (3.6)	3 (4.4)	.73
ENI (%)	124 (45.1)	30 (44.1)	1.0

Note:—ENI indicates early neurologic improvement.

$P < .001$; aOR, 2.59; 95% CI, 1.26–5.65; $P = .012$ for 90-day mRS 3–6). When defined as 90-day mRS 4–6, futile recanalization was observed in 57% of patients with VSS 3–4 versus 34.5% of those with VSS 0–2 (OR, 2.51; 95% CI, 1.45–4.40; $P < .001$; aOR, 1.34; 95% CI, 0.7–2.57; $P = .38$ for a 90-day mRS 4–6). Rates of symptomatic ICH and death were similar in both groups. Among patients with VSS 3–4 who had a 90-day outcome available ($n = 70$), none of the patients with unsuccessful recanalization ($n = 5$) had a 90-day mRS 0–2 compared with 7/65 (20%) patients with successful recanalization. Among those with VSS 0–2 and a 90-day outcome available ($n = 295$), 9/37 (24%) patients with unsuccessful recanalization had a 90-day mRS 0–2, compared with 132/258 (51%) patients with successful recanalization (OR, 0.31; 95% CI, 0.13–0.65; $P = .003$).

DISCUSSION

In this multicenter, prospective observational study, we found that patients with moderate-to-severe WMD had significantly worse functional outcomes at 90 days in terms of functional independence compared with those with no-to-minimal WMD (18% versus 45%; $P < .001$). A significant overall shift toward worse outcomes was also observed, though the rates of successful recanalization and hemorrhagic complications were not significantly different between the 2 groups. An increasing shift toward a worse outcome with each incremental grade of VSS may imply an underlying dose response between WMD and outcomes and suggests a possible causal relationship. Furthermore, the odds of futile recanalization were nearly 4-fold higher in patients with moderate-to-severe WMD.

Acquired WMD is common with aging and has heterogeneous clinical and pathologic correlates. It most frequently represents the sequelae of chronic, inadequately controlled hypertension, which was an overwhelmingly common risk factor and probably the major driver of WMD in the current cohort. However, smoking, diabetes, cerebral amyloid angiopathy, rare hereditary cerebral small-vessel diseases, and even migraines have been reported to be linked to WMD.[16,17] The presence of WMD on imaging is a useful biomarker for compromised cognitive performance, particularly on measures of memory and processing speed.[17,18] Common pathologic correlates of WMD include those commonly implicated in neurodegeneration, such as elevated markers of axonal damage, the presence of activated microglia, and disorganization of aquaporin-4 localization on vessel-associated astrocytes.[19-22]

Mechanisms by which WMD may exert a negative effect on outcomes following an acute stroke are multifold. First, it is associated with disruption of endothelial function, resulting in damage to the microvascular integrity, and blood-brain barrier dysfunction, resulting in extravasation of blood products and hemorrhagic complications.[23] Second, it may reduce the ischemic resilience of the cerebral tissue to a sudden lack of blood flow.[24] Third, it can cause ongoing platelet activation and increased propensity for thrombosis, resulting in higher final infarct volumes.[25] The resulting clinical consequences include not only worse outcomes with the incident stroke but also subsequent increased cognitive decline and rates of recurrent strokes.[26,27]

Outcomes of patients with moderate-to-severe WMD in acute reperfusion have mainly been studied in the context of intravenous thrombolysis. There is an increased rate of symptomatic ICH in patients with moderate-to-severe WMD.[10,28] However, post hoc analysis of randomized data suggests that patients with moderate-to-severe WMD continue to derive the benefit from intravenous thrombolysis with an overall improvement in functional outcomes, compared with no thrombolytic treatment.[28] A limited number of studies have reported the effect of WMD on outcomes after EVT.[29-32] All of these studies were retrospective in design, most were single-center, likely included patients treated with older EVT devices, and included a relatively small number of patients.

The results of these studies have been variable. One study showed no difference in functional outcomes,[29] and others have shown a worse functional outcome in moderate-to-severe WMD.[30,32] All the studies have consistently reported no difference in rates of hemorrhagic complications in contrast to similar studies involving intravenous thrombolysis. It is plausible that blood vessels rendered "leaky" from the microvascular damage from underlying WMD are more susceptible to the lytic effects of systemic thrombolysis. However, as the field of acute stroke

advances, a heightened understanding of how varying substrates impact recovery will not only impact patient selection but may also lead to new targets for neurorestorative therapies.

Our study has the inherent limitations of an observational study. Most important, we did not include patients with baseline disability, likely introducing a selection bias. It is plausible that the outcomes may change after factoring the patients' disabled statuses, because patients with moderate-to-severe WMD are more likely to have pre-existing disability. Additionally, due to selection bias inherent to the inclusion criteria, our study population might not reflect patients with the most severe WMD and, therefore, may underestimate the negative impact of WMD on outcomes after EVT. Furthermore, without a placebo arm, it is impossible to know whether the effect of EVT is truly attenuated in patients with WMD. We may have been underpowered to detect a significant effect of WMD of hemorrhage rates. Our study is strengthened by a relatively large number of patients compared with prior studies, and its multi-institutional design makes the results more generalizable. Additionally, the patients included in this study are representative of the modern EVT population.

Our findings should be validated in large EVT cohorts, particularly those in randomized trials.

CONCLUSIONS

Moderate-to-severe WMD is associated with decreased rates of functional independence in patients undergoing EVT; however, there are no significant differences in the rates of procedural success or intracranial hemorrhage. Currently, our data cannot support withholding EVT on the basis of the severity of WMD but may provide some reassurance that the rate of symptomatic hemorrhage may not be significantly higher. Future analyses of randomized trial data are needed to understand whether the treatment effect of EVT is truly diminished in patients with moderate-to-severe WMD.

Disclosures: Eva A. Mistry—*UNRELATED*: *Grants/Grants Pending*: National Institutes of Health/National Institute of Neurological Disorders and Stroke, Vanderbilt Faculty Research Scholars Program, University of Cincinnati Gardner Neuroscience Institute, and Society of Vascular and Interventional Neurology, *Comments*: K23NS113858.* James E. Siegler—*RELATED*: *Grant:* National Institutes of Health, *Comments*: U10 NS086474 grant*; *Support for Travel to Meetings for the Study or Other Purposes*: American Heart Association, *Comments*: Junior Investigator Travel Award; *UNRELATED*: *Payment for Lectures Including Service on Speakers Bureaus*: Tufts Medical Center and Lahey Hospital & Medical Center, Boston, Massachusetts, *Comments*: Grand Rounds honoraria. Scott E. Kasner—*UNRELATED*: *Consultancy*: Medtronic, Bayer, Bristol-Myers Squibb; *Grants/Grants Pending*: W. L. Gore & Associates, Bayer, Bristol-Myers Squibb*; *Royalties*: Up-to-Date. Rohan Chitale—*UNRELATED*: *Grants/Grants Pending*: Cerenovus*; *Payment for Lectures Including Service on Speakers Bureaus*: Medtronic.* Michael Froehler—*UNRELATED*: *Consultancy*: Balt USA, Corindus Vascular Robotics, Genentech, Medtronic, Stryker, Viz.ai; *Employment*: Vanderbilt University Medical Center; *Grants/Grants Pending*: National Institutes of Health, Genentech, Stryker, Medtronic, MicroVention, Penumbra, Endophys.* Shadi Yaghi—*UNRELATED*: *Consultancy*: Medtronic.* Pooja Khatri—*UNRELATED*: *Consultancy*: Lumosa Therapeutics, Genentech, *Comments*: Data and Safety Monitoring Board (Lumosa), trial Principal Investigator (Genentech)*; *Expert Testimony*: medicolegal consultation*; *Grants/Grants Pending*: Cerenovus, Nervive.* *Money paid to the institution.

REFERENCES

1. Powers WJ, Rabinstein AA, Ackerson T, et al; American Heart Association Stroke Council. **2018 guidelines for the early management of patients with acute ischemic stroke: a guideline for healthcare professionals from the American Heart Association/American Stroke Association.** *Stroke* 2018;49:e46–110 CrossRef Medline
2. Goyal M, Menon BK, van Zwam WH, et al; HERMES Collaborators. **Endovascular thrombectomy after large-vessel ischaemic stroke: a meta-analysis of individual patient data from five randomised trials.** *Lancet* 2016;387:1723–31 CrossRef Medline
3. Smith EE, Saver JL, Cox M, et al. **Increase in endovascular therapy in Get with the Guidelines-Stroke after the Publication of Pivotal Trials.** *Circulation* 2017;136:2303–10 CrossRef Medline
4. Albers GW, Marks MP, Kemp S, et al; DEFUSE 3 Investigators. **Thrombectomy for stroke at 6 to 16 hours with selection by perfusion imaging.** *N Engl J Med* 2018;378:708–18 CrossRef Medline
5. Nogueira RG, Jadhav AP, Haussen DC, et al; DAWN Trial Investigators. **Thrombectomy 6 to 24 hours after stroke with a mismatch between deficit and infarct.** *N Engl J Med* 2018;378:11–21 CrossRef Medline
6. Roman LS, Menon BK, Blasco J, et al; HERMES Collaborators. **Imaging features and safety and efficacy of endovascular stroke treatment: a meta-analysis of individual patient-level data.** *Lancet Neurol* 2018;17:895–904 CrossRef Medline
7. The TELSA trial. **Thrombectomy for Emergent Salvage of Large Anterior Circulation Ischemic Stroke.** https://www.cms.gov/Medicare/Coverage/IDE/Approved-IDE-Studies-Items/G190006-NCT03805308. Accessed January 31, 2020
8. Sarraj A, Hassan AE, Savitz S, et al. **Outcomes of endovascular thrombectomy vs medical management alone in patients with large ischemic cores: a secondary analysis of the Optimizing Patient's Selection for Endovascular Treatment in Acute Ischemic Stroke (select) study.** *JAMA Neurol* 2019; Jul 29. [Epub ahead of print] CrossRef Medline
9. Nagel S, Bouslama M, Krause LU, et al. **Mechanical thrombectomy in patients with milder strokes and large vessel occlusions.** *Stroke* 2018;49:2391–97 CrossRef Medline
10. Kongbunkiat K, Wilson D, Kasemsap N, et al. **Leukoaraiosis, intracerebral hemorrhage, and functional outcome after acute stroke thrombolysis.** *Neurology* 2017;88:638–45 CrossRef Medline
11. Smith EE. **Leukoaraiosis and stroke.** *Stroke* 2010;41:S139–43 CrossRef Medline
12. Mistry EA, Sucharew H, Mistry AM, et al. **Blood Pressure after Endovascular Therapy for Ischemic Stroke (BEST): a multicenter prospective cohort study.** *Stroke* 2019;50:3449–55 CrossRef Medline
13. van Swieten JC, Hijdra A, Koudstaal PJ, et al. **Grading white matter lesions on CT and MRI: a simple scale.** *J Neurol Neurosurg Psychiatry* 1990;53:1080–83 CrossRef Medline
14. Boulouis G, Bricout N, Benhassen W, et al. **White matter hyperintensity burden in patients with ischemic stroke treated with thrombectomy.** *Neurology* 2019;93:e1498–1506 CrossRef Medline
15. Pantoni L, Simoni M, Pracucci G, et al. **Visual rating scales for age-related white matter changes (leukoaraiosis): can the heterogeneity be reduced?** *Stroke* 2002;33:2827–33 CrossRef Medline
16. Erdelyi-Botor S, Aradi M, Kamson DO, et al. **Changes of migraine-related white matter hyperintensities after 3 years: a longitudinal MRI study.** *Headache* 2015;55:55–70 CrossRef Medline
17. Habes M, Erus G, Toledo JB, et al. **White matter hyperintensities and imaging patterns of brain ageing in the general population.** *Brain* 2016;139:1164–79 CrossRef Medline
18. Schrag M, Kirshner H. **Neuropsychological effects of cerebral amyloid angiopathy.** *Curr Neurol Neurosci Rep* 2016;16:76 CrossRef Medline
19. Chen A, Akinyemi RO, Hase Y, et al. **Frontal white matter hyperintensities, clasmatodendrosis and gliovascular abnormalities in ageing and post-stroke dementia.** *Brain* 2016;139:242–58 CrossRef Medline
20. Moore EE, Hohman TJ, Badami FS, et al. **Neurofilament relates to white matter microstructure in older adults.** *Neurobiol Aging* 2018;70:233–41 CrossRef Medline
21. Osborn KE, Alverio JM, Dumitrescu L, et al. **Adverse vascular risk relates to cerebrospinal fluid biomarker evidence of axonal injury**

in the presence of Alzheimer's disease pathology. *J Alzheimers Dis* 2019;71:281–90 CrossRef Medline

22. Raz N, Yang Y, Dahle CL, et al. **Volume of white matter hyperintensities in healthy adults: contribution of age, vascular risk factors, and inflammation-related genetic variants.** *Biochim Biophys Acta* 2012;1822:361–69 CrossRef Medline
23. del Zoppo GJ, von Kummer R, Hamann GF. **Ischaemic damage of brain microvessels: inherent risks for thrombolytic treatment in stroke.** *J Neurol Neurosurg Psychiatry* 1998;65:1–9 CrossRef Medline
24. Henninger N, Khan MA, Zhang J, et al. **Leukoaraiosis predicts cortical infarct volume after distal middle cerebral artery occlusion.** *Stroke* 2014;45:689–95 CrossRef Medline
25. Iwamoto T, Kubo H, Takasaki M. **Platelet activation in the cerebral circulation in different subtypes of ischemic stroke and Binswanger's disease.** *Stroke* 1995;26:52–56 CrossRef Medline
26. Inzitari D, Pracucci G, Poggesi A, et al; LADIS Study Group. **Changes in white matter as determinant of global functional decline in older independent outpatients: three-year follow-up of LADIS (Leukoaraiosis and Disability] study cohort.** *BMJ* 2009;339: b2477 CrossRef Medline
27. Vermeer SE, Hollander M, van Dijk EJ, et al, Rotterdam Scan Study. **Silent brain infarcts and white matter lesions increase stroke risk in the general population: the Rotterdam Scan study.** *Stroke* 2003;34:1126–29 CrossRef Medline
28. Demchuk AM, Khan F, Hill MD, et al; NINDS rt-PA Stroke Study Group. **Importance of leukoaraiosis on CT for tissue plasminogen activator decision making: evaluation of the NINDS rt-PA Stroke study.** *Cerebrovasc Dis* 2008;26:120–25 CrossRef Medline
29. Atchaneeyasakul K, Leslie-Mazwi T, Donahue K, et al. **White matter hyperintensity volume and outcome of mechanical thrombectomy with Stentriever in acute ischemic stroke.** *Stroke* 2017;48:2892–94 CrossRef Medline
30. Guo Y, Zi W, Wan Y, et al. **Leukoaraiosis severity and outcomes after mechanical thrombectomy with stent-retriever devices in acute ischemic stroke.** *J Neurointerv Surg* 2019;11:137–40 CrossRef Medline
31. Shi ZS, Loh Y, Liebeskind DS, et al. **Leukoaraiosis predicts parenchymal hematoma after mechanical thrombectomy in acute ischemic stroke.** *Stroke* 2012;43:1806–11 CrossRef Medline
32. Zhang J, Puri AS, Khan MA, et al. **Leukoaraiosis predicts a poor 90-day outcome after endovascular stroke therapy.** *AJNR Am J Neuroradiol* 2014;35:2070–75 CrossRef Medline

Glasgow Coma Scale on Presentation Predicts Outcome in Endovascular Treatment for Acute Posterior Large-Vessel Occlusion

A.H. Chiu, D.A. Hince, and W. McAuliffe

ABSTRACT

SUMMARY: Use of mechanical thrombectomy for stroke has increased since the publication of trials describing outcome improvement when used in the anterior circulation. These results, however, cannot be directly translated to the posterior circulation. While a high NIHSS score has demonstrated an association with poor outcomes in posterior stroke, the NIHSS is weighted toward hemispheric disease, and complex scores potentially delay definitive imaging diagnosis. We performed a retrospective analysis to ascertain whether any rapidly obtainable demographic or clinical and imaging data have a correlation with patient outcome post-thrombectomy. Seventy-three cases were audited between September 2010 and October 2017. Presenting with a Glasgow Coma Scale score of >13 meant that the odds of reaching the primary end point of functional independence (defined as a 90-day modified Rankin Scale score of 0–2) were 5.70 times greater; similarly, presenting with a posterior circulation ASPECTS of >9 resulted in the odds of reaching the primary end point being 4.03 times greater. *Older age correlated to a lower odds of independence* (0.97, $p = .04$).

ABBREVIATIONS: F-mTICI = final modified TICI score; GCS = Glasgow Coma Scale; I-mTICI = initial modified TICI score; MT = mechanical thrombectomy; mTICI = modified TICI; PC = posterior circulation; PLVO = posterior large-vessel occlusion; RACE = Rapid Arterial oCclusion Evaluation

The caseload of mechanical thrombectomy (MT) for stroke has increased since the publication of trials[1-6] describing the benefit in the anterior circulation. Given the questionable efficacy of IV-tPA in the treatment of posterior circulation stroke, endovascular treatment has long been considered an option for posterior large-vessel occlusion (PLVO).[6-8] Trials pertaining to the anterior circulation, however, cannot be translated directly to PLVO. While a high NIHSS score has also been associated with poor outcomes in posterior stroke,[9,10] this association has been questioned,[11,12] given that the NIHSS is weighted toward hemispheric disease.[13] Other scales[14] have been suggested to increase the accuracy in posterior strokes; however, the use of these complex scores potentially delays the imaging diagnosis, which is unarguably more definitive for guiding management. We thus sought to identify whether any rapidly obtainable demographic or clinical- and imaging-related data that are routinely collected for PLVO have a correlation with outcome.

Received October 18, 2019; accepted after revision February 19, 2020.

From the Neurological Intervention and Imaging Service of Western Australia (A.H.C., W.M.), Western Australia Health, Sir Charles Gairdner, Royal Perth, and Fiona Stanley Hospitals, Perth, Australia; Medical School, Division of Medicine (A.H.C., W.M.), University of Western Australia, Perth, Australia; and Institute for Health Research (D.A.H.), University of Notre Dame, Fremantle, Australia.

Please address correspondence to Albert H. Chiu, MBBS (Hons.) FRANZCR CCINR, Neurological Intervention and Imaging Service of Western Australia, Sir Charles Gairdner Hospital, 1st Floor, G Block, Hospital Ave, Nedlands WA 6009, Australia; e-mail: albert.h.chiu@gmail.com

Indicates article with supplemental on-line table.

http://dx.doi.org/10.3174/ajnr.A6497

MATERIALS AND METHODS

Background

Our neurointerventional service has, for >10 years, been organized as a single multisite state department encompassing 3 tertiary/quaternary hospitals, providing all elective and acute neurovascular services. During data collection, stroke care underwent an evolution from a neurology-driven thrombolysis service (organized per hospital) to a state-wide MT-driven system. Ambulance triage using the Rapid Arterial oCclusion Evaluation score (RACE)[15] was implemented in 2016. Ambulances would be diverted to 1 of 2 MT centers on the basis of the RACE, and on arrival to the emergency department, a "code stroke" was activated.

As the service grew, the decision to proceed to MT evolved. Use of the NIHSS became sporadic, given the nature of PLVO but also because of the availability of RACE and increasingly expeditious transfer to CT. The NIHSS was hence not included in the study. Imaging protocols were hospital-dependent but included noncontrast CT brain and CTA; use of perfusion varied. MR imaging was not performed routinely before intervention. Decision-making evolved to a parallel model with neurology and neurointervention teams attending every code stroke, with the

decision for IV-tPA and/or MT made collaboratively. MT was performed with the patient under general anesthetic using stent retriever a or suction techniques, with use of balloon-guide catheters and/or distal-access catheters per operator preference.

Data Collection

This was a retrospective analysis of a prospectively collected audit data base encompassing all cases at all 3 hospitals. Adult patients treated between September 2010 and October 2017 with MT for an intracranial PLVO were included. Demographics collected include age, sex, and time of onset (or wake-up/unknown-onset). Clinical parameters collected included the Glasgow Coma Scale (GCS) score on presentation, and whether IV-tPA was administered. Imaging was reviewed, and the extent of infarction on pretreatment noncontrast brain CT was graded per the posterior circulation ASPECTS (PC-ASPECTS) score.[16] The presence of posterior communicating arteries and the level of occlusion were assessed on CTA; if this assessment was not possible, information was sought on treatment angiography. Thrombectomy-related data included the initial modified TICI (I-mTICI) score, final modified TICI score (F-mTICI; both with modified TICI [mTICI] 3 defined by the entire basilar territory), and time of recanalization. Safety data recorded included procedural complications, separated into clinically relevant or technical (intracranial perforation/extravasation, nonterritory embolism, or vessel dissection), imaging complications on routine day 1 noncontrast brain CT (subarachnoid/intraparenchymal hemorrhage, subdivided into symptomatic/asymptomatic), and clinically relevant access complications (vascular occlusion, percutaneous thrombin treatment, transfusion, or surgical repair). The 3-month mRS score was determined at routine 3-month outpatient clinic. The primary end point was defined as functional independence, which was defined as a 3-month mRS of $\leq$2. The diagnosis for the cause of stroke (cardiogenic, intracranial/extracranial atheroma, dissection, paradoxical, iatrogenic, or otherwise) was recorded. Missing data were retrieved from medical records and the PACS.

Statistical Analysis

Descriptive data are presented using means/SDs, median/interquartile ranges, and frequency/percentage as appropriate. The relationship between mRS and predictors of interest (time to recanalization, GCS, IV-tPA, sex, age, and PC-ASPECTS) was considered using univariable and multivariable logistic regression models. The multivariable model was developed using backward elimination, and $P < .05$ was used to determine predictor inclusion in the model. The association between mRS and F-mTICI (dichotomized as 0–2a versus 2b–3) was assessed using the Fisher exact test because this variable perfectly predicts the mRS and therefore a logistic model cannot be fitted. Similarly, the relationship between mRS and I-mTICI was considered with the Fisher test because of the small sample size in the 2b–3 group. The sensitivity, specificity, and area under the curve for significant predictors of interest were determined using a cutoff value that produced the maximum product of sensitivity and specificity in predicting the primary end point.[17] The probability cutoff from the final multivariable model was determined in the same way and was used to assess the prediction performance of this model. A bootstrap procedure (with 100 repetitions) was used to determine the 95% confidence interval for these cut-points. All analyses were conducted using STATA, Version 15.0 (StataCorp, College Station, Texas), and $P < .05$ was considered significant.

The study was reviewed and approved by the local institutional review board for audit processes (Governance Evidence Knowledge Outcomes [GEKO] System, Department of Health, Western Australia).

RESULTS

Seventy-nine cases were recorded; 6 patients were excluded due to incomplete follow-up data. Of the 73 remaining, 26 patients (35.62%) were women. Ages ranged from 18 to 92 years (mean, 64.11 $\pm$ 15.51 years). The time of onset of stroke was unknown in 14 patients (19.18%), and the median presentation GCS was 10 (interquartile range, 8). A breakdown of presentation PC-ASPECTS, posterior communicating artery status, and level of occlusion is given in Table 1. IV-tPA was administered in 11/73 patients (15.07%). I-mTICI 0 was seen in 66/73 (90.41%); F-mTICI $\geq$ 2b was achieved in 63 (86.30%). Further breakdown is provided in Table 1. The median total time of ictus to recanalization was 6.5 hours (interquartile range, 8.2 hours).

The procedural complication rate was 4.11% (3.80% when including 6 patients with missing 3-month data); this consisted of 2 cases of perforation, and 1 technical complication (dissection) that was non-flow-limiting and did not contribute to patient deterioration.

Postprocedurally, there were 2 cases of new symptomatic intraparenchymal hemorrhage (considered natural history), 1 symptomatic SAH (1 of the perforations), and 1 of access complication requiring both percutaneous thrombin injection and blood transfusion, for a delayed complication rate of 5.48% (5.06% when including 6 patients with missing 3-month data). Final outcomes are listed in the On-line Table.

At 3-month follow-up, 25 patients (34.25%) reached the primary end point (mRS $\leq$ 2). The most common cause for PLVO was cardiogenic with 26/73 cases (35.62%), followed by intracranial atheroma in 20 (27.40%); details are provided in Table 2. Twenty-five patients (34.25%) died.

GCS, PC-ASPECTS, and age were found to be significant predictors (Table 3). Presenting with a GCS of >13 meant that the odds of reaching the primary end point were 5.70 times greater; similarly, presenting with a PC-ASPECTS of >9 resulted in the odds of reaching the primary end point being 4.03 times greater. No cut-point could be found for age. These are also significant on the multivariable model; a predicted probability of 0.32 (95% CI, 0.18–0.46) has a sensitivity of 0.83 (95% CI, 0.61–0.95) and specificity of 0.71 (95% CI, 0.55–0.84) for mRS $\leq$ 2. This produces an area under the receiver operating characteristic curve of 0.77 (95% CI, 0.55–0.84). Details are listed in Table 4. No correlation was seen for IV-tPA, sex, or time from ictus to recanalization (Table 3). F-mTICI $\geq$ 2b was significant for predicting mRS $\leq$ 2, whereas I-mTICI was not (Table 5). Given the difficulty in meaningfully categorizing the level of occlusion and the robustness of the posterior communicating arteries, the frequencies were found

Table 1: Initial and final mTICI for the 73 patients with complete data

Category	No. (%)
Level of occlusion	
RVA, no LVA	2
RVA, small LVA	1
RVA, large LVA	0
LVA, no RVA	0
LVA, small RVA	1
LVA, large RVA	0
Bilateral VA	1
Lower basilar trunk	22
Upper basilar trunk	9
Basilar apex	29
RPCA	2
LPCA	5
Bilateral PCA	1
PC-ASPECTS	
10	23
9	8
8	14
7	10
6	5
5	2
4	1
3	1
2	0
1	0
0	0
No data	9
PcomA	
None	30
1, <1 mm	9
1, ≥1 mm	4
2, both <1 mm	7
2, 1 <1 mm; 1 ≥1 mm	9
2, both ≥1 mm	12
No data	2
I-mTICI	
0	66 (90.41)
1	5 (6.85)
2b	1 (1.37)
2c	1 (1.37)
F-mTICI	
0	6 (8.22)
1	3 (4.11)
2a	1 (1.37)
2b	20 (27.40)
2c	7 (9.59)
3	36 (49.32)
F-mTICI ranges	
0–2a	10 (13.70)
2b–3	63 (86.30)

Note:—PcomA indicates posterior communicating artery; RVA, right vertebral artery; LVA, left vertebral artery; VA, vertebral artery; RPCA, right posterior cerebral artery; LPCA, left posterior cerebral artery; PCA, posterior cerebral artery.

to be too small to model; however, a breakdown is provided in Table 1.

For completeness, in the 6 patients who had incomplete follow-up data, 2 were women. All presented with an I-mTICI of 0. F-mTICI consisted of 0 ($n = 1$), 2a ($n = 2$), 2b ($n = 1$), and 3 ($n = 2$). Causes of stroke were cardiogenic ($n = 1$), extracranial atheroma ($n = 1$), iatrogenic ($n = 1$), intracranial atheroma ($n = 2$), and unknown ($n = 1$).

Table 2: Final documented causes for posterior circulatory occlusion in the 73 patients with complete data

Cause	No. (%)
Cardiogenic	26 (35.62)
Intracranial atheroma	20 (27.40)
Unknown	9 (12.33)
Dissection	7 (9.59)
Other NOS	5 (6.85)
Iatrogenic	3 (4.11)
Extracranial atheroma	2 (2.74)
Paradoxical	1 (1.37)

Note:—NOS indicates not otherwise specified.

DISCUSSION

With MT, our workflow surrounding patients with stroke has changed to prehospital activation, assessment by multiple specialties, and patient transfer from the ambulance to the emergency department, through imaging, and potentially to the neurointerventional suite. Because of the potential time lost, there is interest in how time may be saved. While complex clinical scores may give an edge to prognostication, even the well-studied NIHSS has not been demonstrated to perform better; Turc et al[18] found, in 1004 patients, that cut-points of NIHSS ≥ 11 and RACE ≥ 5 both achieved accuracies of 79% for large-vessel occlusion, but with the NIHSS only demonstrating a 5% improvement in the false-negative rate (27% versus 33%, respectively) and an inferior false-positive rate (17% versus 15%, respectively). Introducing more scores increases interoperator variability, especially when a mix of junior and senior clinicians is involved, as is the reality of acute stroke care. The additive value of these scores to actual patient care, in this time-sensitive environment, must hence be questioned.

Most studies suggest poorer outcomes for PLVO compared with anterior circulatory large-vessel occlusion,[19,20] but these also generally demonstrate a longer ictus-to-recanalization time. Alawieh et al,[21] however published an analysis of 536 patients in which there was no significant difference in onset-to-groin times between anterior and posterior circulation thrombectomies (or procedural times) and correlating equivalent functional outcomes. Although we did not find an association between ictus to recanalization and outcome, the above study continues to reinforce the need to minimize time lost.

Our results are notable in that favorable GCS and PC-ASPECTS scores predict significant odds of functional independence. GCS demonstrated a trend toward significance in an earlier article by Mourand et al,[22] albeit with a smaller population of 31 patients. The GCS has been considered a biomarker for outcome previously; however, in these studies it was either used in a different timeframe, in patients treated without thrombolysis or thrombectomy, solely with thrombolysis, or with outdated devices such as the Merci Retriever System (Concentric Medical, Mountain View, CA),[23-25] all of which have little relevance to modern thrombectomy. The relevance of established infarct at presentation to outcome is self-explanatory, but the cut-point of >9 suggests that any established infarction is clinically relevant. While a cut-point for age could not be established, for each year of increasing age, a 3%–5%

Table 3: Univariable and multivariable odds ratios for the association between each predictor variable and binary mRS (where mRS >2 is the reference group)

Predictor	No.	Univariable OR	95% CI	*P*	Multivariable OR[a]	95% CI	*P*
Time to recanalization	67	1.01	–0.99–1.03	.37			
GCS	73	1.18	1.04–1.33	.01	1.21	1.04–1.42	.001
IV-tPA							
No	62	1.00					
Yes	11	1.12	0.29–4.25	.87			
Sex							
F	26	1.00					
M	47	1.28	0.46–3.55	.64			
Age (yr)	73	0.97	0.94–1.00	.04	0.96	0.92–1.00	.05
PC-ASPECTS	64	1.66	1.12–2.47	.01	1.77	1.14–2.73	.01

[a] OR from the final model multivariable model ($n = 64$).

Table 4: Univariable odds ratios, sensitivities, specificities, and area under ROC curves for the association between each predictor variable and binary mRS (where mRS >2 is the reference group)

Predictor	Positive Group	OR (95% CI)	Sensitivity (95% CI)	Specificity (95% CI)	AUC (95% CI)
GCS	GCS > 13	5.70 (1.97–16.47)	0.60 (0.39–0.79)	0.79 (0.65–0.90)	0.70 (0.58–0.81)
PC-ASPECTS	>9	4.03 (1.36–11.98)	0.57 (0.35–0.77)	0.76 (0.60–0.88)	0.66 (0.54–0.78)
Age (yr)	<68.5	1.50 (0.56–4.07)[a]	0.64 (0.43–0.82)	0.46 (0.31–0.61)	0.55 (0.43–0.69)
Multivariable model	Pr <0.32	11.48 (3.22–40.91)	0.83 (0.61–0.95)	0.71 (0.55–0.84)	0.77 (0.55–0.84)

Note:—AUC indicates area under the curve; Pr, predicted probability from the model; ROC, receiver operating characteristic.
[a] Not significant.

Table 5: Cross-tabulation and χ^2 analyses for the association between mRS (0–2 vs 3–6) and binary mTICI measures in the 73 patients with complete data

	mRS		
	0–2	3–6	*P*[1]
F-mTICI			
0–2a	0	10	
2b–3	25	38	.01
I-mTICI			
0-2a	24	47	
2b–3	1	1	.63

decrease in the odds of mRS ≤ 2 is also expected and confirms the long-reported association of age with outcome in stroke.[9,26,27] A F-mTICI ≥ 2b was also significant for mRS ≤ 2, similar to other studies for the posterior circulation, confirming the importance of reperfusion, similar to that in the anterior circulation.[3,28] Our outcomes for mTICI ≥ 2b (86.30%) and mRS ≤ 2 (34.25%) are comparable with those in other articles specifically assessing endovascular treatment of basilar artery occlusion[9,10,28-30] and on the lower end of reported mortality rates of 25%–47%.[10,29]

Our study has a number of limitations. First, the nature of this single-service cohort means that there is self-adjudication. Second, patient numbers analyzed remained low; however, this finding reflects the lower proportion of PLVO as a part of stroke presentations overall. This number has affected some of our analyses, such as our ability to analyze the effect of the level of occlusion and the robustness of collaterals; however, we resisted the urge to further group these because doing so would create categories that share little clinical similarity. Third, there is heterogeneity in our prehospital process, in-hospital management, and endovascular therapy during the 7-year data collection, but this reflects the real-life evolution of treatment. It is possible that current outcomes may be better. Last, we did not seek to assess a broader range of clinical parameters such as serum glucose level, medical history, anticoagulation and other medications, and, of course, the NIHSS and hence could not include these in the analysis. However, this feature reflects the reality of endovascular stroke care: Much of the information above may not be immediately available at time of decision making.

CONCLUSIONS

Our study suggests that the presentation GCS, a rapidly calculated and well-understood clinical score for all clinician groups and seniorities, has correlation with patient outcome after posterior circulation MT. Absence of an identifiable infarction on presentation CT portends a better prognosis. We also confirm that functional independence is affected by recanalization and age.

Given the poor outcome of untreated PLVO, there is a tendency to treat patients regardless of presentation status and at longer timeframes. While this practice theoretically gives the patient the best possible chance of recovery, if through future research a point of futility can be established, then better use of health care resources can be established. The result of our study furthers this aim and, in the meantime, may give some guidance to clinical decision-making and informed consent.

Disclosures: Dana A. Hince—*RELATED*: *Grant*: Sir Charles Gairdner Hospital, *Comments*: The institute I work for has a tendered agreement with Sir Charles Gairdner Hospital to provide statistical support/data analysis to employees of that institution. My income is not dependent on this source, and I have received no money for the work I completed for this article.* *Money paid to the institution.

REFERENCES

1. Campbell BC, Mitchell PJ, Kleinig TJ, et al; EXTEND-IA Investigators. **Endovascular therapy for ischemic stroke with perfusion-imaging selection.** *N Engl J Med* 2015;372:1009–18 CrossRef Medline

2. Berkhemer OA, Fransen PS, Beumer D, et al; MR CLEAN Investigators. **A randomized trial of intraarterial treatment for acute ischemic stroke.** *N Engl J Med* 2015;372:11–20 CrossRef Medline
3. Goyal M, Demchuk AM, Menon BK, et al; ESCAPE Trial Investigators. **Randomized assessment of rapid endovascular treatment of ischemic stroke.** *N Engl J Med* 2015;372:1019–30 CrossRef Medline
4. Saver JL, Goyal M, Bonafé A, et al; SWIFT PRIME Investigators. **Stent-retriever thrombectomy after intravenous t-PA vs. t-PA alone in stroke.** *N Engl J Med* 2015;372:2285–95 CrossRef Medline
5. Jovin TG, Chamorro A, Cobo E, et al; REVASCAT Trial Investigators. **Thrombectomy within 8 hours after symptom onset in ischemic stroke.** *N Engl J Med* 2015;372:2296–2306 CrossRef Medline
6. Bracard S, Ducrocq X, Mas JL, et al; THRACE investigators. **Mechanical Thrombectomy After Intravenous Alteplase versus Alteplase Alone after Stroke (THRACE): a randomised controlled trial.** *Lancet Neurol* 2016;15:1138–47 CrossRef Medline
7. Nagel S, Kellert L, Möhlenbruch M, et al. **Improved clinical outcome after acute basilar artery occlusion since the introduction of endovascular thrombectomy devices.** *Cerebrovasc Dis* 2013;36:394–400 CrossRef Medline
8. Schonewille WJ, Wijman CA, Michel P, et al; BASICS study group. **Treatment and outcomes of acute basilar artery occlusion in the Basilar Artery International Cooperation Study (BASICS): a prospective registry study.** *Lancet Neurol* 2009;8:724–30 CrossRef Medline
9. Singer OC, Berkefeld J, Nolte CH, et al; ENDOSTROKE Study Group. **Mechanical recanalization in basilar artery occlusion: the ENDOSTROKE study.** *Ann Neurol* 2015;77:415–24 CrossRef Medline
10. Luo G, Mo D, Tong X, et al. **Factors associated with 90-day outcomes of patients with acute posterior circulation stroke treated by mechanical thrombectomy.** *World Neurosurg* 2018;109:e318–28 CrossRef Medline
11. Inoa V, Aron AW, Staff I, et al. **Lower NIH stroke scale scores are required to accurately predict a good prognosis in posterior circulation stroke.** *Cerebrovasc Dis* 2014;37:251–55 CrossRef Medline
12. Heldner MR, Zubler C, Mattle HP, et al. **National Institutes of Health stroke scale score and vessel occlusion in 2152 patients with acute ischemic stroke.** *Stroke* 2013;44:1153–57 CrossRef Medline
13. Schneck MJ. **Current stroke scales may be partly responsible for worse outcomes in posterior circulation stroke.** *Stroke* 2018;49:2565–66 CrossRef Medline
14. Olivato S, Nizzoli S, Cavazzuti M, et al. **e-NIHSS: an expanded National Institutes of Health Stroke Scale weighted for anterior and posterior circulation strokes.** *J Stroke Cerebrovasc Dis* 2016;25:2953–57 CrossRef Medline
15. Pérez de la Ossa N, Carrera D, Gorchs M, et al. **Design and validation of a prehospital stroke scale to predict large arterial occlusion: the rapid arterial occlusion evaluation scale.** *Stroke* 2014;45:87–91 CrossRef Medline
16. Puetz V, Sylaja PN, Coutts SB, et al. **Extent of hypoattenuation on CT angiography source images predicts functional outcome in patients with basilar artery occlusion.** *Stroke* 2008;39:2485–90 CrossRef Medline
17. Liu X. **Classification accuracy and cut point selection.** *Stat Med* 2012;31:2676–86 CrossRef Medline
18. Turc G, Maïer B, Naggara O, et al. **Clinical scales do not reliably identify acute ischemic stroke patients with large-artery occlusion.** *Stroke* 2016;47:1466–72 CrossRef Medline
19. Alonso de Leciñana M, Kawiorski MM, Ximénez-Carrillo Á, et al; Madrid Stroke Network. **Mechanical thrombectomy for basilar artery thrombosis: a comparison of outcomes with anterior circulation occlusions.** *J Neurointerv Surg* 2017;9:1173–78 CrossRef Medline
20. Serles W, Gattringer T, Mutzenbach S, et al; Austrian Stroke Unit Registry Collaborators. **Endovascular stroke therapy in Austria: a nationwide 1-year experience.** *Eur J Neurol* 2016;23:906–11 CrossRef Medline
21. Alawieh A, Vargas J, Turner RD, et al. **Equivalent favorable outcomes possible after thrombectomy for posterior circulation large vessel occlusion compared with the anterior circulation: the MUSC experience.** *J Neurointerv Surg* 2018;10:735–40 CrossRef Medline
22. Mourand I, Machi P, Milhaud D, et al. **Mechanical thrombectomy with the Solitaire device in acute basilar artery occlusion.** *J Neurointerv Surg* 2014;6:200–04 CrossRef Medline
23. Mansour OY, Megahed MM, Elghany E. **Acute ischemic stroke prognostication, comparison between Glasgow Coma Score, NIHS Scale and Full Outline of UnResponsiveness Score in intensive care unit.** *Alexandria Journal of Medicine* 2015;51:247–53 CrossRef
24. Tsao JW, Hemphill JC, Johnston SC, et al. **Initial Glasgow Coma Scale score predicts outcome following thrombolysis for posterior circulation stroke.** *Arch Neurol* 2005;62:1126–29 CrossRef Medline
25. Chandra RV, Law CP, Yan B, et al. **Glasgow Coma Scale does not predict outcome post-intra-arterial treatment for basilar artery thrombosis.** *AJNR Am J Neuroradiol* 2011;32:576–80 CrossRef Medline
26. Nakayama H, Jørgensen HS, Raaschou HO, et al. **The influence of age on stroke outcome: the Copenhagen Stroke Study.** *Stroke* 1994;25:808–13 CrossRef Medline
27. Greving JP, Schonewille WJ, Wijman CA, et al; BASICS Study Group. **Predicting outcome after acute basilar artery occlusion based on admission characteristics.** *Neurology* 2012;78:1058–63 CrossRef Medline
28. Mokin M, Sonig A, Sivakanthan S, et al. **Clinical and procedural predictors of outcomes from the endovascular treatment of posterior circulation strokes.** *Stroke* 2016;47:782–88 CrossRef Medline
29. Bouslama M, Haussen DC, Aghaebrahim A, et al. **Predictors of good outcome after endovascular therapy for vertebrobasilar occlusion stroke.** *Stroke* 2017;48:3252–57 CrossRef Medline
30. Gory B, Eldesouky I, Sivan-Hoffmann R, et al. **Outcomes of stent retriever thrombectomy in basilar artery occlusion: an observational study and systematic review.** *J Neurol Neurosurg Psychiatry* 2016;87:520–25 CrossRef Medline

Is Histologic Thrombus Composition in Acute Stroke Linked to Stroke Etiology or to Interventional Parameters?

J. Goebel, B.-J. Gaida, I. Wanke, C. Kleinschnitz, M. Koehrmann, M. Forsting, C. Moenninghoff, A. Radbruch, and A. Junker

ABSTRACT

BACKGROUND AND PURPOSE: Detailed insight into the composition of thrombi retrieved from patients with ischemic stroke by mechanical thrombectomy might improve pathophysiologic understanding and therapy. Thus, this study searched for links between histologic thrombus composition and stroke subtypes and mechanical thrombectomy results.

MATERIALS AND METHODS: Thrombi from 85 patients who had undergone mechanical thrombectomy for acute ischemic stroke between December 2016 and March 2018 were studied retrospectively. Thrombi were examined histologically. Preinterventional imaging features, stroke subtypes, and interventional parameters were re-analyzed. Statistical analysis was performed with the Kruskal-Wallis test, Mann-Whitney *U* test, or Spearman correlation as appropriate.

RESULTS: Cardioembolic thrombi had a higher percentage of macrophages and a tendency toward more platelets than thrombi of large-artery atherosclerotic stenosis ($P = .021$ and .003) or the embolic stroke of undetermined source ($P = .037$ and .099) subtype. Thrombi prone to fragmentation required the combined use of contact aspiration and stent retrieval ($P = .021$) and were associated with an increased number of retrieving maneuvers ($P = .001$), longer procedural times ($P = .001$), and a higher lymphocyte content ($P = .035$).

CONCLUSIONS: We interpreted the higher macrophage and platelet content in cardioembolic thrombi compared with large-artery atherosclerotic stenosis or embolic stroke of undetermined source thrombi as an indication that the latter type might be derived from an atherosclerotic plaque rather than from an undetermined cardiac source. The extent of thrombus fragmentation was associated with a more challenging mechanical thrombectomy and a higher lymphocyte content of the thrombi. Thus, thrombus fragmentation not only might be caused by the recanalization procedure but also might be a feature of a lymphocyte-rich, difficult-to-retrieve subgroup of thrombi.

ABBREVIATIONS: ESUS = embolic stroke of undetermined source; H&E = hematoxylin-eosin; LAA = large-artery atherosclerotic stenosis; MT = mechanical thrombectomy; mTICI = modified TICI; RBC = red blood cells; WBC = white blood cells

The demonstrated efficacy of the endovascular therapeutic approach to the occlusion of large vessels in the anterior circulation initiated a fundamental change in stroke therapy. This currently consists of the combination of thrombolysis with intravenous rtPA and mechanical endovascular thrombectomy (MT).[1-6]

With the increasing performance of MT to extract the occluding thrombus, more thromboembolic material has become available for further analysis. Several studies of thrombus composition in acute ischemic stroke have been published, but a comparison of their data is difficult because of a lack of standardization, often with conflicting results.[7,8] In addition, only a small number of thrombi have been investigated, often with no differentiation between fibrin and platelets or among the different subtypes of white blood cells (WBC). Therefore, the current study searched for the following: 1) histologic differences between the different stroke subtypes with regard to thrombus composition—that is, the proportions of fibrin, platelets, red blood cells (RBC), WBC, macrophages, lymphocytes, and granulocytes and the extent of thrombus fragmentation; and 2) correlations between thrombus composition and the parameters of the MT.

MATERIALS AND METHODS

Patients presenting at our center with acute ischemic stroke between December 2016 and March 2018 were recruited for MT and subsequent statistical analysis with the approval of the local

Received August 15, 2019; accepted after revision January 24, 2020.

From the Departments of Diagnostic and Interventional Radiology and Neuroradiology (J.G., I.W., M.F., C.M., A.R.) and Neuropathology (A.J.), and Clinic of Neurology (C.K., M.K.), University Hospital Essen, Essen, Germany; and Neuroradiological Centre (B.-J.G.), Clinic Hirslanden, Zurich, Switzerland.

Please address correspondence to Juliane Goebel, MD, Department of Diagnostic and Interventional Radiology and Neuroradiology, University Hospital Essen, Hufelandstr 55, 45147 Essen, Germany; e-mail: Juliane.Goebel@uk-essen.de

Indicates article with supplemental on-line table.

Indicates article with supplemental on-line photos.

http://dx.doi.org/10.3174/ajnr.A6467

Table 1: Antibodies and staining procedures

Antigen	Source	Pretreatment	Dilution
CD68 (Ki-M1P)	Dr Klapper, Institute for Pathology, Kiel, Germany	None	1:10,000
CD45 (LCA) (mouse monoclonal, 2B11 + PD7/26)	Dako, Hamburg, Germany	Citrate	1:1000

Note:—LCA indicates leukocyte common antigen.

ethics committee of the medical faculty of the university Duisburg-Essen, Germany.

A total of 136 consecutive patients underwent MT during this period (On-line Fig 1). Patients from whom thrombotic material suitable for histopathologic analysis was obtained during MT were included in the further analysis. Patient characteristics were extracted from the electronic medical records. The subtypes of ischemic stroke were classified according to Hart.[9]

Preinterventional Imaging

Unenhanced brain CT and contrast-enhanced CTA of the supra-aortic brain-supplying arteries (Somatom Definition Flash or Definition AS+ scanner; Siemens, Erlangen, Germany) were performed in all patients either in our center or in the referring hospital. All available unenhanced brain CT scans were retrospectively re-analyzed for the presence or absence of the dense artery sign, for thrombus density calculated as the average of 2 Hounsfield unit measurements in the occlusion indicated by CTA and/or the dense artery sign, and for early ischemic changes according to the ASPECTS in cases of middle cerebral artery ischemia.[10]

Mechanical Thrombectomy

MT using an aspiration catheter and/or a stent retriever was performed with the patient under general anesthesia in a biplanar DSA system (Allura Xper FD20; Philips Healthcare, Best, the Netherlands). By means of the Seldinger technique, a guiding catheter was inserted transfemorally, the large vessel proximal to the suspected occlusion was probed, and selective DSA was performed using Ultravist 300 as contrast agent (iopromide; Bayer HealthCare, Berlin, Germany). After identification of the arterial occlusion, a distal access or aspiration catheter was introduced coaxially (5F Sofia distal access catheter or 6F Sofia Plus aspiration catheter, MicroVention, Aliso Viejo, California; 3MAX/4MAX/5MAX or ACE 64 reperfusion catheter, Penumbra, Alameda, California) over a microwire (Traxcess14, MicroVention; Transend EX, Stryker, Kalamazoo, Michigan) and, if possible, docked onto the thrombus. Subsequently, direct contact thrombus aspiration was performed using a VacLok syringe (Merit Medical, South Jordan, Utah). If recanalization was not sufficient, the aspiration maneuver was repeated or, as an alternative, a stent retriever (Solitaire FR, Medtronic, Minneapolis, Minnesota; Trevo XP Provue System, Stryker; EmboTrap II Revascularization Device, Cerenovus, Galway, Ireland; Separator 3D System, Penumbra) was inserted, positioned in the thrombus, and 1 or multiple stent-retrieving maneuvers were then performed under constant aspiration. The thrombi were collected in a sterile manner, and those thrombi suitable for histopathologic analysis were immediately preserved in formalin. The records of the endovascular procedures were re-analyzed for interventional parameters, including the time interval between stroke onset and MT, the duration of MT, the endovascular devices/technique used, the number of retrieving maneuvers, and interventional complications. The achieved global recanalization success was quantified using the modified TICI (mTICI) scale.[11]

Histology and Immunohistochemistry

All investigations were performed on 1-μm sections. Histochemical and immunohistochemical staining was used to determine the quantitative composition of the thrombi. The stains used were hematoxylin-eosin (H&E) for RBC (appears reddish), Ladewig trichrome stain for fibrin deposits (appears brick red), Elastica van Gieson stain for collagen fibers (appears reddish), Von Kossa stain for calcifications (stains black, On-line Fig 2), naphthol AS-D chloroacetate stain for granulocytes (detected by their esterase content, On-line Fig 3), and Prussian blue staining for iron ions in siderophages. In addition, immunohistochemical staining for CD68 (positive for Ki-M1P, macrophages, and activated platelets, their size allowing exact quantification) and for CD45 (positive for leukocyte common antigen and lymphocytes) was performed (On-line Fig 3). Pretreatments and antibody dilutions were performed as described in Table 1. In brief, the endogenous peroxidase activity was first blocked by incubating the sections in 3% H_2O_2 in phosphate-buffered saline. This step was followed by a blocking step with 10% fetal calf serum in phosphate-buffered saline for 10 minutes at room temperature, followed by incubation with the primary antibody for 1 hour at room temperature. The sections were then incubated with the secondary antibody (biotin-labeled antibody). Because the sections were stained using the Dako-Autostainer-Plus (Agilent Technologies, Santa Clara, California), the ZytoChemPlus horseradish peroxidase polymer system (mouse/rabbit) (REF:POLHRP-100, Dako, Hamburg, Germany) was used for detection. Cell nucleus counterstaining was performed with hematoxylin.

The stained sections were digitized using a Leica slide scanner (Leica Biosystems, Wetzlar, Germany). From the scanned files, either the whole thrombus area (H&E for RBC quantification, Ladewig trichrome for fibrin quantification) or the whole thrombus area divided into subareas with an edge length of 1000 μm (CD68 for monocytes/macrophages and activated platelets, CD45 for leukocytes) was extracted and analyzed using ImageJ software (National Institutes of Health, Bethesda, Maryland).[12] After we adjusted the hue, saturation, and brightness, we adjusted the "color threshold" so that colored particles or colored areas could be determined using the "Analyze Particles" function in ImageJ.[13] Regions with densely packed RBC or platelets and areas of dense fibrin deposition were included in the evaluation as coherent areas (On-line Fig 4).

The applied staining methods also allowed an age estimation of the thrombi. Because the Prussian blue stain,

Table 2: Baseline characteristics and preinterventional imaging results of the studied patients[a]

Characteristics and Results	
Total No. of patients	85
Sex (No.)	37 Men/48 women
Age (yr)	72.0 ± 12.9
Vascular risk factors (No.) (multiple choices possible)	
Atrial fibrillation	50 (58.8%)
Hypertension	70 (82.4%)
Diabetes	24 (28.2%)
High blood cholesterol levels	53 (62.4%)
Smoking	19 (22.4%)
Excessive alcohol intake	1 (1.2%)
Obesity	7 (8.2%)
Heart disease other than atrial fibrillation	44 (51.8%)
Patients with previous ischemic stroke (No.)	18 (21.2%)
Subtypes of ischemic stroke (No.)	
Major-risk source cardiogenic embolism	51 (60.0%)
Large-artery atherosclerotic stenosis	16 (18.8%)
ESUS	17 (20.0%)
Unusual (eg, dissection)	1 (1.2%)
Initial NIHSS score	13 (0–28)
Initial stroke imaging (No.)	
CT	83
DSA	2
Occlusion site (No.)	
Internal carotid artery (intracranial)	28 (32.9%)
MCA, M1 segment	36 (42.4%)
MCA, M2 segment	10 (11.8%)
Basilar artery	9 (10.6%)
Anterior cerebral artery	1 (1.2%)
Posterior cerebral artery	1 (1.2%)
Dense artery sign ($n = 71$ patients)[b]	43 (60.6%)
Mean thrombus attenuation (HU) (67 patients)[b]	58 (41–149)
Initial ASPECTS (in MCA ischemia; $n = 64$ patients)[b]	10 (3–10)
Patients given IV tPA (No.)	52 (61.2%)
OTT ($n = 56$ patients) (min)[b]	172 (96–782)

Note:—OTT indicates time interval between symptom onset and start of thrombectomy.
[a] Data are given as number (percent of total), mean ± SD, or median (range).
[b] Data were not available from all 85 patients (On-line Table 1).

indicating iron ions in siderophages, turns positive approximately 72 hours after coagulation, the absence of any blue coloration indicated a thrombus age of <72 hours. In addition, the intermingling of thrombi with collagen fibers, reddish in Elastica van Gieson staining, would argue for their reorganization, a finding that does not occur in fresh thrombi (<72 hours) (On-line Fig 2). Furthermore, calcifications (visualized by the Von Kossa staining) are not found in fresh thrombi (On-line Fig 2).

The areas occupied by fibrin, platelets, RBC, and WBC (including macrophages, lymphocytes, and granulocytes) were quantified as percentages. Furthermore, we investigated the presence of siderophages, collagen fibers, calcifications, and the number of histologic fragments of the thrombi.

Statistical Analysis

Statistical analysis was performed with the SPSS software package (Version 25.0; IBM, Armonk, New York). Normal distribution was determined with the Kolmogorov-Smirnov test. Data are given as frequency counts and percentage values, medians and ranges, and means and SDs, as appropriate. The Kruskal-Wallis test was used to evaluate overall group differences between stroke subtypes in thrombus composition (fibrin, platelets, RBC, WBC, macrophages, lymphocytes, granulocytes, number of thrombus fragments). In case of significant overall group differences, pair-wise comparisons of stroke subtypes were performed with the Kruskal-Wallis 1-way ANOVA for multiple samples with a Bonferroni correction. To investigate a possible influence of thrombus composition on MT, we performed a Kruskal-Wallis test (with post hoc Bonferroni correction for the second step of analysis) or a Spearman rank correlation analysis, as appropriate. Finally, a Mann-Whitney *U* test was used to determine whether rtPA administration resulted in differences in fibrin content or fragmentation of the thrombi. A *P* value < .05 was considered statistically significant.

RESULTS

Patients, Preinterventional Imaging, and Interventional Parameters

In 2 of the 136 initially recruited consecutive patients with acute ischemic stroke selected for MT, intravenous rtPA completely dissolved the occluding thrombi (On-line Fig 1). In the remaining 134 patients, MT failed in 25 patients (mTICI 0 in 16 patients, mTICI 1 in 2 patients, and mTICI 2a in 7 patients) and was successful in 109 patients (mTICI 2b in 45 patients and mTICI 3 in 64 patients). In 48 patients, no evaluable thromboembolic material was extracted. Thrombi suitable for histopathologic analysis were retrieved from 86 patients, but 1 of these was excluded due to the use of a nonstandard recanalization technique. Thus 85 patients and their thrombi were included in this study.

Baseline characteristics, subtype of stroke, and preinterventional imaging results of the studied patients are shown in Table 2. Forty-five patients were directly admitted to our center as emergency patients (52.9%), 33 patients (38.8%) were referred to us by other hospitals, 5 patients developed an acute cerebral artery occlusion as in-patients in our hospital (5.9%), and in 2 patients (2.4%), artery occlusion was diagnosed during an angiography. The initial CT was not available for re-analysis in 11 of the patients transferred for MT from other hospitals to our center. Interventional and posttherapeutic parameters, including the duration of MT, global recanalization success, and the ultimately successful

Table 3: Interventional parameters including revascularization rates and data on histopathologic thrombus composition[a]

Parameters	
Duration of thrombectomy (interval between first and last obtained DSA; $n = 83$ patients) (min)[b]	46 (4–260)
Achieved tissue reperfusion (No.)	
mTICI 0	5 (5.9%)
mTICI 1	1 (1.2%)
mTICI 2a	2 (2.4%)
mTICI 2b	34 (40.0%)
mTICI 3	43 (50.6%)
Ultimately successful recanalization technique (No.)	
Aspiration (number of passes, median and range) 2 (1–8)	47 (55.3%)
Stent retrieval (number of passes, median and range) 2 (1–5)	23 (27.1%)
Combined aspiration and stent retrieval (number of passes, median and range) 3 (2–8)	15 (17.6%)
Occurrence of endovascular complications (No.)	19 (22.4%)
Occurrence of symptomatic hemorrhage (No.)	2 (2.4%)
ASPECTS 24 hr postthrombectomy ($n = 73$ patients)[b]	8 (0–10)
NIHSS score at 2–14 days postthrombectomy ($n = 66$ patients)[b]	3 (0–21)
Thrombus components (% from thrombus profile)	
Fibrin	40.9 (2.8–68.2)
Platelets	16.1 (1.9–81.1)
RBC	41.7 (1.2–89.9)
WBC	2.6 (0.4–8.5)
Macrophages	0.7 (0.0–5.2)
Lymphocytes	0.3 (0.0–1.7)
Granulocytes	1.5 (0.0–7.1)
No. of thrombus fragments	8 (2–47)

Note:— DSA indicates digital subtraction angriography.
[a] Data are given as number and percentage or median and range.
[b] Data were not available in all 85 patients (On-line Table 1).

recanalization technique with the number of retrieval maneuvers, are given in Table 3.

Histologic Thrombus Composition

The quantitative contributions of fibrin, platelets, RBC, and WBC to the investigated thrombi are shown in Fig 1. The percentage distribution of the different thrombus components is shown in Table 3. Because blue staining for iron ions in siderophages was always negative and neither calcifications nor collagen fibers were detected, all thrombi were classified as fresh (ie, <3 days old).

Subtypes of Stroke. Because there was just 1 patient with an unusual stroke subtype, statistical comparisons were possible only in cardioembolic, large-artery atherosclerotic stenosis (LAA), and embolic stroke of undetermined source (ESUS) subtypes.

The proportion of macrophages was significantly higher in cardioembolic thrombi (0.9%, 0.1%–3.3%) than in LAA (0.3%, 0.1%–3.8%; $P = .021$) or ESUS thrombi (0.4%, 0.0%–5.2%; $P = .037$; Fig 2). Cardioembolic thrombi contained a higher proportion of platelets (19.1%, 3.6%–81.1%) than LAA thrombi (10.3%, 2.3%–25.1%; $P = .003$) and showed a tendency toward a higher platelet proportion compared with ESUS thrombi (12.2%, 1.9%–39.7%; $P = .099$; Fig 2). LAA and ESUS thrombi did not differ significantly with regard to platelet or macrophage content, nor were other differences in thrombus composition found between stroke subtypes.

Mechanical Thrombectomy. Thrombi retrieved from patients who had received intravenous rtPA contained significantly less fibrin (38.4%, 2.8%–66.4%) than those from patients without rtPA administration (42.4%, 20.1%–68.2%; $P = .027$), whereas no correlation was found between rtPA administration and the extent of thrombus fragmentation. With regard to the ultimately successful recanalization technique, thrombi that could only be retrieved using a combination of contact aspiration and stent retrieval had a significantly smaller proportion of platelets (11.5%, 2.5%–35.3%) than those that were removed by stent retrieval alone (18.4%, 5.2%–39.7%; $P = .034$; Fig 2). Thrombi that were only extractable using the combination technique had a significantly higher number of fragments (13, 3–40) than thrombi extractable by contact aspiration (8, 2–35; $P = .021$) or stent retrieval alone (7, 2–47; $P = .006$; Fig 2). There was a weak correlation between the number of thrombus fragments and the required number of retrieving maneuvers ($r = 0.365$, $P = .001$), procedural time ($r = 0.356$, $P = .001$), and percentage of lymphocytes in the thrombi ($r = 0.229$, $P = .035$).

DISCUSSION

This study showed, first, that cardioembolic thrombi had a higher percentage of macrophages and a trend toward a higher percentage of platelets than thrombi of other stroke subtypes and, second, thrombi presenting as severely fragmented for histologic work-up had a higher lymphocyte content and often required the combined application of contact aspiration and stent retrieval, as well as more retrieving maneuvers and longer procedure times for their removal.

Regarding stroke etiology, we observed a higher percentage of macrophages and a trend toward a higher percentage of platelets in cardioembolic thrombi than in LAA or ESUS thrombi, while there were no such differences between LAA and ESUS stroke-subtype thrombi. We interpreted this finding as an indication that ESUS represents an embolism from an atherosclerotic plaque rather than from an undetermined cardiac embolic source. This is in line with the results of Boeckh-Behrens et al[14] and Sporns et al,[15] who reported higher WBC and fibrin/platelet content in cardioembolic thrombi, and with the findings of Maekawa et al,[16] who reported an association between fibrin-rich thrombi and the cardioembolic stroke subtype, though the latter did not differentiate between fibrin and thrombocytes. The few published studies with small numbers of examined thrombi did not find any association between thrombus composition and stroke subtype.[17-19] In addition, contrary to our results, Kim et al[20] reported a higher

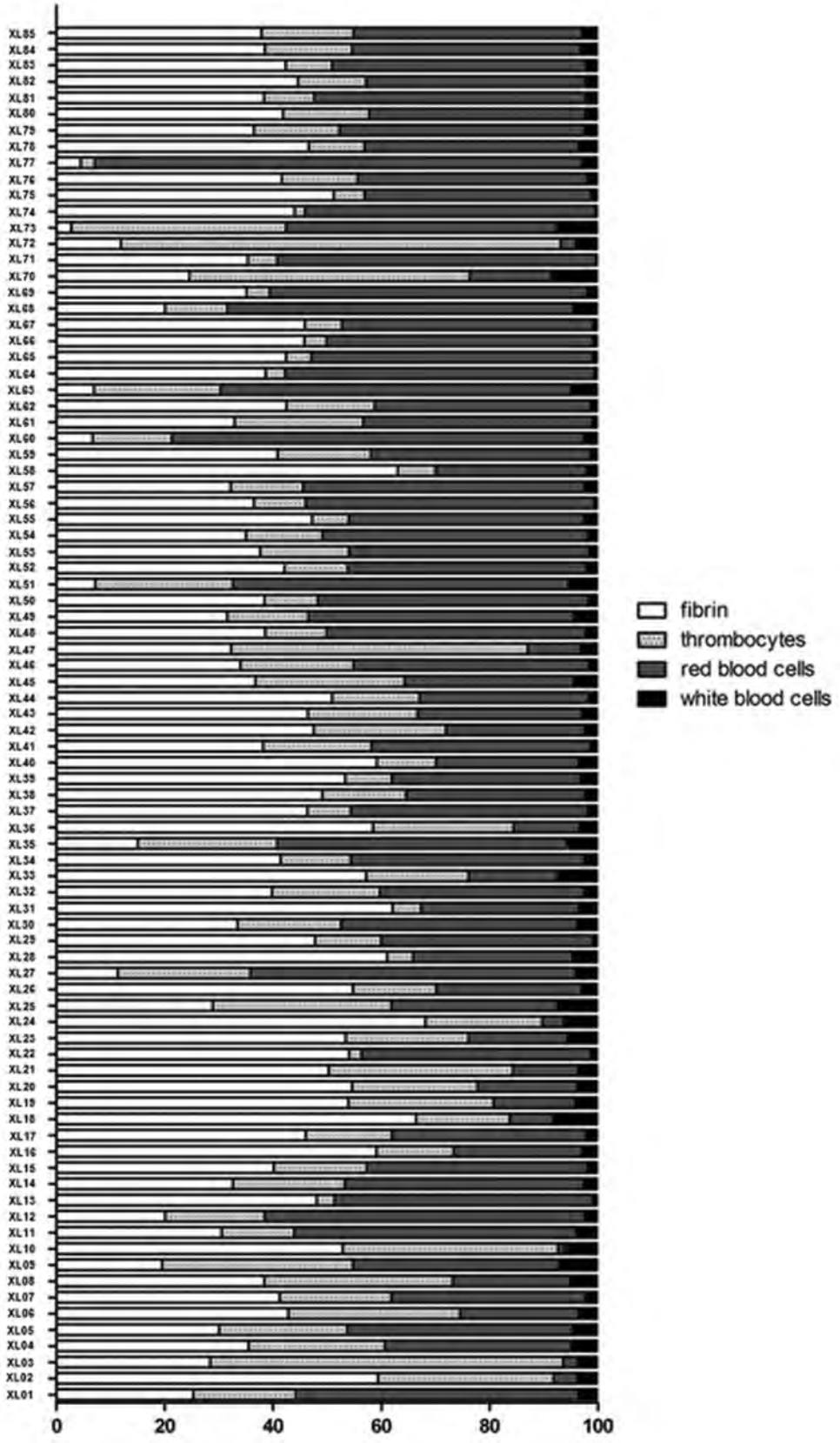

FIG 1. Percentages of the different clot components. Each investigated thrombus is shown in its quantitative composition of fibrin, platelets, red blood cells, and white blood cells (including macrophages, leukocytes, and granulocytes).

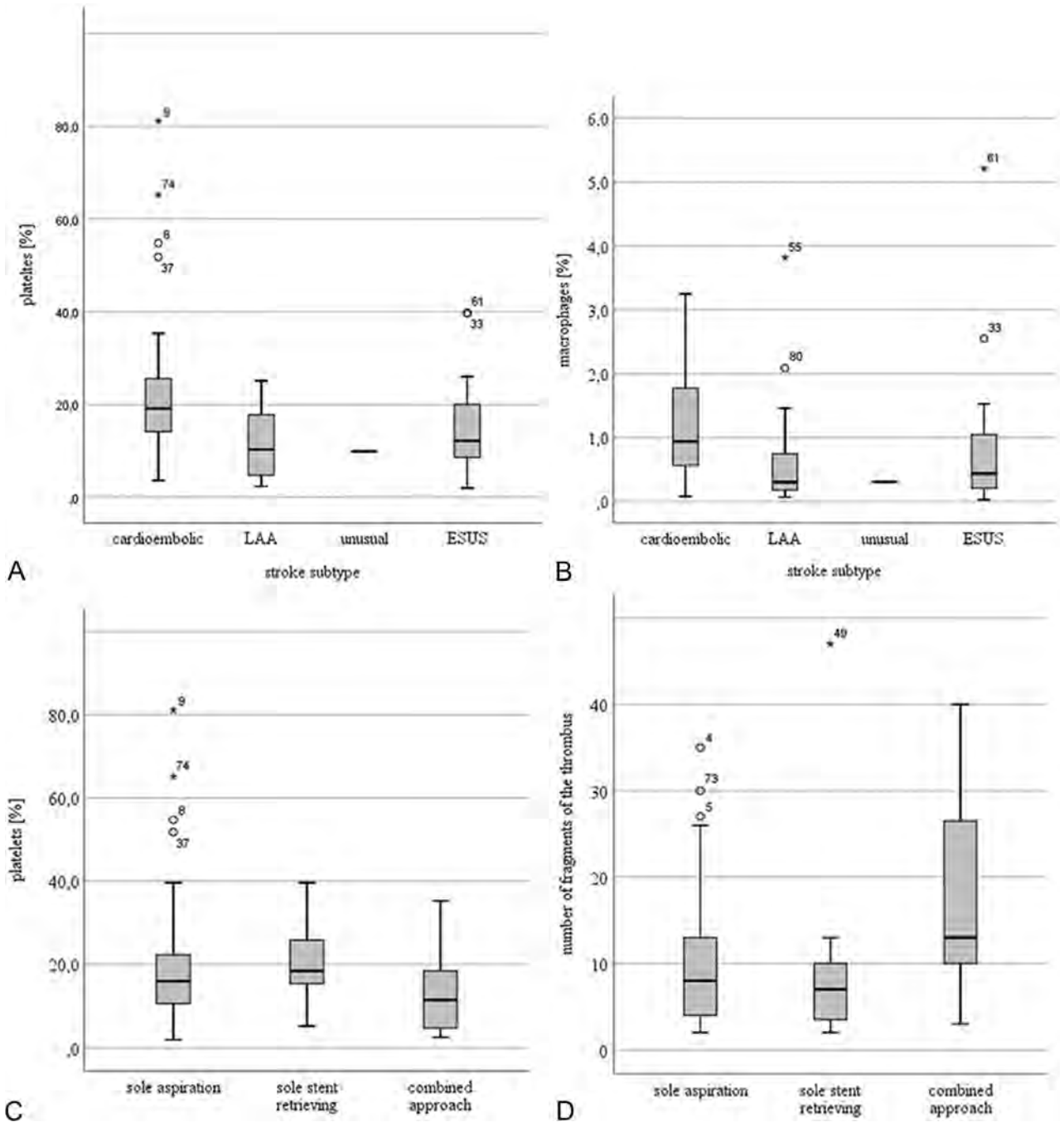

FIG 2. Differences between the different stroke subtypes in the proportions of platelets and macrophages (subunits *A* and *B*) and differences between the individual thrombi in the proportions of platelets and the number of fragments that were ultimately retrieved by contact aspiration alone, stent retrieval alone, or a combination of the 2 techniques (subunits *C* and *D*).

proportion of RBC and a lower proportion of fibrin in cardioembolic thrombi than in LAA thrombi. Nevertheless, because only 8 LAA thrombi were included in their study, its validity might be questionable.

Most interesting, we found significant relationships between thrombus composition and parameters of the MT procedure as described above. This finding raises the following the question: Was, for example, increased thrombus fragmentation caused by the MT procedure itself, because thrombus fragmentation with peripheral embolization is a known complication of MT, or was the tendency of some thrombi to fragment due to their composition?[21] It is possible that thrombi prone to fragmentation are more difficult to remove by MT and require more retrieving maneuvers consecutively, resulting in a longer procedural time. The additionally observed relationship between lymphocyte content and the degree of thrombus fragmentation supports the assumption of a lymphocyte-rich subgroup of thrombi that are susceptible to fragmentation. This would support the hypothesis that the greater extent of thrombus fragmentation was not exclusively due to the recanalization procedure but was, to a certain

degree, an inherent tendency for these thrombi to fragment. Because lymphocytes are known to play a role in thrombus formation,[19] might they not conceivably also make the thrombus more prone to fragmentation? Our findings are partly in line with those of Kaesmacher et al,[22] who reported an association between a higher content of neutrophil granulocytes and increased periprocedural thrombus fragmentation but found no relationship between thrombus stability and the overall WBC content. We found that thrombi that had required the combined approach of contact aspiration and stent retrieval for their extraction had a lower proportion of platelets than those that could be extracted by stent retrieval alone. We are not quite sure how to interpret this finding, and the results of other studies on this topic are of no assistance because they did not differentiate between platelets and fibrin.[16,17,22-24]

Our study has several limitations. The first of these is a selection bias. We were obviously able to examine only those thrombi that could be retrieved, thus excluding thrombectomy-resistant thrombi. A second limitation is the small number of retrieved thrombi and the skewed distribution between the different stroke subtypes. Finally, we had no information on the prevalence of primarily fragmented thrombi because the preinterventional imaging was unenhanced brain CT and CTA and we directly probed the large vessel proximal to the suspected occlusion during MT.

CONCLUSIONS

We found that cardioembolic thrombi had a higher percentage of macrophages and a tendency toward a higher percentage of platelets than thrombi of the LAA or ESUS stroke subtype. We interpreted this finding as an indication that ESUS represents embolism from an atherosclerotic plaque rather than from an undetermined cardiac embolic source. Moreover, we observed an association between the extent of thrombus fragmentation and both a more challenging mechanical thrombectomy and a higher lymphocyte content. Thus, thrombus fragmentation might be caused not only by the recanalization procedure but might also be due to an inherent feature of lymphocyte-rich and difficult-to-retrieve thrombi.

ACKNOWLEDGMENTS

We thank Dr Klapper (Institute for Pathology, Kiel, Germany) for the kind donation of antibodies against CD68 (Ki-M1P) and Nicole Macha for excellent technical assistance.

Disclosures: Isabel Wanke—*UNRELATED*: *Consultancy*: Stryker Osteonics SA, *Comments*: Steering Committee for Neuroform Atlas Stent for Intracranial Aneurysm Treatment (ATLAS EU PMCF, microstent), less than €800 per year; *Payment for Lectures Including Service on Speakers Bureaus*: Bayer Health, *Comments*: 2 lectures per year (2× €1000). Christoph Moenninghoff—*UNRELATED*: *Payment for Lectures Including Service on Speakers Bureaus*: Teva Pharmaceutical Industries, *Comments*: payment for 1 lecture; *Payment for Manuscript Preparation*: Bayer Pharmaceuticals, *Comments*: payment for 1 MRA image set preparation; *Travel/Accommodations/Meeting Expenses Unrelated to Activities Listed*: MicroVention, Stryker, *Comments*: several neurointerventional meetings. Alexander Radbruch—*UNRELATED*: *Other*: Study support from Guerbet and Bayer, personal fees from Bayer, Guerbet, Siemens, Sanofi, GE Healthcare, and Bracco.

REFERENCES

1. Berkhemer OA, Fransen PS, Beumer D, et al; MR CLEAN Investigators. **A randomized trial of intraarterial treatment for acute ischemic stroke.** *N Engl J Med* 2015;372:11–20 CrossRef Medline
2. Goyal M, Demchuk AM, Menon BK, et al; ESCAPE Trial Investigators. **Randomized assessment of rapid endovascular treatment of ischemic stroke.** *N Engl J Med* 2015;372:1019–30 CrossRef Medline
3. Campbell BC, Mitchell PJ, Kleinig TJ, et al; EXTEND-IA Investigators. **Endovascular therapy for ischemic stroke with perfusion-imaging selection.** *N Engl J Med* 2015;372:1009–18 CrossRef Medline
4. Saver JL, Goyal M, Bonafe A, et al; SWIFT PRIME Investigators. **Stent-retriever thrombectomy after intravenous t-PA vs. T-PA alone in stroke.** *N Engl J Med* 2015;372:2285–95 CrossRef Medline
5. Jovin TG, Chamorro A, Cobo E, et al; REVASCAT Trial Investigators. **Thrombectomy within 8 hours after symptom onset in ischemic stroke.** *N Engl J Med* 2015;372:2296–2306 CrossRef Medline
6. Goyal M, Menon BK, van Zwam WH, et al; HERMES Collaborators. **Endovascular thrombectomy after large-vessel ischaemic stroke: a meta-analysis of individual patient data from five randomised trials.** *Lancet* 2016;387:1723–31 CrossRef Medline
7. Brinjikji W, Duffy S, Burrows A, et al. **Correlation of imaging and histopathology of thrombi in acute ischemic stroke with etiology and outcome: a systematic review.** *J Neurointerv Surg* 2017;9:529–34 CrossRef Medline
8. De Meyer SF, Andersson T, Baxter B, et al; Clot Summit Group. **Analyses of thrombi in acute ischemic stroke: a consensus statement on current knowledge and future directions.** *Int J Stroke* 2017;12:606–14 CrossRef Medline
9. Hart RG, Diener HC, Coutts SB, et al; Cryptogenic Stroke/ESUS International Working Group. **Embolic strokes of undetermined source: the case for a new clinical construct.** *Lancet Neurol* 2014;13:429–38 CrossRef Medline
10. Barber PA, Demchuk AM, Zhang J, et al. **Validity and reliability of a quantitative computed tomography score in predicting outcome of hyperacute stroke before thrombolytic therapy: ASPECTS study group: Alberta Stroke Programme Early CT Score.** *Lancet* 2000;355:1670–74 CrossRef Medline
11. Zaidat OO, Yoo AJ, Khatri P, et al; STIR Thrombolysis in Cerebral Infarction (TICI) Task Force. **Recommendations on angiographic revascularization grading standards for acute ischemic stroke: a consensus statement.** *Stroke* 2013;44:2650–63 CrossRef Medline
12. Schindelin J, Rueden CT, Hiner MC, et al. **The ImageJ ecosystem: an open platform for biomedical image analysis.** *Mol Reprod Dev* 2015;82:518–29 CrossRef Medline
13. Voigt D, Scheidt U, Derfuss T, et al. **Expression of the antioxidative enzyme peroxiredoxin 2 in multiple sclerosis lesions in relation to inflammation.** *Int J Mol Sci* 2017;18 CrossRef Medline
14. Boeckh-Behrens T, Kleine JF, Zimmer C, et al. **Thrombus histology suggests cardioembolic cause in cryptogenic stroke.** *Stroke* 2016;47:1864–71 CrossRef Medline
15. Sporns PB, Hanning U, Schwindt W, et al. **Ischemic stroke: what does the histological composition tell us about the origin of the thrombus?** *Stroke* 2017;48:2206–10 CrossRef Medline
16. Maekawa K, Shibata M, Nakajima H, et al. **Erythrocyte-rich thrombus is associated with reduced number of maneuvers and procedure time in patients with acute ischemic stroke undergoing mechanical thrombectomy.** *Cerebrovasc Dis Extra* 2018;8:39–49 CrossRef Medline
17. Liebeskind DS, Sanossian N, Yong WH, et al. **CT and MRI early vessel signs reflect clot composition in acute stroke.** *Stroke* 2011;42:1237–43 CrossRef Medline
18. Simons N, Mitchell P, Dowling R, et al. **Thrombus composition in acute ischemic stroke: A histopathological study of thrombus extracted by endovascular retrieval.** *J Neuroradiol* 2015;42:86–92 CrossRef Medline
19. Schuhmann MK, Gunreben I, Kleinschnitz C, et al. **Immuno-histochemical analysis of cerebral thrombi retrieved by mechanical**

thrombectomy from patients with acute ischemic stroke. *Int J Mol Sci* 2016;17:298 CrossRef Medline

20. Kim SK, Yoon W, Kim TS, et al. **Histologic analysis of retrieved clots in acute ischemic stroke: correlation with stroke etiology and gradient-echo MRI.** *AJNR Am J Neuroradiol* 2015;36:1756–62 CrossRef Medline
21. Gralla J, Schroth G, Remonda L, et al. **Mechanical thrombectomy for acute ischemic stroke: thrombus-device interaction, efficiency, and complications in vivo.** *Stroke* 2006;37:3019–24 CrossRef Medline
22. Kaesmacher J, Boeckh-Behrens T, Simon S, et al. **Risk of thrombus fragmentation during endovascular stroke treatment.** *AJNR Am J Neuroradiol* 2017;38:991–98 CrossRef Medline
23. Hashimoto T, Hayakawa M, Funatsu N, et al. **Histopathologic analysis of retrieved thrombi associated with successful reperfusion after acute stroke thrombectomy.** *Stroke* 2016;47:3035–37 CrossRef Medline
24. Boeckh-Behrens T, Schubert M, Forschler A, et al. **The impact of histological clot composition in embolic stroke.** *Clin Neuroradiol* 2016; 26:189–97 CrossRef Medline

The FRED for Cerebral Aneurysms of the Posterior Circulation: A Subgroup Analysis of the EuFRED Registry

C.J. Griessenauer, M.A. Möhlenbruch, P. Hendrix, C. Ulfert, C. Islak, M. Sonnberger, T. Engelhorn, E. Müller-Thies-Broussalis, T. Finkenzeller, M. Holtmannspötter, J.-H. Buhk, W. Reith, A. Simgen, H. Janssen, N. Kocer, and M. Killer-Oberpfalzer

ABSTRACT

BACKGROUND AND PURPOSE: Flow diversion for the posterior circulation remains a promising treatment option for selected posterior circulation aneurysms. The Flow-Redirection Intraluminal Device (FRED) system has not been previously assessed in a large cohort of patients with posterior circulation aneurysms. The purpose of the present study was to assess safety and efficacy of FRED in this location.

MATERIALS AND METHODS: Consecutive patients with posterior circulation aneurysms treated at 8 centers participating in the European FRED study (EuFRED) between April 2012 and January 2019 were retrospectively reviewed. Complication and radiographic and functional outcomes were evaluated.

RESULTS: Eighty-four patients (median age, 54 years) with 84 posterior circulation aneurysms were treated with the FRED. A total of 25 aneurysms (29.8%) had previously ruptured, even though most aneurysms were diagnosed incidentally (45.2%). The intradural vertebral artery was the most common location (50%), and saccular, the most common morphology (40.5%). The median size was 7 mm. There were 8 (9.5%) symptomatic thromboembolic and no hemorrhagic complications. Thromboembolic complications occurred mostly (90.9%) in nonsaccular aneurysms. On last follow-up at a median of 24 months, 78.2% of aneurysms were completely occluded. Functional outcome at a median of 27 months was favorable in 94% of patients. All mortalities occurred in patients with acute subarachnoid hemorrhage and its sequelae.

CONCLUSIONS: The largest cohort of posterior circulation aneurysms treated with the FRED to date demonstrated favorable safety and efficacy profiles of the device for this indication. Treatment in the setting of acute subarachnoid hemorrhage was strongly related to mortality, regardless of whether procedural complications occurred.

Flow diversion for aneurysms of the posterior circulation continues to be more controversial than other endovascular treatment modalities in that location. Whereas it is established in the anterior circulation, flow diversion in the posterior circulation remains "off-label" according to the FDA, which has not granted approval to any flow-diverting device for that indication. Still, flow-diverting stents are used at increasing frequency in those locations.[1-3] The largest studies on posterior circulation flow diversion are currently available for the Pipeline Embolization Device (PED; Covidien, Irvine, California).[4,5] Aneurysms of the vertebral artery have been found to be particularly amenable to flow diversion.[5,6] Larger cohorts of other flow diverters used in the posterior circulation are currently lacking. Here, we performed a subgroup analysis of posterior circulation cases treated with the Flow-Redirection Endoluminal Device (FRED; MicroVention, Tustin, California) at centers participating in the European FRED study (EuFRED).[7]

MATERIALS AND METHODS

Study Design and Data Collection

The EuFRED study was a retrospective, multicenter postmarket registry of consecutive patients with intracranial aneurysms treated with the FRED at European high-volume neurovascular

Received October 23, 2019; accepted after revision January 14, 2020.

From the Research Institute of Neurointervention (C.J.G., E.M.-T.-B., M.K.-O.), Paracelsus Medical University, Salzburg, Austria; Department of Neurosurgery (C.J.G.), Geisinger, Danville, Pennsylvania; Department of Neuroradiology (M.A.M., C.U.), Heidelberg University Hospital, Heidelberg, Germany; Department of Neurosurgery (P.H.), Saarland University Medical Center and Saarland University Faculty of Medicine, Homburg/Saar, Germany; Department of Neuroradiology (C.I., N.K.), Cerrahpasa Medical School, Istanbul University, Istanbul, Turkey; Department of Neuroradiology (M.S.), Kepler Universitätsklinikum, Linz, Austria; Department of Neuroradiology (T.E.), University Hospital Erlangen, Erlangen, Germany; Institute of Radiology and Neuroradiology (T.F., M.H.), Klinikum Nuernberg Sued, Paracelsus Medical University, Nuernberg, Germany; Department of Neuroradiology (T.F.), Klinikum Weiden, Weiden, Bavaria, Germany; Department of Neuroradiology (J.-H.B.), University Hospital Hamburg Eppendorf, Hamburg, Germany; Clinic for Diagnostic and Interventional Neuroradiology (W.R., A.S.), Universitätsklinikum des Saarlandes, Homburg/Saar, Homburg, Saarland, Germany; and Institute for Neuroradiology (H.J.), Klinikum Ingolstadt, Ingolstadt, Germany.

Due to equal contributions, the 2 last authors share senior authorship.

Please address correspondence to Christoph J. Griessenauer, MD, Department of Neurosurgery, Geisinger, 100 N Academy Ave, Danville, PA 17822; e-mail: christoph.griessenauer@gmail.com; @cgriessenauer

Indicates article with supplemental on-line table.

http://dx.doi.org/10.3174/ajnr.A6447

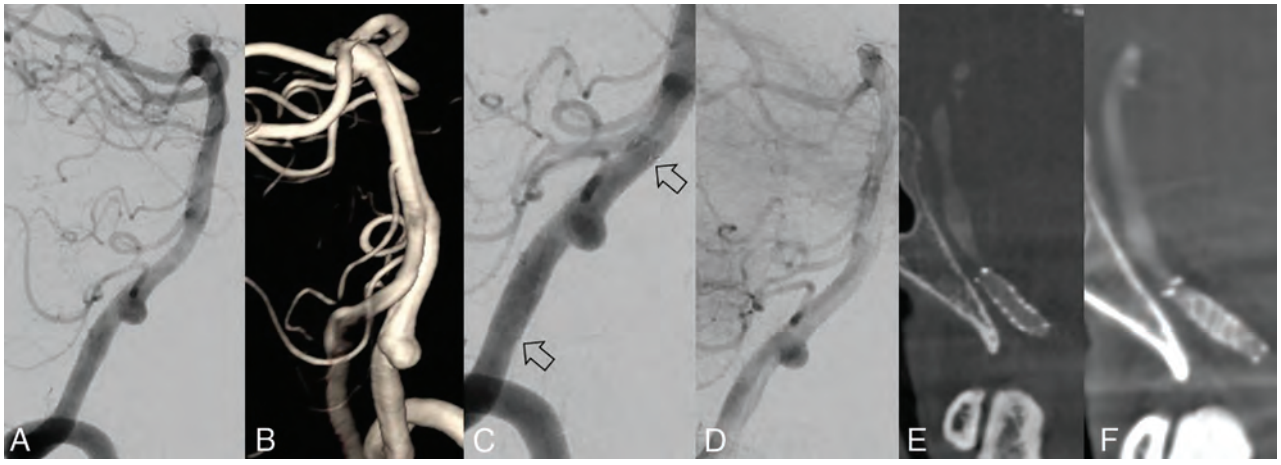

FIG 1. A 66-year-old woman presenting with an unruptured left vertebral artery aneurysm measuring 5 mm in maximum diameter. *A*, Lateral view of a left vertebral artery digital subtraction angiogram. *B*, Rotational 3D reconstruction. *C*, Angiogram post-FRED placement (*arrows* show the proximal and distal ends of the flow diverter). *D*, Stasis in the aneurysm after flow-diverter placement. *E*, Conebeam CT with contrast 1 month after stent placement shows complete occlusion of the aneurysm. *F*, Confirmation of aneurysm occlusion at 1 year.

centers as previously described.[7] The decision to use the FRED was at practitioner discretion to reflect real-world indications. An independent study nurse not involved in the clinical decision-making collected all raw data of the original EuFRED dataset. For this subgroup analysis of the posterior circulation aneurysms treated, 8 centers that had treated posterior circulation aneurysms provided additional consecutive cases up to January 2019. Aneurysms were classified according to the morphology as saccular, fusiform, dissecting, and blister/pseudoaneurysm with and without intraluminal thrombus, with the maximum diameter measured in millimiters. The categorization of aneurysm morphology was performed at the individual centers and in accordance with prior classification of posterior circulation aneurysms treated with flow diversion.[5] Details on platelet function testing and antiplatelet regimen were obtained. Complications were classified as thromboembolic, hemorrhagic, and other and divided in symptomatic and asymptomatic. Clinical and imaging follow-up time points were at the discretion of the participating center as was the imaging technique. Angiographic outcome was evaluated locally at the individual center by a radiologist not involved in the procedure and graded as completely occluded, near-completely occluded with neck remnant, or incompletely occluded. Functional outcomes were assessed locally and by using the mRS. Internal review board approval was obtained at all participating institutions, and all patients signed approved consent forms.

Statistical Analyses

Continuous variables are presented as median and range, and categoric variables are presented as frequency and percentage. Analyses were performed using χ^2 and Fisher exact tests. P values $< .05$ were considered statistically significant.

RESULTS

Baseline Patient and Aneurysm Characteristics

A total of 84 aneurysms in 84 patients (median age, 54 years) were treated with the FRED. All patients with electively treated aneurysms had a good preprocedural functional status (mRS, 0–2). A history of aneurysm rupture was present in 25 (29.8%) aneurysms, with 12 aneurysms (14.3%) treated in the acute phase (within 48 hours) of aneurysm rupture. The intradural vertebral artery (50%) (Fig 1) and basilar artery (26.1%) were the most common locations of the aneurysm. The aneurysms were saccular (40.5%), fusiform (25.0%), dissecting (22.6%), or blister (11.9%) and had a median maximum diameter of 7 mm (range, 2–67 mm). Intraluminal thrombus was present in 8.3% of aneurysms (Table 1).

Treatment Characteristics and Outcomes

Most aneurysms were treated with a single FRED (95.2%). Adjunctive coiling was performed in 16.7%. Platelet function testing was available in 95.2% of cases and resulted in a regimen change in 2.4%. The most common postprocedural antiplatelet medication regimen was aspirin and clopidogrel (86.9%). Of the 12 aneurysms treated in the acute setting of subarachnoid hemorrhage, 9 patients (75%) were started on tirofiban and transitioned to aspirin and clopidogrel (8 patients) or aspirin and ticagrelor (1 patient), while 2 (16.7%) were loaded with aspirin and clopidogrel, and 1 (8.3%), with aspirin and ticagrelor. There were 11 (13.1%) thromboembolic infarctions, most frequently affecting the cerebellum and occurring mostly in nonsaccular aneurysms (90.9%). Symptomatic infarctions occurred in 8 (9.5%) patients. Imaging follow-up was available for 77 (91.7%) patients. Imaging modalities included MRA (50%), DSA (45.6%), conebeam CT with IV contrast (2.9%), and CTA (1.5%). At a median follow-up of 24 months, 78.2% of aneurysms were completely and 9% near-completely occluded. Retreatment with another flow diverter was performed in 7.1% of patients (Fig 2). Functional outcome at a median of 27 months was favorable in 94% of patients (mRS, 0–2) and available for 98.8% of patients. There were 5 (6%) mortalities, all occurring in patients treated in the acute setting of subarachnoid hemorrhage. In one of those patients, mortality was due to a thromboembolic infarction from the flow-diversion procedure (Table 2).

Table 1: Baseline characteristics

Parameter	No.
No. of patients	84
No. of aneurysms	84
Females	42 (50.0%)
Median age (range) (yr)	54 (15–81)
Pretreatment mRS of patients without SAH	58
0	53 (91.4%)
1	4 (6.9%)
2	1 (1.7%)
3–5	0 (0.0%)
Index aneurysm presentation	
Acute SAH (within 48 hours)	12 (14.3%)
<2 weeks since SAH	6 (7.1%)
>2 weeks since SAH	7 (8.3%)
Stroke	2 (2.4%)
Brain stem compression	5 (6.0%)
Brain stem infarction	2 (2.4%)
Incidental	38 (45.2%)
Other[a]	12 (14.3%)
Aneurysm location	
Vertebral artery (intradural)	42 (50%)
Basilar artery	22 (26.1%)
Posterior cerebral artery	7 (8.3%)
Superior cerebellar artery	4 (4.8%)
Vertebral artery (extradural)	4 (4.8%)
Posterior inferior cerebellar artery	3 (3.6%)
Vertebrobasilar junction	2 (2.4%)
Aneurysm morphology	
Saccular	34 (40.5%)
Fusiform	21 (25.0%)
Dissecting	19 (22.6%)
Blister/pseudoaneurysm	10 (11.9%)
Index aneurysm pretreated[b]	7 (8.3%)
Aneurysm size (median) (range) (mm)	7 (2–67)
Intra-aneurysmal thrombus	7 (8.3%)

[a] Other Headache ($n = 7$), vertigo ($n = 1$), syncope ($n = 1$), TIA (1), dizziness ($n = 1$), Traumatic brain injury ($n = 1$).
[b] Pretreatment endovascular ($n = 6$), endovascular, and open microsurgery ($n = 1$).

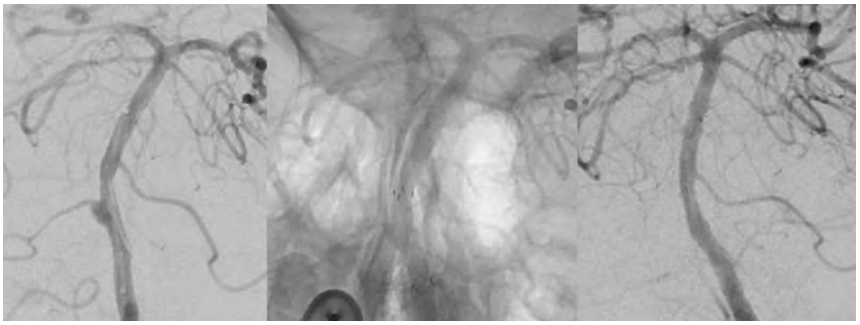

FIG 2. A 68-year-old male patient who had an SAH with a Hunt and Hess score of 3 (*left*). Diagnostic angiography reveals a 3-mm dissecting aneurysm of the basilar artery at the origin of the anterior inferior cerebellar artery (*middle*). Implantation of a FRED into the basilar artery with good wall apposition and complete coverage of the aneurysm neck and anterior inferior cerebellar artery origin was achieved. The patient was administered tirofiban for the first 24 hours after implantation (*right*). During recovery, the patient presented with cranial nerve IX to XII palsies and slight hemiparesis on the left. MR imaging showed only minimal DWI lesions in both cerebellar hemispheres (MRI not shown). Diagnostic angiography 7 days after the primary intervention revealed occlusion of the aneurysm and occlusion of the anterior inferior cerebellar artery. The patient recovered to a mRS 2 after 3 months.

Predictors of Complication and Occlusion Status at Last Follow-Up

The small number of cases with complications and incomplete occlusion status limited the ability to perform statistical analysis. All thromboembolic complications occurred in aneurysms not treated with adjunctive coiling, albeit this relationship did not reach statistical significance. All patients with thromboembolic complications had undergone platelet function testing, and no adjustments to the antiplatelet regimen were warranted. There were no associations of occlusion status or complications with any of the recorded variables (On-line Table).

DISCUSSION

The present cohort is the largest reported on the FRED for aneurysms of the posterior cerebral circulation. The FRED was successfully implanted in 84 patients with 84 aneurysms, most commonly located along the intradural vertebral artery. Symptomatic thromboembolic complications occurred in 9.5% of patients, whereas no hemorrhagic complications were reported. Complete or near-complete occlusion was achieved in 87.2% of aneurysms at a median follow-up of 24 months. At a median clinical follow-up of 27 months, all living patients had a favorable functional outcome. Mortalities occurred only in patients treated in the acute setting of subarachnoid hemorrhage.

The Flow-Redirection Intraluminal Device

The FRED is a dual-layer braided device with an inner low-porosity stent that acts as the flow diverter and an outer part that serves as a scaffold for the inner stent. The EuFRED study with 579 aneurysms treated with the FRED is the largest to date. In aneurysms followed for >1 year, complete occlusion was achieved in 95.3%. Transient morbidity, permanent morbidity, and mortality rates were 3.2%, 0.8%, and 1.5%, respectively.[7]

The Italian core lab–adjudicated FRED registry included 165 aneurysms.[8] Device-related morbidity and mortality occurred in 6.1% and 2.4% of patients. Complete or near-complete occlusion at 12 to 24 months was 77% and 19%, respectively. The study also included 29 aneurysms in the posterior circulation. Even though this subgroup was not discussed in detail, posterior circulation aneurysms contributed to mortality in particular. Among the 6 delayed deaths, 3 occurred in basilar artery aneurysms.[8]

The Safety and efficacy Analysis of FRED Embolic device in aneurysm treatment (SAFE) study is the third largest on FRED, enrolling 103 aneurysms; posterior circulation aneurysms were not included.[9]

In the United States, the FRED is not approved currently. Still, in a comparative study of EuFRED anterior circulation aneurysms matched to aneurysms treated with the PED at US centers, both safety and efficacy profiles

Table 2: Treatment characteristics and outcomes

Parameter	No.
No. of FREDs per aneurysm	
1 FRED	80 (95.2%)
2 FREDs	3 (3.6%)
4 FREDs	1 (1.2%)
Adjunctive coiling required	14 (16.7%)
Platelet function testing	80 (95.2%)
Antiplatelet regimen changed after testing	2 (2.4%)
Postprocedural antiplatelet regimen	
ASA + clopidogrel	62 (73.8%)
Tirofiban loading followed by ASA + clopidogrel	11 (13.1%)
ASA + ticagrelor	6 (7.1%)
Prasugrel	3 (3.6%)
ASA + prasugrel	1 (1.2%)
ASA + tirofiban + ticagrelor	1 (1.2%)
Thromboembolic infarction due to procedure	11 (13.1%)
Symptomatic thromboembolic complication	8 (9.5%)
Location of infarction	
Cerebellum	7 (8.3%)
Brain stem	2 (2.4%)
Posterior cerebral artery territory	1 (1.2%)
Thalamus	1 (1.2%)
Hemorrhagic complications	0 (0.0%)
Other complications	3 (3.6%)
Parent artery occlusion	2 (2.4%)
Time of radiographic follow-up (median) (range) (mo)[a]	24 (0.03–72)
Occlusion status last imaging follow-up[a]	
Complete occlusion (100%)	61 (78.2%)
Near-complete occlusion (>90%)	7 (9%)
Incomplete occlusion (<90%)	10 (12.8%)
Imaging technique[b]	
MRA	34 (50%)
DSA	31 (45.6%)
Conebeam CT with IV contrast	2 (2.9%)
CTA	1 (1.5%)
Retreatment[c]	6 (7.1%)
Time of functional outcome follow-up (median) (range) (mo)[d]	27 (0.03–72)
Functional outcome[e]	
mRS 0–2	78 (94%)
mRS 3–5	0
mRS 6	5 (6%)

Note:—ASA indicates acetylsalicylic acid.
[a] Data missing in 6 patients.
[b] Data missing in 16 patients.
[c] Data missing in 1 patient.
[d] Data missing in 6 patients.
[e] Data missing in 1 patient.

of both flow diverters were comparable.[10] To overcome the limitation of short angiographic follow-up of 6.6 months in the initial EuFRED publication,[7] we updated both angiographic and clinical follow-up for the current study. With median follow-ups of 24 and 27 months, respectively, this study also presents some of the longest follow-up data on the FRED.[8,9]

Occlusion of Posterior Circulation Aneurysms with Flow Diverters

Per FDA regulations, flow diversion in the posterior circulation continues to be considered off-label. Nevertheless, flow diversion is increasingly used for posterior circulation aneurysms with most data available for the PED.[4-6,11]

The largest single-center series on posterior circulation aneurysms treated with either the PED or the p64 (phenox, Bochum, Germany) included 58 nonsaccular aneurysms.[11] The cohort represents the most challenging aneurysm morphologies in the posterior circulation.[6] Angiographic occlusion or minor remnants were reported in 100% (5/5) of dolichoectatic, 95.5% (21/22) of fusiform, and 63.2% (12/19) of transitional morphology at a mean follow-up of 25.2 months. Up to 8.3 flow diverters were used, on average, in fusiform basilar artery aneurysms. A meta-analysis of nonsaccular posterior circulation aneurysms treated with flow diverters reported the average device number at 4.33 per aneurysm.[6] In contrast, the present study included 50 nonsaccular aneurysms classified as fusiform, dissecting, and blister, with a median diameter of 7 mm. The median number of FREDs used was 1. Among patients with angiographic follow-up and nonsaccular aneurysms, the rates of complete and near-complete occlusion were 81.8% and 4.6%, respectively, at 18.5 months. Given the complexity of these lesions, however, any comparison must be interpreted with caution. Still, data are promising in terms of occlusion of some of the most challenging cerebral aneurysms.

The second largest single-center series was published in 2019, including 55 aneurysms treated with the PED.[4] The classification of aneurysms was similar to that in the current study as saccular, fusiform, and dissecting/pseudoaneurysm. One PED was used in 84% of procedures. Angiographic follow-up was short, with only 8 aneurysms imaged at 24 months. On last follow-up, however, complete occlusion or trace filling was achieved in 72% and 9%, respectively, which is comparable with the present study, especially given the shorter follow-up.

The largest series on posterior circulation flow diversion was a multicenter study, including 131 aneurysms, all treated with the PED.[5] At a median of 11 months, complete or near-complete occlusion was achieved in 78.1% of aneurysms, with dissecting and fusiform aneurysms occluding most and least frequently, respectively. A predictor of occlusion in dissecting aneurysms was age, with older aneurysms occluding less often, a relationship that has also been demonstrated for anterior circulation aneurysms after flow diversion.[12] In fusiform aneurysms, no predictors of occlusion were identified. Assessed variables were aneurysm size and location, intraluminal thrombus, adjunctive coiling, and the number of devices used. Saccular aneurysms of the basilar artery occluded less often than saccular aneurysms in other posterior circulation locations, though this relationship was not significant ($P = .08$).[5]

Complications Associated with Posterior Circulation Flow Diversion

The posterior circulation is characterized by unique neurovascular anatomy with end arterial perforating vessels to the brain stem arising from the distal vertebral artery, basilar trunk, and proximal posterior cerebral arteries. Placement of flow diverters inevitably results in coverage of smaller or larger side branches of the vertebrobasilar system.[13]

Reported morbidity and mortality are important. An aforementioned meta-analysis of 131 posterior circulation aneurysms treated with flow diversion reported overall morbidity and mortality rates of 26% and 21%, respectively. Favorable clinical outcome (mRS, ≤2) was most frequently achieved in the vertebral

artery as opposed to other locations, likely owing to the relative paucity of perforators in that location.[6] In the present study, 11 thromboembolic complications occurred. Even though there was not a predilection for a specific location, 10 of 11 (90.9%) thromboembolic complications occurred in nonsaccular aneurysms, and 5 of 11 (45.5%), in aneurysms that had previously ruptured.

The multicenter study of 131 posterior circulation aneurysms treated with the PED also identified fusiform aneurysm morphology as a risk factor for major complications.[5] Nevertheless, data from the present study show that even nonsaccular aneurysms of the posterior circulation can be treated safely with flow diverters as long as treatment is performed in unruptured aneurysms. Several key aspects, as summarized by Bhogal et al,[11] are critical to minimize complications. These include rigorous platelet function testing and regimen adjustments, performed in 95.2% of patients in the current study; treatment of not acutely symptomatic patients, either due to rupture or brain stem compression or ischemia; the use of fewer flow diverters per aneurysm (median of 1 in the current series); and adjunctive coiling. Applying those principles in the current study may have explained the very favorable safety profile.

Strengths and Limitations

The most significant limitation is the heterogeneity of posterior circulation aneurysms. Given their variability in size and involvement of various segments of the posterior circulation tree, comparative analyses are challenging. Thus, any related study is exposed to significant selection bias across different neurovascular centers and individual neurovascular practitioners. Data collection was performed at the individual institution and was not core lab–adjudicated, introducing potential bias. Nevertheless, the dataset was nearly complete. The inclusion of multiple institutions, on the other hand, improved the generalizability of the findings. Another limitation was variability in the type of platelet function test used at the individual institution, albeit most patients underwent platelet function testing.

CONCLUSIONS

The largest cohort of posterior circulation aneurysms treated with the FRED to date demonstrated favorable safety and efficacy profiles of the device for this indication. Regardless of location and morphology, flow diversion using the FRED represents a viable treatment option for those challenging lesions. Thromboembolic complications occurred mostly in nonsaccular aneurysms. Treatment in the setting of acute subarachnoid hemorrhage, however, was strongly related to mortality, regardless of whether procedural complications occurred.

Disclosures: Markus A. Möhlenbruch—*UNRELATED*: *Board Membership*: Codman Neurovascular; *Consultancy*: Medtronic, MicroVention, Stryker*; *Grants/Grants Pending*: Balt, MicroVention*; *Payment for Lectures Including Service on Speakers Bureaus*: Medtronic, MicroVention, phenox, Stryker.* Christian Ulfert—*UNRELATED*: *Payment for Lectures Including Service on Speakers Bureaus*: Cerenovus; *Travel/Accommodations/Meeting Expenses Unrelated to Activities Listed*: Stryker, MicroVention, Balt. Markus Holtmannspötter—*UNRELATED*: *Consultancy*: Medtronic, MicroVention, Sequent Medical, Stryker, Mentice, Route 92, *Comments*: consultancy and proctoring agreement; *Payment for Lectures Including Service on Speakers Bureaus*: Medtronic, MicroVention, Sequent Medical. Jan-Hendrik Buhk—*UNRELATED*: *Consultancy*: Acandis, Cerenovus, Codman Neurovascular, Medtronic, MicroVention, Stryker, *Comments*: consultancy and proctoring. Naci Kocer—*UNRELATED*: *Consultancy*: MicroVention, Medtronic, *Comments*: consultant and proctorship agreement; *Payment for Lectures Including Service on Speakers Bureaus*: MicroVention, *Comments*: lectures on FRED. Hendrik Janssen—*UNRELATED*: *Consultancy*: MicroVention/Sequent Medical, *Comments*: proctor*; *Travel/Accommodations/Meeting Expenses Unrelated to Activities Listed*: MicroVention, *Comments*: travel expenses for conferences.* Monika Killer-Oberpfalzer—*RELATED*: *Grant*: MicroVention/Terumo*; *Consulting Fee or Honorarium*: MicroVention/Terumo; *UNRELATED*: *Consultancy*: Medtronic, Stryker, Cerus; *Grant*: MicroVention/Terumo, *Comments*: research grant*; *Support for Travel to Meetings for the Study or Other Purposes*: MicroVention/Terumo; *Travel/Accommodations/Meeting Expenses Unrelated to Activities Listed*: MicroVention, Stryker, Medtronic. Civan Islak—*UNRELATED*: *Consultancy*: MicroVention; *Patents (Planned, Pending or Issued)*: US 2015/0327868A1.*Money paid to institution.

REFERENCES

1. Petr O, Brinjikji W, Cloft H, et al. **Current trends and results of endovascular treatment of unruptured intracranial aneurysms at a single institution in the flow-diverter era.** *AJNR Am J Neuroradiol* 2016;37:1106–13 CrossRef Medline
2. Ogilvy CS, Jordan NJ, Ascanio LC, et al. **Surgical and endovascular comprehensive treatment outcomes of unruptured intracranial aneurysms: reduction of treatment bias.** *World Neurosurg* 2019;126:e878–87 CrossRef Medline
3. Wang CB, Shi WW, Zhang GX, et al. **Flow diverter treatment of posterior circulation aneurysms: a meta-analysis.** *Neuroradiology* 2016;58:391–400 CrossRef Medline
4. Bender MT, Colby GP, Jiang B, et al. **Flow diversion of posterior circulation cerebral aneurysms: a single-institution series of 59 cases.** *Neurosurgery* 2019;84:206–16 CrossRef Medline
5. Griessenauer CJ, Ogilvy CS, Adeeb N, et al. **Pipeline embolization of posterior circulation aneurysms: a multicenter study of 131 aneurysms.** *J Neurosurg* 2018;130:923–35 CrossRef Medline
6. Kiyofuji S, Graffeo CS, Perry A, et al. **Meta-analysis of treatment outcomes of posterior circulation non-saccular aneurysms by flow diverters.** *J Neurointerv Surg* 2018;10:493–99 CrossRef Medline
7. Killer-Oberpfalzer M, Kocer N, Griessenauer CJ, et al. **European multicenter study for the evaluation of a dual-layer flow-diverting stent for treatment of wide-neck intracranial aneurysms: the European Flow-Redirection Intraluminal Device Study.** *AJNR Am J Neuroradiol* 2018;39:841–47 CrossRef Medline
8. Piano M, Valvassori L, Lozupone E, et al. **FRED Italian Registry: a multicenter experience with the Flow Re-direction Endoluminal Device for intracranial aneurysms.** *J Neurosurg* 2019;1–8 CrossRef Medline
9. Pierot L, Spelle L, Berge J, et al. **SAFE study (Safety and efficacy Analysis of FRED Embolic device in aneurysm treatment): 1-year clinical and anatomical results.** *J Neurointerv Surg* 2019;11:184–89 CrossRef Medline
10. Griessenauer CJ, Thomas AJ, Enriquez-Marulanda A, et al. **Comparison of Pipeline Embolization Device and Flow Re-Direction Endoluminal Device flow diverters for internal carotid artery aneurysms: a propensity score-matched cohort study.** *Neurosurgery* 2019;85:E249–55 CrossRef Medline
11. Bhogal P, Pérez MA, Ganslandt O, et al. **Treatment of posterior circulation non-saccular aneurysms with flow diverters: a single-center experience and review of 56 patients.** *J Neurointerv Surg* 2017;9:471–81 CrossRef Medline
12. Adeeb N, Moore JM, Wirtz M, et al. **Predictors of incomplete occlusion following Pipeline embolization of intracranial aneurysms: is it less effective in older patients?** *AJNR Am J Neuroradiol* 2017;38:2295–300 CrossRef Medline
13. Adeeb N, Griessenauer CJ, Dmytriw AA, et al. **Risk of branch occlusion and ischemic complications with the Pipeline embolization device in the treatment of posterior circulation aneurysms.** *AJNR Am J Neuroradiol* 2018;39:1303–09 CrossRef Medline

Efficacy and Safety of Flow-Diverter Therapy for Recurrent Aneurysms after Stent-Assisted Coiling

K.Y. Park, J.Y. Yeon, B.M. Kim, P. Jeon, J.-H. Kim, C.K. Jang, D.J. Kim, J.W. Lee, Y.B. Kim, J. Chung, D.H. Song, H.G. Park, and J.S. Park

ABSTRACT

BACKGROUND AND PURPOSE: Flow-diverter treatment for previously stented aneurysms has been reported to be less effective and prone to complications. In this study, we evaluated the effectiveness and safety of flow diverters for recurrent aneurysms after stent-assisted coiling.

MATERIALS AND METHODS: Patients who underwent flow-diverter placement for recurrent aneurysms after stent-assisted coiling between March 2015 and March 2019 were recruited. Clinical and radiographic characteristics and clinical and angiographic outcomes were retrospectively evaluated.

RESULTS: Among 133 patients who underwent flow-diverter insertion, 17 (male/female ratio = 5:12; mean age, 53.8 years) were treated for recurrent aneurysms after stent placement with ($n = 16$) or without ($n = 1$) coiling. Eight patients initially presented with subarachnoid hemorrhage; 7, with headache; and 2, with visual field defects. Angiographic morphology included large/giant saccular in 12 patients, dissecting in 2, fusiform in 1, traumatic pseudoaneurysm in 1, and ruptured blood blister-like aneurysm in 1. The duration between the first treatment and flow-diverter placement ranged from 2 weeks to 15 months (median, 6 months). Flow-diverter placement was successful in all cases without any complications. All patients had favorable outcomes (mRS, 0–2), without any newly appearing symptoms. Aneurysms were followed up with conventional angiography at least once in 6–18 months. Sixteen aneurysms showed complete occlusion, and 1 aneurysm was enlarged.

CONCLUSIONS: Results from this case series investigating flow-diverter placement for recurrent aneurysms after stent-assisted coiling suggested that the procedure is safe and effective. Further study in a larger population may be warranted.

ABBREVIATIONS: LVIS = low-profile visualized intraluminal support; PED = Pipeline Embolization Device; SAC = stent-assisted coiling

Endovascular coil embolization is a standard treatment for intracranial aneurysms. However, its durability and potential for angiographic recurrence are still major shortcomings.[1,2] Although stent placement with coiling can help enhance durability, the recurrence rate is reported to be approximately up to 14.9%, even after successful stent-assisted coiling (SAC).[3] Conversely, retreatment of previously stented aneurysms is challenging for both neurosurgeons and neurointerventionalists due to its questionable efficacy and safety.[4,5] Thus, neither conventional clipping nor coiling has provided reasonable outcomes as a retreatment technique for recurrent aneurysms after SAC.

Following the introduction of the early version of the Pipeline Embolization Device (PED; Medtronic, Minneapolis, Minnesota),[6,7] flow diverters have gained increasing acceptance for aneurysm treatment. In particular, these were useful for the treatment of complex and complicated aneurysms, such as large or giant, dissecting, and blood blister-like aneurysms. Additionally, these types of aneurysms were also susceptible to recurrence.[8-11] Thus, flow diverters may be an alternative treatment option for recurrent aneurysms after SAC. Unfortunately, previous studies on flow-diverter treatment for previously stented aneurysms reported some technical issues and unfavorable results.[12-16] Nelson et al[12] reported that 1 in 4 aneurysms previously treated with another stent was not occluded at

Received October 11, 2019; accepted after revision January 27, 2020.

From the Department of Neurosurgery (K.Y.P., C.K.J., J.W.L., Y.B.K., J.C.), Yonsei University College of Medicine, Seoul, Republic of Korea; Department of Neurosurgery (J.Y.Y.), Sungkyunkwan University School of Medicine, Seoul, Republic of Korea; Department of Radiology (B.M.K., J.-H.K., D.J.K., D.H.S., H.G.P., J.S.P.), Severance Stroke Center, Severance Hospital, Yonsei University College of Medicine, Seoul, Republic of Korea; and Department of Radiology (P.J.), Samsung Medical Center, Sungkyunkwan University School of Medicine, Seoul, Republic of Korea.

K.Y. Park and J.Y. Yeon contributed equally.

Please address correspondence to Byung Moon Kim, MD, PhD, Interventional Neuroradiology, Severance Stroke Center, Department of Radiology, Yonsei University College of Medicine, Severance Hospital, 50-1, Yonsei-ro, Seodaemun-gu, Seoul, Republic of Korea; e-mail: bmoon21@hanmail.net; bmoon21@yuhs.ac

Indicates article with supplemental on-line table.

http://dx.doi.org/10.3174/ajnr.A6476

180 days after PED placement. Fischer et al[13] reported that the adverse event rate was 13%, and the successful occlusion rate was 65% in 30 cases of PED for recurrent aneurysms after SAC. Daou et al[15] reported that the complete occlusion rate was 55.6%, with a 14.3% complication rate in PEDs after SAC. However, recent neurointerventional techniques and devices may be helpful in overcoming these technical issues, and more acceptable outcomes are expected.

In the present study, we report on the effectiveness and safety of flow-diverter treatment for recurrent aneurysms after SAC.

MATERIALS AND METHODS

The institutional review board of each hospital approved this study and waived the requirement for patient informed consent due to its retrospective design. After the introduction of the PED, patients who underwent flow-diverter placement for the treatment of recurrent aneurysms after SAC in 5 hospitals between March 2015 and March 2019 were recruited.

Planning of flow-diverter treatment was based on consensus by a multidisciplinary team meeting after the careful evaluation of 3D angiograms. Flow-diverter placement was chosen as a retreatment method after agreement that the initial aneurysm was large/giant, ruptured dissecting, or blood blister-like. On the basis of previous results, those types of aneurysms were thought to be prone to re-recurrence, even if retreatment was successful with additional coil insertion.

In cases in which dual-antiplatelet medication was stopped or changed to aspirin monotherapy before the PED retreatment procedure, dual-antiplatelet medication (aspirin, 100 mg, and clopidogrel, 75 mg) was resumed for at least 5 days. Because no patient showed resistance on the antiplatelet resistance test at the initial SAC and no patient had thromboembolic events during follow-up, an additional antiplatelet resistance test before PED placement was not routinely performed. After the completion of treatment, the dual-antiplatelet medication was maintained for at least 6 months, and subsequently, the regimen was changed to aspirin monotherapy, which was continued indefinitely.

All clinical and radiologic data were obtained from the electronic medical records and a prospectively registered aneurysm data base. Data were retrospectively reviewed.

Flow-Diverter Placement

All procedures were conducted with the patient under general anesthesia. A 5F intermediate catheter was used in all except 3 cases, combined with a 6F or 7F Shuttle guide sheath (Cook, Bloomington, Indiana) or a 6F Neuron MAX (Penumbra, Alameda, California). The routine procedural details were as follows: 1) After the placement of a 5F intermediate catheter (Sofia; MicroVention, Aliso Viejo, California; Navien, Medtronic, Minneapolis, Minnesota; Revive, Codman Neurovascular, Raynham, Massachusetts) within a 6F or 7F Shuttle or a 6F Neuron MAX catheter, the Marksman catheter (Medtronic) was introduced and advanced over a 0.014-inch guidewire into 1 branch of the parent artery beyond the stented segment; 2) the intermediate catheter was advanced over the Marksman catheter and microwire as far as possible beyond the stented segment of the parent artery; 3) the size-matched flow diverter was introduced and placed to span the entire stented segment; if required, multiple flow diverters were used to span the entire stented segment; and 4) if an immediate postimplantation angiogram or flat panel CT image showed equivocal apposition of the flow diverter and a previously placed stent in the segment where a metallic artifact due to the coil mass was not prominent, or if the apposition between the PED and the preplaced stent could not be assessed due to the surrounding coil mass (Fig 1), balloon angioplasty was performed for better apposition between the preplaced stent and the flow diverter.

Clinical and Angiographic Follow-Up

Routine clinical follow-up was performed at 1, 3, 6, and 18 months. Routine angiographic follow-up was performed at 6 months. If the 6-month angiogram did not show complete occlusion of the aneurysm, further follow-up angiographies were scheduled at 12 months and 18–24 months.

Outcome Measurements

Procedural success was defined as the full expansion of the flow diverter spanning the entire stented segment of the parent artery.

Clinical outcomes were assessed with the mRS at the latest clinical follow-up. Treatment-related morbidity was defined as the development of any new deficit due to treatment-related complications that were still present at discharge. Treatment-related mortality was defined as death of the patient from treatment-related complications during admission or clinical follow-up. In addition, any treatment-related complication other than neurologic complication was evaluated. Follow-up angiographic outcomes were assessed according to the Raymond class, in which class 1 is defined as complete occlusion; class 2, as neck remnant; and class 3, as sac remnant.[17]

The procedural success rate, treatment-related morbidity and mortality, and clinical and angiographic follow-up outcomes were retrospectively assessed.

Statistical Analysis

Because this study included the results of a single arm of flow-diverter insertion for recurrent aneurysms after SAC, without comparison with other types of treatment, only descriptive statistics are presented. All data are presented as mean and range for continuous variables and number and percentage for categoric variables.

RESULTS

Among 133 patients who underwent flow-diverter insertion, 17 (male/female ratio = 5:12; mean age, 53.8 years) were treated for recurrent aneurysms after stent placement with ($n = 16$) or without ($n = 1$) coiling. Baseline characteristics of patients and aneurysms and follow-up clinical and angiographic outcomes are shown in the On-line Table.

Eight patients initially presented with subarachnoid hemorrhage; 7, with headache; and 2, with a visual field defect. Except for 1 patient (case 7, Fig 1) who presented with a ruptured ICA fusiform aneurysm and had end-stage renal disease, no patient had an underlying comorbidity. The aneurysm types included large/giant saccular in 12 patients, dissecting in 2, fusiform in 1

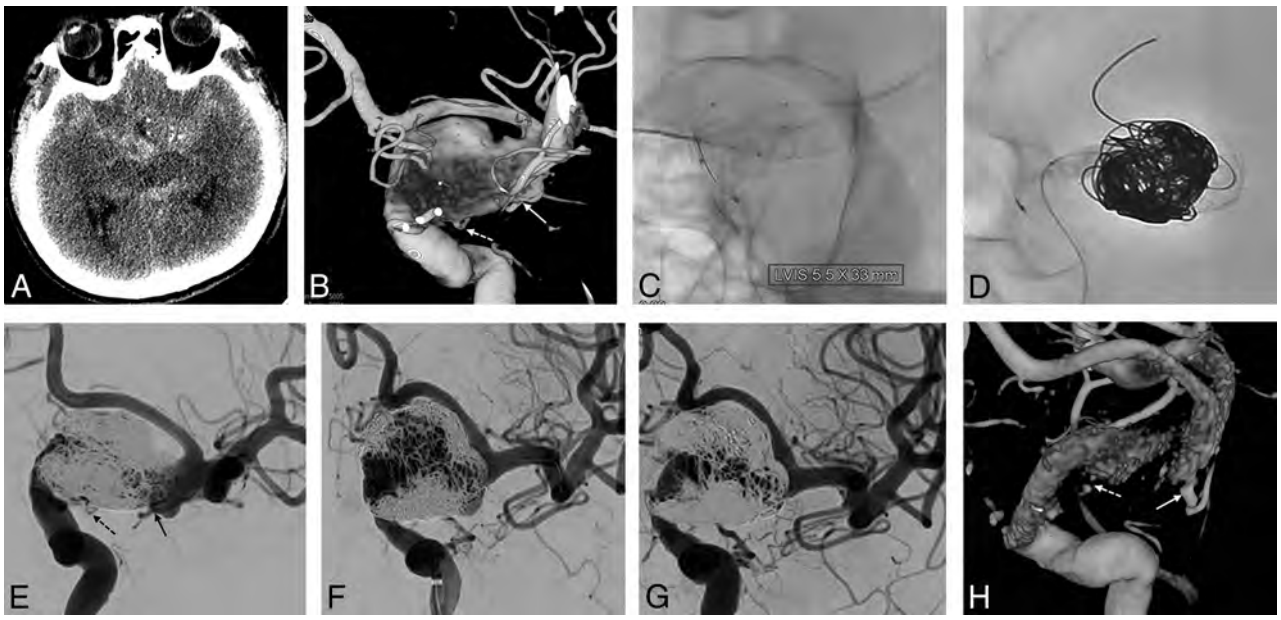

FIG 1. A 54-year-old man with subarachnoid hemorrhage. *A*, A nonenhanced CT image shows a diffuse subarachnoid hemorrhage in the basal cistern. *B*, A 3D volume-reconstruction image shows a fusiform aneurysm of the left distal ICA. Both the anterior choroidal (*solid arrow*) and posterior communicating (*dashed arrow*) arteries arise from the fusiform aneurysm. *C*, Three LVIS Blue devices are deployed in a telescopic manner from the ICA cavernous segment to the middle cerebral artery M1 segment. *D*, Coil embolization performed using the balloon-in-stent technique. *E*, Immediate postembolization shows near-complete embolization. Both the anterior choroidal (*solid arrow*) and posterior communicating (*dashed arrow*) arteries are saved. *F*, One-year follow-up angiogram shows a major recurrence. Note that the left anterior cerebral artery is tented due to the mass effect of the fusiform aneurysm. *G*, One-year follow-up angiogram after Pipeline Embolization Device implantation shows complete occlusion. *H*, Subtracted 3D reconstruction image shows a well-remodeled ICA with both anterior choroidal (*solid arrow*) and posterior communicating (*dashed arrow*) arteries saved.

(Fig 1), traumatic pseudoaneurysm in 1, and blood blister-like in 1; and the aneurysm locations were the ICA intradural segment in 13 patients, ICA cavernous segment in 1, MCA in 2, and anterior communicating artery in 1 (Fig 2). The types of stents initially used were the Enterprise (Codman Neurovascular) in 11 patients and the Low-Profile Visualized Intraluminal Support (LVIS; MicroVention), Blue, or Jr in 6. Flow-diverter placement was successful in all patients. At retreatment, the mRS was 0 in nine, 1 in four, 2 in 2, and 3 in 2 patients, respectively. The duration between the first treatment and flow-diverter placement ranged from 2 weeks to 15 months (median, 6 months). One patient was retreated 2 weeks after initial treatment. The patient (case 17) had a ruptured blood blister-like aneurysm and showed aneurysm enlargement from 3.5 to 5 mm at 2 weeks' follow-up angiography after overlapping of 3 LVIS stents as the initial treatment. Due to fear of rehemorrhage, the patient was urgently retreated with 2 PEDs.

A single PED was used in 14; two PEDs, in 2; and 3 PEDs, in 1 patient. Of a total of 21 PEDs, PED Classic and PED Flex were used in 7 and 14, respectively. In every case, the previously stented segment was completely covered by the PED. Balloon angioplasty was performed because incomplete expansion or poor apposition of the PED was suspected in 4 cases, and the apposition between the PED and the preplaced stent could not be assessed due to a surrounding coil mass in the fusiform aneurysm (case 7, Fig 1). There was no difference in the frequency of balloon angioplasty between PED Classic (2 of 7 patients, 28.6%) and PED Flex (3 of 10 patients, 30%). There were no periprocedural neurologic or other complications including vascular injury, access site complication, and contrast material–induced kidney injury.

At the most recent follow-up (mean, 22 months; range, 6–48 months), all patients had favorable outcomes (mRS, 0–2), without any newly appearing neurologic deficits. All aneurysms were followed up with conventional angiography at least once, 6–18 months after PED placement. Sixteen aneurysms (94.1%) showed complete occlusion; however, 1 initially ruptured dissecting MCA aneurysm (case 15) was enlarged. This enlarged dissecting aneurysm underwent a third treatment using an additional flow-diverter placement and has not yet undergone follow-up angiography. Asymptomatic in-stent stenosis (>50%) was observed in 1 case on follow-up angiography.

DISCUSSION

In this case series, all aneurysms were successfully retreated using the PED without any complications. Furthermore, although the initial aneurysms (large-/giant-sized, ruptured dissecting, or blood blister-like) were prone to re-recurrence even after successful retreatment with additional coil insertion, 94.1% of the aneurysms retreated using flow diverters had complete occlusion on follow-up angiography.

During the coiling procedure for an intracranial aneurysm, a stent may be used for multiple purposes, such as preservation of a parent or branch artery, prevention of microcatheter kickback, and increased durability. Despite these advantages, SAC has not been widespread until recently due to its technical difficulty and possible complications. However, with the recent development of

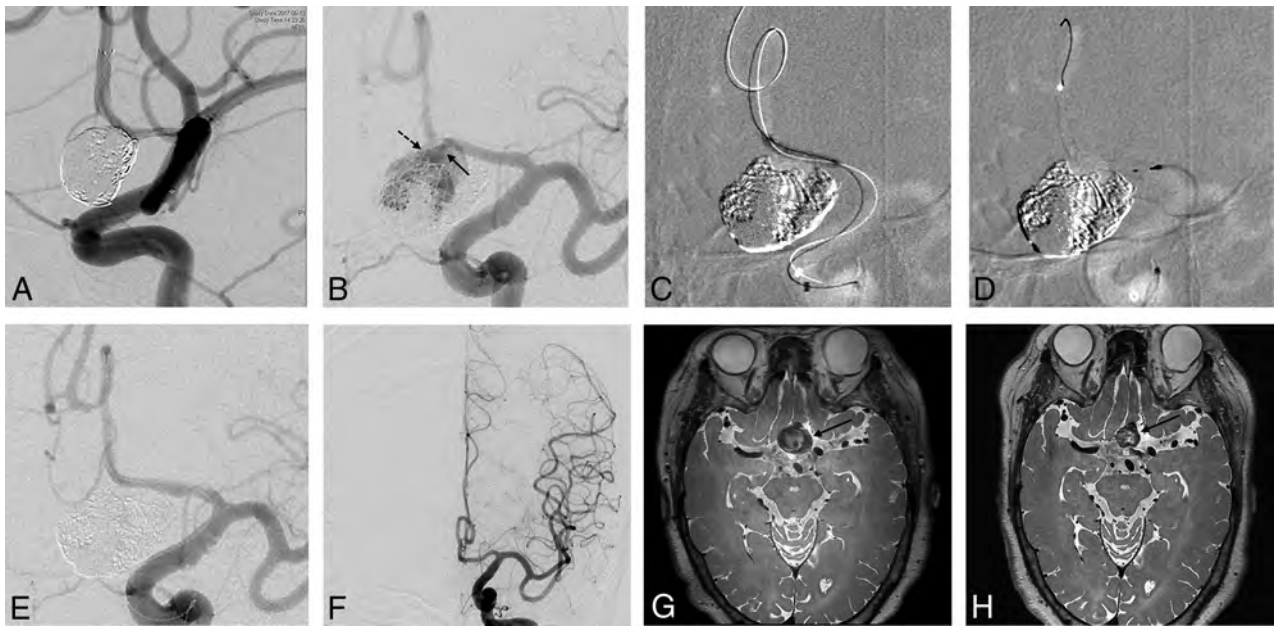

FIG 2. A 67-year-old woman with a partially thrombosed giant aneurysm at the anterior communicating artery. *A*, Angiogram immediately after LVIS Jr–assisted coiling shows complete occlusion of the aneurysm sac. *B*, The 14-month follow-up angiogram shows a major recurrence with occlusion of the stent. The left anterior cerebral artery A2 segment is supplied through the recurrent aneurysm sac. Note blood flow from the A1 segment through the aneurysm sac to the A2 segment. The *solid arrow* indicates the inflow from A1 into the aneurysm sac, and the *dashed arrow* indicates the outflow from the aneurysm sac to A2. *C*, The A2 segment is navigated through the inside of the stent using a 0.0165-inch microcatheter and a 0.014-inch microwire. Next, balloon angioplasty is performed to open the occluded stented segment of the anterior cerebral artery using a Gateway balloon (Stryker, Kalamazoo, Michigan). *D*, The Pipeline Flex is deployed spanning the entire stented segment. *E*, An angiogram immediately after PED implantation shows complete occlusion of the recurrent aneurysm. *F*, The 10-month follow-up angiogram shows complete occlusion of the aneurysm. MR image before PED implantation (*G*) and at 10-month follow-up (*H*) show the decreased size of the thrombosed giant aneurysm (*solid arrow*).

low-profile stents, SAC may be an easier and safer procedure than those using previous stents.[18-20] Currently, SAC has become more common and is used in up to 32.7% of all endovascular coiling.[21] However, because a recurrence after SAC is not uncommon, management after recurrence is an important clinical issue that remains controversial.

Surgical retreatment for previously stented aneurysms is challenging and complicated because direct manipulation of the stented artery or extrusion of the previous coil mass is required, which is associated with a risk of thromboembolism and arterial tearing. Thus, endovascular coil addition with or without a stent has been widely accepted as a retreatment technique for recurrent aneurysms after SAC.[22,23] However, this conventional endovascular retreatment cannot fully overcome the risk of repeat recurrences because most target aneurysms in this study were vulnerable to recurrence by nature.

Flow diverters are a new treatment strategy for intracranial aneurysms. The flow diverter gradually occludes an aneurysm within an organized thrombus by enhancing an intra-aneurysmal flow diversion[24] and neointima formation.[25] Consequently, flow-diverter treatment has a lower probability of recurrence than conventional coiling, even in lesions vulnerable to recurrence. Therefore, a flow diverter might be a better treatment option for recurrent aneurysms even after SAC. However, in previous studies, flow-diverter treatment after stent placement was reportedly less effective and more complicated, with 40.9%–75.0% occlusion rates and a higher complication rate, up to 16.7%.[12-16]

These unfavorable results may stem from several technical issues regarding flow-diverter deployment within a previously placed stent. First, the microwire may go through the strut of a previous stent and potentially traverse in an "in-out-in" fashion. This phenomenon results in incomplete opening of the flow diverter. However, in most cases in the present study, this drawback was overcome by advancing the 5F intermediate catheter distally over the Marksman catheter, which promised the inner lumen and the central axis of the previous stent. This method ensures that the intermediate catheter cannot traverse the previous stent in the "in-out-in" fashion, though the microwire and microcatheter may.[26] Second, the previously placed stent strut or coil interrupts the visibility of the flow diverter, and the entire process of flow-diverter deployment cannot be easily identified using fluoroscopy. Thus, incomplete expansion of the flow diverter may potentially occur despite using a size-matched flow diverter and may be a main cause of thromboembolic complications and less effective flow diversion. In the present study, when a postimplantation angiogram or flat panel CT image showed equivocal apposition of the flow diverter in the segment where a metallic artifact due to coil mass was not prominent or when the wall apposition of the PED could not be assessed due to the surrounding coil mass, balloon angioplasty was performed. Balloon angioplasty was helpful for better apposition of the flow diverter to the previous stent.[27] Third, during the deployment of the flow diverter within the previously stented artery, the usual drag-and-drop technique can cause anchoring of the flow diverter to the previous stent, followed by a stretch of the flow

diverter. Therefore, instead of the drag-and-drop technique, direct deployment of the flow diverter to its final location may be helpful for the retreatment of stented aneurysms.[14,28]

Finally, if the previous stent did not sufficiently appose the vessel wall, blood flow may occur between the stent and vessel wall, referred to as an endoleak. The risk of endoleak is greater in cases with a previous stent than in those with a previous flow diverter[28] and may become an obstacle to flow diversion and neointima formation. Therefore, careful review and selection of patients are mandatory before using flow-diverter treatment for recurrent aneurysms after SAC. In addition, the flow diverter should be deployed to span the entire length of the previously placed stent, and both proximal and distal ends of the flow diverter should contact the normal parent artery, without interposition of the previous stent struts. Although an unrecognized gap may exist between the parent artery and the previously placed stent, the gap could be a semi-closed space and gradually obliterated if the flow diverter fully covered the entire length of the stent.

The present study demonstrated better clinical and angiographic outcomes compared with those of previous studies. This improved outcome may be largely due to rapid development of neurointerventional devices, including a new generation of PED (PED Flex), and intermediate catheters. In addition, the operators' gaining more experience in PED placement may also partly contribute to the improved results.

In the present study, a selection bias existed due to the retrospective design. The treatment strategy for every patient was determined after in-depth discussion among vascular neurosurgeons and interventional neuroradiologists for better clinical and anatomic outcomes. However, the present study was focused on demonstrating that flow-diverter treatment can be a retreatment option for specific situations such as SAC instead of the standard treatment (coil addition). Another limitation was the relatively small case series with a short-term follow-up. However, once complete occlusion of the aneurysm was achieved with the flow diverter, recurrence was extremely rare; therefore, long-term follow-up did not appear necessary. Further studies with larger populations are warranted to determine cases that are appropriate for flow-diverter treatment for recurrences after SAC.

CONCLUSIONS

In this case series, flow-diverter treatment for recurrent aneurysms after SAC was demonstrated to be safe and effective. Further study in a larger population is warranted.

ACKNOWLEDGMENTS

We would like to thank Editage (www.editage.co.kr) for English language editing.

Disclosures: Dong Joon Kim—*UNRELATED*: *Travel/Accommodations/Meeting Expenses Unrelated to Activities Listed*: Stryker Pacific Limited.

REFERENCES

1. Raymond J, Guilbert F, Weill A, et al. **Long-term angiographic recurrences after selective endovascular treatment of aneurysms with detachable coils.** *Stroke* 2003;34:1398–403 CrossRef Medline
2. Molyneux AJ, Birks J, Clarke A, et al. **The durability of endovascular coiling versus neurosurgical clipping of ruptured cerebral aneurysms: 18-year follow-up of the UK cohort of the International Subarachnoid Aneurysm Trial (ISAT).** *Lancet* 2015;385:691–97 CrossRef Medline
3. Piotin M, Blanc R, Spelle L, et al. **Stent-assisted coiling of intracranial aneurysms: clinical and angiographic results in 216 consecutive aneurysms.** *Stroke* 2010;41:110–15 CrossRef Medline
4. Liu JJ, Nielsen TH, Abhinav K, et al. **Surgical treatment of recurrent previously coiled and/or stent-coiled intracerebral aneurysms: a single-center experience in a series of 75 patients.** *World Neurosurg* 2019 Jan 11. [Epub ahead of print] CrossRef Medline
5. Muskens IS, Hertgers O, Lycklama À Nijeholt GJ, et al. **Outcomes of retreatment for intracranial aneurysms: a meta-analysis.** *Neurosurgery* 2019;85:750–61 CrossRef Medline
6. Kallmes DF, Ding YH, Dai D, et al. **A new endoluminal, flow-disrupting device for treatment of saccular aneurysms.** *Stroke* 2007;38:2346–52 CrossRef Medline
7. Fiorella D, Woo HH, Albuquerque FC, et al. **Definitive reconstruction of circumferential, fusiform intracranial aneurysms with the Pipeline Embolization Device.** *Neurosurgery* 2008;62:1115–20 CrossRef Medline
8. Kim BM, Shin YS, Baik MW, et al. **Pipeline Embolization Device for large/giant or fusiform aneurysms: an initial multi-center experience in Korea.** *Neurointervention* 2016;11:10–17 CrossRef Medline
9. Oishi H, Teranishi K, Yatomi K, et al. **Flow diverter therapy using a Pipeline Embolization Device for 100 unruptured large and giant internal carotid artery aneurysms in a single center in a Japanese population.** *Neurol Med Chir (Tokyo)* 2018;58:461–67 CrossRef Medline
10. Fang YB, Lin A, Kostynskyy A, et al. **Endovascular treatment of intracranial vertebrobasilar artery dissecting aneurysms: parent artery occlusion versus flow diverter.** *Eur J Radiol* 2018;99:68–75 CrossRef Medline
11. Zhu D, Yan Y, Zhao P, et al. **Safety and efficacy of flow diverter treatment for blood blister-like aneurysm: a systematic review and meta-analysis.** *World Neurosurg* 2018;118:e79–86 CrossRef Medline
12. Nelson PK, Lylyk P, Szikora I, et al. **The Pipeline Embolization Device for the Intracranial Treatment of Aneurysms trial.** *AJNR Am J Neuroradiol* 2011;32:34–40 CrossRef Medline
13. Fischer S, Vajda Z, Aguilar Perez M, et al. **Pipeline Embolization Device (PED) for neurovascular reconstruction: initial experience in the treatment of 101 intracranial aneurysms and dissections.** *Neuroradiology* 2012;54:369–82 CrossRef Medline
14. Chalouhi N, Chitale R, Starke RM, et al. **Treatment of recurrent intracranial aneurysms with the Pipeline Embolization Device.** *J Neurointerv Surg* 2014;6:19–23 CrossRef Medline
15. Daou B, Starke RM, Chalouhi N, et al. **Pipeline Embolization Device in the treatment of recurrent previously stented cerebral aneurysms.** *AJNR Am J Neuroradiol* 2016;37:849–55 CrossRef Medline
16. Heiferman DM, Billingsley JT, Kasliwal MK, et al. **Use of flow-diverting stents as salvage treatment following failed stent-assisted embolization of intracranial aneurysms.** *J Neurointerv Surg* 2016;8:692–95 CrossRef Medline
17. Roy D, Milot G, Raymond J. **Endovascular treatment of unruptured aneurysms.** *Stroke* 2001;32:1998–2004 CrossRef Medline
18. Shankar JJ, Quateen A, Weill A, et al. **Canadian Registry of LVIS Jr for Treatment of Intracranial Aneurysms (CaRLA).** *J Neurointerv Surg* 2017;9:849–53 CrossRef Medline
19. Park KY, Kim BM, Kim DJ, et al. **Y-configuration stenting for coiling of wide-neck bifurcation aneurysms using Low-profile Visualized Intraluminal Support Junior.** *J Neurointerv Surg* 2019;11:400–04 CrossRef Medline
20. Caragliano AA, Papa R, Pitrone A, et al. **The low-profile Neuroform Atlas stent in the treatment of wide-necked intracranial aneurysms: immediate and midterm results—an Italian multicenter registry.** *J Neuroradiol*. 2019 Apr 2. [Epub ahead of print]
21. Turk AS, Johnston SC, Hetts S, et al. **Geographic differences in endovascular treatment and retreatment of cerebral aneurysms.** *AJNR Am J Neuroradiol* 2016;37:2055–59 CrossRef Medline

22. Hauck EF, Natarajan SK, Hopkins LN, et al. **Salvage Neuroform stent-assisted coiling for recurrent giant aneurysm after waffle-cone treatment.** *J Neurointerv Surg* 2011;3:27–79 CrossRef Medline
23. Song Y, Wang Y, Li C, et al. **Retreatment and outcomes of recurrent intracranial vertebral artery dissecting aneurysms after stent assisted coiling: a single center experience.** *PLoS One* 2014;9:e113027 CrossRef Medline
24. Narata AP, de Moura FS, Larrabide I, et al. **The role of hemodynamics in intracranial bifurcation arteries after aneurysm treatment with flow-diverter stents.** *AJNR Am J Neuroradiol* 2018;39:323–30 CrossRef Medline
25. Lee JY, Cho YD, Kang HS, et al. **Healing of aneurysm after treatment using flow diverter stent: histopathological study in experimental canine carotid side wall aneurysm.** *J Korean Neurosurg Soc* 2020;63:34–44 CrossRef Medline
26. Mascitelli JR, Wei D, Oxley TJ, et al. **A technical consideration when using flow diversion for recurrent aneurysms following stent-assisted coiling.** *J Neurointerv Surg* 2017;9:e24 CrossRef Medline
27. Kühn AL, Rodrigues KM, Wakhloo AK, et al. **Endovascular techniques for achievement of better flow diverter wall apposition.** *Interv Neuroradiol* 2019;25:344–47 CrossRef Medline
28. Bender MT, Vo CD, Jiang B, et al. **Pipeline embolization for salvage treatment of previously stented residual and recurrent cerebral aneurysms.** *Interv Neurol* 2018;7:359–69 CrossRef Medline

Complications of Endovascular Treatments for Brain Arteriovenous Malformations: A Nationwide Surveillance

K. Sato, Y. Matsumoto, T. Tominaga, T. Satow, K. Iihara, and N. Sakai,
for the Japanese Registry of Neuroendovascular Therapy Investigators

ABSTRACT

BACKGROUND AND PURPOSE: Embolization is widely performed to treat brain arteriovenous malformations, but little has been reported on factors contributing to complications. We retrospectively reviewed a nationwide surveillance to identify risk factors contributing to complications and short-term clinical outcomes in the endovascular treatment of brain arteriovenous malformations.

MATERIALS AND METHODS: Data for endovascular treatment of brain arteriovenous malformations were extracted from the Japanese nationwide surveillance. Patient characteristics, brain arteriovenous malformation features, procedures, angiographic results, complications, and clinical outcomes at 30 days postprocedure were analyzed.

RESULTS: A total of 1042 endovascular procedures (788 patients; mean, 1.43 ± 0.85 procedures per patient) performed in 111 institutions from 2010 to 2014 were reviewed. Liquid materials were used in 976 procedures (93.7%): to perform presurgical embolization in 638 procedures (61.2%), preradiosurgical embolization in 160 (15.4%), and as sole endovascular treatment in 231 (22.2%). Complete or near-complete obliteration of brain arteriovenous malformations was obtained in 386 procedures (37.0%). Procedure-related complications occurred in 136 procedures (13.1%), including hemorrhagic complications in 59 (5.7%) and ischemic complications in 57 (5.5%). Univariate analysis identified deep venous drainage, associated aneurysms, infratentorial location, and preradiosurgical embolization as statistically significant risk factors for complications. Multivariate analysis showed that embolization of brain arteriovenous malformations in the infratentorial location was significantly associated with complications. Patients with complications due to endovascular procedures had worse clinical outcomes 30 days after the procedures than those without complications.

CONCLUSIONS: Complications arising after endovascular treatment of brain arteriovenous malformations are not negligible even though they may play a role in adjunctive therapy, especially in the management of infratentorial brain arteriovenous malformations.

ABBREVIATIONS: bAVM = brain arteriovenous malformation; JR-NET = Japanese Registry of Neuroendovascular Therapy

Brain arteriovenous malformations (bAVMs) are rare lesions characterized by the presence of a nidus containing abnormal tortuous vascular channels between feeding arteries and draining veins without an intervening capillary network.[1] AVMs most commonly result in hemorrhage, which carries a mortality rate of 10%∼15% and a morbidity rate up to 50%.[2] The annual hemorrhage rate for AVMs is between 2% and 4% per year.[3-6] The main goal of therapy is complete AVM obliteration, which prevents future hemorrhage. Current treatment options include microsurgery, radiosurgery, embolization, or a combination of therapies.[7]

Endovascular embolization has typically been reserved as an adjunctive therapy in the management of bAVMs, either for preoperative devascularization or preradiosurgical volume reduction.[8] In addition, palliative or target embolization may be used in high-risk components of bAVMs to stabilize symptomatic lesions.[9] Recent technical advances, including flow-

Received October 14, 2019; accepted after revision January 10, 2020.

From the Department of Neuroendovascular Therapy (K.S., Y.M.), Kohnan Hospital, Sendai, Japan; Department of Neurosurgery (T.T.), Tohoku Graduate School of Medicine, Sendai, Japan; Department of Neurosurgery (T.S.), National Cerebral and Cardiovascular Center, Suita, Japan; Department of Neurosurgery (K.I.), Graduate School of Medical Sciences, Kyushu University, Fukuoka, Japan; and Department of Neurosurgery (N.S.), Kobe City Medical Center General Hospital, Kobe, Japan.

This study was supported, in part, by a Grant-in-Aid (Junkanki-Kaihatsu H24-4-3) from the National Cerebral and Cardiovascular Center, Japan, and by Hatazaki Foundation, Kobe, Japan.

Please address correspondence to Kenichi Sato, MD, Department of Neuroendovascular Therapy, Kohnan Hospital, 4-20-1 Nagamachi-minami, Taihaku-ku, Sendai, Japan, 982-8523; e-mail: kenmina@nsg.med.tohoku.ac.jp

Indicates open access to non-subscribers at www.ajnr.org
Indicates article with supplemental on-line tables.
http://dx.doi.org/10.3174/ajnr.A6470

directed microcatheters and liquid embolic materials such as *n*-BCA and ethylene-vinyl alcohol copolymer (Onyx; Medtronic, Irvine, California), make it possible to treat bAVMs with embolization alone in selected cases.[10-12] With expanded capabilities, appropriate patient selection and risk estimation for the endovascular procedure for treatment of bAVMs becomes paramount. Nonetheless, studies of the complications of embolization using multicenter data collection have been scarce.

In this study, we retrospectively reviewed a nationwide surveillance to elucidate notable risk factors of procedure-related complications and short-term clinical outcomes after endovascular treatment of bAVMs.

MATERIALS AND METHODS

Data Extraction

The Japanese Registry of Neuroendovascular Therapy (JR-NET) is a nationwide retrospective registration study. Clinical and procedural data were enrolled through a Web site constructed by the Translation Research Informatics Center (Kobe, Japan) and anonymously reviewed by the principal investigators. The institutional review board at Kobe City Medical Center General Hospital approved the study protocol of JR-NET. Because of the retrospective observational nature of the study, written informed consent was not obtained from patients. Previous studies have been reported on data from JR-NET1 and JR-NET2, which were conducted from 2005 to 2006 and 2007 to 2009, respectively.[13,14] A total of 40,169 endovascular procedures were reviewed in the JR-NET3 study from 2010 to 2014, including 1063 procedures (2.7% of all procedures) for bAVMs treated by embolization. After excluding incomplete or duplicate data, we analyzed 1042 procedures performed for bAVMs for which detailed data were available.

JR-NET studies were performed according to the principles of the Declaration of Helsinki.

Evaluation

The dataset of patients with bAVMs obtained from JR-NET3 included the following: basic information (patient age, sex, symptoms, mRS score before the procedure, and mRS 30 days after the procedure) and detailed information about the lesions (nidus location, maximal diameter, involvement of the eloquent brain area, associated aneurysms, and the features of the draining vein, including deep venous drainage, occlusion, stenosis, and varix). AVMs were also classified according to the Spetzler-Martin grading system.[15] Procedural data were documented, including the number of participating physicians, the number of procedures, scheduled or emergency procedures, embolization strategy, sensory-evoked potential and/or motor-evoked potential monitoring, provocation test, type of microcatheter and embolic material used, the number of feeding vessels cannulated, embolization results, and complications. The embolization strategy was defined as curative, target, presurgical, or preradiosurgical. Procedure-related complications were classified as hemorrhagic (AVM rupture and vessel perforation), ischemic (vessel occlusion and distal embolism), or others. Clinical outcomes 30 days after endovascular procedures were dichotomized into favorable (mRS 0–2) or poor (mRS 3–6) for statistical analysis.

Statistical Analysis

Statistical analyses were performed using JMP software (Version 12; SAS Institute, Cary, North Carolina). Numeric data are expressed as mean ± SD. Group comparisons of mean and categoric data were performed using the Student *t* test and Pearson χ^2 test as appropriate. *P* values $< .05$ were considered statistically significant. A multivariate statistical analysis of factors related to the occurrence of complications was performed using a logistic regression model. Variables found to be significant in the univariate analysis were selected for testing in the final model.

RESULTS

Patient Characteristics

Table 1 summarizes the baseline characteristics of the study population. We reviewed 788 patients (471 males [59.8%]; age range, 0–90 years; mean, 41.3 years of age) with bAVMs who underwent a total of 1042 embolization procedures (1.43 ± 0.85 procedures per patient) in 111 institutions between January 2010 and December 2014. Clinical presentation was hemorrhage in 548 patients (69.5%), while 110 patients were asymptomatic. A Spetzler-Martin grade was determined for 752 of the treated AVMs (95.4%). There were 136 grade I (17.3%), 273 grade II (34.6%), 224 grade III (28.4%), 98 grade IV (12.4%), and 21 grade V (2.7%) lesions. AVMs were located in the cortical regions in 574 patients (72.8%), were deep-seated in 35 (4.4%), in the cerebellum in 126 (16.0%), and in the brain stem in 17 (2.2%). Associated aneurysms were found in 146 AVMs (18.5%), including flow-related arterial aneurysms in 92 AVMs (11.7%) and intranidal aneurysms in 45 (5.7%). Abnormalities of the drainage route were detected in 290 AVMs (36.4%), including occlusion of the draining vein in 12 (1.5%), stenosis in 92 (11.7%), and venous varix in 186 (23.6%).

Modalities of Treatment

Endovascular treatment for bAVMs included presurgical embolization in 638 procedures (61.2%), preradiosurgical embolization in 160 (15.4%), target embolization in 144 (13.8%), and curative embolization in 87 (8.3%). The purposes of the endovascular procedure were unknown in 13 (1.2%). Presurgical embolization was performed in patients with AVMs of Spetzler-Martin grade I in 107 (16.8%) procedures, grade II in 224 (35.1%), grade III in 165 (25.9%), grade IV in 91 (14.3%), and grade V in 50 (7.8%) (Online Table 1). Of all embolization procedures, 124 (11.9%) were performed as an emergency procedure. Provocation and evoked-potentials were monitored in 117 (11.2%) and 39 (3.7%) procedures, respectively. Coils were used in 165 embolization procedures (15.8%); *n*-BCA, in 627 (60.2%); and Onyx, in 432 (41.5%). An average of 3.3 embolization sessions per procedure was achieved. All procedures were performed via a transarterial approach.

Treatment Results

Technical success was achieved in 1023 procedures (98.2%). Curative embolization achieved complete obliteration of the nidus in 55.2% (48 procedures) and near-complete obliteration in 27.6% (24 procedures). Overall, endovascular procedures resulted in complete or near-complete obliteration of the AVM in 37.0% (386 procedures) and partial

Table 1: Summary of baseline characteristics

Characteristics	
No. of patients	788
Age (mean) (yr)	41.3 ± 19.9
Male (No.) (%)	471 (59.8%)
Clinical presentation (No.) (%)	
Hemorrhage	548 (69.5%)
NHND	130 (16.5%)
Asymptomatic	110 (14.0%)
Preprocedural mRS (No.) (%)	
0	562 (71.3%)
1	84 (10.7%)
2	44 (5.6%)
3	34 (4.3%)
4	27 (3.4%)
5	15 (1.9%)
Unknown	22
Spetzler-Martin grade (No.) (%)	
I	136 (17.3%)
II	273 (34.6%)
III	224 (28.4%)
IV	98 (12.4%)
V	21 (2.7%)
Unknown	36 (4.6%)
Size (No.) (%)	
<3 cm	443 (56.2%)
3–6 cm	278 (35.3%)
>6 cm	38 (3.8%)
Deep venous drainage (No.) (%)	438 (55.6%)
Eloquence (No.) (%)	318 (40.4%)
Location (No.) (%)	
Cortical	574 (72.8%)
Deep	35 (4.4%)
Cerebellum	126 (16.0%)
Brain stem	17 (2.2%)
Others	36 (4.6%)
Associated aneurysm (No.) (%)	146 (18.5%)
Flow-related	92 (11.7%)
Intranidal	45 (5.7%)
Unrelated	9 (1.1%)
Abnormality of drainage route (No.) (%)	
Occlusion	12 (1.5%)
Stenosis	92 (11.7%)
Varix	186 (23.6%)

Note:—NHND indicates nonhemorrhagic neurologic deficit.

obliteration in 60.3% (628 procedures). No morphologic changes were observed in the remaining 17 AVMs (1.6%) based on postoperative radiologic examinations.

Complications

Complications occurred in 136 embolization procedures (13.1%), with hemorrhage observed in 59 (5.7%) and ischemia in 57 (5.5%). Hemorrhagic complications included AVM rupture in 26 procedures (2.4%) and vessel perforation or rupture due to catheterization in 33 (3.2%). AVM rupture occurred intraoperatively in 8 procedures (30.8% of patients with AVM rupture), within 24 hours after endovascular procedures in 9 (34.6%), within 7 days in 5 (19.2%), and within 30 days in 4 (15.4%). Of the cases of AVM rupture, 12 patients (46.2% of patients with AVM rupture) underwent emergency open surgery for removal of a hematoma as well as ruptured AVMs after embolization. Procedures with AVM rupture were associated with severe persistent disability in 8 patients (30.8% of patients with AVM rupture), mild persistent disability in 2 (7.7%), and transient neurologic deficits in 6 (23.1%). Death occurred in 2 patients (7.7%) with AVM rupture. There was no significant difference in patient characteristics, morphologic features of AVM, and the strategy, embolic materials, or results of the embolization between procedures with AVM rupture and those without.

Ischemic complications included normal artery occlusion in 34 procedures (59.6% of patients with ischemic complications), distal thrombotic embolism in 20 (35.1%), and arterial dissection due to catheterization in 3 (5.3%). Procedures with ischemic complications were associated with severe persistent disability in 9 patients (15.8% of patients with ischemic complications), mild persistent disability in 13 (22.8%), and transient neurologic deficits in 12 (21.1%).

Univariate analyses in regard to AVM features revealed that deep venous drainage ($P < .01$), infratentorial location including the cerebellum ($P < .01$) and/or brain stem ($P < .01$), and the presence of flow-related aneurysms ($P = .01$) were significantly correlated with procedure-related complications, while cortical location had a negative correlation with complications ($P < .01$, On-line Table 2). In relation to the type of endovascular procedure, preradiosurgical embolization was associated with procedure-related complications ($P < .05$, Table 2). Infrantentorial location, including the cerebellum (OR, 2.38; 95% CI, 1.25–3.16) and brain stem (OR, 2.14; 95% CI, 1.48–10.13), remained significantly associated with procedure-related complications in a multivariate analysis ($P < .01$). AVM rupture (7/147, 4.8%) and ischemia (14/147, 9.5%) occurred more frequently in cerebellar AVMs than AVMs in other regions (16/895, 1.8%, $P < .05$, and 40/895, 4.5%, $P < .01$, respectively), while ischemic complications (6/20, 30%) occurred more frequently in brain stem AVMs than in other regions (48/1022, 4.7%, $P < .01$).

Clinical Outcomes

The 30-day morbidity and mortality rates were 291 (27.9%) and 8 (0.8%) of 1042 procedures, respectively. Two of the 8 deaths were accompanied by hemorrhagic complications (AVM rupture, $n = 2$). Endovascular procedures with complications were significantly associated with worse outcome compared with procedures without complications ($P < .05$, Table 3).

To determine the risk factors associated with the deterioration of mRS scores, we compared the procedures that led to worse mRS scores 30 days after the endovascular procedures and those in which mRS scores of patients improved or did not change (On-line Table 3). Univariate analyses revealed that older age ($P \leq .001$), hemorrhagic presentation ($P \leq .001$), nidus size ≤3 cm ($P = .001$), infratentorial nidus location ($P \leq .001$), presurgical embolization ($P = .021$), complete obliteration ($P = .003$), and procedure-related complications ($P \leq .001$) were significantly correlated with the deterioration of mRS scores 30 days after endovascular treatment. Older age ($P = .026$; OR, 0.99; 95% CI, 0.99–1.0), hemorrhagic presentation ($P \leq .001$; OR, 4.05; 95% CI, 2.91–5.73), presurgical embolization ($P = .002$; OR, 1.56; 95% CI, 1.17–2.09), complete obliteration ($P = .021$; OR, 1.71; 95% CI, 1.08–2.69), and procedure-related complications ($P \leq .001$; OR, 2.02; 95% CI, 1.36–3.02) remained significantly associated with the deterioration of mRS scores 30 days after endovascular treatment in a multivariate analysis.

Table 2: Endovascular procedures

	Total	Complication		*P* Value		OR (95% CI)
		Yes	No	Uni-	Multi-	
No. of procedures (%)	1042	136 (13.1%)	906 (86.9%)			
Emergency (No.) (%)	124	13 (9.6%)	111 (10.6%)	.366		
Provocation test (No.) (%)	117 (11.2%)	8 (5.9%)	109 (12.0%)	.059		
SEP and/or MEP monitoring (No.) (%)	39 (3.7%)	7 (5.1%)	32 (3.5%)	.561		
No. of treatments (No.) (%)						
Initial	778 (75.6%)	104 (76.5%)	684 (75.5%)	.48		
Second and more	254 (24.4%)	32 (23.5%)	222 (24.5%)	.48		
Strategy (No.) (%)						
Curative	87 (8.3%)	17 (12.5%)	70 (7.7%)	.061		
Target	144 (13.8%)	15 (11.0%)	129 (14.2%)	.312		
Presurgical	638 (61.2%)	74 (54.4%)	564 (62.3%)	.08		
Preradiosurgical	160 (15.4%)	29 (21.3%)	131 (14.5%)	.038	.074	1.13 (0.96–2.44)
No. of approaches (mean)		3.2 ± 1.2	3.3 ± 1.5	.28		
Embolic material (No.) (%)						
Coils	165 (15.8%)	16 (11.8%)	149 (15.3%)	.163		
n-BCA	627 (60.2%)	83 (61.0%)	544 (60.0%)	.827		
Onyx	432 (41.5%)	64 (47.1%)	368 (40.6%)	.073		
Results (No.) (%)						
Complete obliteration	101 (9.7%)	18 (13.2%)	83 (9.2%)	.134		
Nearly complete	285 (27.3%)	38 (27.9%)	247 (27.3%)	.869		
Partial	628 (60.3%)	76 (55.9%)	552 (60.9%)	.262		
Unchanged	17 (1.6%)	3 (2.2%)	14 (1.5%)	.571		

Note:—SEP indicates sensory-evoked potential; MEP, motor-evoked potential.

Table 3: mRS at 30 days after endovascular procedure

	Total	Complications		Univariate (*P* Value)
		Yes	No	
No. of Procedures (%)	1042	136 (13.1%)	906 (86.9%)	
mRS score (No.) (%)				
0–2	743 (71.3%)	87 (64.0%)	656 (72.4%)	.046
3–6	299 (28.7%)	49 (36.0%)	250 (27.6%)	.046

DISCUSSION

We reviewed 1042 AVM embolization procedures using data extracted from a nationwide surveillance (JR-NET3). Of all the cases reviewed, 13.1% experienced complications, including hemorrhage in 5.7% and ischemia in 5.5%, which are consistent with the reported rates of complications in 6.4%–21% of procedures.[16-22] Multivariate analysis showed that embolization for infratentorial AVMs was significantly associated with complications. To our knowledge, this study includes the largest number of patients with bAVMs treated by endovascular procedures across multiple centers since the advent of current neuroendovascular techniques.

With the advances in neuroendovascular treatment throughout the past 2 decades, new techniques and devices have improved the possibility for successful embolization of bAVMs, alone or in combination with other therapeutic modalities.[17,23,24] Despite the fairly large number of patients with bAVMs who are treated with embolization, published data on complications associated with embolization procedures are surprisingly scarce or only based on the experience of a single institution. Refinement of bAVM risk assessment for endovascular treatment is imperative in ensuring favorable outcome.[25]

In the pre-Onyx era, endovascular treatment for bAVMs was deemed to carry a procedural risk related to the Spetzler-Martin grade, number of embolizations treated, and the patient characteristics (increased age and absence of pretreatment neurologic deficits).[26,27] After the introduction of Onyx for AVM embolizations, Bell et al[25] reported their experience of transarterial embolization in 126 patients with bAVMs and concluded that procedure-related complications did not correlate with the Spetzler-Martin grade, but with a novel endovascular grading scale incorporating the number of feeding arteries, eloquence, and the presence of an arteriovenous fistula component. Pan et al[19] categorized complications of AVM embolization using liquid materials into technique-related and non-technique-related. Technique-related complications, such as those induced by navigation or removal of the microcatheter and migration of embolic materials, can be overcome by further improvement in the endovascular procedures and devices. Complications unrelated to the endovascular technique are mainly associated with angioarchitectural characteristics of bAVMs, including eloquent cortical location or exclusive deep venous drainage.[19] Baharvahdat et al[16] analyzed 846 embolization procedures performed in their institution during a 10-year period and reported that hemorrhagic complications occurred in 11% of cases, including periprocedural arterial perforation (48%) and AVM rupture (52%). They also identified premature venous occlusion as an independent predictor of severe hemorrhagic complication. Reportedly higher volumes of embolic agent injected in a single session and deposition on the venous outflow before complete occlusion of the bAVM could account for severe hemorrhagic complications.[18,28]

In the present study, although the volume of injected liquid agent was not evaluated, the use of Onyx was not associated with higher complication rates, probably because >60% of the

performed endovascular procedures were planned as presurgical embolizations followed by early surgical resection of the embolized AVMs and not as a curative embolization. By contrast, preradiosurgical embolization was significantly associated with procedure-related complications in univariate statistical analysis. This finding might be because preradiosurgical embolizations are mainly performed for bAVMs in locations not suitable for surgical removal, such as AVMs in the eloquent or deep-seated locations, both of which are reportedly associated with a higher risk of complications after embolization.[19] The use of Onyx in such locations does not preclude complications in the preradiosurgical embolization (On-line Table 4). Considering that embolization before radiosurgery can decrease the rate of AVM obliteration, preradiosurgical AVM embolization should be decided prudently.[29]

Patients with infratentorial AVMs have worse outcomes than those with supratentorial lesions.[30] They are more likely to present with hemorrhage, with annual rates of hemorrhage ranging from 4.4% to 11.6%, compared with all AVMs (2%–4%), and with an annual rehemorrhage rate of 34.4% for ruptured AVMs managed conservatively.[31] Infratentorial AVMs are more frequently associated with feeding artery aneurysms than supratentorial AVMs (25% versus 5%).[32-34] Associated aneurysms are the source of bleeding in 10.5% of cases of infratentorial AVMs, but in only 1.7% of cases of supratentorial AVMs.[34,35] Hemorrhages occurring from infratentorial AVMs are more likely to be symptomatic, with a mortality rate of 60% due to their presence in the narrow confines of the posterior fossa and the proximity to highly eloquent structures.[30,31,36]

These findings support an aggressive management for infratentorial AVMs both before and after rupture. However, infratentorial AVMs have also been reported to be difficult to treat with open surgery[37,38] or stereotactic radiosurgery,[39,40] and multimodal treatments including embolization have been recommended.[41] The present study shows that embolization of infratentorial AVMs could also involve procedure-related complications with a significantly higher rate. Vessel tortuosity, a lower safety margin of eloquent areas, or frequent association with flow-related aneurysms might complicate embolization of infratentorial AVMs. A meticulous treatment plan is mandatory because procedure-related complications tend to be severe following the endovascular treatment of infratentorial AVMs.

The JR-NET study group previously reported the procedural complications of endovascular treatment for bAVMs (JR-NET1 and 2)[14] after analyzing the data from 987 endovascular procedures for bAVMs performed from January 2005 and December 2009. We observed some differences in the results of bAVM embolizations between the present study and JR-NET1 and JR-NET2, possibly because of Onyx being approved for presurgical embolization in September 2009. As a result, Onyx was used as an embolic material in only 54 (5.5%) procedures assessed in JR-NET1 and JR-NET2, while 432 (41.5%) procedures in the present study were performed using Onyx.

The introduction of Onyx might lead to a higher rate of AVM occlusion and procedure-related complications, changing the risk factors for endovascular treatments of bAVMs. In the present study, we did not observe any significant change in the annual rate of complete obliteration and procedure-related complications since Onyx has become widespread in the endovascular treatment of bAVMs in Japan (data not shown). Moreover, the recent advances in the field of embolization techniques such as transvenous embolization[42] and the introduction of dual-lumen balloon microcatheters[43] or the detachable-tip microcatheters[44] for liquid embolic material are expected to improve the rate of nidus occlusion with fewer complications, though none are currently available in Japan.

This study has some limitations, including its retrospective nature and short-term follow-up period. The clinical outcomes for patients with bAVMs treated by an operation or radiosurgery after embolization were not available, so we could not determine the mRS scores 30 days after presurgical embolization to assess whether the outcomes or complications of open surgery led to any score change in these patients. Long-term outcomes, including recanalization and bleeding rates after curative embolization, were also not available. We extracted data from JR-NET3, which includes the data from 111 major neurointerventional registered centers but may not represent the nationwide total. Future studies evaluating the long-term clinical outcomes, including recanalization and bleeding rates after embolizations, may be warranted, and further analysis could include a heterogeneous population of multiple medical centers in Japan as well as in other countries.

CONCLUSIONS

We observed that complications of endovascular treatment may result in worse outcomes in patients with bAVMs. Thus, interventionalists should be aware of potential complications, especially in the management of infratentorial AVMs.

ACKNOWLEDGMENTS

The JR-NET3 Study Group: Co-Principal Investigators: Nobuyuki Sakai, Kobe City Medical Center General Hospital, Kobe, Japan; Koji Iihara, Kyushu University, Fukuoka, Japan; and Tetsu Satow, National Cerebral and Cardiovascular Center, Suita, Japan; Investigators: Masayuki Ezura, Sendai Medical Center, Sendai, Japan; Akio Hyodo, Dokkyo Medical University Saitama Medical Center, Koshigaya, Japan; Shigeru Miyachi, Aichi Medical University, Aichi, Japan; Susumu Miyamoto, Kyoto University, Kyoto, Japan; Yoji Nagai, Kobe University, Kobe, Japan; Kunihiro Nishimura, National Cerebral and Cardiovascular Center, Suita, Japan; and Kazunori Toyoda, National Cerebral and Cardiovascular Center, Suita, Japan; Coinvestigators: Toshiyuki Fujinaka, Osaka Medical Center, Osaka, Japan; Toshio Higashi, Fukuoka University, Fukuoka, Japan; Masaru Hirohata, Kurume University, Kurume, Japan; Akira Ishii, Kyoto University, Kyoto, Japan; Hirotoshi Imamura, Kobe City Medical Center General Hospital, Kobe, Japan; Yasushi Ito, Shinrakuen Hospital, Niigata, Japan; Naoya Kuwayama, Toyama University, Toyama, Japan; Hidenori Oishi, Juntendo University, Tokyo, Japan; Yuji Matsumaru, Tsukuba University, Tsukuba, Japan; Yasushi Matsumoto, Kohnan Hospital, Sendai, Japan; Ichiro Nakahara, Fujita Medical University, Aichi, Japan; Chiaki Sakai, Hyogo College of Medicine, Nishinomiya, Japan; Kenji Sugiu, Okayama University, Okayama, Japan; Tomoaki Terada, Showa University Fujigaoka Hospital, Kanagawa, Japan; Shinichi Yoshimura,

Hyogo College of Medicine, Nishinomiya, Japan; and Certified Specialist of Japanese Society of Neuroendovascular Therapy.

Disclosures: Yasushi Matsumoto—*UNRELATED*: *Payment for Lectures Including Service on Speakers Bureaus*: Medtronic, Stryker, Medicos Hirata, KANEKA MEDIX. Nobuyuki Sakai—*RELATED*: *Grant*: Terumo; *UNRELATED*: *Board Membership*: Terumo; *Consultancy*: BioMedical Solutions; *Grants/Grants Pending*: Daiichi-Sankyo, Terumo*; *Payment for Lectures Including Service on Speakers Bureaus*: Medtronic, Stryker, Terumo. Koji Iihara—*UNRELATED*: Biomedical Solutions: practical research project for lifestyle-related diseases by the Japan Agency for Medical Research and Development, grants-in-aid from the Japanese Ministry of Health, Labor and Welfare, KAKENHI. *Money paid to the institution.

REFERENCES

1. Fleetwood IG, Steinberg GK. **Arteriovenous malformations.** *Lancet* 2002;359:863–73 CrossRef Medline
2. Arteriovenous Malformation Study Group**. Arteriovenous malformations of the brain in adults.** *N Engl J Med* 1999;340:1812–18 CrossRef Medline
3. Brown RD Jr, Wiebers DO, Forbes G, et al. **The natural history of unruptured intracranial arteriovenous malformations.** *J Neurosurg* 1988;68:352–57 CrossRef Medline
4. Mast H, Young WL, Koennecke HC, et al. **Risk of spontaneous haemorrhage after diagnosis of cerebral arteriovenous malformation.** *Lancet* 1997;350:1065–68 CrossRef Medline
5. Ondra SL, Troupp H, George ED, et al. **The natural history of symptomatic arteriovenous malformations of the brain: a 24-year follow-up assessment.** *J Neurosurg* 1990;73:387–91 CrossRef Medline
6. Gross BA, Du R. **Natural history of cerebral arteriovenous malformations: a meta-analysis.** *J Neurosurg* 2013;118:437–43 CrossRef Medline
7. Darsaut TH, Guzman R, Marcellus ML, et al. **Management of pediatric intracranial arteriovenous malformations: experience with multimodality therapy.** *Neurosurgery* 2011;69:540–56 CrossRef Medline
8. Ogilvy CS, Stieg PE, Awad I, et al; Special Writing Group of the Stroke Council, American Stroke Association. **AHA Scientific Statement: recommendations for the management of intracranial arteriovenous malformations—a statement for healthcare professionals from a special writing group of the Stroke Council, American Stroke Association.** *Stroke* 2001;32:1458–71 CrossRef Medline
9. Alexander MD, Hippe DS, Cooke DL, et al. **Targeted embolization of aneurysms associated with brain arteriovenous malformations at high risk for surgical resection: a case-control study.** *Neurosurgery* 2018;82:343–49 CrossRef Medline
10. Potts MB, Zumofen DW, Raz E, et al. **Curing arteriovenous malformations using embolization.** *Neurosurg Focus* 2014;37:E19 CrossRef Medline
11. van Rooij WJ, Jacobs S, Sluzewski M, et al. **Curative embolization of brain arteriovenous malformations with Onyx: patient selection, embolization technique, and results.** *AJNR Am J Neuroradiol* 2012;33:1299–304 CrossRef Medline
12. Valavanis A, Yaş argil MG. **The endovascular treatment of brain arteriovenous malformations.** *Adv Tech Stand Neurosurg* 1998;24:131–214 CrossRef Medline
13. Sakai N, Yoshimura S, Taki W, et al; Japanese Registry of Neuroendovascular Therapy Investigators. **Recent trends in neuroendovascular therapy in Japan: analysis of a nationwide survey: Japanese Registry of Neuroendovascular Therapy (JR-NET) 1 and 2.** *Neurol Med Chir (Tokyo)* 2014;54:1–8 CrossRef Medline
14. Kondo R, Matsumoto Y, Endo H, et al. **Endovascular embolization of cerebral arteriovenous malformations: results of the Japanese Registry of Neuroendovascular Therapy (JR-NET) 1 and 2.** *Neurol Med Chir (Tokyo)* 2014;54:54–62 CrossRef
15. Spetzler RF, Martin NA. **A proposed grading system for arteriovenous malformations.** *J Neurosurg* 1986;65:476–83 CrossRef Medline
16. Baharvahdat H, Blanc R, Termechi R, et al. **Hemorrhagic complications after endovascular treatment of cerebral arteriovenous malformations.** *AJNR Am J Neuroradiol* 2014;35:978–83 CrossRef Medline
17. Cronqvist M, Wirestam R, Ramgren B, et al. **Endovascular treatment of intracerebral arteriovenous malformations: procedural safety, complications, and results evaluated by MR imaging, including diffusion and perfusion imaging.** *AJNR Am J Neuroradiol* 2006;27:162–76 Medline
18. Ovalle F, Shay SD, Mericle RA. **Delayed intracerebral hemorrhage after uneventful embolization of brain arteriovenous malformations is related to volume of embolic agent administered: multivariate analysis of 13 predictive factors.** *Neurosurgery* 2012;70:313–20 CrossRef Medline
19. Pan J, He H, Feng L, et al. **Angioarchitectural characteristics associated with complications of embolization in supratentorial brain arteriovenous malformation.** *AJNR Am J Neuroradiol* 2014;35:354–59 CrossRef Medline
20. Panagiotopoulos V, Gizewski E, Asgari S, et al. **Embolization of intracranial arteriovenous malformations with ethylene-vinyl alcohol copolymer (Onyx).** *AJNR Am J Neuroradiol* 2009;30:99–106 CrossRef Medline
21. Saatci I, Geyik S, Yavuz K, et al. **Endovascular treatment of brain arteriovenous malformations with prolonged intranidal Onyx injection technique: long-term results in 350 consecutive patients with complete endovascular treatment course.** *J Neurosurg* 2011;115:78–88 CrossRef Medline
22. Starke RM, Komotar RJ, Otten ML, et al. **Adjuvant embolization with N-butyl cyanoacrylate in the treatment of cerebral arteriovenous malformations: outcomes, complications, and predictors of neurologic deficits.** *Stroke* 2009;40:2783–90 CrossRef Medline
23. Crowley RW, Ducruet AF, McDougall CG, et al. **Endovascular advances for brain arteriovenous malformations.** *Neurosurgery* 2014;74:S74–82 CrossRef Medline
24. Van Beijnum J, van der Worp HB, Buis DR, et al. **Treatment of brain arteriovenous malformations: a systematic review and meta-analysis.** *JAMA* 2011;306:2011–19 CrossRef Medline
25. Bell DL, Leslie-Mazwi TM, Yoo AJ, et al. **Application of a novel brain arteriovenous malformation endovascular grading scale for transarterial embolization.** *AJNR Am J Neuroradiol* 2015;36:1303–09 CrossRef Medline
26. Kim LJ, Albuquerque FC, Spetzler RF, et al. **Postembolization neurological deficits in cerebral arteriovenous malformations: stratification by arteriovenous malformation grade.** *Neurosurgery* 2006;58:53–59; discussion 53–59 CrossRef Medline
27. Hartmann A, Pile-Spellman J, Stapf C, et al. **Risk of endovascular treatment of brain arteriovenous malformations.** *Stroke* 2002;33:1816–20 CrossRef Medline
28. Heidenreich JO, Hartlieb S, Stendel R, et al. **Bleeding complications after endovascular therapy of cerebral arteriovenous malformations.** *AJNR Am J Neuroradiol* 2006;27:313–16 Medline
29. Xu F, Zhong J, Ray A, et al. **Stereotactic radiosurgery with and without embolization for intracranial arteriovenous malformations: a systematic review and meta-analysis.** *Neurosurg Focus* 2014;37:E16 CrossRef Medline
30. Abla AA, Nelson J, Rutledge WC, et al. **The natural history of AVM hemorrhage in the posterior fossa: comparison of hematoma volumes and neurological outcomes in patients with ruptured infra- and supratentorial AVMs.** *Neurosurg Focus* 2014;37:E6 CrossRef Medline
31. Arnaout OM, Gross BA, Eddleman CS, et al. **Posterior fossa arteriovenous malformations.** *Neurosurg Focus* 2009;26:E12 CrossRef Medline
32. Kouznetsov E, Weill A, Ghostine JS, et al. **Association between posterior fossa arteriovenous malformations and prenidal aneurysm rupture: potential impact on management.** *Neurosurg Focus* 2014;37:E4 CrossRef Medline

33. Westphal M, Grzyska U. **Clinical significance of pedicle aneurysms on feeding vessels, especially those located in infratentorial arteriovenous malformations.** *J Neurosurg* 2000;92:995–1001 CrossRef Medline
34. Schmidt NO, Reitz M, Raimund F, et al. **Clinical relevance of associated aneurysms with arteriovenous malformations of the posterior fossa.** *Acta Neurochir Suppl* 2011;112:131–35 CrossRef Medline
35. da Costa L, Thines L, Dehdashti AR, et al. **Management and clinical outcome of posterior fossa arteriovenous malformations: report on a single-centre 15-year experience.** *J Neurol Neurosurg Psychiatry* 2009;80:376–79 CrossRef Medline
36. Fults D, Kelly DL Jr. **Natural history of arteriovenous malformations of the brain: a clinical study.** *Neurosurgery* 1984;15:658–62 CrossRef Medline
37. Rodríguez-Hernández A, Kim H, Pourmohamad T, et al; University of California, San Francisco Arteriovenous Malformation Study Project. **Cerebellar arteriovenous malformations: anatomic subtypes, surgical results, and increased predictive accuracy of the supplementary grading system.** *Neurosurgery* 2012;71:1111–24 CrossRef Medline
38. Han SJ, Englot DJ, Kim H, et al. **Brainstem arteriovenous malformations: anatomical subtypes, assessment of "occlusion in situ" technique, and microsurgical results.** *J Neurosurg* 2015;122:107–17 CrossRef Medline
39. Bowden G, Kano H, Tonetti D, et al. **Stereotactic radiosurgery for arteriovenous malformations of the cerebellum.** *J Neurosurg* 2014;120:583–90 CrossRef Medline
40. Koga T, Shin M, Terahara A, et al. **Outcomes of radiosurgery for brainstem arteriovenous malformations.** *Neurosurgery* 2011;69:45–51 CrossRef Medline
41. Kelly ME, Guzman R, Sinclair J, et al. **Multimodality treatment of posterior fossa arteriovenous malformations.** *J Neurosurg* 2008;108:1152–61 CrossRef Medline
42. Mendes GA, Kalani MY, Iosif C, et al. **Transvenous curative embolization of cerebral arteriovenous malformations: a prospective cohort study.** *Neurosurgery* 2018;83:957–64 CrossRef Medline
43. Spiotta AM, James RF, Lowe SR, et al. **Balloon-augmented Onyx embolization of cerebral arteriovenous malformations using a dual-lumen balloon: a multicenter experience.** *J Neurointerv Surg* 2015;7:721–27 CrossRef Medline
44. Flores BC, See AP, Weiner GM, et al. **Use of Apollo detachable-tip microcatheter for endovascular embolization of arteriovenous malformations and arteriovenous fistulas.** *J Neurosurg* 2018;130:963–71 CrossRef Medline

Treatment Outcomes of Endovascular Embolization Only in Patients with Unruptured Brain Arteriovenous Malformations: A Subgroup Analysis of ARUBA (A Randomized Trial of Unruptured Brain Arteriovenous Malformations)

A.I. Qureshi, O. Saeed, S. Sahito, I. Lobanova, J. Liaqat, F. Siddiq, and C.R. Gomez

ABSTRACT

BACKGROUND AND PURPOSE: Endovascular embolization only has been advocated for treatment of brain arteriovenous malformations in recent trials. Our aim was to evaluate the results of embolization only in a cohort of patients who were enrolled in the A Randomized Trial of Unruptured Brain Arteriovenous Malformations (ARUBA) study at 39 clinical sites in 9 countries.

MATERIALS AND METHODS: We analyzed the rates and severity of stroke and death in patients who underwent embolization only. Events were identified through in-person neurologic follow-up visits performed at 6-month intervals during the first 2 years and annually, with telephone contact every 6 months thereafter. All event-related data were reviewed by independent adjudicators.

RESULTS: Among 30 patients who had embolization planned, 26 underwent embolization only. A total of 13 stroke events were reported in the follow-up period among 26 subjects (ischemic, hemorrhagic, or both in 4, 7, and 2 subjects, respectively). The adverse event occurred after the first embolization in 11 of 13 patients. One patient had a major motor deficit, and 2 patients developed major visual field deficits. One event was fatal. The modified Rankin Scale score was 0–2 at last follow-up in 11 of the 12 stroke survivors. Estimated stroke-free survival was 46% at 12 months.

CONCLUSIONS: Although the rates of stroke and/or death were high in patients treated with embolization only in ARUBA, the rates of favorable outcomes following stroke were high during follow-up.

ABBREVIATION: BAVM = brain arteriovenous malformations

A Randomized Trial of Unruptured Brain Arteriovenous Malformations (ARUBA) reported the risk of death and symptomatic stroke in 223 patients with an unruptured brain arteriovenous malformation (BAVM) randomized to either medical management alone or medical management with interventional therapy.[1] For 114 patients allocated to interventional therapy, brain arteriovenous malformations were treated by neurosurgery alone ($n = 5$), embolization alone ($n = 30$), or radiation therapy alone ($n = 31$) or using a multimodal approach ($n = 28$). The study was discontinued after the Data and Safety Monitoring Board appointed by the National Institute of Neurological Disorders and Stroke of the National Institutes of Health recommended halting randomization because the composite end point of death or symptomatic stroke had occurred in 10.1% patients in the medical management group compared with 30.7% in the interventional therapy group, which exceeded the prespecified stopping boundary.

Questions have been raised regarding the high-rate use of primary (rather than adjunct) endovascular treatment in the ARUBA trial, and other authors have recommended an in-depth analysis of adverse events in patients who were treated with embolization only in the trial.[2,3] Embolization as a primary treatment for BAVM has been reported in approximately

Received August 23, 2019; accepted after revision January 20, 2020.

From the Zeenat Qureshi Stroke Institute (A.I.Q., O.S., S.S., I.L., J.L.), St. Cloud, Minnesota; Department of Neurology (A.I.Q., C.R.G.) and Division of Neurological Surgery (F.S.), University of Missouri, Colombia, Missouri; Department of Neurology (O.S.), University of Tennessee Health Science Center, Memphis, Tennessee; Department of Neurology (S.S.), JFK Medical Center, Edison, New Jersey; and Pakistan Emirates Military Hospital (J.L.), Rawalpindi, Pakistan.

Paper previously presented as poster at: Annual Meeting of the American Academy of Neurology, May 4–10, 2019; Philadelphia, Pennsylvania.

Please address correspondence to Adnan I. Qureshi, MD, University of Missouri, Department of Neurology, One Hospital Dr., CE507, Columbia, MO 6521; e-mail: qureshai@gmail.com

Indicates article with supplemental on-line tables.

http://dx.doi.org/10.3174/ajnr.A6443

2%–10% of the patients in other studies, which is much lower than the 26% use rate in ARUBA.[4,5] Furthermore, considerable variation in the rates of severe complications with embolization (overall, 6.6%; range, 0%–28%) was seen between studies for unruptured and ruptured BAVMs in a meta-analysis, highlighting the role of study-specific in-depth analysis.[6]

We performed an in-depth analysis of the results of endovascular embolization only in patients with BAVMs treated in ARUBA trial.

MATERIALS AND METHODS

We acquired the public use of ARUBA dataset files from the National Institute of Neurological Disorders and Stroke clinical research archives. The design of the ARUBA trial has been described previously.[1] The trial was a prospective, multicenter, randomized controlled trial involving 39 active clinical sites in 9 countries. All patients included were 18 years of age or older with an unruptured BAVM diagnosed by conventional angiography, MR imaging or MR angiography, or CT or CT angiography, with no imaging evidence of previous BAVM-related intracerebral hemorrhage or any previous interventional treatment attempt (endovascular, surgical, radiation therapy), or who were considered untreatable by the local investigators.

Patients who had concomitant vascular or brain disease that interfered with/or contraindicated any interventional therapy type (stenosis/occlusion of neck artery) or known allergy to iodine contrast agents were excluded. The trial excluded patients with multifocal BAVMs, arteriovenous or spinal fistula, vein of Galen type malformation, cavernous malformation, dural arteriovenous fistula, developmental venous anomaly, neurocutaneous syndrome such as cerebroretinal angiomatosis (von Hippel-Lindau syndrome), encephalo-trigeminal syndrome (Sturge-Weber) or Wyburn-Mason syndrome, Moyamoya-type changes, or hereditary hemorrhagic telangiectasia (Osler-Weber-Rendu disease).

Participating sites had experience with the management of at least 10 BAVMs per year, the presence of a multidisciplinary arteriovenous malformation treatment team, and documented academic interest in BAVM research. The choice of endovascular treatment in patients allocated to the interventional therapy group was made by local ARUBA investigators as the technique to achieve complete eradication of the BAVM. Baseline imaging (MR imaging or MR angiography, CT or CT angiography, or conventional angiography) was collected after enrollment for each patient. Additionally, all baseline imaging studies were subject to independent centralized adjudication for diagnostic accuracy. Lesion eradication was confirmed on the basis of conventional angiography and central adjudication.

Patients were actively screened for the possibility of new stroke, neurologic deficits, seizures, headaches, or any other clinically important event during in-person neurologic follow-up visits scheduled at 6-month intervals during the first 2 years and then annually or with telephone contact, which was performed every 6 months to supplement annual clinic visits after the first 2 years of randomization. Stroke was defined as a clinically symptomatic event (any new focal neurologic deficit, seizure, or new-onset headache) that was associated with imaging findings of hemorrhage or infarction. Hemorrhage was defined as fresh intracranial blood on head CT or MR imaging or in the CSF. Infarction was defined as a new ischemic lesion on cranial CT or MR imaging (diffusion-weighted, T2-weighted, or fluid-attenuated inversion recovery MR imaging). Any imaging studies related to neurologic adverse events were systematically collected in electronic format and included in the material for independent clinical event adjudication. All primary and secondary outcome events were adjudicated by an independent panel of 4 distinguished academic community members (neurology, interventional neuroradiology, neurosurgery, and radiosurgery).[7] If a stroke related to a BAVM occurred, the patient was seen within 48 hours of the event by a designated neurologist, and the data coordinating center was notified within 72 hours. The decision as to whether to continue with treatment and plans for the type of treatment were made by the treating team.

We selected all the patients in whom endovascular treatment was the only treatment used and reviewed the individual data elements in the public use trial dataset. For patients who developed a stroke event, we collected age and sex, BAVM location and size, Spetzler-Martin grade, number of embolizations, symptoms, stroke subtype (ischemic or hemorrhage), time interval between embolization and the stroke event, and the modified Rankin Scale score at last follow-up. We reviewed the description of events and classified them into visual field deficits, motor deficits, level of consciousness deficits, and others. Visual field deficits were classified as major if complete hemianopsia was reported. Motor deficits were classified as major if hemiplegia or both upper and lower extremities were involved. We also classified a deficit as major if at follow-up, the modified Rankin Scale score was >2.

Statistical Analysis

The analysis was predominantly descriptive. We calculated the 1-month rate of stroke and death as the proportion of patients who experienced the event relative to total number at risk. We compared the baseline, clinical, and angiographic variables of patients who were treated using embolization only according to whether they had a stroke event. We used the χ^2 test and ANOVA for categoric and continuous variables, respectively. Time to stroke event or death after embolization or the last known follow-up period in stroke-free patients was used to estimate the proportion of patients who would be alive and stroke-free at 12 months using Kaplan-Meier analysis and life tables. All data were analyzed using SPSS Statistics for Windows, Version 23.00, 64-bit edition (IBM, Armonk, New York).

RESULTS

Thirty patients of 116 randomized to interventional treatment were scheduled to have embolization. Of the 30 patients with intended embolization, only 26 patients underwent embolization. In 1 patient, the diagnosis of BAVM was not confirmed on the pretreatment angiogram. In 3 patients, the microcatheter could not be placed in the target feeders for safe or effective

embolization. Of the 26 patients, embolization was performed using Onyx (Covidien, Irvine, California) in 21 patients; Histoacryl (Braun, Melsungen, Germany) in 3 patients; and *N*-butyl cyanoacrylate and Glubran Tiss (Aspide Medical, La Talaudiére, France) in 1 patient each. The mean age of subjects was 43.7 ±11.1 years; 14 were men. The initial presentation was seizure with headache ($n = 3$), headache alone ($n = 6$), seizure alone ($n = 11$), focal deficits with seizure ($n = 1$), and focal deficits alone ($n = 3$). The BAVM was graded as Spetzler-Martin grades I, II, III, and IV in 7, 10, 8, and 1 subjects, respectively. The baseline clinical and angiographic characteristics of the subjects are presented in On-line Table 1. The average number of embolizations per subject was 3.2 (range, 1–9).

The median follow-up period after embolization was 11.8 ± 9.4 months (range, 0–30 months). A total of 13 stroke events were reported during the follow-up period among 26 subjects (69.8 per 1000 person-days follow-up). The strokes were reported as ischemic, hemorrhagic, or both in 4, 7, and 2 subjects, respectively. The adverse event occurred after first embolization in 11 of 13 patients.

The proportion of women among those who experienced stroke was significantly higher (69.2% versus 30.8%, $P = .02$). There was a higher proportion of subjects who developed stroke in subjects with Spetzler-Martin grades III and IV. The maximum BAVM size (anterior-posterior length) was nonsignificantly greater in patients who had a stroke (26.4 ± 14.2 mm versus 19.9 ± 6.3 mm, $P = .1$), and the side of the lesion was not associated with the occurrence of stroke (On-line Table 1). There appeared to be a higher prevalence of unrelated aneurysms and deep venous drainage among patients with stroke events. There was no difference in the mean number of embolizations in those who had stroke events (3.6 ± 2.5 versus 2.7 ± 1.4, $P = .3$).

A review of description of events demonstrated that episodic headache, bruit in the ear, or unilateral myosis occurred in 3 patients without any other neurologic deficits. One stroke event was fatal. Of the 12 stroke survivors, the modified Rankin Scale score was 0–2 at last follow-up in 11 subjects. One patient had a major motor deficit, and 2 patients developed major visual field deficits. The fatal stroke occurred in a 61-year-old woman who underwent embolization with Onyx for reduction of the BAVM nidus before stereotactic radiosurgery (On-line Table 2). The subject developed new-onset coma secondary to intracerebral hemorrhage 9 days after embolization and died a day later subsequent to withdrawal of care. Two patients developed homonymous hemianopsia deficits immediately postembolization with MR imaging demonstrating infarction in relevant distributions. Two others developed partial visual field deficits. One patient with a partial visual field had concurrent occipital headaches, and a second patient had skew deviation and partial upper gaze palsy. Three patients developed intraparenchymal hemorrhages, of which 1 was only associated with transient headache and the other 2 were associated with hemiplegia. Two patients developed upper extremity weakness postembolization (1 preceded by seizures). The estimated stroke-free survival was 46% at 12 months.

DISCUSSION

Key Results

We provide a detailed description of the stroke events that occurred in patients in the ARUBA trial who underwent embolization only. Stroke or death or both within 1 month following the procedure occurred in 15.4% of patients. Four patients met the definition of having a major neurologic deficit. Intracerebral hemorrhage occurred in 9 of 13 patients with a stroke event. One stroke event was fatal. One patient developed a major motor deficit, and 2 patients developed major visual field deficits. In the patient who developed a major motor deficit, the deficit occurred after 101 days, so it may be considered related to the disease process rather than the procedure. Some events were minor, such as episodic headache, bruit in the ear, or unilateral myosis occurring in 3 patients without any other neurologic deficits. The modified Rankin Scale score was 0–2 at last follow-up in 11 of the 12 stroke survivors. Therefore, major disability was infrequent among patients who actually had a stroke postembolization.

Limitations

This is a retrospective analysis of prospectively collected data. The issues regarding patient and procedure selection within the ARUBA trial have been mentioned earlier. Without in-depth procedural data, the relationship between individual components of the procedure and stroke and/or death cannot be determined. Furthermore, issues like intraprocedural anticoagulation and postprocedural blood pressure control could not be evaluated. We included patients who underwent only embolization, but it is possible that in some patients, additional treatment such as surgical excision or radiation therapy would have been performed in the absence of any stroke or death.

Interpretation

Certain aspects are important to understand before interpretation of the results. All the patients analyzed underwent embolization-only; therefore, our analysis avoids contamination by the consequences of surgery or radiosurgery. However, in some patients, additional surgery or radiation therapy may have been planned but was not performed, either due to good results or complications associated with embolization. We did not have data regarding the percentage of angiographic obliteration following the embolization, which prevented us from performing more in-depth analysis.

The rates of stroke events appeared higher than in the Brain Arteriovenous Malformations Embolization with Onyx (BRAVO) study, which included patients with BAVMs treatable using an endovascular approach who were included if the treatment was partially or completely performed using Onyx.[8] Patients who had experienced recent intracranial bleeding (in the month before the first embolization session) were excluded. Posttreatment intracerebral hemorrhage occurred in 10 of 117 patients who had undergone 237 embolization sessions. Nonhemorrhagic deficits occurred in 16 of 117 patients (9 were transient). The overall rate of any stroke event was 26 (22%) of 117 patients treated. Five (4.3%) patients died due to treatment-related complications similar to the 1 (3.8%) of 26 patients in the ARUBA trial. However, the rate of major stroke was 5.1% in the BRAVO trial and 15.3% in the ARUBA trial (there

were some differences in defining major stroke between the trials). There were 2 important differences between the 2 trials: The rate of patients with Spetzler-Martin AVM grades IV (22% versus 4%) and ruptured BAVM (34% versus none) was higher in the BRAVO trial. Most interesting, the rate of postembolization intracerebral hemorrhage was higher in unruptured AVMs (11.7%) than in ruptured AVMs (2.5%). Similarly, total obliteration was less common in unruptured AVMs (18.7%) than in ruptured AVMs (32.5%).

A single-center retrospective review of patients with unruptured BAVMs who met the inclusion criteria of ARUBA and underwent primary Onyx embolization[9] reported a 1-month rate of 13% for stroke or death and 3% for death following the procedure. Six of the 8 stroke events or death were intracerebral hemorrhages. It is possible that primary embolization of unruptured BAVMs is associated with a higher risk than ruptured BAVMs. There are certain attributes of BAVMs that are more prevalent in patients with ruptured BAVMs, such as intranidal fistulas[10] and flow-related aneurysms,[11] deep venous drainage,[10] small nidus size,[12] high feeding mean arterial pressure,[12]deep location,[13] venous stenosis,[14] a single draining vein,[15] and slow filling of feeding arteries.[16] It remains unclear whether certain angiographic characteristics in unruptured BAVMs predispose to an increased risk associated with embolization. Some studies have not found such a relationship.[17,18]

There is no consensus regarding the interpretation of the results of the ARUBA trial. Opinions vary as follows: 1) no implications because the trial design was full of flaws and not representative of current practices;[3] 2) a more limited role of embolization with more emphasis on surgery and radiation therapy;[19-21] and 3) a limited role for any treatment technique with greater emphasis on conservative management in the treatment of unruptured BAVMs.[1] The American Heart Association/American Stroke Association Scientific Statement acknowledges that the optimal approach to management of unruptured BAVMs remains a subject of debate because of insufficient high-quality, consistent evidence about the lifetime risks of intracerebral hemorrhage and its predictors and the complications associated with treatment.[22]

Generalizability

The implications of this analysis need to be discussed. The analysis provides more details regarding the stroke events and associated characteristics of patients and BAVMs. The analysis is an important step in understanding how to modify current practices when choosing embolization for unruptured BAVMs. Minor stroke events perhaps may not have the same significance compared with major events (in regard to disability and resource use), yet they may be classified as stroke events.[23] In the ARUBA trial, only 2 of 13 stroke events resulted in moderate-to-severe disability, categorized by a modified Rankin Scale score of >2 at last follow-up. Minor postembolization deficits may be acceptable if the treatment is effective in preventing major stroke and disability during follow-up,[24] considering that the incidence of first-ever hemorrhage in untreated patients with BAVM during follow-up was as follows: 0–9 years, 4.6%; 30–39 years, 21%; and 60–69 years, 40.0% in 1 study. The first intracranial hemorrhage was fatal in 4.6% of the patients. Approximately 28% of treated and untreated patients had a moderate-to-severe disability by the Oxford Handicap Scale at a mean follow-up of 10 years.[25,26] Primary or recurrent hemorrhage in patients with BAVM resulted in moderate-to-severe disability (modified Rankin Scale score, >2) in approximately 40% of patients. Crawford et al[27] reported that there was a 42% risk of intracerebral hemorrhage, a 29% risk of death, an 18% risk of epilepsy, and a 27% risk of having a neurologic handicap by 20 years after diagnosis in patients with BAVMs without treatment.

CONCLUSIONS

A simulation analysis demonstrated that the risk of intervention in unruptured BAVMs would have to be reduced by 50% to achieve equivalence and by 80% to achieve superiority to medical management on the basis of the results of ARUBA trial.[28] Newer embolization techniques have the promise of increasing the efficacy of treatment, though safety and long-term effectiveness remain unclear. There are some encouraging initial data supporting the role of targeted embolization focusing on selected regions such as intranidal aneurysms or high-flow fistulas[29-31] in achieving a better balance in the risk-benefit ratio. A transvenous approach and embolization of BAVMs that are supplied by very narrow and tortuous arterial pedicles may have the potential to increase the curative rates.[32,33] The American Heart Association/American Stroke Association Scientific Statement[22] recommends further clinical studies to investigate the reproducibility of the findings of ARUBA and to investigate whether the balance of risk between conservative management and intervention is different in specific groups. Certain trials are already underway such as the Treatment of Brain AVMs (TOBAS) study and the Transvenous Approach for the Treatment of Cerebral Arteriovenous Malformations (TATAM) study to add additional information regarding the role of embolization in BAVM treatment.

REFERENCES

1. Mohr JP, Parides MK, Stapf C, et al; international ARUBA investigators. **Medical management with or without interventional therapy for unruptured brain arteriovenous malformations (ARUBA): a multicentre, non-blinded, randomised trial.** *Lancet* 2014;383:614–21 CrossRef Medline
2. Russin J, Spetzler R. **Commentary: the ARUBA trial.** *Neurosurgery* 2014;75:E96–97 CrossRef Medline
3. Bambakidis NC, Cockroft KM, Hirsch JA, et al. **The case against a randomized trial of unruptured brain arteriovenous malformations: misinterpretation of a flawed study.** *Stroke* 2014;45:2808–10 CrossRef Medline
4. Link TW, Winston G, Schwarz JT, et al. **Treatment of unruptured brain arteriovenous malformations: a single-center experience of 86 patients and a critique of the A Randomized Trial of Unruptured Brain Arteriovenous Malformations (ARUBA) Trial.** *World Neurosurg* 2018;120:e1156–62 CrossRef Medline
5. Rutledge WC, Abla AA, Nelson J, et al. **Treatment and outcomes of ARUBA-eligible patients with unruptured brain arteriovenous malformations at a single institution.** *Neurosurg Focus* 2014;37:E8 CrossRef Medline
6. van Beijnum J, van der Worp HB, Buis DR, et al. **Treatment of brain arteriovenous malformations: a systematic review and meta-analysis.** *JAMA* 2011;306:2011–19 CrossRef Medline

7. Mohr JP, Moskowitz AJ, Parides M, et al. **Hull down on the horizon: A Randomized trial of Unruptured Brain Arteriovenous malformations (ARUBA) trial.** *Stroke* 2012;43:1744–45 CrossRef Medline
8. Pierot L, Cognard C, Herbreteau D, et al. **Endovascular treatment of brain arteriovenous malformations using a liquid embolic agent: results of a prospective, multicentre study (BRAVO).** *Eur Radiol* 2013;23:2838–45 CrossRef Medline
9. Singfer U, Hemelsoet D, Vanlangenhove P, et al. **Unruptured brain arteriovenous malformations: primary Onyx embolization in ARUBA (A Randomized Trial of Unruptured Brain Arteriovenous Malformations)-eligible patients.** *Stroke* 2017;48:3393–96 CrossRef Medline
10. Marks MP, Lane B, Steinberg GK, et al. **Hemorrhage in intracerebral arteriovenous malformations: angiographic determinants.** *Radiology* 1990;176:807–13 CrossRef Medline
11. Willinsky R, Lasjaunias P, Terbrugge K, et al. **Brain arteriovenous malformations: analysis of the angio-architecture in relationship to hemorrhage (based on 152 patients explored and/or treated at the Hopital de Bicetre between 1981 and 1986).** *J Neuroradiol* 1988;15:225–37 Medline
12. Kader A, Young WL, Pile-Spellman J, et al. **The influence of hemodynamic and anatomic factors on hemorrhage from cerebral arteriovenous malformations.** *Neurosurgery* 1994;34:801–07; discussion 807–08 CrossRef Medline
13. Turjman F, Massoud TF, Vinuela F, et al. **Correlation of the angioarchitectural features of cerebral arteriovenous malformations with clinical presentation of hemorrhage.** *Neurosurgery* 1995;37:856–60; discussion 860–62 CrossRef Medline
14. Nataf F, Meder JF, Roux FX, et al. **Angioarchitecture associated with haemorrhage in cerebral arteriovenous malformations: a prognostic statistical model.** *Neuroradiology* 1997;39:52–58 CrossRef Medline
15. Shi X, Wang Z, Yu C. **An analysis of the correlation between angiographic and clinical findings in cerebral arteriovenous malformations.** *Chin Med Sci J* 1993;8:35–37 Medline
16. Asadi H, Kok HK, Looby S, et al. **Outcomes and complications after endovascular treatment of brain arteriovenous malformations: a prognostication attempt using artificial intelligence.** *World Neurosurg* 2016;96:562–69.e561 CrossRef Medline
17. Ledezma CJ, Hoh BL, Carter BS, et al. **Complications of cerebral arteriovenous malformation embolization: multivariate analysis of predictive factors.** *Neurosurgery* 2006;58:602–11; discussion 602–11 CrossRef Medline
18. Lv X, Wu Z, Jiang C, et al. **Complication risk of endovascular embolization for cerebral arteriovenous malformation.** *Eur J Radiol* 2011;80:776–79 CrossRef Medline
19. Karlsson B, Jokura H, Yang HC, et al. **The NASSAU (New ASSessment of cerebral Arteriovenous malformations yet Unruptured) analysis: are the results from the ARUBA trial also applicable to unruptured arteriovenous malformations deemed suitable for gamma knife surgery?** *Neurosurgery* 2018;85:E118–24 CrossRef Medline
20. Wong J, Slomovic A, Ibrahim G, et al. **Microsurgery for ARUBA trial (A Randomized Trial of Unruptured Brain Arteriovenous Malformation)-eligible unruptured brain arteriovenous malformations.** *Stroke* 2017;48:136–44 CrossRef Medline
21. Ding D, Starke RM, Kano H, et al. **Radiosurgery for cerebral arteriovenous malformations in A Randomized Trial of Unruptured Brain Arteriovenous Malformations (ARUBA)-eligible patients: a multicenter study.** *Stroke* 2016;47:342–49 CrossRef Medline
22. Derdeyn CP, Zipfel GJ, Albuquerque FC, et al; American Heart Association Stroke Council. **Management of brain arteriovenous malformations: A Scientific Statement for Healthcare Professionals from the American Heart Association/American Stroke Association.** *Stroke* 2017;48:e200–24 CrossRef Medline
23. Staubach S, Hein-Rothweiler R, Hochadel M, et al. **Predictors of minor versus major stroke during carotid artery stenting: results from the Carotid Artery Stenting (CAS) registry of the Arbeitsgemeinschaft Leitende Kardiologische Krankenhausarzte (ALKK.).** *Clin Res Cardiol* 2014;103:345–51 CrossRef Medline
24. ApSimon HT, Reef H, Phadke RV, et al. **A population-based study of brain arteriovenous malformation: long-term treatment outcomes.** *Stroke* 2002;33:2794–800 CrossRef Medline
25. Halim AX, Johnston SC, Singh V, et al. **Longitudinal risk of intracranial hemorrhage in patients with arteriovenous malformation of the brain within a defined population.** *Stroke* 2004;35:1697–702 CrossRef Medline
26. van Beijnum J, Lovelock CE, Cordonnier C, et al; SIVMS Steering Committee and the Oxford Vascular Study. **Outcome after spontaneous and arteriovenous malformation-related intracerebral haemorrhage: population-based studies.** *Brain* 2009;132:537–43 CrossRef Medline
27. Crawford PM, West CR, Chadwick DW, et al. **Arteriovenous malformations of the brain: natural history in unoperated patients.** *J Neurol Neurosurg Psychiatry* 1986;49:1–10 CrossRef Medline
28. Joyce C, Gomez CR. **Reimagining ARUBA: theoretical optimization of the treatment of unruptured brain arteriovenous malformations.** *J Stroke Cerebrovasc Dis* 2018;27:3100–07 CrossRef Medline
29. Sun Y, Jin H, Li Y, et al. **Target embolization of associated aneurysms in ruptured arteriovenous malformations.** *World Neurosurg* 2017;101:26–32 CrossRef Medline
30. Sahlein DH, Mora P, Becske T, et al. **Nidal embolization of brain arteriovenous malformations: rates of cure, partial embolization, and clinical outcome.** *J Neurosurg* 2012;117:65–77 CrossRef Medline
31. Le Feuvre D, Taylor A. **Target embolization of AVMs: identification of sites and results of treatment.** *Interv Neuroradiol* 2007;13:389–94 CrossRef Medline
32. Iosif C, Mendes GA, Saleme S, et al. **Endovascular transvenous cure for ruptured brain arteriovenous malformations in complex cases with high Spetzler-Martin grades.** *J Neurosurg* 2015;122:1229–38 CrossRef Medline
33. Wang MZ, Qiu HC, Wang S, et al. **A new technique for transvenous embolization of brain arteriovenous malformations in hybrid operation.** *Chin Med J* 2018;131:2993–96 CrossRef Medline

Intermixed Dimethyl-Sulfoxide–Based Nonadhesive Liquid Embolic Agents Delivered Serially via the Same Microcatheter for Cerebral AVM Treatment

A. Sirakov, K. Minkin, and S. Sirakov

ABSTRACT

BACKGROUND AND PURPOSE: Conventional nonadhesive liquid embolic agents currently are the criterion standard for endovascular embolization of cerebral AVMs. However, inadequate distal penetration into the nidus and unstable proximal plug formation are the major limitations of this approach and of the currently available embolic materials. The aim of this study was to evaluate the hypothetic efficacy of combining liquid embolic agents with different properties and viscosities for use in endovascular embolization of cerebral AVMs.

MATERIALS AND METHODS: From March 2018 to March 2019, sixteen patients with cerebral AVMs (12 women, 4 men; age range, 33–61 years) underwent endovascular embolization with combined liquid embolic agents delivered serially via a single microcatheter. The procedure consists of initial embolization with PHIL 30%, followed by Menox 18 through the same microcatheter. According to the Spetzler-Martin scale, 11 (68.75%) AVMs were grades I–II, 4 (25%) were grade III, and 1 (6.25%) was grade IV. Angiographic, technical, and clinical outcomes were analyzed independently.

RESULTS: Combined PHIL and Menox embolization through the same microcatheter via 21 pedicles was performed in these 16 patients. Once the length of the reflux reached approximately 2 cm, PHIL 30% was switched to Menox 18. Antegrade flow and distal penetration of the serially applied liquid embolic agents were observed in all 16 cases. The ability to completely control the flow of the materials and avoid any dangerous proximal reflux was noted in all performed embolizations. The estimated average size reduction of the treated AVMs was 85%, ranging from 50% to 100%. Complete embolization was achieved in 10/16 or 62.5% of the cases. There was no procedure-related complication during or after the embolization. No mortality or postprocedural clinical worsening was seen. Clinical success and complete obliteration were confirmed with at least 1 follow-up angiography in 10/16 patients.

CONCLUSIONS: Serial delivery of nonadhesive liquid embolic agents via the same microcatheter was safe and effective in our study and may be a potential technique for routine AVM treatment. However, further investigations are required to validate the safety and the efficacy of the method.

ABBREVIATIONS: DMSO = dimethyl-sulfoxide; EVOH = ethylene-vinyl alcohol copolymer; LEA = liquid embolic agent

Liquid embolic agents are primarily used for treatment of cerebral AVMs.[1] The most widely used liquid embolic agents are the nonadhesive ethylene-vinyl alcohol copolymers (EVOHs): Onyx (Covidien, Irvine, California), SQUID (Emboflu, Gland, Switzerland), Menox (Meril Life Sciences, Gujarat India), and polyhydroxyethylmethacrylate copolymer—Precipitating Hydrophobic Injectable Liquid (PHIL; MicroVention, Tustin, California), along with the well-known *n*-BCA.[2-4] The major limitation of the conventional EVOH embolization technique is that on some occasions, it is difficult to control the reflux of the material at the level of microcatheter tip and the formation of a stable proximal plug. Establishing a stable proximal plug is crucial because it allows better distal antegrade nidal penetration. Technically speaking, EVOHs with extra-low viscosity could improve the distal penetration of the embolic agent. Currently, the only commercially available extra-low-viscosity formulation of EVOH is SQUID 12.[5]

Initial experience with the recently introduced liquid embolic agent PHIL has shown that this agent may, due to its intrinsic properties, address the limitation of its nonadhesive EVOH competitors in terms of proximal plug formation.[6]

We sought to explore whether 2 different, serially applied nonadhesive liquid embolic agents via the same microcatheter

Received November 5, 2019; accepted after revision January 10, 2020.

From the Radiology Department (A.S., S.S.) and Neurosurgery Department (K.M.), UH St Ivan Rilski, Sofia, Bulgaria

Please address correspondence to Stanimir Sirakov, MD, PhD, UH St Ivan Rilski, 15 Academic Ivan Geshov boulevard, Sofia, Bulgaria; e-mail: ssirakov@bsunivers.com; @AlexanderSirak1

http://dx.doi.org/10.3174/ajnr.A6453

could increase the embolization success rate of cerebral AVMs. We hypothesized that using liquid embolic agents with different properties and viscosities could improve the AVM embolization with less proximal reflux. The technical aspects of this approach were evaluated as were immediate clinical and angiographic results.

MATERIALS AND METHODS

The study protocol was reviewed and approved according to the local institutional policy, and appropriate consent was obtained from each patient. From March 2018 to March 2019, in a single-center institution, a total of 16 patients with cerebral AVMs underwent endovascular embolization with combined liquid embolic agents (LEAs) serially delivered via a single microcatheter. All patient demographics, AVM angioarchitecture, procedural details, pre- and postprocedural mRS scores, and clinical data were collected (Table 1). The study population consisted of 12 women and 4 men, with ages ranging from 33 to 61 years. The most common clinical presentation was hemorrhage in 75% of patients (12/16), with the remaining 25% (4/16) presenting with headaches and epileptic seizures. Based on the size, eloquence, and venous drainage of the lesions per the Spetzler-Martin scale, 11 (68.75%) AVMs were grades I–II, 4 (25%) were grade III, and 1 (6.25%) was grade IV. Low-grade AVMs (Spetzler-Martin grades I and II) were intended to be definitively treated, while staged endovascular embolization was planned for larger AVMs, rendering them suitable for subsequent microsurgical resection. None of the included patients had any previous microsurgical or endovascular treatment.

Table 1: Baseline characteristics of the treated patients

Variable	Value
Age (yr)	
Mean	33.5
Median	42
Range	33–61
Sex (No.) (%)	
Male	25% (4)
Female	75% (12)
Presentation (No.) (%)	
Hemorrhage	75% (12)
Neurologic deficit	–
Headache	12.5% (2)
Epilepsy	12.5% (2)
Asymptomatic	–
Size (%) (No.)	
≤30 mm	75% (12)
≥30 mm	25% (4)
No. of arterial feeders (%)	
Single	43.7% (7)
Multiple	56.3% (9)
Venous pattern (No.) (%)	
Superficial	68.7% (11)
Deep	18.7% (3)
Deep and superficial	12.5% (2)
Spetzler-Martin score	
I	31.2% (5)
II	37.5% (6)
III	25% (4)
IV	6.3% (1)
mRS prior to embolization	
1	68.7% (11)
2	25% (4)
3	6.3% (1)

Note:—– indicates absence of particular determinant; mRS, modified ranking score.

Description of the Technique

All procedures were performed with the patient under general anesthesia in a dedicated neuroangiography suite. During the procedures, systolic blood pressure was maintained between 80 and 100 mm Hg to prevent any possible migration of embolic material to the venous compartment of the AVM. Catheterization of the right distal radial artery was performed in all 16 patients. A 6F guiding catheter was then introduced into the appropriate feeding artery over an exchange-length wire using standard techniques. The choice of arterial feeders most suitable for intermixed embolization was made by the treating physician on a case-by-case basis. Dimethyl-sulfoxide (DMSO)-compatible Apollo microcatheters (Covidien) were delivered over a 0.010- or 0.008-inch microwire into the selected feeding pedicle and its desired segment with the tip positioned as close as possible to the nidus of the AVM. The hub lumen and the dead space of the microcatheter were then primed with 0.25 mL of DMSO.

The basis of the embolization technique was to first perform primary injections with PHIL 30% to optimize the initial plug formation. As soon as the length of injected PHIL reached 1.5 cm or was close to the proximal marker of the microcatheter, Menox 18 was applied as a second embolic agent via the same microcatheter. Additional DMSO was not injected between applications of the 2 liquid embolic agents. Because a solid proximal plug was already formed, Menox, due to its different intrinsic properties, was able to penetrate more distally and thus achieve an optimized AVM embolization via the same microcatheter. On completion of the endovascular embolization, control contrast injections were performed through the guide catheter and the microcatheter was subsequently removed from the pedicle under fluoroscopy. This technique was performed in all cases (Fig 1). No pressure-cooker technique or any other antireflux modifications were used in this cohort.[7]

At the end of each embolization session and for each microcatheter used, the amount of traction force required to successfully retrieve the catheter was individually assessed. The perceived difficulty (eg, easy, moderate, strong) was subjectively documented by the main operator following every microcatheter removal.

Distal detachable tips of the microcatheters used were carefully examined under stereomicroscopy for any evidence of adherent or mixed embolic material fragments.

Angiographic results were determined by estimating the percentage of nidus reduction observed in the last intraprocedural angiogram. All angiograms were blindly and independently reviewed by 2 outside interventionists. Final verdict and complete interpretation of the data were reached through a consensus session.

Study Outcome Measures

As per our institutional routine protocol, the first follow-up with DSA combined with clinical evaluation was performed 6 months

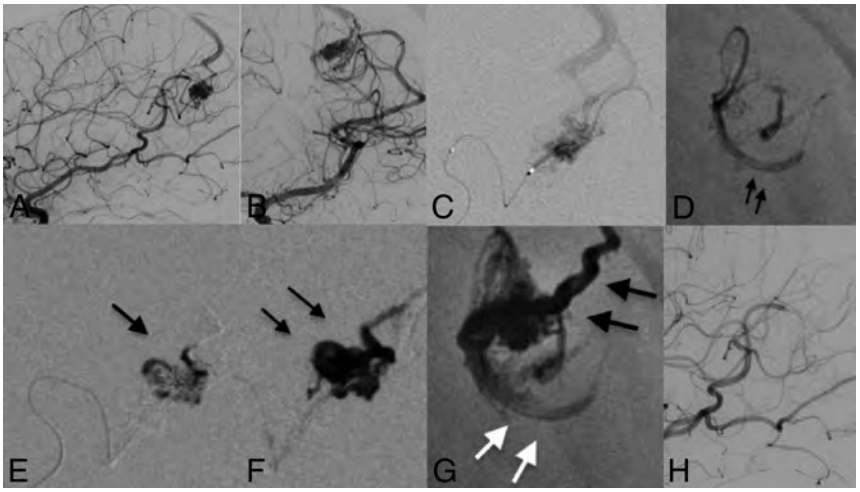

FIG 1. A 35-year-old female patient who presented with left-sided headache and seizures. DSA revealed a left parietal (*A* and *B*) AVM supplied by the left MCA. The AVM was drained by the superficial cortical vein to the superior sagittal sinus. An Apollo microcatheter was positioned into a distal arterial feeder arising from the left MCA (*C*). A PHIL 30 plug was created with 2 rounds of injections (*D*, *arrows*). After 1.2 mL of PHIL 30 was injected into the AVM, embolization was continued with Menox 18 (*E* and *F*) to ensure successful distal and continuous penetration. No further proximal reflux was observed (*G*). Note the different radiopacities of the used liquid embolic agents (*black arrows*, Menox 18; *white arrows*, PHIL 30.) At the end of the procedure, 100% size reduction was achieved by delivering a total amount of 2.7 mL of embolic material from 1 feeder during 1 session (*H*).

Table 2: Embolization characteristics and technical results[a]

Study Group (n = 16)	Value	
Applied LEA	PHIL 30	Menox 18
Total fluoroscopy time (sec)	2460 (900–3761)	
Total injection time (sec)	55 (51–70)	325 (480–980)
Time per single injection (sec)	5.8 (6.6–12.1)	21.1 (12–50.1)
Injection pause time (sec)	0.4 (1.1–2.2)	1.1 (0.4–30)
Injections (No.)	4.1 (2–5)	11 (8–35)
Total volume of LEA per procedure (mL)	0.9 (0.7–2.3)	4.1 (1.2–6)

[a] Data are presented as median (lower quartile; upper quartile).

after the treatment. A cranial MR imaging and clinical assessment were performed on discharge after each endovascular session and on each follow-up if considered mandatory. The neurologic examination was performed by a neurologist or a certified stroke nurse and recorded using the mRS.

Primary End Points

The primary end points were complete nidal occlusion of Spetzler-Martin grade I–II AVMs, with the rate of favorable clinical outcomes defined as mRS 0–2 at 30 days after embolization.

Secondary End Points

Secondary outcomes included either intraprocedural or postprocedural intervention-related complications leading to permanent neurologic deficits. Other secondary outcomes included parent vessel injury, extravasation of the applied LEAs, rerupture of the AVM, the degree of the nidal obliteration, and the occurrence of intervention-related stroke or death. Technical complications were defined as unsuccessful microcatheter retrieval, microcatheter occlusion, and any adverse physiologic changes due to the combination of both agents.

RESULTS

Combined PHIL and Menox embolization was performed in all 16 patients. Fast and solid proximal plug formation was achieved in all cases via initial applications of PHIL 30%. Proximal plug formation with PHIL 30% was performed without difficulty in 21 pedicles, and the embolization proceeded accordingly. Successful and continuous application of the second embolic agent, Menox 18, was performed in all patients. Antegrade flow of the EVOH material into the nidal components was observed in all 16 cases. The mean volume of PHIL used was 0.9 mL (range, 0.7–2.3 mL), and the mean volume of EVOH injected was 4.1 mL (range, 1.2–6 mL). We noted mean injections pause times of 0.4 seconds for the PHIL and 1.1 seconds for the EVOH with a mean time under fluoroscopy of just 41 minutes per procedure. Technical results are summarized in Table 2.

No microcatheter remained irreversibly trapped in the plug, and no technical complications such as microcatheter occlusion or rapid tantalum sedimentation occurred. Six detachable distal tips of the used microcatheters were successfully retrieved. Among those 6 microcatheters, in 2 of them, adherent microscopic particles of the liquid embolic cast and structural crack scratches were noted over the most distal portion of the tip.

No adverse physiologic changes such as vessel injury, embolic agent extravasation, or microcatheter rupture were observed.

Angiographic Outcomes and Follow-Up Examinations

AVM volume was calculated using the method of Pasqualin et al.[8] Adequate nidal penetration was achieved in all cases. The estimated average size reduction of the treated AVMs was 85%, ranging from 50% to 100%. We achieved complete angiographic obliteration of the nidus in 10/16 (62.5%) patients after the initial session with serially combined LEAs, all of whom had small AVMs (Spetzler-Martin grade I or II) (Fig 2). Favorable clinical outcome and complete obliteration were confirmed with at least 1 follow-up angiography after a mean of 5.1 months (range, 3–6 months) in each of the 10 patients.

Partial embolization was achieved in 6/16 (37.5%) patients. One of those patients underwent microsurgical resection of the nidus due to enlargement of the intraparenchymal hematoma that was present during radiologic examination at admission.

Planned embolization via the same method was performed for the remaining 5/16 (31.25%) patients to achieve sufficient

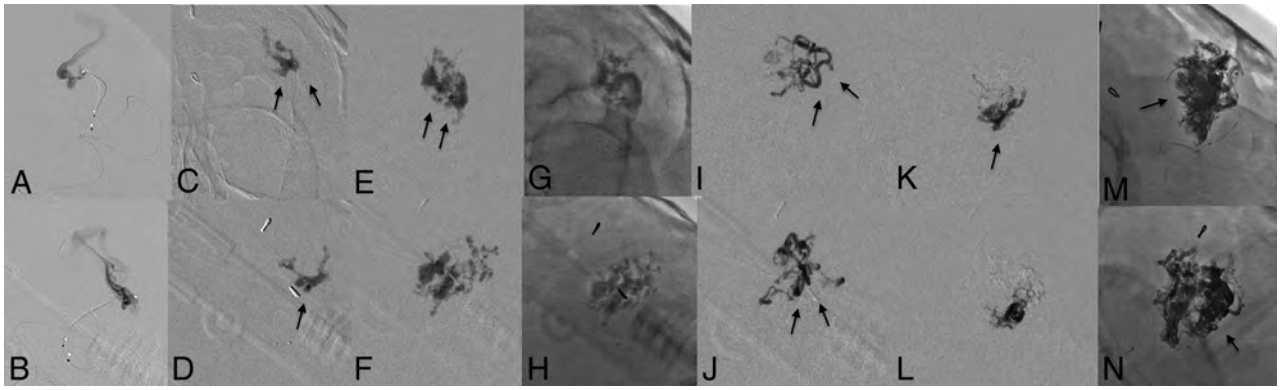

FIG 2. Step-by-step embolization of a ruptured left-sided parietal AVM, Spetzler-Martin grade II. The tip of the microcatheter was placed into the nidus (*A* and *B*). Initial injections of PHIL 30 (*C*, *D*, *E*, *F*, *G*, and *H*; *arrows*) were needed to create a stable proximal plug. The embolic material was switched with Menox 18 to successfully achieve distal and continuous nidal penetration (*I–L*; *arrows*). Note the distal extent of the Menox agent (*M*, *N*, *arrow*) and the different radio-opacities of the applied LEAs.

AVM nidal occlusion suitable for subsequent radiosurgery or surgical resection.

There was no procedure-related complication during or after the embolization. No mortality or worsening mRS postprocedurally was seen in this cohort.

DISCUSSION

Today, dimethyl-sulfoxide–based nonadhesive embolic agents are the main tool used for the multimodality treatment of cerebral AVMs.[9] EVOH was pioneered in the neurointerventional field and quickly became proclaimed the criterion standard for curative AVM embolization.[10] This liquid embolic material is thought to be an easily manageable agent. Its greatest advantage of slowly controllable embolization and the ability to initiate and interrupt injections may reduce the risk of any dangerous migration of the embolic mass. However, the major limitation of EVOH is that its nonadhesive nature limits control over the direction of polymer flow and can lead to excessive reflux, which may result in incomplete nidal embolization or dangerous proximal backflow and obstruction of normal arterial feeders. Usually, this issue can be addressed by intentionally allowing the agent to cover a small portion of the detachable tip of the microcatheter, creating a proximal "plug."[11] This process often requires multiple short cycles of repeat injections, thereby increasing the total duration of the procedure as well as the risk of vessel rupture or rapid tantalum sedimentation inside the microcatheter.[12] The waiting time between applications of the agent to ensure an appropriate degree of hardening of the LEA is important because not waiting long enough can lead to premature embolization of the feeding artery. On the other hand, the flow pattern through the nidus can be somehow redirected by allowing the already-injected material to harden and thus creating a new low-resistance channel.[13] All of these shortcomings are associated with the effect of the plug and properties of the EVOH technique.

The polylactide-co-glycolide and polyhydroxyethylmethacrylate copolymer PHIL is a nonadhesive and inherently radio-opaque LEA. Initial experience with this agent has revealed the potential advantages of this LEA over the standard EVOH technique. Reported differences include the ability to create a faster and stable proximal plug, a constant degree of distal nidal penetration, and consistent visibility due to the presence of iodine as its radio-opacity component. The material is available in 3 different concentrations and viscosities: PHIL 25, 30, and 35. Higher concentrations are preferred in the presence of a fistulous component, whereas lower concentrations are used to achieve better distal penetration. It has already been demonstrated that the successful outcome of embolization can be based on the effect of the proximal plug and the viscosity of the material used.[14,15]

Both Menox 18 and PHIL are DMSO-based liquid embolic agents that require DMSO-compatible microcatheters to enable a safe and efficient embolization process. Special emphasis is placed on the need for deliberation when choosing the most appropriate embolic material. Depending on the specific angioarchitecture and the geometry of the feeding arteries, use or even the combination of liquid embolic agents is often required. In our experience, combined injections of PHIL and Menox via the same microcatheter have been technically possible and safe, offering the advantage of switching between agents without the additional application of DMSO. The lesser layering effect and higher viscosity of PHIL 30 offer better properties of the proximal plug, thus ensuring successful distal penetration of Menox 18, which has 50% lower viscosity (36 cSt, PHIL 30, versus 18 cSt, Menox 18). More specifically, the initial injection of PHIL 30 creates a proximal stop that successfully blocks the flow and creates a distinctive change in the pressure gradient within the nidus, thus supporting the forward, more distal penetration of Menox due to its lower viscosity. We believe this may limit potentially dangerous proximal backflow and decrease the amount of embolic agent used. We noted a mean time under fluoroscopy of only 41 minutes and relatively shorter EVOH pause times.

From our routinely collected data, we performed direct comparisons among the Menox or PHIL infiltration times using this approach versus the conventional method. The reported injection pause times and the mean fluoroscopy times were relatively shorter than those we observe on a daily basis in comparison with injections of EVOH or PHIL as stand-alone liquid embolic agents.[16,17] However, direct head-to-head comparison is difficult

to perform with great accuracy because each AVM has distinct anatomic and flow characteristics.

Serial application of EVOH and PHIL via the same microcatheter was reported by Koçer et al[6] in a single case scenario during their preliminary experience with PHIL. The authors did not report any technical complications or adverse physiologic changes due to the combination of both agents.

Recently, Xu et al[18] described an efficient method of combining regular and diluted viscosities of EVOH to treat cerebral AVMs. The proposed method consists of initial embolization with regular-viscosity formulations of EVOH, followed by injection of a lower viscosity mixture of 1.5 mL of EVOH diluted with 0.5 mL of DMSO through the same microcatheter. The technique was performed in 15 patients with a reported average of 90% (range, 55%–100%) estimated size reduction. In 6 patients, the AVMs were completely obliterated. Control over the proximal reflux and success of the technique was achieved in 80% of the cases.

In regards to fluid resistance to deformation, extra-low-viscosity formulations of the established nonadhesive LEAs, PHIL 25% low viscosity and SQUID 12. As mentioned above, of the commercially available precipitating, nonadhesive embolic agents, SQUID 12 is the only extra-low-viscosity version so far with a growing body of literature supporting the effectiveness of this agent when used for embolization of vascular malformations.[19,20] Several experimental studies investigated the improved features of PHIL 25% low-viscosity and SQUID 12 formulations.[21,22] Both reports confirmed the embolization extent and the distal penetration to be higher for the low-viscosity agents compared with the standard ones. All investigated embolic agents demonstrated optimal flow control and a significantly lower amount of reflux. This aspect can be highly relevant in clinical practice. However, the authors suggested conceivable drawbacks of extra-low-viscosity LEAs in terms of early distal embolization, thus increasing the risk of premature obliteration of the draining veins or unintentional embolization of vital vasculature. Nevertheless, the yielded technical results suggest that for selected types of vascular lesions, the low-viscosity LEAs can be the preferred agents over the currently available standard-viscosity LEAs (eg, Onyx 18, SQUID 18, Menox 18, and PHIL 25%).

Several antireflux modifications are being developed to gain better control over the flow during embolization. The so-called pressure-cooker technique is designed to create an antireflux plug by trapping the detachable part of the microcatheter used for Onyx delivery via coils and glue. Successful execution of this method is reported to obtain a better forceful and controlled EVOH embolization.

The emergence of DMSO-compatible balloons provides better reflux control and improved flow conditions when using nonadhesive LEAs, allowing the agents to travel more distally.[23] Difficulties in navigation in distal arterial sites and the risks of vessel rupture due to balloon overinflation exist in this technique.[24] Using double-lumen balloon catheters with even smaller diameters may reduce the technical complications and increase the embolization rates.[25] In this context, commercially available prototypes of extra-small balloon microcatheters can be extremely advantageous and make untreatable lesions curable.

Our initial experience with combining nonadhesive liquid embolic agents with different viscosities for AVM treatment yielded promising results. The average estimated size reduction of the nidus was 85%. Total endovascular obliteration in 1 endovascular session was achieved in more than half of the included patients (10/16). In our initial-but-limited experience with this method, we did not observe an increased risk of inadequate nidal embolization, retraction failures, or any occasions in which the used LEAs precipitated and blocked the microcatheter.

Limitations

Despite being the largest clinical study of the treatment of cerebral AVMs with combined liquid embolic agents delivered via the same microcatheter reported to date, our study has several important limitations. First, this is a single-center experience, and the technical results are limited by the authors' individual techniques and experiences. Second, the sample is relatively small. Thus, the results of our study should be interpreted with caution because they may not be widely applicable to general practice. Last, pharmacoeconomics in developing countries holds promise for patients with certain neurovascular diseases, particularly those who require multiple treatment modalities. Unfortunately, this issue was the only reason for particularly choosing Menox 18 over the other available EVOHs. The same is true for the use of PHIL 30% for the initial plug formation followed by further embolization with PHIL 25%.

CONCLUSIONS

Combined nonadhesive liquid embolic agents delivered via the same microcatheter have the potential to facilitate and increase the success rate of endovascular embolization of cerebral AVMs while carrying risks similar to those of other available approaches. Due to the relatively small size of our study, further investigations are required to validate the safety and the efficacy of the method.

REFERENCES

1. Potts MB, Zumofen DW, Raz E, et al. **Curing arteriovenous malformations using embolization.** *Neurosurg Focus* 2014;37:E19 CrossRef Medline
2. Loh Y, Duckwiler GR; Onyx Trial Investigators. **A prospective, multicenter, randomized trial of the Onyx liquid embolic system and N-butyl cyanoacrylate embolization of cerebral arteriovenous malformations.** *J Neurosurg* 2010;113:733–41 CrossRef Medline
3. Samaniego EA, Kalousek V, Abdo G, et al. **Preliminary experience with Precipitating Hydrophobic Injectable Liquid (PHIL) in treating cerebral AVMs.** *J Neurointerv Surg* 2016;8:1253–55 CrossRef Medline
4. Akmangit I, Daglioglu E, Kaya T, et al. **Preliminary experience with Squid: a new liquid embolizing agent for AVM, AV fistulas and tumors.** *Turk Neurosurg* 2014;24:565–70 CrossRef Medline
5. Pedicelli A, Lozupone E, Valente I, et al. **Pre-operative direct puncture embolization of head and neck hypervascular tumors using SQUID 12.** *Interv Neuroradiol* 2019 Dec 19. [Epub ahead of print] CrossRef Medline
6. Koçer N, Hanımoğlu H, Batur Ş, et al. **Preliminary experience with precipitating hydrophobic injectable liquid in brain arteriovenous malformations.** *Diagn Interv Radiology* 2016;22:184–89 CrossRef Medline

7. Chapot R, Stracke P, Velasco A, et al. **The pressure-cooker technique for the treatment of brain AVMs.** *J Neuroradiol* 2014;41:87–91 CrossRef Medline
8. Pasqualin A, Cioffi F, Barone G, et al. **The relevance of anatomic and hemodynamic factors to a classification of cerebral arteriovenous malformations.** *Neurosurgery* 1991;28:370–79 CrossRef Medline
9. Davies JM, Yanamadala V, Lawton MT. **Comparative effectiveness of treatments for cerebral arteriovenous malformations: trends in nationwide outcomes from 2000 to 2009.** *Neurosurg Focus* 2012;33: E11 CrossRef Medline
10. Vaidya S, Tozer K, Chen J. **An overview of embolic agents.** *Semin Intervent Radiol* 2008;25:204–15 CrossRef Medline
11. Brzozowski K, Ziecina P, Piasecki P, et al. **Effectiveness of ONYX liquid embolic agent in endovascular treatment of cerebral arteriovenous malformations - own experience.** *Eur Congr Radiol* 2011
12. Ayad M, Eskioglu E, Mericle RA. **Onyx®: a unique neuroembolic agent.** *Expert Rev Med Devices* 2006;3:705–15 CrossRef Medline
13. Crowley RW, Ducruet AF, McDougall CG, et al. **Endovascular advances for brain arteriovenous malformations.** *Neurosurgery* 2014;74:S74–82 CrossRef Medline
14. Lv X, Wu Z, Li Y. **Arteriovenous malformation in the brain: a theoretical study explaining the behavior of liquid embolic agents during endovascular treatment.** *Neuroradiol J* 2013;26:661–68 CrossRef Medline
15. Vollherbst DF, Sommer CM, Ulfert C, et al. **Liquid embolic agents for endovascular embolization: evaluation of an established (Onyx) and a novel (PHIL) embolic agent in an in vitro AVM model.** *AJNR Am J Neuroradiol* 2017;38:1377–82 CrossRef Medline
16. Sirakov S, Sirakov A, Minkin K, et al. **Initial experience with the new ethylene vinyl alcohol copolymer based liquid embolic agent Menox in the endovascular treatment of cerebral arteriovenous malformations.** *J Neurointerv Surg* 2019;11:1040–44 CrossRef Medline
17. Sirakov SS, Sirakov A, Minkin K, et al. **Initial experience with precipitating hydrophobic injectable liquid in cerebral arteriovenous malformations.** *Interv Neuroradiol* 2019;25:58–65 CrossRef Medline
18. Xu H, Wang L, Guan S, et al. **Embolization of brain arteriovenous malformations with the diluted Onyx technique: initial experience.** *Neuroradiology* 2019;61:471–78 CrossRef Medline
19. Gioppo A, Faragò G, Caldiera V, et al. **Medial tentorial dural arteriovenous fistula embolization: single experience with embolic liquid polymer SQUID and review of the literature.** *World Neurosurg* 2017;107:1050.e1–e7 CrossRef Medline
20. Erbahceci Salik A, Islim F, Akgul A, et al. **Concomitant transarterial and transvenous embolization of a pelvic arteriovenous malformation using a new liquid embolic agent, Squid-12 and detachable coils.** *Case Rep Vasc Med* 2014;2014:972870–75 CrossRef Medline
21. Vollherbst DF, Otto R, Hantz M, et al. **Investigation of a new version of the liquid embolic agent PHIL with extra-low-viscosity in an endovascular embolization model.** *AJNR Am J Neuroradiol* 2018;39:1696–1702 CrossRef Medline
22. Samaniego EA, Derdeyn CP, Hayakawa M, et al. **In vivo evaluation of the new PHIL low viscosity in a swine rete mirabile model.** *Interv Neuroradiol* 2018;24:706–12 CrossRef Medline
23. Spiotta AM, James RF, Lowe SR, et al. **Balloon-augmented Onyx embolization of cerebral arteriovenous malformations using a dual-lumen balloon: a multicenter experience.** *J Neurointerv Surg* 2015;7:721–27 CrossRef Medline
24. Jagadeesan BD, Grigoryan M, Hassan AE, et al. **Endovascular balloon-assisted embolization of intracranial and cervical arteriovenous malformations using dual-lumen coaxial balloon microcatheters and Onyx: initial experience.** *Oper Neurosurg* 2013;73:ons238–43 CrossRef Medline
25. Vollherbst DF, Otto R, Do TD, et al. **Extra-small dual-lumen microballoon catheters can improve endovascular embolization: an experimental in vivo and in vitro study.** *J Neurointerv Surg* 2018;10:1092–96 CrossRef Medline

Facial Nerve Arterial Arcade Supply in Dural Arteriovenous Fistulas: Anatomy and Treatment Strategies

K.D. Bhatia, H. Kortman, H. Lee, T. Waelchli, I. Radovanovic, J.D. Schaafsma, V.M. Pereira, and T. Krings

ABSTRACT

BACKGROUND AND PURPOSE: Endovascular treatment of petrous dural AVFs may carry a risk of iatrogenic facial nerve palsy if the facial nerve arterial arcade, an anastomotic arterial arch that supplies the geniculate ganglion, is not respected or recognized. Our purpose was to demonstrate that the use of a treatment strategy algorithm incorporating detailed angiographic anatomic assessment allows identification of the facial nerve arterial arcade and therefore safe endovascular treatment.

MATERIALS AND METHODS: This was a retrospective cohort study of consecutive petrous dural AVF cases managed at Toronto Western Hospital between 2006 and 2018. Our standard of care consists of detailed angiographic assessment followed by multidisciplinary discussion on management. Arterial supply, primary and secondary treatments undertaken, angiographic outcomes, and clinical outcomes were assessed by 2 independent fellowship-trained interventional neuroradiologists.

RESULTS: Fifteen patients had 15 fistulas localized over the petrous temporal bone. Fistulas in all 15 patients had direct cortical venous drainage and received at least partial supply from the facial nerve arterial arcade. Following multidisciplinary evaluation, treatment was performed by endovascular embolization in 8 patients (53%) and microsurgical disconnection in 7 patients (47%). All patients had long-term angiographic cure, and none developed iatrogenic facial nerve palsy.

CONCLUSIONS: By means of our treatment strategy based on detailed angiographic assessment and multidisciplinary discussion, approximately half of our patients with petrous AVFs were cured by endovascular treatment, half were cured by an operation, and all had preserved facial nerve function.

ABBREVIATIONS: EVOH = ethylene-vinyl alcohol copolymer; MMA = middle meningeal artery; TAE transarterial embolization; TVE = transvenous embolization

The arterial arcade of the facial nerve is an anastomotic arch of arteries traversing the petrous temporal bone that supplies the geniculate ganglion and tympanic segment of the facial nerve.[1,2] Care must be taken during embolization from the proximal aspect of external carotid artery branches to avoid occlusion of the facial nerve arterial arcade, which may result in iatrogenic facial nerve (Bell) palsy.[3,4] The risk of occluding the facial nerve arterial arcade is particularly elevated when embolizing petrous dural AVFs because these lesions are frequently supplied by the vessels that form the arterial arcade.[1,3,5,6]

Anatomy

Two arteries form the facial nerve arterial arcade: 1) the petrous branch of the middle meningeal artery (MMA), and 2) the stylomastoid branch of the posterior auricular or occipital artery (Fig 1).[1,3,7] Branches of these 2 arteries anastomose adjacent to the geniculate ganglion.[2,3] The arcade can be reinforced by the inferior tympanic artery, a branch of the ascending pharyngeal artery that travels to the tympanic cavity alongside the Jacobson nerve.[5,7]

The petrous branch of the MMA usually arises within the first 10 mm distal to the entry of the MMA to the middle cranial fossa via the foramen spinosum but can arise just proximal to the foramen.[5,8-10] It then extends posterolaterally toward the hiatus of the facial nerve canal where it gives off small branches to supply the greater petrosal nerve, which travels in the canal.[8,10] The artery travels within the canal (25%) or external to it (75%), piercing the petrous bone more laterally before supplying the geniculate

Received October 26, 2019; accepted after revision January 14, 2020.

From the Division of Neuroradiology (K.D.B., H.K., H.L., V.M.P., T.K.), Joint Department of Medical Imaging; Division of Neurosurgery (T.W., I.R., V.M.P., T.K.), Department of Surgery; and Division of Neurology (J.D.S.), Department of Medicine, Toronto Western Hospital, Toronto, Ontario, Canada.

Please address correspondence to Kartik Dev Bhatia, MD, Division of Neuroradiology, Level 3, Toronto Western Hospital, 399 Bathurst St, Toronto, M5T 2S8, ON, Canada; e-mail: Kartik.bhatia@uhn.ca

Indicates article with supplemental on-line tables.

Indicates article with supplemental on-line photo.

http://dx.doi.org/10.3174/ajnr.A6449

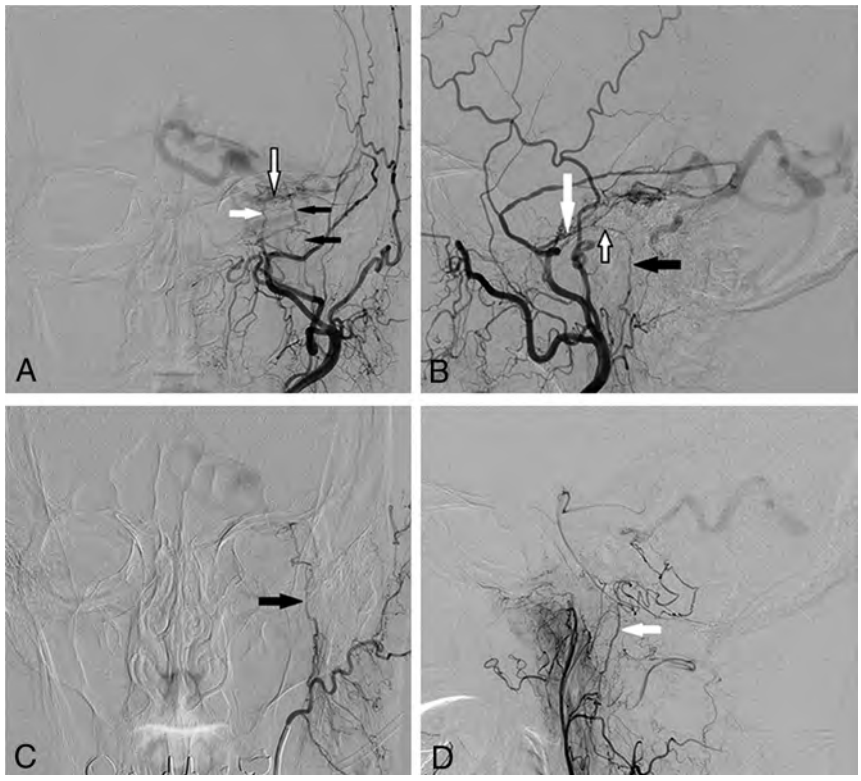

FIG 1. DSA images via left external carotid artery injection from a patient with a left petrous AVF (patient 5) demonstrate the anatomy of the facial nerve arterial arcade. *A*, Anterior-posterior projection demonstrates supply to the fistula by the petrous branch of the left MMA (*white arrow*), stylomastoid branch of the left posterior auricular artery (*black arrows*), and the anastomotic arcade between these 2 arteries (*black-border arrow*). *B*, Lateral projection shows the petrous branch of the MMA (*white arrow*), stylomastoid artery (*black arrow*), and the anastomotic facial nerve arterial arcade (*black-border arrow*). *C*, Anterior-posterior projection during selective injection of the left posterior auricular artery confirms supply to the fistula from the left stylomastoid artery (*black arrow*). *D*, Lateral projection during selective left ascending pharyngeal artery injection demonstrates additional supply to the AVF from its hypoglossal branch (*white arrow*).

ganglion by 1–3 small branches and then supplying the second (tympanic) segment of the intraosseous facial nerve.[3,8,10]

The stylomastoid artery can arise from the posterior auricular artery, from the proximal third of the occipital artery, or from a common trunk of these 2 arteries.[1,3] Traveling superiorly through the stylomastoid foramen and lying anterior or anteromedial to the facial nerve, it provides arterial supply to the third (mastoid) intraosseous segment of the facial nerve.[7,8,11] The artery then ascends to the level of the facial genu and the tympanic cavity where it divides into several branches and provides additional supply to the second (tympanic) segment of the nerve.[7,8] Here, a network of its branches anastomoses with branches of the petrous branch of the MMA to form the facial nerve arterial arcade (Fig 1).[7] These arteries are, in the absence of shunts, most often too small to be detected on conventional angiography.[2]

Rationale for the Study

Petrous dural AVFs drain into cortical veins (most often the superior petrosal vein, ie, vein of Dandy) rather than directly into dural venous sinuses.[6] They are therefore high-grade fistulas (Borden III, Cognard III–IV)[12,13] and thus warrant treatment due to their well described risk of subsequent neurologic deterioration or rupture.[6,14] At our institution, we use management principles based on detailed angiographic anatomic assessment and multidisciplinary discussion (retrospectively summarized in our treatment algorithm shown in Fig 2) to avoid iatrogenic facial nerve palsy while achieving angiographic cure. In this study, we assess the treatment approaches and outcomes using these principles.

MATERIALS AND METHODS

Ethics approval for this study was granted by the Research Ethics Board of the University Health Network, Toronto (approval No. 19-5018).

Study Design and Selection Criteria

This was a retrospective study of a cohort of patients with intracranial AVFs managed at Toronto Western Hospital between 2006 and 2018. Inclusion criteria were the following: 1) confirmed diagnosis of intracranial AVF on DSA with the fistula point localized over the petrous temporal bone, and 2) follow-up DSA or time-resolved MRA after an interventional or conservative management. All included cases underwent data collection and imaging analysis.

Data Collection and Analysis

In all cases, 6-vessel cerebral angiography, high-frame-rate magnified acquisitions, and 3D rotational angiography with MPRs were undertaken for treatment planning. Clinical data points were obtained from the electronic patient records. Baseline and follow-up DSA and MRA for each patient were independently reviewed by 2 fellowship-trained interventional neuroradiologists (K.D.B. and H.K.). Disagreements were resolved by consensus; otherwise, they were resolved by the supervising senior interventional neuroradiologist (T.K.). We assessed the following imaging characteristics of each petrous AVF: location, arterial supply (in particular supply by vessels that form the facial nerve arterial arcade), venous drainage, Borden[12] and Cognard[13] classifications, endovascular approach, embolic agents used, angiographic outcome after primary treatment, and long-term angiographic outcome.

Treatment Planning

All AVF cases were discussed in a multidisciplinary conference among neurologists, radiosurgeons, cerebrovascular neurosurgeons, and interventional neuroradiologists to decide on management. On the basis of our review of the conference minutes for these cases, the

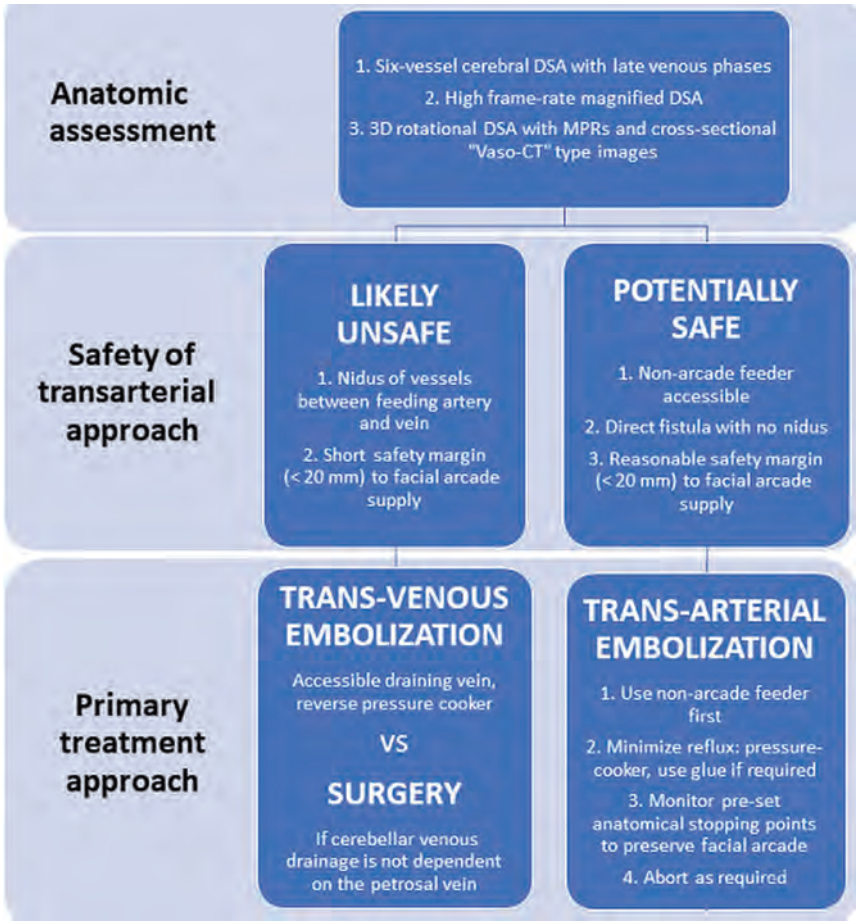

FIG 2. Retrospective summary of our treatment strategy algorithm for petrous dural AVFs.

primary treatment choice was determined by taking a stepwise approach. First, consensus agreement was reached that conservative treatment was not indicated in these cases due to the direct cortical venous drainage that occurs in petrous AVFs. Second, anatomic factors were assessed that would allow a safe endovascular treatment through an arterial, venous, or combined approach. For this article, we have retrospectively summarized the management principles outlined in the conference minutes for these cases in a treatment algorithm, shown in Fig 2.

Factors favoring an attempt at primary transarterial embolization (TAE) included the following: 1) accessible nonarcade arterial feeders supplying the AVF, 2) a direct arteriovenous fistulous point without an intervening nidus, and 3) a reasonable safety margin (for our purposes defined as the ability to place the distal end of the embolization microcatheter a minimum of 20 mm distal to the origin of or communication points with vessels of the facial nerve arterial arcade) for reflux of the embolic agent while preserving facial nerve arterial supply. The choice of a minimum distance of 20 mm was based on our experience of the working margin required to safely withdraw the microcatheter once glue begins to reflux and, for pressure-cooker/ethylene-vinyl alcohol copolymer (EVOH) approaches, the minimum detachable tip length available in a dimethyl-sulfoxide-compatible microcatheter (15 mm tip, Apollo Onyx Delivery Microcatheter; Medtronic, Irvine, California).

In the absence of favorable features for TAE, transvenous embolization (TVE) would be considered if there was an accessible draining vein that could be safely occluded. In the remaining cases or if endovascular treatment was unsuccessful, microsurgical disconnection was recommended.

RESULTS

Fifteen patients (5 women; mean age, 63.5 years) had 15 dural AVFs with the fistulous point localized over the petrous temporal bone (8.7% of all patients with dural arteriovenous fistulas managed at our center). Clinical presentations are detailed in On-line Table 1. All 15 petrous shunts had direct cortical venous drainage (Borden type III),[1] 6 were Cognard type III (cortical venous drainage), and 9 were Cognard type IV (ie, with cortical venous ectasia).[13] Angiographic characteristics are detailed in On-line Table 2.

Arterial Supply and Venous Drainage

All 15 patients (100%) demonstrated arterial supply to the AVF from either or both vessels involved in the facial nerve arterial arcade. The petrous branch of the MMA was seen in 13 patients (87%), while the stylomastoid artery was seen in 9 cases (60%); both vessels were involved in 7 cases (47%). Additional nonarcade supply to the fistulas discussed herein is outlined in On-line Table 2. The venous drainage outflow pathways were through cortical veins in all cases (superior petrosal vein, $n = 13$; subtemporal vein, $n = 2$). The detailed drainage patterns are summarized in On-line Table 3.

Primary Treatment Choice

Using the treatment strategy algorithm outlined in Fig 2, the multidisciplinary conference opinion for the primary treatment approach was TAE in 8 cases, TVE in 3 cases, and an operation in 4 cases. One patient initially declined an operation and chose the alternative option of gamma knife radiosurgery but subsequently underwent microsurgical disconnection because of residual AVF filling 2 years later.

Treatment Outcomes

The primary and secondary treatments undertaken, curative treatment, complications, and long-term angiographic and functional outcomes are summarized in On-line Table 4.

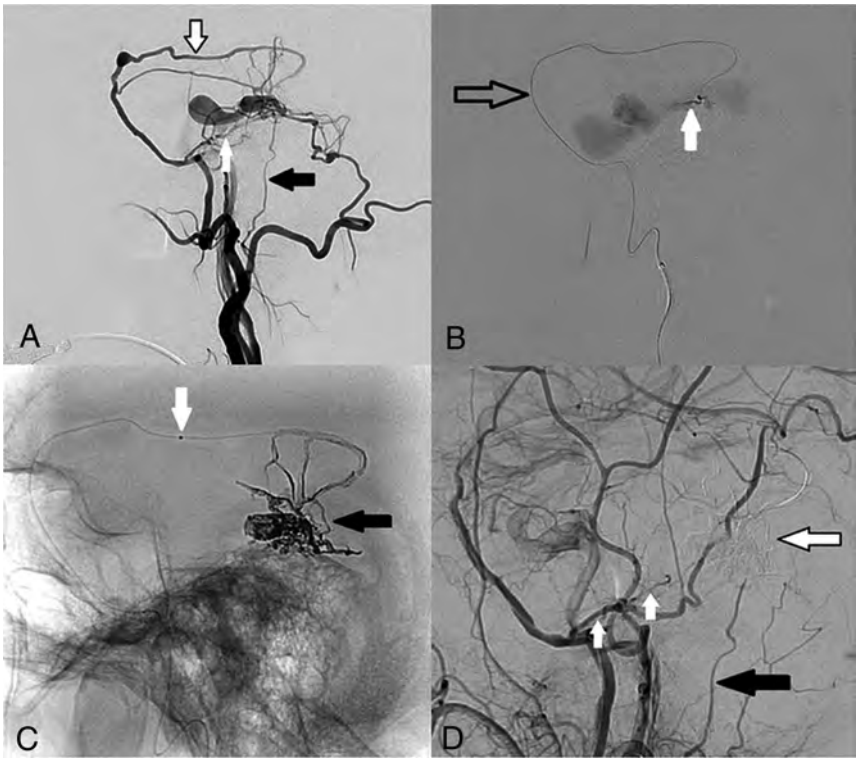

FIG 3. DSA and transarterial embolization using EVOH copolymer of a right-sided Borden III/Cognard IV petrous dural AVF. All images are in the lateral projection. *A*, Right external carotid artery injection demonstrates arterial supply to the AVF from the squamous temporal branch of the right MMA (*black-border arrow*) from an enlarged petrous branch of the MMA (*white arrow*) and from an enlarged stylomastoid artery (*black arrow*). Note that the facial nerve arterial arcade is formed by the latter 2 vessels. *B*, A microcatheter is present in the squamous branch of the MMA (*black-border arrow*). Microcatheter injection DSA from a distal point in the vessel demonstrates the fistulous point (*white arrow*) entering an ectatic petrosal varix. *C*, Spot film following EVOH embolization via the squamous branch of the MMA demonstrates the EVOH cast (*black arrow*) across the fistulous point and into the venous sac. The proximal marker of the detachable tip is visible (*white arrow*). *D*, Magnified right common carotid artery injection following embolization demonstrates the subtracted EVOH cast (*black-border arrow*) with no remnant filling of the AVF. The petrous branch of the MMA (*white arrows*) and the stylomastoid artery (*black arrow*) remain patent after treatment. The patient had preserved facial nerve function postprocedure.

Of the 8 patients with primary TAE, 5 had angiographic cure after a single session. All 5 of these patients were treated using liquid embolic agents (glue 4, EVOH 1) to occlude the fistulous point, with the microcatheter placed distally in the squamous (nonpetrous) branch of the middle meningeal artery in all cases and additional glue embolization via the meningohypophyseal trunk in 1 case. An example of TAE (patient 3) using EVOH via the squamous branch of the MMA is demonstrated in Fig 3.

One case with TAE with angiographic cure (patient 1) was complicated by pial arterial infarction due to the passage of glue droplets across an external carotid–internal carotid anastomosis, in this case most likely between the squamous branch of the middle meningeal artery and the lateral tentorial branch of the meningohypophyseal trunk. The TAE session was aborted in 2 cases due to inability to gain a distal or safe microcatheter position (patients 2 and 13), and in a third case (patient 5), only partial fistula reduction was achieved; these cases underwent curative surgical treatment. All 3 cases of primary TVE (patients 7, 14, and 15) were cured using a reverse pressure-cooker technique (On-line Figure).

Microsurgical disconnection was recommended as the primary treatment in 4 cases in which an endovascular approach was deemed too dangerous (Fig 2) and as the secondary treatment in 3 unsuccessful TAE cases (see above). In all 7 cases, an extended retrosigmoid approach was used to expose and occlude the draining petrosal vein with subsequent angiographic cure. One primary surgical case (patient 6) was complicated by hemorrhagic venous infarction of the ipsilateral cerebellum.

In summary, all 15 patients had long-term angiographic cure, and none developed iatrogenic facial nerve palsy. Approximately half of these patients ($n = 8$) had cure by endovascular treatment, and half ($n = 7$), by microsurgical disconnection. Two patients (patient 1: TAE and patient 6: an operation) had significant treatment-related neurologic complications resulting in permanent worsening of their mRS at presentation by 1 point.

DISCUSSION

Endovascular treatment of petrous AVFs supplied by vessels of the facial nerve arterial arcade is associated with certain strategic and technical challenges to preserve facial nerve function. In our cohort, all patients with petrous AVFs had at least partial arterial supply to the fistula from vessels of the facial nerve arterial arcade. In addition, these patients warranted interventional treatment due to direct cortical venous drainage in all cases, in keeping with the known venous drainage pattern of lateral epidural shunts into cortical veins.[15] Because of these challenges, some groups have adopted a primary surgical approach for petrous AVFs.[14,16,17] Use of the principles outlined retrospectively in our treatment strategy algorithm (Fig 2) resulted in endovascular cure in approximately half of cases (8/15: 53%) and surgical cure in the other half (7/15: 47%), with preserved facial nerve function in all cases.

Surgical Treatment

Surgical management of AVFs is based on the principle that microsurgical disconnection of the draining vein will cure the AVF.[18] Lawton et al[17] recommended use of an extended retrosigmoid approach for petrosal AVFs to expose and occlude the superior petrosal (Dandy) vein as it enters the superior petrosal sinus. This involves lateral positioning for a vertical trajectory to

the cerebellopontine angle and anterior mobilization of the skeletonized sigmoid sinus, allowing ideal visualization of the petrous-tentorial angle.[14,17,18] In the series of Lawton et al of 8 patients with petrosal AVFs, all patients underwent presurgical TAE to minimize blood loss.[17] Therefore, when safe to do so, an attempt at endovascular treatment is still the recommended primary approach.[6,18]

The surgical goal of disconnecting the superior petrosal vein carries a risk of cerebellar venous infarction if the ipsilateral cerebellum is dependent on the petrosal vein complex for drainage.[19] This complication is well-described following petrosal vein sacrifice during microvascular decompression for trigeminal neuralgia (4%–7% in larger series).[19,20] The rate of neurologic deterioration following an operation for petrosal AVFs may be even higher (13%–33% in small series, including facial nerve palsy, hemiparesis from venous infarct, and death from intraoperative cerebellar edema).[17,21] Surgical management of petrosal AVFs, therefore, requires careful assessment of the cerebellar venous drainage pattern on DSA to ensure that the petrosal vein can be safely sacrificed.

Transarterial Embolization

The treatment goal for curative TAE is occlusion of the fistulous point and the foot of the draining vein.[22] A safe TAE approach to petrosal AVFs is optimized by detailed analysis of high-frame-rate magnified angiography and 3D rotational angiography with MPRs.[23,24] Anatomic factors that best allow safe TAE are outlined in the Materials and Methods section and in Fig 2.[25,26] If such favorable factors are not present, then TVE may be considered.[27] Otherwise, a primary surgical disconnection is suggested by our group (Fig 2).

The advantage of glue in petrosal AVFs is the ability to rapidly penetrate the fistulous point while minimizing reflux toward the facial arcade if a distal wedged position can be achieved.[25] However, if a distal perifistulous microcatheter position cannot be achieved or the microcatheter is not retrieved at the appropriate moment of the injection, there may be glue inflow or reflux into the facial nerve arterial arcade. Other complications may involve gluing of the microcatheter tip so that it cannot be retrieved or nontarget embolization of pial arteries across external carotid–internal carotid anastomoses (ie, branches of the inferolateral or meningohypophyseal trunks), resulting in arterial infarction (as occurred in patient 1 in our series).[1,28] Thus, the use of liquid embolic agents requires extensive experience with the agent, a distal microcatheter position, and a thorough knowledge of the external carotid–internal carotid anastomoses and cranial nerve supply in this region.[1,25,28]

EVOH can be injected more slowly without the need for rapid removal of the microcatheter (Fig 3), but it is associated with longer radiation times and risks of reflux into both external carotid–internal carotid anastomoses and cranial nerve supply.[29,30] EVOH was used for TAE in 1 patient in our series (patient 3, Fig 3) with injection performed via the squamous branch of the MMA through a detachable-tip microcatheter. The use of detachable-tip microcatheters, which can also be combined with a pressure-cooker technique, in which a coil/glue plug is deployed over the detachable tip by a second microcatheter to minimize EVOH reflux, allows controlled embolization if there is a reasonable anatomic safety margin back to the facial arcade (the shortest available detachable-tip length is 15 mm).[31] The presence of an intervening nidus between the embolization point and the venous drainage increases the potential for reflux of the embolic agent across nidal channels into the facial nerve arterial arcade (Fig 2 and On-line Figure).

Transvenous Embolization

TVE of petrosal AVFs may be considered when there are relative anatomic contraindications to TAE or TAE has failed to occlude the fistula.[27] Safe TVE requires successful navigation of the microcatheter to the foot of the draining vein, limited tortuosity of the draining vein, and absence of normal cortical venous drainage into the target vein (Fig 2 and On-line Figure).[32] To achieve retrograde flow of the embolic agent toward the fistula point, a reverse pressure-cooker (dual microcatheter) technique (On-line Figure) or a dual-lumen balloon may be required.[32-34] Given the need for navigation in pial veins, this approach requires experience to prevent potentially catastrophic venous hemorrhagic complications and, thus, in the authors' opinion, should be performed only in centers with experience in pial transvenous approaches.

Utility of Our Treatment Strategy Algorithm

Our retrospective treatment-strategy algorithm (Fig 2) is based on detailed angiographic assessment and multidisciplinary discussion, with the aim of primary TAE or TVE when safe to do so. Safe microsurgical disconnection requires careful evaluation of the venous drainage of the cerebellum on preoperative DSA to ensure nondependence on the petrosal vein complex. Advancements in detachable-tip microcatheters, liquid embolics, and treatment strategies (eg, pressure-cooker technique) potentially allow greater rates of endovascular cure.[17,35]

Limitations

This study is limited by its retrospective nature and relatively small sample size.

CONCLUSIONS

Petrous AVFs are always supplied by arteries of the facial nerve arterial arcade and always have cortical venous drainage. This raises the risk of iatrogenic facial nerve palsy via endovascular arterial routes during clinically necessary treatments. Using the principles outlined in our treatment-strategy algorithm, approximately half of our patients were cured by endovascular treatment, half were cured by an operation, and all had preserved facial nerve function.

Disclosures: Kartik D. Bhatia—*UNRELATED*: *Employment*: University Health Network, Toronto, *Comments*: paid employment as clinical fellow in interventional neuroradiology at the University Health Network, Toronto. Timo Krings—*UNRELATED*: *Consultancy*: Stryker, Medtronic, Penumbra; *Royalties*: Thieme; *Stock/Stock Options*: Marblehead.

REFERENCES

1. Geibprasert S, Pongpech S, Armstrong D, et al. **Dangerous extracranial-intracranial anastomoses and supply to the cranial nerves:**

vessels the neurointerventionalist needs to know. *AJNR Am J Neuroradiol* 2009;30:1459–68 CrossRef Medline
2. Ozanne A, Pereira V, Krings T, et al. **Arterial vascularization of the cranial nerves.** *Neuroimaging Clin N Am* 2008;18:431–39 CrossRef Medline
3. Lapresle J, Lasjaunias P. **Cranial nerve ischaemic arterial syndromes: a review.** *Brain* 1986;109:207–16 CrossRef Medline
4. Lasjaunias P, Doyon D, Edouard A. **Post-embolisation lower motor neurone facial paralysis: report of one case, discussion, prevention (author's transl**.) [in French]. *Ann Otolaryngol Chir Cervicofac* 1978;95:595–602 Medline
5. Merland JJ, Moret J, Lasjaunias P, et al. **Cranial osseous and meningeal blood supply (author's transl**) [in French]. *J Neuroradiol* 1977;4:335–36 Medline
6. Li J, Ren J, Du S, et al. **Dural arteriovenous fistulas at the petrous apex.** *World Neurosurg* 2018;119:e968–76 CrossRef Medline
7. Minatogawa T, Kumoi T, Hosomi H, et al. **The blood supply of the facial nerve in the human temporal bone.** *Auris Nasus Larynx* 1980;7:7–18 CrossRef Medline
8. Dozõić A, Cetković M, Marinković S, et al. **Vascularisation of the geniculate ganglion.** *Folia Morphol (Warsz)* 2014;73:414–21 CrossRef Medline
9. Natali AL, Leo JT. **Neuroanatomy, Middle Meningeal Arteries.** StatPearls [Internet]. October 2018. https://www.ncbi.nlm.nih.gov/books/NBK519545/. Accessed September 14, 2019
10. El-Khouly H, Fernandez-Miranda J, Rhoton AL Jr. **Blood supply of the facial nerve in the middle fossa: the petrosal artery.** *Neurosurgery* 2008;62(5 Suppl 2):ONS297–303; discussion ONS303–294 CrossRef Medline
11. Upile T, Jerjes W, Nouraei SA, et al. **The stylomastoid artery as an anatomical landmark to the facial nerve during parotid surgery: a clinico-anatomic study.** *World J Surg Oncol* 2009;7:71 CrossRef Medline
12. Borden JA, Wu JK, Shucart WA. **A proposed classification for spinal and cranial dural arteriovenous fistulous malformations and implications for treatment.** *J Neurosurg* 1995;82:166–79 CrossRef Medline
13. Cognard C, Gobin YP, Pierot L, et al. **Cerebral dural arteriovenous fistulas: clinical and angiographic correlation with a revised classification of venous drainage.** *Radiology* 1995;194:671–80 CrossRef Medline
14. Westermaier T, Bendszus M, Solymosi L, et al. **Surgical treatment of dural arteriovenous fistulas of the petrous apex.** *World Neurosurg* 2012;77:e597–613 CrossRef Medline
15. Geibprasert S, Pereira V, Krings T, et al. **Dural arteriovenous shunts: a new classification of craniospinal epidural venous anatomical bases and clinical correlations.** *Stroke* 2008;39:2783–94 CrossRef Medline
16. Youssef PP, Schuette AJ, Cawley CM, et al. **Advances in surgical approaches to dural fistulas.** *Neurosurgery* 2014;74(Suppl 1):S32–41 CrossRef Medline
17. Lawton MT, Sanchez-Mejia RO, Pham D, et al. **Tentorial dural arteriovenous fistulae: operative strategies and microsurgical results for six types.** *Neurosurgery* 2008;62:110–124; discussion 124–15 CrossRef Medline
18. Radovanovic I, Wallace M. Cranial dural arterovenous fistula disconnection. In: Jandial R, McCormick P, Black P, eds. *Core Techniques in Operative Neurosurgery*. Philadelphia: Elsevier; 2019
19. Narayan V, Savardekar AR, Patra DP, et al. **Safety profile of superior petrosal vein (the vein of Dandy) sacrifice in neurosurgical procedures: a systematic review.** *Neurosurg Focus* 2018;45:E3 CrossRef Medline
20. Liebelt BD, Barber SM, Desai VR, et al. **Superior petrosal vein sacrifice during microvascular decompression: perioperative complication rates and comparison with venous preservation.** *World Neurosurg* 2017;104:788–94 CrossRef Medline
21. Gross BA, Du R. **Surgical treatment of high grade dural arteriovenous fistulae.** *J Clin Neurosci* 2013;20:1527–32 CrossRef Medline
22. Gross BA, Albuquerque FC, Moon K, et al. **Evolution of treatment and a detailed analysis of occlusion, recurrence, and clinical outcomes in an endovascular library of 260 dural arteriovenous fistulas.** *J Neurosurg* 2017;126:1884–93 CrossRef Medline
23. Gailloud P, Oishi S, Carpenter J, et al. **Three-dimensional digital angiography: new tool for simultaneous three-dimensional rendering of vascular and osseous information during rotational angiography.** *AJNR Am J Neuroradiol* 2004;25:571–73 Medline
24. Kiyosue H, Tanoue S, Okahara M, et al. **Angioarchitecture of transverse-sigmoid sinus dural arteriovenous fistulas: evaluation of shunted pouches by multiplanar reformatted images of rotational angiography.** *AJNR Am J Neuroradiol* 2013;34:1612–20 CrossRef Medline
25. Lasjaunias P, Berenstein A, terBrugge K. Clinical and endovascular treatment aspects in adults. In: *Surgical Neuroangiography*. Vol 2. 2nd ed. Heidleberg: Springer-Verlag; 2004
26. Baltsavias G, Spiessberger A, Hothorn T, et al. **Cranial dural arteriovenous shunts, Part 4: clinical presentation of the shunts with leptomeningeal venous drainage.** *Neurosurg Rev* 2015;38:283–91; discussion 291 CrossRef Medline
27. Signorelli F, Gory B, Maduri R, et al. **Intracranial dural arteriovenous fistulas: a review of their current management based on emerging knowledge.** *J Neurosurg Sci* 2017;61:193–206 CrossRef Medline
28. Koyanagi M, Kobayashi T, Oda M, et al. **Dural arteriovenous fistula in the falx cerebri treated with transarterial embolization using n-butyl cyanoacrylate.** *Surg Neurol Int* 2016;7:S1057–59 CrossRef Medline
29. Velat GJ, Reavey-Cantwell JF, Sistrom C, et al. **Comparison of N-butyl cyanoacrylate and Onyx for the embolization of intracranial arteriovenous malformations: analysis of fluoroscopy and procedure times.** *Neurosurgery* 2008;63:ONS73–78; discussion ONS78–80 CrossRef Medline
30. Chen J, Crane B, Niparko J, et al. **Direct intraoperative confirmation of penetration of ethylene vinyl alcohol copolymer (Onyx) into the vasa nervosa of the facial nerve.** *J Neurointerv Surg* 2012;4:435–47 CrossRef Medline
31. Chapot R, Stracke P, Velasco A, et al. **The pressure cooker technique for the treatment of brain AVMs.** *J Neuroradiol* 2014;41:87–91 CrossRef Medline
32. Abecassis IJ, Nerva JD, Ghodke BV, et al. **The dual microcatheter technique for transvenous embolization of dural arteriovenous fistulae.** *J Neurointerv Surg* 2017;9:578–82 CrossRef Medline
33. Zhang G, Zhu S, Wu P, et al. **The transvenous pressure cooker technique: a treatment for brain arteriovenous malformations.** *Interv Neuroradiol* 2017;23:194–99 CrossRef Medline
34. Ye M, Zhang P. **Transvenous balloon-assisted Onyx embolization of dural arteriovenous fistulas of hypoglossal canal.** *Neuroradiology* 2018;60:971–78 CrossRef Medline
35. Colby GP, Coon AL, Huang J, et al. **Historical perspective of treatments of cranial arteriovenous malformations and dural arteriovenous fistulas.** *Neurosurg Clin N Am* 2012;23:15–25 CrossRef Medline

Assessment of Apparent Internal Carotid Tandem Occlusion on High-Resolution Vessel Wall Imaging: Comparison with Digital Subtraction Angiography

S. Chai, Z. Sheng, W. Xie, C. Wang, S. Liu, R. Tang, C. Cao, W. Xin, Z. Guo, B. Chang, X. Yang, J. Zhu, and S. Xia

ABSTRACT

BACKGROUND AND PURPOSE: Not all tandem occlusions diagnosed on traditional vascular imaging modalities, such as MRA, represent actual complete ICA occlusion. This study aimed to explore the utility of high-resolution vessel wall imaging in identifying true ICA tandem occlusions and screening patients for their suitability for endovascular recanalization.

MATERIALS AND METHODS: Patients with no signal in the ICA on MRA were retrospectively reviewed. Two neuroradiologists independently reviewed their high-resolution vessel wall images to assess whether there were true tandem occlusions and categorized all cases into intracranial ICA occlusion, extracranial ICA occlusion, tandem occlusion, or near-occlusion. DSA classified patient images into the same 4 categories, which were used as the comparison with high-resolution vessel wall imaging. The suitability for recanalization of occluded vessels was evaluated on high-resolution vessel wall imaging compared with DSA.

RESULTS: Forty-five patients with no ICA signal on MRA who had available high-resolution vessel wall imaging and DSA images were included. Among the 34 patients (34/45, 75.6%) with tandem occlusions on DSA, 18 cases also showed tandem occlusions on high-resolution vessel wall imaging. The remaining 16 patients, intracranial ICA, extracranial ICA occlusions and near-occlusions were found in 2, 6, and 8 patients, respectively, on the basis of high-resolution vessel wall imaging. A total of 20 cases (20/45, 44.4%) were considered suitable for recanalization on the basis of both DSA and high-resolution vessel wall imaging. Among the 25 patients deemed unsuitable for recanalization by DSA, 11 were deemed suitable for recanalization by high-resolution vessel wall imaging.

CONCLUSIONS: High-resolution vessel wall imaging could allow identification of true ICA tandem occlusion in patients with an absence of signal on MRA. Findings on high-resolution vessel wall imaging can be used to screen more suitable candidates for recanalization therapy.

ABBREVIATIONS: EICA = extracranial ICA; IICA = intracranial ICA; HR-VWI = High-resolution vessel wall imaging

Internal carotid artery occlusion is a relatively uncommon-yet-important cause of TIAs and cerebral infarction.[1] Tandem occlusion of the ICA, typically diagnosed on Doppler sonography, CTA, or MRA by the absence of flow, contrast media, or signal of the extracranial ICA (EICA) concomitant ipsilateral to the intracranial ICA (IICA), is often associated with a poor prognosis due to a low arterial recanalization rate.[2-4]

However, not all tandem occlusions identified on these luminal imaging modalities represent actual complete ICA occlusion. Near-occlusion with or without full collapse (defined as prominent carotid bulb stenosis with a string-like or otherwise normal-appearing distal lumen)[5,6] and isolated intracranial or extracranial occlusion caused by atherosclerosis or dissection may masquerade as complete occlusion of the ICA.[7-10] In these cases of slow blood flow and altered flow dynamics, CTA or MRA acquisition can "outrun" the arrival of a blood signal or contrast media,

Received October 17, 2019; accepted after revision January 15, 2020.

From the Department of Radiology (S.C., W. Xie, S.L., R.T., S.X.), First Central Clinical College, Tianjin Medical University, Tianjin, China; Departments of Radiology and (S.C., W. Xie, S.L., R.T., S.X.), Tianjin First Central Hospital, Tianjin, China; Neurosurgery (Z.S., C.W., B.C.), Tianjin First Central Hospital, Tianjin, China; Department of Neurosurgery (W. Xin, X.Y.), Tianjin Medical University General Hospital, Tianjin, China; Department of Radiology (C.C.), Tianjin Huanhu Hospital, Tianjin, China; Department of Neurosurgery (Z.G.), Tianjin TEDA Hospital, Tianjin, China; and MR Collaboration (J.Z.), Siemens Healthcare Ltd., Beijing, China.

This work was supported by a grant from the National Natural Science Foundation of China (NSFC 81871342).

Please address correspondence to Shuang Xia, PhD, Department of Radiology, Tianjin First Central Hospital, No. 24, Fukang Rd, Nan Kai District, Tianjin, China; e-mail: xiashuang77@163.com

Indicates open access to non-subscribers at www.ajnr.org
Indicates article with supplemental on-line tables.
Indicates article with supplemental on-line photos.
http://dx.doi.org/10.3174/ajnr.A6452

resulting in inadequate arterial angiography and the appearance of an occlusion. This process can confound planning for recanalization treatment because many neurointerventionists would offer surgery to patients with apparent tandem occlusion on conventional luminal imaging if focal occlusion or near-occlusion was confirmed during intraoperative angiography.[11-14] The process can also cause misclassification of patients with isolated ICA occlusion or near-occlusion during clinical trial screening if the evaluation is based solely on CTA or MRA. Consequently, accurate noninvasive imaging is necessary to visualize the true occlusion site and to help screen potential candidates for recanalization therapy.

High-resolution vessel wall imaging (HR-VWI) techniques allow direct characterization of the vessel wall and intraluminal status by suppressing the signal in flowing blood,[15] providing information about the location, length, and etiology of the occlusion and the presence or absence of intraluminal thrombus.[16,17] To the best of our knowledge, our study is the first to determine whether HR-VWI would enable superior identification of true tandem occlusions.

We hypothesized that HR-VWI could more accurately identify true tandem occlusion in patients with apparent ICA occlusion detected on MRA. The aims of this study were to explore the utility of HR-VWI for identifying true ICA tandem occlusions and to determine the suitability for endovascular recanalization in patients with an absence of signal on MRA compared with DSA.

MATERIALS AND METHODS

Patient Selection and Data Collection

This retrospective study was approved by the research ethics board at Tianjin First Central Hospital (project identification No. 2018N133KY), and the informed consent requirement was waived. A total of 355 diagnostic HR-VWI scans were obtained from September 2016 to November 2018. Patients who had apparent tandem ICA occlusion on MRA and underwent both HR-VWI and DSA examinations were included in the study. The exclusion criteria were the following: 1) the presence of ICA signal, 2) the absence of DSA images for comparison, 3) insufficient vessel coverage or uninterpretable images due to motion artifacts, and 4) nonatherosclerotic or dissection occlusion, including Moyamoya disease, vasculitis, and trauma.

The patient data, including demographics, vascular risk factors (hypertension, hyperlipidemia, diabetes mellitus, coronary disease, prior stroke history, smoking, and alcohol intake), and their NIHSS scores, were retrospectively collected. The interval time from the HR-VWI examination to symptom onset and the time between HR-VWI and DSA were also recorded.

MR Imaging Protocols

All patients underwent routine brain MR imaging examinations and HR-VWI on a 3T system (Magnetom Prisma; Siemens, Erlangen, Germany) with a standard 64-channel head coil. Routine brain MRIs, including DWI and TOF-MRA, were initially performed for assessment of acute infarction and the vessels, respectively. The HR-VWI was performed by an inversion-recovery sampling perfection with application-optimized contrasts by using different flip angle evolution (IR-SPACE; Siemens) sequence to visualize the intraluminal status by suppressing blood flow and CSF signal, with the following parameters: TR = 900 ms; TE = 15 ms; flip angle = 120°; FOV = 240 × 210 mm^2; matrix = 384 × 336; 240 slices with 0.55-mm section thickness; reconstructed voxel size = 0.55 × 0.55 × 0.55 mm^3; and acquisition time = 7 minutes 43 seconds. Image reconstruction was performed with the 3D function of the PACS. On-line Table 1 shows more detailed sequence parameters.

MRA Analysis

All baseline MRA images were assessed by 2 diagnostic neuroradiologists (with 3 and 7 years of experience in neuroimaging, respectively) who were blinded to the DSA and HR-VWI findings for the apparent tandem occlusion in the ICA. "Apparent tandem occlusion" was defined as the absence of signal in the extracranial ICA concomitant ipsilateral to the intracranial ICA.

HR-VWI Analysis

Two additional diagnostic neuroradiologists (both with 3 years of experience in HR-VWI interpretation) who were both blinded to the DSA findings and clinical treatment information separately reviewed the HR-VWI and determined the presence or absence of occlusions from the carotid bulb to the circle of Willis. "Occlusion" was defined as discontinuation of lumen >5 mm in length,[18] which presented as no black-blood signal on HR-VWI.

The horizontal segment of the carotid canal was used as the landmark to divide the ICA into extracranial and intracranial segments. The occlusion types were categorized as EICA occlusion, IICA occlusion, tandem occlusion, and near-occlusion with or without full collapse. "Tandem occlusion" was defined as cervical carotid occlusion with a concomitant intracranial occlusion.[19] Near-occlusion with and without full collapse was distinguished by prominent carotid bulb plaque with a string-like or more normal distal lumen, respectively. On-line Figure 1 shows different occlusion types on HR-VWI. The morphologic characteristics, including distal ICA reconstitution and the occlusion segment, were recorded. "Reconstitution" was defined as the ICA distal to the occlusion being visible. Segments of the ICA were evaluated on the basis of the classification criteria proposed by Bouthillier et al.[20]

To evaluate intraobserver agreement, 1 reader reassessed the same images and measured vessel occlusion length 3 months after the first reading session. The measurement method of vessel occlusion length is shown on On-line Fig 2*A*. The cause of the occlusion, thrombus, or dissection with intramural hematoma was recorded, according to previously published parameters.[21]

Identification of Candidates Suitable for Endovascular Recanalization on the Basis of Occluded Vascular Features

Criteria of apparent suitability for endovascular recanalization based on occlusion segment, occlusion type, and distal ICA reconstitution were proposed.[2,22,23] Therefore, the vessels were further classified into 4 groups based on these morphologic features as follows:

1. Suitable for recanalization: near-occlusion without full collapse.
2. Probably suitable for recanalization: focal occlusion at or above the clinoid segment, tandem occlusion with distal ICA reconstitution before the clinoid segment, and near-occlusion with full collapse.
3. Probably unsuitable for recanalization: tandem occlusion with distal ICA reconstitution at or above the clinoid segment.
4. Not suitable for recanalization: tandem occlusion without reconstitution.

DSA Analysis

Conventional selective cerebral angiography was performed using the transfemoral approach, including cervical and intracranial views in the anterior-posterior and lateral projections on the biplane angiography suite system (Allura Xper FD20 biplane system; Philips Healthcare, Best, the Netherlands). The injected volume of the contrast media was 6–8 mL.

Two interventional neuroradiologists (with 6 and 7 years of experience in interventional neuroradiology, respectively) reviewed all the DSA images in a blinded fashion to classify those images into the same 4 occlusion types, including IICA occlusion, EICA occlusion, tandem occlusion, and near-occlusion. The morphologic characteristics, including distal ICA reconstitution and occlusion segment, were defined using criteria similar to that for HR-VWI. If DSA showed no occlusion but only high-grade (90%–99%) stenosis in the carotid bulb with or without narrowing of the poststenotic ICA, the finding was deemed to show near-occlusion.[24] The vessel occlusion length was measured by 1 of the readers (On-line Fig 2*B*). The suitability of the occluded vessels for endovascular recanalization was also classified into 4 groups using the same criteria as used for HR-VWI. Reperfusion was graded in patients who underwent recanalization treatment according to modified TICI perfusion categories, and procedural success was defined as TICI 2b or 3.[7]

Statistical Analysis

Statistical analysis was performed using SPSS, Version 22.0 (IBM, Armonk, New York) and GraphPad Prism software 5.0 (GraphPad Software, San Diego, California). Categoric variables were reported as proportions. Intra- and interneuroradiologist agreement regarding the qualitative parameters associated with the suitability for endovascular recanalization, occlusion site and reconstitution, were assessed using the Cohen κ. Disagreements in the interpretation of occlusion categories and suitability for endovascular recanalization were resolved by consensus review of the images. The Fisher exact test was used to calculate the statistical differences in the categoric proportions from contingency table analysis.

RESULTS

Patient Characteristics

In total, 355 patients with HR-VWI examinations were retrospectively analyzed; 78 patients were found to have an absence of signal in the ICA on MRA. Fifteen patients without DSA data for comparison were excluded; 4 patients were excluded due to insufficient vessel coverage or motion artifacts.

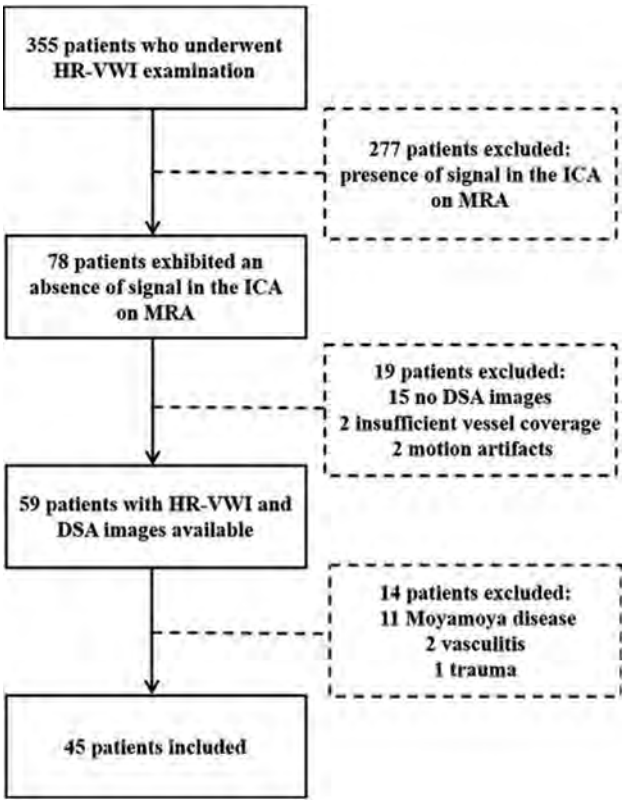

FIG 1. Flow chart of patient selection.

Patients with other causes of ICA occlusion, including 11 with Moyamoya disease, 2 with vasculitis, and 1 with trauma were also ruled out. Finally, 45 patients were included in the current study for analysis (Fig 1).

Of the 45 patients, 39 (86.7%) were men and 6 (13.3%) were women, with an average age of 62 years. The median and mean interval time between HR-VWI scanning and DSA was 6.0 ± 3.5 days (ranging from 1 to 15 days). More demographics and baseline characteristics are presented in On-line Table 2.

Assessment Reproducibility

Interobserver agreement coefficients regarding the occlusion category, reconstitution, and suitability for recanalization on HR-VWI and DSA were almost perfect (On-line Table 3). Agreement coefficients were interpreted according to the methods described by Kundel and Polansky.[25] Intraobserver agreement for the above qualitative analysis on HR-VWI was excellent, with κ (95% CI) = 0.968 (0.907–1.000), 0.941 (0.861–1.000), and 0.945 (0.837–1.000), respectively.

Findings on HR-VWI

Among the 45 included cases with apparent occlusions on MRA, HR-VWI showed tandem occlusion in 18 cases (18/45, 40.0%). All 18 cases also showed tandem occlusions on DSA (Table 1). Figure 2 shows an example of a case with matching classifications of tandem occlusion on both DSA and HR-VWI. In addition, dissection with intramural hematoma was detected on HR-VWI in 33.3% (6/18) of the cases of tandem occlusion.

Table 1: Different types of occlusion on HR-VWI versus DSA

HR-VWI	DSA				Total
	IICA Occlusion	EICA Occlusion	Tandem Occlusion	Near-Occlusion	
IICA occlusion	4 (8.9%)	0 (0.0%)	2 (4.4%)	0 (0.0%)	6 (13.3%)
EICA occlusion	0 (0.0%)	1 (2.2%)	6 (13.3%)	0 (0.0%)	7 (15.6%)
Tandem occlusion[a]	0 (0.0%)	0 (0.0%)	18 (40.0%)	0 (0.0%)	18 (40.0%)
Near-occlusion	0 (0.0%)	0 (0.0%)	8 (17.8%)	6 (13.3%)	14 (31.1%)
Total	4 (8.9%)	1 (2.2%)	34 (75.6%)	6 (13.3%)	45 (100%)

[a] Tandem occlusion, concomitant extracranial ICA ipsilateral to the intracranial ICA occlusion. Fisher exact test: $P < .001$.

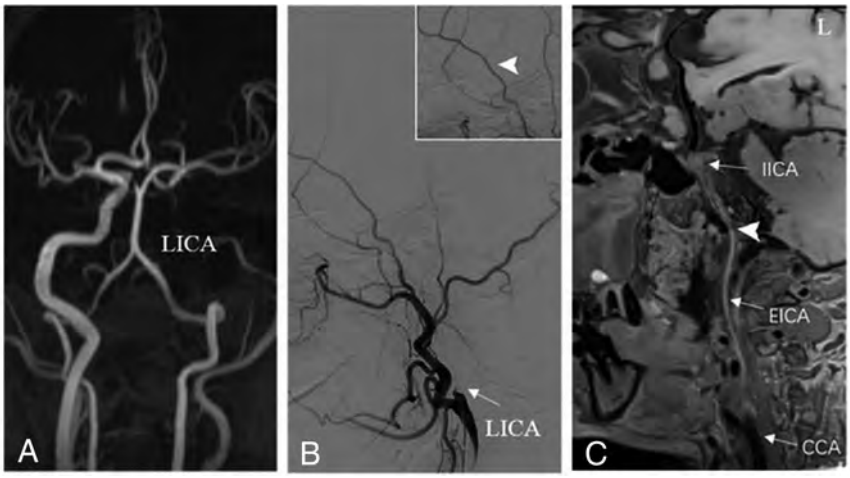

FIG 2. An example of tandem occlusion of the ICA. *A*, MRA shows an absence of signal in the left ICA. *B*, DSA presents contrast cutoff (*arrow*) at the level of the carotid bulb with distal ICA reconstitution (*arrowhead*). *C*, HR-VWI shows occlusion from the carotid bulb to the clinoid segment of the left ICA (*arrowhead*), with reconstitution at the supraclinoid segment, which was considered unsuitable for recanalization. LICA indicates left ICA.

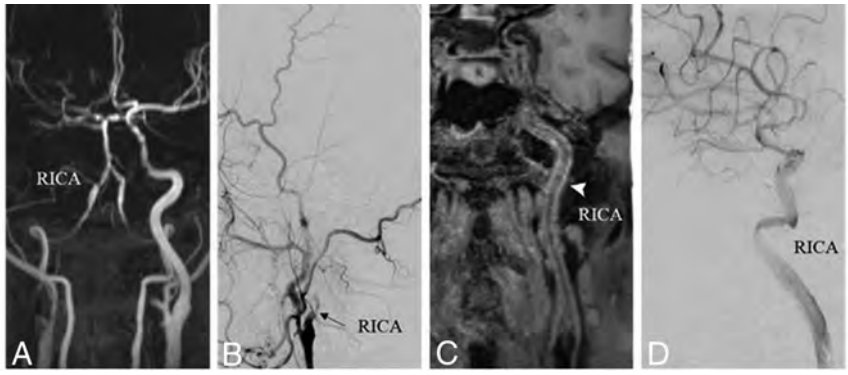

FIG 3. An example of apparent right internal carotid tandem occlusion on MRA (*A*) and preoperative DSA (*B*, *arrow*). *C*, HR-VWI shows a patent ICA with a narrow residual cavity (*arrowhead*), defined as near-occlusion with full collapse, which was considered suitable for recanalization. *D*, Postoperative DSA demonstrates successful recanalization with TICI 3. RICA indicates right ICA.

In the 27 (60%) remaining vessels, no tandem occlusions were found. Instead, IICA occlusions, EICA occlusions, and near-occlusions were observed in 6 (13.3%), 7 (15.6%), and 14 (31.1%) cases, respectively. Of the 14 near-occlusion cases, 5 were near-occlusion without full collapse and 9 were near-occlusion with full collapse (Table 1 and On line Fig 3*A*). Therefore, near-occlusion with full collapse was most frequently categorized as tandem occlusion by DSA. Figure 3 depicts a case with apparent internal carotid tandem occlusion on MRA and preoperative DSA, which was shown to display near-occlusion with full collapse on HR-VWI.

Findings on DSA

ICA tandem occlusions were detected on DSA in 34 of 45 (75.6%) cases. Sixteen patients (47.1%) had tandem occlusion on DSA, but HR-VWI showed IICA occlusion in 2, EICA occlusion in 6, and near-occlusion in 8 patients. The remaining 11 (24.4%) patients without tandem occlusion on DSA were correctly ruled out on HR-VWI. Among these patients, near-occlusion was observed in 6 (13.3%) (of which 5 showed near-occlusion without full collapse and 1 showed near-occlusion with full collapse), isolated IICA occlusion was seen in 4 (36.4%), and EICA occlusion in 1 (2.2%) (Table 1 and On-line Fig 3*A*).

The length distribution of the tandem occlusion with the 2 imaging methods is presented in On line Fig 3*B*. The length of occlusion measured on HR-VWI was significantly shorter than that shown on DSA ($P < .001$).

Suitability for Recanalization Evaluated by HR-VWI versus DSA

A total of 20 patients were deemed suitable for recanalization by both DSA and HR-VWI (Table 2). The extent of occlusion in these patients (n = 20) included 5 occlusions from the bulb to the cavernous ICA, 4 from the bulb to the petrous ICA, 1 at the cervical ICA, 4 localized at the supraclinoid ICA, 1 near-occlusion with full collapse at the ICA, and 5 near-occlusions without full collapse at the ICA. These numbers were 2, 2, 7, 6, 9, and 5, respectively, evaluated by HR-VWI (Fig 4).

In the remaining 25 patients who were deemed unsuitable for recanalization by DSA, 11 were found to be suitable for recanalization on the basis of HR-VWI, and 14 were considered

Table 2: Performance of HR-VWI versus DSA in assessing tandem occlusion and suitability for recanalization of ICA[a]

	DSA		HR-VWI	
	Present	Absent	Suitable	Unsuitable
HR-VWI present	18 (40.0%)	0 (0.0%)	4 (8.9%)	14 (31.1%)
HR-VWI absent	16 (35.6%)	11 (24.4%)	27 (60.0%)	0 (0.0%)
DSA (suitability for recanalization)				
Suitable	9 (20.0%)	11 (24.4%)	20 (44.4%)	0 (0.0%)
Unsuitable	25 (55.6%)	0 (0.0%)	11 (24.4%)	14 (31.1%)

[a] "Present" means tandem occlusion–positive; "Absent" means tandem occlusion–negative. The table shows the proportional relationship between the presence of tandem occlusion and the suitablity for recanalization. The percentage was calculated on the basis of a total number of patients of 45.

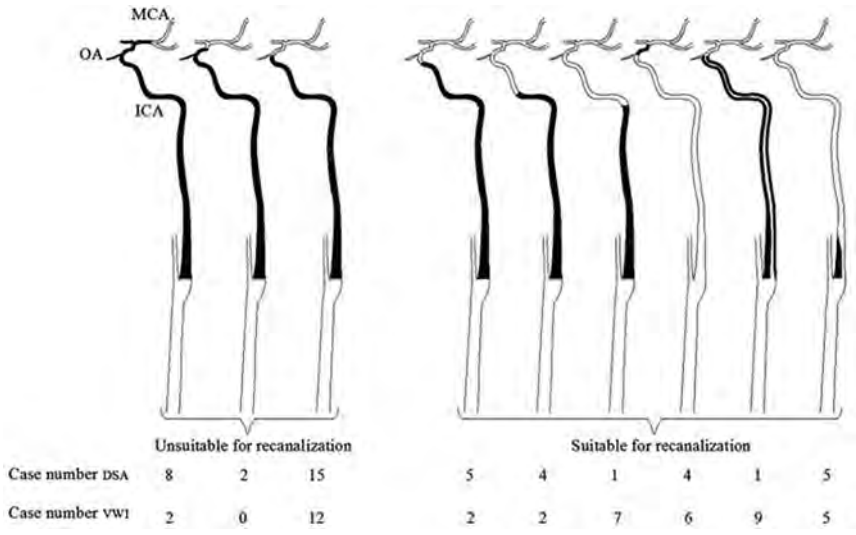

FIG 4. The extent of occlusion of 45 patients and their suitability for recanalization evaluated by DSA and VWI. The black part represents occlusion or near-occlusion. OA indicates ophthalmic artery.

unsuitable for recanalization by both HR-VWI and DSA (Table 2). The extent of occlusion in these 25 patients included 15 occlusions from the carotid bulb to the clinoid segment with reconstitution at the supraclinoid segment of the ICA, 2 occlusions from the bulb to the supraclinoid ICA, and 8 occlusions from the bulb to the MCA. These numbers were 12, 2, and 0, respectively, evaluated by HR-VWI (Fig 4).

Surgical Results for Endovascular Recanalization

Twelve patients underwent recanalization surgery successfully with TICI 2b or 3 among the 20 patients deemed suitable for recanalization by both DSA and HR-VWI. One patient presented with a history of recurrent stroke and underwent the operation successfully, with TICI 3 in the 11 patients deemed suitable for recanalization by HR-VWI but unsuitable by DSA. No operation was performed in the 14 patients deemed unsuitable for recanalization evaluated by both HR-VWI and DSA.

DISCUSSION

This study demonstrates that HR-VWI could allow identification of true ICA tandem occlusion in patients with apparent tandem occlusion on MRA. Furthermore, we proposed a method for preoperative evaluation of recanalization.

The study also shows that the arteries in approximately half of the patients with an apparent tandem ICA occlusion on DSA had patent or focal occlusion on HR-VWI. This finding may be due to the existence of pseudo-occlusion on luminal imaging techniques, including TOF-MRA, CTA, and DSA. Previous studies have indicated that even specialized radiologists may not be reliably able to distinguish true cervical occlusion from pseudo-occlusion in patients with ICA nonattenuation on single-phase CTA.[8] Many studies have advocated the use of DSA to diagnose pseudo-occlusion. However, in the series studied by Grossberg et al,[7] 71% of patients also showed a pseudo-occlusion on DSA. The authors considered microcatheter exploration to be the only method able to accurately diagnose the location of the occlusion. This method, however, was invasive, with a substantial number of risks and potential complications. Thus, the noninvasive HR-VWI could serve as a more convenient technique for the identification of true ICA tandem occlusion.

Prominent proximal stenosis or occlusion of the extracranial carotid or distal occlusions in the intracranial ICA could give the appearance that the ICA was totally occluded on luminal imaging. The findings in our study were consistent with those of other recent studies.[26-28] Patients with isolated vessel occlusion or near-occlusion could have overestimation and exaggeration on images captured with these luminal imaging techniques. Normal blood flow may be interrupted, possibly leading to an absence of signal or nonattenuation.[8,29,30] To the best of our knowledge, there is no existing literature focusing on whether HR-VWI would enable superior identification of true tandem occlusion. As a result, the literature available to evaluate true ICA tandem occlusion using HR-VWI is limited. However, excellent interobserver agreement in our study suggests that detection of true occlusion sites by HR-VWI in patients with an absence of signal on MRA is highly reproducible.

Recent research has shown that technical success rates in patients with reconstitution below the clinoid segment on preprocedural CTA were significantly higher than in those with reconstitution at or above the clinoid segment.[22] Therefore, we regarded the clinoid segment as the standard for suitability of

endovascular recanalization. Because DSA was also used for recanalization-procedure planning, a false-positive finding of tandem occlusion suggested that patients might be candidates for the recanalization treatment. This could significantly impact decision-making for some patients who might otherwise be excluded from selection as candidates for recanalization.[31]

Notably, 10 patients in our study had intramural hematomas, which have previously been described as being characteristic of dissection.[32,33] Because the treatment for dissection is different from that of an isolated thrombus, this finding further proves the importance of HR-VWI.

Our study had several limitations. First, given the reliance on HR-VWI, there was a potential for ascertainment bias because these kinds of studies may have not been documented in previous literature and it was often difficult to have a criterion standard to confirm the occlusions. Second, this was a retrospective study with a relatively small sample size, but compared with other trials that focus on tandem or pseudo-occlusion,[8,31,34-36] we had a similar or even relatively larger sample size. Third, although we proposed a method to identify candidates for recanalization, this method could not be well-validated due to a limited number of surgery cases. Therefore, larger sample sizes are needed in the future to validate the accuracy of the identification method. Finally, we could not completely exclude the possibility of recanalization during the period between HR-VWI and the DSA examination; the spontaneous recanalization rate of ICA occlusion is low, and the intervals are usually long, with an average interval of >1 year.[37,38] We believe that the chance of spontaneous recanalization in our patients was small because the intervals between HR-VWI and DSA were short, with mean intervals of 6.8 days.

CONCLUSIONS

Compared with DSA, HR-VWI could allow identification of true ICA tandem occlusion in patients with an absence of signal on MRA. Findings on HR-VWI can be used to identify more suitable candidates for recanalization therapy.

ACKNOWLEDGMENTS

We would like to thank the study team and all the study participants.

REFERENCES

1. Flaherty ML, Flemming KD, McClelland R, et al. **Population-based study of symptomatic internal carotid artery occlusion: incidence and long-term follow-up.** *Stroke* 2004;35:e349–52 CrossRef Medline
2. Goyal M, Menon BK, van Zwam WH, et al; HERMES Collaborators. **Endovascular thrombectomy after large-vessel ischaemic stroke: a meta-analysis of individual patient data from five randomised trials.** *Lancet* 2016;387:1723–31 CrossRef Medline
3. Rubiera M, Ribo M, Delgado-Mederos R, et al. **Tandem internal carotid artery/middle cerebral artery occlusion: an independent predictor of poor outcome after systemic thrombolysis.** *Stroke* 2006;37:2301–05 CrossRef Medline
4. Verlato F, Camporese G, Bernardi E, et al. **Clinical outcome of patients with internal carotid artery occlusion: a prospective follow-up study.** *J Vasc Surg* 2000;32:293–98 CrossRef Medline
5. Bartlett ES, Walters TD, Symons SP, et al. **Diagnosing carotid stenosis near-occlusion by using CT angiography.** *AJNR Am J Neuroradiol* 2006;27:632–37 Medline
6. Fox AJ, Eliasziw M, Rothwell PM, et al. **Identification, prognosis, and management of patients with carotid artery near occlusion.** *AJNR Am J Neuroradiol* 2005;26:2086–94 Medline
7. Grossberg JA, Haussen DC, Cardoso FB, et al. **Cervical carotid pseudo-occlusions and false dissections: intracranial occlusions masquerading as extracranial occlusions.** *Stroke* 2017;48:774–77 CrossRef Medline
8. Diouf A, Fahed R, Gaha M, et al. **Cervical internal carotid occlusion versus pseudo-occlusion at CT angiography in the context of acute stroke: an accuracy, interobserver, and intraobserver agreement study.** *Radiology* 2018;286:1008–15 CrossRef Medline
9. Lee D, Heo SH, Kim EJ, et al. **Pseudo-occlusion of the extracranial carotid artery caused by intracranial carotid artery stenosis.** *Neurol Sci* 2012;33:1201–03 CrossRef Medline
10. Kao HL, Lin MS, Wang CS, et al. **Feasibility of endovascular recanalization for symptomatic cervical internal carotid artery occlusion.** *J Am Coll Cardiol* 2007;49:765–71 CrossRef Medline
11. Gil-Peralta A, González A, González-Marcos JR, et al. **Internal carotid artery stenting in patients with symptomatic atheromatous pseudo-occlusion.** *Cerebrovasc Dis* 2004;17(Suppl 1):105–12 CrossRef Medline
12. O'Leary DH, Mattle H, Potter JE. **Atheromatous pseudo-occlusion of the internal carotid artery.** *Stroke* 1989;20:1168–73 CrossRef Medline
13. Greiner C, Wassmann H, Palkovic S, et al. **Revascularization procedures in internal carotid artery pseudo-occlusion.** *Acta Neurochir (Wien)* 2004;146:237–43; discussion 243 CrossRef Medline
14. Rothwell PM, Eliasziw M, Gutnikov SA, et al; Carotid Endarterectomy Trialists' Collaboration. **Analysis of pooled data from the randomised controlled trials of endarterectomy for symptomatic carotid stenosis.** *Lancet* 2003;361:107–16 CrossRef Medline
15. Bhogal P, Navaei E, Makalanda HL, et al. **Intracranial vessel wall MRI.** *Clin Radiol* 2016;71:293–303 CrossRef Medline
16. Naggara O, Louillet F, Touzé E, et al. **Added value of high-resolution MR imaging in the diagnosis of vertebral artery dissection.** *AJNR Am J Neuroradiol* 2010;31:1707–12 CrossRef Medline
17. Ryoo S, Lee MJ, Cha J, et al. **Differential vascular pathophysiologic types of intracranial atherosclerotic stroke: a high-resolution wall magnetic resonance imaging study.** *Stroke* 2015;46:2815–21 CrossRef Medline
18. Chen YH, Leong WS, Lin MS, et al. **Predictors for successful endovascular intervention in chronic carotid artery total occlusion.** *JACC Cardiovasc Interv* 2016;9:1825–32 CrossRef Medline
19. Malik AM, Vora NA, Lin R, et al. **Endovascular treatment of tandem extracranial/intracranial anterior circulation occlusions: preliminary single-center experience.** *Stroke* 2011;42:1653–57 CrossRef Medline
20. Bouthillier A, van Loveren HR, Keller JT. **Segments of the internal carotid artery: a new classification.** *Neurosurgery* 1996;38:425–32; discussion 432–33 CrossRef Medline
21. Bachmann R, Nassenstein I, Kooijman H, et al. **High-resolution magnetic resonance imaging (MRI) at 3.0 Tesla in the short-term follow-up of patients with proven cervical artery dissection.** *Invest Radiol* 2007;42:460–66 CrossRef Medline
22. Chen YH, Kao HL. **Predicting procedure successful rate and 1-year patency after endovascular recanalization for chronic carotid artery occlusion by CT angiography.** *Int J Cardiol* 2017;229:59 CrossRef Medline
23. Marnat G, Mourand I, Eker O, et al. **Endovascular management of tandem occlusion stroke related to internal carotid artery dissection using a distal to proximal approach: insight from the RECOST study.** *AJNR Am J Neuroradiol* 2016;37:1281–88 CrossRef Medline
24. Chen CJ, Lee TH, Hsu HL, et al. **Multi-slice CT angiography in diagnosing total versus near occlusions of the internal carotid**

artery: comparison with catheter angiography. *Stroke* 2004;35:83–85 CrossRef Medline

25. Kundel HL, Polansky M. **Measurement of observer agreement.** *Radiology* 2003;228:303–08 CrossRef Medline
26. Duijsens HM, Spaander F, van Dijk LC, et al. **Endovascular treatment in patients with acute ischemic stroke and apparent occlusion of the extracranial internal carotid artery on CTA.** *J Neurointerv Surg* 2015;7:709–14 CrossRef Medline
27. Kim JJ, Dillon WP, Glastonbury CM, et al. **Sixty-four-section multidetector CT angiography of carotid arteries: a systematic analysis of image quality and artifacts.** *AJNR Am J Neuroradiol* 2010;31:91–99 CrossRef Medline
28. Marquering HA, Nederkoorn PJ, Beenen LF, et al. **Carotid pseudo-occlusion on CTA in patients with acute ischemic stroke: a concerning observation.** *Clin Neurol Neurosurg* 2013;115:1591–94 CrossRef Medline
29. Huston J, Lewis BD, Wiebers DO, et al. **Carotid artery: prospective blinded comparison of two-dimensional time-of-flight MR angiography with conventional angiography and duplex US.** *Radiology* 1993;186:339–44 CrossRef Medline
30. Atlas SW. **MR angiography in neurologic disease.** *Radiology* 1994;193:1–16 CrossRef Medline
31. Ng FC, Choi PM, Datta M, et al. **Perfusion-derived dynamic 4D CT angiography identifies carotid pseudo-occlusion in hyperacute stroke.** *J Neuroimaging* 2016;26:588–91 CrossRef Medline
32. Bachmann R, Nassenstein I, Kooijman H, et al. **Spontaneous acute dissection of the internal carotid artery: high-resolution magnetic resonance imaging at 3.0 Tesla with a dedicated surface coil.** *Invest Radiol* 2006;41:105–11 CrossRef Medline
33. Coppenrath E, Lenz O, Sommer N, et al. **Clinical significance of intraluminal contrast enhancement in patients with spontaneous cervical artery dissection: a black-blood MRI study.** *Rofo* 2017;189:624–31 CrossRef Medline
34. Fujimoto S, Toyoda K, Kishikawa K, et al. **Accuracy of conventional plus transoral carotid ultrasonography in distinguishing pseudo-occlusion from total occlusion of the internal carotid artery.** *Cerebrovasc Dis* 2006;22:170–76 CrossRef Medline
35. Kappelhof M, Marquering HA, Berkhemer OA, et al; MR CLEAN Investigators. **Accuracy of CT angiography for differentiating pseudo-occlusion from true occlusion or high-grade stenosis of the extracranial ICA in acute ischemic stroke: a retrospective MR CLEAN substudy.** *AJNR Am J Neuroradiol* 2018;39:892–98 CrossRef Medline
36. Park SE, Choi DS, Baek HJ, et al. **Endovascular therapy of acute ischemic stroke related to tandem occlusion: comparison of occlusion and severe stenosis of the proximal cervical internal carotid artery.** *Br J Radiol* 2018 Dec 3:20180051. [Epub ahead of print] CrossRef Medline
37. Shchanitsyn IN, Maksyushina TD, Titova YI, et al. **Spontaneous recanalization of chronic occlusion of the internal carotid artery** [in English, Russian]. *Angiol Sosud Khir* 2015;21:124–35 Medline
38. Nozaki T, Hiramatsu H, Yamashita S, et al. **Spontaneous multiple-channel recanalization of internal carotid artery occlusion with unusual radiological features.** *Clin Neuroradiol* 2014;24:73–75 CrossRef Medline

Radiomics Study of Thyroid Ultrasound for Predicting *BRAF* Mutation in Papillary Thyroid Carcinoma: Preliminary Results

M.-r. Kwon, J.H. Shin, H. Park, H. Cho, S.Y. Hahn, and K.W. Park

ABSTRACT

BACKGROUND AND PURPOSE: It is not known how radiomics using ultrasound images contribute to the detection of BRAF mutation. This study aimed to evaluate whether a radiomics study of gray-scale ultrasound can predict the presence or absence of *B-Raf proto-oncogene, serine/threonine kinase* (*BRAF*) mutation in papillary thyroid cancer.

MATERIALS AND METHODS: The study retrospectively included 96 thyroid nodules that were surgically confirmed papillary thyroid cancers between January 2012 and June 2013. *BRAF* mutation was positive in 48 nodules and negative in 48 nodules. For analysis, ROIs from the nodules were demarcated manually on both longitudinal and transverse sonographic images. We extracted a total of 86 radiomics features derived from histogram parameters, gray-level co-occurrence matrix, intensity size zone matrix, and shape features. These features were used to build 3 different classifier models, including logistic regression, support vector machine, and random forest using 5-fold cross-validation. The performance including accuracy, sensitivity, specificity, positive predictive value, negative predictive value, and area under the receiver operating characteristic curve, of the different models was evaluated.

RESULTS: The incidence of high-suspicion nodules diagnosed on ultrasound was higher in the *BRAF* mutation–positive group than in the mutation–negative group ($P = .004$). The radiomics approach demonstrated that all classification models showed moderate performance for predicting the presence of *BRAF* mutation in papillary thyroid cancers with an area under the curve value of 0.651, accuracy of 64.3%, sensitivity of 66.8%, and specificity of 61.8%, on average, for the 3 models.

CONCLUSIONS: Radiomics study using thyroid sonography is limited in predicting the *BRAF* mutation status of papillary thyroid carcinoma. Further studies will be needed to validate our results using various diagnostic methods.

ABBREVIATIONS: AUC = area under the receiver operating characteristic curve; GLCM = gray-level co-occurrence matrix; ISZM = intensity size zone matrix; K-TIRADS = Korean Thyroid Imaging Reporting and Data System; mRMR = minimum redundancy maximum relevance; PTC = papillary thyroid carcinoma; US = ultrasound

Papillary thyroid carcinoma (PTC) is the most common type of thyroid malignancy and accounts for the rapidly increasing incidence of thyroid cancer worldwide.[1,2] The *B-Raf proto-oncogene, serine/threonine kinase* (*BRAF*) mutation plays a central role in the pathogenesis of PTC, promoting carcinogenesis through the action of the mitogen-activated protein kinase pathway.[3,4] The frequency of the *BRAF* mutation in PTC has been reported to range from 29% to 83% and is known to be the most common genetic alteration in PTC.[5,6] Many studies have reported that the *BRAF* mutation is associated with poor clinicopathologic outcomes, such as a high incidence of advanced clinical stage, extrathyroidal extension, and increased recurrence.[6-9] These results suggest that preoperative knowledge of the *BRAF* mutation status can be helpful in categorizing patients as

Received August 9, 2019; accepted after revision December 17.

From the Department of Radiology (M.-r.K., J.H.S., S.Y.H., K.W.P.), Samsung Medical Center, Sungkyunkwan University School of Medicine, Seoul, Republic of Korea; Department of Radiology (M.-r.K.), Kangbuk Samsung Hospital, Sungkyunkwan University School of Medicine, Seoul, Republic of Korea; Center for Neuroscience Imaging Research/School of Electronic and Electrical Engineering (H.P.), Sungkyunkwan University, Suwon, Korea; and Center for Neuroscience Imaging Research/Department of Electronic and Computer Engineering (H.C.), Sungkyunkwan University, Suwon, Korea.

Jung Hee Shin and Hyunjin Park contributed equally to this study.

This work was supported by the Institute for Basic Science (grant No. IBS-R015-D1), the National Research Foundation of Korea (grant No. NRF-2019R1H1A2079721), the Ministry of Science and ICT of Korea under the Information Technology Research Center support program (grant No. IITP-2019-2018-0-01798) supervised by the Institute for Information and Communication Technology Promotion, and the Institute for Information and Communication Technology Promotion grant funded by the Korean government under the AI Graduate School Support Program (grant No. 2019-0-00421).

Please address correspondence to Hyunjin Park, PhD, Center for Neuroscience Imaging Research/School of Electronic and Electrical Engineering, Sungkyunkwan University, Suwon, 16419, Korea; e-mail: hyunjinp@skku.edu

Indicates open access to non-subscribers at www.ajnr.org
Indicates article with supplemental on-line tables.
Indicates article with supplemental on-line photo.
http://dx.doi.org/10.3174/ajnr.A6505

high risk and planning an appropriate treatment strategy. According to 2015 American Thyroid Association guidelines, active surveillance of PTC has emerged as a safe alternative to surgical intervention in low-risk patient with PTCs.[10] In this era, preoperative knowledge of the *BRAF* mutation status can be one of preoperative modulators for planning an appropriate treatment strategy, such as the determination of an early surgical intervention.

Several studies have investigated whether gray-scale ultrasound (US) findings could predict the presence of the *BRAF* mutation in PTC and have reported controversial results. Kabaker et al[11] reported that most of the suspicious US findings, including a taller-than-wide shape, ill-defined margin, hypoechogenicity, calcifications, and absent halo were associated with *BRAF* mutation positivity, and Hahn et al[12] reported that hypoechogenicity and nonparallel orientation were associated with *BRAF* mutation positivity. Conversely, other studies have found no close correlation between suspicious US features and the *BRAF* mutation.[9,13,14]

With these various results, visual interpretation of US images has limitations, including a high dependency on the radiologist's experience and interobserver variation. In addition, substantial objective information from the image may not be evaluated through visual interpretation. Radiomics, which automatically extracts innumerable high-dimensional features from images, has recently emerged and shows promising results for decision support.[15] Previous studies have reported that histograms and texture analyses of US are useful for differentiating benign and malignant thyroid nodules.[16-21] To our knowledge, there have been no published studies aimed at identifying the presence of *BRAF* mutation using radiomics features of US.

Therefore, the purpose of this study was to evaluate whether radiomics study of gray-scale US could predict the presence or absence of *BRAF* mutation in PTC.

MATERIALS AND METHODS

Patient Selection

The institutional review board of our institution (Samsung Medical Center) approved this retrospective study. We retrospectively reviewed our institutional data base to identify patients with surgically confirmed PTC who underwent preoperative thyroid US and successful DNA sequencing for *BRAF* mutations between January 2012 and June 2013. The exclusion criteria were as follows: 1) nodule diameter of <10 mm in small nodules because the ROI method has lower accuracy and current guidelines do not recommend fine-needle aspiration for nodules with a diameter of <10 mm;[22,23] 2) lack of precise correlation between pathology, the *BRAF* mutation study, and US findings in patients with multiple nodules; and 3) both transverse and longitudinal US images not being available. Finally, this study included a total of 96 PTCs from 96 patients (mean age, 44.9 $\pm$ 13.2 years; range, 19–77 years). The final surgical diagnoses and *BRAF* mutation results of the thyroid nodules were analyzed.

US Examinations and Image Evaluation

All patients underwent preoperative thyroid US using an iU22 Vision 2010 machine (Philips Healthcare, Seattle, Washington) with a commercially available 7- to 12-MHz linear-array transducer. All scans were performed by 1 of 7 radiologists with between 2 and 15 years of experience in thyroid US. Longitudinal and transverse images were obtained for each nodule.

One radiologist (M.-r.K.) retrospectively reviewed preoperative US and assessed image features, and another radiologist (J.H.S.) with 15 years of experience in thyroid US supervised this step. According to the Korean Thyroid Imaging Reporting and Data System (K-TIRADS),[22] all thyroid nodules were evaluated for internal content, echogenicity, shape, orientation, margin, and calcifications. The final category assessment was divided into 5 categories according to the K-TIRADS as follows: category 1, no nodule; category 2, benign nodule; category 3, low-suspicion nodule; category 4, intermediate-suspicion nodule; and category 5, high-suspicion nodule.

Radiomics Feature Analysis

The most representative transverse and longitudinal images of each tumor were selected for radiomics feature extraction. An ROI in the thyroid tumor was delineated manually along the border of each tumor on representative US images using MRIcron software (http://www.mricro.com/mricron) by 2 radiologists (M.-r.K. and J.H.S.). The intraclass correlation coefficient was computed to assess the reproducibility of features using 2 sets of ROIs. The first set of ROIs was used for the radiomics analysis.

A total of 86 radiomics features were extracted using open-source radiomics software, Py-Radiomics (https://www.radiomics.io/pyradiomics.html).[24] Forty-three features were computed for each technique (transverse and longitudinal images). Features computed from both orientations were considered. The features were grouped into shape (6 features), histogram-based (19 features), intensity size zone matrix (ISZM, 2 features), and gray-level co-occurrence matrix (GLCM, 16 features). The histogram-based features were computed from 64-bin histograms calculated over the intratumoral intensity range. The GLCM features assess textural information and reflect intratumoral heterogeneity using a 2D histogram with 64 bins. A total of 8 matrices corresponding to eight 2D directions with an offset of 1 were computed and then averaged to yield a single matrix. The averaged matrix was used to compute the GLCM features. The ISZM features were also related to texture using blobs of similar intensity and differing sizes. We constructed a 32×256 matrix in which the first dimension was binned intensity and the second dimension was the size of the blobs. Further details regarding the features are given in On-line Tables 1–3.

Due to the lack of external validation data, we applied 5-fold cross-validation to separate our data into training and test sets to reduce overfitting. Models were built using the training set only and tested on a left-out test set. Each model was trained using 80% of the data ($n = 77$) and later tested on the remaining 20% of the data ($n = 18$). Feature selection was performed using minimum redundancy maximum relevance (mRMR) from the training set.[25] The number of

chosen features of mRMR was set using a grid search between 3 and 11. Within the cross-validation, the optimal number of features was chosen on the basis of the maximum performance in the test set on average for the 3 classifiers (On-line Figure). The selected features were used as input to train 3 different classifier models, including logistic regression, support vector machine using the linear kernel, and random forest with 50 trees. As for tuning the hyperparameters of the support vector machine, we tried different kernels, including linear, quadratic, and radial basis functions for the support vector machine, and linear kernel worked the best. The random forest classifier has feature-selection capabilities. However, the other 2 models, logistic regression and support vector machine, do not have such capabilities. We adopted an external feature-selection procedure (ie, mRMR) so that all 3 models were subjected to the same feature-selection procedure. The trained classifiers were further tested on a left-out test fold. Because we adopted 5-fold cross-validation, we repeated the procedures of feature selection, model training, and testing steps 5 times, each time leaving out a different test fold. The performance of the classifier models was assessed on the basis of accuracy, sensitivity, specificity, positive predictive value, negative predictive value, and area under the receiver operating characteristic curve (AUC).

Statistical Analysis

To compare *BRAF* mutation–positive and –negative PTCs, we analyzed categoric variables using a χ^2 or Fisher exact test, while continuous variables were analyzed using a Student *t* test. A *P* value $<$ .05 was considered statistically significant.

Table 1: Clinical and tumor characteristics of study population

	BRAF (+) PTC (*n* = 48)	*BRAF* (−) PTC (*n* = 48)	*P* Value
Age (mean) (yr)	46.9 ± 13.8	42.8 ± 12.4	.13
Sex			.27
M	11 (22.9)	7 (14.6)	
F	37 (77.1)	41 (85.4)	
Tumor size (mean) (cm)	1.59 ± 0.57	1.87 ± 1.05	.12
Central lymph node metastasis			.15
No	16 (33.3)	24 (50.0)	
Yes	32 (66.7)	24 (50.0)	
Lateral lymph node metastasis			>.99
No	38 (79.2)	38 (79.2)	
Yes	10 (20.8)	10 (20.8)	

Table 2: Relationship between *BRAF* mutation and US imaging characteristics by visual assessment of papillary thyroid carcinomas

	BRAF (+) PTC (*n* = 48)	*BRAF* (−) PTC (*n* = 48)	*P* Value
Internal content			.16
Solid	46 (95.8)	41 (85.4)	
Predominantly solid	2 (4.2)	7 (14.6)	
Echogenicity			.012
Markedly hypoechoic	20 (41.7)	8 (16.7)	
Hypoechoic	23 (47.9)	26 (54.2)	
Isoechoic	5 (10.4)	13 (27.1)	
Hyperechoic	0 (0.0)	1 (2.1)	
Shape			.08
Irregular	12 (25.0)	20 (41.7)	
Round to oval	36 (75.0)	28 (58.3)	
Orientation			.007
Nonparallel	26 (54.2)	13 (27.1)	
Parallel	22 (45.8)	35 (72.9)	
Margin			.66
Spiculated/microlobulated	35 (72.9)	31 (64.6)	
Ill-defined	4 (8.3)	6 (12.5)	
Smooth	9 (18.8)	11 (22.9)	
Calcification			.33
No	18 (37.5)	16 (33.3)	
Microcalcification	19 (39.6)	22 (45.8)	
Macrocalcification	6 (12.5)	9 (18.8)	
Rim calcification	5 (10.4)	1 (2.1)	
Final K-TIRADS category			.004
3 (Low suspicion)	1 (2.1)	3 (6.3)	
4 (Intermediate suspicion)	9 (18.8)	22 (45.8)	
5 (High suspicion)	38 (79.2)	23 (47.9)	

RESULTS

The clinical, pathologic, and imaging findings of 96 patients are shown in Tables 1 and 2. Among the total of 96 patients, 78 were women (mean age, 45.1 ± 13.9 years; range, 19–77 years) and 18 were men (mean age, 43.9 ± 10.2 years; range, 21–62 years).

The 96 nodules consisted of 48 *BRAF* mutation–positive PTCs and 48 *BRAF* mutation–negative PTCs. Clinical characteristics, including patient age and sex, were not significantly different. The mean tumor size was 1.73 ± 0.85 cm (range, 1–6 cm). The mean tumor size was not significantly different between the 2 groups (BRAF mutation–positive group: 1.59 ± 0.57 cm; *BRAF* mutation–negative group: 1.87 ± 1.05 cm, $P = .12$). Central and lateral lymph node metastases were not significantly different ($P = .15$ and $P = 1.00$, respectively). Among US characteristics, echogenicity was significantly different between the 2 groups ($P = .012$). *BRAF* mutation positive groups significantly showed nonparallel orientation ($P = .007$) (Table 2). The incidence of K-TIRADS category 5 (high suspicion) was higher than that of K-TIRADS 3 (low suspicion) or 4 (intermediate suspicion) in the *BRAF* mutation–positive group ($P = .004$). The intraclass correlation coefficient of 86 features was a mean of 0.89 ± of 0.09 as shown in On-line Table 4.

We adopted 5-fold cross-validation; thus, the selected features varied from fold to fold. There were 2 features that were selected >3 times: the mean

(histogram) of the longitudinal image and informational measure of correlation (GLCM) of the longitudinal image. We reported the mean values of the performance metric along with confidence intervals over the 5 folds in On-line Table 5. The averages for the 3 classifier models were as follows: accuracy, 64.3% (range, 63.68%–64.68%); sensitivity, 66.8% (range, 64.67%–70.89%); and specificity, 61.8% (range, 58.22%–64.67%). The receiver operating characteristic of the 3 models yielded a relatively low AUC of 0.65 on average (range, 0.6446–0.6562) (Figure).

We also performed a different feature-selection approach (ie, Pearson correlation–based feature selection) to see if it led to better performance. We computed the correlation between all possible pairs of features, and if the correlation exceeded 0.5, we kept the feature that had a higher correlation with the mutation status for a given pair of features. After feature selection, 3 models were trained and tested. The results of 3 classifiers using a simple Pearson correlation–based feature selection are given in On-line Table 6. Results showed that training performance was better than those using the mRMR feature selection, but test performance was worse, which implied that models were overfitting. The averages for the 3 classifier models were as follows: accuracy, 58.6% (range, 56.16%–60.42%); sensitivity, 63.9% (range, 60.44%–66.89%); and specificity, 53.8% (range, 52.22%–56.67%). The receiver operating characteristic of the 3 models yielded a relatively low AUC of 0.61 on average. The test performance in terms of AUC showed the lower bound of the confidence interval as 0.52, slightly above the chance level (ie, 0.50).

DISCUSSION

Since the introduction of radiomics, many previous studies have tried to investigate the relationship between image characteristics and genetic mutations in various malignancies, including lung, colon, brain, and breast cancers.[26-29] They proposed a CT- or MR imaging–based radiomics model to detect gene mutation status as a noninvasive method. These models were useful to predict the presence of gene mutations in malignancies.

To our knowledge, this is the first study to apply radiomics in the estimation of *BRAF* mutation in patients with PTC. We evaluated the ability of radiomics, using various machine learning approaches, to help predict the presence of the *BRAF* mutation in patients with PTC. In our study, *BRAF*-mutated PTCs tended to show nonparallel orientation and marked hypoechogenicity, similar to findings in some previous studies.[12,13] Although visual assessment of thyroid nodules suggested that high-suspicion findings on US were significantly more frequent in *BRAF*-mutated PTCs, radiomics demonstrated that all classification models failed to show excellent performance for predicting the presence of *BRAF* mutation in PTCs.

Radiomics is usually performed using tomographic images, including CT, MR imaging, or PET images because these modalities can acquire 3D volume data and data acquisition can be standardized by setting scan parameters of the machines so that they are identical.[15] US has several limitations in quantitative analysis in contrast to tomographic images: Only 2D data can be acquired through this technique along with lack of representative features due to a limited amount of image data, operator dependency, and dependency on US machines.[30] These factors may have

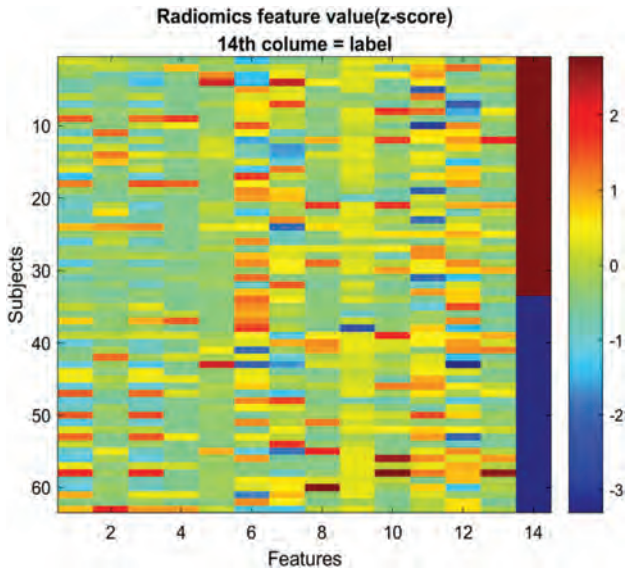

FIGURE. Heatmap showing the correlation of radiomics features with *BRAF* mutation prediction after feature selection using mRMR. Red indicates higher correlation relative to blue.

affected our results. However, US is the most widely used standard imaging tool in thyroid pathology and is very helpful in discriminating between malignant and benign thyroid nodules. Until now, a number of studies have been published that have reported that quantitative features extracted from US images have favorable results.[16-21] Further studies with a larger amount of data will be necessary.

In our study, 3 different classifiers were applied to demonstrate the effectiveness of the chosen features. A simple model, such as logistic regression, has few parameters and is interpretable; conversely, complex models, such as support vector machine and random forest, are difficult to interpret and have many parameters. No superiority among the classifiers was noted in this study, and the difference among the AUCs of the 3 classifiers was very small; this finding indicates that choosing any classifier did not affect the overall performance. One possible reason for this result could be that the selected features were not very effective; thus, the results remained comparable regardless of the simple or complex classifier model.

In many studies using machine learning, the performance of the unseen test set tends to be lower than that of the training set because data overfitting might occur in the training set. In particular, using too many trees in the random forest classifier might inflate the performance measures in the training set.[31] We conducted a Pearson correlation, one of the other ways to perform feature selection. Results showed that training performance increased, but test performance decreased; these findings imply that the selected features overfitted the training data.

Two features, mean (histogram-based feature) and informational measures of correlation (texture feature) of the longitudinal image, were selected >3 times. Thus, they were important features to explain the *BRAF* mutation. There was a relatively small overlap between the 2 features when we computed a Pearson correlation ($r = 0.15$ with $P = .14$). The mean value reflects echogenicity of the ROI, which is compatible with our visual assessment

of US images.[16] The informational measure of correlation is related to the heterogeneity of the ROI and thus could have a potential correlation with pathology. *BRAF* genetic alterations coexist in thyroid tumors in which some cells provide a basis for mutation and others do not have mutations, forming intratumor heterogeneity. Intratumor heterogeneity may foster tumor evolution and adaptation.[32,33]

Our study had several limitations. First, this was a retrospective study from a single institution, which introduces the possibility of selection bias. Additionally, the small datasets in our study made it difficult to achieve reliable results. With added samples, applying deep learning approaches combined with electronic medical records might be possible; this process might improve the overall performance. Second, although preoperative US was performed with the same US machine set with similar parameters to avoid equipment-based variability, this feature and patient-related factors may still have influenced the pixel intensity of US images.[30] Third, we focused on predicting the *BRAF* status of patients with papillary thyroid cancer. Our main goal was not to contrast healthy controls and patients with papillary thyroid cancer. Still, including healthy controls would lead to less positive bias. Last, the lack of external validation data is also a limitation of this study. Our results from this study need to be further validated in a larger dataset to better assess their potential clinical use.

CONCLUSIONS

Our preliminary study shows that radiomics study of thyroid US was limited in predicting *BRAF* mutation in PTC.

Disclosures: Hyunjin Park—*RELATED*: *Grant*: Institute for Basic Science, National Research Foundation of Korea, Ministry of Science and information and communication technology, Institute for Information and Communication Technology Promotion.* *Money paid to the institution.

REFERENCES

1. Davies L, Welch HG. **Increasing incidence of thyroid cancer in the United States, 1973–2002.** *JAMA* 2006;295:2164–67 CrossRef Medline
2. Leenhardt L, Grosclaude P, Cherie-Challine L; Thyroid Cancer Committee. **Increased incidence of thyroid carcinoma in France: a true epidemic or thyroid nodule management effects? Report from the French Thyroid Cancer Committee.** *Thyroid* 2004;14:1056–60 CrossRef Medline
3. Xing M. **BRAF mutation in thyroid cancer.** *Endocr Relat Cancer* 2005;12:245–62 CrossRef Medline
4. Melck AL, Yip L, Carty SE. **The utility of BRAF testing in the management of papillary thyroid cancer.** *Oncologist* 2010;15:1285–93 CrossRef Medline
5. Kim KH, Kang DW, Kim SH, et al. **Mutations of the BRAF gene in papillary thyroid carcinoma in a Korean population.** *Yonsei Med J* 2004;45:818–21 CrossRef Medline
6. Lee JH, Lee ES, Kim YS. **Clinicopathologic significance of BRAF V600E mutation in papillary carcinomas of the thyroid: a meta-analysis.** *Cancer* 2007;110:38–46 CrossRef Medline
7. Xing M, Westra WH, Tufano RP, et al. **BRAF mutation predicts a poorer clinical prognosis for papillary thyroid cancer.** *J Clin Endocrinol Metab* 2005;90:6373–79 CrossRef Medline
8. Nikiforova MN, Kimura ET, Gandhi M, et al. **BRAF mutations in thyroid tumors are restricted to papillary carcinomas and anaplastic or poorly differentiated carcinomas arising from papillary carcinomas.** *J Clin Endocrinol Metab* 2003;88:5399–404 CrossRef Medline
9. Kwak JY, Kim EK, Chung WY, et al. **Association of BRAFV600E mutation with poor clinical prognostic factors and US features in Korean patients with papillary thyroid microcarcinoma.** *Radiology* 2009;253:854–60 CrossRef Medline
10. Haugen BR, Alexander EK, Bible KC, et al**. 2015 American Thyroid Association Management Guidelines for Adult Patients with Thyroid Nodules and Differentiated Thyroid Cancer: The American Thyroid Association Guidelines Task Force on Thyroid Nodules and Differentiated Thyroid Cancer.** *Thyroid* 2016;26:1–133 CrossRef Medline
11. Kabaker AS, Tublin ME, Nikiforov YE, et al. **Suspicious ultrasound characteristics predict BRAF V600E-positive papillary thyroid carcinoma.** *Thyroid* 2012;22:585–89 CrossRef Medline
12. Hahn SY, Kim TH, Ki CS, et al. **Ultrasound and clinicopathological features of papillary thyroid carcinomas with BRAF and TERT promoter mutations.** *Oncotarget* 2017;8:108946–57 CrossRef Medline
13. Hwang J, Shin JH, Han BK, et al. **Papillary thyroid carcinoma with BRAFV600E mutation: sonographic prediction.** *AJR Am J Roentgenol* 2010;194:W425–30 CrossRef Medline
14. Li Q, Yuan J, Wang Y, et al. **Association between the BRAF V600E mutation and ultrasound features of the thyroid in thyroid papillary carcinoma.** *Oncol Lett* 2017;14:1439–44 CrossRef Medline
15. Gillies RJ, Kinahan PE, Hricak H. **Radiomics: images are more than pictures, they are data.** *Radiology* 2016;278:563–77 CrossRef Medline
16. Kwon MR, Shin JH, Hahn SY, et al. **Histogram analysis of greyscale sonograms to differentiate between the subtypes of follicular variant of papillary thyroid cancer.** *Clin Radiol* 2018;73:591e1–e7 Medline Medline
17. Song G, Xue F, Zhang C. **A model using texture features to differentiate the nature of thyroid nodules on sonography.** *J Ultrasound Med* 2015;34:1753–60 CrossRef Medline
18. Chen SJ, Chang CY, Chang KY, et al. **Classification of the thyroid nodules based on characteristic sonographic textural feature and correlated histopathology using hierarchical support vector machines.** *Ultrasound Med Biol* 2010;36:2018–26 CrossRef Medline
19. Nam SJ, Yoo J, Lee HS, et al. **Quantitative evaluation for differentiating malignant and benign thyroid nodules using histogram analysis of grayscale sonograms.** *J Ultrasound Med* 2016;35:775–82 CrossRef Medline
20. Grani G, D'Alessandri M, Carbotta G, et al. **Grey-scale analysis improves the ultrasonographic evaluation of thyroid nodules.** *Medicine (Baltimore)* 2015;94:e1129 CrossRef Medline
21. Bhatia KS, Lam AC, Pang SW, et al. **Feasibility study of texture analysis using ultrasound shear wave elastography to predict malignancy in thyroid nodules.** *Ultrasound Med Biol* 2016;42:1671–80 CrossRef Medline
22. Shin JH, Baek JH, Chung J, et al; Korean Society of Thyroid Radiology (KSThR) and Korean Society of Radiology. **Ultrasonography diagnosis and imaging-based management of thyroid nodules: revised Korean Society of Thyroid Radiology consensus statement and recommendations.** *Korean J Radiol* 2016;17:370–95 CrossRef Medline
23. Tessler FN, Middleton WD, Grant EG, et al. **ACR Thyroid Imaging, Reporting and Data System (TI-RADS): White Paper of the ACR TI-RADS Committee.** *J Am Coll Radiol* 2017;14:587–95 CrossRef Medline
24. van Griethuysen JJ, Fedorov A, Parmar C, et al. **Computational radiomics system to decode the radiographic phenotype.** *Cancer Res* 2017;77:e104-07 CrossRef Medline
25. Peng H, Long F, Ding C. **Feature selection based on mutual information: criteria of max-dependency, max-relevance, and min-redundancy.** *IEEE Trans Pattern Anal Mach Intell* 2005;27:1226–23 CrossRef Medline
26. Yang L, Dong D, Fang M, et al. **Can CT-based radiomics signature predict KRAS/NRAS/BRAF mutations in colorectal cancer?** *Eur Radio* 2018;28:2058–67 CrossRef Medline
27. Liu Y, Kim J, Balagurunathan Y, et al. **Radiomic features are associated with EGFR mutation status in lung adenocarcinomas.** *Clin Lung Cancer* 2016;17:441–48e6 CrossRef Medline

28. Li H, Zhu Y, Burnside ES, et al. **MR imaging radiomics signatures for predicting the risk of breast cancer recurrence as given by research versions of MammaPrint, Oncotype DX, and PAM50 gene assays.** *Radiology* 2016;281:382–91 CrossRef Medline
29. Chen X, Tong Y, Shi Z, et al. **Noninvasive molecular diagnosis of craniopharyngioma with MRI-based radiomics approach.** *BMC Neurol* 2019;19:6 CrossRef Medline
30. Lee SE, Han K, Kwak JY, et al. **Radiomics of US texture features in differential diagnosis between triple-negative breast cancer and fibroadenoma.** *Sci Rep* 2018;8:13546 CrossRef Medline
31. Breiman L. **Random forests.** *Machine Learning* 2001;45:5–32 CrossRef
32. Guerra A, Sapio MR, Marotta V, et al. **The primary occurrence of BRAF(V600E) is a rare clonal event in papillary thyroid carcinoma.** *J Clin Endocrinol Metab* 2012;97:517–24 CrossRef Medline
33. Guerra A, Fugazzola L, Marotta V, et al. **A high percentage of BRAFV600E alleles in papillary thyroid carcinoma predicts a poorer outcome.** *J Clin Endocrinol Metab* 2012;97:2333–40 CrossRef Medline

Comparison of Enhancement of the Vestibular Perilymph between Variable and Constant Flip Angle–Delayed 3D-FLAIR Sequences in Menière Disease

S. Nahmani, A. Vaussy, C. Hautefort, J.-P. Guichard, A. Guillonet, E. Houdart, A. Attyé, and M. Eliezer

ABSTRACT

BACKGROUND AND PURPOSE: Endolymphatic hydrops in patients with Menière disease relies on delayed postcontrast 3D-FLAIR sequences. The purpose of this study was to compare the degree of perilymphatic enhancement and the detection rate of endolymphatic hydrops using constant and variable flip angles sequences.

MATERIALS AND METHODS: This was a retrospective study performed in 16 patients with Menière disease who underwent 3T MR imaging 4 hours after gadolinium injection using two 3D-FLAIR sequences with a constant flip angle at 140° for the first and a heavily-T2 variable flip angle for the second. The signal intensity ratio was measured using the ROI method. We graded endolymphatic hydrops and evaluated the cochlear blood-labyrinth barrier impairment.

RESULTS: Both for symptomatic and asymptomatic ears, the median signal intensity ratio was significantly higher with the constant flip angle than with the heavily-T2 variable flip angle (7.16 versus 1.54 and 7.00 versus 1.45, $P < .001$). Cochlear blood-labyrinth barrier impairment was observed in 4/18 symptomatic ears with the heavily-T2 variable flip angle versus 8/19 with constant flip angle sequences. With heavily-T2 variable flip angle sequences, endolymphatic hydrops was observed in 7–10/19 symptomatic ears versus 12/19 ears with constant flip angle sequences. We found a significant association between the clinical symptomatology and the presence of endolymphatic hydrops with constant flip angle but not with heavily-T2 variable flip angle sequences. Interreader agreement was always perfect with constant flip angle sequences while it was fair-to-moderate with heavily-T2 variable flip angle sequences.

CONCLUSIONS: 3D-FLAIR constant flip angle sequences provide a higher signal intensity ratio and are superior to heavily-T2 variable flip angle sequences in reliably evaluating the cochlear blood-labyrinth barrier impairment and the endolymphatic space.

ABBREVIATIONS: BLB = blood-labyrinth barrier; CFA = constant flip angle; EH = endolymphatic hydrops; hVFA = heavily-T2 variable flip angle; MD = Menière disease; SIR = signal intensity ratio; VFA = variable flip angle

Menière Disease (MD), consisting of recurrent spells of spontaneous vertigo and fluctuating aural symptoms, is associated with endolymphatic hydrops (EH), which is an accumulation of excessive endolymph fluid in the inner ear, but also with blood-labyrinth barrier (BLB) impairment.[1-3]

During the past decade, to define EH on MR imaging, most studies have used the semiquantitative grading system introduced by the nakashima et al., while some authors have suggested that this grading system was not specific.[2] On the basis of these findings, an anatomic grading system based on the saccular morphology in combination with cochlear BLB impairment has been introduced.[4,5]

There are 2 reported methods for contrast media administration: intratympanic and intravenous.[6,7] The main advantage of an intratympanic administration is a higher perilymphatic contrast, allowing the use of 3D-real inversion recovery sequences, which are less sensitive to gadolinium but enable the visualization of endolymph, perilymph, and bone in a single image.[8,9] However, due to its invasiveness, the intratympanic method has been replaced by the intravenous method.[9] It requires a shorter waiting time (4 hours) and allows the evaluation of the permeability of the BLB in both ears. 3D-FLAIR sequences, which are more sensitive to T1-shortening than 3D-real inversion recovery sequences, were adjusted to enable the best evaluation of EH.[10]

Received July 26, 2019; accepted after revision February 12, 2020.

From the Departments of Neuroradiology (S.N., J.-P.G., A.G., E.H., M.E.), and Head and Neck Surgery (C.H.), Lariboisiere University Hospital, Paris, France; Siemens Healthineers (A.V.), Saint-Denis, France; and Department of Neuroradiology and MRI (A.A.), Grenoble Alpes University Hospital, SFR RMN Neurosciences, Grenoble, France.

Please address correspondence to Michael Eliezer, MD, Neuroradiology Unit, Lariboisière University Hospital, 75010 Paris, France; e-mail: michael.eliezer@aphp.fr

Indicates article with supplemental on-line table.

http://dx.doi.org/10.3174/ajnr.A6483

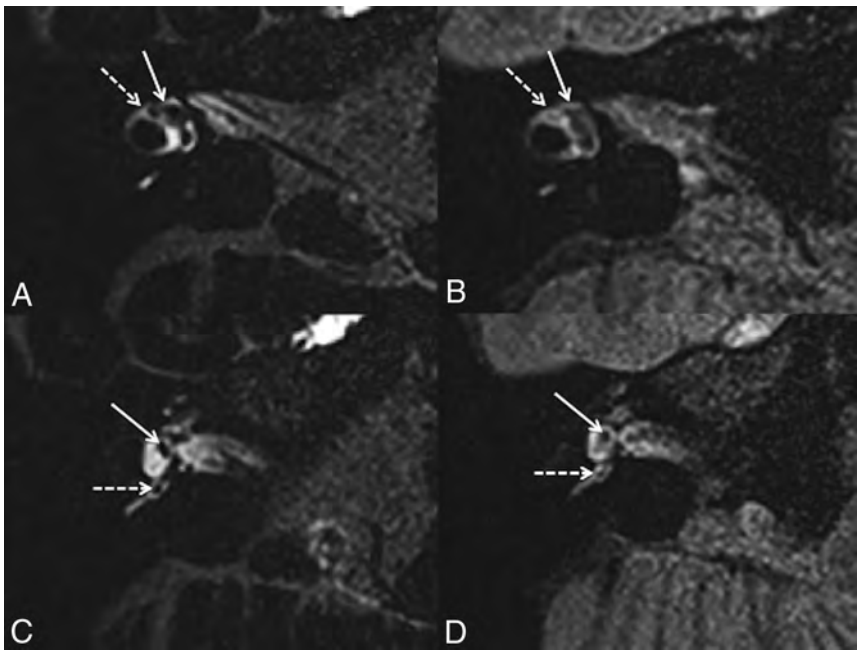

FIG 1. A 42-year-old woman with right possible MD. Axial 3D-FLAIR CFA at the level of the lateral semicircular canal (*A*) shows a normal utricle (*white arrow*) and lateral ampulla (*right dotted arrow*). *C*, Axial 3D-FLAIR CFA through the inferior part of the vestibule shows a normal saccule (*white arrow*) and posterior ampulla (*white dotted arrow*). Axial 3D-FLAIR heavily-T2 VFA at the level of the lateral semicircular canal (*B*) shows a normal utricle (*white arrow*), while the lateral ampulla (*right dotted arrow*) is barely visible. *D*, Axial 3D-FLAIR heavily-T2 VFA through the inferior part of the vestibule shows a normal saccule (*white arrow*) and posterior ampulla (*white dotted arrow*).

In the same way, a postprocessing technique implying a fusion of gray-scale inverted positive endolymph with native positive perilymph images has been developed to overcome the lower contrast obtained after intravenous injection.[11] Other authors reported that 3D-FLAIR sequences using a constant flip angle (CFA) instead of a variable flip angle (VFA), without postprocessing, were self-sufficient to provide a good contrast-to-noise ratio.[12-14] However, to this day, VFA sequences remain more widespread than CFA sequences because of their lower specific absorption rate deposition and enable reducing scan times by increasing the echo-train length without blurring.[15]

In a previous study, Naganawa et al[16] stated that the 3D-FLAIR heavily-T2 variable flip angle (hVFA) was superior to CFA sequences in improving the contrast-to-noise ratio and the recognition of the endolymphatic space compartments. Yet, different acquisition parameters between both sequences were used; thus, no proper comparison should be made.

The purpose of this study was to compare the degree of perilymphatic enhancement and the detection rate of EH in patients with MD using CFA and hVFA sequences with equivalent technical parameters.

MATERIALS AND METHODS

Patients

This was a retrospective imaging study approved by our institutional review board (Lariboisiere University Hospital; IRB 2214440) and conducted between December 2018 and March 2019. Patients with a clinical diagnosis of definite, probable, and possible MD based on the 1995 American Academy of Otolaryngology-Head and Neck Surgery recommendations were included.[17] Patients with a history of intratympanic treatment or operations were excluded.

Audiometric Test

The mean pure-tone average hearing levels measured at 500, 1000, 2000, and 4000 Hz in each ear were evaluated. When symptoms were bilateral, we considered both ears as symptomatic.

Imaging

MR imaging examinations were performed on a 3T Magnetom Skyra scanner (Siemens, Erlangen, Germany) with a head/neck 64 coil. All patients underwent MR imaging 4 hours after a single intravenous dose of gadobutrol (Gadovist, 0.1 mmol/kg, 1 mmol/mL; Bayer Schering Pharma, Berlin, Germany), which provided high contrast in the labyrinth.[18] We performed two 3D-FLAIR MR imaging sequences. The first was acquired with a CFA (140°) and the second with a VFA.

We performed the 3D-FLAIR sequences with the following parameters: FOV = 140 × 140 mm, TR = 10,000 ms, TE = 640 ms, TI = 2600 ms, matrix size = 256 × 256 mm, NEX = 2, generalized autocalibrating partially parallel acquisition = 2, section thickness = 0.8 mm, scan time = 7 minutes 50 seconds.

Imaging Analysis

For each patient, MR images were evaluated independently with Carestream Vue (Carestream health) 12.1 by 2 readers (A = S.N. and B = M.E.) with, respectively, 1 and 6 years of experience in inner ear imaging, blinded to the clinical data.

Quantitative Assessment. Quantitative assessment of the BLB permeability was performed with the ROI method, as previously reported.[14] A 5-mm^2 circular ROI was placed in the basal turn of the cochlea and a 50-mm^2 circular ROI was placed at the same level in the medulla. The signal intensity ratio (SIR) was defined as the signal intensity of the basal turn divided by that of the medulla. The mean SIR value was calculated for each ear.

Qualitative Assessment. We verified the presence of the following structures (Fig 1): 1) the saccule, an area of hypointense signal located at the medial and anterior walls of the vestibule at the level of the oval window;[19,20] 2) the utricle, an elliptic area of hypointense signal located in the superior part of the vestibule at the level of the lateral semicircular canal;[19,20] and 3) the ampulla of each semicircular canal, an area of hypointense signal surrounded by perilymphatic fluid.

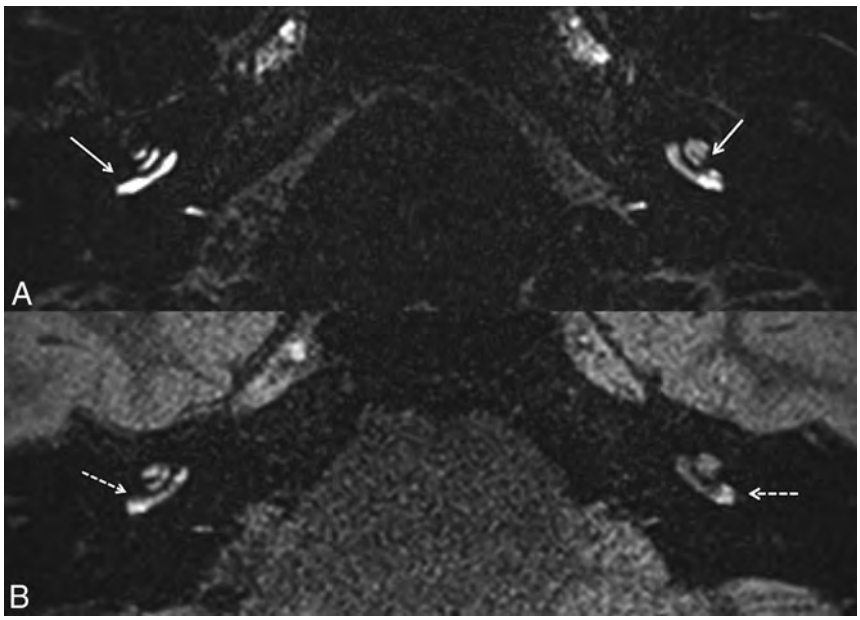

FIG 2. A 63-year-old woman with right definite MD. *A*, Axial CFA at the level of the basal turn of the cochlea shows a marked right cochlear BLB impairment compared with the left side (*white arrow*). *B*, The right cochlear BLB impairment (*white dotted arrow*) is less obvious with hVFA.

We used a modified EH grading system according to Bernaerts et al[5] and defined the presence of EH when the saccule became equal to or larger than the utricle or when there was a confluence of the saccule and utricle.[4] We also assessed the presence of cochlear BLB impairment, defined as a subjective marked perilymphatic enhancement in the basal turn of the cochlea (0, no BLB impairment; 1, BLB impairment) relative to the contralateral cochlea, as previously reported.[5]

A visual assessment based on a binary scale was performed to evaluate the distinction between the utricle and the saccule, and the ampullas from the perilymphatic space (0, no distinction; 1, distinction).

Statistical Analysis

Data were analyzed using R statistical and computing software, Version 3.3.2 (http://www.r-project.org/). Comparison of SIR between CFA and hVFA sequences was assessed with the Wilcoxon signed ranked test. Comparison of the SIR between symptomatic and asymptomatic ears was assessed by the Mann-Whitney test. Comparison for visual assessment between CFA and hVFA sequences was made using the Fisher exact test. Interreader agreement was calculated with the Cohen κ coefficient, to evaluate the reproducibility of the qualitative analysis. Continuous data were expressed as medians (Q1; Q3) and ranges. Categoric data were expressed as frequencies and percentages. Significance was set at $P < .05$.

RESULTS

Population

Sixteen patients with MD (10 women and 6 men, 7 with right-sided MD, 6 with left-sided MD, and 3 with bilateral MD) with a median age of 46 years (Q1: 43 years, Q3: 52 years; range, 35–68 years) were included in this study. A total of 32 ears were analyzed, including 19 symptomatic and 13 asymptomatic ears.

The median of the pure-tone average levels in the symptomatic ears was 23 dB (Q1: 17 dB, Q3: 50 dB; range, 4–73 dB), and 15 dB (Q1: 15 dB, Q3: 19 dB; range, 3–34 dB) in the asymptomatic ears.

MR Imaging Data

Quantitative Analysis. For the symptomatic ears, the SIR was significantly lower with hVFA (median, 1.54; Q1: 1.44, Q3: 1.84; range, 0.93–2.55) than with CFA (median, 7.16; Q1: 5.65, Q3: 8.46; range, 4.39–15.71) ($P < .001$).

For the asymptomatic ears, there were also significant differences in the SIR between hVFA (median, 1.45; Q1: 1.30, Q3: 1.68; range, 1.10–1.91) and CFA sequences (median, 7; Q1: 5.85, Q3: 7.6; range, 4.65–11.04) ($P < .001$).

No significant differences in the SIR were found between symptomatic and asymptomatic ears, either with CFA ($P = .70$) or hVFA sequences ($P = .25$).

Qualitative Analysis. Cochlear Blood Labyrinth Barrier Impairment. With hVFA sequences (Fig 2), cochlear BLB impairment was observed in 6/32 ears (18.7%) (6/19 symptomatic and 0/13 asymptomatic ears) according to reader A and 4/32 ears (12.5%) according to reader B (4/19 symptomatic, 0/13 asymptomatic ears). The Cohen κ coefficient was 0.53. There was no significant association between cochlear BLB impairment and clinical symptomatology ($P = .06$ for reader A and $P = .12$ for reader B).

With CFA sequences (Fig 2), cochlear BLB impairment was observed in 8/32 ears (25.0%) according to both readers (8/19 symptomatic and 0/13 asymptomatic ears). Interreader agreement was perfect (Cohen κ coefficient = 1). There was a significant association between cochlear BLB impairment and clinical symptomatology ($P = .01$).

Data are summarized in the On-line Table.

Endolymphatic Hydrops. With hVFA sequences (Fig 3), EH was observed in 13/32 ears (40.6%) according to reader A (10/19 symptomatic and 3/13 asymptomatic ears) and 10/32 ears (31.3%) according to reader B (7/19 symptomatic and 3/13 asymptomatic ears). The Cohen κ coefficient was 0.26. There was no significant association between the clinical symptomatology and the presence of EH ($P = .15$, OR = 3.55; 95% CI, 0.63–26.62; and $P = .47$, OR = 1.90; 95% CI, 0.32–14.47, according to readers A and B respectively).

With CFA sequences (Fig 3), both readers reported EH in 14/32 ears (43.7%: 12/19 symptomatic and 2/13 asymptomatic ears). The Cohen κ coefficient was 1. We found a significant association between the clinical symptomatology and the presence of EH ($P = .01$, OR = 8.73; 95% CI, 1.33 – 103.73).

Data are summarized in the On-line Table.

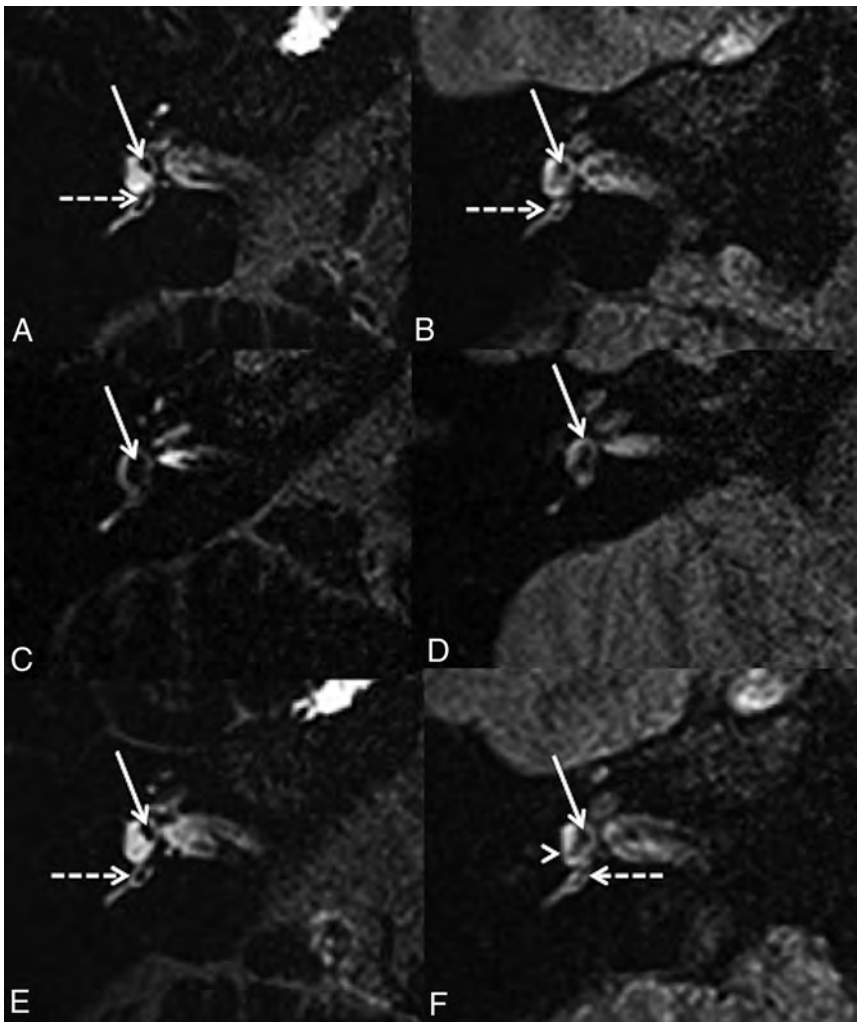

FIG 3. A 42-year-old woman with right possible MD. Right axial CFA (*A*) and hVFA (*B*) sequences through the inferior part of the vestibule show a normal saccule (*white arrow*) and posterior ampulla (*white dotted arrow*) in both sequences. A 43-year-old man with a right definite MD. Right axial CFA (*C*) and hVFA (*D*) sequences through the inferior part of the vestibule show saccular hydrops (*white arrow*) in both sequences. A 35-year-old woman with a right possible MD. Right axial CFA (*E*) and hVFA (*F*) sequences through the inferior part of the vestibule and the posterior ampulla (*white dotted arrow*). With the CFA sequence, the right saccule appears normal (*white arrow*). With the hVFA sequence, reader A described a right saccular hydrops, while reader B defined the right saccule as normal. The saccule (*white arrow*) and the posterior and lower parts of the utricle (*white arrowhead*) were confluent without expansion of these 2 structures.

Endolymphatic Space Evaluation. With hVFA sequences (Fig 3), the distinction between the utricle and the saccule was not possible in 13/32 ears (40.6%) according to reader A (8/19 symptomatic and 5/13 asymptomatic ears) and 13/32 ears (40.6%) according to reader B (9/19 symptomatic and 4/13 asymptomatic ears). The Cohen κ coefficient was 0.35. For both readers, there were no significant differences in the distinction between the utricle and the saccule whether the patient was symptomatic or not ($P = 1$ for reader A and $P = .47$ for reader B). Among the ears in which the distinction between the saccule and the utricle was not possible, EH was described in only 6/13 ears (46.2%) according to reader A and 9/13 ears (69.2%) according to reader B.

The distinction of the posterior ampulla was not possible in 12/32 ears (37.5%) according to reader A (8/19 symptomatic and 4/13 asymptomatic ears) and 10/32 ears (31.3%) according to reader B (8/19 symptomatic and 2/13 asymptomatic ears). The Cohen κ coefficient was 0.31. The distinction of the lateral ampulla was not possible in 17/32 ears (53.1%) according to reader A (10/19 symptomatic and 7/13 asymptomatic ears) and 21/32 (65.6%) according to reader B (12/19 symptomatic and 9/13 asymptomatic ears). The Cohen κ coefficient was 0.49. For both readers, the absence of discrimination of the ampullas was not significantly related to the clinically symptomatic ear or the presence of endolymphatic hydrops.

With CFA sequences (Fig 3), the distinction between the utricle and the saccule was not possible in 10/32 ears (31.3%) for both readers (9/19 symptomatic and 1/13 asymptomatic ears). The Cohen κ coefficient was 1. Among the 10 ears in which the distinction between the utricle and the saccule was not possible, EH was identified in all ears according to both readers. There was a significant association between the absence of utricle/saccule discrimination and the clinically symptomatic ear (OR = 0.09; 95% CI, 0.01–0.93; $P = .02$).

The distinction of the lateral and posterior ampullas was always observed for both readers. Interreader agreement was perfect (Cohen κ coefficient = 1).

Data are summarized in the Online Table.

DISCUSSION

We demonstrated that CFA was superior to hVFA sequences for evaluating the SIR, cochlear BLB impairment, and the endolymphatic space, with high reliability.

MR imaging evaluation of the endolymphatic space is based on the difference in signal between the endolymphatic and perilymphatic spaces due to the selective enhancement of the perilymphatic space after contrast media administration. In our study, SIR, which is an indirect evaluation of the contrast-to-noise ratio, was significantly higher with CFA than hVFA sequences. Naganawa et al[11] have reported the opposite association, yet the parameters of these 2 sequences were not strictly similar; thus, no proper comparison should be made.

In the literature, hVFA sequences are most commonly used for the diagnosis of EH because they allow keeping the high signal amplitude through the long readout duration.[15] After a 90°

radiofrequency pulse, equally spaced 180° radiofrequency pulses are the most appropriate ones to refocus transverse magnetization generating a train of spin echoes without compromising longitudinal relaxation. However, constant high flip angle refocusing radiofrequency pulses are responsible for high-power deposition in tissues, which must be monitored in the brain due to the specific absorption rate regulatory limits (2 W/kg).[15] VFA radiofrequency pulses have been designed to provide higher signal amplitude and low specific absorption rate deposition, by maintaining a transverse magnetization as well as using longitudinal magnetization to contribute to the signal during sequence readouts. It is based on the principle of stimulated echo, which cannot be reached by a 180° CFA. One of the consequences is a decrease in contrast in T1 due to a permanent residual transverse magnetization but also lower flip angle values. This is an obvious impediment in the EH imaging, in which the main focus is to highlight the shortening of the longitudinal relaxation induced by gadolinium. Thus, a constant 140° radiofrequency pulse has been found to be the best compromise to limit stimulated echoes, as well as specific absorption rate deposition. In our study, specific absorption rate deposition was around 0.03–0.05 W/kg with hVFA and 0.16–0.22 W/kg with CFA sequences.

We found a strong correlation between the cochlear BLB impairment and the symptomatic ear with CFA ($P = .01$) but not with hVFA sequences ($P = .06$ for reader A and $P = .13$ for reader B). Hydrops protocol enables the assessment of not only the endolymphatic space but also the permeability of the BLB, which might be slightly impaired in MD but also in various inner ear diseases.[13,14,21-24] Various authors have demonstrated that some patients with MD could also have cochlear BLB impairment, either isolated or in association with EH.[5,25] Therefore, we recommend the use of CFA instead of hVFA sequences to evaluate the permeability of the BLB with a high reliability.

The distinction between the utricle and the saccule is crucial because the diagnosis of EH on MR imaging relies on the presence of saccular dilation.[4] However, in cases of severe dilation, one can observe an expansion of the dilation from the saccule to the utricle, making it impossible to distinguish these 2 structures. With CFA sequences, this distinction was not possible in 10 ears because EH was identified in all of them according to both readers. By contrast, with hVFA sequences, the utricle and the saccule could not be distinguished in 7 and 4 ears (respectively, for readers A and B), while no sign of EH was observed. Indeed, we observed cases in which the saccule and the utricle were not dilated but seemed to be confluent at a focal point with surrounding perilymphatic space.

EH in the asymptomatic ears was observed in 3 patients with MD with hVFA and CFA sequences. However, with hVFA sequences, both readers were in agreement on only 1 of these 3 patients. In the literature, the rate of EH in asymptomatic ears on MR imaging ranges from 20% to 65%.[26,27] Here, we propose the hypothesis that previously published discrepancies may be related to the use of different flip angle parameters in addition to the disease itself.

The distinction of the ampullas from the surrounding perilymphatic space is a strong indicator of the spatial resolution of the sequence, which is highly recommended for hydrops protocol. Although ampullar hydrops is uncommon, lately, it has been reported that some patients with atypical acute vestibular syndrome could present with a collapse of the endolymphatic space of the pars superior (utricle and ampullas).[28] With CFA sequences, the visualization of the ampullas was possible in all cases, while this evaluation was more inconsistent with hVFA sequences.

Therapeutic Applications

The treatment of MD is based on lifestyle change and various drug therapies for the management of vertigo.[29] More invasive treatments such as endolymphatic sac surgery, vestibular nerve section, or intratympanic drugs can be suggested in cases of medical treatment failure.[30-32] The pathophysiologic effect of endolymphatic sac surgery is still widely discussed and could be further discussed in light of results from the MR imaging hydrops protocol, suggesting that vestibular neurectomy should be preferred to control vertigo in patients without saccular hydrops.

Our study has several limitations, first, by its retrospective nature. Second, because 15% of patients with MD might present with EH on the contralateral asymptomatic ear, the presence of a control group would have been interesting. We had no possibility of quantifying the volume of the vestibular endolymphatic space in vivo; thus, it was not possible to assess whether the observed radiologic hydrops is well-correlated with the true presence of an endolymphatic hydrops in histopathology. Another limitation of our study was the small number of patients, which could explain some nonsignificant results. However, those results were only related to the hVFA sequences but never to the CFA sequences.

CONCLUSIONS

The diagnosis of EH in patients with MD can be difficult on MR imaging because it requires fine analysis of small anatomic structures. When performing hydrops protocol, radiologists should keep in mind that FLAIR sequences require optimal parameters to evaluate the endolymphatic space and the permeability of the BLB accurately. We demonstrated that CFA sequences provided higher SIR and were superior to hVFA sequences in reliably evaluating the cochlear BLB impairment and the endolymphatic space.

ACKNOWLEDGMENTS

We thank Pamela Haylock (Lariboisiere University Hospital) for critically editing the manuscript.

Disclosures: Alexis Vaussy—*UNRELATED*: *Employment*: Siemens Healthineers France, *Comments*: current MR Clinical Scientist position within the company. Arnaud Attyé—*UNRELATED*: *Consultancy*: Pixyl Medical, *Comments*: I have a consulting service agreement with occasional consultant activities; *OTHER RELATIONSHIPS*: I have conducted previous MRI studies on healthy volunteers' inner ears using research funds from Guerbet SA.

REFERENCES

1. Altmann F, Fowler EP Jr. **Histological findings in Meniere's symptom complex.** *Ann Otol Rhinol Laryngol* 1943;52:52–80

2. Nakashima T, Naganawa S, Pyykko I, et al. **Grading of endolymphatic hydrops using magnetic resonance imaging.** *Acta Oto-Laryngol Suppl* 2009:5–8 CrossRef Medline
3. Tagaya M, Yamazaki M, Teranishi M, et al. **Endolymphatic hydrops and blood-labyrinth barrier in Ménière's disease.** *Acta Otolaryngol* 2011;131:474–79 CrossRef Medline
4. Attyé A, Eliezer M, Boudiaf N, et al. **MRI of endolymphatic hydrops in patients with Meniere's disease: a case-controlled study with a simplified classification based on saccular morphology.** *Eur Radiology* 2017;27:3138–46 CrossRef Medline
5. Bernaerts A, Vanspauwen R, Blaivie C, et al. **The value of four stage vestibular hydrops grading and asymmetric perilymphatic enhancement in the diagnosis of Menière's disease on MRI.** *Neuroradiology* 2019;61:421–29 CrossRef Medline
6. Naganawa S, Komada T, Fukatsu H, et al. **Observation of contrast enhancement in the cochlear fluid space of healthy subjects using a 3D-FLAIR sequence at 3 Tesla.** *Eur Radiol* 2006;16:733–37 CrossRef Medline
7. Naganawa S, Yamazaki M, Kawai H, et al. **Visualization of endolymphatic hydrops in Ménière's disease with single-dose intravenous gadolinium-based contrast media using heavily T(2)-weighted 3D-FLAIR.** *Magn Reson Med Sci* 2010;9:237–42 CrossRef Medline
8. Yamazaki M, Naganawa S, Tagaya M, et al. **Comparison of contrast effect on the cochlear perilymph after intratympanic and intravenous gadolinium injection.** *AJNR Am J Neuroradiol* 2012;33:773–78 CrossRef Medline
9. Li Y, Sha Y, Wang F, et al. **Comprehensive comparison of MR image quality between intratympanic and intravenous gadolinium injection using 3D real IR sequences.** *Acta Otolaryngol* 2019;139:659–64 CrossRef Medline
10. Naganawa S. **The technical and clinical features of 3D-FLAIR in neuroimaging.** *Magn Reson Med Sci* 2015;14:93–106 CrossRef Medline
11. Naganawa S, Yamazaki M, Kawai H, et al. **Imaging of Ménière's disease after intravenous administration of single-dose gadodiamide: utility of subtraction images with different inversion time.** *Magn Reson Med Sci* 2012;11:213–19 CrossRef Medline
12. Sepahdari AR, Ishiyama G, Vorasubin N, et al. **Delayed intravenous contrast-enhanced 3D FLAIR MRI in Meniere's disease: correlation of quantitative measures of endolymphatic hydrops with hearing.** *Clin Imaging* 2015;39:26–31 CrossRef Medline
13. Eliezer M, Maquet C, Horion J, et al. **Detection of intralabyrinthine abnormalities using post-contrast delayed 3D-FLAIR MRI sequences in patients with acute vestibular syndrome.** *Eur Radiol* 2019;29:2760–69 CrossRef Medline
14. Pakdaman MN, Ishiyama G, Ishiyama A, et al. **Blood-labyrinth barrier permeability in Menière disease and idiopathic sudden sensorineural hearing loss: findings on delayed postcontrast 3D-FLAIR MRI.** *AJNR Am J Neuroradiol* 2016;37:1903–08 CrossRef Medline
15. Mugler JP. **Optimized three-dimensional fast-spin-echo MRI.** *J Magn Reson Imaging* 2014;39:745–67 CrossRef Medline
16. Naganawa S, Kawai H, Sone M, et al. **Increased sensitivity to low concentration gadolinium contrast by optimized heavily T2-weighted 3D-FLAIR to visualize endolymphatic space.** *Magn Reson Med Sci* 2010;9:73–80 CrossRef Medline
17. **Committee on Hearing and Equilibrium guidelines for the evaluation of results of treatment of conductive hearing loss: American Academy of Otolaryngology-Head and Neck Surgery Foundation, Inc.** *Otolaryngol Head Neck Surg* 1995;113:186–87 CrossRef Medline
18. Eliezer M, Poillon G, Gillibert A, et al. **Comparison of enhancement of the vestibular perilymph between gadoterate meglumine and gadobutrol at 3-Tesla in Meniere's disease.** *Diagn Interv Imaging* 2018;99:271–77 CrossRef Medline
19. Merchant SN, Nadol JB. *Schuknecht's Pathology of the Ear*. 3rd ed. Shelton: McGraw-Hill Medical; 2010
20. Lane JI, Witte RJ, Bolster B, et al. **State of the art: 3T imaging of the membranous labyrinth.** *AJNR Am J Neuroradiol* 2008;29:1436–40 CrossRef Medline
21. Naganawa S, Kawai H, Taoka T, et al. **Cochlear lymph fluid signal increase in patients with otosclerosis after intravenous administration of gadodiamide.** *Magn Reson Med Sci* 2016;15:308–15 CrossRef Medline
22. Byun H, Chung JH, Lee SH, et al. **The clinical value of 4-hour delayed-enhanced 3D-FLAIR MR images in sudden hearing loss.** *Clin Otolaryngol* 2019;44:336–42 CrossRef Medline
23. Eliezer M, Toupet M, Guichard J-P, et al. **Cochleovestibular artery syndrome: consideration based on VHIT, VEMP, and inner ear MRI.** *J Neurol* 2019;266:2327–29 CrossRef Medline
24. Eliezer M, Verillaud B, Guichard J-P, et al. **Labyrinthine infarction caused by vertebral artery dissection: consideration based on MRI.** *J Neurol* 2019;266:2575–77 CrossRef Medline
25. Kahn L, Hautefort C, Guichard JP, et al. **Relationship between video head impulse test, ocular and cervical vestibular evoked myogenic potentials and compartmental magnetic resonance imaging classification in Menière's disease.** *Laryngoscope* 2019 Nov 19. [Epub ahead of print] CrossRef Medline
26. Barath K, Schuknecht B, Naldi AM, et al. **Detection and grading of endolymphatic hydrops in Menière disease using MR imaging.** *AJNR Am J Neuroradiol* 2014;35:1387–92 CrossRef Medline
27. Pyykkö I, Nakashima T, Yoshida T, et al. **Meniere's disease: a reappraisal supported by a variable latency of symptoms and the MRI visualisation of endolymphatic hydrops.** *BMJ Open* 2013;3:e001555 CrossRef
28. Eliezer M, Attyé A, Guichard JP, et al. **Vestibular atelectasis: myth or reality?.** *Laryngoscope* 2019;129:1689–95 CrossRef Medline
29. Sajjadi H, Paparella MM. **Meniere's disease.** *Lancet* 2008;372:406–14 CrossRef Medline
30. Sood AJ, Lambert PR, Nguyen SA, et al. **Endolymphatic sac surgery for Ménière's disease: a systematic review and meta-analysis.** *Otol Neurotol* 2014;35:1033–45 CrossRef Medline
31. Tewary AK, Riley N, Kerr AG. **Long-term results of vestibular nerve section.** *J Laryngol Otol* 1998;112:1150–53 CrossRef Medline
32. Miller MW, Agrawal Y. **Intratympanic therapies for Menière's disease.** *Curr Otorhinolaryngol Rep* 2014;2:137–43 CrossRef Medline

Involvement of the Olfactory Apparatus by Gliomas

X. Wu, Y. Li, C.M. Glastonbury, and S. Cha

ABSTRACT

SUMMARY: The olfactory bulbs and tracts are central nervous system white matter tracts maintained by central neuroglia. Although rare, gliomas can originate from and progress to involve the olfactory apparatus. Through a Health Insurance Portability and Accountability Act–compliant retrospective review of the institutional teaching files and brain MR imaging reports spanning 10 years, we identified 12 cases of gliomas involving the olfactory bulbs and tracts, including 6 cases of glioblastoma, 2 cases of anaplastic oligodendroglioma, and 1 case each of pilocytic astrocytoma, diffuse (grade II) astrocytoma, anaplastic astrocytoma (grade III), and diffuse midline glioma. All except the pilocytic astrocytoma occurred in patients with known primary glial tumors elsewhere. Imaging findings of olfactory tumor involvement ranged from well-demarcated enhancing masses to ill-defined enhancing infiltrative lesions to nonenhancing masslike FLAIR signal abnormality within the olfactory tracts. Familiarity with the imaging findings of glioma involvement of the olfactory nerves is important for timely diagnosis and treatment of recurrent gliomas and to distinguish them from other disease processes.

ABBREVIATIONS: GBM = glioblastoma multiforme; TMZ = temozolomide; EGFR = epidermal growth factor receptor; IDH1 = Isocitrate dehydrogenase 1; MGMT = O6-methylguanine methyltransferase

The olfactory bulbs and tracts are central nervous system white matter tracts extending directly to the cerebrum, maintained by a combination of specialized olfactory ensheathing cells and central neuroglia, including astrocytes and oligodendrocytes.[1] As a result, gliomas can rarely originate from and progress to involve the olfactory apparatus. Relatively common neoplasms that involve the olfactory grooves include meningiomas arising from the anterior cranial fossa dura and sinonasal malignancies extending intracranially such as squamous cell carcinoma and esthesioneuroblastoma.[2] These entities have characteristic imaging findings, and the purpose of this article is to characterize the range of imaging findings of gliomas that affect the olfactory bulbs and tracts and to differentiate them from other masses of the anterior cranial fossa.

Received November 7, 2019; accepted after revision January 25, 2020.

From the Department of Radiology and Imaging Sciences (X.W.), Emory University, Atlanta, Georgia; Departments of Clinical Radiology (Y.L., C.M.G.), Otolaryngology Head and Neck Surgery (C.M.G.), Radiation Oncology (C.M.G.), Radiology (S.C.), and Neurological Surgery (S.C.), University of California, San Francisco, San Francisco, California.

Drs Glastonbury and Cha contributed equally to this work.

Paper previously presented at: Annual Meeting of the American Society of Neuroradiology and the Foundation of the ASNR Symposium, June 2–7, 2018; Vancouver, British Columbia, Canada.

Please address correspondence to Xin Wu, MD, Department of Radiology and Imaging Science, Emory University, 1364 Clifton Rd NE, Suite BG 20, Atlanta, GA 30322; e-mail: xin.wu@emory.edu; @CynXinWu

Indicates article with supplemental on-line table.

http://dx.doi.org/10.3174/ajnr.A6471

Case Series

A Health Insurance Portability and Accountability Act–compliant retrospective search through University of California San Francisco radiology institutional teaching files and radiology reports for patients with olfactory masses was conducted, with an inclusion criterion of a known history of glioma or pathologically proved glial neoplastic involvement of the olfactory nerve. Twelve patients (3 women and 9 men) were identified with glial masses involving the olfactory bulbs. Patient ages ranged from 10 to 74 years (On-line Table). A single case of primary pilocytic astrocytoma originating from the olfactory bulb was identified. The remaining 11 patients had known pre-existing glial tumors elsewhere, with multicentric or progressive involvement of the olfactory bulb/tract. There were 6 cases of glioblastomas, 2 cases of anaplastic oligodendrogliomas, and 1 case each of diffuse astrocytoma, anaplastic astrocytoma, and diffuse midline glioma.

Case 1. A 27-year-old man presented with mild hyperprolactinemia and underwent a dedicated pituitary and sella protocol MR imaging, on which a well-circumscribed uniformly enhancing mass was seen to arise from the left olfactory groove, with mild surrounding dural thickening and enhancement (Fig 1). There

was no tumor extension through the cribriform plate, and no other intracranial lesions were identified on follow-up brain imaging. On further questioning, the patient revealed partial anosmia. The radiology interpretation favored a diagnosis of meningioma, and the operative note even indicated a dural tail associated with the mass, which was inseparable from the left olfactory nerve. The final pathologic diagnosis yielded pilocytic astrocytoma, World Health Organization grade I.

Case 2. A 51-year-old man with a history of left frontal lobe grade II astrocytoma treated 12 years prior by surgical resection and temozolomide (TMZ) was found to have nonenhancing masslike T2-weighted/FLAIR signal abnormality in the olfactory nerve ipsilateral to his original tumor, concerning for slowly progressive recurrence.

Case 3. A 46-year-old woman was originally diagnosed with grade III diffuse anaplastic oligodendroglioma of the left inferior frontal lobe, treated with resection and chemoradiation. She presented to our institution 8 years after the initial treatment for continued follow-up. During the subsequent 8 years, the tumor demonstrated subtle and slow progression during multiple examinations, as manifested by progressive nonenhancing masslike FLAIR signal abnormality involving the left anterior perforated substance and olfactory nerve (Fig 2).

Case 4. A 53-year-old male patient with a right temporal anaplastic oligodendroglioma had undergone subtotal resection 7 years prior followed by chemoradiation. He demonstrated slowly progressive bulky nonenhancing disease involving the olfactory cortex and olfactory bulb (Fig 3).

Case 5. A 10-year-old boy presented for continued management of his orbital rhabdomyosarcoma, originally diagnosed and treated 8 years prior. On his initial (pretreatment) imaging, a right anterior temporal mass was also identified. On further work-up and biopsy, this tumor was found to represent a grade III anaplastic astrocytoma. Abnormal nonenhancing nodular T2 hyperintensity was present along the olfactory nerve, though there was no definite involvement of the ipsilateral olfactory cortex (Fig 4). Signal abnormality was also seen in the bilateral internal auditory canals and along the expected course of the left abducens nerve, likely due to leptomeningeal disease spread.

Case 6. A 15-year-old male patient presented with diffuse midline glioma diagnosed 2 years prior, when he underwent treatment with chemoradiation. One year after the diagnosis, additional treatment was required with radiation, nivolumab, and bevacizumab. Imaging demonstrated diffuse nonenhancing T2/FLAIR signal abnormality of the bilateral frontotemporal lobes and olfactory nerves (Fig 5).

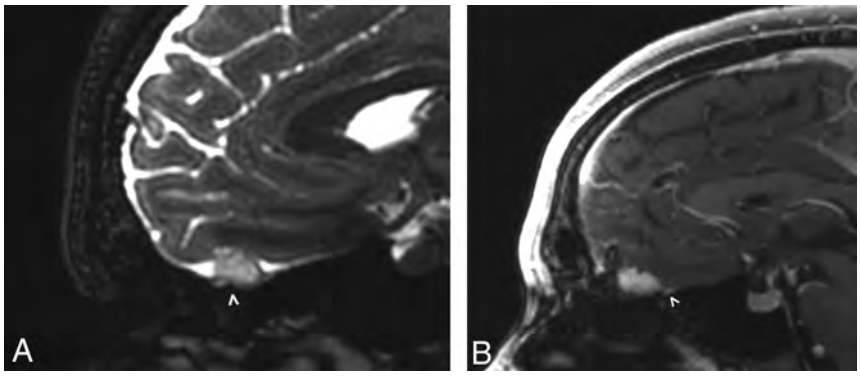

FIG 1. A 27-year-old man with mild hyperprolactinemia (case 1). Sagittal FIESTA (*A*) demonstrates a T2 hyperintense apparent extra-axial mass (*arrowhead*) within the left anterior cranial fossa. On the sagittal postcontrast T1-weighted image (*B*), the mass has uniform enhancement with a subtle adjacent dural tail (*arrowhead*). On imaging, this was believed to be a meningioma, but at resection, it was determined to be a pilocytic astrocytoma.

Case 7. A 61-year-old woman originally presented with a right temporal lobe mass diagnosed as *Isocitrate dehydrogenase 1* (*IDH1*) R132H wild-type, *epidermal growth factor receptor* (*EGFR*)-amplified, *O6-methylguanine methyltransferase* (*MGMT*) unmethylated glioblastoma multiforme (GBM), which underwent partial resection, radiation, and TMZ therapy. A year later, there was a new nodular enhancing mass within the surgical bed compatible with disease progression. The contralateral olfactory nerve also demonstrated progressive masslike FLAIR signal abnormality as well as enhancement, compatible with multicentric disease recurrence and progression.

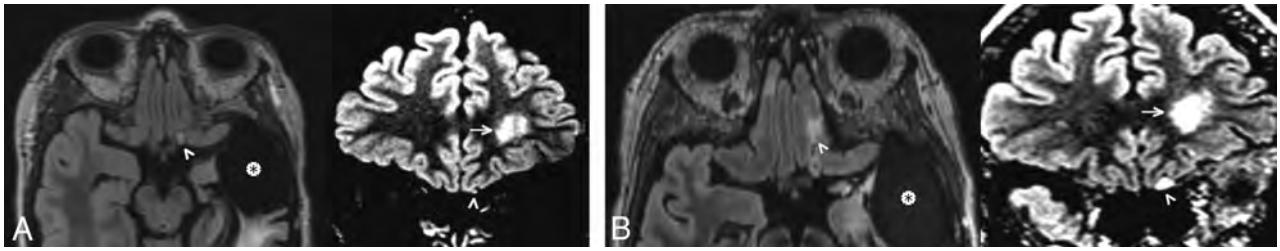

FIG 2. A 46-year-old woman with left inferior frontal grade III diffuse anaplastic oligodendroglioma previously treated with resection and chemoradiation (case 3). Axial and coronal FLAIR images obtained 8 years after the initial treatment (*A*) demonstrate a left temporal resection cavity (*asterisk*) and unchanged FLAIR signal in the left frontal lobe (*arrow*). There is subtle nodular FLAIR signal abnormality (*arrowheads*) of the left olfactory bulb. Axial and coronal FLAIR images obtained 16 years after the initial treatment (*B*) show minimal change around the resection cavity (*asterisk*) but progressive enlargement of the hyperintense left olfactory bulb (*arrowheads*).

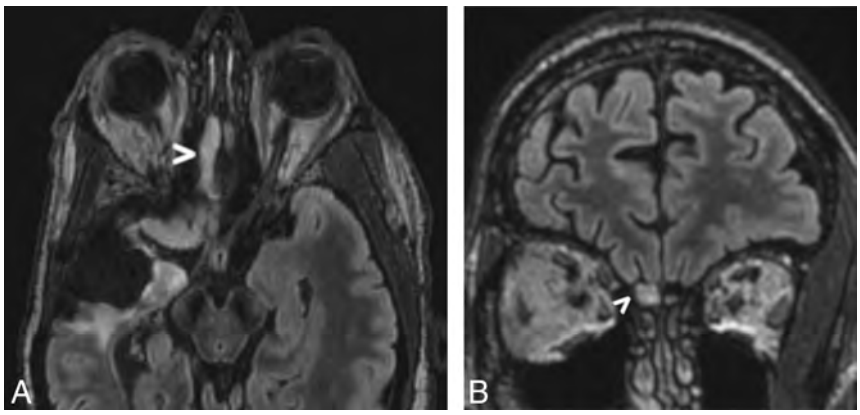

FIG 3. A 53-year-old man with a right temporal anaplastic oligodendroglioma previously treated with subtotal resection and chemoradiation (case 4). Axial FLAIR image (*A*) obtained 7 years after the initial treatment demonstrates masslike FLAIR signal abnormality within the right olfactory cortex as well as the right olfactory tract and bulb (*arrowhead*), compatible with oligodendroglioma involvement. Coronal FLAIR image (*B*) obtained at the same time illustrates an asymmetric masslike FLAIR signal abnormality within the right olfactory tract and bulb (*arrowhead*), while the contralateral olfactory bulb remains normal in caliber.

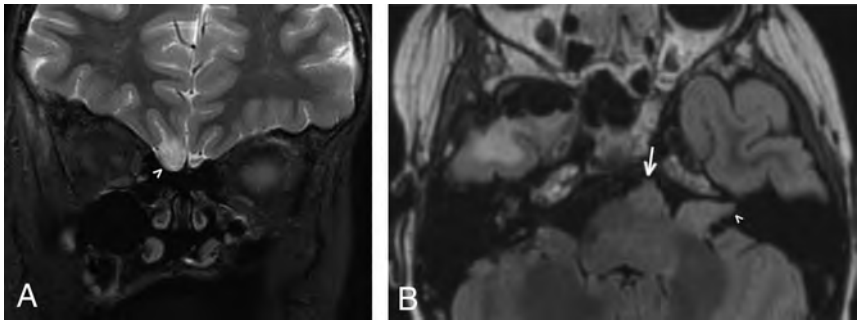

FIG 4. A 10-year-old boy with right anterior temporal grade III anaplastic astrocytoma detected 8 years prior (case 5). Coronal FLAIR image (*A*) demonstrates a nonenhancing masslike signal abnormality within the right olfactory tract (*arrowhead*), while an axial FLAIR image (*B*) obtained at the same time demonstrates a nonenhancing masslike signal abnormality within the left internal auditory canal (*arrowhead*) as well as in the prepontine cistern, along the presumed location of the left abducens nerve/CN VI (*arrow*). Combined, findings are compatible with leptomeningeal disease spread involving multiple cranial nerves.

Case 8. A 69-year-old woman presented with a large left frontal *IDH1* R132H wild-type, *MGMT*-unmethylated, and *EGFR*-unamplified GBM with sarcomatous features. She underwent radiation therapy with concurrent TMZ. When the tumor progressed, she underwent adjuvant TMZ followed by a MEDI4736 vaccine trial and bevacizumab. A nodular enhancing mass developed in the left olfactory groove during treatment, inseparable from the olfactory nerve.

Case 9. A 74-year-old man presented with a right frontal GBM, which did not involve the olfactory cortex. He was then found to have an enhancing nodular mass involving the contralateral olfactory nerve compatible with progressive disease.

Case 10. A 37-year-old man presented with a nonenhancing left olfactory nerve mass and a history of GBM centered in the right frontal operculum, resected 4 years prior (Fig 6). The mass was resected and was demonstrated to be glioblastoma.

Case 11. A 36-year-old man with an *IDH1* wild-type, p53-positive, *phosphatase and tensin homolog*–intact, *EGFR*-negative GBM centered in the corpus callosum underwent treatment with radiation and TMZ. One year later, he presented with abnormal enlargement and patchy enhancement in the left olfactory nerve accompanied by extensive masslike FLAIR signal abnormality in the ipsilateral olfactory cortex. There was progressive worsening of the masslike signal abnormality and enhancement within the left olfactory nerve during studies spanning the next 3 months (Fig 7).

Case 12. A 31-year-old man was originally diagnosed with right frontal lobe grade III anaplastic astrocytoma 6 years prior. On presentation to our institution, the tumor had undergone transformation to an *IDH1*-mutant, *EGFR*-negative, *MGMT*-methylated GBM, which was 1p19q-codeleted. There was bulky nonenhancing signal abnormality in the right gyrus rectus, orbitofrontal gyrus, anterior temporal lobe, and olfactory nerve, compatible with progressive disease involvement (Fig 8).

DISCUSSION

The first cranial nerve (CN I), also known as the olfactory nerve, is a purely sensory nerve that supplies the sensation of smell via specialized olfactory sensory neurons that arise from the nasal mucosa of the superior nasal cavity. Extending through the cribriform plate, small fibers of unmyelinated bipolar olfactory nerve cells synapse with secondary mitral and tufted neurons in the olfactory bulbs. Also known as projection neurons, these mitral and tufted neurons form myelinated olfactory tracts that lie within the bony olfactory sulcus and groove in the medial-most portions of the floor of the anterior cranial fossa. The olfactory tracts directly project to the olfactory cortices bilaterally, which include the posterior orbitofrontal gyrus, amygdala, and uncus, where the sensation of smell is synthesized and processed.[3,4]

Our study of 12 patients with glioma involving the olfactory bulbs and tracts highlights an uncommon-but-clinically important phenomenon. All except 1 of the cases represented secondary involvement through direct infiltration of tumor or multifocal/multicentric disease in patients with known glioma diagnoses, including anaplastic oligodendroglioma, diffuse and anaplastic

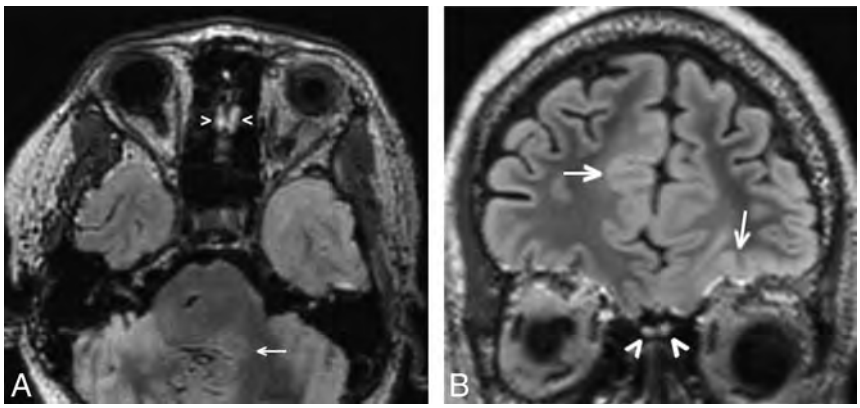

FIG 5. A 15-year-old boy presenting for follow-up of diffuse midline glioma initially diagnosed 2 years earlier and treated with chemoradiation (case 6). An axial FLAIR image (*A*) demonstrates nonenhancing T2/FLAIR signal abnormality of the bilateral olfactory nerves (*arrowheads*) and left dorsal pons (*arrow*), as well as cortical thickening and signal abnormality in the left anterior temporal lobe. Coronal FLAIR image (*B*) illustrates thickening and FLAIR signal abnormality involving the bilateral olfactory nerves (*arrowheads*) as well as multiple cortical areas in the bilateral frontal lobes (*arrows*). Findings are compatible with multifocal glioma involvement.

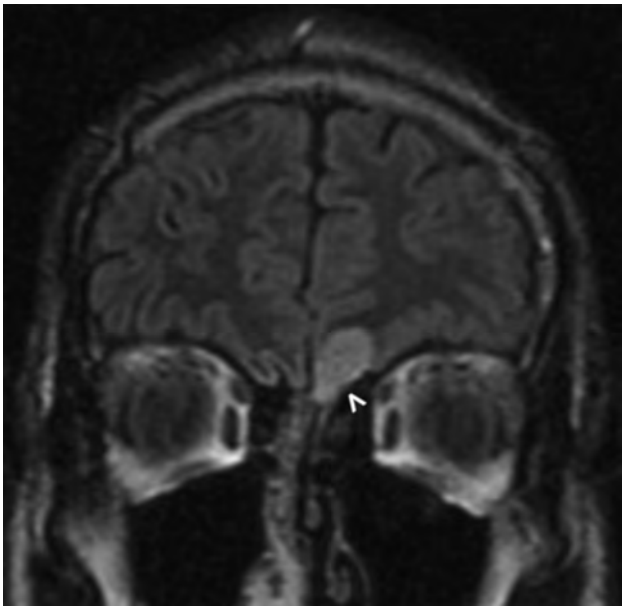

FIG 6. A 37-year-old man with a history of right frontal operculum GBM resected 4 years prior (case 10). Coronal FLAIR image demonstrates masslike FLAIR signal abnormality in the left olfactory nerve and surrounding left inferior frontal lobe (*arrowhead*), pathologically proved to reflect disease recurrence on resection.

astrocytomas, diffuse midline glioma, and GBM. None of the gliomas in our series demonstrated osseous destruction, extension through the skull base, or involvement of the olfactory recess. The lack of these features distinguishes these tumors radiographically from other aggressive lesions common to this site, including enthesioneuroblastoma, aggressive primary osseous lesions, and intracranial extension of primary head and neck neoplasms, such as squamous cell carcinoma.[5,6]

In all patients with GBM, olfactory bulb and tract involvement represented progression of previously treated disease elsewhere in the cerebrum. In 3 cases, the olfactory nerve affected was located contralateral to the site of the originally treated tumor, compatible with the underlying multifocal/infiltrative nature of GBM. From animal studies, there is evidence that GBM cancer-initiating cells may have special affinity for the subventricular zones and olfactory bulbs, mimicking the behavior or neural stem cells.[7] This mechanism potentially explains the tropism for the olfactory system that is demonstrated by progressive gliomas in our series.

Typically, the imaging characteristics of progressive olfactory tract involvement mirrored those of the pre-existing glial tumor. In our series, 4 of the 6 patients with GBM had enhancing disease involving the olfactory bulb, while 2 patients had nonenhancing infiltrative lesions. For 4 of the 6 patients, the *IDH1* genotyping was available. Of these patients, 1 patient with secondary *IDH1*-mutant disease demonstrated nonenhancing involvement of the olfactory nerve, while 3 patients with *IDH1* wild-type disease all demonstrated enhancing tumor along the olfactory nerve. These findings are compatible with the most common MR imaging appearance of *IDH1* wild-type versus mutant GBMs.[8]

In 1 case with a pre-existing glial tumor, there was widespread intracranial disease, including involvement of multiple cranial nerves, raising suspicion for leptomeningeal spread of disease, which resulted in the signal abnormality involving the olfactory nerve. However, in 6 of the remaining 10 progressive cases, there was concurrent or prior involvement of ipsilateral olfactory cortex by tumor, supporting the hypothesis of direct tumor progression through parenchymal glial tracts.

The sole case of primary glioma arising from the olfactory bulbs in our series was a pilocytic astrocytoma, which mimicked a meningioma on imaging as well as during surgical resection. While often seen in the setting of meningiomas, dural enhancement and thickening (also known as the dural tail sign) are nonspecific and have been reported with a variety of peripherally located parenchymal lesions.[9] More specifically, supratentorial pilocytic astrocytomas adjacent to the cerebral convexity and anterior clinoid process have been reported to mimic meningiomas.[10,11]

To our knowledge, this is the first time that a primary glial neoplasm has been reported to arise from the olfactory tract. Although a case report has previously reported olfactory groove involvement by a large pleomorphic xanthoastrocytoma, it is unclear whether the lesion originated from the inferior frontal lobe parenchyma or olfactory tracts on the basis of imaging and intraoperative findings.[12] Primary ganglioglioma, which contains both glial and neuronal cells, has previously been reported to involve the olfactory cortex and olfactory nerve.[13] Primary tumors arising from olfactory ensheathing cells have also been previously described.[14] These

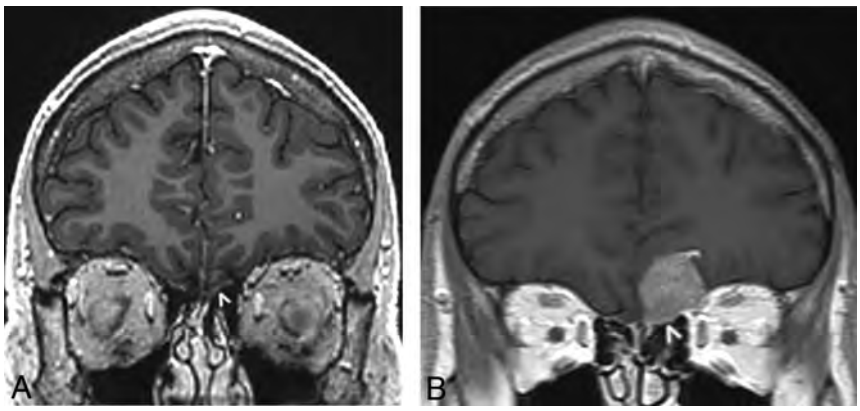

FIG 7. A 36-year-old man with a history of *IDH1* wild-type GBM centered in the corpus callosum, treated with radiation and TMZ (case 11). Coronal postcontrast T1-weighted echo-spoiled gradient echo image (*A*) obtained 1 year from initial treatment demonstrates abnormal enlargement and patchy enhancement of the left olfactory nerve (*arrowhead*). On a follow-up coronal postcontrast T1-weighted spin-echo image obtained 3 months later (*B*), the enhancing mass has enlarged (*arrowhead*) and appears to involve the leptomeningeal space, compatible with progressive recurrence.

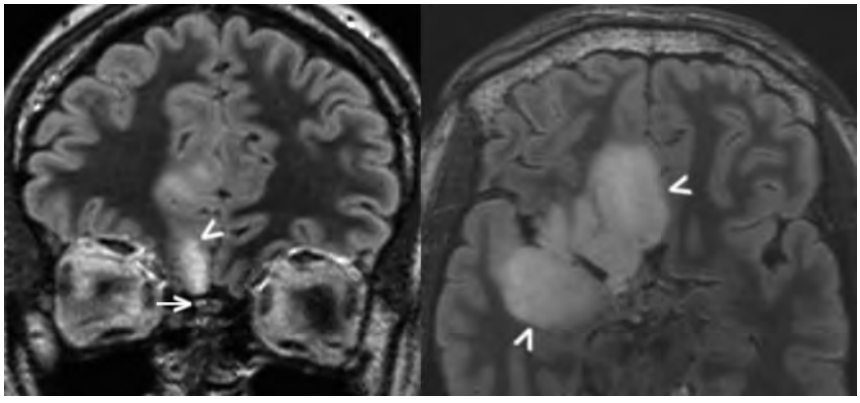

FIG 8. A 31-year-old man originally treated for right frontal lobe grade III anaplastic astrocytoma 6 years prior and now presenting with tumor transformation to an *IDH1*-mutant, 1p19q-codeleted GBM (case 12). Coronal and axial FLAIR images on re-presentation demonstrate a bulky nonenhancing masslike signal abnormality involving the right olfactory cortex (*arrowheads*) and olfactory nerve (*arrow*), compatible with GBM involvement.

tumors can histologically resemble olfactory groove schwannomas, which are entities of unclear origin because Schwann cells are not found in the olfactory system, though various developmental and nondevelopmental theories have been proposed to explain the origin of these tumors.[15-17] These lesions can all appear similar radiologically as enhancing olfactory groove masses, which may remodel but not erode the skull base.

In all our cases, olfactory nerve involvement was detected on imaging follow-up of the patients' known gliomas or work-up for an unrelated symptom/laboratory findings without a related symptom. In at least 3 of the progressive glioma cases, abnormal signal intensity could be seen in the olfactory nerve on retrospective review of examinations performed when the finding was first reported. This highlights the importance of including the olfactory nerves in one's search pattern, because our study suggests that most patients would not present with new olfactory-related symptoms.

One of the limitations of this study is the lack of pathologic confirmation for most cases in which there was suspected involvement of the olfactory nerve by progressive glioma. In most of these cases, the ipsilateral olfactory nerve was involved or progressive disease was evident in other parts of the brain parenchyma. Thus, treatment strategies were altered on the basis of a combination of clinical and radiologic evidence of disease progression because pathologic confirmation would have demanded invasive procedures, which were not favored in risk-benefit analyses. In the single case in which a biopsy was obtained to confirm progressive disease (case 10), olfactory involvement represented the sole site of suspected recurrence and was located contralateral to the site of the previously resected tumor, thus presenting a diagnostic dilemma, which required pathologic confirmation.

CONCLUSIONS

Awareness and early detection of unusual occurrence or recurrence of gliomas involving the olfactory bulb and tract are important for diagnosis and proper clinical management. Because it can be a subtle site of tumor recurrence, the olfactory groove is an important search pattern for accurate and early diagnosis of tumor recurrence in a patient with a diagnosis of glioma, especially if the patient's tumor previously involved the olfactory cortex. Furthermore, gliomas can rarely arise from the olfactory nerve, appear discrete, and mimic meningiomas.

REFERENCES

1. Garcia-Gonzalez D, Murcia-Belmonte V, Clemente D, et al. **Olfactory system and demyelination.** *Anat Rec (Hoboken)* 2013;296:1424–34 CrossRef Medline
2. Francies O, Makalanda L, Paraskevopolous D, et al. **Imaging review of the anterior skull base.** *Acta Radiology Open* 2018;7:20584601 18776487 CrossRef Medline
3. Rea P. Olfactory Nerve. In Rea P, ed. *Clinical Anatomy of the Cranial Nerves*. San Diego: Academic Press; 2014:1–6
4. Som PM, Curtin HD. *Head and Neck Imaging*. St. Louis: Mosby; 1996
5. Dublin AB, Bobinski M. **Imaging characteristics of olfactory neuroblastoma (esthesioneuroblastoma).** *J Neurol Surg B Skull Base* 2016;77:1–5 CrossRef Medline
6. Hudgins PA, Baugnon KL. **Head and neck: skull base imaging.** *Neurosurgery* 2018;82:255–67 CrossRef Medline

7. Kroonen J, Nassen J, Boulanger YG, et al. **Human glioblastoma-initiating cells invade specifically the subventricular zones and olfactory bulbs of mice after striatal injection.** *Int J Cancer* 2011;129:574–85 CrossRef Medline
8. Yamashita K, Hiwatashi A, Togao O, et al. **MR imaging-based analysis of glioblastoma multiforme: estimation of IDH1 mutation status.** *AJNR Am J Neuroradiol* 2016;37:58–65 CrossRef Medline
9. Guermazi A, Lafitte F, Miaux Y, et al. **The dural tail sign: beyond meningioma.** *Clin Radiology* 2005;60:171–88 CrossRef Medline
10. Lee JH, Sung SK, Choi CH. **Supratentorial pilocytic astrocytoma mimicking convexity meningioma with early anaplastic transformation: a case report.** *Brain Tumor Res Treat* 2017;5:105–09 CrossRef Medline
11. Hong CS, Lehman NL, Sauvageau E. **A pilocytic astrocytoma mimicking a clinoidal meningioma.** *Case Rep Radiology* 2014;2014:524 574 CrossRef Medline
12. Kaku MV, Bhat DI, Shukla D, et al. **Pleomorphic xanthoastrocytoma arising from olfactory groove: a rare location for a rare tumor.** *Pediatr Neurosurg* 2013;49:292–96 CrossRef Medline
13. Singla N, Gupta K, Kapoor A. **Ganglioglioma arising from olfactory sheath: a rare site of an uncommon tumor.** *J Clin Neurosci* 2016;28:182–84 CrossRef Medline
14. Darie I, Riffaud L, Saikali S, et al. **Olfactory ensheathing cell tumour: case report and literature review.** *J Neurooncol* 2010;100:285–89 CrossRef Medline
15. Praharaj SS, Vajramani GV, Santosh V, et al. **Solitary olfactory groove schwannoma: case report with review of the literature.** *Clin Neurol Neurosurg* 1999;101:26–28 CrossRef Medline
16. Murakami M, Tsukahara T, Hatano T, et al. **Olfactory groove schwannoma: case report.** *Neurol Med Chir (Tokyo)* 2004;44:191–94 CrossRef Medline
17. Li YP, Jiang S, Zhou PZ, et al. **Solitary olfactory schwannoma without olfactory dysfunction: a new case report and literature review.** *Neurol Sci* 2012;33:137–42 CrossRef Medline

Advanced ADC Histogram, Perfusion, and Permeability Metrics Show an Association with Survival and Pseudoprogression in Newly Diagnosed Diffuse Intrinsic Pontine Glioma: A Report from the Pediatric Brain Tumor Consortium

S. Vajapeyam, D. Brown, C. Billups, Z. Patay, G. Vezina, M.S. Shiroishi, M. Law, P. Baxter, A. Onar-Thomas, J.R. Fangusaro, I.J. Dunkel, and T.Y. Poussaint

ABSTRACT

BACKGROUND AND PURPOSE: Diffuse intrinsic pontine glioma is a lethal childhood brain cancer with dismal prognosis and MR imaging is the primary methodology used for diagnosis and monitoring. Our aim was to determine whether advanced diffusion, perfusion, and permeability MR imaging metrics predict survival and pseudoprogression in children with newly diagnosed diffuse intrinsic pontine glioma.

MATERIALS AND METHODS: A clinical trial using the poly (adenosine diphosphate ribose) polymerase (PARP) inhibitor veliparib concurrently with radiation therapy, followed by maintenance therapy with veliparib + temozolomide, in children with diffuse intrinsic pontine glioma was conducted by the Pediatric Brain Tumor Consortium. Standard MR imaging, DWI, dynamic contrast-enhanced perfusion, and DSC perfusion were performed at baseline and approximately every 2 months throughout treatment. ADC histogram metrics of T2-weighted FLAIR and enhancing tumor volume, dynamic contrast-enhanced permeability metrics for enhancing tumors, and tumor relative CBV from DSC perfusion MR imaging were calculated. Baseline values, post-radiation therapy changes, and longitudinal trends for all metrics were evaluated for associations with survival and pseudoprogression.

RESULTS: Fifty children were evaluable for survival analyses. Higher baseline relative CBV was associated with shorter progression-free survival ($P = .02$, $Q = 0.089$) and overall survival ($P = .006$, $Q = 0.055$). Associations of higher baseline mean transfer constant from the blood plasma into the extravascular extracellular space with shorter progression-free survival ($P = .03$, $Q = 0.105$) and overall survival ($P = .03$, $Q = 0.102$) trended toward significance. An increase in relative CBV with time was associated with shorter progression-free survival ($P < .001$, $Q < 0.001$) and overall survival ($P = .004$, $Q = 0.043$). Associations of longitudinal mean extravascular extracellular volume fraction with progression-free survival ($P = .03$, $Q = 0.104$) and overall survival ($P = .03$, $Q = 0.105$) and maximum transfer constant from the blood plasma into the extravascular extracellular space with progression-free survival ($P = .03$, $Q = 0.102$) trended toward significance. Greater increases with time were associated with worse outcomes. True radiologic progression showed greater post-radiation therapy decreases in mode_ADC_FLAIR compared with pseudoprogression (means, −268.15 versus −26.11, $P = .01$.)

CONCLUSIONS: ADC histogram, perfusion, and permeability MR imaging metrics in diffuse intrinsic pontine glioma are useful in predicting survival and pseudoprogression.

ABBREVIATIONS: DCE = dynamic contrast-enhanced; DIPG = diffuse intrinsic pontine glioma; K_{ep} = rate constant from extravascular extracellular space back into blood plasma; K^{trans} = transfer constant from blood plasma into extravascular extracellular space; OS = overall survival; PBTC = Pediatric Brain Tumor Consortium; PFS = progression-free survival; rCBV = relative CBV; RT = radiation therapy; TMZ = temozolomide; v_e = extravascular extracellular volume fraction; v_p = blood-plasma volume fraction

Received November 21, 2019; accepted after revision February 10, 2020.

From the Radiology (S.V., T.Y.P.), Boston Children's Hospital and Harvard Medical School, Boston, Massachusetts; DF/HCC Tumor Imaging Metrics Core (D.B.), Massachusetts General Hospital, Boston, Massachusetts; Biostatistics (C.B., A.O.-T.) and Diagnostic Imaging (Z.P.), St. Jude Children's Research Hospital, Memphis, Tennessee; Radiology (G.V.), Children's National Medical Center, Washington, DC; Radiology (M.S.S.), Keck Medical Center of USC, Los Angeles, California; Neuroscience (M.L.), Monash University, Melbourne, Australia; Cancer and Hematology Center (P.B.), Texas Children's Hospital, Houston, Texas; Aflac Cancer and Blood Disorders Center (J.R.F.), Children's Healthcare of Atlanta, Atlanta, Georgia; and Pediatrics (I.J.D.), Memorial Sloan Kettering Cancer Center, New York, New York.

This work was supported by the National Institutes of Health (UM1 CA081457 and P30 CA008748), the Pediatric Brain Tumor Consortium Foundation, the Pediatric Brain Tumor Foundation of the United States, and the American Lebanese Syrian Associated Charities.

Paper previously presented at: Annual Meeting of the American Society of Neuroradiology, May 18–23, 2019; Boston, Massachusetts.

Please address correspondence to Sridhar Vajapeyam, PhD, Boston Children's Hospital and Harvard Medical School, Department of Radiology, 300 Longwood Ave, Boston, MA 02115; e-mail: sridhar.vajapeyam@childrens.harvard.edu

Indicates open access to non-subscribers at www.ajnr.org

Indicates article with supplemental on-line tables.

http://dx.doi.org/10.3174/ajnr.A6499

Diffuseintrinsic pontine gliomas (DIPGs) represent 80% of all brain stem gliomas, and brain stem tumors constitute approximately 10%–15% of pediatric CNS tumors.[1] The prognosis for DIPG has been uniformly dismal, with >90% of patients succumbing to the disease within 2 years of diagnosis, with a median overall survival of 9 months.[2] Radiation therapy (RT) has shown transient improvement of neurologic symptoms and marginal survival benefit.[3]

In this study, we assessed associations between survival and imaging metrics derived from advanced diffusion, perfusion, and permeability MR imaging data in a cohort of patients with newly diagnosed DIPG treated with veliparib concurrent with RT, followed by maintenance therapy of veliparib plus temozolomide (TMZ) treated in a Pediatric Brain Tumor Consortium (PBTC) Phase I/II trial. Poly (adenosine diphospate ribose) polymerase (PARP) inhibitors such as veliparib have been shown to overcome TMZ resistance while also increasing radiosensitivity.[4,5] Advanced ADC histogram metrics have been shown to correlate with survival[6] in DIPG, whereas perfusion and permeability metrics have shown associations with survival as well as pseudoprogression[7-9] in pediatric and adult gliomas. We therefore explored the utility of these imaging metrics to predict pseudoprogression versus early true progression.

MATERIALS AND METHODS

Patients and Treatment Protocol

Fifty-three children (33 girls, 20 boys; median age 6.6 years; range, 2.5–12.9 years) with newly diagnosed DIPGs were enrolled in a Phase II PBTC trial (PBTC-033, NCT01514201) to determine the efficacy of administering veliparib concurrently with radiation therapy, followed by maintenance therapy with veliparib and temozolomide (TMZ). All patients received photon radiation with a planned target volume of 5400 cGy administered in 30 fractions of 180 cGy and a 50-mg/m^2 dose of veliparib, followed by maintenance therapy with veliparib at 25 mg/m^2 two times a day and TMZ at 135 mg/m^2/day for 5 days every 28 days.

Imaging and Image Analysis

MR Imaging Evaluation. Standard MR imaging (which included axial T2, axial T2-weighted FLAIR and axial pre- and postcontrast T1-weighted images) was performed within 2 weeks before registration; at the end of radiation therapy (week 10); within 1 week before courses 3, 5, and 8 of maintenance therapy; and at the end of treatment. Images were transferred to a Vitrea workstation (Vital Images, Minnetonka, Minnesota), and 3D FLAIR and enhancing tumor volumes were calculated from the axial T2-weighted FLAIR and axial postcontrast T1-weighted images, respectively. DSC perfusion, dynamic contrast-enhanced (DCE) permeability imaging, and DTI were performed at the same time points as standard MR imaging through week 26 (6 months from the initiation of treatment).

DCE Permeability Imaging and Analysis. All patients underwent a DCE-MR imaging protocol as follows: 1) variable flip angle echo-spoiled gradient-echo T1-mapping sequences using flip angles of 15°, 10°, 5°, and 2°; TR = 5 seconds; TE = minimum; FOV = 240 mm; section thickness = 5 mm; 2) A 3D fast gradient-echo DCE-MR imaging axial sequence of 50 phases, 7 seconds apart, with flip angle = 15°, TR = 4 seconds, TE = minimum. FOV, section thickness, and scan locations were identical to those in the T1-mapping sequences to allow the use of the T1-maps to calculate permeability metrics. A bolus of gadobutrol (0.05 mmol/kg of body weight) was injected 20 seconds after the start of scanning.

DCE-MR images were transferred to a DynaCAD workstation (https://www.invivocorp.com/solutions; Invivo, Gainesville, Florida) for automated processing using OmniLook software. Voxelwise T1-maps were generated from the variable flip angle images as described in Fram et al,[10] and the 2-compartment extended Tofts model[11] was used to generate maps of the pharmacokinetic parameters, namely transfer constant from the blood plasma into the extravascular extracellular space (K^{trans}), rate constant from extravascular extracellular space back into blood plasma (k_{ep}), extravascular extracellular volume fraction (v_e), and blood plasma volume fraction (v_p). ROIs were drawn on each section of tumor around contrast-enhancing portions of the tumor by an imaging data analyst or by a PhD scientist and verified by a Certificate of Added Qualification–certified neuroradiologist, and the mean (over voxels) and SDs of each of the variables were recorded for statistical analysis.

DSC Perfusion Imaging and Analysis. An axial 2D T2* gradient recalled-echo EPI sequence was used with TR = 2000 ms, TE = 23 ms, section thickness = 5.0 mm with a 2-mm gap, flip angle = 60°, and 50–60 time points. With the bolus for the DCE-MR imaging serving as preloading, another bolus injection of 0.05 mmol/kg body weight of gadobutrol was administered 20 seconds after start of scanning, followed by a 10-mL saline flush. Corrected CBV maps[12] were generated off-line and normalized using an ROI selected in normal-appearing white matter. A 2D ROI corresponding to the area of greatest enhancement in the tumor was selected in the normalized relative CBV (rCBV) map and used as the rCBV of the tumor.

DTI Acquisition and ADC Histogram Analysis. DTI data were acquired with the following acquisition parameters on a 3T scanner: section thickness = 2.2 mm, TR = 8800 ms, TE = 88 ms, FOV = 220 mm, b-value = 1000 s/mm^2, 35 directions. Due to their superior anatomic contrast, axial B_0 images from the DTI sequence were registered to the axial FLAIR images using the mutual information algorithm in FSL (www.fmrib.ox.ac.uk/fsl),[13,14] and the same transformation matrix was used on the ADC maps to register them to the FLAIR images. Axial postcontrast images were also similarly registered to FLAIR images. 3D ROIs comprising the tumor FLAIR volume and the postcontrast enhancing tumor volume were automatically generated using the thresholding feature in Fiji (https://imagej.net/Fiji/Downloads).[15] The ADC values of the voxels in FLAIR and enhancing volumes were then used to generate the ADC_FLAIR and ADC_enhancing volumes, respectively. These volumes were thresholded using a uniform range of 600–2600 $\times$ 10^{-6} mm^2/s to automatically exclude cysts, necrosis, and hemorrhage, and corresponding ADC_FLAIR and ADC_enhancing histograms were generated. Histogram

metrics used for statistical analysis were the number of peaks (unimodal or bimodal), mean, SD, skewness, and kurtosis of these histograms. In the case of tumors showing bimodal ADC histograms, the lower peak was measured for mean and SD, and skewness and kurtosis were not recorded.

For each of the imaging metrics, the baseline value, the post-RT change (defined as the value at the 10-week post-RT scan minus the baseline value), and the time-dependent longitudinal change in the metric during the course of treatment were examined for associations with progression-free survival (PFS), overall survival (OS), and pseudoprogression.

For patients suspected of having pseudoprogression during the first 6 months of therapy, the treating physician had the option of allowing the patient to continue protocol treatment and repeat the disease assessment in 4–6 weeks. Pseudoprogression was defined as tumors that met the ≥25% progressive disease threshold by bidimensional MR imaging area but improved spontaneously to a size of stable disease or smaller compared with initial imaging on subsequent scans. Provided that the patient did not show clinical deterioration consistent with tumor progression and subsequent MR imaging demonstrated tumor regression or stable disease, the patient could remain on treatment. If the repeat MR imaging after 4–6 weeks showed true radiographic disease progression, rather than pseudoprogression, then the date of progression was the date of the initial MR imaging, not the follow-up scan.

Statistical Methods

To examine associations between imaging parameters and outcome, we used only eligible and evaluable Phase II patients. OS was defined as the time interval from the date of treatment to the date of death from any cause or to the date of last follow-up. PFS was defined as the time interval from the date of treatment to the earliest date of failure (disease progression or death from any cause) for patients who failed or to the date of last contact for patients who had not failed.

Exact Wilcoxon rank sum tests were used to compare distributions of continuous imaging metrics among patient groups. For each of the imaging metrics, the baseline value, the post-RT change (defined as the value at the 10-week post-RT scan minus the baseline value), and the time-dependent longitudinal change in the metrics during the course of treatment were examined for associations with outcome (PFS and OS) using Cox regression models. Overall survival was compared among those with pseudoprogression versus those with true early progression using an exact log-rank test. For exploratory analyses examining associations with outcome (OS and PFS), unadjusted P values are reported along with Q values based on the false discovery rate, given the large number of statistical tests performed. These were calculated using the fdrtool package in R (http://www.r-project.org).[16,17] Q values less than a fixed threshold of 0.1 were considered significant.

RESULTS

Patients

Of 53 patients enrolled in the study, 1 patient withdrew before therapy and 2 patients received <1 full dose of veliparib, leaving 50 patients evaluable for survival analyses. Forty-three patients died, and 45 experienced a PFS event. Seven patients had suspected pseudoprogression confirmed by repeat imaging and were compared with 20 patients identified as having true progression in the first 6 months of treatment. None of the patients had intratumoral hemorrhage, and no biopsy was performed.

MR Imaging Evaluation

Most of the tumors were T1-hypointense and T2-hyperintense at presentation. Larger baseline tumor volumes on FLAIR were associated with worse PFS ($P = .01$, $Q = 0.079$) but not OS. Larger enhancing tumor volumes at baseline were associated with worse OS ($P = .005$, $Q = 0.047$) and PFS ($P = .01$, $Q = 0.070$). Larger percentage increases in FLAIR tumor volume with RT correlated with worse PFS ($P = .01$, $Q = 0.084$). Larger increases in enhancing tumor volume with RT correlated with worse PFS ($P = .01$, $Q = 0.078$). Volumetric analysis showed no difference between pseudoprogression and true early progression groups.

DCE Permeability

Associations of higher baseline mean K^{trans} ($n = 22$) and shorter OS ($P = .03$, $Q = 0.102$) and PFS ($P = .03$, $Q = 0.105$) trended toward significance. When analyzed as continuous time-dependent variables, associations of mean v_e with PFS ($P = .03$, $Q = 0.104$) and OS ($P = .03$, $Q = 0.105$) and maximum K^{trans} with PFS ($P = .03$, $Q = 0.102$) trended toward significance. Greater increases with time were associated with worse outcomes (Fig 1). Permeability metrics showed no difference between pseudoprogression and true early progression groups.

DSC Perfusion

Higher baseline rCBV was associated with shorter PFS ($P = .02$, $Q = 0.089$) and OS ($P = .006$, $Q = 0.055$). When analyzed as a time-dependent variable, an increase in rCBV with time was associated with shorter OS ($P = .004$, $Q = 0.043$) and PFS ($P < .001$, $Q < 0.001$). Post-RT change in rCBV was not associated with survival or pseudoprogression.

ADC Histogram Analyses

Associations of higher baseline mode_ADC_enhancing with longer PFS ($P = .03$, $Q = 0.106$) and of greater post-RT increase in skewness_ADC_FLAIR with longer PFS ($P = .03$, $Q = 0.102$) trended toward significance. Mode_ADC_FLAIR showed a greater decrease after RT for true early progression compared with tumors that showed pseudoprogression (means, −268.15 versus −26.11, $P = .01$) (Fig 2).

A complete set of results of all relevant statistical tests can be found in the On-line Tables 1–7.

DISCUSSION

While some early studies concluded that standard imaging could not predict survival in DIPG,[18] several more recent studies have shown metrics derived from standard imaging, such as baseline and post-RT changes on FLAIR, enhancing tumor volume, and the presence or absence of enhancement at baseline, are correlated with survival.[19-21] Our results showing associations between larger baseline FLAIR and enhancing tumor

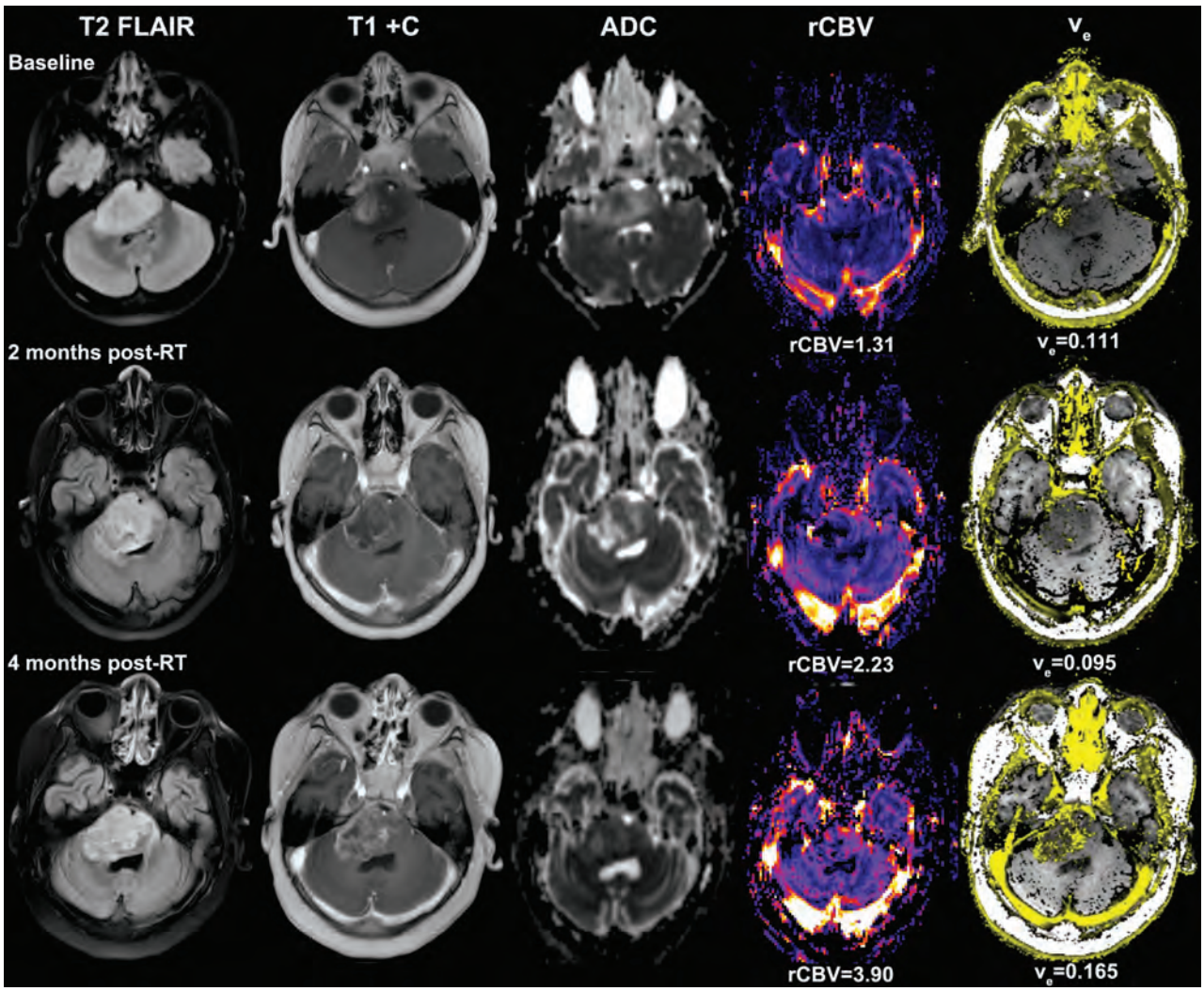

FIG 1. Large increase with time in rCBV and mean v_e in a 6.6-year-old female short-term survivor (OS = 124 days) with DIPG. Increase in rCBV with time was associated with shorter PFS ($P = .004$, $Q = 0.043$) and OS ($P < .001$, $Q < 0.001$). An increase in mean v_e was marginally associated with shorter PFS ($P = .028$, $Q = 0.104$) and OS ($P = .030$, $Q = 0.105$).

volumes and survival are further confirmation of the role of standard MR imaging in predicting survival.

Advanced MR imaging techniques such as DSC and DCE-MR perfusion imaging,[22-24] arterial spin-labeling,[8] diffusion imaging including ADC histograms and functional diffusion maps,[6,22,25] MR spectroscopy,[26] and PET[27] have proved increasingly useful in characterizing the heterogeneity in DIPG for predicting survival and may even provide insight into molecular subgroups.[28,29]

Our DCE-MR imaging findings show that increased baseline mean K^{trans} was associated with shorter survival, which again suggests that greater perfusion in enhancing tumors indicates a worse prognosis. The association of increased v_e and shorter survival found in this study is consistent with an earlier report linking higher v_e to higher grade tumors in a pediatric population.[30] V_e is the extravascular extracellular volume fraction of the tissue and, thus, is dependent on the cellularity as well as the vascularity of the tumor. Because both cellularity and vascularity change with treatment, our findings suggest that the rate of change of v_e during the course of treatment could be used to monitor the efficacy of treatment: A rapid increase in v_e may indicate an ineffective treatment regimen.

Our findings of higher baseline rCBV as well as an increase of rCBV during treatment being associated with shorter survival is in agreement with earlier findings reported by Hipp et al[24] as well as other studies showing that enhancement at baseline and across time is associated with a worse prognosis.[20,21] Sedlacik et al,[23] however, found that tumors with a higher baseline cerebral blood flow measured by DSC and a higher increase in these metrics through RT had a longer PFS. Similarly, Calmon et al[8] found that higher rCBV measured immediately following RT correlated with longer PFS. Higher baseline rCBV has, however, been linked to increased angiogenesis[31] and a biopsy-confirmed higher grade in DIPG.[32] The lack of consistent DSC perfusion findings in DIPG is likely due to differences in acquisition and postprocessing parameters, susceptibility artifacts associated with the location of the tumor in the brain stem, and also the challenges of choosing a representative 2D tumor ROI, given the tumor

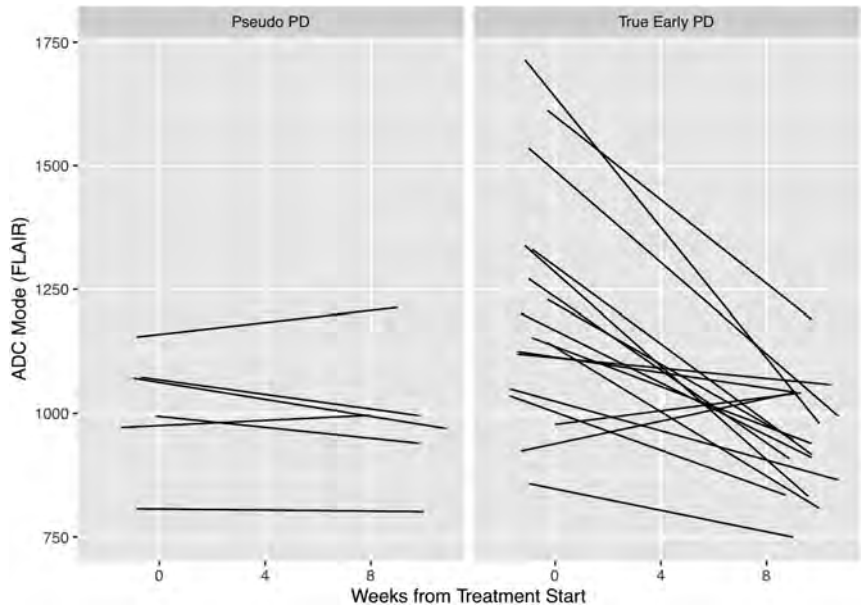

FIG 2. Post-RT change in mode_ADC_FLAIR for pseudoprogression cases on the left and true early progression on the right. The striking difference between groups is evident. Note the sharp drop between baseline and post-RT scans in the mode of ADC_FLAIR for true early progression cases on the right compared with the pseudoprogression cases on the left (means, −268.15 versus −26.11; $P = .0099$). All ADC values are in 10^{-6} mm^2/s.

heterogeneity seen in DIPG. In addition, it has been shown that there are rapid changes in cerebral blood volume and flow in DIPG both during RT and also immediately following RT.[23] The time point when DSC perfusion is measured during therapy is therefore critical and may also explain the divergent findings in the literature.

A greater post-RT increase in skewness_ADC_FLAIR implies a larger post-RT drop in ADC and was associated with longer survival in our study, and correlates with published data from a large cohort.[6] The drop in ADC could be due to a decrease in vasogenic edema, indicating that the radiation therapy is effective.[6]

We report on 7/50 (14%) cases of pseudoprogression in this DIPG cohort. A post-RT decrease in mode_ADC_FLAIR was significantly lower in those showing pseudoprogression compared with those who went on to show true early progression in our study. While pseudoprogression is well-documented in adult glioblastomas treated with RT + TMZ, typically seen within the first 3 months after radiation,[33] there are very few reports on DIPG. Chassot et al[34] reported 4/22 (18%) cases of pseudoprogression in children with DIPG treated with RT + TMZ and found no difference in overall survival between pseudoprogression and true progression cases. Carceller et al[35] reported 6/44 (13.6%) cases of pseudoprogression in a DIPG cohort treated with various different treatment regimens and found no difference in overall survival between pseudoprogression and true progression groups. We also observed no evidence of a significant difference in overall survival among our patients with pseudoprogression versus those with true early progression ($P = .75$). In a peptide-based vaccine DIPG trial, Ceschin et al[36] found that parametric response maps of ADC were able to retrospectively identify 4/21 (19%) cases of pseudoprogression and reported better overall survival in these cases. More recently, Calmon et al[37] reported 19/43 (44%) cases of pseudoprogression in a DIPG cohort treated with RT along with various concurrent chemotherapy agents in 37 of the cases. There are thus very few cases of pseudoprogression reported in the literature, confounded by the fact that they have all undergone varying treatment regimens. In addition, the definition of pseudoprogression is inconsistent across these reports and affects the frequency of the occurrence of pseudoprogression reported.

While most previous studies have retrospectively compared diffusion and perfusion properties of pseudoprogression and true progression groups at the time of radiologic progression,[7,9,36,38,39] our results show post-RT changes in ADC histograms that precede radiologic progression and could be used to predict pseudoprogression. A recent report by Calmon et al[37] found differences in post-RT changes in DSC perfusion between pseudoprogression and true progression groups, confirming the usefulness of looking at post-RT changes in DIPG as a predictive radiologic marker of pseudoprogression. Because pseudoprogression is most often seen within the first 3 months after RT, it is plausible that radiosensitivity and response to radiation affect the incidence of pseudoprogression.

Our understanding of DIPG has changed in the past few years with the advent of biopsy for DIPG and the subsequent discovery of novel histone and genetic mutations.[29] This study preceded many of these findings and could benefit from genetic and molecular information available from biopsy data. The methodology outlined in this study, particularly the 3D volumetric ADC histogram analyses, may be particularly well-suited to study these tumors. Future work will focus on correlating these advanced diffusion, perfusion, and permeability metrics with molecular signatures.

CONCLUSIONS

The data from this study demonstrate that higher baseline FLAIR and enhancing tumor volumes, rCBV, and mean K^{trans} are all associated with shorter survival in newly diagnosed DIPGs treated with veliparib given concurrently with focal radiation, followed by maintenance therapy of veliparib + TMZ in children with DIPG. Smaller percentage increases in FLAIR tumor volume, smaller increases in enhancing tumor volume, smaller increases in skewness of ADC_FLAIR, and larger decreases of mean_ADC_enhancing were associated with longer survival. Higher increases with time in rCBV and v_e in the course of treatment were associated with shorter survival. Tumors with pseudoprogression had a smaller post-RT

decrease in mode_ADC_FLAIR than those that had true early progressive disease. These results incorporating advanced diffusion, perfusion, and permeability metrics and the association with survival and pseudoprogression will need to be validated in larger prospective clinical trials.

Disclosures: Sridhar Vajapeyam—*RELATED*: *Grant*: National Institutes of Health.* Ira J. Dunkel—*UNRELATED*: *Consultancy*: Apexigen, Bristol-Myers Squibb, Celgene, Pfizer, Roche, *Comments*: all unpaid or de minimis compensation; *Grants/Grants Pending*: Bristol-Myers Squibb, Genentech, Novartis, *Comments*: Funds were provided to my institution to cover the cost of clinical trials for which I was institutional Principal Investigator.* Tina Young Poussaint—*RELATED*: *Grant*: Pediatric Brain Tumor Consortium Neuroimaging Center Grant, *Comments*: National Institutes of Health subcontract from the Pediatric Brain Tumor Consortium*; *UNRELATED*: *Royalties*: Springer, *Comments*: *Atlas of Pediatric Brain Tumors*. Patricia Baxter—*RELATED*: *Grant*: National Cancer Institute, *Comments*: Pediatric Brain Tumor Consortium (UO1) (2UM1CA081457)*; *Support for Travel to Meetings for the Study or Other Purposes*: Pediatric Brain Tumor Consortium (UO1) (2UM1CA081457).* Arzu Onar-Thomas—*RELATED*: *Grant*: National Cancer Institute Cancer Therapy Evaluation Program Pediatric Brain Tumor Consortium grant (2UM1CA081457)*; *UNRELATED*: *Consultancy*: Roche, Eli Lilly, *Comments*: participation on Pediatric Advisory Committee for 1 specific project for each company; *Grants/Grants Pending*: Pfizer, Celgene, Apexigen, Novartis, Merck, *Comments*: grants for clinical trial costs conducted by the Pediatric Brain Tumor Consortium.* *Money paid to the institution.

REFERENCES

1. Ostrom QT, Gittleman H, Truitt G, et al. **CBTRUS statistical report: primary brain and other central nervous system tumors diagnosed in the United States in 2011-2015.** *Neuro Oncol* 2018;20:iv1–86 CrossRef Medline
2. Hargrave D, Bartels U, Bouffet E, **Diffuse brainstem glioma in children: critical review of clinical trials.** *Lancet Oncol* 2006;7:241–48 CrossRef Medline
3. Gallitto M, Lazarev S, Wasserman I, et al. **Role of radiation therapy in the management of diffuse intrinsic pontine glioma: a systematic review.** *Adv Radiat Oncol* 2019;4:520–31 CrossRef Medline
4. Lemasson B, Wang H, Galban S, et al. **Evaluation of concurrent radiation, temozolomide and ABT-888 treatment followed by maintenance therapy with temozolomide and ABT-888 in a genetically engineered glioblastoma mouse model.** *Neoplasia* 2016;18:82–89 CrossRef Medline
5. Yuan AL, Ricks CB, Bohm AK, et al. **ABT-888 restores sensitivity in temozolomide resistant glioma cells and xenografts.** *PLoS One* 2018;13:e0202860 CrossRef Medline
6. Poussaint TY, Vajapeyam S, Ricci KI, et al. **Apparent diffusion coefficient histogram metrics correlate with survival in diffuse intrinsic pontine glioma: a report from the Pediatric Brain Tumor Consortium.** *Neuro Oncol* 2016;18:725–34 CrossRef Medline
7. Wan B, Wang S, Tu M, et al. **The diagnostic performance of perfusion MRI for differentiating glioma recurrence from pseudoprogression: a meta-analysis.** *Medicine (Baltimore)* 2017;96:e6333 CrossRef Medline
8. Calmon R, Puget S, Varlet P, et al. **Multimodal magnetic resonance imaging of treatment-induced changes to diffuse infiltrating pontine gliomas in children and correlation to patient progression-free survival.** *Int J Radiat Oncol Biol Phys* 2017;99:476–85 CrossRef Medline
9. Thomas AA, Arevalo-Perez J, Kaley T, et al. **Dynamic contrast enhanced T1 MRI perfusion differentiates pseudoprogression from recurrent glioblastoma.** *J Neurooncol* 2015;125:183–90 CrossRef Medline
10. Fram EK, Herfkens RJ, Johnson GA, et al. **Rapid calculation of T1 using variable flip angle gradient refocused imaging.** *Magn Reson Imaging* 1987;5:201–08 CrossRef Medline
11. Tofts PS. **Modeling tracer kinetics in dynamic Gd-DTPA MR imaging.** *J Magn Reson Imaging* 1997;7:91–101 CrossRef Medline
12. Boxerman JL, Schmainda KM, Weisskoff RM. **Relative cerebral blood volume maps corrected for contrast agent extravasation significantly correlate with glioma tumor grade, whereas uncorrected maps do not.** *AJNR Am J Neuroradiol* 2006;27:859–67 Medline
13. Jenkinson M, Bannister P, Brady M, et al. **Improved optimization for the robust and accurate linear registration and motion correction of brain images.** *Neuroimage* 2002;17:825–41 CrossRef Medline
14. Jenkinson M, Beckmann CF, Behrens TE, et al. **FSL.** *Neuroimage* 2012;62:782–90 CrossRef Medline
15. Schindelin J, Arganda-Carreras I, Frise E, et al. **Fiji: an open-source platform for biological-image analysis.** *Nat Methods* 2012;9:676–82 CrossRef Medline
16. Strimmer K. **fdrtool: a versatile R package for estimating local and tail area-based false discovery rates.** *Bioinformatics* 2008;24:1461–62 CrossRef Medline
17. Benjamini Y, Hochberg Y. **Controlling the false discovery rate: a practical and powerful approach to multiple testing.** *Journal of the Royal Statistical Society: Series B (Methodological)* 1995;57:289–300 CrossRef
18. Hargrave D, Chuang N, Bouffet E. **Conventional MRI cannot predict survival in childhood diffuse intrinsic pontine glioma.** *J Neurooncol* 2008;86:313–19 CrossRef Medline
19. Kilburn LB, Kocak M, Baxter P, et al. **A Pediatric Brain Tumor Consortium phase II trial of capecitabine rapidly disintegrating tablets with concomitant radiation therapy in children with newly diagnosed diffuse intrinsic pontine gliomas.** *Pediatr Blood Cancer* 2018;65 CrossRef Medline
20. Poussaint TY, Kocak M, Vajapeyam S, et al. **MRI as a central component of clinical trials analysis in brainstem glioma: a report from the Pediatric Brain Tumor Consortium (PBTC).** *Neuro Oncol* 2011;13:417–27 CrossRef Medline
21. Jansen MH, Veldhuijzen van Zanten SE, Sanchez Aliaga E, et al. **Survival prediction model of children with diffuse intrinsic pontine glioma based on clinical and radiological criteria.** *Neuro Oncol* 2015;17:160–66 CrossRef Medline
22. Lobel U, Sedlacik J, Reddick WE, et al. **Quantitative diffusion-weighted and dynamic susceptibility-weighted contrast-enhanced perfusion MR imaging analysis of T2 hypointense lesion components in pediatric diffuse intrinsic pontine glioma.** *AJNR Am J Neuroradiol* 2011;32:315–22 CrossRef Medline
23. Sedlacik J, Winchell A, Kocak M, et al. **MR imaging assessment of tumor perfusion and 3D segmented volume at baseline, during treatment, and at tumor progression in children with newly diagnosed diffuse intrinsic pontine glioma.** *AJNR Am J Neuroradiol* 2013;34:1450–55 CrossRef Medline
24. Hipp SJ, Steffen-Smith E, Hammoud D, et al. **Predicting outcome of children with diffuse intrinsic pontine gliomas using multiparametric imaging.** *Neuro Oncol* 2011;13:904–09 CrossRef Medline
25. Ceschin R, Kocak M, Vajapeyam S, et al. **Quantifying radiation therapy response using apparent diffusion coefficient (ADC) parametric mapping of pediatric diffuse intrinsic pontine glioma: a report from the Pediatric Brain Tumor Consortium.** *J Neurooncol* 2019;143:79–86 CrossRef Medline
26. Lobel U, Hwang S, Edwards A, et al. **Discrepant longitudinal volumetric and metabolic evolution of diffuse intrinsic pontine gliomas during treatment: implications for current response assessment strategies.** *Neuroradiology* 2016;58:1027–34 CrossRef Medline
27. Zukotynski K, Vajapeyam S, Fahey FH, et al. **Correlation of 18F-FDG PET and MR apparent diffusion coefficient (ADC) histogram metrics with survival in diffuse intrinsic pontine glioma: a report from the pediatric brain tumor consortium.** *J Nucl Med* 2017;58:1264–69 CrossRef Medline
28. Lober RM, Cho YJ, Tang Y, et al. **Diffusion-weighted MRI derived apparent diffusion coefficient identifies prognostically distinct subgroups of pediatric diffuse intrinsic pontine glioma.** *J Neurooncol* 2014;117:175–82 CrossRef Medline
29. Castel D, Philippe C, Calmon R, et al. **Histone H3F3A and HIST1H3B K27M mutations define two subgroups of diffuse intrinsic pontine gliomas with different prognosis and phenotypes.** *Acta Neuropathol* 2015;130:815–27 CrossRef Medline
30. Vajapeyam S, Stamoulis C, Ricci K, et al. **Automated processing of dynamic contrast-enhanced MRI: correlation of advanced**

pharmacokinetic metrics with tumor grade in pediatric brain tumors. *AJNR Am J Neuroradiol* 2017;38:170–75 CrossRef Medline

31. Conway AE, Reddick WE, Li Y, et al. **"Occult" post-contrast signal enhancement in pediatric diffuse intrinsic pontine glioma is the MRI marker of angiogenesis?** *Neuroradiology* 2014;56:405–12 CrossRef Medline
32. Kilday JP, Pringle C, Kamaly-Asl ID, et al. **RADI-15: perfusion imaging in presumed pediatric diffuse intrinsic pontine glioma: a UK regional analysis.** *Neuro Oncol* 2018;20(Suppl 2):i172–73 CrossRef
33. Zikou A, Sioka C, Alexiou GA, et al. **Radiation necrosis, pseudoprogression, pseudoresponse, and tumor recurrence: imaging challenges for the evaluation of treated gliomas.** *Contrast Media Mol Imaging* 2018;2018:6828396 CrossRef Medline
34. Chassot A, Canale S, Varlet P, et al. **Radiotherapy with concurrent and adjuvant temozolomide in children with newly diagnosed diffuse intrinsic pontine glioma.** *J Neurooncol* 2012;106:399–407 CrossRef Medline
35. Carceller F, Fowkes LA, Khabra K, et al. **Pseudoprogression in children, adolescents and young adults with non-brainstem high grade glioma and diffuse intrinsic pontine glioma.** *J Neurooncol* 2016;129:109–21 CrossRef Medline
36. Ceschin R, Kurland BF, Abberbock SR, et al. **Parametric response mapping of apparent diffusion coefficient as an imaging biomarker to distinguish pseudoprogression from true tumor progression in peptide-based vaccine therapy for pediatric diffuse intrinsic pontine glioma.** *AJNR Am J Neuroradiol* 2015;36:2170–76 CrossRef Medline
37. Calmon R, Puget S, Varlet P, et al. **Cerebral blood flow changes after radiation therapy identifies pseudoprogression in diffuse intrinsic pontine gliomas.** *Neuro Oncol* 2018;20:994–1002 CrossRef Medline
38. Carceller F, Jerome NP, Fowkes LA, et al. **Post-radiotherapy apparent diffusion coefficient (ADC) in children and young adults with high-grade gliomas and diffuse intrinsic pontine gliomas.** *Pediatr Hematol Oncol* 2019;36:103–12 CrossRef Medline
39. Song YS, Choi SH, Park CK, et al. **True progression versus pseudoprogression in the treatment of glioblastomas: a comparison study of normalized cerebral blood volume and apparent diffusion coefficient by histogram analysis.** *Korean J Radiol* 2013;14:662–72 CrossRef Medline

Increased Notching of the Corpus Callosum in Fetal Alcohol Spectrum Disorder: A Callosal Misunderstanding?

E. Schneble, C. Lack, M. Zapadka, C.M. Pfeifer, D.M.E. Bardo, J. Cagley, J. Acharya, A.P. Klein, M. Balla, J.T. Obayashi, D. Ross, D.R. Pettersson, and J.M. Pollock

ABSTRACT

BACKGROUND AND PURPOSE: In the medicolegal literature, notching of the corpus callosum has been reported to be associated with fetal alcohol spectrum disorders. Our purpose was to analyze the prevalence of notching of the corpus callosum in a fetal alcohol spectrum disorders group and a healthy population to determine whether notching occurs with increased frequency in the fetal alcohol spectrum disorders population.

MATERIALS AND METHODS: We performed a multicenter search for cases of fetal alcohol spectrum disorders and included all patients who had a sagittal T1-weighted brain MR imaging. Patients with concomitant intracranial pathology were excluded. The corpus callosum was examined for notches using previously published methods. A χ^2 test was used to compare the fetal alcohol spectrum disorders and healthy groups.

RESULTS: Thirty-three of 59 patients with fetal alcohol spectrum disorders (0–44 years of age) identified across all centers had corpus callosum notching. Of these, 8 had an anterior corpus callosum notch (prevalence, 13.6%), 23 had a posterior corpus callosum notch (prevalence, 39%), and 2 patients demonstrated undulated morphology (prevalence, 3.4%). In the healthy population, the anterior notch prevalence was 139/875 (15.8%), posterior notch prevalence was 378/875 (43.2%), and undulating prevalence was 37/875 (4.2%). There was no significant difference among the anterior ($P = .635$), posterior ($P = .526$), and undulating ($P = .755$) notch prevalence in the fetal alcohol spectrum disorders and healthy groups.

CONCLUSIONS: There was no significant difference in notching of the corpus callosum between patients with fetal alcohol spectrum disorders and the healthy population. Although reported to be a marker of fetal alcohol spectrum disorders, notching of the corpus callosum should not be viewed as a specific finding associated with fetal alcohol spectrum disorders.

ABBREVIATIONS: CC = corpus callosum; FAS = fetal alcohol syndrome; FASD = fetal alcohol spectrum disorders

Fetal alcohol syndrome (FAS) was first described >45 years ago[1] with detrimental effects of prenatal alcohol exposure on the developing brain that are now well-known.[2-5] The nondiagnostic umbrella term, fetal alcohol spectrum disorders (FASD), is used to describe the spectrum of disorders occurring from in utero alcohol exposure. Estimated to affect approximately 2%–5% of live births in the United States, Canada, and Western Europe,[6] the range of neuropsychologic deficits associated with FASD is independent from formal FAS diagnostic criteria, which mandate the presence of midline craniofacial anomalies.[7] Instead, dysmorphology of intracranial midline structures such as the corpus callosum (CC) are implicated in FASD in addition to other neurocognitive and psychiatric disorders.[3,4,8-11]

The CC is the largest white matter tract in the brain and is an integral structure in the transmission and synthesis of complex information between the 2 hemispheres. The CC may be disproportionally affected by prenatal alcohol exposure given that most callosal fibers are formed in utero during a period of rapid growth between 12 and 16–20 weeks of gestation.[12,13] Although the total number of callosal fibers is fixed at birth, this structure continues to develop in the postnatal period due to fiber myelination,

Received October 8, 2019; accepted after revision February 10, 2020.

From the Departments of Radiology (E.S., D.R.P., J.M.P.), and Neurological Surgery (J.T.O., D.R.), Oregon Health & Science University, Portland, Oregon; Operative Care Division (D.R.), Portland Veterans Administration Hospital, Portland, Oregon; Department of Radiology (C.L., M.Z.), Wake Forest University, Winston-Salem, North Carolina; Department of Radiology (C.M.P.), University of Texas Southwestern Medical Center, Dallas, Texas; Department of Radiology (D.M.E.B.), Phoenix Children's Hospital, Phoenix, Arizona; Department of Radiology (J.C.), Legacy Emanuel, Portland, Oregon; Department of Radiology (J.A.), University of Southern California, Keck School of Medicine, Los Angeles, California; and Department of Radiology (A.P.K., M.B.), Medical College of Wisconsin, Milwaukee, Wisconsin.

Please address correspondence to Jeffrey M. Pollock, MD, Department of Radiology, Oregon Health & Science University, 3181 SW Sam Jackson Park Rd CR 135, Portland, OR, 97239; e-mail: pollockj@ohsu.edu

http://dx.doi.org/10.3174/ajnr.A6475

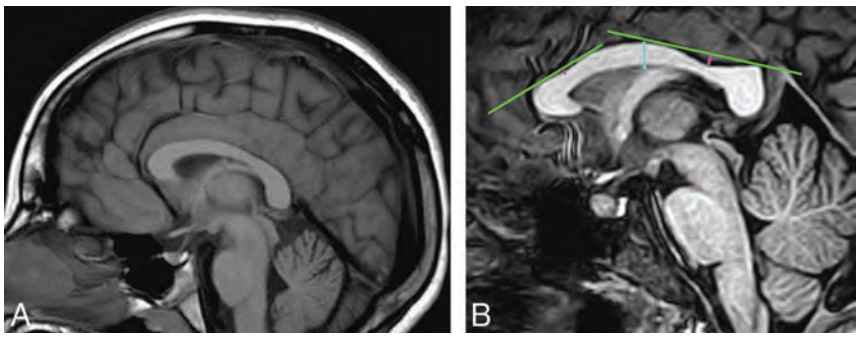

FIGURE. Midsagittal T1-weighted images. *A*, A normal corpus callosum with no notch. *B*, A corpus callosum with anterior and posterior notches measuring 1 and 3 mm in depth (*pink lines*), respectively. A "notch" was defined as a depression in the dorsal surface whose depth was at least 1 mm from a *tangential green line* to the surface of the CC. Notches are classified as either anterior or posterior on the basis of their relationship to the midcallosal body (*blue line*).

redirection, and pruning throughout the first 2 decades of life.[14,15] These varying rates and timing of CC component development result in a dynamic morphology throughout both gestation and early life,[16,17] with additional alterations in CC morphology visualized throughout the life span.[18-20]

The clarity of corpus callosum visualization with MR imaging lends itself to statistical shape analysis, a field that is used in the US court system for legal defense.[21] A 1995 article by Riley et al[8] remains frequently cited in the medicolegal literature for establishing focal abnormalities of the CC as part of the FAS spectrum.[21] Subsequent literature suggests focal thinning or concavity of the CC, which the current authors refer to as "notching," to be an indicator of brain damage from fetal alcohol exposure.[21,22]

The goal of this study was to further characterize the CC in the FASD population. Specifically, we sought to compare the prevalence of dorsal notching in a patient group with known FASD with the prevalence of dorsal notching in a population with no history of FASD and no gross abnormalities on brain MR imaging. Recent studies have suggested that focal concavities along the anterior and posterior surfaces of the CC are manifestations of normal growth and development.[23,24] An analysis of >1600 brain MR imaging studies by Krause et al[24] showed a CC notch in 50% of men and women. In addition, the lack of identified notches in the first week of life led the authors to suggest that notching is an acquired characteristic of normal CC development. Furthermore, the overall prevalence of notching was found to be greater than the expected prevalence of FASD, suggesting that notching is a normal morphologic feature and not pathognomonic of FASD.[24]

Building on recent work[23,24] examining CC notching in a healthy population, we used the same methodology to characterize the dorsal contour of the corpus callosum within an FASD group. The goal of this study was to determine whether notching along the dorsal surface of the CC is more prevalent in FASD compared with a healthy population.

MATERIALS AND METHODS

This retrospective, multicenter study was approved by the respective institutional review board with a waiver of patient consent. Subjects were obtained from an ICD-10 search of the electronic medical record for an FASD diagnosis with available MR imaging examinations of the brain that met the inclusion criteria. Imaging was reviewed and patients were excluded for any intracranial abnormality including but not limited to tumor, stroke, infection, migrational or structural abnormalities to include partial or complete corpus callosum dysgenesis, and surgery.

All MR imaging was performed using 1.5T or 3T machines. T1-weighted sagittal slices were obtained with 1- to 4-mm section thickness. A team of neuroradiologists from 7 medical centers throughout the United States visually inspected the dorsal surface of each CC on a midline sagittal T1-weighted image obtained at respective institutions. The morphology of each corpus callosum was assessed using a previously described protocol.[24] A CC was designated "normal" if the dorsal surface contained no notching (Fig 1*A*). A "notch" was defined as a focal concavity in the dorsal surface, the depth of which was at least 1 mm from a tangential line to the surface of the CC (Fig 1*B*). The location of the notch was recorded as anterior or posterior with the midbody of the CC separating the 2 locations. The CC was considered "undulating" if >2 notches involving both the anterior and posterior CC were present. Each center submitted measurements and anonymized images of their cases.

Age-matched data from prior work analyzing 1639 unique brain MR imaging studies with normal findings using identical methodology and inclusion and exclusion criteria were used to define the radiographically healthy control group with no clinical history of FASD.[24]

Statistical Analysis

Statistical analysis with a χ^2 test was performed to determine whether there were significant differences among anterior, posterior, and undulating notch prevalence in FASD compared with a healthy population. Values were calculated in Excel (Microsoft, Redmond, Washington) and were then imported into SPSS Statistics, Version 24 (IBM, Armonk, New York). Statistical analysis was performed using SPSS. P values $< .05$ were considered significant.

RESULTS

One hundred forty-one patients with a clinical diagnosis of FASD were initially identified. Ninety-six of those patients had adequate MR imaging examination findings. Fifty-nine of the patients with FASD (0–44 years of age; mean, 11.5 years) with MR imaging met all the inclusion and exclusion criteria. A spectrum of structural abnormalities was the most common reason for the 37 exclusions (23 dysgenesis of the CC, 8 cortical migration abnormalities, 3 Chiari 1 malformations, and 3 cases of periventricular leukomalacia). Eight notches of the anterior CC were identified in the FASD group (prevalence, 13.6%). Twenty-three patients had

Review summary

	FASD	Non-FASD Control Group	FASD (Excluded Due to Structural Abnormality)
Brain MR imaging studies reviewed (No.)	59	875	37
Brain MR imaging studies with notches (No.) (%)	33 (55.9%)	554 (63.3%)	11 (29.7%)
Posterior position (No.) (%)	23 (39%)	378 (43.2%)	10 (27%)
Anterior position (No.) (%)	8 (13.6%)	139 (15.8%)	1 (2.7%)
Undulating, >2 notches (No.) (%)	2 (3.4%)	37 (4.2%)	0 (0%)

a posterior CC notch (prevalence, 39%). Two patients demonstrated undulated morphology (prevalence, 3.4%). In the healthy age-matched control group, the anterior notch prevalence was 139/875 (15.8%), the posterior notch prevalence was 378/875 (43.2%), and the undulating prevalence was 37/875 (4.2%). There was no significant difference among the anterior ($P = .635$), posterior ($P = .526$), and undulating ($P = .755$) notch prevalence in the FASD and healthy groups (Table).

We also reviewed the 37 patients with FASD who were initially excluded due to structural abnormalities and found 1 anterior notch (prevalence, 2.7%) and 10 posterior notches (prevalence, 27%). There was no significant difference in the FASD groups designated "structurally normal" and having "structurally abnormal" findings between the anterior ($P = .076$) and posterior ($P = .230$) notch prevalence. There was no significant difference between the prevalence of anterior ($P = .086$) and posterior ($P = .129$) notches among the FASD group, the FASD group with structural abnormalities, and healthy age-matched controls.

DISCUSSION

In our multicenter study population, there was no significant difference in CC notching between our subjects with FASD and healthy populations. Although the developing CC may be susceptible to the effects of prenatal alcohol exposure, focal notching was not found to have an increased prevalence in our FASD population compared with age-matched controls. These findings conflict with the medicolegal use of MR imaging to suggest that notching of the CC is evidence of an individual having FASD.[21]

In an era in which the US judicial system is increasingly willing to accept brain imaging as evidence of injury or pre-existing conditions, the importance of defining both normal and pathologic morphology is paramount. This study builds on recent work examining MR imaging characteristics of the CC that found dorsal notching as both an acquired and dynamic feature of normal corpus callosum development. This prior examination of 1639 MR imaging examinations with normal findings also served as the age-matched control group of the current study. In this study, the authors noted increasing prevalence ($P < .001$) and depth ($P = .028$) of anterior notching with increasing age as well as decreasing prevalence of posterior notching as age increased ($P < .001$).[24] Although the study of Krause et al[24] was not adequately powered to perform a dedicated cohort study of the FASD population, lack of notching in the first week of life led the authors to suggest that notching can be an anatomic, not pathologic, feature of normal development. These findings are corroborated by our multicenter analysis of an FASD population, which demonstrates that the prevalence of notching is not increased in the FASD group compared with an age-matched control population. Thus, the neuroradiologist should recognize notching as a common finding on brain MRIs and not a pathologic finding specific for FASD.

MR imaging has served as a tool to describe brain morphologic differences in FASD populations in relation to associated cognitive deficits.[2-4,25] However, much remains unknown regarding the impact of prenatal alcohol exposure on the developing brain without a diagnostic pattern of abnormalities yet available on MR imaging examinations.[26] A single anatomic feature such as focal thinning or notching is unlikely to be a suitable marker of FASD, given the complex process involving the development and maturation of the corpus callosum. Whereas the effects of intrauterine alcohol exposure occur on a spectrum, so do the morphologic features of the corpus callosum within a healthy population.

A limitation of this study is the narrow focus of solely examining the dorsal surface of the CC. Although this is a multicenter study, the regional and global characteristics that may affect CC morphology were not quantified. In addition, the current study is not a longitudinal study because patients were not tracked along their dedicated life span, a critical gap across the available MR imaging literature.[9] Due to the purely radiographic nature of this study, we do not have any clinical data of the potential functional deficits of the patients or a quantitative assessment of alcohol exposure that these patients experienced in utero. Last, a retrospective review of both the healthy and FASD populations leads to an inherent selection bias. These findings may be further confounded by excluding studies with concomitant pathology.

CONCLUSIONS

In the medicolegal field, focal concavity or notching has been considered a diagnostic structural finding associated with FASD.[21] Whereas prior studies have suggested corpus callosum notching to be a manifestation of normal development and growth, our multicenter study sought to compare the prevalence of notching in FASD to a healthy population. Lack of a significant difference of notching between FASD and healthy groups suggests that notching of the corpus callosum should not be viewed as a specific finding associated with FASD. This study does not contradict other dysmorphias of fetal alcohol exposure but broadens prior work suggesting CC notching to be a normal anatomic feature without pathognomonic correlation to FASD.

Disclosures: Dianna M.E. Bardo—*UNRELATED*: *Consultancy*: Knonkiljke Philips NV, Guerbet*; *Royalties:* Thieme Publishing; *Travel/Accommodations/Meeting Expenses Unrelated to Activities Listed*, money paid to the individual: Knonkiljke Philips NV, Guerbet; *Other*: Bracco, *Comments*: research support.* *Money paid to the institution.

REFERENCES

1. Jones KL, Smith DW, Ulleland CN, et al. **Pattern of malformation in offspring of chronic alcoholic mothers.** *Lancet* 1973;1:1267–71 CrossRef Medline
2. Archibald SL, Fennema-Notestine C, Gamst A, et al. **Brain dysmorphology in individuals with severe prenatal alcohol exposure.** *Dev Med Child Neurol* 2001;43:148–54 Medline
3. Sowell ER, Mattson SN, Thompson PM, et al. **Mapping callosal morphology and cognitive correlates: effects of heavy prenatal alcohol exposure.** *Neurology* 2001;57:235–44 CrossRef Medline
4. Yang Y, Phillips OR, Kan E, et al. **Callosal thickness reductions relate to facial dysmorphology in fetal alcohol spectrum disorders.** *Alcohol Clin Exp Res* 2012;36:798–806 CrossRef Medline
5. Holzman C, Paneth N, Little R, et al. **Perinatal brain injury in premature infants born to mothers using alcohol in pregnancy: Neonatal Brain Hemorrhage Study Team.** *Pediatrics* 1995;95:66–73 Medline
6. May PA, Baete A, Russo J, et al. **Prevalence and characteristics of fetal alcohol spectrum disorders.** *Pediatrics* 2014;134:855–66 CrossRef Medline
7. Mattson SN, Riley EP, Gramling L, et al. **Neuropsychological comparison of alcohol-exposed children with or without physical features of fetal alcohol syndrome.** *Neuropsychology* 1998;12:146–53 CrossRef Medline
8. Riley EP, Mattson SN, Sowell ER, et al. **Abnormalities of the corpus callosum in children prenatally exposed to alcohol.** *Alcohol Clin Exp Res* 1995;19:1198–1202 CrossRef Medline
9. Donald KA, Eastman E, Howells FM, et al. **Neuroimaging effects of prenatal alcohol exposure on the developing human brain: a magnetic resonance imaging review.** *Acta Neuropsychiatr* 2015;27:251–69 CrossRef Medline
10. Norman AL, Crocker N, Mattson SN, et al. **Neuroimaging and fetal alcohol spectrum disorders.** *Dev Disabil Res Rev* 2009;15:209–17 CrossRef Medline
11. Barkovich AJ, Kjos BO, Jackson DE Jr, et al. **Normal maturation of the neonatal and infant brain: MR imaging at 1.5 T.** *Radiology* 1988;166:173–80 CrossRef Medline
12. Achiron R, Achiron A. **Development of the human fetal corpus callosum: a high-resolution, cross-sectional sonographic study.** *Ultrasound Obstet Gynecol* 2001;18:343–47 CrossRef Medline
13. Malinger G, Zakut H. **The corpus callosum: normal fetal development as shown by transvaginal sonography.** *AJR Am J Roentgenol* 1993;161:1041–43 CrossRef Medline
14. Knyazeva MG. **Splenium of corpus callosum: patterns of interhemispheric interaction in children and adults.** *Neural Plast* 2013;2013:639430 CrossRef Medline
15. Vannucci RC, Barron TF, Vannucci SJ. **Development of the corpus callosum: an MRI study.** *Dev Neurosci* 2017;39:97–106 CrossRef Medline
16. Tanaka-Arakawa MM, Matsui M, Tanaka C, et al. **Developmental changes in the corpus callosum from infancy to early adulthood: a structural magnetic resonance imaging study.** *PLoS One* 2015;10:e0118760 CrossRef Medline
17. Luders E, Thompson PM, Toga AW. **The development of the corpus callosum in the healthy human brain.** *J Neurosci* 2010;30:10985–90 CrossRef Medline
18. Allen LS, Richey MF, Chai YM, et al. **Sex differences in the corpus callosum of the living human being.** *J Neurosci* 1991;11:933–42 Medline
19. Doraiswamy PM, Figiel GS, Husain MM, et al. **Aging of the human corpus callosum: magnetic resonance imaging in normal volunteers.** *J Neuropsychiatry Clin Neurosci* 1991;3:392–97 CrossRef Medline
20. Hayakawa K, Konishi Y, Matsuda T, et al. **Development and aging of brain midline structures: assessment with MR imaging.** *Radiology* 1989;172:171–77 CrossRef Medline
21. Mardia K, Bookstein F, Kent J. **Alcohol, babies and the death penalty: saving lives by analysing the shape of the brain.** *Significance* 2013;10:12–16 CrossRef
22. Bookstein FL, Connor PD, Huggins JE, et al. **Many infants prenatally exposed to high levels of alcohol show one particular anomaly of the corpus callosum.** *Alcohol Clin Exp Res* 2007;31:868–79 CrossRef Medline
23. Simpson LN, Schneble EJ, Griffin ED, et al. **Morphological changes of the dorsal contour of the corpus callosum during the first two years of life.** *Pediatr Radiol* 2019 Dec 16. [Epub ahead of print] CrossRef Medline
24. Krause KL, Howard D, Pettersson DR, et al. **Defining the normal dorsal contour of the corpus callosum with time.** *AJNR Am J Neuroradiol* 2019;40:86–91 CrossRef Medline
25. Moore EM, Migliorini R, Infante MA, et al. **Fetal alcohol spectrum disorders: recent neuroimaging findings.** *Curr Dev Disord Rep* 2014;1:161–72 CrossRef Medline
26. Treit S, Jeffery D, Beaulieu C, et al. **Radiological findings on structural magnetic resonance imaging in fetal alcohol spectrum disorders and healthy controls.** *Alcohol Clin Exp Res* 2020;44:455–62 CrossRef

Thalamic Massa Intermedia in Children with and without Midline Brain Malformations

M.T. Whitehead and N. Najim

ABSTRACT

BACKGROUND AND PURPOSE: The massa intermedia is a normal midline transventricular thalamic connection. Massa intermedia aberrations are common in schizophrenia, Chiari II malformation, X-linked hydrocephalus, Cornelia de Lange syndrome, and diencephalic-mesencephalic junction dysplasia, among others. We have noticed that massa intermedia abnormalities often accompany other midline malformations. The massa intermedia has never been formally evaluated in a group of exclusively pediatric patients, to our knowledge. We sought to compare and contrast the prevalence, size, and location of the massa intermedia in pediatric patients with and without congenital midline brain abnormalities.

MATERIALS AND METHODS: Successive 3T brain MR imaging examinations from pediatric patients with and without midline malformations were procured from the imaging data base at a pediatric hospital. Massa intermedia presence, size, morphology, and position were determined using 3D-TIWI with 1-mm isotropic resolution. The brain commissures, septum pellucidum, hypothalamus, hippocampus, vermis, and brain stem were evaluated to determine whether alterations were related to or predictive of massa intermedia abnormalities.

RESULTS: The massa intermedia was more frequently absent, dysmorphic, and/or displaced in patients with additional midline abnormalities than in those without. The massa intermedia was absent in 40% of patients with midline malformations versus 12% of patients with normal findings ($P < .001$). Massa intermedia absence, surface area, and morphology were predictable by various attributes and alterations of the commissures, hippocampus, hypothalamus, vermis, brain stem, and third ventricle.

CONCLUSIONS: Most pediatric patients have a thalamic massa intermedia centered in the anterior/superior third ventricle. Massa intermedia abnormalities are commonly associated with other midline malformations. Normal-variant massa intermedia absence is a diagnosis of exclusion.

ABBREVIATION: MI = massa intermedia

The massa intermedia (MI) is a normal midline transventricular thalamic link that develops around 13–17 weeks' gestational age.[1-3] It is not considered a commissure because no reciprocal interhemispheric connections have been found within it in humans. Nonetheless, its cytoarchitecture suggests that it is functionally active.[4] The MI comprises neurons and neuropil with circularly oriented fibers postulated to represent neurosphere correlates (neuronal and glial progenitors).[4,5] Stria medullaris fibers that modulate motivation and mood may cross through the MI as suggested by DTI tractography.[6] In a separate DTI study, Damle et al[5] showed that MI size correlates with anterior thalamic radiation integrity and mediates the relationship between age and attention in healthy female subjects.

Animal studies have also enhanced our understanding of MI anatomy and potential functions. Widespread frontal, perirolandic/pericruciate, and limbic axonal MI crossings have been documented histologically in monkeys, rats, and cats.[7] Crossing nigro-caudate and caudo-caudate connections have also been identified.[8] A rhesus monkey study demonstrated loss of the normal crossed tactile placing response in stroke-induced monkeys following concurrent transection of the corpus callosum and MI but not in stroke-induced monkeys after callosotomy alone, suggesting that the paralytic effect of cortical damage may be dampened with an intact MI and accentuated without it.[9]

Received October 21, 2019; accepted after revision January 22, 2020.

From the Department of Radiology (M.T.W., N.N.), Children's National Hospital, Washington, DC; and The George Washington University Hospital (M.T.W.), Washington, DC.

Please address correspondence to Matthew T. Whitehead, MD, Children's National Hospital, 111 Michigan Ave NW, Washington, DC, 20010; e-mail: MWhitehe@childrensnational.org

Indicates article with supplemental on-line table.

http://dx.doi.org/10.3174/ajnr.A6446

Multiple studies have shown that the MI may be small or absent more frequently in patients with schizophrenia spectrum disorders.[2,10-15] It may also be small in borderline personality and bipolar disorders.[16,17] MI abnormalities can also occur in association with Chiari II malformation, X-linked hydrocephalus, Cornelia de Lange syndrome, and diencephalic-mesencephalic junction dysplasia, among others.[18-22]

The thalamic massa intermedia has never been formally evaluated in a group of exclusively pediatric patients, to our knowledge. We have observed that the MI is commonly absent, small, thickened, and/or displaced in patients with additional midline abnormalities. We sought to compare and contrast the prevalence, size, and location of the MI in 3T MR imaging examinations with normal findings in pediatric patients with and without congenital midline brain abnormalities and to determine whether there are structural variables that can predict MI abnormalities.

MATERIALS AND METHODS

After Children's National Hospital institutional review board approval, the MR imaging data base at a single academic pediatric hospital was searched for all consecutive 3T brain MR imaging examinations performed during 8 years (2012–2019) from pediatric patients (0–18 years of age) using the following key words/phrases: "normal brain," "midline abnormality," "agenesis," "dysgenesis," and "hypogenesis." These terms were selected because they are a common lexicon used in neuroradiology reports from our institution to describe various midline malformations of the telencephalon, diencephalon, hindbrain, face, and skull. Each study was reviewed to verify the lack of abnormalities in the healthy group and the presence of ≥1 congenital midline abnormality in the abnormal group. Examinations with excessive motion artifacts, lack of 3D-T1WI, prior surgical intervention, tumor, and clastic lesions other than mild gliosis were excluded. In the healthy group, developmental delay and seizures were additional exclusion criteria. Age, sex, and examination indications were documented. Medical records were reviewed to clarify history and document diagnoses.

All MR imaging studies were performed on a 3T scanner (Signa HDxt Optima; GE Healthcare, Milwaukee, Wisconsin). Pulse sequences included a 3D sagittal echo-spoiled gradient-echo T1WI with 3 plane reformats, T2WI, T2-FLAIR, susceptibility-weighted (T2* weighted angiography), and DTI with 7 directions of encoding. 3D echo-spoiled gradient-echo T1WI parameters were the following: TE/TR = 3/8 ms, TI = 450 ms, flip angle = 12°, section thickness = 1 mm, section spacing = 0.5 mm, matrix = 256 × 256, FOV = 40–58 × 16–24 cm (based on head size). All examinations were evaluated, in consensus, by a board-certified neuroradiologist and pediatric neuroradiologist with 6 years of practice experience following certification (M.T.W.) and a second reader that had completed an Accreditation Council for Graduate Medical Education Pediatric Radiology Fellowship.

3D-T1WI was used to evaluate the MI presence, morphology (normal/thin/thick), location (third ventricle quadrant center),[23] anterior-posterior diameter, craniocaudal diameter, and surface area. The corpus callosum (presence, morphology, length, surface area, and diameters of the genu, rostrum, and splenium) and anterior commissure (presence, morphology, surface area, and anterior-posterior and craniocaudal diameters) were assessed using sagittal 3D-T1WI. The transverse diameters of the MI, anterior commissure, and third ventricle were measured on reformatted axial 3D-T1WI. Additional brain structures were assessed qualitatively in the following manner: septum pellucidum (normal/cavum/hypoplastic/absent), fornix (normal/hypoplastic/absent), hypothalamus (normal/interhypothalamic adhesion), hippocampus (normal/under-rotated/dysplastic/sclerosis), vermis (normal/hypoplastic/dysplastic ± hypoplastic), and brain stem (normal/hypoplastic/dysplastic ± hypoplastic).

Using descriptive data derived from the healthy group, 2 SDs from the mean upper and lower bound cut points were determined for the MI, corpus callosum, and anterior commissure continuous data. Measurements falling below and above these boundaries were classified as "thin/hypoplastic" and "thickened/dysplastic," respectively.

Statistical Methods

Normal Gaussian distribution of the data means was confirmed by a Shapiro-Wilk test. Subsequently, 2-tailed unpaired *t* tests were used to compare the continuous data means within and between the healthy and midline abnormality groups. χ^2 tests were used to evaluate categoric variable distribution differences within and between groups. Multiple logistic and linear regression analyses were conducted to determine whether there were age, sex, or MR imaging predictors of MI absence, size, or morphology. Additionally, logistic regression analyses were used to determine whether age predicted MI absence after controlling for sex. $P < .05$ was considered significant.

RESULTS

The healthy group comprised 111 examinations from 105 unique patients after excluding 4 cases (3D-T1WI lacking, $n = 3$; motion, $n = 1$). Six examinations from 5 patients were follow-ups. The most common primary indications were headache ($n = 83$) and encephalopathy ($n = 11$). The midline abnormality group consisted of 119 examinations from 103 patients after excluding 6 (catheters, $n = 3$; normal, $n = 2$; glioma, $n = 1$). Sixteen examinations from 14 patients were follow-ups. The most common primary indications in the abnormal group were fetal imaging with abnormal findings ($n = 32$), seizures ($n = 16$), dysmorphia ($n = 15$), and developmental delay ($n = 10$); a unifying diagnosis was achieved in 36/103 (35%), 19 (53%) of which were genetic diagnoses and 17 (47%) of which were clinical/imaging diagnoses, most commonly septo-optic dysplasia ($n = 6$) and Dandy-Walker malformation ($n = 4$). The average age of the healthy group was 11.7 ± 5.3 years (range, 9 days to 18 years) versus 4.1 ± 5.5 years (range, 1 day to 18 years) in the midline abnormality group ($P < .001$). There was no significant sex difference between groups ($P = .78$) (Table).

MI absence was more common in patients with midline abnormalities (41/103; 40%) than in patients with normal findings (13/105; 12%) ($P < .001$) (Figs 1–4). It was absent in 4/4 (100%) Dandy-Walker Malformation cases and 1/6 (17%) septo-optic dysplasia cases. The MI was duplicated in 1 case from the midline abnormality group. The MI transverse diameter was the only MI measurement with a statistical difference between

Demographic and structural variables in healthy and midline abnormality groups

	Healthy Group (Avg ± SD)	Midline Group (Avg ± SD)	Total (Avg ± SD)	*P*
Age (yr)	11.7 ± 5.3	4.1 ± 5.5	7.9 ± 6.6	.001
Sex	*n* = 55 f (52%)	*n* = 52 f (50%)	*n* = 107 f (51%)	.78
MI present	*n* = 92 (88%)	*n* = 62 (60%)	*n* = 154 (74%)	.001
Morphology	*n* = 89 (n); 3(T)	*n* = 45 (n); 10(T); 7(t)	*n* = 134 (n); 13(T); 7(t)	.001
tr (mm)	1.5 ± 0.2	2 ± 0.2	1.7 ± 1	.002
ap (mm)	7.3 ± 2.3	6.8 ± 3.9	7 ± 3.1	.144
cc (mm)	6.7 ± 5.6	6.1 ± 3.5	6.4 ± 4.9	.202
Area (mm^2)	42.9 ± 23.9	44.2 ± 48.9	43.2 ± 35.9	.458
Location	*n* = 84 (a/s); 6 (p/s); 2 (p/i)	*n* = 34 (a/s); 14 (p/s); 3 (p/i); 1 (a/i); 10 (all)	*n* = 118 (a/s); 20 (p/s); 5 (p/i); 1 (a/i); 10 (all)	.001
CC present	*n* = 105 (100%)	*n* = 70 (68%)	*n* = 175 (84%)	.001
Morphology	*n* = 105 (n)	*n* = 13 (n); 6 (h); 46 (h/d); 5 (d)	*n* = 118 (n); 6 (h); 46 (h/); (5d)	.001
Length (mm)	68.2 ± 7.6	39.9 ± 21.5	57 ± 20.2	.001
Genu (mm)	10.5 ± 2	7.4 ± 10	9.3 ± 6.6	.007
Body (mm)	5.7 ± 1.2	3.5 ± 2.2	4.9 ± 1.9	.001
Splen (mm)	10.3 ± 2	4.7 ± 2.9	8.4 ± 3.6	.001
Area (mm^2)	546 ± 129	214 ± 199	415 ± 228	.001
AC present	*n* = 105 (100%)	*n* = 101 (98%)	*n* = 206 (99%)	.151
Morphology	*n* = 105 (n)	*n* = 41 (n); 53 (h); 7 (T)	*n* = 146 (n); 53 (h); 7 (T)	.001
tr (mm)	1.8 ± 0.4	3.9 ± 1.5	2.8 ± 1.5	.001
ap (mm)	2.6 ± 0.7	1.7 ± 1.1	2.2 ± 1	.001
cc (mm)	3.5 ± 1	2.2 ± 1.3	2.9 ± 1.3	.001
Area (mm^2)	8.1 ± 3.8	4.4 ± 5.1	6.3 ± 4.9	.001
Septum pellucidum	*n* = 96 (n); 9 (c)	*n* = 13 (n); 7 (c); 47 (a); 36 (h)	*n* = 109 (n); 16 (c); 47 (a); 36 (h)	.001
Fornix	*n* = 105 (n)	*n* = 36 (n); 25 (a); 42 (h)	*n* = 141 (n); 25 (a); 42 (h)	.001
Hypothalamus	*n* = 105 (n)	*n* = 84 (n); 19 (IHA)	*n* = 189 (n); 19 (IHA)	.001
Hippocampus	*n* = 87 (n); 18 (u)	*n* = 11 (n); 88 (u); 2 (d); 2 (mts)	*n* = 98 (n); 106 (u); 2 (d); 2 (mts)	.001
Brain stem	*n* = 105 (n)	*n* = 67 (n); 18 (h); 18 (d)	*n* = 172 (n); 18 (h); 18 (d)	.001
Vermis	*n* = 105 (n)	*n* = 77 (n); 15 (h); 11 (d)	*n* = 182 (n); 15 (h); 11 (d)	.001
3rd Ventricle (mm)	2.8 ± 0.9	5.5 ± 3.3	4.1 ± 2.8	.001

Note:—Avg indicates average; tr, transverse diameter; ap, anteroposterior diameter; cc, craniocaudal diameter; CC, corpus callosum; Splen, splenium; AC, anterior commissure; n, normal; T, thick; t, thin; a/s, anterior/superior quadrant of 3rd ventricle; a/i, anterior-inferior; p/s, posterior-superior; p/i, posterior-inferior; all, all quadrants; h, hypoplastic; h/d, hypogenetic ± dysgenetic; d, dysgenetic/dysplastic; c, cavum; a, absent; IHA, interhypothalamic adhesion; u, under-rotated; mts, hippocampal sclerosis; f, female.

groups. The MI mean surface area was not significantly different between groups (healthy group, 43 ± 24 mm; range, 6–140 mm; abnormal group, 44 ± 49 mm; range, 2–214 mm; $P = .46$). However, the MI morphology differed and was almost always normal in examinations with normal findings (89/92, 97%) and frequently-but-less commonly normal in patients with midline abnormalities (45/62, 73%) ($P < .001$) (Figs 5 and 6). Furthermore, the MI location differed between groups; in examinations with normal findings, it was almost always centered in the anterior/superior quadrant of the third ventricle ($n = 84$, 91%) and was more variable in patients with midline abnormalities ($P < .001$). Neither MI presence nor surface area nor morphology was predictable on the basis of age or sex ($P > .05$). There was no significant change in the presence, size, morphology, or location of the MI on any of the 6 follow-up examinations in the healthy group; however, 6/11 (55%) follow-up examinations from patients with an MI in the abnormal group had interval MI volume loss. When the MI surface area remained stable on follow-up, there was no significant change in third ventricle diameter in either group ($P > .67$). However, the third ventricle diameter significantly increased when the MI surface area decreased ($P = .013$). Specific data of additional groups are presented in the Table.

Logistic regression analysis showed that the odds of an absent MI were 1.5 times greater (OR, 0.68; 95% CI, 0.59–0.79; $P < .001$) with every 1-mm increase in the third ventricle transverse diameter and 1.7 times greater (OR, 0.6; 95% CI, 0.48–0.75; $P < .001$) with every 1-mm increase in the anterior commissure transverse diameter in both groups combined. Furthermore, third ventricle diameter and anterior commissure diameter were strong predictors of MI surface area and morphology in both groups combined ($P < .001$). Corpus callosum presence was predictive of MI presence (OR, 3.9; 95% CI, 1.8–8.5; $P < .001$) and MI area ($P = .002$) in both groups combined. Interhypothalamic adhesions were predictive of MI surface area and morphology in both groups combined ($P < .03$). Hippocampal abnormalities tripled the odds of MI absence (OR, 0.33; 95% CI, 0.17–0.65; $P < .001$) and were predictive of MI surface area and morphology abnormalities ($P < .02$) in both groups combined. Brain stem hypoplasia or dysplasia or both were predictive of MI surface area and morphology in both groups combined ($P < .001$). The odds of MI absence were 2.4 times greater in patients with vermian hypoplasia and/or dysplasia (OR, 0.42; 95% CI, 0.24–0.73; $P = .002$) in both groups combined (On-line Table).

DISCUSSION

The thalamic massa intermedia is more commonly absent (40% versus 12%), dysmorphic, and/or displaced in children with other structural midline brain abnormalities than in those without. MI

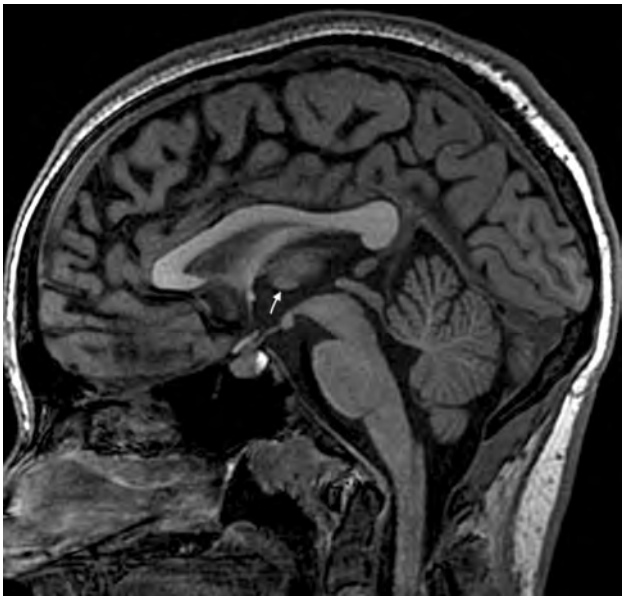

FIG 1. Sagittal midline T1WI from a brain MR imaging with normal findings in a 17-year-old adolescent girl with retroauricular pain depicting the normal thalamic MI centered in the anterior/superior portion of the third ventricle (*arrow*).

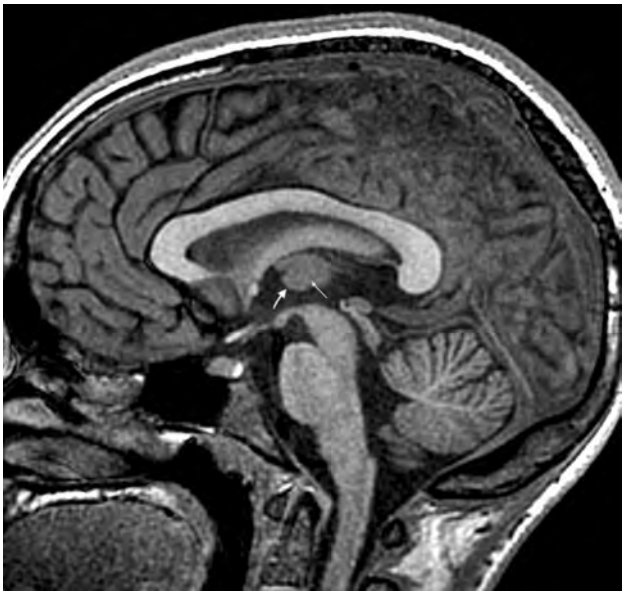

FIG 2. Sagittal midline T1WI from a brain MR imaging with normal findings in an 11-year-old girl with headache, showing a normal MI with part of its superior and posterior margin volume averaged with the medial thalami in a patient with a small third ventricle (*large arrow*). This appearance has the potential to compromise MI evaluation both qualitatively and quantitatively. However, a faint marginal distinction is often seen when carefully analyzed (*small arrow*).

absence, surface area, and morphology are predictable by various attributes and abnormalities involving the corpus callosum, anterior commissure, hippocampus, hypothalamus, vermis, brain stem, and third ventricle.

Midline brain malformations are often multiple and may involve the MI. For example, the MI diameter is generally smaller

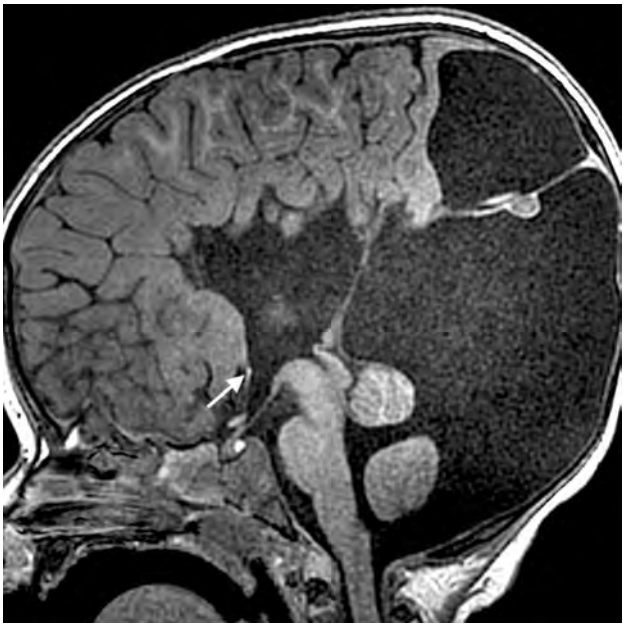

FIG 3. Sagittal midline T1WI demonstrating MI absence in association with multiple additional midline abnormalities, including marked enlargement of the fourth ventricle/posterior fossa and under-rotation of a hypoplastic/dysplastic vermis (Dandy-Walker malformation), hypoplasia of the anterior commissure (*arrow*), pontine hypoplasia, and agenesis of the corpus callosum.

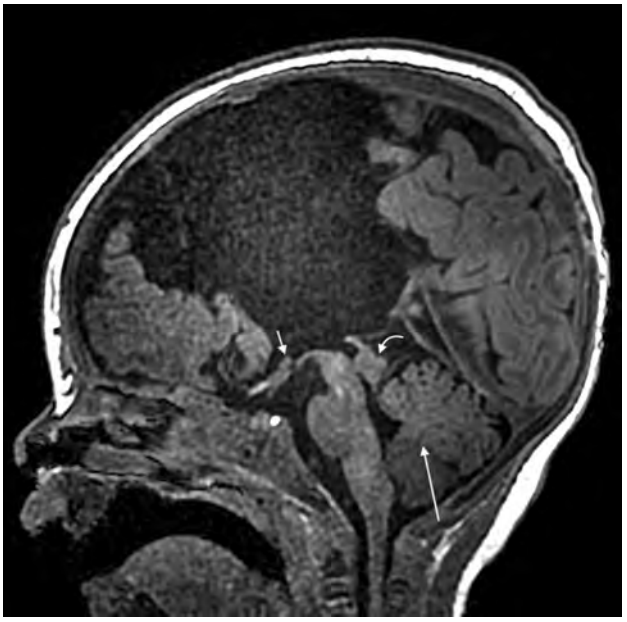

FIG 4. Sagittal midline T1WI showing MI absence in association with multiple additional midline abnormalities in a patient with septo-preoptic holoprosencephaly. Additional findings include agenesis of the corpus callosum, interhypothalamic adhesion (*small straight arrow*), tectal dysplasia (*small curved arrow*), and hypoplasia of the vermis (*long straight arrow*).

in fetuses with corpus callosum agenesis.[24] In our experience, the MI is an often-neglected midline brain component on MR imaging, perhaps due to lack of familiarity/awareness, perceived lack of importance, and/or satisfaction with the search when other

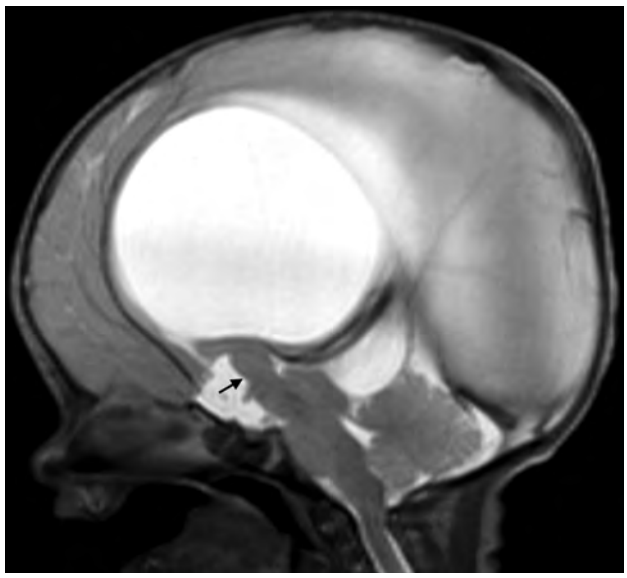

FIG 5. Sagittal midline T2WI from a patient with diencephalic-mesencephalic junction dysplasia showing a thickened thalamic massa intermedia connected to the midbrain (*arrow*). The midbrain is dysplastic with associated aqueductal stenosis and consequent hydrocephalus.

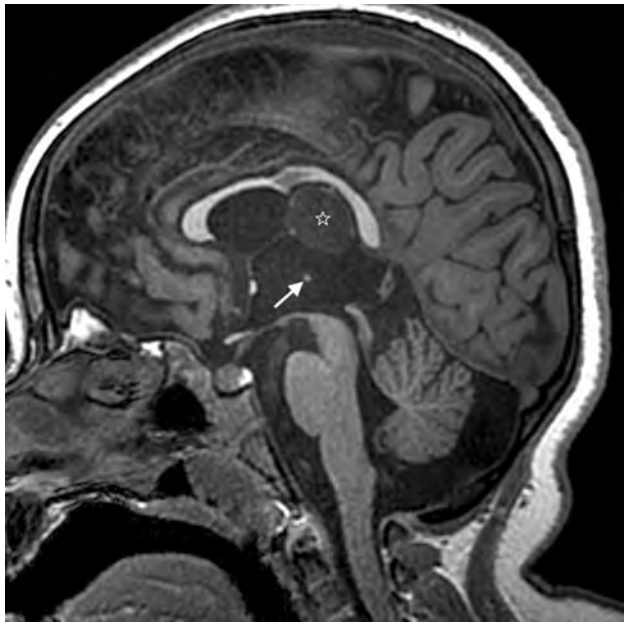

FIG 6. Sagittal midline T1WI depicting MI thinning/hypoplasia in a patient with Aicardi syndrome (*arrow*). Other findings include callosal dysgenesis and a pericallosal arachnoid cyst (*star*).

abnormalities exist. However, 1 midline abnormality should heighten radiologists' suspicion for others, and all abnormalities should be carefully documented in an effort to diagnose an underlying syndrome/disorder, or at least to lay the groundwork for a future diagnosis. Massa intermedia abnormalities can be a clue to the presence of additional abnormalities.

The MI mean surface area was 43 ± 24 mm^2 in examinations with normal findings. This is congruent with previous pathology literature comprising mostly adult specimens (mean surface area range, 13–46 mm^2).[25-28] Although the average MI surface area did not significantly differ between groups, MI dysmorphology was more common in the midline abnormality group (27% versus 3%). MI dysmorphology has been reported in several diseases. Chiari II malformation–related MI thickening may be the best-known disease-associated condition.[18] Yamasaki et al[19] found MI thickening in all 6 patients with X-linked hydrocephalus examined by MR imaging. Loss of function *L1 cell adhesion molecule* (*L1CAM*) gene defects seems to result in the most severe neuroimaging phenotype, with 100% prevalence of MI thickening.[20] In diencephalic-mesencephalic junction dysplasia, the MI may be dysplastic and connected to the midbrain.[22] MI thickening was also demonstrated in 60% (3/5) of patients with 6q terminal deletion syndrome.[29]

MI size tends to decrease with age in adults.[15,25,30] However, the association between MI abnormality and age has not been previously addressed in children. We found no relationship between age and MI abnormalities. On the other hand, the MI surface area decreased in more than one-third of follow-up examinations in the midline abnormality group. The transverse diameters of the MI, anterior commissure, and third ventricle were correlated variables, and the MI area was inversely related to them. Prior studies have also shown inverse relationships between the third ventricle diameter and MI thickness.[3,10,24,30,31] Acquired MI absence can occur secondary to hydrocephalus-induced rupture.[32] If we add our findings to the existing literature, it seems that MI volume loss and/or absence can occur in 3 main scenarios: 1) congenital, decreased or lack of the normal MI constraint leading to third ventriculomegaly; 2) acquired, primary or secondary MI volume loss associated with loss of cerebral volume; and 3) acquired, increased third ventricular pressure/dilation causing stretching or rupture.

MI duplication has been sparsely described on postmortem examination and imaging.[26,28,33-35] By means of MR imaging, it has been shown in Dandy-Walker continuum and in a patient with a presumed-but-unknown genetic disorder.[33,34] The MI was duplicated in 1 of our patients with midline malformations, including callosal dysgenesis and anterior commissure hypoplasia.

Previous literature mainly from adult subjects has shown the prevalence of MI absence in healthy subjects to be 2%–25%; this wide range is probably related to varied imaging and pathology techniques used in its assessment.[2,3,5,11-13,15,25-28,31,36] Two prior imaging studies, one primarily and the other exclusively in adults, performed using 3T MR imaging and 1-mm-thick sections akin to our study, found the normal prevalence of MI absence to be 4%–10%.[35] Similar to these, we discovered MI absence in 12% of pediatric patients with otherwise normal MR imaging findings. MI absence may be present at a higher rate in association with other brain malformations. For instance, the MI was absent in greater than one-third of patients with Cornelia de Lange syndrome in 1 study.[21] We determined that the MI was more likely to be absent in children with additional structural midline brain abnormalities. Furthermore, the MI was absent in all of our patients with Dandy-Walker malformation and infrequently in septo-optic dysplasia.

Reported MI sex differences have been conflicting, but many studies have suggested a higher prevalence of MI absence and decreased MI volume in males compared with

females.[5,23,27,28,31,36] In contrast, we found no significant sex differences between groups among the variables examined. It is possible that the reported sexual dimorphism of the MI may be present only in the adult population.

MI location impacts local CSF flow dynamics.[23] The maximum pressure within the third ventricle can vary up to 50% on the basis of MI location.[23] In healthy patients, the MI tends to be centered in the anterior/superior quadrant of the third ventricle.[26,28] Our findings are in agreement. However, it was significantly more variable in location in the midline abnormality group.

Hippocampal abnormalities increased the likelihood of MI absence, altered surface area, and abnormal morphology. Animal studies have demonstrated functional connectivity between the medial temporal lobes and MI. In felines with amygdaloid-stimulation-induced seizure kindling, the MI plays a role in interhemispheric ictal propagation.[37] MI-induced kindling in rats resembles an amygdaloid kindling response.[38] N-methyl-D-aspartate injection into the MI induces seizures and facilitates limbic kindling in rats.[39,40] However, under-rotation, or "incomplete hippocampal inversion" may be found in up to 17% of healthy subjects, similar to our findings in the brain MR imaging group with normal findings.[41]

MI absence, surface area, and morphology were predicted by the presence of an interhypothalamic adhesion. Congenital interhypothalamic adhesions may be markers of additional midline abnormalities.[42-45]

Several limitations warrant mention. We acknowledge that MI prevalence and size cannot be verified without histologic correlation. However, 3-plane high-resolution T1WIs were carefully scrutinized to make determinations. Furthermore, MI prevalence and size in the healthy group are within the range previously reported for healthy adults. Even with current state-of-the-art MR imaging techniques, however, MI absence may be underappreciated because volume averaging remains a challenge, especially when the third ventricle is small (Fig 2). Therefore, there is a tendency to underdiagnose MI absence and overestimate MI size with neuroimaging. Another limitation is that the mean age between groups was statistically different, with the abnormal group being imaged at a younger age on average. This difference was unavoidable given the retrospective nature of the study. Nonetheless, there was no difference within or between groups with regard to MI absence, area, or morphology. Another potential limitation is that most patients in the healthy group were imaged due to headache symptoms, making pediatric migraine a potential-albeit-unlikely confounding variable. Finally, few unified diagnoses were known in the midline abnormality group, limiting disease-specific generalizability. Future work would be useful to determine whether disease-specific MI abnormalities exist.

CONCLUSIONS

Most pediatric patients have a thalamic massa intermedia centered in the anterior/superior third ventricle. The MI is more frequently absent, dysmorphic, and/or displaced in pediatric patients with additional midline abnormalities than in those without. These findings support the notion that the MI cannot be ignored during MR imaging assessment of the brain. It can be a clue to the presence of additional abnormalities. Normal-variant MI absence is a diagnosis of exclusion, which should only be proposed when it is isolated and in patients without any associated clinical deficits.

REFERENCES

1. O'Rahilly R, Müller F. **Ventricular system and choroid plexuses of the human brain during the embryonic period proper.** *Am J Anat* 1990;189:285–302 CrossRef Medline
2. Trzesniak C, Linares IM, Coimbra ÉR, et al. **Adhesio interthalamica and cavum septum pellucidum in mesial temporal lobe epilepsy.** *Brain Imaging Behav* 2016;10:849–56 CrossRef Medline
3. Yasaka K, Akai H, Kunimatsu A, et al. **Factors associated with the size of the adhesio interthalamica based on 3.0-T magnetic resonance images.** *Acta Radiol* 2019;60:113–19 CrossRef Medline
4. Laslo P, Slobodan M, Nela P, et al. **Specific circular organization of the neurons of human interthalamic adhesion and of periventricular thalamic region.** *Int J Neurosci* 2005;115:669–79 CrossRef Medline
5. Damle NR, Ikuta T, John M, et al. **Relationship among interthalamic adhesion size, thalamic anatomy and neuropsychological functions in healthy volunteers.** *Brain Struct Funct* 2017;222:2183–92 CrossRef Medline
6. Kochanski RB, Dawe R, Kocak M, et al. **Identification of stria medullaris fibers in the massa intermedia using diffusion tensor imaging.** *World Neurosurg* 2018;112:e497–504 CrossRef Medline
7. Molinari M, Minciacchi D, Bentivoglio M, et al. **Efferent fibers from the motor cortex terminate bilaterally in the thalamus of rats and cats.** *Exp Brain Res* 1985;57:305–12 CrossRef Medline
8. Pritzel M, Sarter M, Morgan S, et al. **Interhemispheric nigrostriatal projections in the rat: bifurcating nigral projections and loci of crossing in the diencephalon.** *Brain Res Bull* 1983;10:385–90 CrossRef Medline
9. Lumley JS. **The role of the massa intermedia in motor performance in the rhesus monkey.** *Brain* 1972;95:347–56 CrossRef Medline
10. Snyder PJ, Bogerts B, Wu H, et al. **Absence of the adhesio interthalamica as a marker of early developmental neuropathology in schizophrenia: an MRI and postmortem histologic study.** *J Neuroimaging* 1998;8:159–63 CrossRef Medline
11. Takahashi T, Suzuki M, Zhou SY, et al. **Prevalence and length of the adhesio interthalamica in schizophrenia spectrum disorders.** *Psychiatry Res* 2008;164:90–94 CrossRef Medline
12. Ceyhan M, Adapınar B, Aksaray G, et al. **Absence and size of massa intermedia in patients with schizophrenia and bipolar disorder.** *Acta Neuropsychiatr* 2008;20:193–98 CrossRef Medline
13. Trzesniak C, Kempton MJ, Busatto GF, et al. **Adhesio interthalamica alterations in schizophrenia spectrum disorders: a systematic review and meta-analysis.** *Prog Neuropsychopharmacol Biol Psychiatry* 2011;35:877–86 CrossRef Medline
14. Trzesniak C, Schaufelberger MS, Duran FL, et al. **Longitudinal follow-up of cavum septum pellucidum and adhesio interthalamicaalterations in first-episode psychosis: a population-based MRI study.** *Psychol Med* 2012;42:2523–34 CrossRef Medline
15. Takahashi T, Nakamura K, Ikeda E, et al. **Longitudinal MRI study of the midline brain regions in first-episode schizophrenia.** *Psychiatry Res* 2013;212:150–53 CrossRef Medline
16. Takahashi T, Malhi GS, Wood SJ, et al. **Midline brain abnormalities in established bipolar affective disorder.** *J Affect Disord* 2010;122:301–05 CrossRef Medline
17. Takahashi T, Chanen AM, Wood SJ, et al. **Midline brain structures in teenagers with first-presentation borderline personality disorder.** *Prog Neuropsychopharmacol Biol Psychiatry* 2009;33:842–46 CrossRef Medline

18. Etus V, Guler TM, Karabagli H. **Third ventricle floor variations and abnormalities in myelomeningocele-associated hydrocephalus: our experience with 455 endoscopic third ventriculostomy procedures.** *Turk Neurosurg* 2017;27:768–71 CrossRef Medline
19. Yamasaki M, Arita N, Hiraga S, et al. **A clinical and neuroradiological study of X-linked hydrocephalus in Japan.** *J Neurosurg* 1995;83:50–55 CrossRef Medline
20. Kanemura Y, Okamoto N, Sakamoto H, et al. **Molecular mechanisms and neuroimaging criteria for severe L1 syndrome with X-linked hydrocephalus.** *J Neurosurg* 2006;105:403–12 CrossRef Medline
21. Whitehead MT, Nagaraj UD, Pearl PL. **Neuroimaging features of Cornelia de Lange syndrome.** *Pediatr Radiol* 2015;45:1198–205 CrossRef Medline
22. Severino M, Tortora D, Pistorio A, et al. **Expanding the spectrum of congenital anomalies of the diencephalic-mesencephalic junction.** *Neuroradiology* 2016;58:33–44 CrossRef Medline
23. Cheng S, Tan K, Bilston LE. **The effects of the interthalamic adhesion position on cerebrospinal fluid dynamics in the cerebral ventricles.** *J Biomech* 2010;43:579–82 CrossRef Medline
24. Birnbaum R, Parodi S, Donarini G, et al. **The third ventricle of the human fetal brain: normative data and pathologic correlation: a 3D transvaginal neurosonography study.** *Prenat Diagn* 2018;38:664–72 CrossRef Medline
25. Davie JC, Baldwin M. **Radiographic-anatomical study of the massa intermedia.** *J Neurosurg* 1967;26:483–87 CrossRef Medline
26. Malobabić S, Puskas L, Blagotić M. **Size and position of the human adhaesio interthalamica.** *Gegenbaurs Morphol Jahrb* 1997;133:175–80 Medline
27. Allen LS, Gorski RA. **Sexual dimorphism of the anterior commissure and massa intermedia of the human brain.** *J Comp Neurol* 1991;312:97–104 CrossRef Medline
28. Pavlović MN, Jovanović ID, Ugrenović SZ, et al. **Position and size of massa intermedia in Serbian brains.** *Folia Morphol (Warsz)* 2019 Apr 17. CrossRef Medline
29. Elia M, Striano P, Fichera M, et al. **6q terminal deletion syndrome associated with a distinctive EEG and clinical pattern: a report of five cases.** *Epilepsia* 2006;47:830–38 CrossRef Medline
30. Rosales RK, Lemay MJ, Yakovley PI. **The development and involution of massa intermedia with regard to age and sex.** *J Neuropathol Exp Neurol* 1968;27:166 Medline
31. Samra KA, Cooper IS. **Radiology of the massa intermedia.** *Radiology* 1968;91:1124–28 CrossRef Medline
32. El Damaty A, Langner S, Schroeder HW. **Ruptured massa intermedia secondary to hydrocephalus.** *World Neurosurg* 2017;97:749.e7–10 CrossRef Medline
33. Tubbs RS, Smyth MD, Oakes WJ, et al. **Duplication of the massa intermedia in a child.** *Pediatr Neurosurg* 2004;40:42–43 CrossRef Medline
34. Whitehead MT. **Thalamic massa intermedia duplication in a dysmorphic 14 month-old toddler.** *J Radiol Case Rep* 2015;9:1–5 CrossRef Medline
35. Baydin S, Gungor A, Baran O, et al. **The double massa intermedia.** *Surg Neurol Int* 2016;7:30 CrossRef Medline
36. Nopoulos PC, Rideout D, Crespo-Facorro B, et al. **Sex differences in the absence of massa intermedia in patients with schizophrenia versus healthy controls.** *Schizophr Res* 2001;48:177–85 CrossRef Medline
37. Hiyoshi T, Wada JA. **Midline thalamic lesion and feline amygdaloid kindling, I: effect of lesion placement prior to kindling.** *Electroencephalogr Clin Neurophysiol* 1988;70:325–38 CrossRef Medline
38. Mori N, Wada JA. **Kindling of the massa intermedia of the thalamus in rats.** *Brain Res* 1992;575:148–50 CrossRef Medline
39. Hirayasu Y, Wada JA. **N-methyl-D-aspartate injection into the massa intermedia facilitates development of limbic kindling in rats.** *Epilepsia* 1992;33:965–70 CrossRef Medline
40. Hirayasu Y, Wada JA. **Convulsive seizures in rats induced by N-methyl-D-aspartate injection into the massa intermedia.** *Brain Res* 1992;577:36–40 CrossRef Medline
41. Cury C, Toro R, Cohen F, et al; IMAGEN Consortium. **Incomplete hippocampal inversion: a comprehensive MRI study of over 2000 subjects.** *Front Neuroanat* 2015;9:160 CrossRef Medline
42. Whitehead MT, Vezina G. **Interhypothalamic adhesion: a series of 13 cases.** *AJNR Am J Neuroradiol* 2014;35:2002–06 CrossRef Medline
43. Ahmed FN, Stence NV, Mirsky DM. **Asymptomatic interhypothalamic adhesions in children.** *AJNR Am J Neuroradiol* 2016;37:726–29 CrossRef Medline
44. Whitehead MT, Vezina G. **Asymptomatic interhypothalamic adhesions in children.** *AJNR Am J Neuroradiol* 2016;37:E35 CrossRef Medline
45. Loubet A, Dargazanli C, Joris Roux C, et al. **Interhypothalamic adhesion and multiple cerebral abnormalities in a 2-year-old boy.** *J Neuroradiol* 2017;44:63–64 CrossRef Medline

Celebrating 35 Years of the AJNR

March 1985 edition

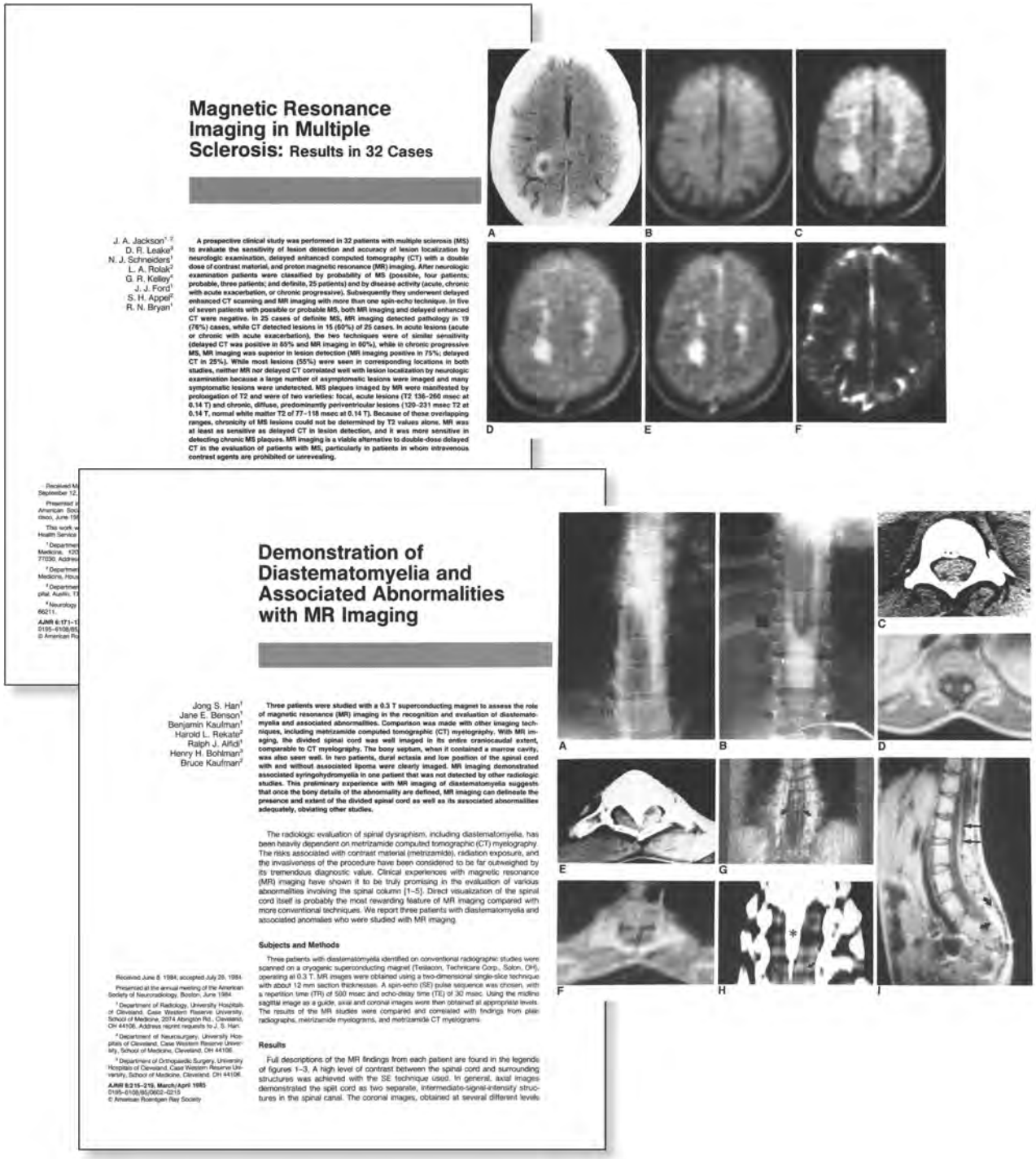

Magnetic Resonance Imaging in Multiple Sclerosis: Results in 32 Cases

J. A. Jackson[1, 2]
D. R. Leake[3]
N. J. Schneiders[1]
L. A. Rolak[2]
G. R. Kelley[4]
J. J. Ford[1]
S. H. Appel[2]
R. N. Bryan[1]

A prospective clinical study was performed in 32 patients with multiple sclerosis (MS) to evaluate the sensitivity of lesion detection and accuracy of lesion localization by neurologic examination, delayed enhanced computed tomography (CT) with a double dose of contrast material, and proton magnetic resonance (MR) imaging. After neurologic examination patients were classified by probability of MS (possible, four patients; probable, three patients; and definite, 25 patients) and by disease activity (acute, chronic with acute exacerbation, or chronic progressive). Subsequently they underwent delayed enhanced CT scanning and MR imaging with more than one spin-echo technique. In five of seven patients with possible or probable MS, both MR imaging and delayed enhanced CT were negative. In 25 cases of definite MS, MR imaging detected pathology in 19 (76%) cases, while CT detected lesions in 15 (60%) of 25 cases. In acute lesions (acute or chronic with acute exacerbation), the two techniques were of similar sensitivity (delayed CT was positive in 85% and MR imaging in 80%), while in chronic progressive MS, MR imaging was superior in lesion detection (MR imaging positive in 75%; delayed CT in 25%). While most lesions (55%) were seen in corresponding locations in both studies, neither MR nor delayed CT correlated well with lesion localization by neurologic examination because a large number of asymptomatic lesions were imaged and many symptomatic lesions were undetected. MS plaques imaged by MR were manifested by prolongation of T2 and were of two varieties: focal, acute lesions (T2 136–260 msec at 0.14 T) and chronic, diffuse, predominantly periventricular lesions (120–231 msec T2 at 0.14 T, normal white matter T2 of 77–118 msec at 0.14 T). Because of these overlapping ranges, chronicity of MS lesions could not be determined by T2 values alone. MR was at least as sensitive as delayed CT in lesion detection, and it was more sensitive in detecting chronic MS plaques. MR imaging is a viable alternative to double-dose delayed CT in the evaluation of patients with MS, particularly in patients in whom intravenous contrast agents are prohibited or unrevealing.

Demonstration of Diastematomyelia and Associated Abnormalities with MR Imaging

Jong S. Han[1]
Jane E. Benson[1]
Benjamin Kaufman[1]
Harold L. Rekate[2]
Ralph J. Alfidi[1]
Henry H. Bohlman[3]
Bruce Kaufman[2]

Three patients were studied with a 0.3 T superconducting magnet to assess the role of magnetic resonance (MR) imaging in the recognition and evaluation of diastematomyelia and associated abnormalities. Comparison was made with other imaging techniques, including metrizamide computed tomographic (CT) myelography. With MR imaging, the divided spinal cord was well imaged in its entire craniocaudal extent, comparable to CT myelography. The bony septum, when it contained a marrow cavity, was also seen well. In two patients, dural ectasia and low position of the spinal cord with and without associated lipoma were clearly imaged. MR imaging demonstrated associated syringohydromyelia in one patient that was not detected by other radiologic studies. This preliminary experience with MR imaging of diastematomyelia suggests that once the bony details of the abnormality are defined, MR imaging can delineate the presence and extent of the divided spinal cord as well as its associated abnormalities adequately, obviating other studies.

The radiologic evaluation of spinal dysraphism, including diastematomyelia, has been heavily dependent on metrizamide computed tomographic (CT) myelography. The risks associated with contrast material (metrizamide), radiation exposure, and the invasiveness of the procedure have been considered to be far outweighed by its tremendous diagnostic value. Clinical experiences with magnetic resonance (MR) imaging have shown it to be truly promising in the evaluation of various abnormalities involving the spinal column [1–5]. Direct visualization of the spinal cord itself is probably the most rewarding feature of MR imaging compared with more conventional techniques. We report three patients with diastematomyelia and associated anomalies who were studied with MR imaging.

Subjects and Methods

Three patients with diastematomyelia identified on conventional radiographic studies were scanned on a cryogenic superconducting magnet (Teslacon, Technicare Corp., Solon, OH), operating at 0.3 T. MR images were obtained using a two-dimensional single-slice technique with about 12 mm section thicknesses. A spin-echo (SE) pulse sequence was chosen, with a repetition time (TR) of 500 msec and echo-delay time (TE) of 30 msec. Using the midline sagittal image as a guide, axial and coronal images were then obtained at appropriate levels. The results of the MR studies were compared and correlated with findings from plain radiographs, metrizamide myelograms, and metrizamide CT myelograms.

Results

Full descriptions of the MR findings from each patient are found in the legends of figures 1–3. A high level of contrast between the spinal cord and surrounding structures was achieved with the SE technique used. In general, axial images demonstrated the split cord as two separate, intermediate-signal-intensity structures in the spinal canal. The coronal images, obtained at several different levels

Received June 8, 1984; accepted July 26, 1984.
Presented at the annual meeting of the American Society of Neuroradiology, Boston, June 1984.

[1] Department of Radiology, University Hospitals of Cleveland, Case Western Reserve University, School of Medicine, 2074 Abington Rd., Cleveland, OH 44106. Address reprint requests to J. S. Han.
[2] Department of Neurosurgery, University Hospitals of Cleveland, Case Western Reserve University, School of Medicine, Cleveland, OH 44106.
[3] Department of Orthopaedic Surgery, University Hospitals of Cleveland, Case Western Reserve University, School of Medicine, Cleveland, OH 44106.

AJNR 6:215–219, March/April 1985
0195-6108/85/0602-0215
© American Roentgen Ray Society

Time to Refine How We Tweet?

I read with great interest the article by Tomblinson et al[1] about the role of hidden metrics for the evaluation of social media effectiveness. I think the topic is quite important while setting a social media strategy for a professional institution like the American Society of Neuroradiology (ASNR), which is spreading knowledge. Beyond the simple gaining of visibility, the presence on social media is meant to drive correct and high-level content, which is invariably stored on the Web sites of official journals and societies.

Luckily, we are not able to properly summarize an article in the short space available on Twitter, and the existence of a robust Web site where all content is available is crucial to preserve the knowledge.

A single post on social media lasts hours, then is forgotten, but we want to deliver science. As correctly highlighted by the authors, we have to think beyond Likes and Retweets because Tweets also are open to users not signed in to Twitter. Users could be interested in the topic of the Tweet and click on the link, with no interaction with the post itself.

http://dx.doi.org/10.3174/ajnr.A6457

I appreciated so much the awareness of the *American Journal of Neuroradiology*/ASNR in including in most of their tweets a link to their Web site. Moreover, quantifying which content is accessed and downloaded and how is important to discern the audience's satisfaction with a specific strategy.

As an example, in the European Society of Neuroradiology, last August, we proposed a review per day on social media channels, with highly interesting preliminary data about downloading of cited articles, regardless of whether they were open access. I am sure that paper can change the way some authors and educators think about health care social media posting, enhancing its use as a driver of content available on a specific (personal) Web site.

REFERENCE

1. Tomblinson P, Wadhwa V, Latimer E, et al. **Publicly available metrics underestimate *AJNR* Twitter impact and follower engagement.** *AJNR Am J Neuroradiol* 2019;40:1994–97 CrossRef Medline

G. D'Anna
Radiology Unit
Humanitas Mater Domini
Castellanza (Varese), Italy

Do the Magic Angle Effects or Susceptibility Effects Affect the Visualization of Nigrosome 1?

I read with great interest the recently published article by Arai et al[1] in the *American Journal of Neuroradiology*. In this article, the authors claimed that the asymmetric visualization of nigrosome 1 is affected by the magic angle and susceptibility. They also suggested that these challenges in visualization are caused by the anatomic slant structure of nigrosome 1. For proper assessment of nigrosome 1 on MR imaging, it is of the utmost importance that researchers should be familiar with its anatomy and obtain high-spatial-resolution imaging to reduce partial-volume effects. In this regard, I am concerned about the methods used by the authors of this article.

First, the authors claimed that the MR imaging visualization of nigrosome 1 is often poor because of the asymmetry of this cell cluster, regardless of whether nigrosome 1 is healthy. I tried to find any relevant studies with regard to the cell cluster asymmetry in nigrosome 1 but to no avail. It, therefore, would be better to add any reference to this description.

Second, it has been reported that the CNS does not show magic angle effects (T2 prolongation at certain angles) because it has no ordered collagen.[2] It, therefore, is implausible to describe that visualization of nigrosome 1 is affected by magic angle effects. Because a multiecho gradient recalled-echo sequence was used in this study, there may be changes of T2* contrast in certain regions of the white matter. It has been shown that the relative orientation of white matter fibers to the B_0 field significantly affects T2* measurements, and the dominant source of this orientation dependency is susceptibility effects from myelin.[3] Myelin, however, is not, or is scarcely, present in nigrosome 1.[4] Thus, neither magic angle effects nor susceptibility effects may affect the image contrast in healthy nigrosome 1.

Third, even if nigrosome 1 visualization is affected by the magic angle effects due to its slant, nigrosome 1 should have higher signal intensity in nontilted head imaging than in tilted head imaging. The opposite results, however, were presented in this study.

Fourth, the authors indicated nigrosome 1 on the susceptibility map in Fig 5.[1] The indicated structures with hypointensity are connected to the slightly hypointense regions below the substantia nigra. Nigrosome 1, however, is located between the 2 hyperintense areas on quantitative susceptibility mapping because it is seen as a hyperintense region between the 2 hypointense regions on SWI (also known as the "swallow tail sign"). Nigrosome 1 is also located more anteriorly than that in Fig 5.[1] The structure indicated by the authors, rather, would be the medial lemniscus (based on the *Duvernoy's Atlas of the Human Brain Stem and Cerebellum*),[5] not nigrosome 1, which is supported by the fact that it shows orientation-dependent signal changes because of its myelin content. It would have been better to test if higher-spatial resolution imaging (eg, $0.5 \times 0.5 \times 1.0\,mm^3$) shows similar results because nigrosome 1 is very small and easily affected by a partial-volume effect.[6]

REFERENCES

1. Arai N, Kan H, Ogawa M, et al. **Visualization of nigrosome 1 from the viewpoint of anatomic structure.** *AJNR Am J Neuroradiol* 2020; 41:86–91 CrossRef Medline
2. Bydder M, Rahal A, Fullerton GD, et al. **The magic angle effect: a source of artifact, determinant of image contrast, and technique for imaging.** *J Magn Reson Imaging* 2007;25:290–300 CrossRef Medline
3. Oh SH, Kim YB, Cho ZH, et al. **Origin of B0 orientation dependent R2(*) (=1/T2(*)) in white matter.** *Neuroimage* 2013;73:71–79 CrossRef Medline
4. Massey LA, Miranda MA, Al-Helli O, et al. **9.4T MR microscopy of the substantia nigra with pathological validation in controls and disease.** *Neuroimage Clin* 2017;13:154–63 CrossRef
5. Naidich TP, Duvernoy HM, Delman BN, et al. *Duvernoy's Atlass of the Human Brain Stem and Cerebellum*. Austria: Springer-Verlag/Wien; 2009
6. Kim EY, Sung YH, Lee J. **Nigrosome 1 imaging: technical considerations and clinical applications.** *Br J Radiol* 2019;92:20180842 CrossRef Medline

E.Y. Kim
Department of Radiology
Gil Medical Center
Gachon University College of Medicine
Incheon, South Korea

http://dx.doi.org/10.3174/ajnr.A6458

REPLY:

We greatly appreciate the interest of Dr Kim in our work and his knowledgeable comments regarding our article that was recently published in the *American Journal of Neuroradiology*.[1] He has highlighted several important points that we will address in this response.

The first implication on the meaning of the asymmetry of the cell cluster, regardless of whether nigrosome-1 is healthy, is important and should be clarified. Our study discussed the visualization of nigrosome-1 asymmetry using clinical MR imaging.[2] We believe that our views are shared by most authors with considerable experience in clinical MR imaging examinations.

Dr Kim suggests that the magic angle effect appears hyperintense because of sequences using a short TE. It is rightfully pointed out that this is an MR imaging phenomenon that is often discussed with regard to fiber structures in orthopedic and neurologic cases, among others. However, we discuss the magic angle that presents universally in the B_0 direction. In particular, the change in the magnitude of the interaction becomes a conspicuous interference along the magic angle because of the dipole–dipole interaction.[3,4] This change affects the MR signal intensity around the boundary between the susceptibility of different tissues. As mentioned earlier in the Discussion section, quantitative susceptibility mapping was performed to support the magic angle. Our response to the third question is the same as previously mentioned. It is not the relation to the fiber array dependency.

Fig 5*A* reveals the quantitative susceptibility mapping, which was not used to describe the nigrosome-1 regions. Quantitative susceptibility mapping eliminates the magic angle effect because of the deconvolution of phase data with a dipole kernel. The imaging techniques that make nigrosome-1 hyperintense (ie, the swallow tail sign) affect the magic angle; therefore, there are differences in image contrasts.

Finally, the volume of nigrosome-1 is 7 slices' worth that was reported in a previous study by Dr Kim (ie, $0.5 \times 0.5 \times 1.0\,mm^3$).[5] The partial volume effect cannot be assumed because our voxel size parameter (ie, $0.63 \times 0.63 \times 1.5\,mm^3$) was slightly larger than that reported by Dr Kim. To be sure, we performed high-resolution (ie, $0.5 \times 0.5 \times 0.9\,mm^3$) imaging (Figure). As indicated, the same result was obtained in Fig 4 of our article, hence, proving that there was no partial volume effect.

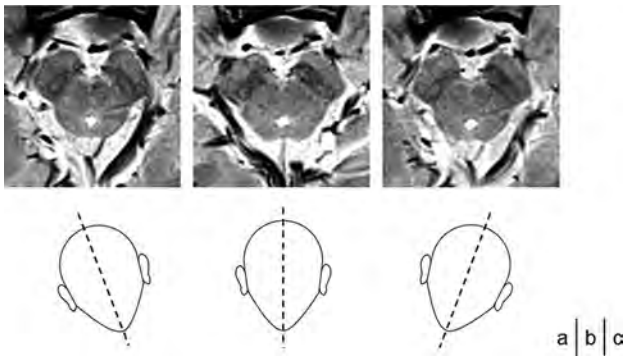

FIGURE. Examples of nigrosome-1 visualization in the B_0 direction using high resolution (ie, $0.5 \times 0.5 \times 0.9\ mm^3$), with a right head tilt (*A*), without a head tilt (*B*), and with a left head tilt (*C*).

REFERENCES

1. Arai N, Kan H, Ogawa M, et al. **Visualization of nigrosome 1 from the viewpoint of anatomic structure.** *AJNR Am J Neuroradiol* 2020;41:86–91 CrossRef Medline
2. Cosottini M, Frosini D, Pesaresi I, et al. **Comparison of 3T and 7T susceptibility-weighted angiography of the substantia nigra in diagnosing Parkinson disease.** *AJNR Am J Neuroradiol* 2015;36:461–66 CrossRef Medline
3. Erickson SJ, Prost RW, Timins ME. **The "magic angle" effect: background physics and clinical relevance.** *Radiology* 1993;188:23–25 CrossRef Medline
4. Wang J, Dong H, Li SW. **Magnetic dipole-dipole interaction induced by the electromagnetic field.** *Phys Rev A* 2018;97:013819 CrossRef
5. Kim EY, Sung YH, Lee J. **Nigrosome 1 imaging: technical considerations and clinical applications.** *Br J Radiol* 2019;92:20180842 CrossRef Medline

N. Arai
Department of Radiology
Nagoya City University Hospital
Nagoya, Japan
H. Kan
Radiological and Medical Laboratory Sciences
Nagoya University Graduate School of Medicine
Nagoya, Japan

http://dx.doi.org/10.3174/ajnr.A6473

Authorship Trends in the *American Journal of Neuroradiology*

The authorship demographics in the *American Journal of Neuroradiology* (*AJNR*) have been changing with time. The clinical demands on neuroradiologists have increased recently. We sought to determine whether there has been a commensurate shift toward more nonradiologist, PhD, multi-institutional, and funded articles being published in the *AJNR*. We assessed *AJNR*-published articles for each branch of neuroradiology (Brain, Spine, Head and Neck, Neurointerventional Radiology [NIR], and Pediatrics [Ped]) to determine changes in the authorship characteristics of those who publish in the *AJNR* across time. We predicted a shift toward multi-institutional, PhD-driven research in all fields except NIR, due to increasing clinical demands on physician neuroradiologists and the need for large datasets for writing definitive articles.

We reviewed 3 months of *AJNR* articles published during 1998, 2003, 2008, 2013, and 2018 and characterized the degrees and specialties of the first authors, funding status, institutional affiliations, and type of article to assess trends across time. Only original publications were included. A binary logistic model was fitted to the data to test the research hypothesis regarding the relationship between the likelihood that multi-institutional and radiology field, and funding were associated with MDs (compared with PhDs).

Tables 1, 2, and 3 present the results of these analyses. Of the 367 original articles, a radiologist was the first author in 280 (76.3%) articles, followed by neurosurgeons (27, 7.4%) and neurologists (26, 7.1%). Three hundred sixteen (86.1%) articles were written by MD or MD-PhD first authors. One hundred forty-five (39.5%) articles were from multiple institutions; 115 articles (31.3%) were mentioned as funded. Of the funded articles, 74 (64.3%) were first-authored by MDs, and 41 (35.7%), by non-MDs. MDs had a gradually decreasing trend of first authorship from 96.6% in 1998 to 72.0% in 2018. Among MDs, radiologists contributed 80% of the original articles in 1998, which decreased to 66.7% in 2013 and increased back to 77.5% in 2018. The regression model showed that multi-institutional studies were associated with MDs as first authors (OR = 6.5; 95% CI, 3.59–11.77). Also, radiologists exceeded all other subspecialties (OR = 3.42; 95% CI, 1.69–6.93) for MD authors.

http://dx.doi.org/10.3174/ajnr.A6463

Characteristics of AJNR *Authors*

By viewing trends in authorship, one can assess the state of the specialty in terms of academic output. In radiology, in which MDs and PhDs own considerable authorship space, these trends can reveal the evolution of research productivity. In a study by Emamzadehfard et al,[1] the country of the first author's institution in published articles in *AJNR* issues from January 2016 to June 2018 was categorized by Brain, Head and Neck, Spine, NIR, and Ped sections. They concluded that contributions to the *AJNR* from non-US authors dominated in the NIR category, likely due to the more restrictive limitations of the FDA on new NIR devices in the United States compared with Europe. Authors from Asian countries contributed more to Head and Neck articles, likely due to the increased prevalence of thyroid and nasopharyngeal carcinomas as well as Epstein-Barr virus infections in Asia. Authors from European countries published more articles than those in Asian countries in Pediatrics, in part due to authoritative and prolific Italian experts in pediatric neuroradiology. The US prominence was foremost in the Spine, and authors from Canada dominated the non-US spine contributions. Overall, the contributions from non-US authors (55.9%) to the *AJNR* exceeded those originating from the United States (44.1%).[1]

Trend Towards PhD Authorship

Our results show a decline of MD authorship from 96.6% in 1998 to 72.0% in 2018 ($P = .003$). What accounts for the shift away from MD first authorship to more PhD-first authored *AJNR* articles in this time period? One possibility is the changing research environment for academic radiologists in the United States, who have taken on more clinical responsibilities, with consequent reduction of academic time, energy, and resources for research. Another factor may be the increasing challenge of obtaining research funding in the United States. Fang and Casadevall[2] documented the lack of academic support granted to American investigators, particularly compared with prior time periods. These findings are in line with our results, which showed the large role of PhD first authors who may benefit from greater resources for research and more funded time.

Table 1: The distribution of first authors, degrees, institutions, funding, and fields across time

	1998		2003		2008		2013		2018	
	Count	%	Count	%	Count	%	Count	%	Count	%
Radiologist vs nonradiologist										
Radiologists	48	80.0%	55	83.3%	52	76.4%	56	66.7%	69	77.5%
Nonradiologists	12	20.0%	11	16.7%	16	23.6%	28	33.3%	20	22.5%
Degree										
Both MD and PhD	1	1.7%	4	6.2%	5	8.6%	9	11.3%	16	18.0%
MD	56	96.6%	56	86.2%	47	81.0%	58	72.5%	64	72.0%
PhD	2	3.4%	5	7.6%	6	10.4%	10	12.5%	8	8.9%
Master of Science	0	0.0%	0	0.0%	0	0.0%	3	3.7%	1	1.1%
Institution										
Multiple institutions	17	28.3%	15	22.7%	19	27.9%	43	51.2%	51	34.5%
Single institution	43	71.7%	51	77.3%	49	72.1%	41	48.8%	38	65.5%
Funding										
Funded	12	20.0%	14	21.2%	17	25.0%	39	46.4%	33	37.1%
Unfunded	48	80.0%	52	78.8%	51	75.0%	45	53.6%	56	62.9%
Field										
Brain	13	21.7%	26	39.4%	30	44.8%	28	33.7%	33	39.8%
Head and Neck	24	40.0%	7	10.7%	9	13.4%	14	16.9%	13	15.7%
IR-Vascular	16	26.7%	14	21.2%	19	28.4%	25	30.1%	22	26.5%
Peds	6	10.0%	13	19.7%	2	3.0%	10	12.0%	5	6.0%
PNS-Spine	1	1.6%	6	9.0%	7	10.4%	6	7.3%	10	12.0%

Note:—IR indicates interventional radiology; PNS, peripheral nervous system.

Table 2: Distribution of radiologists versus nonradiologists in the field of neuro-IR

Field	Nonradiologist (Count)	Radiologist (Count)
Non-IR	57	214
Neuro-IR	30	66

Table 3: Regression model of predictor factors and association with radiology versus nonradiology

Predictor Factor	Exp(B)	95% CI for Exp(B)		*P* Value
Funding (funded vs unfunded)[a]	0.662	0.372	1.178	.160
Degree (PhD vs MD)	0.826	0.351	1.947	.663
Field				
Head and neck				.019
Brain	1.911	1.012	3.611	.046
Spine	2.551	0.860	7.564	.091
Neuro-IR	1.269	0.696	2.315	.437
Pediatric	6.758	1.900	24.035	.003
Year				
1998				.029
2003	2.856	1.295	6.299	.009
2008	2.271	1.065	4.843	.034
2013	1.601	0.819	3.128	.169
2018	2.414	1.232	4.732	.010

Note:—Exp(B) indicates exponential of the regression coefficient.
[a] Studies we are analyzing that were funded or non-funded.

Funded versus Unfunded Research

We found a concomitant increasing trend toward funded articles in the *AJNR*. Lim et al[3] studied the publishing of funded original articles in 2 major American radiology journals, the *American Journal of Roentgenology* (*AJR*) and *Radiology*, between 2001 and 2010. They showed that only 26.9% (1758 of 6542) of original articles were funded, a proportion that is remarkably low in comparison with other specialties, but close to the 31.3% of *AJNR* articles that we report herein.[3] One study documented that 77% of the original articles published in the major medical and neurologic journals in 1991 were funded.[4] While the trend in the *AJNR* is toward an increase in funded original articles, radiology literature still trails other specialties significantly in the publication of funded studies.

Radiologist versus Nonradiologist Authorship in the AJNR

In our study, we show that of the 367 original articles, radiologists were the first authors in 280 (76.3%) articles, followed by neurosurgeons (27, 7.4%) and neurologists (26, 7.1%). Lim et al[3] also evaluated the contributions of radiologists versus nonradiologists in original radiology articles and found that although radiologists still have the most prominent role in radiology research, 12.4% (811 of 6542) of articles had a nonradiologist as the first author, including 15.4% in *Radiology* (541 of 3571).[3] One contributing factor to high number nonradiologist contributions was likely the growth in multidisciplinary collaborative studies among radiologists and clinicians from other medical specialties in which the first author was not a radiologist. Additionally, many nonradiologists who are performing radiology or radiology-related research may be choosing to submit their publications to radiology journals rather than clinical journals. This possibility may be particularly true in NIR, in which neurosurgeons and neurologists have a greater participation rate than diagnostic neuroradiologists. These trends indicate that radiology research is spreading throughout the clinical literature with more interplay between radiologists and nonradiologists. In summary, MDs and radiologists still dominate authorship in the *AJNR*; however, there are trends from 1998 to 2018 toward more PhD-authored, multi-institutional, and funded articles.

Disclosures: David Yousem—*UNRELATED*: *Expert Testimony*: Witness fees; *Payment for Lectures Including Service on Speakers Bureaus*: MRI Online, American College of Radiology; *Royalties*: Elsevier, Analytical Informatics Institute, money paid to individual.

REFERENCES

1. Emamzadehfard S, Eslami V, Yousem DM, et al. **Disproportionate international contributions to subspecialties of neuroradiology in the American Journal of Neuroradiology.** *AJNR Am J Neuroradiol* 2019;40:E3–4 CrossRef Medline
2. Fang FC, Casadevall A. **NIH peer review reform: change we need, or lipstick on a pig?** *Infect Immun* 2009;77:929–32 CrossRef Medline
3. Lim KJ, Yoon DY, Yun EJ, et al. **Characteristics and trends of radiology research: a survey of original articles published in AJR and Radiology between 2001 and 2010.** *Radiology* 2012;264:796–802 CrossRef Medline
4. Stein MD, Rubenstein L, Wachtel TJ. **Who pays for published research?** *JAMA* 1993;269:781–82 Medline

S. Emamzadehfard
Department of Radiology
University of Texas Health Science Center
San Antonio, Texas

A. Taree
Icahn School of Medicine at Mount Sinai
New York, New York

D.M. Yousem
Johns Hopkins Medical Institution
Baltimore, Maryland

In the article "Artery of Davidoff and Schechter Supply in Dural Arteriovenous Fistulas" (*AJNR Am J Neuroradiol* 2020;41:300–04), the institutional affiliations for T. Wälchli were listed incorrectly. The correct affiliations are as follows:

Joint Department of Medical Imaging and Division of Neurosurgery, Department of Surgery, Toronto Western Hospital, Toronto, Ontario, Canada.

Department of Fundamental Neurobiology, Krembil Research Institute, Toronto Western Hospital, University Health Network, University of Toronto, Toronto, Ontario, Canada.

Group of CNS Angiogenesis and Neurovascular Link, Neuroscience Center Zurich, University of Zurich, Swiss Federal Institute of Technology (ETH) Zurich, and University Hospital Zurich, Zurich, Switzerland.

Division of Neurosurgery, University Hospital Zurich, Zurich, Switzerland.

http://dx.doi.org/10.3174/ajnr.A6518